THE CDF IIb DETECTOR

TECHNICAL DESIGN REPORT

The CDF IIb Collaboration

September 2002

Contents

Chapter 1

Overview

1.1 Introduction

The physics program at the Fermilab Tevatron Collider will continue to explore the high energy frontier of particle physics until the commissioning of the LHC at CERN in 2007. The luminosity increase provided by the Main Injector and Recycler, along with the upgrades of the collider detectors, will provide unique opportunities for the discovery of light Higgs bosons, supersymmetric particles and other evidence for physics beyond the Standard Model. Full exploitation of these opportunities with the CDF detector will require upgrades beyond those implemented for the first stage (Run IIa) of the Tevatron's Run II physics program. Most of the Run IIa upgrades are described in a Technical Design Report [1]. The upgraded CDF detector, including beyond-the-baseline enhancements [2], was installed in February of 2001, and is now collecting data from $p\bar{p}$ collisions at $\sqrt{s}$ of 1.96 TeV.

Since the design of CDF's Run IIa upgrades, the long term plans for Tevatron Collider operation have evolved, projecting integrated luminosities well beyond the initial goal of 2 fb^{-1}. It is now anticipated that collection of physics data will continue until at least 15 fb^{-1} of integrated luminosity is collected by both the CDF and D0 experiments. This will result in 7.5 times the total radiation dose specified for the Run IIa CDF upgrade, and will require the replacement of the inner silicon microstrip detectors (L00 and SVXII). Furthermore, the increase in instantaneous luminosity to $5x10^{32}$ $cm^{-2}s^{-1}$ will compromise the performance of other detector, trigger and data acquisition systems. The upgrade of these components, beyond the original Run IIa design, is referred to as the CDF IIb Project. These CDF Run IIb detector upgrades are described in this document, which will not duplicate a description of the previous upgrades described in the original CDF Run IIa Technical Design Report [1].

We devote the rest of Chapter 1 to a history of CDF's data taking, a tabulation of our design goals, and a brief overview of the detector and project plan.

In Chapter 2 we motivate the detector design with a review of the physics program, extrapolating from our understanding of Run I to the prospects for Run II.

Chapter 3 describes the motivation for the need to replace the inner silicon detectors, SVX II and L00. A baseline replacement detector is proposed that meets the needs of the experiment, and establishes the scope of the project. Chapter 4 describes studies used to support the design of the baseline Run IIb silicon detector.

Chapter 5 describes the replacement of the Central Preradiator Chamber system.

Chapter 6 describes the data acquisition system with bandwidth increases needed for the Run IIb instantaneous luminosity.

Chapter 7 describes the installation scenario.

1.2 History

The Collider Detector at Fermilab (CDF) is a general purpose experiment for the study of $p\bar{p}$ collisions at $\sqrt{s} = 1.8$ TeV at the Fermilab Tevatron Collider. First collisions were produced and detected in October of 1985, and the Tevatron and CDF performance have evolved together to yield data sets of ever increasing sensitivity:

- ~ 25 nb^{-1} in 1987
- ~ 4.5 pb^{-1} in 1988-1989 (Run 0)
- ~ 19 pb^{-1} in 1992-1993 (Run Ia)
- ~ 90 pb^{-1} in 1994-1996 (Run Ib)

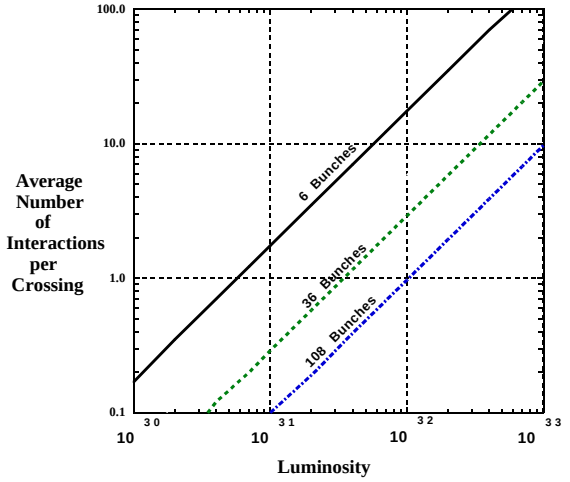

Figure 1.1: $\bar{N}$ for various conditions at CDF. 36 bunches $\equiv$ 396 ns crossings, 108 bunches $\equiv$ 132 ns crossings

- ~ 2000 pb^{-1} in 2001-2004 (Run IIa, anticipated)
- $\sim$ 13000 pb^{-1} in 2004-2007 (Run IIb, anticipated)

During the 1988 run the Tevatron met and surpassed its design luminosity of 1×10^{30}cm^{-2}s^{-1}. The 1994 accumulation utilized instantaneous Tevatron luminosities in excess of 2×10^{31}cm^{-2}s^{-1}.

The particle physics returns from this steadily evolving sensitivity include the discovery of the top quark and an accurate measurement of its mass $m_t = 176.1 \pm 6.6$, precision measurement of $m_W = 80.433 \pm 0.079$ GeV/c^2, measurement of the inclusive jet cross section out to transverse energies of 400 GeV, precision measurement of many b hadron properties, and many of the most stringent limits on non-standard processes. The complete CDF physics archive (see Chapter 8), as of September 2001, is a collection of over 200 published papers ranging over the full state of the art in hadron collider physics.

1.3 Accelerator Configuration for Run IIb

The stated goal of Tevatron Run IIb is the accumulation of 15 fb^{-1} at $\sqrt{s} = 1.96$ TeV, using luminosities up to 5×10^{32}cm^{-2}s^{-1}. This modest increase in the Tevatron energy over Run I has a significant physics benefit, (for instance increasing the $t\bar{t}$ yield by 40%) but little impact on the detector performance. Detector issues are driven instead by the luminosity, the number of bunches, and the time between crossings. During Run IIb operation, we anticipate that the $p\bar{p}$ crossing time will be both 396 ns and 132 ns. This time structure is unchanged from the Run IIa specification, so no modifications are needed solely due to bunch spacing. The number of bunches and the luminosity together determine a key design input, $\bar{N}$, the average number of overlapping interactions in a given beam crossing. $\bar{N}$ is displayed as a function of luminosity and crossing rate in Fig 1.1. The detector design for Run IIb specifies running conditions with $\bar{N} \sim 5$.

1.4 The CDF II Detector

CDF II is a general purpose solenoidal detector which combines precision charged particle tracking with fast projective calorimetry and fine grained muon detection.

The detector is shown in a solid cutaway view on the cover of this report, and in an elevation view in Fig. 1.2. Tracking systems are contained in a superconducting solenoid, 1.5 m in radius and 4.8 m in length, which generates a 1.4 T magnetic field parallel to the beam axis. Calorimetry and muon systems are all outside the solenoid. The main features of the detector systems are summarized below and described in greater detail in [1]. We use a coordinate system where the polar angle θ is measured from the proton direction, the azimuthal angle ϕ is measured from the Tevatron plane, and the pseudo-rapidity is defined as $\eta = -\ln(\tan(\theta/2))$.

1.4.1 Tracking Systems

Efficient, precision charged particle tracking is at the heart of the CDF analysis technique. To meet our physics goals we must maintain or improve the efficiency of our tracking at high luminosity.

For Run II, we have an optimized "integrated tracking system" shown schematically in Fig. 1.3. At large radii, an open cell drift chamber, the COT, covers the region $|\eta| \leq 1.0$. Inside the COT, a silicon "inner tracker" is built from two components. A micro-vertex detector at very small radii establishes the ultimate impact parameter resolution. Two additional silicon layers at intermediate radii provide p_T resolution and b-tagging in the forward region 1.0

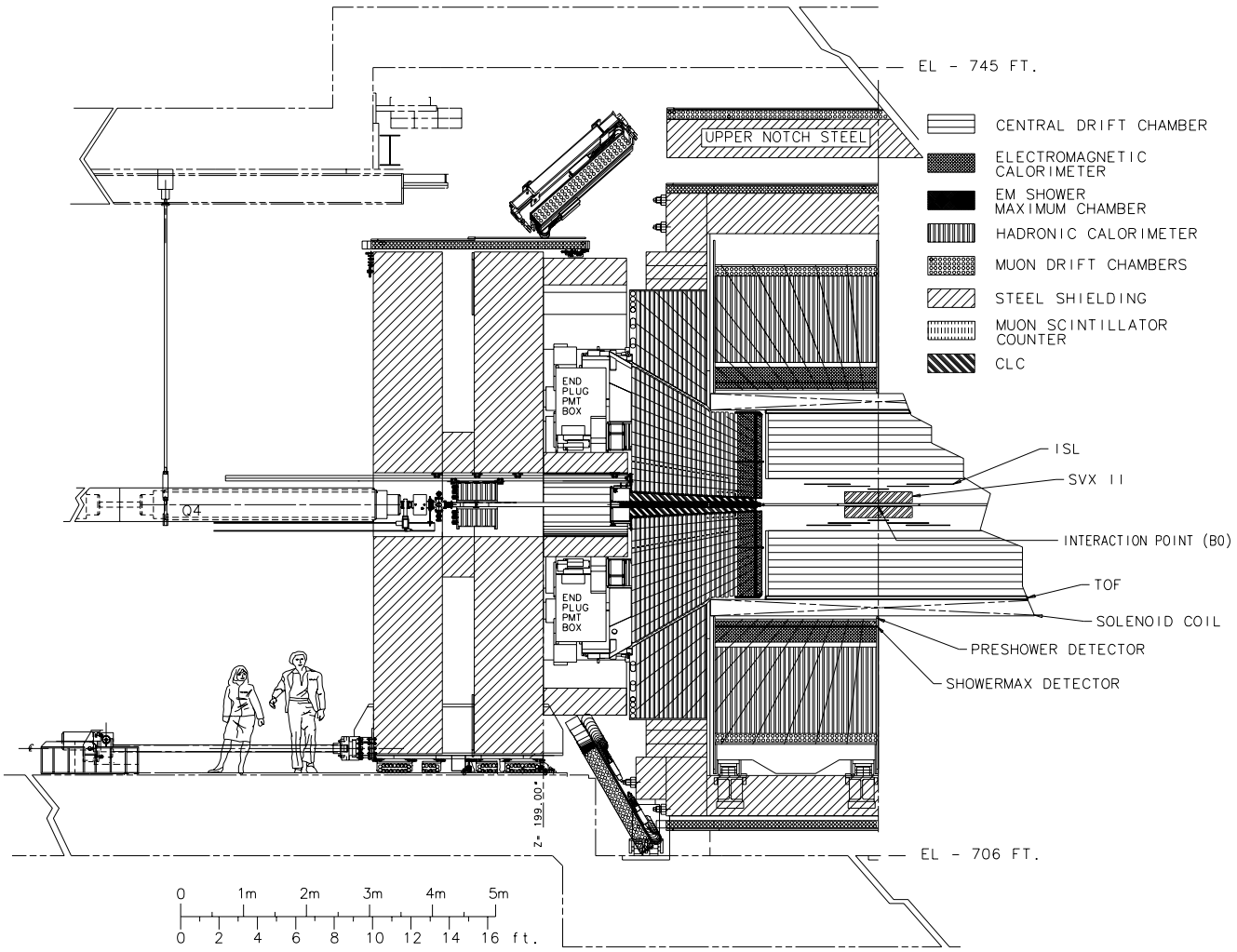

Figure 1.2: Elevation view of one half of the CDF II detector

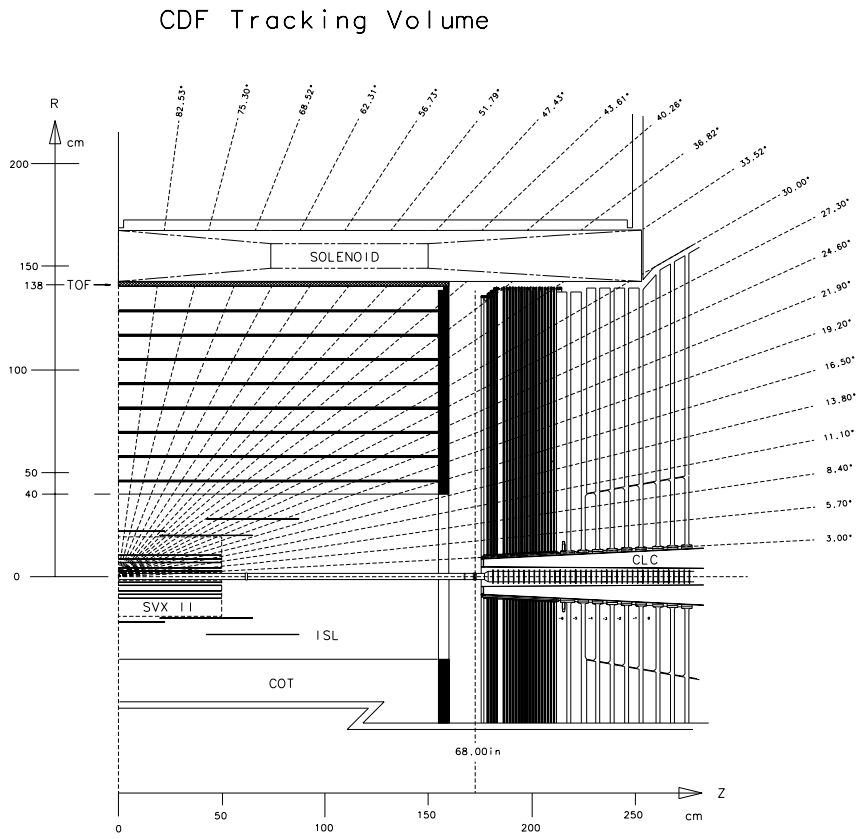

Figure 1.3: Longitudinal View of the CDF II Tracking System

$\leq |\eta| \leq 2.0$, and *stand-alone* silicon tracking over the full region $|\eta| \leq 2.0$.

As discussed in [1], stand-alone silicon segments allow integrated tracking algorithms which maximize tracking performance over the whole region $|\eta| \leq 2.0$. We showed there that a good signal to noise ratio for the silicon segments requires at least five measurements. In the central region, the stand-alone silicon segment can be linked to the full COT track to give excellent p_T and impact parameter resolution. Beyond $|\eta| = 1.0$, where the COT acceptance and efficiency falls precipitously, a seventh silicon layer at 28 cm is required in order to recover acceptable p_T and impact parameter resolution for a stand-alone silicon track (not segment!) in that region. These strengths of the silicon tracking system will be preserved and modestly improved by the replacement detector proposed for Run IIb.

The main parameters of the integrated tracking system are summarized in Tables 1.1,1.2. The performance is benchmarked in [1].

1.4.1.1 Central Outer Tracker: COT

Tracking in the region $|\eta| \leq 1.0$ will be done with an open cell drift chamber, the COT, covering radii between 44 and 132 cm. This device will be retained for Run IIb.

The COT uses small drift cells and a fast gas to limit drift times to less than 100 ns. The basic drift cell has a line of 12 sense wires alternating with shaper wires every 3.8 mm, running down the middle of two gold-on-mylar cathode planes which are separated by $\sim$ 2 cm. Four axial and four stereo super-

COT	
Radial coverage	44 to 132 cm
Number of superlayers	8
Measurements per superlayer	12
Readout coordinates of SLs	$+3^\circ$ 0 -3° 0 $+3^\circ$ 0 -3 0°
M aximum drift distance	0.88 cm
Resolution per measurement	180 μm
Rapidity coverage	$\|\eta\| \leq 1.0$
Number of channels	30,240
Material thickness	1.3% X_0
ISL	
Radial coverage	20 to 28 cm
Number of layers	one for $\|\eta\| < 1$; two for $1 < \|\eta\| < 2$
Readout coordinates	r-ϕ and r-uv (1.2° stereo) (all layers)
Readout pitch	110 μm (axial); 146 μm (stereo)
Resolution per measurement	16 μm (axial)
Total length	174 cm
Rapidity coverage	$\|\eta\| \leq 1.9$
Number of channels	268,800
Material thickness	2% X_0

Table 1.1: Design parameters of the tracking system components common to Runs IIa and IIb.

layers provide 96 measurements between 44 and 132 cm, requiring a total of 2,520 drift cells and 30,240 readout channels. The wires and cathode planes are strung between two precision milled endplates, and the complete chamber is roughly 1.3% of a radiation length at normal incidence.

The COT is currently operating in Run IIa. The detector has operated very well up to this point.

1.4.1.2 ISL: Intermediate Silicon Layers

Another section of the tracking system that will remain unchanged for Run IIb is the Intermediate Silicon Layers (ISL). In the central region, a single ISL layer is placed at a radius of 22 cm. This layer has not yet been commissioned in Run IIa, since a cooling problem has made its operation impossible. The prospects for repair of this cooling problem are not yet clear. In the plug region, $1.0 \leq |\eta| \leq 2.0$, two layers of silicon are placed at radii of 20 cm and 28 cm. SVX II and ISL together are a single functional system which provides stand-alone silicon tracking and b-tagging over the full region $|\eta| \leq 2.0$.

Double sided silicon is used with 55 μm strip pitch on the axial side and 73 μm pitch on the stereo side with a 1.2° stereo angle. Every other strip is read out to reduce the total channel count to 268,800. Due to charge sharing through the intermediate strips, the single hit resolution perpendicular to the strip direction will be ≤ 16 μm on the axial side and ≤ 23 μm on the stereo side. The ISL readout electronics are identical to the SVX II, and will be reused for Run IIb.

1.4.1.3 SVX IIb

The design of the Run IIb inner tracker is very similar to the combination of the Run IIa SVXII plus L00, but will be more radiation tolerant and easier to build. The fundamental changes from the Run IIa design are driven by the high radiation environment of Run IIb. The SVX3D chip would not survive and is also no longer available. We are fortunate however, that technology has advanced in the intervening years and it is now standard to use a 0.25 μm process which naturally radiation hard. Design of the SVX4 chip for Run IIb began over a year ago and submission of a full chip is imminent. Details of the chip design are discussed in Chapter 3.

The double sided sensors used in SVXII are also incapable of surviving the Run IIb radiation dosages. Here we benefit from the extensive research and de-

	SVX II/L00	SVX IIb
Radial coverage	1.3 to 10.7 cm	1.9 to 16.6 cm
Number of layers	6	6
Readout coordinates	r-ϕ on one side of all layers	r-ϕ on one side of all layers
Stereo side	none, r-z, r-z, r-uv, r-z, r-uv (uv $\equiv 1.2^\circ$ stereo)	none, r-z, r-z, r-z, r-uv, r-uv, r-z (uv $\equiv 2.5^\circ$ stereo)
Readout pitch	50-65 μm r-ϕ; 60-150 μm stereo	50-88 μm r-ϕ, 88-92 μm stereo
Total length	87.0 cm	112.0 cm
Rapidity coverage	$\|\eta\| \leq 2.0$	$\|\eta\| \leq 2.0$
Number of channels	405,504	520,704
Power dissipated	3.0 KW	3.0 KW

Table 1.2: A comparison between the design parameters of the Run IIa detectors (SVX II/L00) and the baseline Run IIb silicon proposal

velopment efforts that have been ongoing for the LHC experiments. The lifetime of single sided sensors is determined by the bias voltage they can withstand (at least $\approx$ 500V is needed) and the temperature of the silicon. In the Run IIb design we plan to use these sensors and also actively cool the silicon.

The new silicon detector has been designed with the following constraints in mind:

- The new detector should retain or improve the tracking capability of the Run IIa detector.
- Interruption of operations should be as short as possible. Six months is the target installation period.
- The new detector must be compatible with the existing data acquisition system.
- The new detector must be compatible with the existing infrastructure; detector space, cable space, and cooling system.
- The new detector must be compatible with the Silicon Vertex Trigger (SVT), so that impact parameter triggering is not compromised.
- Little time is available for construction, so the number of parts must be kept to a minimum.

We believe that the baseline design presented in Chapter 3 meets all these criteria.

Table 1.2 shows a comparison of the Run IIa and IIb silicon detectors. Briefly, the Run IIb detector will have 6 axial layers and two small angle stereo layers as did SVXII+L00. It also includes a set of 90^o stereo layers similar to those in SVXII. In Run IIb however, the active silicon will be more evenly spaced in radius and will cover a larger area. The stereo tracking will be improved over Run IIa by reducing the pitch on the small angle and 90^o sensors, using a larger angle on the small angle stereo layers and by locating a 90^o layer at large radius where the occupancy is low.

The Run IIb design is fundamentally different from the Run IIa detector in that a single stave (ladder in the Run IIa language) design is used for all but the inner two layers. This will significantly simplify the construction and prototyping processes. These staves have axial sensors on one side and stereo on the other. The design is essentially independent of whether the stereo side contains 90^o or small angle sensors. If further study and experience with Run IIa data indicate that the particular choice presented in Chapter 3 should change, this will not impact the schedule or the prototyping efforts already underway. The smallest layer, mounted on the beampipe, is a simplified version of the Run IIa L00 design. Because of space constraints, the layer outside the beampipe layer requires a unique stave design; the outer layer stave is too large, but it would be difficult to build another layer in the style of L00. The design presented in Chapter 3 introduces a minimum number of staves with a different design (12, compared to 156 outer layer staves) and is derived from the stave design of the outer layers.

$\|\eta\|$ Range	$\Delta\phi$	$\Delta\eta$
0. - 1.1 (1.2 h)	15°	~ 0.1
1.1 (1.2 h) - 1.8	7.5°	~ 0.1
1.8 - 2.1	7.5°	~ 0.16
2.1 - 3.64	15°	0.2 - 0.6

Table 1.3: CDF II Calorimeter Segmentation

	Central	Plug
EM:		
Thickness	$19X_0, 1\lambda$	$21X_0, 1\lambda$
Sample (Pb)	$0.6X_0$	$0.8X_0$
Sample (scint.)	5 mm	4.5 mm
WLS	sheet	fiber
Light yield	160 pe/GeV	300 pe/GeV
Sampling res.	$11.6\%/\sqrt{E_T}$	$14\%/\sqrt{E}$
Stoch. res.	$14\%/\sqrt{E_T}$	$16\%/\sqrt{E}$
SM size (cm)	$1.4\phi\times$(1.6-2.0)Z	0.5×0.5 UV
Pre-shower size	$1.4\phi \times 65$Z cm	by tower
Hadron:		
Thickness	4.5λ	7λ
Sample (Fe)	1 in. C, 2 in. W	2 in.
Sample (scint.)	10 mm	6 mm
WLS	finger	fiber
Light yield	~ 40 pe/GeV	39 pe/GeV

Table 1.4: Central and Plug Calorimeter Comparison

1.4.2 Calorimeter Systems

Outside the solenoid, scintillator-based calorimetry covers the region $|\eta| \leq 3.0$ with separate electromagnetic and hadronic measurements with a segmentation given in Table 1.3. The CDF calorimeters have obviously played a key role in the physics program by measuring electron and photon energies, jet energies, and net transverse energy flow. The ability to match tracks with projective towers and EM shower position in the central region has lead to a powerful analysis and calibration framework, including an understanding of the absolute jet energy scale to 2.5%.

For Run II, the existing scintillator-based central calorimeters will continue to perform well. The central and plug calorimeters both have fast enough energy measurement response times to take full advantage of the 132 ns bunch spacing. Shower maximum and pre-shower functions in the plug upgrade are also fast enough, while the wire chamber pre-shower and shower maximum in the central system will need to integrate several bunches. The shower maximum detector in the central calorimeter is inaccessible, so this deficiency cannot be addressed in any reasonable time scale. The preshower detector will be replaced for Run IIb by a scintillator based detector with the same response time available to the plug calorimeter. A general comparison of the central and plug calorimeters is given in Table 1.4.

1.4.3 Muon Systems

CDF II uses four systems of scintillators and proportional chambers in the detection of muons over the region $|\eta| \leq 1.5$. The absorbers for these systems are the calorimeter steel, the magnet return yoke, additional steel walls, and the steel from the Run I forward muon toroids. The geometric and engineering problems of covering the full η region using these absorbers leads to the four logical systems. As seen in Table 1.5, they are all functionally similar. The CDF II tracking system provides a capability for muon momentum reconstruction over this full region of pseudorapidity.

1.4.4 Electronics and Triggering

The CDF electronics systems have been substantially altered to handle Run II accelerator conditions. The increased instantaneous luminosity requires a similar increase in data transfer rates. However it is the reduced separation between accelerator bunches that has the greatest impact, necessitating a new architecture for the readout system.

Figure 1.4 shows the functional block diagram of the readout electronics. To accommodate a 132 ns bunch-crossing time and a 4 μs decision time for the first trigger level, all front-end electronics are fully pipelined, with on-board buffering for 42 beam crossings. Data from the calorimeters, the central tracking chamber, and the muon detectors are sent to the Level-1 trigger system, which determines whether a $\bar{p}p$ collision is sufficiently interesting to hold the data for the Level-2 trigger hardware. The Level-1 trigger is a synchronous system with a decision reaching each front-end card at the end of the 42-crossing pipeline. Upon a Level-1 trigger accept, the data on each front-end card are transferred to one of four local Level-2 buffers. The second trigger level is an asynchronous system with an average decision time of 20 μs.

	CMU	CMP/CSP	CMX/CSX	IMU
Pseudo-rapidity coverage	$\lvert\eta\rvert \leq\sim 0.6$	$\lvert\eta\rvert \leq\sim 0.6$	$\sim 0.6 \leq \lvert\eta\rvert \leq\sim 1.0$	$\sim 1.0 \leq \lvert\eta\rvert \leq\sim 1.5$
Drift tube cross-section	2.68 x 6.35 cm	2.5 x 15 cm	2.5 x 15 cm	2.5 x 8.4 cm
Drift tube length	226 cm	640 cm	180 cm	363 cm
Max drift time	800 ns	1.4 μs	1.4 μs	800 ns
Total drift tubes (present)	2304	864	1536	none
Total drift tubes (Run II)	2304	1076	2208	1728
Scintillation counter thickness		2.5 cm	1.5 cm	2.5 cm
Scintillation counter width		30 cm	30-40 cm	17 cm
Scintillation counter length		320 cm	180 cm	180 cm
Total counters (present)		128	256	none
Total counters (Run II)		269	324	864
Pion interaction lengths	5.5	7.8	6.2	6.2-20
Minimum detectable muon p_T	1.4 GeV/c	2.2 GeV/c	1.4 GeV/c	1.4-2.0 GeV/c
Multiple scattering resolution	12 cm/p (GeV/p)	15 cm/p	13 cm/p	13-25 cm/p

Table 1.5: Design Parameters of the CDF II Muon Detectors. Pion interaction lengths and multiple scattering are computed at a reference angle of $\theta = 90^\circ$ in CMU and CMP/CSP, at an angle of $\theta = 55^\circ$ in CMX/CSX, and show the range of values for the IMU.

A Level-2 trigger accept flags an event for readout. Data are collected in DAQ buffers and then transferred via a network switch to a Level-3 CPU node, where the complete event is assembled, analyzed, and, if accepted, written out to permanent storage. These events can also be viewed by online monitoring programs running on other workstations.

1.4.4.1 Data Acquisition

A block diagram of the data acquisition system is shown in Fig. 1.5. Timing signals associated with the beam crossing are distributed to each crate by the Master-Clock subsystem. Trigger decision information is distributed by the Trigger-System-Interface subsystem. Commercial processors read data from modules in their local crate and deliver it to the VME Readout Boards (VRBs) and the Event-Building subsystem. This system concentrates the data and delivers it to the Level-3 trigger subsystem through a commercial network switch. The Level-3 trigger is a "farm" of parallel processors, each fully analyzing a single event. The Data-Logging subsystem delivers events to mass storage and also to online monitoring processes to verify that the detector, trigger, and data acquisition system are functioning correctly. Our plans for data acquisition during Run IIb are described in Chapter 6.

1.4.4.2 Trigger

In Run Ib, the trigger had to reduce the raw collision rate by a factor of 10^5 to reach < 10 Hz, an event rate that could be written to magnetic tape. With an order of magnitude increase in luminosity for Run II, the trigger must have a larger rejection factor while maintaining high efficiency for the broad range of physics topics we study.

We use a tiered "deadtimeless" trigger architecture. The event is considered sequentially at three levels of approximation, with each level providing sufficient rate reduction for the next level to have minimal deadtime. Level-1 and Level-2 use custom hardware on a limited subset of the data and Level-3 uses a processor farm running on the full event readout. The trigger, like the DAQ, is fully pipelined.

The block diagram for the CDF II trigger system is presented in Fig. 1.6. Events accepted by the Level-1 system are processed by the Level-2 hardware. The Silicon Vertex Tracker (SVT) provides, for the first time in a hadron-collider experiment, the ability to trigger on tracks with large impact parameters. This will make accessible a large number of important processes involving hadronic decay of b-quarks, such as $Z \rightarrow b\bar{b}$, $B^0 \rightarrow \pi^+\pi^-$, and exotic processes like SUSY and Technicolor that copiously produce b quarks. The Level-2 system will have improved momentum resolution for tracks, finer

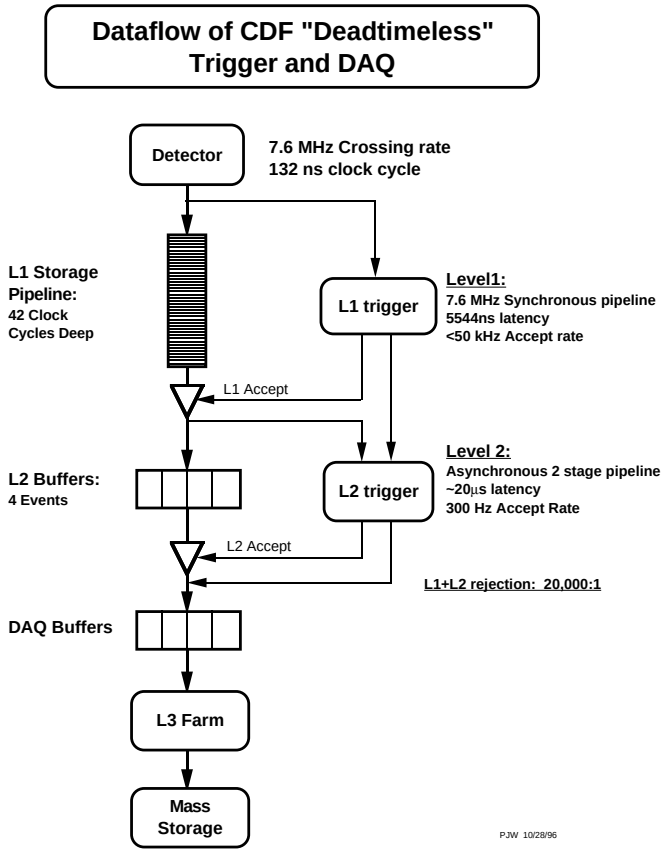

Figure 1.4: Functional block diagram of the CDF II data flow

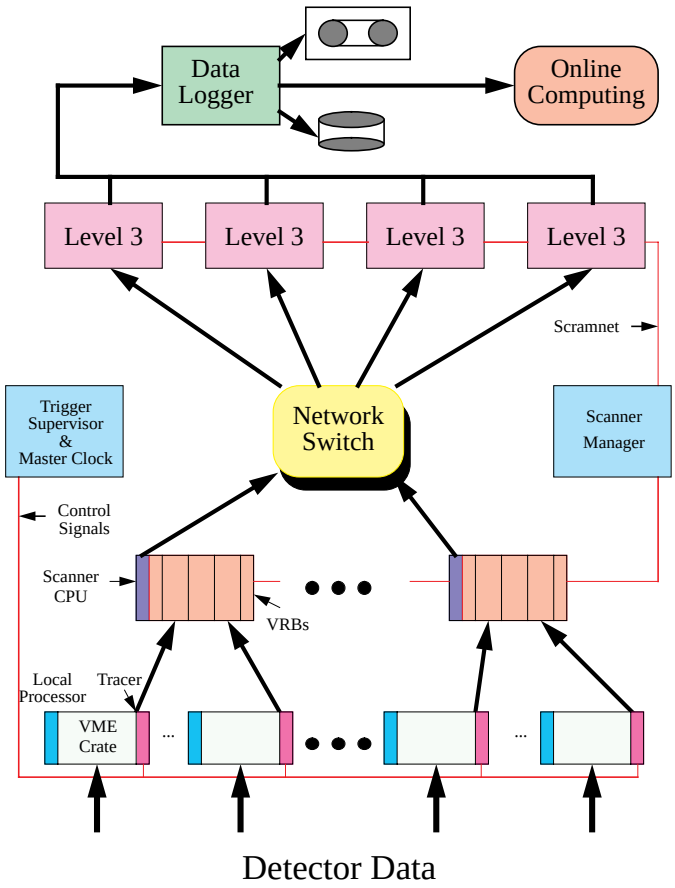

Figure 1.5: A schematic of the CDF II Data Acquisition system, showing data flow from the front-end and trigger VME crates to the Online Computing system.

angular matching between muon stubs and central tracks, and data from the central shower-max detector (CES) for improved identification of electrons and photons. Jet reconstruction is provided by the Level-2 cluster finder, which, although rebuilt for the new architecture, retains the same algorithm used successfully in previous running. The Level-2 trigger is being commissioned at this time, and is not yet full operational.

The trigger system is very flexible and will be able to accommodate over 100 separate trigger selections. With a 40 kHz accept rate at Level-1 and a 1000 Hz rate out of Level-2, we expect to limit deadtime to $< 10\%$ at full luminosity, while writing events to mass storage at 30-50 Hz.

1.5 The CDF II Upgrade Plan

Our goal is to install and recommission CDF for the resumption of data taking as quickly as possible. Every effort will be made to minimize the time that the installation of this project takes away from operations.

This document is the TECHNICAL DESCRIPTION of the baseline CDF II detector. Additional documents describe the managerial, cost, and schedule aspects of the project:

- CDF Run IIb Project Management Plan
- Memoranda of Understanding (MOU) and Work Plans for each subproject
- Cost and Schedule Plan
  - Task-based resource-loaded schedule, including labor estimates
  - Cost Estimate and Work Breakdown Structure (WBS), including contingency analysis
  - WBS Dictionary
  - Financial Plan for U.S. and non-U.S. funding

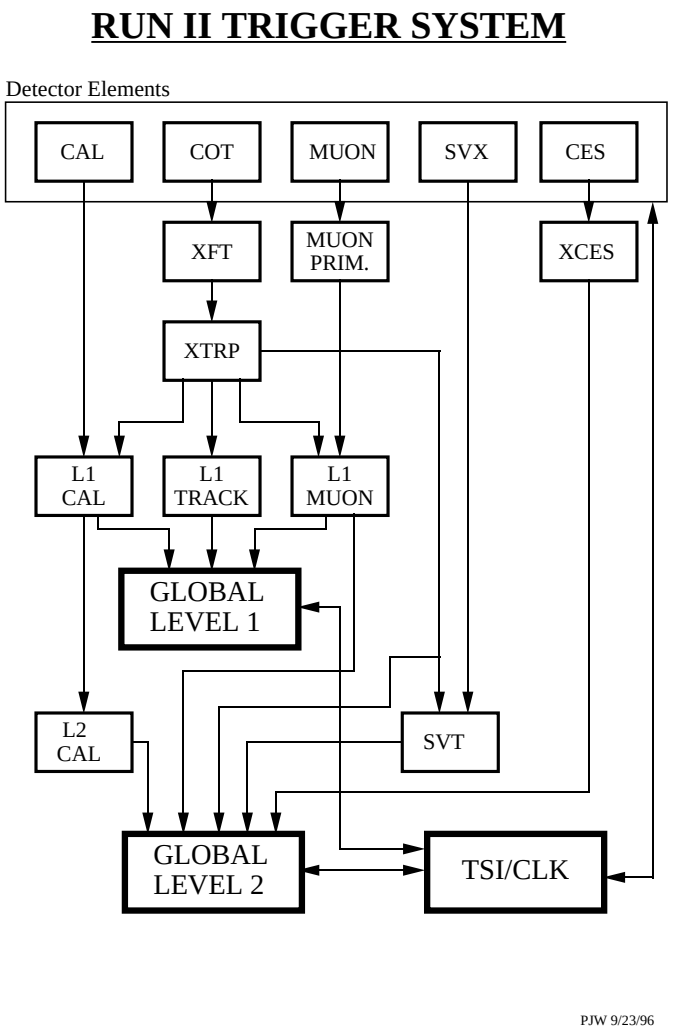

Figure 1.6: Block diagram of the CDF II trigger system.

1.5.1 Outlook

The baseline scope of the detector proposed here meets every goal for a rejuvenated detector capable of operations with the Tevatron + Main Injector at $\mathcal{L} = 5 \times 10^{32}\text{cm}^{-2}\text{s}^{-1}$, 132 ns bunch spacings, and to last through 15 fb^{-1} of integrated luminosity.

- The tracking system will be a fully optimized combination of drift chamber and silicon with powerful redundancy that insures excellent pattern recognition, momentum resolution, and b-tagging out to $|\eta| = 2$, even in the presence of multiple interactions.

- The calorimetry will be exclusively scintillator based, fast, and have resolution equal to or better than the existing detector.

- The muon system will have almost full azimuthal coverage in the central region, and expanded coverage out to $|\eta| = 2.0$.

- The electronics will be fully compliant with 132 ns or 396 ns bunch crossing in every channel, and the data acquisition system and Level-3 trigger will be capable of 1000 Hz operation.

- The trigger will be deadtimeless, ready for every crossing, with tracking information at Level-1 and impact parameter discrimination at Level-2.

This design reflects the accumulated experience of a decade of physics with CDF at the Tevatron. With CDF II and anticipated data sets in excess of 15fb^{-1}in Run II, we look forward to major discoveries at Fermilab in the years to come.

Bibliography

[1] "The CDF II Detector Technical Design Report", The CDF II Collaboration, FERMILAB-Pub-96/390-E, November 1996.

Chapter 2

Physics Goals

2.1 Overview

In this chapter we will describe the physics goals of the CDF II experiment, and the connection between the physics and the detector design. Our physics plan includes six complementary lines of attack on the open questions of the Standard Model:

- search for a light Higgs boson
- characterization of the properties of the top quark
- a global precision electroweak program
- direct search for new phenomena
- tests of QCD at large Q^2
- constraint of the CKM matrix with B hadrons

This physics program is comprehensive in its methods and its scope. It has classic precision measurements, such as m_W and α_s, taken to a new level of accuracy; it has a survey of newly discovered territory, in the first complete study of the top quark; and it extends our reach for new phenomena into a regime where current theoretical speculation suggests new structure. We believe that the power of the CDF II detector combined with the sensitivity of the Run II data sets will result in a significant advance in our understanding of the behavior of elementary particles, if not outright discovery of physics beyond the Standard Model.

In this chapter we will justify this claim. We begin with a summary of our conclusions and then turn to each of the six topics in detail. Since the CDF II experiment re-uses or extends many of the same detector technologies and strategies as its predecessor, the physics analyses of Run II will employ many of the techniques refined during Run I. The physics projections and detector specifications will therefore frequently appeal to a brief review of the current status. We note that our conclusions have the power of direct extrapolations from a well tuned device in a well measured environment.

Table 2.1 shows the expected yields for some benchmark processes with 15 $\text{fb}^{-1}$of Tevatron collisions recorded by the CDF II detector. These are the numbers of identified events available for offline analysis. The statistical precision of Run II, combined with capability of the CDF II detector, will provide rich programs of measurement in each of the six sub-fields, summarized below.

2.1.1 Higgs Boson Physics

The origin of electroweak symmetry breaking is one of the most fundamental questions in elementary particle physics. One explanation is the existence of Higgs bosons. Fits to precision electroweak data suggest that one of the Higgs bosons should be light (below 200 GeV/c^2), and the minimal supersymmetric model requires a Higgs boson with mass less than about 130 GeV/c^2 . These facts make the search for light Higgs bosons one of the most important goals of experimental elementary particle physics. The CDF and D0 experiments have the opportunity to make this discovery in Tevatron Run II. This search directly drives our plan to upgrade the CDF detector to a configuration that will operate with B tagging capabilities at instantaneous luminosities of $5 \times 10^{32} cm^{-2} s^{-1}$ and integrated luminosities approaching 30 fb^{-1}. The details of the Tevatron search strategy for a light Higgs boson have been explored in a Fermilab Higgs Workshop [2]. A brief summary of this workshop and the CDF plans for Higgs boson searches are presented in Section 2.2 .

Mode	Yield (15 fb^{-1})
TOP	
dilepton	1125
$W + 3j * b$	6750
$W + 4j * b$	5440
$W + 4j * bb$	1350
VECTOR BOSONS	
$W \to l\nu$ (e,μ)	32M
$Z \to l^+l^-$(e,μ)	4.5M
$W\gamma, W \to e\nu$	30K
$Z\gamma, Z \to e^+e^-$	13.5K
$W^+W^- \to l\nu l\nu$	1500
$W^+Z^- \to l\nu ll$	375
QCD	
j + X, $|\eta| \leq 1.0, E_T \geq$300 GeV	48K
jj + X, $M_{jj} \geq 600$ GeV	225K
γ + X, $p_T(\gamma) \geq 25$ GeV	45M
$\gamma\gamma$ + X, $p_T(\gamma_1, \gamma_2) \geq 12$ GeV	105 K
$W+ \geq 1j$, $E_T(W) \geq 100$ GeV	75K
$Z+ \geq 1j$, $E_T(Z) \geq$100 GeV	7.5K
B	
$B^0 \to J/\psi K_S$	150K
$B^0 \to \pi^+\pi^-$	38K
$B_s \to J/\psi\phi$	60K

Table 2.1: Representative yields for known processes, after selection. We use the CDF Run I selections modified for increased coverage of the CDF II detector (see text) and we assume 2.0 TeV collisions. $j \equiv$ jet, and $j*b \equiv$ b-tagged jet.

2.1.2 Properties of the Top Quark

A sample of almost 7,000 b-tagged, identified events will allow a detailed survey of the properties of the top quark. A review of this program is given in Section 2.3.

The top mass will be measured with a precision conservatively estimated to be 2.0 GeV/c^2. The total cross section will be measured to 6%, and non-standard production mechanisms will be resolvable down to total cross sections of $\sim$ 90 fb. The branching fraction to b quarks will be measured to 1%, decays to non-W states may be explored at the level of 3%, and branching ratios to the various W helicity states will be measured with uncertainties of order 1%. The magnitude of any FCNC decay will be probed down to branching fractions of 0.5% or less. We will isolate the electroweak production of single top, allowing a cross section measurement with an uncertainty of 12%, and inference of $|V_{tb}|$ with a precision of 6%.

The final top physics program will undoubtedly be richer than this list, which should be interpreted as a catalog of probable sensitivities for the baseline top survey and whatever surprises the top may have in store.

2.1.3 A Precision Electroweak Program

The study of the weak vector bosons at the Tevatron is anchored in the leptonic decay modes. The new plug, intermediate muon system and integrated tracking will give triggerable electron coverage out to $|\eta| = 2.0$, triggerable muon coverage out to $|\eta|$ of at least 1.2 and taggable muon coverage out to $|\eta| = 2.0$. This will double the number of $W \to e\nu$ events and *triple* the acceptance for Z's and dibosons in the electron and muon channels. A data set of 15 fb^{-1}in combination with the acceptance and precision of the CDF II detector results in the comprehensive program in electroweak physics discussed in detail in Section 2.4.

One of our main goals is the measurement of m_W with a precision of $\pm$20 MeV/c^2. The combined precision on m_W and m_{top} will allow inference of the Standard Model Higgs mass m_H with precision of 30%.

The W decay width, Γ_W will be measured to 15 MeV, a factor of twelve improvement on the LEP-II expectation. The precision on A_{FB} at the Z^0 pole will be sufficient to improve on the measurement of $sin^2\theta_W^{eff}$ over LEP and SLD results, and measurement off the pole will be sensitive to new phenomena at high mass scales. Limits on anomalous WWV and ZZγ couplings, bolstered by the forward tracking and lepton identification, will surpass those of LEP-II. The W charge asymmetry measurement, also augmented by unambiguous lepton ID in the plug region, will provide much improved constraints on parton distribution functions.

2.1.4 Search for New Phenomena

The CDF II experiment will search for new objects at and above the electroweak scale. There is at present a great deal of theoretical activity focussed on new phenomena in this regime, with predictions from models invoking supersymmetry, technicolor, and new U(1) symmetries. The magnitude of the top quark mass

and speculation about an excess in the top cross-section have led to other theoretical predictions about phenomena well within our reach in Run II, such as topcolor. Search strategies for these and other models are discussed in Section 2.5.

We will be sensitive to charginos up to 130 GeV/c^2, to gluinos up to 270 GeV/c^2, and to stop squarks up to 150 GeV/c^2. Second generation lepto-quarks can be observed up to masses of 300 GeV/c^2, new vector bosons can be probed up to masses of 900 GeV/c^2, and excited quarks up to 800 GeV/c^2. Quark compositeness can be observed up to a scale of approximately 5 TeV. These are all model dependent limits, and, as in the case of the top survey above, we believe that our catalog of prospects here is best interpreted as a list of probable sensitivities for the real surprises waiting at the electroweak scale.

2.1.5 Precision QCD at Large Q^2

The QCD sector of the Standard Model will be stringently tested using the production and fragmentation properties of jets, and the production properties of W/Z bosons, Drell-Yan lepton pairs, and direct photons. We will evaluate the precision of QCD calculations beyond leading order (higher order perturbative calculations and soft gluon resummation corrections), and determine the fundamental input ingredients, namely parton distribution functions and the running coupling constant α_s.

The precision of QCD measurements at CDF II with 15 fb^{-1}will provide sensitivity to many sources of new physics. For example, the strong coupling constant α_s will be measured over the entire range (10's GeV)$^2 < Q^2 <$ (500 GeV)^2, and deviations from the Standard Model running could signal loop contributions from new particles. A direct search for the substructure of quarks at the level of 10^{-19}m will be possible with high E_T jets and the production angular distribution of di-jets. Finally a broad range of searches will be carried out for the decays of massive particles to various combinations of jets, W/Z bosons, photons and neutrinos via missing E_T.

2.1.6 Constraining the CKM Matrix

CDF II plans to take advantage of the copious production of the various species of b hadrons at the Tevatron to make measurements which will test the consistency of the Standard (CKM) Model of weak quark mixing and *CP* violation. By extending the capabilities developed in Run I into Run II, CDF II expects to be able to measure *CP* asymmetries in $B^0 \to J/\psi K_S$ and $B^0 \to \pi^+\pi^-$ decays with a precision comparable to the e^+e^- colliders. Complementary information will come from a sensitive search for *CP* violation in $B_s \to J/\psi\phi$ decays. The effects of mixing in the $B_s^0 - \bar{B}_s^0$ system will be measured, allowing a determination of the ratio of CKM elements $|V_{td}/V_{ts}|$ over the full range allowed by the Standard Model.

In addition CDF II will continue to improve the precision on measurements of b hadron decay properties (*e.g.* B^0 vs. B^+ lifetimes) and pursue the observation and study of rare decays (*e.g.* $B^0 \to K^{*0}\mu^+\mu^-$). The physics of heavier b hadrons, for instance B_c, will be the exclusive domain of the Tevatron collider for at least the next decade. An overview of CDF II expectations for B physics in Run II is given in Section 2.7.

2.1.7 Detailed Discussion

The scientific prospects for CDF II are discussed in the following sections of this chapter.

The physics opportunities provide much of the rationale for the CDF II design choices, and the discovery prospects detailed here underscore our excitement about completing this upgrade and returning to high luminosity data taking at the Tevatron Collider as quickly as possible.

2.2 Higgs physics in Run 2b

The search of the origin of electroweak symmetry breaking is the central question in high energy physics today. The most recent fits to the world's combined electroweak data[1] favor the existence of a Standard-Model-like Higgs with mass in the range 100-200 GeV. The lower limit on the Higgs mass from the LEP2 experiments is 113.4 GeV; the data from all four experiments show a 2-sigma excess at a Higgs mass of about 115 GeV.

The Tevatron experiments have the opportunity, in the years before the LHC turns on, to search for the Higgs both in the Standard Model (SM) and in supersymmetry, using a variety of search channels discussed here. The Run 2b upgrades, and in particular the replacement for the Run 2a silicon vertex detector, are crucial to carrying out this physics program.

2.2.1 Standard Model Higgs

Events with a SM scalar Higgs can be produced at the Tevatron in several ways. The most copious production mode is gluon-gluon fusion via a heavy quark loop, giving a single Higgs produced. The Higgs can also be produced in association with a W or Z boson via its couplings to the vector bosons. Figure 2.1 shows the production cross section for various modes as a function of Higgs mass.

Figure 2.2 shows the branching ratios of the Standard Model Higgs as a function of Higgs mass. In the range below about 135 GeV Higgs mass, the decay to $b\bar{b}$ dominates, and for larger masses the decay to W pairs dominates.

In the gluon fusion case, for low mass Higgs, there is an overwhelming background from QCD production of $b\bar{b}$ pairs. The WH and ZH modes, however, have been extensively studied[2] and lead to several distinct signatures in which a Higgs signal can be observed with sufficient integrated luminosity.

2.2.2 Low-mass Higgs

For low mass (< 135 GeV) Higgs, the most sensitive signatures arise from the leptonic decays of the W and Z, and are denoted $\ell\nu b\bar{b}$, $\nu\bar{\nu}b\bar{b}$, and $\ell^+\ell^- b\bar{b}$. Hadronic decays of the W and Z lead to the $q\bar{q}b\bar{b}$ final state which suffers from large backgrounds from QCD multijet production.

In Run 1 in CDF, all four of these channels were studied, and led to limits on the Higgs cross section times branching ratio to $b\bar{b}$ as depicted in Figure 2.3. As the plot shows, the Run 1 limits are more than an order of magnitude above the expected Standard Model cross section, naturally provoking the question of whether and how this search can be carried out in Run 2.

Improvements to the detector, coupled with much higher instantaneous luminosity in Run 2 lead to greatly enhanced sensitivity in the Standard Model Higgs search. Unlike the Run 1 detector, the CDF Run 2 detector has a silicon vertex detector covering the entire luminous region, and has measurements of the z coordinates of tracks. Overall, the tracking coverage out to nearly $|\eta| = 2$ and the new muon chambers lead to greatly improved acceptance for Higgs. For the missing E_T channel ($\nu\bar{\nu}b\bar{b}$) channel, the trigger efficiency can be improved by using the silicon vertex trigger (SVT) to tag the jets. Coupled with the fact that the accelerator is expected to deliver a data sample over a hundred times larger than that in Run 1, the overall sensitivity of the Higgs search is dramatically improved in Run 2.

Beyond the improvements to the detector itself, maximizing the sensitivity of the search for the Higgs depends most critically on attaining the best possible $b\bar{b}$ mass resolution, and attaining the best possible b jet tagging efficiency and purity, and understanding and controlling the main irreducible backgrounds from vector boson plus heavy flavor production.

In Run 1 the top quark discovery and subsequent determination of its mass demonstrated that one could use jet information, even jets from b quarks, which have a significant semileptonic branching ratio, to determine the top mass. The case of the Higgs is simpler than that of the top, which suffers from large combinatorics. For the Higgs, the mass resolution is limited by basic physics (missing energy from neutrinos and gluon radiation) and detector resolution.

The benefit of making corrections for missing neutrinos is illustrated by CDF's search in Run 1 for $Z \to b\bar{b}$. Figure 2.4 shows the successive effects of correcting for overall missing energy, and muon p_T, and more general jet energy corrections. The mass resolution attained in this analysis was 13.5%; for a 120 GeV Higgs (in the background-dominated process $Z \to b\bar{b}$) the resolution predicted is 12%.

One can improve upon the jet energy corrections employed in most Run 1 analyses by making the best possible use of all detector information, including tracking, shower max, calorimeter, and muon cham-

bers. Figure 2.5 shows the improvement to jet energy resolution possible by determining jet energy from an optimum linear combination of all jet information. Using all information results in a 30% improvement in jet energy resolution.

A great deal of simulation and calibration work remains and is presently underway. Optimistically, by putting together all the best kinematic corrections with optimal jet energy corrections, we hope to eventually achieve 10-12% mass resolution for the Higgs in the main low-mass search channels. (This is not as good as the $Z \to b\bar{b}$ case because there is additional missing energy in the Higgs channels due to neutrinos from W and Z decay.)

Figure 2.6 shows the raw mass distribution and Figure 2.7 shows the background-subtracted signal in the $\ell\nu b\bar{b}$ case, for a 120 GeV SM Higgs, combining data from both CDF and DØ representing 15 fb^{-1} integrated luminosity, assuming a 10% $b\bar{b}$ mass resolution, which is what was assumed (optimistically) in the Tevatron Run 2 Higgs report. The figure clearly illustrates that even with the best resolution attainable, discovering the Higgs remains a major challenge.

2.2.3 High-mass Higgs

For larger Higgs masses (> 135 GeV), the Higgs decays predominantly to $WW^{(*)}$. Two modes have been shown[2] to be sensitive in this mass range: $\ell\nu\bar{\ell}\bar{\nu}$ (from gluon fusion production of single Higgs) and $\ell^{\pm}\ell^{\pm}jj$ (from tri-vector-boson final states).

The critical issues in these search modes are accurate estimation of the very large ($\sim$10 pb) WW background in the $\ell\nu\bar{\ell}\bar{\nu}$ case and channel and estimation of the $t\bar{t}$ and W/Z+jets backgrounds in the like-sign dilepton channel.

2.2.4 SM Higgs Reach in Run 2

The integrated luminosity required to discover or exclude the Standard Model Higgs, combining all search channels and combining the data from CDF and DØ , is shown in figure 2.8. The lower edge of the bands is the nominal estimate of the Run 2 study, and the bands extend upward with a width of about 30%, indicating the systematic uncertainty in attainable mass resolution, b tagging efficiency, and other parameters.

The figure clearly shows that discovering a SM (or SM-like) Higgs at the 5-sigma level requires a very large data sample: even with 15 fb^{-1}, the mass reach is about 120 GeV at best. A 95% CL exclusion can, however, be attained over the entire mass range 115-190 GeV with the integrated luminosity foreseen in Run 2b.

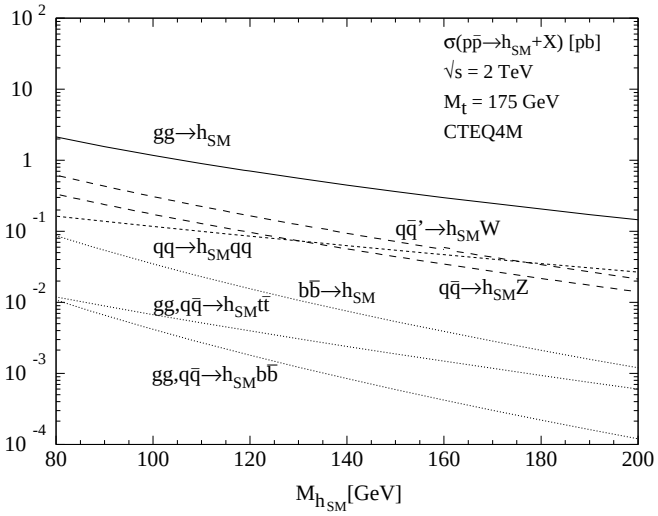

Figure 2.1: Production cross section for Standard Model Higgs at the Tevatron as a function of Higgs mass.

The $b\bar{b}$ mass resolution assumed in making these estimates is 10% in the central part of the distribution. This represents a significant improvement over the 14-15% resolution achieved in this analysis in Run 1, which did not benefit from the more detailed corrections described above and developed after the analysis was completed. A great deal of effort, presently underway, is needed to understand the jet energy corrections to the level required to attain 10% resolution. The required integrated luminosity for Higgs discovery scales linearly with this resolution.

The estimates of required integrated luminosity assume that the b tagging efficiency and purity are essentially the same as in Run 1 in CDF, per taggable jet. The better geometric coverage of the Run 2a and 2b silicon systems, however, is taken into account and leads to a much larger taggable jet efficiency. Since the required integrated luminosity scales inversely with the *square* of the tagging efficiency (assuming constant mistagging rates), however, there is a potentially great payoff for developing high-efficiency algorithms for b-tagging. Any such algorithms depend crucially on the quality of the information coming from the silicon vertex tracking system; the Run 2b silicon system has indeed been designed to optimize the performance in high-E_T b jet tagging.

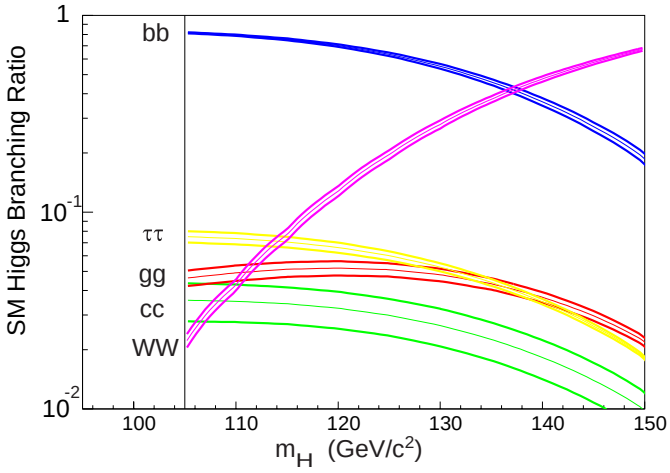

Figure 2.2: Branching ratios for Standard Model Higgs.

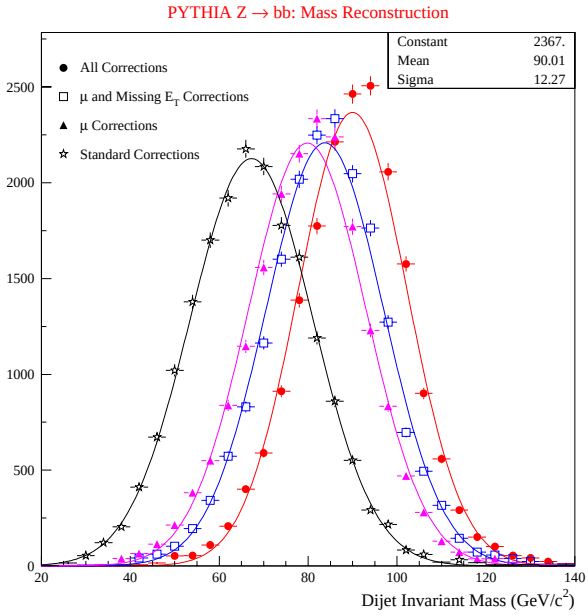

Figure 2.4: Mass resolution improvement for $Z \rightarrow b\bar{b}$ events as successive corrections are applied. After all corrections the resolution is 12%.

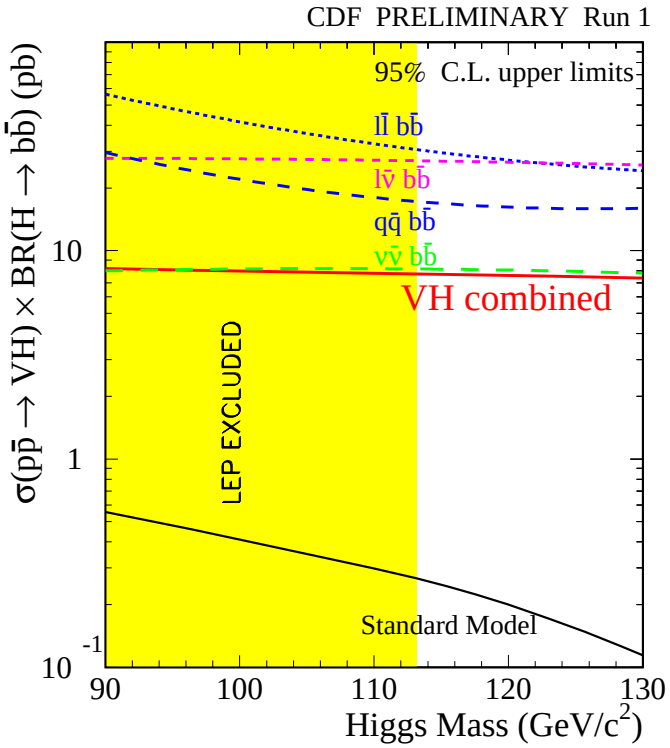

Figure 2.3: Limits on SM Higgs cross section times branching ratio to $b\bar{b}$ from CDF in Run 1.

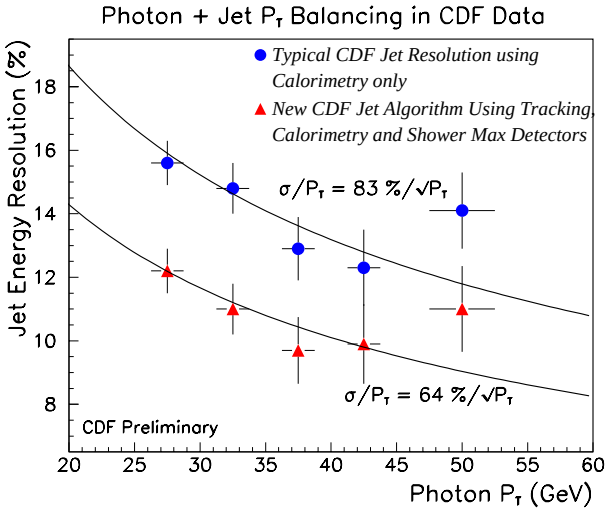

Figure 2.5: Jet energy resolution as a function of jet E_T, comparing standard corrections based on calorimeter only with energy determination combining information from tracking detetors, calorimetry, and shower max.

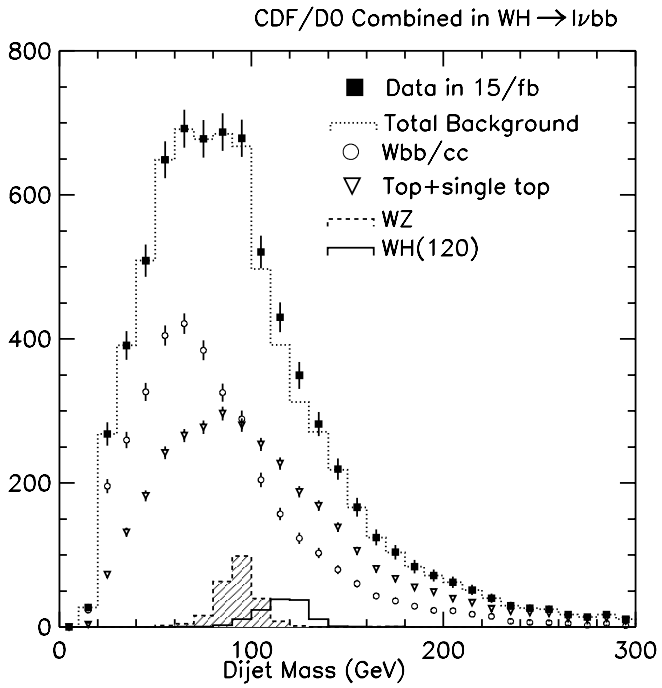

Figure 2.6: Distribution of $b\bar{b}$ mass in the $\ell\nu b\bar{b}$ Higgs search channel, showing expected background sources and expected signal from 120 GeV SM Higgs, combining 15 fb^{-1} of data from CDF and DØ .

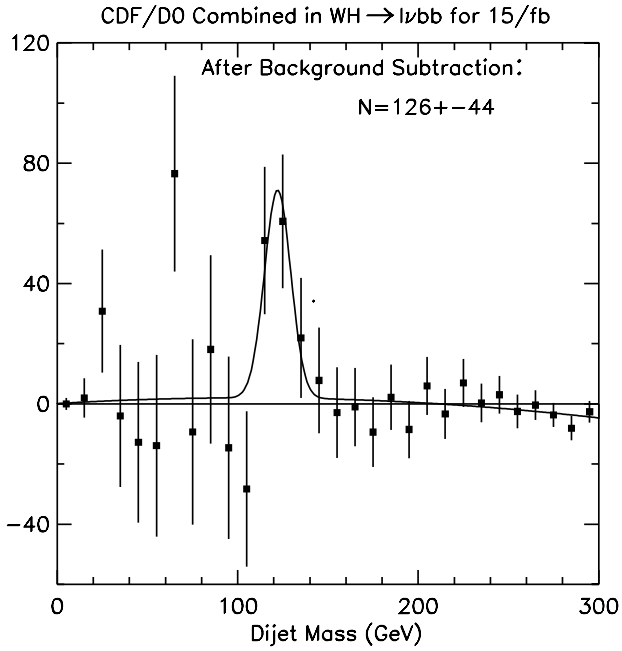

Figure 2.7: Background subtracted $b\bar{b}$ mass distribution in the $\ell\nu b\bar{b}$ channel, showing expected signal from 120 GeV SM Higgs, combining 15 fb^{-1} of data from CDF and DØ .

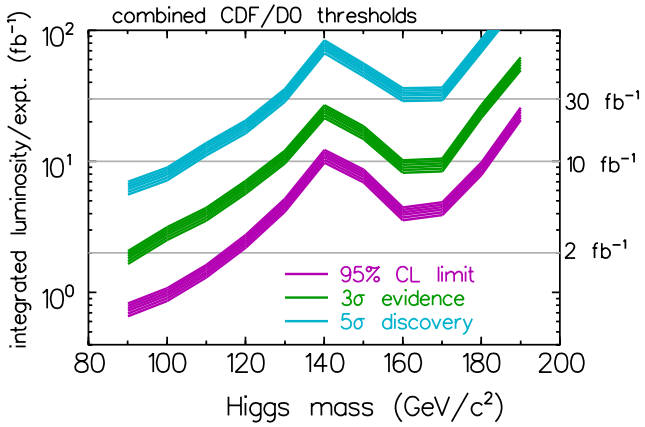

Figure 2.8: The integrated luminosity required per experiment to either exclude a SM Higgs boson at 95% CL or discover it at the 3σ or 5σ level, as a function of the Higgs mass. These results are based on the combined statistical power of both CDF and DØ and combining all search channels.

2.2.5 SUSY Higgs

In the context of the minimal supersymmetric standard model (MSSM) the Higgs sector has two doublets, one coupling to up-type quarks and the other to down-type quarks and leptons. There are five physical Higgs boson states, denoted h, A, H, and $H^{\pm}$. The masses and couplings of the Higgses are determined by two parameters, usually taken to be m_A and $\tan\beta$ (the ratio of the vacuum expectation value of the two Higgs doublets), with corrections from the scalar top mixing parameters.

The light scalar h can appear very Standard-Model-like or nearly so over a larger range of MSSM parameter space. In this scenario the results of the search for the SM Higgs produced in the WH and ZH modes are directly interpretable. Figure 2.9 shows the range in the space of m_A versus $\tan\beta$ in which a 5-sigma discovery can be made, as a function of integrated luminosity, for one choice of stop mixing.

More interesting is the case of large $\tan\beta$. Since the coupling of the neutral Higgses ($h/A/H$) to down-type quarks is proportional to $\tan\beta$, there is an enhancement factor of $\tan^2\beta$ for the production of $b\bar{b}\phi, \phi = h, A, H$ relative to the SM rate appearing in figure 2.1. This leads to distinct final states with four b jets; if we demand that at least three of the jets be tagged, the background from QCD multijet processes is relatively small. In Run 1, CDF searched

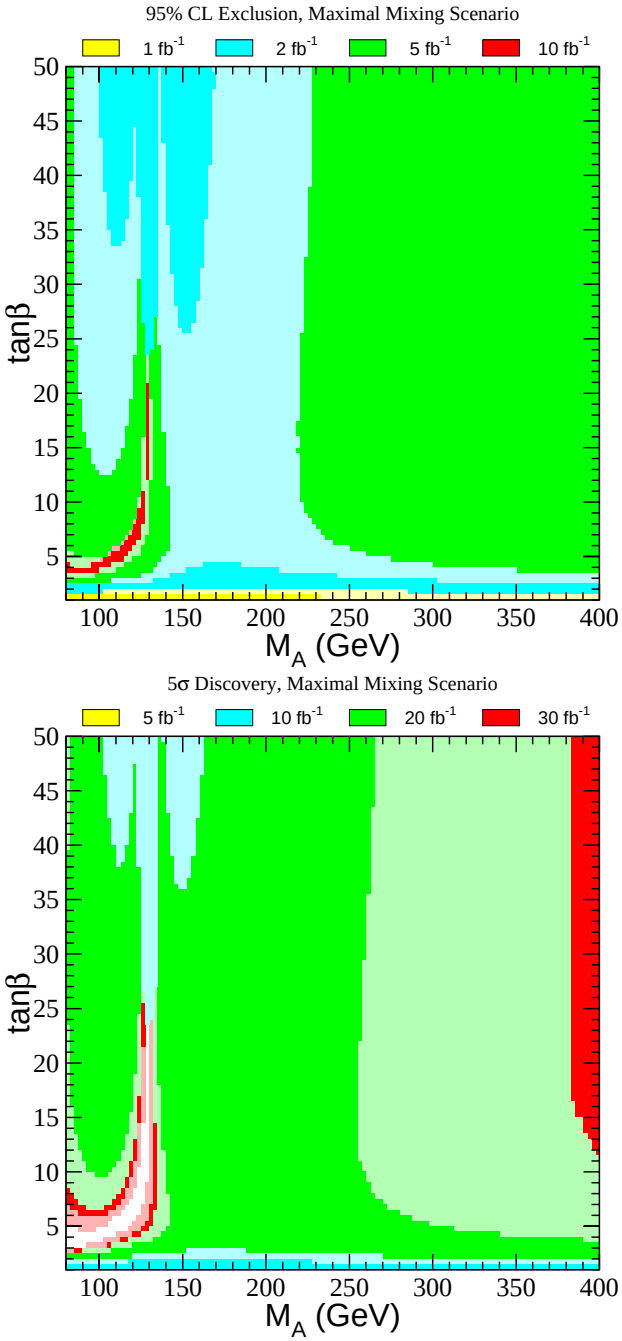

Figure 2.9: Regions of MSSM Higgs parameter space where 95% exclusion can be attained (above) and where 5σ discovery is possible (below), using SM Higgs search results.

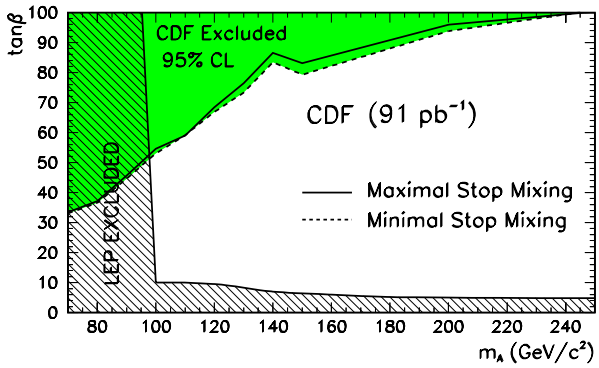

Figure 2.10: CDF limits on MSSM Higgs using $b\bar{b}b\bar{b}$ final state.

for this process, and from the null result excluded a large swath of MSSM parameter space inaccessible to LEP, as shown in figure 2.10.

Based on the Run 1 analysis, and taking into account the improved b-tagging efficiency, Figure 2.11 shows the regions of m_A versus $\tan\beta$ that CDF can cover for different integrated luminosities. It is interesting to note that the sensitive region in this analysis includes the region which is difficult to cover using the results of the SM Higgs search (shown in Figure 2.8). For this analysis the Run 2b silicon vertex system plays an absolutely crucial role: the accepted signal rate is proportional to the cube of the b tagging efficiency!

2.2.6 Summary

With an upgraded detector and more than an order of magnitude larger instantaneous luminosity the CDF experiment, combined with DØ , has a significant chance of discovering a SM (or SM-like) Higgs boson in Run 2. If the Higgs mass is larger than about 130 GeV, the experiment is sensitive to the WW decay modes in two main channels. The experiment also has the chance to discover the Higgs in the MSSM, if $\tan\beta$ is large, via the striking four-b-quark final state.

The key experimental issues are maintaining the excellent secondary vertex tagging efficiency throughout the run, and working hard to understand and improve the dijet mass resolution. Clearly the physics motivation for the Run 2b upgrade to the silicon vertex system is strong, and without it this physics cannot be addressed at all.

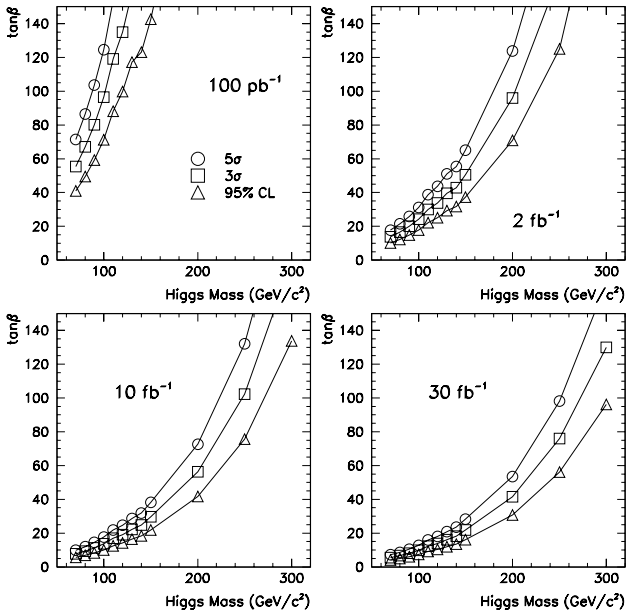

Figure 2.11: Anticipated limits in the plane of $\tan\beta$ versus $m(A)$ using $b\bar{b}b\bar{b}$ final state.

Bibliography

[1] LEP Electroweak Working Group at CERN (see http://lepewwg.web.cern.ch/LEPEWWG/).

[2] Report of the Higgs Working Group of the Tevatron Run 2b SUSY/Higgs Workshop, M. Carena *et al.*, eds., unpublished. (See hep-ph/9910338 at the LANL preprint server.)

2.3 Properties of the Top Quark

The top quark, with mass ~ 175 GeV/c^2, is strongly coupled to the electroweak symmetry breaking mechanism, and decays to a real W and a b-quark before hadronizing. A program to characterize the properties of this unconventional fermion is an obvious scientific priority. The accessibility of the top quark at the Fermilab Tevatron, in conjunction with the planned luminosity and detector upgrades for Run II, creates a new arena for experimental particle physics at an existing facility, and we should fully exploit this unique opportunity over the next decade.

Tevatron Run I brought the discovery of the top quark, the first direct measurements of its mass and cross section [2, 3, 4], and valuable first experience in top quark physics. We established techniques to identify b-quark jets using secondary vertices and soft leptons from the decays $B \to \ell\nu X$ as well as establish the essential utility of b-tagging in the isolation of the top signal. We established techniques for the accurate measurement of the mass and decay kinematics of a heavy object in final states with jets, and the essential utility of *in situ* jet calibration techniques. We have explored a variety of other measurements, all of them presently limited by statistics. [44, 47, 48, 49, 50, 51, 52, 53, 54, 55, 56, 57, 45]

Armed with this experience, we have just embarked on Run IIa, a new physics program with an expected delivered luminosity of 2 fb^{-1}here at the Tevatron [1]. With this data in hand, we expect to make significant contributions to our current understanding of the top quark as discussed in the Run II Technical Design Report (TDR) [35].

This document takes as a basis the Run II TDR but takes it one step further by examining the top quark physics potential with 15 fb^{-1}worth of data. We will show that the CDF IIb detector will be capable of a complete characterization of the main properties of the top quark, and we will establish the probable precisions that can be achieved using 15 fb^{-1}of Tevatron collider data.

Since Run IIa is still in its infancy, we are not currently able to report any new physics results. Instead, we begin by reviewing the top analysis results of Run I. Next, we discuss the impact of the detector upgrade components on the top physics of Run IIb. Finally we describe the Run IIb top physics program, including yields, the mass measurement, production properties, branching ratios, and decays.

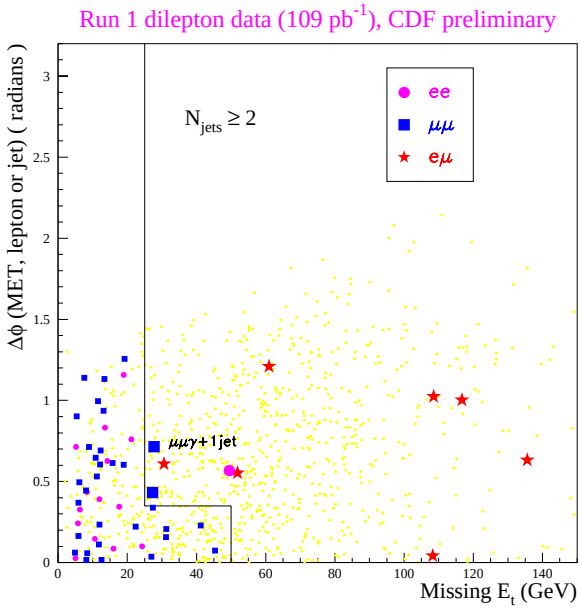

Figure 2.12: $\Delta\phi$ vs. $\not\!\!E_T$ in the dilepton sample. The small grey dots are the result of a $t\bar{t}$ Monte Carlo simulation with $m_{top} = 175$ GeV/c^2.

2.3.1 Review of Run I Analysis

Using 19.3 pb^{-1} from Run Ia, CDF presented initial evidence for the top quark in the spring of 1994 [2]. A year later, with an additional 48 pb^{-1} from Run Ib, CDF confirmed its original evidence for the top quark[3]. Upon completion of Run I in 1996, CDF wrote a series of papers describing the current state of understanding of the top quark utilizing the 105 pb^{-1} Run I dataset. We summarize here the results of those first measurements in this new area of physics.

2.3.1.1 Dilepton Mode

In the standard model, the t and $\bar{t}$-quarks both decay almost exclusively to a W-boson and a b-quark. In the "dilepton" channel, both W's decay leptonically ($W \to \ell\nu$), and we search for leptonic W decays to an electron or a muon. The nominal signature in this channel is two high-P_T leptons, missing transverse energy (from the two ν's), and two jets from the b-quarks. Acceptance for this channel is small, mostly due to the product branching ratio of both W's decaying leptonically (only about 5%). In the 105 pb^{-1} from Run I, CDF observed 7 $e\mu$ events, 2 $\mu\mu$ events, and 1 ee event. Figure 2.12 shows the 10 candidate events in the parameter space $\Delta\phi$ (the angle between the $\not\!\!E_T$ and the nearest lepton or jet) vs $\not\!\!E_T$ (the missing transverse energy) as well as where

one would expect top to lie. The background estimate for the dilepton channel is 2.4 ± 0.4 events[3]. Although not an *a priori* part of the search, we examine the jets in dilepton events for indications that they originated from b-quarks. In the 10 dilepton events, we find 6 jets in 4 events (1 $\mu\mu$ and 3 $e\mu$) which are identified ("tagged") as b-jets. This provides evidence for b-quarks produced in association with two W's, as expected from the decay of a $t\bar{t}$ pair.

CDF has also investigated top decays involving the τ-lepton. We have searched for dilepton events with one high-p_T electron or muon and one hadronically decaying τ-lepton which is identified using tracking and calorimeter quantities[7]. As in the $e\mu, ee$, or $\mu\mu$ channel two jets from b-quarks and significant missing transverse energy are required. Due to the additional undetectable τ-neutrino, the τ hadronic branching ratio and the lower efficiency for τ identification, the acceptance in this channel is considerably smaller than in the case of $e\mu, ee$, or $\mu\mu$. In 105 pb^{-1} we expect about 1 event from $t\bar{t}$ and 2 events from background. We observe 4 candidate events (2 $e\tau$ and 2 $\mu\tau$). There are 4 jets in 3 candidate events that are identified as b-jets ("tagged"). More data with excellent tracking will enable us to conclusively establish this "all 3^{rd} generation" decay mode of the top quark, which is important for charged Higgs searches and tests of weak universality.

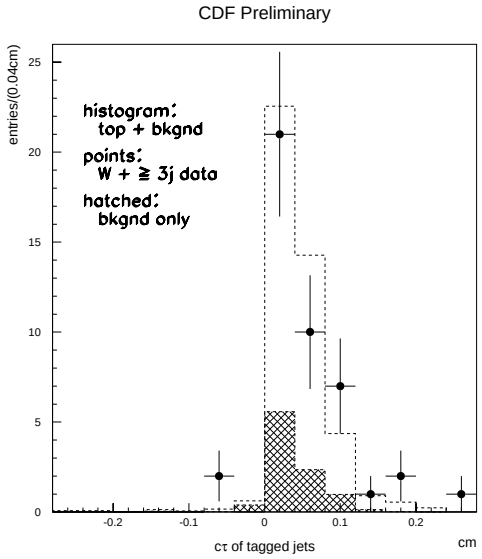

Figure 2.13: The proper time distribution for the b-tagged jets in the signal region (W+$\geq$ 3 jets). The open histogram shows the expected distribution of b's from 175 GeV/c^2 $t\bar{t}$ Monte Carlo simulation. The shaded histogram indicates the background in W+jet events.

2.3.1.2 Lepton + Jets Mode

In this channel, one of the W's decays leptonically to either an electron or muon (plus neutrino) and the other W decays hadronically to a pair of quarks. The nominal signature is a lepton, missing transverse energy (the neutrino from the leptonic W decay), and four jets; two from the b-quarks and two from the decay of the W. Approximately 30% of the $t\bar{t}$ events have this decay signature. Our lepton+jets selection requires that a leptonic W decay be accompanied by at least three central ($|\eta| < 2.0$) jets for an event to be considered part of the sample.

The background from W+multijet production is large. However, $t\bar{t}$ events contain two b-quark jets, and these can be distinguished from gluon and light quark jets in the background using two b-quark tagging techniques. The first technique locates a displaced vertex using the silicon-vertex detector (SVX Tag). The second locates a low-P_T electron or muon primarily from the semileptonic decay of a b-quark or sequential c-quark (SLT Tag). The efficiency for tagging a $t\bar{t}$ event is $(43 \pm 4)\%$ and $(20 \pm 3)\%$ for the SVX and SLT algorithms, respectively. In 105 pb^{-1}, 37 SVX tags are observed in 29 events. The background, in the 29 SVX tagged events, is estimated from a combination of data and Monte Carlo simulation to be 8.0 ± 1.1 events. Using the SLT tagging algorithm, 44 tags are found in 40 events. The background here is estimated to be 25.2 ± 3.8 events. The two samples have 10 events in common[3]. Figure 2.14 (upper left) shows the jet multiplicity spectrum for the SVX b-tags and the background.

In the 1 and 2-jet bins, we expect little contribution from $t\bar{t}$ events. The predicted background and the observed number of events agree well in the 1-jet bin, and agree at the 1.5 sigma level in the 2-jet bin as well. In the 3 and $\geq$4-jet bins, a clear excess of tagged events is observed. Fig. 2.13 shows the proper time distribution expected for b-tagged jets in the signal region ($\geq$ 3 jets), compared with that for the SVX b-tagged jets in the data: the tagged jets are consistent with b decays.

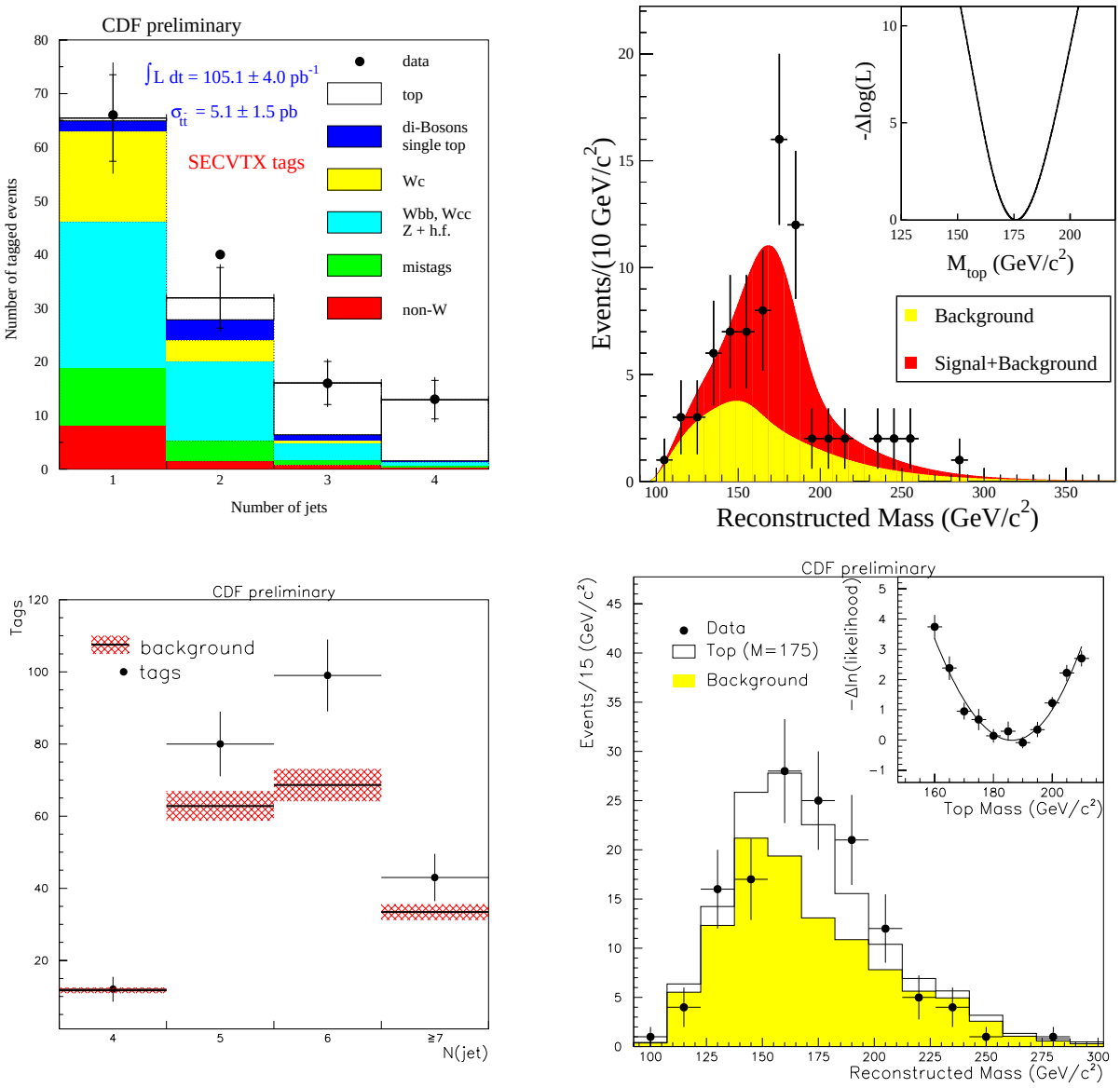

Figure 2.14: **Top Left:** The jet multiplicity distribution in SVX tagged W+jet events. Closed circles are are number of b-tagged events in each bin and shaded areas are the background prediction for the number of tagged events and its uncertainty. **Top Right:** Mass spectrum using the optimized mass sample in lepton+jet events using 105 pb^{-1} of data. The yellow (light) shaded area is the expectation from background. The red shaded area (dark) is the expectation for background plus top production. The points are the data. The likelihood fit is shown as an inset. **Bottom Left:** The jet multiplicity distribution for the all-hadronic mode. The dark circles represent the observed number of b-tags in each jet multiplicity bin and the hatched areas represent the background prediction as well as its estimated uncertainty. **Bottom Right:** Mass spectrum for all-hadronic b-tagged events in 105 pb^{-1} of data. The shaded area is the expectation from background. The histogram is from background plus top production. The likelihood fit is shown as an inset.

2.3.1.3 All Hadronic Mode

We have found a clear signal in the all-hadronic decay channel for $t\bar{t}$ events. In this decay mode there are six final state jets, four of which come from the hadronic decays of the two W's and two from the b-quarks. Approximately 44% of $t\bar{t}$ events have this decay signature. Achieving a reasonable signal-to-background ratio is the challenge in this data set which is dominated by QCD multijet production. In order to isolate a signal and maintain efficiency, we require at least five well-separated jets, one of which must be SVX b-tagged. After additional topological cuts, we find 222 tags in 187 events with an estimated background of 151 $\pm$ 10 events. Figure 2.14 (lower left) shows the jet multiplicity spectrum for the all-hadronic channel. In the 4-jet bin where we expect little contribution from $t\bar{t}$ events, the background and observed tags are in good agreement(12 observed vs 11.7 expected). Where we expect to see a signal for $t\bar{t}$, in the 5, 6, and $\geq$7-jet bins, an excess of tags is observed over the background predictions. [8]

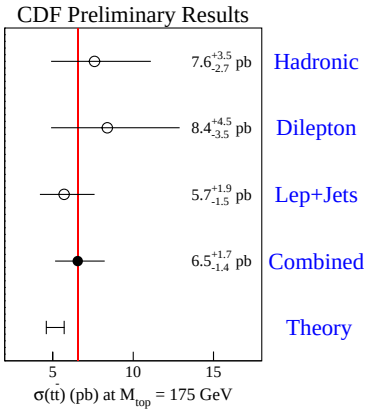

Figure 2.15: The measured cross section for $t\bar{t}$ production for each of the separate production channels measured at CDF as well as our combined measurement. The vertical line represents our average value. The bottom most point is an indication of the current theoretical calculations evaluated at a top mass of 175 GeV/c^2.

2.3.1.4 Kinematic Discrimination

In addition to the search techniques based on the dileptons and b-quark tagging, CDF has isolated $t\bar{t}$ events based on the kinematical properties predicted from Monte Carlo simulations. These methods use the lepton+jets event sample but do not rely on b-tagging to reduce the background. One technique examines the jet E_T spectra of the second and third highest E_T jets [5]. The second technique uses the total transverse energy of the event [6]. In both cases, there is a clear $t\bar{t}$ component in our data.

2.3.1.5 $t\bar{t}$ Production Cross Section

The counting experiments which lead to a confirmed signal can be turned directly into measurements of the $t\bar{t}$ production rate. Figure 2.15 shows the $t\bar{t}$ production cross section measured in several channels in comparison to recent theoretical predictions. Our best measurement is obtained from the weighted average of the counting experiments performed in the dilepton channel, the two lepton+jets channels, SVX b-tagging and SLT b-tagging, and the all-hadronic channel. With 105 pb^{-1} of data, we measure a production cross section by combining the measurements in each of the separate channels to be $6.5^{+1.7}_{-1.4}$ pb[36, 37]. The production cross section in the individual decay channels are found to be $5.7^{+1.9}_{-1.5}$ pb for the Lepton+jets mode [36], $8.4^{+4.5}_{-3.5}$ pb for the dilepton mode [38], and $7.6^{+3.5}_{-2.7}$ pb for the hadronic mode [39]. A theoretical cross section calculation by Mangano *et al.* predicts 5.2 pb[18] at 175 GeV/c^2, and other recent theoretical cross sections are within approximately 10% of this value.[18, 19]

2.3.1.6 Top Quark Mass

The top quark mass has been measured in three different channels. The primary method is based on fully reconstructing the $t\bar{t}$ system with lepton+jets events. These events must contain a lepton and at least four jets such that each final state parton can be assigned to an observed jet or lepton. The reconstruction is performed using a constrained fitting technique which selects the best assignment of observed jets to final state partons based on the lowest χ^2. Without any b-tagging information there are 24 combinations which must be considered (12 parton assignments $\times$ 2 possible longitudinal momentum components for the neutrino). When one or two jets are tagged as b-quarks, the number of combinations is reduced to 12 and 4, respectively. In order to make the best use of the data sets for measuring the top quark

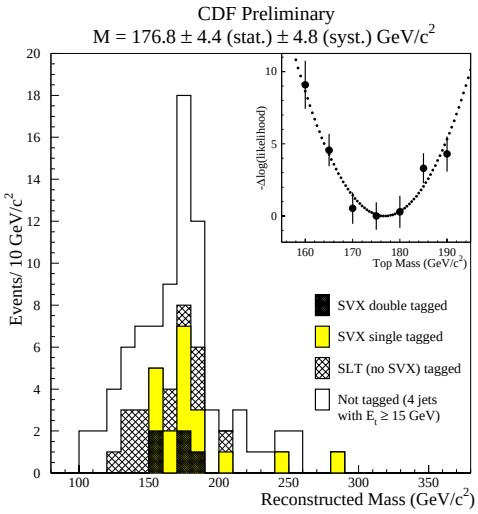

Figure 2.16: The optimized lepton+jets top quark mass plot for each of the four data samples. The light shaded area is the background expectation. The darker shaded region is the shape of the background + top expected for a top mass of 175 GeV/^{2}.The insert in each plot shows the -Δlog(likelihood) for the data in comparison to mass spectra derived from Monte Carlo samples of various m_{top} for that particular set of selection cuts. This technique results in a measured top quark mass of 176.1 ± 5.1 (stat.) ± 5.3 (syst.) GeV/c^2.

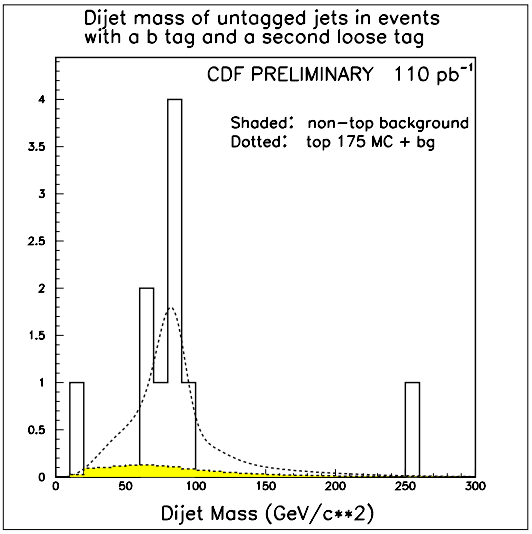

Figure 2.17: The M_{jj}^W distribution is shown for data (solid), expected top+background (dashed), and background (shaded), for W+4 jet events which contain two b-tagged jets. The value of M_{jj}^W is 79.8 ± 6.2 GeV/c^2. The top mass from this subsample has been determined to be 174.8 ± 9.7 GeV/c^2.

mass, the lepton+jets sample is divided into four orthogonal subsamples based on b-tagging: the SVX single-tagged set, the SVX double-tagged set, the SLT-only tagged set, and the not-tagged set [13]. The backgrounds are determined separately for each subset. The mass is determined by combining the likelihood functions defined in each subsample to extract a single optimized measurement of the top quark mass. This method currently yields the world's best top mass measurement of 176.1 ± 5.1 (stat.) ± 5.3 (syst.) GeV/c^2[3] (see Figure 2.16). The systematic uncertainty is dominated by the uncertainty in final state gluon radiation and the detector energy scale.

The same constrained fitting technique was also used to reconstruct the top mass in the all-hadronic channel where at least one b-tag was required; the result is seen in Figure 2.14 (lower right). Applying a maximum likelihood technique to the data in this channel results in a top mass of 186 ± 10 (stat.) ± 5.7 (syst.) GeV/c^2.

Reconstructing a top mass in the dilepton channel is difficult because this system is underconstrained due to the two undetected neutrinos. To solve this problem, we scan the two neutrinos and top mass to determine a probability function. Given the top mass, W mass, η_{ν_1}, η_{ν_2}, the two b jets, and two leptons, one can solve for the top mass independently and compare the predicted missing energy with the measured as a weight estimator. This technique gives a top mass from dileptons of 167.4 ± 10.3 (stat.) ± 4.8 (syst.) GeV/c^2.

In the subsample of lepton+$\geq$ 4-jet events where two b-tags are required, we have looked for evidence of the decay of the hadronic W-boson. Fig. 2.17 shows the reconstructed mass of the unconstrained jet-jet system. A fit yields a jet-jet mass of 79.8 ± 6.2 GeV/c^2 [15]. This will be an important *in situ* technique for jet energy scale calibration in Run II. The top mass from this double b-tagged subsample has been determined to be 174.8 ± 8 (stat.) ± 6 (syst.) GeV/c^2.[14]

2.3.2 Lessons from Run I

- The detector should have the greatest possible acceptance for high-p_T electrons and muons from

the chain $t \to W \to l\nu$.

- The detector should have the greatest possible acceptance and efficiency for tagging b-jets. This is a question of geometrical coverage, efficiency, and signal-to-noise ratio, most importantly for secondary vertex finding but also for soft lepton identification.

- Precision measurement of the top mass requires that the detector have *in situ* capability for understanding the systematics of jet energy calibration, including the ability to accumulate large samples triggered on low-p_T charged tracks, inclusive photons, and inclusive $W \to l\nu$ and $Z \to ll$.

- Understanding of b-tagging systematics has relied on the ability to accumulate a large, reasonably pure control sample of inclusive b-jets using low-p_T inclusive lepton triggers. We anticipate doing this again, with some demand on DAQ bandwidth. However, we have learned that jets containing $b \to cl\nu_l X$ are a biased control sample, and we believe that a large sample of b-jets collected with a secondary vertex trigger will be extremely useful.

2.3.3 Impact of Upgrades on Top Physics

The impact of the CDF IIb upgrades is to maintain the significant increases in overall top acceptance that will be achieved in Run IIa and to maintain that increased acceptance and precision at high luminosity and maintain the precision for large integrated luminosity.

- **Silicon Vertex Detector (SVX IIb)**: SVXII was not built to survive the radiation levels that it would be exposed to for Run IIb. Layer 00 as well as the three innermost layers of SVXII need to be replaced in order to complete Run IIb with reasonable detector performance and thus meet our physics goals. Time constraints on the length of the Run IIa to IIb shutdown require that all of SVXII be replaced. The goal of the replacement device is to have comparable performance to SVXII - the one now in place for Run IIa. Since SVXII is still being commissioned, comparisons will be made between the Run I silicon and the proposed SVXII replacement.

  In top physics, the name of the game is acceptance and purity. The tagging of b-quarks from top quark decays will be greatly improved in the long, 7-layer device from what was used in run I. Increasing the length of the silicon from 52 cm to 96 cm will extend the region of "contained b-jets" to cover the entire interaction region. With seven measurements in two views for any given track, it will be possible to make stringent track quality requirements, reducing the level of mistags, while still improving the overall track finding efficiency.

  Taking all of these factors into account, we anticipate that the SVX II replacement will increase the efficiency for tagging at least one b-jet in a $t\bar{t}$ event to better than 65% (a 60% increase over the Run 1 efficiency), and will raise the double b-tag efficiency to 20% (a 200% increase from Run I performance) [23].

  Finally we point out that the 3D capability of the the new silicon detector will allow a precision measurement of the primary vertex in the event, improving a variety of measurements including the E_t/P_t of the primary leptons, the E_t of the jets, and the missing transverse energy.

- **Central Outer Tracker (COT) Upgrade**: The top analysis of Run I depended crucially on the large central tracking chamber. Similarly, the success of Run IIa top analysis will depend upon the performance of the Central Outer Tracker (COT). As luminosities increase for Run IIB, the inner superlayers of the COT will become less effective due to an increase in occupancy. Although track finding utilizing the outer superlayers will still be possible, the ability to point back to the silicon will be degraded due to low hit usage on the inner superlayers. On complicated events such as those found in $t\bar{t}$, this effect would be extremely detrimental to our ability to reconstruct the event properly. Thus deadening the sense wires at large $|\eta|$ would give back most of the fine performance expected in the Run IIA COT.

- **Muon Detection System**: In the Run I top analysis, only "central" muons were used as the primary lepton - that is those muons which were detected in the region covered by the CMU and CMP detectors. Muons that passed through the

Channel	Acc. A_{IB} (Run Ib)	Acc.,A_{II} (Run IIb)	Run I Results	Run IIb Yield (w/ A_{II})
Produced $t\bar{t}$	-	-	525	100k
Dileptons (ee,$\mu\mu$,$e\mu$)	0.78%	1.1%	10	1200
Tau dileptons ($e\tau$, $\mu\tau$)	0.12%	0.14%	4	142
lepton+$\geq$3j	9.2%	11.2%	324	10000
lepton+$\geq$3j w/ $\geq$1 b tag	3.7%	7.3%	34	7425
mass sample w/ $\geq$1 b SVX tag	3.0%	5.8%	20	6000
mass sample w/ $\geq$2 b SVX tags	0.52%	1.8%	5	1800

Table 2.2:
Acceptance and yield of $t\bar{t}$ events for a Run IIb upgraded detector. The yield is determined using the theoretical cross section (6.8 pb) at m_{top} = 175 GeV/c^2, $\sqrt{s}$ = 2 TeV, and 15 fb^{-1} data sample. For comparison, the acceptances for Run Ib are shown as well as the number of events seen in Run 1 prior to background subtraction. The acceptances include branching ratios and leptonic and kinematic selection (*e.g.* jet counting).

CMX detector (at higher $|\eta|$) were used to identify secondary leptons only — the very high rates and dynamic prescales used in the trigger proved too difficult to untangle. Much of this problem has been addressed for Run IIA by substantially increasing the steel shielding between the interaction region and these counters. This shielding should reduce the number of fake hits such that the trigger rates in the CMX region will be manageable.

Since the drift times in the muon chambers are now appreciably longer than the bunch crossing, scintillation counters, which shadow all of the muon chambers, were added so that muon stubs can be assigned to a particular bunch crossing. Some of this scintillator, like those mounted on the CMX muon arch chambers were installed in Run I and are now showing signs of aging. Current aging projections show that the performance of these counters will be substantially degraded in the next 2-3 years. If it is not replaced, this region of rapidity unusable for top physics in Run IIb. This loss would decrease the muon acceptance by approximately 10% from Run IIA.

- **Central Calorimeter**: With the increased luminosity and smaller bunch spacing of Run IIB, the central preshower and central crack chambers will need replacement. Their relatively poor segmentation and slow readout times will render these detectors useless in this new environment. The loss of these detectors will cripple both electron and photon identification - both critical to top quark physics. The central preradiator in Run I offered a factor of 2 to 3 more rejection of charged pions that pass all other cuts using tracking, calorimetry, and shower maximum information. This extra rejection is crucial in minimizing background in soft electron ID for b-jet tagging (SLT).

2.3.4 Event Yield

To estimate the yield of top events, we extrapolate from our current measured acceptance in Run I using the theoretical cross section (6.8 *pb*) at m_{top} = 175 GeV/c^2 and $\sqrt{s}$ = 2 TeV [22, 11].

At $\sqrt{s}$ =2 TeV, the $t\bar{t}$ cross section is approximately 40% higher than at $\sqrt{s}$=1.8 TeV. We assume that the additional lepton and b-tagging acceptance outlined in Sec. 2.3.3 above can be incorporated while maintaining a signal-to-background ratio comparable to the Run I analysis.

Table 2.2 summarizes the acceptance and yields for various decay channels in the Run II configuration. The Run Ib acceptances are shown for comparison. A data sample of 15 fb^{-1} at the Tevatron will provide over 7500 identified b-tagged $t\bar{t}$ events.

2.3.5 Measurement of the Top Quark Mass

The top quark mass will be one of the most important electroweak measurements made at the Tevatron. In

combination with the W mass, m_t gives information about the mass of the standard model Higgs boson. The precision electroweak program and the W mass measurement are discussed in the electroweak section of Chapter 2. Figure 2.14 shows how the predicted top and W mass measurements constrain the Higgs mass. In that figure, the uncertainty on the top mass is taken as 4 GeV/c^2.

Currently, the statistical and systematic uncertainties on CDF's top mass measurement are both about 5 GeV. The statistical uncertainty should scale as $1/\sqrt{N}$. Using the yields in Table 2.2, we anticipate that the statistical uncertainty on the top mass in the optimized lepton+$\geq$ 4-jet sample will be much less than 1 GeV/c^2. Thus in Run IIb, the overall uncertainty will be dominated by systematics. In fact, we expect approximately 1800 double-tagged lepton+$\geq$ 4-jet events on tape with a 15 fb^{-1}data sample. That one sample alone is sufficiently large that the statistical uncertainty will be less than 1 GeV. Since both b-jets are identified in the double-tagged subsample, it may turn out that the systematics for these events are better understood. If this is the case, there would be no need to include the other 3 subsamples (no-tag, single SVX tag, SLT tag) as was done in Run I.

Almost all of the systematic uncertainties in the top mass measurement are coupled to the reliability of the Monte Carlo models for the spectrum of fit masses in signal and background. Assuming the theory model is accurate, most of the uncertainty is related to resolution effects. Instrumental contributions include calorimeter nonlinearity, losses in cracks, dead zones, and absolute energy scale. A larger and more difficult part of the energy resolution concerns the reliability of the extrapolation to parton energies. Ultimately, it may be our understanding of QCD and not the detector which limits the mass resolution.

Many of these issues can be addressed by *in situ* calibration procedures. For example, Z+jet events are used to understand the systematic uncertainty due to energy scale and gluon radiation, two of the dominant uncertainties. In 15 fb^{-1}, we expect to have 200K (525) Z's with 1 (4) or more jets. The effect of gluon radiation will also be studied in large statistics samples of W+jets, γ+jets, and $b\bar{b}$ events. In addition, the mass peak from $W \to qq'$ (see Figure 2.17) in the lepton + jets top sample allows an energy scale calibration *in exactly the same events and environment* as the mass measurement. [1].

In any case, if all systematic effects can be measured or otherwise connected with mean quantities in large statistics control samples, the systematic uncertainties should also scale as $1/\sqrt{\mathcal{L}}$. We can conservatively assume in this case that we can reduce our systematic error to ≈ 2 GeV/c^2.

2.3.6 Production Cross Section, $\sigma_{t\bar{t}}$

An accurate measurement of the $t\bar{t}$ production cross section is a precision test of QCD. A cross section which is significantly higher than the theoretical expectation would be a sign of non-standard model production mechanisms, for example the decay of a heavy resonant state into $t\bar{t}$ pairs or anomalous couplings in QCD. As in the case of the top mass, large statistics in the lepton+jets mode imply that systematic uncertainties will be the limiting factor in the cross section measurement.

For the acceptance, the reliability of jet counting and b-tagging are at issue. Initial state radiation can be examined using a sample of Z+jets, while the jet energy threshold uncertainty can be addressed as in the top mass discussion. With 15 fb^{-1} of data it will be possible to measure the b-tagging efficiency *in top events*, using dilepton events selected without a b-tag and the ratio of single to double tags in lepton+jets events. We assume that these studies will give uncertainties that scale as $\sqrt{N}$. Hence we expect of order a 3 fold improvement in these systematic uncertainties from what was estimated for Run IIa.

With large samples, one can measure the bottom and charm content as a function of jet multiplicity in W + jet events using the $c\tau$ distribution of the tagged jets and use this to tune the Monte Carlo models for W+$\geq$ 3-jet backgrounds. Finally, in Run II and beyond, the luminosity will be measured either through the $W \to l\nu$ rate, or the mean number of interactions per crossing, and we will assume 5% for the future precision of the luminosity normalization.

Accounting for all effects we find that the total $t\bar{t}$ cross section can be measured with a precision of $\approx$ 5% for 15 fb^{-1}. This will challenge QCD, and provide a sensitive test for non-standard production and decay mechanisms.

2.3.7 Measurement of a t → W Branching Fraction

The ratio of the $t\bar{t}$ cross section measured using dilepton events to that measured using lepton+jets events is a test for non-standard model decay modes of the top quark. Since the cross section in each case assumes that each top decays into W-bosons, a ratio different from 1.0 would signal decays *without* a W-boson, such as charged Higgs (t → H^+ b) or light supersymmetric top (stop). The reach for a particular non-standard decay is model dependent, but we can say that with 15 fb^{-1} of data, we will be able to measure the basic dilepton to lepton+jets ratio to 8%, and the top branching fraction to W in association with b with a precision of 5%.

2.3.8 Measurement of a t → b Branching Fraction

In the standard model with 3 generations, existing experimental constraints and the unitarity of the CKM matrix require $V_{tb} \simeq 1$, predicting that the weak decay of the top will proceed almost exclusively through W + b. In events containing a W, the top branching fraction to b's is related to the CKM element according to:

$$\begin{aligned} B_b &= B(t \to W(b)) \\ &= \frac{\sigma(t \to Wb)}{\sigma(t \to Wq)} \\ &= \frac{|V_{tb}|^2}{|V_{td}|^2 + |V_{ts}|^2 + |V_{tb}|^2} \end{aligned}$$

The notation above is meant to indicate that a W has been required in the final state, and this is not the decay fraction to W+b, but the fraction of decays with W's which *also* contain b's. Since the standard analysis identifies $t\bar{t}$ events by requiring at least 1 W and 1 b, $B(t \to W(b))$ is measured from the number and distribution of tagged b-jets in top events. Four different techniques can be used to measure this distribution: [20, 21]

- The ratio of double b-tagged to single b-tagged events in the b-tagged lepton+jets sample: requiring one b-jet to be tagged leaves the second jet unbiased, and from a known tagging efficiency, one can extract the branching ratio from the ratio of tagged to untagged "second jets". [20]
- The ratio of single b-tagged to no b-tagged events in a lepton+jets sample in which kinematic criteria have been applied: since there is no a-priori tag requirement, we can extract the branching ratio from the ratio of single tagged events to not-tagged events. An ideal sample for this is the W+4 jet mass sample prior to applying the χ^2 cut. [21]
- The number of b-tagged jets in the dilepton sample: Since b-tagging is not required to identify tops decaying to dileptons, the whole b-tag multiplicity distribution in these events contains information on $B(t \to W(b))$. Despite the smaller branching fraction to dileptons, the statistical powers of the dilepton and lepton+jets samples are comparable.
- The distribution of double tags: If there are two tagging algorithms (soft leptons and secondary vertex), one can compare the number of times that events tagged by both algorithms have both tags in the same jet vs. the number of times the tags are in different jets. Small values of $B(t \to Wb)/B(t \to Wq)$ result in large values of the same to different jet ratio.

These techniques are not exclusive, and can be combined. We have used a maximum likelihood estimator to do this combination in Run I data. With 105 pb^{-1}, CDF has a ±25% statistical uncertainty on the branching fraction, but only an ±11% systematic uncertainty. The systematic uncertainty is dominated by the uncertainty on the tagging efficiency, which is measured in the data using b-rich inclusive lepton samples. This uncertainty should fall as $1/\sqrt{N}$. The small non-$t\bar{t}$ backgrounds will be measured to high accuracy by Run II. For Run II, we expect to measure $B(t \to W(b))$ to 3.0%.

2.3.9 Anomalous Couplings and Weak Universality

Since the top quark is so heavy, it is possible that the physics of the underlying theory may manifest itself via new non-universal top interactions. The top quark is unique in that it decays prior to hadronization and therefore the decay products carry helicity information related to the fundamental couplings. In the standard model, the top quark decays only to longitudinal or left-handed W's, where the ratio is given by

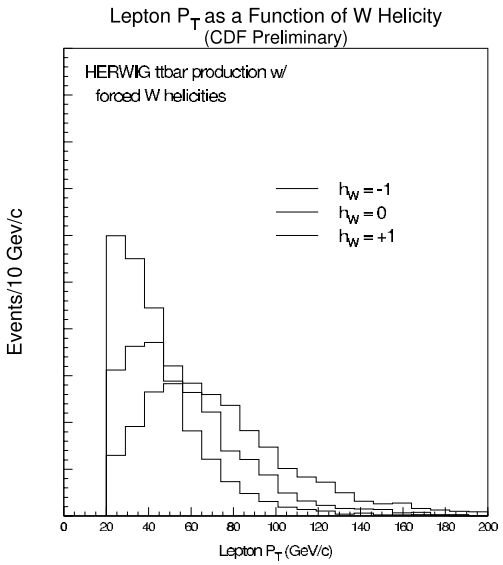

Figure 2.18: The lepton Pt as a function of W helicity for 175 GeV $t\bar{t}$ events

$$\frac{W_{long}}{W_{left}} = \frac{1}{2}\left(\frac{m_{top}}{m_W}\right)^2$$

For $m_{top} = 175.9$ GeV/c^2, the branching fraction to longitudinal W's is 70.6±1.6%. In many cases non-universal top couplings will appear as as a departure of B($t \to bW_{\rm long}$) from the standard value and we use this quantity as our precision benchmark for probes of anomalous weak couplings.

Experimentally, we have two ways to access the polarization state of the decay W. The first way and perhaps the most obvious way is through the charged lepton helicity angle, $cos\theta_e^*$ which can be measured in the lab frame as

$$\cos\theta_e^* \approx \frac{2M_{eb}^2}{m_{eb\nu}^2 - M_W^2} - 1 \qquad (2.1)$$

The resulting distribution can then be fit to a superposition of W helicity amplitudes in order to measure any possible contribution of non-universal weak couplings in the top decay.

The second way uses the shape of the lepton Pt spectra. The idea here is that the charged lepton from the left handed W tends to move opposite to the W direction while that from the longitudinal W tends to be perpendicular to the W direction. In the lab frame, this implies that leptons from longitudinal W's have a somewhat harder Pt distribution than those from the left-handed W's. See Figure 2.18 for an illustration using Herwig MC.

For Run 1 data, it turned out that both techniques have roughly equal statistical sensitivity, but P_T offers many advantages over the angular distribution. It eliminates systematic uncertainties related to parton combinatorics and neutrino reconstruction in the mass fitter and as a variable is more accurately measured.

The following cuts were used in the Run 1 analysis [40, 41]. We start with the cuts used in the $t\bar{t}$ cross-section analysis for event selection and then pick 4 subsets out of this W+3 jet heavy flavor data set.

- A displaced vertex tag identified by our algorithm SECVTX.
- A 4th lower energy jet ($E_T > 8$ GeV) and a soft lepton tag (SLT) within a cone of 0.4 of one of the 3 leading jets and NOT have a SECVTX tag
- A 4th high energy jet ($E_T > 15$ GeV) and a mass fitter value $\chi^2 < 10$.
- Standard dilepton search criteria

A likelihood procedure is performed using the lepton Pt as a variable to determine the fraction of top quarks which decay to longitudinal W bosons. For 105 pb-1, the fraction of top quarks which decay longitudinally is 0.91 ± 0.37 (stat) ± 0.13 (syst). The fraction of top quarks which decay to right handed W bosons (helicity of +1) is measured to be 0.11 ± 0.15 (stat) ± 0.06 (syst). The dominant systematic contributions are due to the uncertainty in top mass and the relative fractions of background contributions.

To date, no study has been performed to see how one would measure this quantity in Run IIb. The data samples will be significantly larger which would help measure the polarization angle. However even with double tagged events, there is still a bias due to mass fitter. It is important to note that even with relatively small data samples in run 1, the systematic uncertainty on this measurement is already quite small. With 15 fb^{-1}of data, we should be able to measure the top quark decay branching fraction to longitudinal W-bosons with a total precision approaching of order 1%. The V+A term in top decay should have similar sensitivity.

2.3.10 Single Top Quark Production

In addition to $t\bar{t}$ pair production via the strong interactions, top quarks can also be produced singly via the electroweak interaction. This process depends on the t-W-b vertex, and the production rate is a measure of the top decay width to W+b and the CKM matrix element $|V_{tb}|^2$. Single top is of theoretical interest because it provides a direct window on the charged-current interaction of the top quark. Unlike the case of top pair production where the electroweak vertex tWb plays a role only in the top quark's decay, in single top, the production cross section contains information on the coupling of top to W and b. Thus the production cross-section for single top contains information on the top partial width.

So far, we have assumed the validity of the Standard Model. Nonstandard couplings could invalidate the above simple extrapolation between V_{tb} and the top width or even render the entire concept of V_{tb} ill defined. Examples of proposed anomalous couplings that could impact single-top production rates include a q^2-dependent form factor at the tWb vertex or new flavor-changing neutral current couplings like tZc or tgc. New particles such as heavy W' boson would also lead to unexpected rates of single top production. Thus measuring single-top production is a win-win proposition. Either we get information on the top width and V_{tb} or we find evidence of new physics.

The two dominant single top processes at the Tevatron are the s-channel mechanism $qq \to t\bar{b}$, referred to here as W^* production, and the t-channel interaction $qb \to qt$, referred to as W-gluon fusion. Other processes become important at higher energies, but are negligible here because they have such heavy final states. Based on theoretical calculations, the W-gluon fusion process is thought to dominate the production with an estimated cross section of 1.7 pb at a 900 GeV Tevatron; the uncertainties on this calculation are on the order of 15%. The W^* production mode is roughly half as large and has an estimated cross section of 0.73 pb with a theoretical uncertainty of 9%. The combined rate for single top production by these two processes is ≈ 2.4 pb, only a little more than a factor of 2 down from the $t\bar{t}$ rate at this energy.

As is the case for $t\bar{t}$, single top events present themselves in the CDF detector as the leptonic or hadronic W decay products accompanied by one or more additional jets. Single top events are interspersed among a vast background of QCD processes which appear as energetic jets in the detector. Since hadronic W decay products are not easily distinguished from ordinary QCD jets, a first step in isolating the single top signal is to demand evidence of a leptonic W-decay as is done with $t\bar{t}$ - namely applying leptonic W selection criteria of a high Pt electron or muon plus large missing energy. As in $t\bar{t}$, dilepton and Z removal cuts are used to reduce unwanted backgrounds further. B-tagging is also used. What remains are backgrounds of W+heavy flavor and $t\bar{t}$ production. Thus, additional cuts are required to separate single top events from these backgrounds.

There are differences between the final states in Wg fusion and W^* production. The final state for W^* production features a second high-P_t central b-jet in addition to the b coming from the top decay $t \to Wb$. The second b in a W-gluon event is expected to be soft and forward and thus not detectable as such in the CDF detector. Furthermore, the Wg event is expected to contain an additional hard forward light-quark jet. Cuts must be developed with these differences in mind to isolate the individual processes.

The data selection criteria that were used to isolate the signal over background in the Run I analysis include:

- High P_T lepton events with 1, 2, or 3 jets with $E_T > 20$ GeV, $|\eta|_{\text{jets}} < 2.4$
- $\not\!\!E_T > 20$ GeV
- $E_T(\text{electron}) > 20$ GeV
- $|\eta|_{\text{electron}} < 1.0$
- Z and Dilepton removal
- At least one jet tagged as a b-jet.
- Reconstruct mass of lepton, neutrino and b-tagged jet to be inside the window $140 < M_{l\nu b} < 210 GeV$
- Fit the H_T distribution where H_T is the energy of the jets, leptons and MET in the event

After selection cuts we expect a 4.3 signal events (W* and Wgluon combined) and 62 background events. Thus we expect a $S/\sqrt{B} = 0.5$. See Table 2.3 for a breakdown by bin and by data sample type. A likelihood fit is then performed based on the variable H_T and a 95

Process	$W+1J$	$W+2J$	$W+3J$
Wg Signal	0.80	1.50	0.71
W^* Signal	0.25	0.80	0.23
$t\bar{t}$ Bckg	0.21	2.28	5.91
QCD Bckg	37.4	13.9	2.7
Total	38.7	18.5	9.6

Table 2.3:
Bin by Bin predictions for the single top processes and backgrounds for a data size of 105 pb.

The above analysis was optimized for a small statistical data set. With the large samples expected in Run IIb, one could remove the 1 jet bin, cut harder on some of the kinematic variables and separate out the two separate single top processes. By just removing the 1 jet bin for large data samples, the S/$\sqrt{B}$=2.9! Based on the theoretical cross section and acceptances from this analysis, one could expect to see roughly 100 W^* events in the W+2 jet bin per fb^{-1} and 150 Wg events per fb^{-1}. Hence in Run IIb, we expect a total sample of single top events to be of order 4000 events on tape. Assuming that the background normalization is understood (through the large statistics top cross section measurement), the statistical precision on the single top cross section using 15 fb^{-1} will be about $\tilde{1}$0%.

Many of the sources of systematic uncertainty in the single top cross section are common to the $t\bar{t}$ cross section discussed earlier. We assume that systematic uncertainties related to selection efficiencies and backgrounds will shrink as $\sqrt{N}$. For the case of 15 fb^{-1} we find that the measurement of the single top cross section will have a total uncertainty of approximately 12%.

The single top cross section is directly proportional to the partial width $\Gamma(t \to Wb)$ and assuming there are no anomalous couplings, this is a direct measure of $|V_{tb}|^2$. There are theoretical uncertainties in converting the cross section to the width, notably for the gluon fusion process. Taking these into account, we anticipate that a measurement of the total single top rate with 15 fb^{-1} will translate in a precision of 6% on $|V_{tb}|$.

The theoretical determination of W* is more reliable than that of W-gluon fusion since initial state effects can be measured in the similar Drell-Yan process, and if the data set is large enough this may afford the best precision on the width. The two processes can be separated by requiring two b-tags since the double tag rate for W* production is close to a factor of 5 more than that of W-gluon fusion.

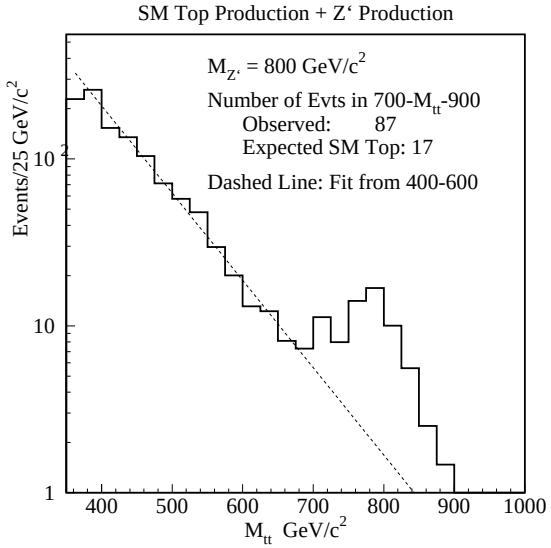

Figure 2.19: A hypothetical $m_{t\bar{t}}$ spectrum with an 800 GeV/c^2 Z′ topcolor boson. The rate is based on the theoretical predicted cross section for $t\bar{t}$ production and Z′ production [31] with 2 fb^{-1}.

2.3.11 Search for Anomalously Large Rare Decays

- $t \to Zc, \gamma c$
- $t \to WZb$
- $t \to W^+W^-c$
- $t \to Hc$

The standard model predicts that the branching fractions of FCNC top decays are around 10^{-10} [29], out of reach for even the LHC. Any observation of such decays will signal new physics. As illustration,

we consider the signal for a flavor changing neutral current decay $t \to c\gamma$ in a $t\bar{t}$ event. If the other top in the event decays in the leptonic channel, the acceptance is almost the same as the standard model lepton+jets mode, and it then becomes a simple matter to scale from present results. The background from $W+\gamma$ + two jets is about 1 fb. Although it is unlikely that this background will be kinematically consistent with $t\bar{t}$ (for example, that $m(\gamma + j) = m(t)$), we take the very conservative assumption that this background is irreducible. We find that 15 fb^{-1} will probe branching fractions for this decay down to 1.0×10^{-3}

Sensitivity to other rare decays can be scaled from this estimate. For the case $t \to Z + c$, where the Z decays to leptons, after adjusting for branching ratios and different backgrounds, we find sensitivity down to of order 0.5%.

2.3.11.1 Dynamical Symmetry Breaking

Because of its large mass, the top quark is an excellent probe for physics beyond the standard model. Theories which implicate top in the electroweak symmetry breaking mechanism, such as a color-octet vector meson associated with a top condensate[33] or multiscale technicolor[34], predict enhancements or changes in the shape of the $t\bar{t}$ invariant mass spectrum ($m_{t\bar{t}}$) and the top quark transverse momentum distribution (P_T^{top}).

CDF performed a search for resonances, $X \to t\bar{t}$, in the $M_{t\bar{t}}$ spectrum by reconstructing $M_{t\bar{t}}$ on an event-by-event basis using the same event sample and constrained fitting techniques used in the top mass measurement, with an additional constraint that the top mass. Effectively once the fit for $M_{t\bar{t}}$ is done, one then looks at the 3 body masses and asks whether they "wanted" to be fit to top. 63 events satisfied the selection criteria. The $M_{t\bar{t}}$ distribution of 63 data events yields a χ^2 of 80% when compared to the hypothesis that the spectrum is comprised of Standard Model $t\bar{t}$ production and the predicted rate of non-$t\bar{t}$ background events. A 95% confidence level cross-section limits for generic objects in the mass range of 400 GeV/c^2 to 1 TeV/c^2 which decay to $t\bar{t}$. These results exclude the existence of a lepto-phobic top-color Z' with masses less than 480 GeV/c^2 for $\Gamma = 0.012$M and 780 GeV/c^2 for $\Gamma = 0.04$M.

In the absence of a signal, limits in Run II will be as high as 1000 GeV/c^2. New resonances with masses below the limit could be observed. For example, Figure 2.19 shows the $M_{t\bar{t}}$ spectrum for 2 fb^{-1} with standard model $t\bar{t}$ production plus the addition of a topcolor Z$'$ at 800 GeV/c^2 [31], where the Z$'$ decays to a $t\bar{t}$ pair. In this theory, the branching fraction of Z$'$ to $t\bar{t}$ pairs is potentially large (50-80%) but depends on the Z$'$ width. In the case shown in Figure 2.19, we would expect 17 events from standard model $t\bar{t}$ production in the range 700$< M_{t\bar{t}} <$ 900 GeV/c^2 and 70 events from Z$' \to t\bar{t}$ in this range. The $M_{t\bar{t}}$ spectrum along with other $t\bar{t}$ production distributions provide an excellent means for searching for new phenomena.

2.3.12 Summary of Top Physics

For the next 5 years, the Tevatron will be the only accelerator capable of producing the top quark. Maintaining the capability of the CDF Run IIa detector is critical for setting limits on rare top searches, understanding the production rates for single top, and first significant measurements of both the top width and V_{tb} as well as on advancing the precision of Run IIa measurements.

The top physics program possible with this sample is summarized in Table 2.4. Measurements of branching ratios, angular distributions, and top production mechanisms with the sensitivities listed in Table 2.4 will provide the first complete characterization of this new fermion and provide another stringent test of the Standard Model. Our catalog of possible measurements is hardly complete. But in the event that the top quark yields surprises, these sensitivities benchmark the capability to explore new physics at the Fermilab Tevatron.

Measurement	15 fb^{-1}	Comment
Yields		
$\mathrm{N_{3jet*b}}$	7500	*identified* events
$\mathrm{N_{4jet*2b}}$	1800	clean m_t sample
δm_t	2	total precision GeV/c^2
Production		
$\delta\sigma_{t\bar{t}}$	6%	test top QCD couplings
$\delta\sigma_{ll}/\sigma_{l+j}$	9%	test non W decay
$\delta\sigma_{t\bar{b}X+b\bar{t}X}$	12%	isolate "single top"
Decay		
$\delta B(t \to W(b))$	1%	from N(bb)/N(bX)
$\delta B(t \to b(W))$	3%	from N(ll)/N(lX)
$\delta\mathrm{B(W_{V+A})}$	1%	$W \to l\,\nu$ helicity
$\delta\mathrm{B(W_{long})}$	1%	$\frac{W_{long}}{W_{left}} = \frac{1}{2}(\frac{m_{top}}{m_W})^2$
$\delta\mathrm{V_{tb}}$	6%	from above
Rare Decays		
B(c γ)	$\leq 1 \times 10^{-3}$	(95% CL)
B(cZ)	$\leq 5 \times 10^{-3}$	(95% CL)
B(Hb)	$\leq 9\%$	from σ_{ll}/σ_{l+j}

Table 2.4: Summary of expected measurement accuracies for an integrated luminosity of 15 fb^{-1}

Bibliography

[1] *Future ElectroWeak Physics at the Fermilab Tevatron: Report of the TeV_2000 Study Group*, Editors D. Amidei and R. Brock Fermilab–Pub–96/082

[2] F. Abe *et al.* (CDF Collaboration), Phys. Rev. D **50**, 2966 (1994); F. Abe *et. al.* (CDF Collaboration), Phys. Rev. Lett. **73**, 225 (1994).

[3] F. Abe *et al.* (CDF Collaboration), Phys. Rev. Lett. **74**, 2626 (1995).

[4] S. Abachi *et al.* (D0 Collaboration), Phys. Rev. Lett. **74**, 2632 (1995).

[5] F. Abe *et al.* (CDF Collaboration), Phys. Rev. D **52**, R2605 (1995).

[6] F. Abe *et al.* (CDF collaboration), Phys. Rev. Lett. **75**, 3997 (1995).

[7] M. Hohlmann, *Observation of Top quarks in the dilepton decay channel* $t\overline{t} \rightarrow e(\mu)\nu_{e(\mu)}\,\tau\nu_\tau\,b\overline{b}$ *Using Hadronic Tau Decays At CDF*, Proc., Lake Louise Winter Institute (1996)

[8] P. Azzi *et al.*, *Hadronic Top Production at CDF*, CDF Note 3679.

[9] R. Hughes, B. Winer, T. Liss, *Combining the SVX, SLT, and Dilepton* $t\bar{t}$ *Cross Sections*, CDF Note 3111.

[10] T. Liss, R. Roser, $t\bar{t}$ *Production Cross Section for 110* pb^{-1}, CDF Note 3481.

[11] A. Beretvas, Int. J. Mod. Phys. A11, 2045 (1996)

[12] P. Azzi *et al.*, $t\bar{t}$ *Production Cross Section in the All-hadronic Channel*, CDF Note 3464.

[13] K. Tollefson *et al.*, *Optimizing the Top Quark Mass Measurement*, CDF Note 3606.

[14] S. Aota *et al.*, *Update to Top Mass on Double b-tagged Events Using Loose Jet Probability Tagging*, CDF Note 3604.

[15] R. Wilkinson *et al.*, *Update to Hadronic W Decays in Double b tagged Top Candidates*, CDF Note 3543.

[16] E. Malkawi, C.-P. Yuan, *A Global Analysis of the Top Quark Couplings to Gauge Bosons*, Phys. Rev. D **50**, R4462 (1994).

[17] E. Laenen, J. Smith, W.L. van Neerven, Phys. Lett. **321B**, 254 (1994).

[18] Catani, Mangano, Nason and Trentadue, CERN Preprint, CERN-TH/96-21 hep-ph/9602208.

[19] E. Berger, Argonne Nat. Lab. Preprint ANL-HEP-PR-95-31

[20] T. LeCompte, R. Roser, *Measurement of* $BF(t \rightarrow Wb)$ *and the CKM Matrix Element* $|V_{tb}|$ *in Top Decays*, CDF Note 3056.

[21] F. Bedeschi, G. Chiarelli, F. Tartarelli, *Measurement of* $BF(t \rightarrow Wb)$ *in Top Decays*, CDF Note 3853.

[22] E. Laenen, private communication.

[23] R. Hughes, R. Roser, from a series of talks at the CDF upgrade meetings

[24] D. Atwood, A. Kagan, T.G. Rizzo, *Constraining Anomalous Top Quark Couplings at the Tevatron*, SLAC-PUB-6580, July 1994.

[25] G. Kane, C.-P. Yuan, and D. Ladinsky, Phys. Rev. D **45**, 124, (1992); D. Atwood, A. Aeppli, and A. Soni, Phys. Rev. Lett. **69**, 2754, (1992); R.S. Chivukula, S.B. Selipsky, E.H. Simmons, Phys. Rev. Lett. **69**, 575, (1992); M.Peskin, talk presented at the *Second International Workshop on Physics and Experiments at a Linear e+e- Collider*, Waikoloa, HI, April 1993; M.Peskin and P. Zerwas, talks presented at the *First International Workshop on Physics and Experiments at a Linear e+e- Collider*, Saariselka, Finland, September 1991.

[26] S. Dawson, Nucl. Phys. **B249**, 42 (1985); S.S.D. Willenbrock and D.A. Dicus, Phys. Rev. D **34**, 155 (1986); S. Dawson and S.S.D. Willenbrock, Nucl. Phys. **B284**, 449 (1987); C.-P. Yuan, Phys. Rev. D **41**, 42 (1990); S. Cortese and R. Petronzio, Phys. Lett. **B253**, 494 (1991); G.V. Jikia and S.R. Slabospitsky, Phys. Lett **B295**, 136 (1992), R.K. Ellis and S. Parke, Phys. Rev. D **46**, 3785 (1992); G. Bordes and B. van Eijk, Z. Phys. **C57**, 81 (1993); G. Bordes and B. van Eijk, Nucl. Phys. **B435**, 23 (1995): T. Stelzer and S. Willenbrock, Phys. Lett. **B357**, 125-130 (1995).

[27] D. Winn, D. Amidei, *Study of the $t \to Wb$ Vertex at CDF*, CDF Note 2914.

[28] D.O.Carlson, C.-P. Yuan, Phys. Lett. **306B**, 386 (1993).

[29] S. Parke, *Summary of Top Quark Physics*, FERMILAB -Conf-94/322-T. Presented at DPF'94, University of New Mexico, Albuquerque, NM, August 2-6, 1994.

[30] T. Stelzer, S. Willenbrock, *Single-Top-Quark Production via $q\bar{q} \to t\bar{b}$*, DTP/95/40, ILL-(TH)-95-30 (1995).

[31] C. Hill, *Topcolor Assisted Technicolor*, Fermilab-Pub-94/395-T

[32] K. Lane, *Top Quarks and Flavor Physics*, BUHEP–95–2.

[33] C. T. Hill, Physics Lett. **266B**, 419 (1991).

[34] K. Lane, E. Eichten, Phys. Lett. **222B**, 274 (1989); K. Lane and M.V. Ramana, Phys. Rev. D **44**, 2678, (1991).

[35] CDF Collaboration, *Technical Design Report for Run II*, Fermilab-pub-96/390-E.

[36] G. Apollinari et al, *Method II measurement of the top cross section with W+3,4 jet events with SECVTX, JPB and SLT tags*, CDF Note 4303.

[37] The Top Group, *The New CDF Run 1 combined $t\bar{t}$ production cross section*, CDF Note 5043.

[38] J. Cassada, P. Tipton, M. Kruse, *Consistency of the Run 1 Top Dilepton Candidate Events with the Top Quark Hypothesis* , CDF Note 4268.

[39] P. Azzi, W. Bokhari, A. Castro, *The effect of the new scale factor on the combined $t\bar{t}$ cross-section in the All Hadronic Channel*, CDF Note 5044.

[40] D. Winn and D. Amidei, *Measurement of W Helicity Fractions in Top Decay*, CDF Note 4464.

[41] D. Winn and D. Amidei, *Update to the Measurement of W Helicity Fractions in Top Decay* , CDF Note 4673.

[42] S. Wolinski P. Savard, *An upper limit on Standard Model single top production in CDF Run 1 data using fitting techniques* , CDF Note 5199.

[43] S. Truitt, P. Savard, *Search for Single Top Production in CDF Run 1 Data* , CDF Note 4978.

[44] First Measurement of Br(t-¿Wb)/Br(t-¿Wq) and Associated Limit on the Cabbibo-Kobayashi-Masakawa Element —Vtb— F. Abe *et al.* (CDF Collaboration), Phys. Rev. Lett. **86**, 3963 (2001).

[45] Measurement of the t-tbar Production Cross Section F. Abe *et al.* (CDF Collaboration), Phys. Rev. **D64**, 032002 (2001).

[46] Measurement of the Top Quark Mass at CDF F. Abe *et al.* (CDF Collaboration), Phys. Rev. **D63**, 032001 (2001).

[47] Measurement of the Helicity of W Boson in Top Quark Decays F. Abe *et al.* (CDF Collaboration), Phys. Rev. Lett. **84**, 216 (2000).

[48] Search for New Particles Decaying to t-tbar in p-pbar Collisions at $\sqrt{s}$ =1.8 TeV F. Abe *et al.* (CDF Collaboration), Phys. Rev. Lett. **85**, 2062 (2000).

[49] Measurement of the Top Quark Mass with the Collider Detector at Fermilab F. Abe *et al.* (CDF Collaboration), Phys. Rev. Lett. **82**, 271 (1999).

[50] Erratum: Measurement of the Top Quark Mass with the Collider Detector at Fermilab F. Abe *et al.* (CDF Collaboration), Phys. Rev. Lett. **82**, 2808 (1999).

[51] Observation of Hadronic W Decays in t-tbar Events with the Collider Detector at Fermilab F. Abe *et al.* (CDF Collaboration), Phys. Rev. Lett. **80**, 5720 (1998).

[52] Measurement of the Top Quark Mass and Production Cross Section from Dilepton Events at CDF F. Abe *et al.* (CDF Collaboration), Phys. Rev. Lett. **80**, 2779 (1998).

[53] Measurement of the t-tbar Production Cross Section in p-pbar Collisions at $\sqrt{s}$ = 1.8 TeV F. Abe *et al.* (CDF Collaboration), Phys. Rev. Lett. **80**, 2773 (1998).

[54] Measurement of the Top Quark Mass F. Abe *et al.* (CDF Collaboration), Phys. Rev. Lett. **80**, 2767 (1998).

[55] Search for FCNC of the Top Quark Decay F. Abe *et al.* (CDF Collaboration), Phys. Rev. Lett. **82**, 2525 (1998).

[56] Search for New Particles Decaying into b-bbar and Produced in Association with W Bosons Decaying into e-nu or mu-nu at the Fermilab Tevatron F. Abe *et al.* (CDF Collaboration), Phys. Rev. Lett. **79**, 3819 (1997).

[57] First Observation of the All-Hadronic Decay of t-tbar pairs F. Abe *et al.* (CDF Collaboration), Phys. Rev. Lett. **79**, 1992 (1997).

2.4 Precision Electroweak Program

2.4.1 Introduction

The comparison of diverse precision experimental measurements to expectations from the Standard Model [1] allows precise tests sensitive to new physics at scales above the electroweak scale, as well as a determination of the Higgs mass within the framework of the model [2]. Global electroweak fits receive contributions from LEP, LEPII and SLC, W mass measurements in $\bar{p}p$ interactions, neutrino neutral current data, and the measurement of the top mass at the Tevatron.

Precision measurement of the top mass and the W mass are primary goals of CDF II. In addition, in the electroweak sector, the W width and leptonic branching ratio, the tri-linear couplings of the W, Z and γ, and the forward-backward charge asymmetry of dileptons at the Z pole and above are important Standard Model parameters. These measurements together will take the global electroweak fit to a new level of precision, and do so completely in the context of a single experiment.

In this section we discuss measurements directly involving the gauge bosons. We begin with a comparison of the the expected event yields of W, Z, and diboson production for Run IIa with 2 fb^{-1} and Run IIb with 15 fb^{-1}, which illustrates the electroweak physics potential (see Table 2.5). We then discuss the CDF Electroweak measurement prospects for Run IIb.

Studies of the Run II sensitivities for Electroweak physics at CDF II, and their competitiveness with LEP-II, LHC and NLC experiments are detailed in the Summary Report of the Workshop on QCD and Weak Boson Physics in Run II [3]. A review of the Run I results on W boson physics can be found in [4].

2.4.2 Impact of Proposed Run IIb Upgrades

Most of the proposed Run IIb upgrades are aimed at maintaining the enhanced detector capabilities that were achieved over Run I by the Run IIa upgrades. Apart from the obvious need to maintain triggering and data acquisition capability in order to record the large data samples, we mention the relevant detector upgrades for electroweak physics.

The momentum measurement from the COT is clearly very important for leptons. At very high instantaneous luminosities, the occupancy in the inner superlayers will hurt pattern recognition and track resolution. The proposed upgrades to the COT inner layers and the silicon detector are both relevant for maintaining track efficiency and quality.

2.4.2.1 Electrons

The detection capabilities for forward electrons and photons were significantly enhanced over Run I by the plug calorimeter and the SVX II+ISL+COT integrated tracking. The charged tracking and momentum information will be better, more efficient, and available over a wider range in η. Plug electrons will significantly improve the yields for W and Z bosons, and allow us to examine some previously inaccessible electroweak physics topics at high η. When considering the purely leptonic decay modes, the acceptance for W bosons is almost doubled, for Z bosons tripled, and for the rarer diboson modes quadrupled by increasing the electron coverage from $|\eta| < 1$ to $|\eta| < 2$. More importantly, the high η leptons and photons provide opportunities for previously inaccessible physics. The high η leptons are very sensitive to physics in the small x region, and the high η leptons and photons are essential to observe the radiation zero in the $W\gamma$ production (see Section 2.4.5).

It is therefore important to preserve the tracking capability to high η. The COT tracking efficiency falls off rapidly beyond $|\eta| \sim 1$. The replacement of the radiation-damaged SVXII with a new silicon detector will maintain tracking capability at high η.

2.4.2.2 Muons

Concerns about the aging and inefficiency of the CSX central muon scintillators have prompted their study and the proposal to eventually replace these counters. These counters are important for triggering and timing of muons and are therefore very important for the electroweak physics goals of Run IIb.

2.4.2.3 Photons

Cosmic rays are a significant background for analyses involving photons and/or $\not\!\!E_T$, such as studies of diboson production. Most electromagnetic showers produced by cosmic rays are out-of-time with the beam crossing. The proposed Run IIb upgrade to add

channel		number of events $\int Ldt = 2$/fb	number of events $\int Ldt = 15$/fb
$W \to e\nu$	(e^c)	1,120,000	8,400,000
$W \to e\nu$	(e^p)	448,000	3,360,000
$W \to \mu\nu$	(μ^c)	672,000	5,040,000
$W \to \mu\nu$	(μ^f)	49,000	368,000
$Z \to ee$	$(e^c, e^{c,p,f})$	146,000	1,095,000
$Z \to \mu\mu$	(μ^c, μ^c)	56,000	420,000
$W\gamma$, $E_T^\gamma > 10$ GeV	$(\gamma^{c,p})$	1,700	12,750
$Z\gamma$, $E_T^\gamma > 10$ GeV	$(\gamma^{c,p})$	509	3,818
$WW \to \ell\nu\ell\nu$		90	675
$WZ \to \ell\nu\ell\ell$		12	90
$ZZ \to \ell\ell\ell\ell$		1.4	10
$WZ \to \ell\nu b\bar{b}$		4	30
$ZZ \to \ell\ell b\bar{b}$		0.5	3

Table 2.5: Expected W, Z, and diboson event yields with 2 fb^{-1} and 15 fb^{-1} when the Run Ib configuration is assumed. c, p, and f for electrons represent Run I CEM, PEM, and FEM, and c and f for muons represent Run I CMU/P and FMU.

timing information to the electromagnetic calorimeter would significantly reduce the cosmic ray background and have a big impact on the sensitivity in diboson analyses. This is exemplified by the $Z\gamma$ coupling measurements in the powerful $Z\gamma \to \nu\nu\gamma$ channel, where photon identification is of paramount importance. With improved photon identification, this channel will become available to CDF in Run IIb.

2.4.3 W Mass

The mass of the W boson is a fundamental parameter of the Standard Model. A direct measurement of M_W can be compared with the prediction from other LEP and SLC results as a test of the SM. In the context of other precise electroweak measurements, direct and precise measurements of M_W and $M_{\rm top}$ provide an indirect constraint on the Higgs boson mass, M_H, via electroweak radiative corrections. The ultimate test of the SM may lie in the comparison of this indirect determination of M_H with its direct observation.

At the Tevatron, the W mass is extracted from a fit to the W transverse mass, M_T^W, and the lepton p_T distributions. The 4 pb^{-1} of the 1988-89 Tevatron Collider run enabled CDF to measure the W mass to be

$$M_W = 79.91 \pm 0.39 \text{ GeV/c}^2 \text{ [6]},$$

and with 19 pb^{-1} from Run Ia CDF measured

$$M_W = 80.41 \pm 0.18 \text{ GeV/c}^2 \text{ [7]}.$$

With 85 pb^{-1} from Run Ib CDF measured

$$M_W = 80.470 \pm 0.089 \text{ GeV/c}^2 \text{ [8]}.$$

The uncertainties in the current Run Ib measurement scale rather well with statistics from the previous measurements; while the difficulty of the measurement has increased, no systematic limitation is yet evident. The fits to the data from Run Ib are shown in Figure 2.21. The uncertainties for the Run Ib measurement are shown in Table 2.6.

Figure 2.20 (a) shows the sensitivity in the M_W-$M_{\rm top}$ plane of the combined CDF W mass measurement of $M_W = 80.433 \pm 0.079$ GeV/c^2 [8] and the top mass measurement $M_{\rm top} = 176.1 \pm 6.6$ GeV/c^2 [5], compared to theoretical predictions based on electroweak radiative corrections [2].

In the Run IIa TDR we made a case that a data set of 2 fb^{-1} will allow CDF II to measure the W mass to ± 40 MeV/c^2, which is comparable to the overall LEP2 expectation ($\sim$ 40 MeV). Figure 2.20 shows the sensitivity in the M_W-$M_{\rm top}$ plane of this estimate when combined with the expected precision $\delta M_{\rm top} = 4$ GeV/c^2 for the same dataset. With a dataset of 15 fb^{-1}, we make the case below that $\delta M_W = 20$ MeV/c^2 (and $\delta M_{\rm top} = 2$ GeV/c^2) is within reach. The precision measurement of the W boson and top quark mass with CDF IIb will allow inference of the Standard Model Higgs boson mass with an uncertainty of $\delta M_H/M_H \sim 30\%$, assuming

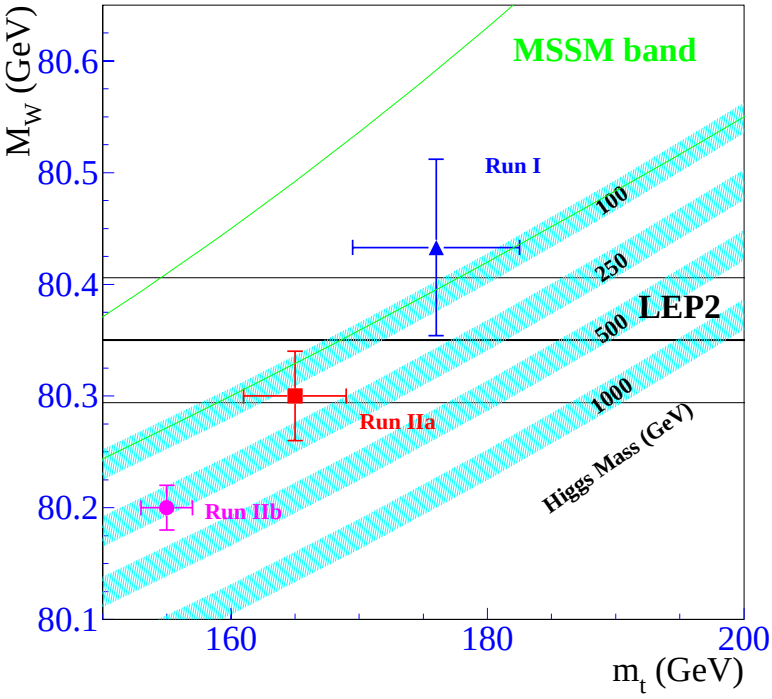

Figure 2.20: The data point labeled "Run I" represents the CDF measurements of M_W and $M_{\rm top}$, and the points labeled "Run IIa" and Run IIb" represent the CDF II estimates for 2 fb^{-1} and 15 fb^{-1}. The curves are from a calculation [2] of the dependence of M_W on $M_{\rm top}$ in the minimal standard model using several Higgs masses. The bands are the uncertainties obtained by folding in quadrature uncertainties on $\alpha(M_Z^2)$, M_Z, and $\alpha_s(M_Z^2)$. Also indicated is the calculation based on a minimal supersymmetric extension of the standard model (MSSM) [9].

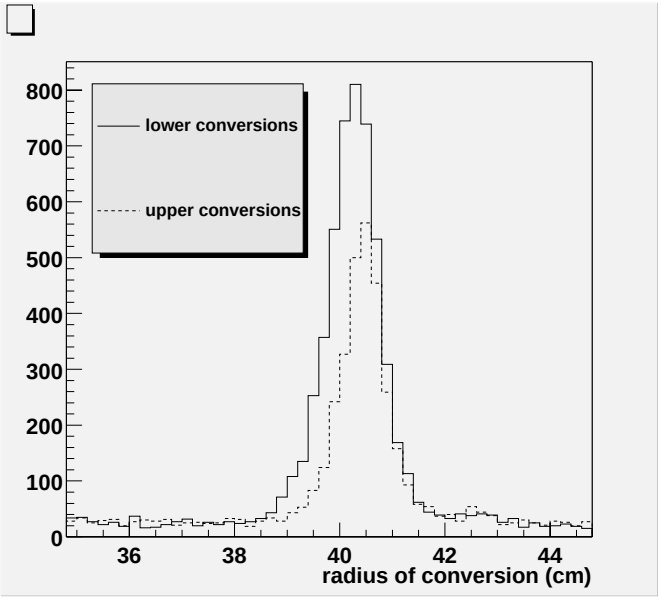

Figure 2.22: The radial distributions for conversions from the Run II commissioning run, in the vicinity of the COT inner wall. An aluminum radiator was attached to the inside of the COT wall on the lower side for calibration.

we will not be limited by the uncertainty in $\alpha(M_Z)$.

For Run II, the statistical uncertainty and most of systematic uncertainties are expected to be reduced significantly compared to Run I. A salient feature of the W mass analyses has been that most of the inputs required for the measurement have been constrained from the collider data. Thus we believe that, with a factor of 7.5 more data, a reduction of the total uncertainty by a factor of 2 is feasible and includes some conservatism. The individual uncertainties are briefly discussed.

2.4.3.1 Statistical Uncertainty

For Run Ib the typical instantaneous luminosity at the beginning of runs was about 2×10^{31} cm^{-2} sec^{-1} and we had about 2.5 extra minimum bias events overlying W and Z events on average. This results in about a 10% loss in statistical precision due to the degraded resolution in the recoil measurement in Run Ib as opposed to Run Ia. For 132 ns operation in Run II the increased number of bunches will more than compensate for the higher luminosity and the number of extra minimum bias events will be to the Run Ia level. This will give us a situation which is better than Run Ib in terms of the statistical power of the data.

2.4.3.2 Track momentum scale and resolution

Scale: Knowledge of material in the tracking volume is of importance in determining the momentum and energy scale. The associated systematics are the uncertainties in the muon energy loss (dE/dx) for the momentum scale and in the radiative shift of the electron E/p peak for the energy scale. Although the amount of material in the tracking volume will be changed we have shown that photon conversions allow us to measure the amount of material in radiation length quite accurately, as illustrated in Figure 2.22 and can reduce the uncertainties on the W mass measurement. During the commissioning run for Run IIa, a precisely-known aluminum radiator

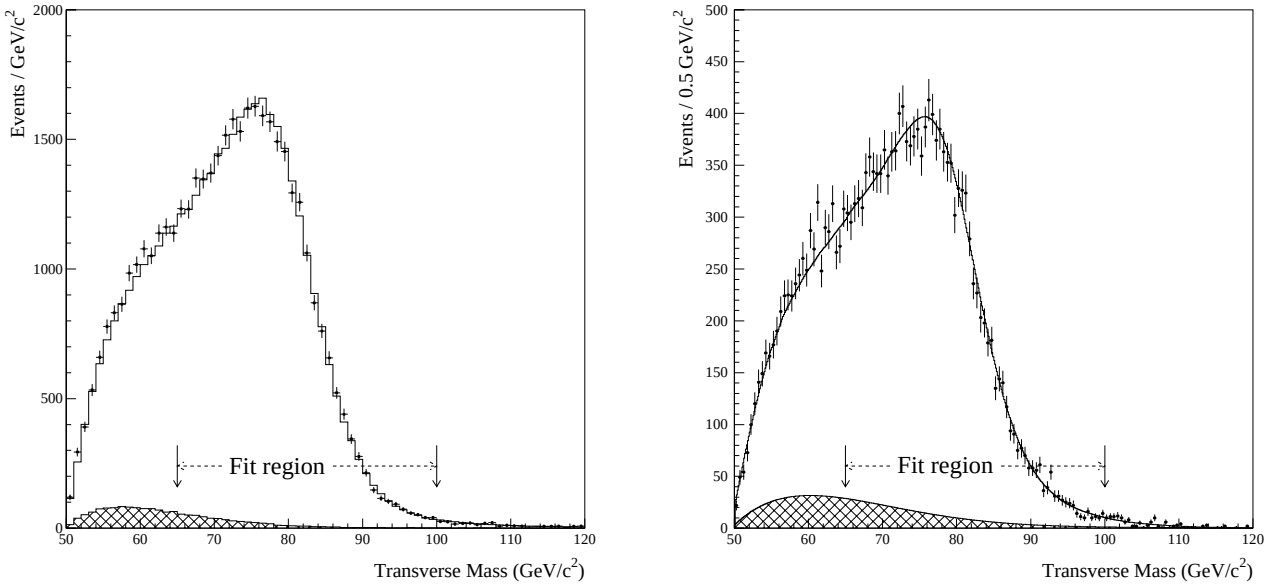

Figure 2.21: Transverse mass distributions and fits for $W \to e\nu$ (left) and $W \to \mu\nu$ (right) from Run Ib.

Source	$W \to e\nu$	$W \to \mu\nu$	common
statistical	65	100	
lepton scale	75	85	
lepton resolution	25	20	
pdfs	15	15	15
p_T^W	15	20	3
recoil	37	35	
higher order QED	20	10	5
trigger, lepton identification bias	-	$15 \oplus 10$	
backgrounds	5	25	
total	92	103	16

Table 2.6: Systematic uncertainties in the W mass (in MeV) in the CDF measurements from the Run 1B data.

Source of Uncertainty	Uncertainty (MeV/c^2)		
	$W \to e\nu$	$W \to \mu\nu$	Common
Statistical	5	8	–
Lepton Energy/Momentum Scale	10	8	8
Lepton Energy/Momentum Resolution	4	3	–
Recoil modeling	3	3	3
Trigger, Event Selection	5	5	–
Backgrounds	5	5	–
p_T^W	5	5	5
PDF	5	5	5
QED radiative corrections	5	5	5
Total Uncertainty	17	17	12
e and μ Combined Uncertainty		15	

Table 2.7: Estimates of uncertainties in the W mass measurement for 15 fb^{-1}.

was placed inside the COT inner wall to provide a calibration reference using conversions.

The dE/dx muon energy loss requires information of the material type in addition to the radiation length. For example, an unknown type of 1% X_o material leads to about 10 MeV uncertainty in the W mass measurement. We have fairly detailed information available on the construction of the Run IIa tracking detectors and do not expect this to be a limitation.

Resolution: It is important to assess the impact of high luminosity running on the track momentum resolution. In Run Ib, the CTC track resolution degraded with luminosity, but could be recovered when SVX hits or the SVX beam position were added to the tracking. For instance, if we compare early Run Ib ($\mathcal{L} \sim 0.2 \times 10^{31}$) to later Run Ib ($\mathcal{L} \sim 1 \times 10^{31}$), the CTC track resolution observed in the width of the J/ψ peak worsens by 35%, but the SVX + CTC track resolution worsens by only 10%. The new tracking system incorporates this linking naturally across all detectors (for $|\eta| \leq 1.0$). It is clearly important here to maintain the tracking capability of the Run IIa SVXII-ISL-COT integrated system.

The M_W uncertainty due to the momentum resolution uncertainty will scale with statistics since the resolution is determined using $Z \to \mu\mu$ events.

2.4.3.3 Calorimeter energy scale and resolution

The dominant uncertainty in the electron energy scale for Run I was from the uncertainty in amount of material in radiation length, and statistics. As described above, the amount of material is expected to be well measured by photon conversion events for Run IIb and the uncertainty should scale with statistics.

The M_W uncertainty due to the energy resolution uncertainty will scale with statistics since the resolution is determined using $Z \to ee$ events.

2.4.3.4 Recoiling energy modeling

The detector response to the recoil energy against W is directly calibrated using $Z \to ee$. Therefore the uncertainty will scale with statistics. For Run II with the muon coverage at high η, $Z \to \mu\mu$ can also be used.

2.4.3.5 W Production model

P_T^W : For the P_T^W spectrum, the P_T^Z distribution from $ee, \mu\mu$ and a new theoretical calculation which includes soft gluon resummation effects and W, Z decays are expected to provide appropriate checks and improved theoretical guidance, and will allow the reduction of the current uncertainty in M_W substantially.

The Run I measurement of $d\sigma/dP_T^Z$ [10] is shown in

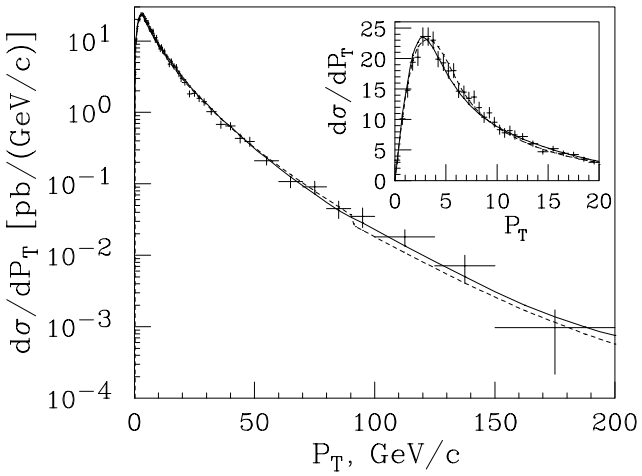

Figure 2.23: The $d\sigma/dp_T$ of e^+e^- pairs in the mass range $66-116$ GeV/c^2. The inset shows the $p_T < 20$ GeV/c region with a linear ordinate. The crosses are the data with all errors included, except the 3.9% luminosity error. The dashed (solid) curve is the EV (Z-only RESBOS) prediction with the cross section normalized to 248 pb.

Fig. 2.23. With 15 fb^{-1} of Run IIb data, the errors in the low P_T^Z region are expected to be 1%, providing a very strong constraint on the theoretical model in the region relevant for the W mass measurement.

Parton Distribution Functions: The Run I uncertainty in PDF's was constrained by the CDF W asymmetry measurement (see Figure 2.24), which will become more precise with statistics. Forward coverage is very important for this measurement since the PDF sensitivity increases with the rapidity coverage. The data in the central region probes the d and u distributions in the x region between 0.02 and 0.15. The forward data probes the region between 0.006 (a new region of x) and 0.35.

However, Monte Carlo studies have shown that the W charge asymmetry does not have the same sensitivity to all aspects of the PDF's as the W mass measurement. Therefore additional measurements are likely to be needed which will constrain PDF's in different ways. The y distributions of Z (y_Z) from dileptons have sensitivity to constrain PDFs, and this may help reducing the PDF uncertainty in M_W. A precise measurement of Z efficiency as a function y_Z in a wide rapidity region is required, which can be measured using the Z sample itself with sufficient statistics. Figure 2.25 shows the Run I measurement [11] of $d\sigma/dy$ for Drell-Yan production. The measurement is completely limited by statistics in Run I, and is likely to remain so even beyond 2 fb^{-1}. For this measurement forward coverage is essential. Similar but additional information on PDF's can be obtained by measuring the lepton rapidity distribution in W decays.

Cross section measurements of Drell-Yan production [12] (especially the low mass region) can be used to get further constraints on PDFs. The Run I Drell-Yan cross section measurements using central electrons are shown in Figure 2.26. The low mass data is sensitive to the very low x region. Run IIb upgrades to the DAQ bandwidth will be important for this program in order to preserve our ability to trigger on low p_T lepton pairs.

The PDF uncertainty can also be reduced by raising the minimum M_T^W for fitting. This will imply a larger statistical uncertainty, and is an example of using the huge Run IIb statistics to reduce systematics and the total uncertainty.

While the PDF uncertainty will warrant attention, it is likely that a program of measurements with collider data will prevent it from dominating the W mass measurement. It should be noted that the combined DØ run I measurement, including the forward calorimeter data, already quotes a PDF uncertainty of 7 MeV [13].

QCD higher order corrections : The effects of higher-order QCD corrections on the W polarization have been calculated at O(α_s^2). The W mass is measured using the low p_T^W sample where the higher order QCD corrections are modest. The uncertainty is negligible in current analyses, and should not be a fundamental problem in the future. This effect has been measured in Run I [14] and the measurement is statistically limited. With Run IIb statistics, a precise measurement of the W polarization as a function of p_T^W will be possible.

QED Radiative corrections : Radiative corrections in M_W are rather large: the shifts in M_W due to the final state radiation are 65 MeV in the $W \to e\nu$ channel and 168 MeV in the $W \to \mu\nu$ channel. For Run Ib, the uncertainty in these shifts due to missing diagrams was estimated to be 20 MeV and 10 MeV for the electron and muon channels respectively. Recently, a more thorough calculation [15] of electroweak radiative W and Z boson production and decay, including initial and final state radiation, fi-

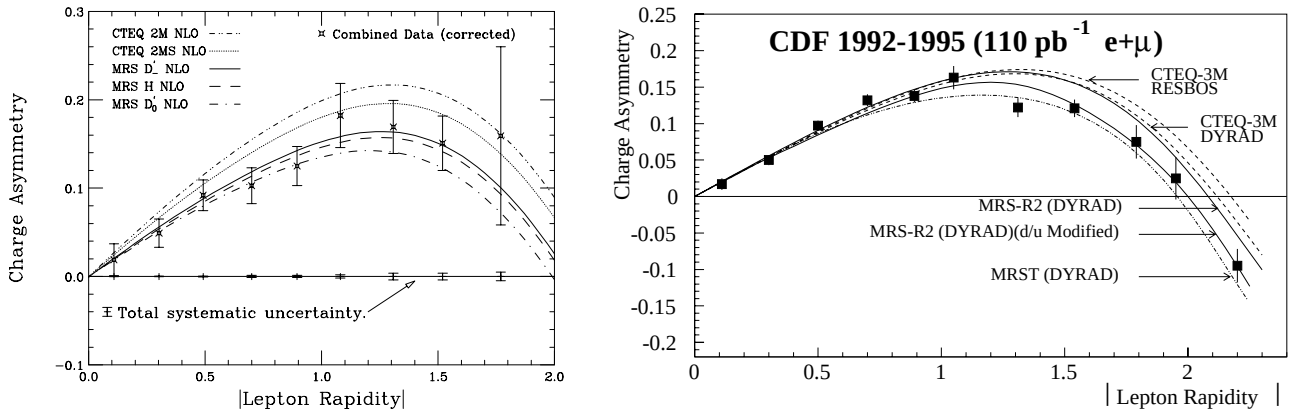

Figure 2.24: Left: Combined Run Ia W charge asymmetry measurement using muons and central and plug electrons. Right: Combined W charge asymmetry using Run Ia and Ib data including the forward muons, showing the effect of the larger rapidity coverage and higher statistics.

nite lepton masses, and finite W, Z width effects. A two-photon calculation is also available [16]. This will make it possible to reduce the error associated with radiative corrections substantially in the future.

2.4.3.6 Backgrounds

The $Z \to \mu\mu$ background (one muon in the central muon chambers and the other muon in high η region) in the $W \to \mu\nu$ sample is the dominant background for this channel and its uncertainty derives from the choice of PDF's and the tracking efficiency at high η. For Run II, the tracking upgrade (well measured ISL+SVXII tracks in the region $1 < |\eta| < 2$) and the forward muon upgrade (muons in the region $1.5 < |\eta| < 3$) together with the muon signature in the plug upgrade calorimeter will remove most of this background and will reduce the uncertainty. This uncertainty does not scale easily with statistics, but forward tracking and muon coverage is clearly very important to control this source of background.

2.4.3.7 Trigger and Selection Bias

For Run Ib, there was a 15 MeV uncertainty due to a possible momentum dependence of the muon triggers in the $W \to \mu\nu$ channel. The measurement of the momentum dependence was statistically limited. The muon selection is also possibly affected by the presence of nearby jets.

For Run IIb, it is important to maintain unbiased triggers. That is, the momentum thresholds should be low enough not to introduce a P_T or E_T dependence above 25 GeV. Also, the lepton selection should not be biased by hadronic activity. This means we must maintain high tracking efficiency as the luminosity increases.

2.4.3.8 W mass summary

We make a conservative estimate that 15 fb^{-1} will allow CDF II to measure the W mass to ± 20 MeV/c^2, which will be a significant improvement over the Run IIa measurement and the world average, giving the Tevatron the leading role in the measurement of this important parameter. Coupled with a commensurate improvement in the top mass precision, this will give the Tevatron the dominant position in constraining the Higgs mass. The estimates of individual uncertainties is shown in Table 2.7.

2.4.4 W Width

The leptonic branching ratio of the W may be inferred from the ratio $R = \sigma \cdot Br(W \to l\nu)/\sigma \cdot Br(Z \to ll)$, using LEP measurements for the Z couplings and a theoretical prediction of the production cross section ratio. It provides a standard model consistency check. For Run Ia [17] CDF measured $Br(W \to e\nu) = 0.109 \pm 0.0033(\text{stat}) \pm 0.0031(\text{syst})$. If one further assumes standard couplings for $W \to e\nu$, one can derive a value for the total width of the W boson, $\Gamma_W = 2.064 \pm 0.0060(\text{stat}) \pm 0.0059(\text{syst})$ GeV. The theoretical uncertainty in the cross section ratio is expected to limit precision to about $\pm 1\%$. However, the upgraded momentum measurement in the region $1 < |\eta| < 2$ should give improved acceptance

systematics, reducing the dependence on the parton distribution functions.

The W width can be measured directly from the shape of the transverse mass distribution (see Figure 2.27). For $M_T^W > 100$ GeV/c^2 resolution effects are under control and using Run Ib in the modes $W \to e\nu$ and $W \to \mu\nu$, CDF measured $\Gamma_W = 2.04 \pm 0.11(\text{stat}) \pm 0.09(\text{syst})$ GeV [19]. The direct measurement of the W width closely follows the measurement of the W mass. The uncertainties will likely scale with statistics allowing a ± 15 MeV measurement for 15 fb^{-1}, much better than the LEP2 expectation of ± 200 MeV, and providing a stringent test of the standard model.

2.4.5 Gauge Boson Couplings

The Standard Model makes specific predictions for the trilinear couplings of the gauge bosons, W, Z, and γ. The nature of these couplings can be investigated via studies of $W\gamma$ and $Z\gamma$ production [20] and WW, WZ and ZZ pair production [21]. The major goals of these studies will be testing the Standard Model prediction(s) and searching for new physics. The Run I results are summarized in Table 2.8 (see also [3] for details).

$W\gamma$ production in $p\bar{p}$ collisions is of special interest due to the SM prediction of a radiation amplitude zero in the charge-signed $Q_W \cdot \cos\theta^*_\gamma$ distribution at ~ -0.3. The radiation zero is also predicted to manifest itself as a "channel" in the charge-signed $Q_W\eta_\ell$ *vs.* $Q_W\eta_\gamma$ 2-dimensional distribution [22], and as a strong "dip" in the charge-signed photon-W decay lepton rapidity difference distribution, $Q_W \cdot (\eta_\gamma - \eta_\ell)$ at ~ -0.3.

By using central and plug electrons and photons, it will be possible in Run IIa to conclusively establish the dip in the photon lepton rapidity difference distribution. On the other hand, for central electrons and photons only, the dip is not statistically significant with Run IIa statistics and will benefit from Run IIb statistics. Also, the increased statistics will help to measure the location of the dip more precisely and provide a better test of the standard model prediction.

Backgrounds from electromagnetic showers induced by cosmic rays are important for diboson analyses. For example, a $W \to e\nu$ event with a cosmic ray would look like a $W\gamma$ event with anomalous $\not\!\!E_T$. Similarly, a $Z \to ee$ event with an overlapping cosmic ray would give an $ee\gamma\not\!\!E_T$ signature. The process $p\bar{p} \to Z^0(\to \nu\bar{\nu}) + \gamma + X$ has large cosmic ray backgrounds. Sensitivity to $Z\gamma$ anomalous couplings is statistics-limited and this channel has the advantage over the $\ell^+\ell^-\gamma$ channel by a factor of 3 in the branching ratio, and almost a factor of 2 in the acceptance. The DØ experiment has taken advantage of its pointing calorimeter to control cosmic ray backgrounds, and has produced the best $Z\gamma$ measurement by using the $\gamma\not\!\!E_T$ channel [23]. By using the EM calorimeter timing information provided by the proposed Run IIb upgrade, the cosmic ray background can be controlled much better and the sensitivity of these diboson analyses will increase significantly.

For Run II, we anticipate that the current results from CDF will undergo further significant improvements with 15 fb^{-1} integrated luminosity, in conjunction with the Run II upgrades of the overall tracking, calorimeter, muon and DAQ systems. Since the acceptance for diboson events increases rapidly with rapidity coverage, it is important to maintain this capability through Run IIb to fully exploit the increased luminosity. The sensitivity for WWV and $ZZ\gamma$ anomalous coupling is limited by the statistics of backgrounds and potential signal and therefore benefits from larger data sizes, improving as $N^{1/4}$. The CDF IIb measurements with 15 fb^{-1} (see Table 2.9) are anticipated to surpass those from LEP-II experiments. The Tevatron also has a significant advantage over LEP-II because the Tevatron can produce all the three ($W\gamma$, WW and WZ) final states and therefore obtain independent sensitivity to the different couplings with fewer assumptions.

In addition to the increased sensitivity to anomalous couplings through potential excesses in the data, 15 fb^{-1} of integrated luminosity makes it possible to *measure* all the diboson production cross sections with good precision. This is particularly true for the WW, WZ and ZZ cross sections which are statistically limited even with 15 fb^{-1} (see Table 2.5). The precise measurements of these cross sections means that we will also be sensitive to *deficits* compared to the predicted cross sections. This will add a whole new dimension to diboson physics and new physics searches, which makes a strong case for going beyond 2 fb^{-1} and acquiring 15 fb^{-1} of data.

The statistics of Run IIb will also make possible for the first time a study of two new diboson channels, $WZ \to l\nu b\bar{b}$ and the ZZ final state. The former channel is very important to understand as a background

Mode ($\ell = e, \mu$)	Luminosity (pb^{-1})	Anomalous Coupling limit (95% C.L.)
$W\gamma \to \ell\nu, \gamma$	20	$-0.7 \leq \lambda \leq 0.7$, $-2.2 \leq \Delta\kappa \leq 2.3$
$WW \to$ dilepton	108	$-0.9 \leq \lambda \leq 0.9$, $-1.0 \leq \Delta\kappa \leq 1.3$
WW and $WZ \to$ leptons + jets	19.6	$-0.81 \leq \lambda \leq 0.84$, $-1.11 \leq \Delta\kappa \leq 1.27$
$Z \to \ell\ell\gamma$	20	$-3.0 \leq h_{30}^{Z} \leq 3.0$, $-0.7 \leq h_{40}^{Z} \leq 0.7$

Table 2.8: 95% C.L. Anomalous gauge boson coupling limits achieved in Run I analyses by the CDF Collaboration.

Mode	Luminosity (fb^{-1})	Anomalous Coupling limit (95% C.L.)
Combined $W\gamma, WW$ and WZ	2	$-0.086 \leq \lambda \leq 0.090$, $-0.12 \leq \Delta\kappa \leq 0.19$
Combined $W\gamma, WW$ and WZ	15	$-0.052 \leq \lambda \leq 0.054$, $-0.073 \leq \Delta\kappa \leq 0.115$
$Z\gamma \to ll\gamma$	15	$-0.045 \leq h_{30}^{Z} \leq 0.045$, $-0.0027 \leq h_{40}^{Z} \leq 0.0027$
$Z\gamma \to \nu\nu\gamma$	15	$-0.019 \leq h_{30}^{Z} \leq 0.019$, $-0.0014 \leq h_{40}^{Z} \leq 0.0014$

Table 2.9: 95% C.L. Anomalous gauge boson coupling limits that might be achieved in run IIb.

to the WH channel for the Higgs search.

2.4.6 Forward-Backward Z Asymmetry

The presence of both vector and axial-vector couplings of electroweak bosons to fermions in the process $q\bar{q} \to Z^0/\gamma \to e^+e^-$ gives rise to an angular asymmetry, "Forward-Backward Asymmetry", in the emission angle of the electron in the rest frame of the electron-positron pair. This asymmetry, A_{FB}, is a direct probe of the relative strengths of the vector and axial-vector couplings over the range of Q^2 being considered. In addition, A_{FB} constrains the properties of any hypothetical heavy neutral gauge bosons not included in the Standard Model. For values of Q^2 significantly larger than M_Z^2, A_{FB} is predicted to be large and positive (approximately 0.5), which makes it sensitive to deviations induced by new physics.

From $\sim$110 pb^{-1} of the Run I dielectron data, CDF has measured[24] A_{FB} to be 0.070 ± 0.016 using a sample of 5463 events in the Z pole region defined by $75 < M_{ee} < 105$ GeV, and 0.43 ± 0.10 using a sample of 183 events in the high mass region defined by $M_{ee} > 105$ GeV. These measurements can be compared with the Standard Model predictions of 0.052 ± 0.002 and 0.528 ± 0.009. Table 2.10 summarizes our measured values for A_{FB} and its uncertainties in both invariant mass regions. The statistical errors are dominant, and the sources of systematic uncertainty (from background level determination and electron pair mass resolution) are expected to scale with statistics as well. This means that these measurements will benefit from increased statistics even beyond 15 fb^{-1}.

In the vicinity of the Z^0 pole it will be possible to extract a precision measurement of $\sin^2\theta_W^{eff}$ from A_{FB}. The uncertainty in $\sin^2\theta_W^{eff}$ should also scale with statistics since A_{FB} is proportional to $(\sin^2\theta_W^{eff} - 0.25)$. Under the assumption that all uncertainties scale with statistics, we expect an uncertainty in A_{FB} of 0.001 and an uncertainty in $\sin^2\theta_W^{eff}$ of 0.0004 with 15 fb^{-1}. The theoretical uncertainty in A_{FB} due to parton distribution uncertainty should be below 0.001, and with further improvements in PDF's should not pose a limitation.

It should be noted that if $\sin^2\theta_W^{eff}$ is measured to within 0.0004 as expected, then the CDF IIb result will improve upon the LEP I and SLD results which measure $\sin^2\theta_W^{eff}$ from jet charge asymmetries in hadronic Z^0 decays with an uncertainty of ~ 0.001. Since the initial and final states are reversed in the two cases, the systematics are also different.

Well above the Z^0 pole, for electron pairs with invariant mass in excess of 105 GeV/c^2, A_{FB} is dominated by Z^0/γ interference, and a large positive value is predicted for A_{FB} with a very flat dependence in electron pair invariant mass. There can be strong variations in A_{FB} with invariant mass due to a variety of exotic physics at higher invariant mass scales, including most Z' or composite Z models [25], and also lepton compositeness models, exchange of lep-

	75 GeV/c^2 < M$_{ee}$ < 105 GeV/c^2		M$_{ee}$ > 105 GeV/c^2	
	CC	CP	CC	CP
Raw event sample	2602	2861	98	85
Background	0^{+2}_{-0}	110 ± 36	1^{+2}_{-1}	1^{+21}_{-1}
Predicted Asymmetry	0.052±0.002		0.528±0.009	
Measured Asymmetry	0.070±0.016		0.43±0.10	
Uncertainty in A$_{FB}$				
Statistical	0.015		0.08	
Background subtraction	0.002		0.04	
Mass Deconvolution	0.003		0.03	
Total uncertainty	0.016		0.10	

Table 2.10: Run I (110 pb^{-1}) measurements of A_{FB}.

toquarks or R-parity violating SUSY particles, and extra dimensions. Moreover, if new physics is discovered at CDF II, A$_{FB}$ measurements will provide discrimination between various models.

As with the measurements of A$_{FB}$ at the Z^0 pole, we expect the uncertainty in the measurements above the Z^0 pole to scale with statistics compared to the Run I measurement [24]. For electron pairs with invariant mass between 105 GeV/c^2 and 195 GeV/c^2, we expect to collect approximately 20,000 events with 15 fb^{-1}. Using this entire sample we expect to measure A$_{FB}$ to within 0.007. For electron pairs with invariant mass above 195 GeV/c^2 (above the LEP 200 maximum $\sqrt{s}$), we expect to collect approximately 2,000 events, which should allow a measurement of A$_{FB}$ to within 0.025. Parton distribution function uncertainty will not significantly affect this sensitivity.

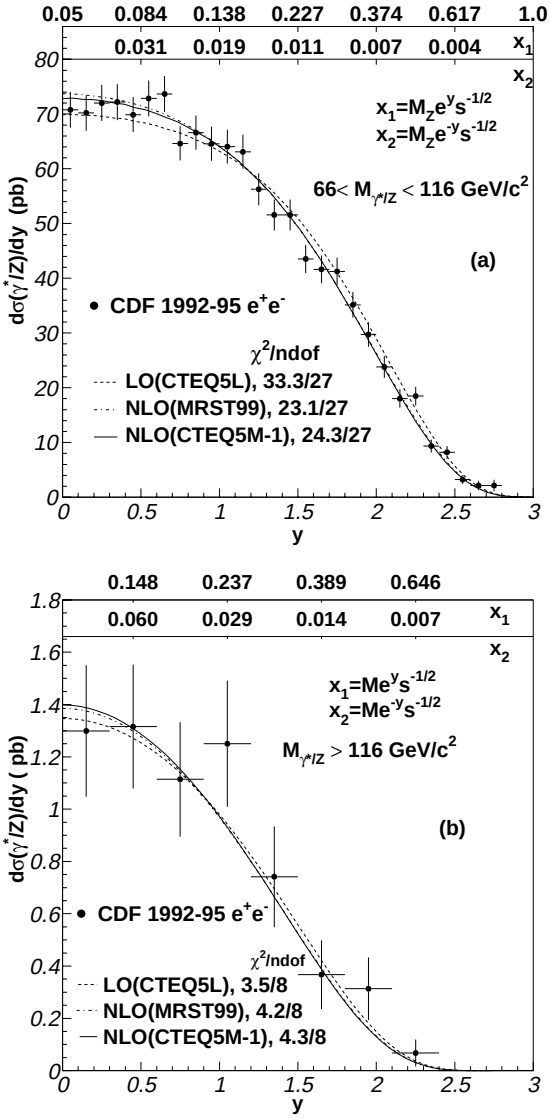

Figure 2.25: $d\sigma/dy$ distributions of e^+e^- pairs in (a) the Z boson mass region, and b the high mass region. The error bars on the data include statistical errors only. The theoretical predictions have been normalized to the data in the Z boson mass region. The top horizontal axes on the figures are the corresponding values of x_1 and x_2 as a function of y. The M used to obtain x_1 and x_2 in (b) is the mean mass over the bin.

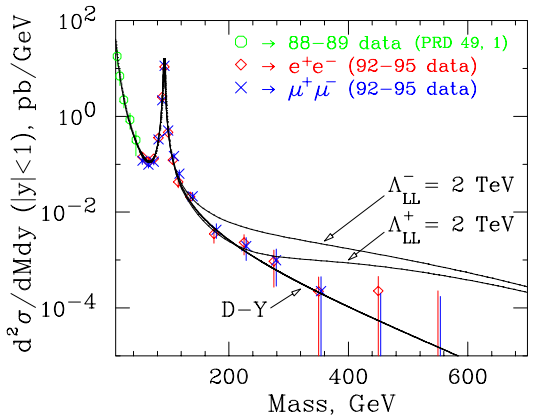

Figure 2.26: Drell-Yan dilepton $(e^+e^-, \mu^+\mu^-)$ production cross section from Run I as a function of the dilepton invariant mass. Also shown are expectations from compositeness models.

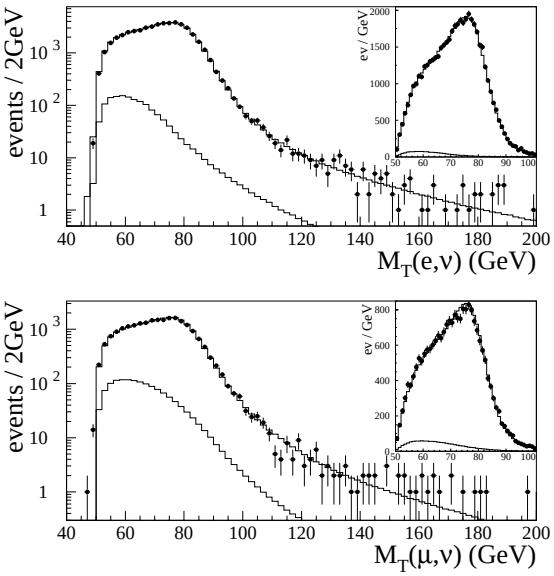

Figure 2.27: Run Ib transverse mass distributions (filled circles) for $W \to e\nu$ (upper) and $W \to \mu\nu$ (lower), with best fit Monte Carlo fits superimposed as a solid curve. The lower curve in each plot shows the sum of the estimated backgrounds. Each inset shows the 50-100 GeV region on a linear scale.

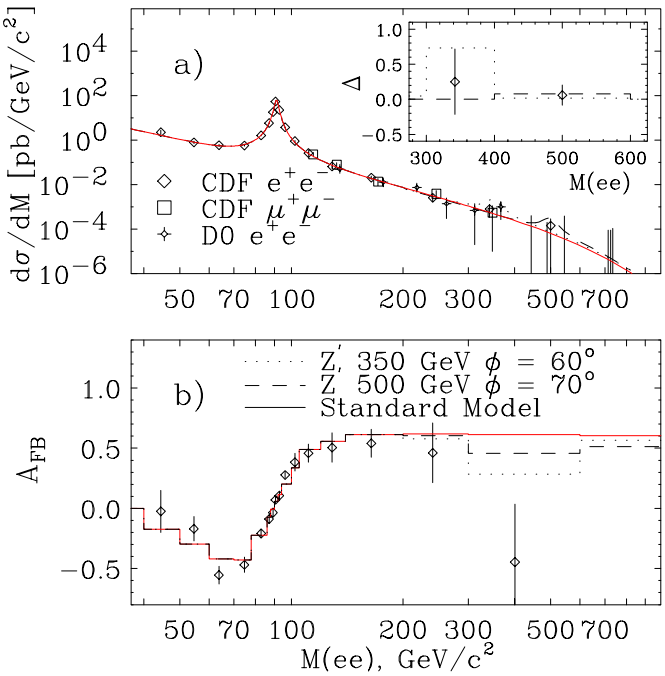

Figure 2.28: (a) $d\sigma/dM$ distribution of e^+e^- and $\mu^+\mu^-$ pairs. All errors (except for the overall 3.9% luminosity error) have been combined in quadrature. The standard model theoretical predictions (solid lines) have been normalized to the data in the Z boson mass region. Also shown are the e^+e^- measurements from DØ. (b) A_{FB} versus mass compared to the standard model expectation (solid line). Also, predicted theoretical curves for $d\sigma/dM$ and A_{FB} with an extra E_6 Z' boson (width of 10%) with $M_{Z'} = 350$ GeV (dotted line) and 500 GeV (dashed line). The inset in (a) shows the difference, "Δ" in fb/GeV/c^2, between the CDF e^+e^- $d\sigma/dM$ data and the standard model prediction (on a linear scale) compared to the expectation from these two Z' models.

Bibliography

[1] S. L. Glashow, Nucl. Phys. **22**, 579 (1961); S. Weinberg, Phys. Rev. Lett. **19**, 1264 (1967); A. Salam, in *Elementary Particle Theory: Relativistic Groups and Analyticity*, ed. N. Svartholm (Almqvist and Wiksell, Stockholm, 1968), p. 367.

[2] G. Degrassi *et al.* Phys. Lett. B **418**, 209 (1998); G. Degrassi, P. Gambino, and A. Sirlin, Phys. Lett. B **394**, 188 (1997).

[3] Summary Report of the Fermilab Workshop on QCD and Weak Boson Physics in Run II, Fermilab-Pub-00/297, November 2000.

[4] R. Thurman-Keup, A. V. Kotwal, M. Tecchio and A. Byon-Wagner, Rev. Mod. Phys. 73, 267 (2001).

[5] T. Affolder *et al.* (CDF Collaboration), Phys. Rev. D **63**, 032003 (2001); B. Abbott *et al.* (D0 Collaboration), Phys. Rev. D **60**, 052001 (1999).

[6] F. Abe *et al.*(CDF), Phys. Rev. **D43**, 2070 (1991).

[7] F. Abe *et al.*(CDF), Phys. Rev. Lett. **75**, 11, (1995); Phys. Rev. **D52**, 4784 (1995).

[8] T. Affolder *et al.*(CDF), Phys. Rev. **D64**, 052001 (2001).

[9] P. Chankowski *et al.*, Nucl. Phys. **B417**, 101 (1994); D. Garcia and J. Sola, Mod. Phys. Lett. A **9**, 211 (1994); A. Dabelstein, W. Hollik and W. Mosle, in *Perspectives for Electroweak Interactions in e^+e^- Collisions*, ed. by B. A. Kniehl (World Scientific, Singapore, 1995) p. 345; D. Pierce *et al.*, Nucl. Phys. **B491**, 3 (1997).

[10] T. Affolder *et al.* (CDF), Phys. Rev. Lett. **84**, 845 (2000).

[11] T. Affolder *et al.*(CDF), Phys. Rev. **D63** 011101 (2001).

[12] F. Abe *et al.*(CDF), Phys. Rev. **D49**, R1 (1994).

[13] B. Abbott *et al.*(DØ), Phys. Rev. Lett. **84**, 222 (2000); Phys. Rev. **D62**, 092006 (2000).

[14] B. Abbott *et al.*(DØ), Phys. Rev. **D63**, 072001 (2001).

[15] U. Baur, S. Keller and D. Wackeroth, Phys. Rev. **D59**, 013002 (1999).

[16] U. Baur and T. Stelzer, Phys. Rev. **D61**, 073007 (2000).

[17] F. Abe *et al.*(CDF), Phys. Rev. Lett. **73**, 220 (1994).

[18] F. Abe *et al.*(CDF), Phys. Rev. **D50**, 5550 (1994).

[19] T. Affolder *et al.*(CDF), Phys. Rev. Lett. **85**, 3347 (2000).

[20] F. Abe, *et al.*, The CDF Collaboration, Phys. Rev. Lett. **74**, 1936 (1995); F. Abe, *et al.*, The CDF Collaboration, Phys. Rev. Lett. **74**, 1941 (1995).

[21] F. Abe, *et al.*, The CDF Collaboration, Phys. Rev. Lett. **75**, 1017 (1995); F. Abe, *et al.*, The CDF Collaboration, Phys. Rev. Lett. **78**, 4537 (1997).

[22] U. Baur, S. Errede and G. Landsberg, Phys. Rev. D**50**, 1917 (1994).

[23] DØ Collaboration, S. Abachi *et al.*, Phys. Rev. Lett. **78**, 3640 (1997).

[24] F. Abe *et al.* (CDF), Phys. Rev. Lett. **77**, 2616 (1996); T. Affolder *et al.* (CDF), hep-ex/0106047, submitted to PRL.

[25] J. L. Rosner, Fermilab Report No. FERMILAB-PUB-95/394-T.

[26] F. Abe *et al.*(CDF), Phys. Rev. Lett. **74**, 850 (1995).

2.5 Search for New Phenomena

2.5.1 Introduction

The Standard Model is widely believed to be incomplete. Indeed, precision electroweak data, combined with the direct search limit from LEP for the Higgs (H^0), are moderately inconsistent.[1, 2] Strong theoretical arguments suggest that new physics should emerge at the scale of electroweak symmetry breaking, for example in scenarios invoking supersymmetry, new strong dynamics, or large extra-dimensions.

If we assume that no discoveries are made in the 2 fb^{-1} Run IIa, nevertheless an order of magnitude increase in integrated luminosity will greatly extend the discovery potential of CDF II. This is despite the fact that, as illustrated in Figure 2.29, the reach in mass grows only logarithmically with integrated luminosity. However, numerous models have been suggested that predict new phenomena at a scale accessible at the Tevatron– for example in models of supersymmetry [3, 4, 5, 6, 7, 8], technicolor [9], gauged flavor symmetries[10], and large extra dimensions [11, 12, 13]. However, in many cases small branching ratios for experimentally viable signatures make detection difficult. In this situation one gains as the square-root of the integrated luminosity. Thus, a large discovery potential for CDF II exists in a high-luminosity Tevatron run.

The situation is well illustrated by the case of supersymmetry in a supergravity (SUGRA) scenario. As part of the Physics at Run II Workshop [14], the SUGRA working group studied five choices of SUGRA parameters (for details, see reference [15].) In SUGRA models, charginos and neutralinos tend to be light (100-200 GeV range) and therefore $\tilde{\chi}\tilde{\chi}$ pair production cross sections tend to dominate. This is illustrated in Table 2.11, where $\tilde{\chi}\tilde{\chi}$ production is dominant for all cases except the fourth where there is a large $\tilde{t}$-pair cross section. An effective search strategy in SUGRA models is therefore to look for tri-lepton final states.[19] However, tri-lepton final states, which might arise from three-body decays (e.g. $\tilde{\chi}_1^{\pm} \to \ell\nu_\ell\tilde{\chi}^0$) or leptonic decays of the τ (particularly in large $\tan\beta$ models such as cases 2,3,5), result in rather small signal cross sections (see Table 2.12). The Standard Model backgrounds from this study are shown in Table 2.13. Whereas with 2 fb^{-1} only case 1 is observable at the 3σ level in the tri-lepton channel, with 15 fb^{-1} all cases except case 4 are observable at this level in this channel.

Table 2.11: Parameter space choices, sparticle masses and total signal cross sections for the five chosen case studies of the mSUGRA group. The total cross section and fractional contribution to the signal from various subprocesses in the five parameter space cases of reference [15].

case	(1)	(2)	(3)	(4)	(5)
σ_{tot}(fb)	404	653	2712	3692	1393
$\tilde{g},\tilde{q}(\%)$	4.3	6.6	50.4	66.2	0.01
$\tilde{g}\tilde{\chi},\tilde{q}\tilde{\chi}(\%)$	2.4	3.6	2.9	1.2	0.01
$\tilde{\chi}\tilde{\chi}(\%)$	85.0	85	45.7	32.6	99.5
$\tilde{l}\tilde{l}(\%)$	8.3	4.7	1.0	0.04	0.4
$\tilde{t}\tilde{t}(\%)$	1.8	1.5	41	65	0.01
$\tilde{\chi}_1^{\pm}\tilde{\chi}_2^0(\%)$	43.8	45	26.5	18	16.7
$\tilde{\chi}_1^{\pm}\tilde{\chi}_1^{\pm}(\%)$	33.5	33	17.6	13	24.6

Table 2.12: The 3ℓ signal (fb) in 5 parameter points (adapted from [15]) The lepton p_T thresholds are 11,7, and 5 GeV.

case	σ fb
(1)	7.39 ± 0.12
(2)	0.93 ± 0.06
(3)	1.08 ± 0.12
(4)	2.72 ± 0.23
(5)	0.63 ± 0.07

An additional analysis was performed for sensitivity in a more general minimal SUGRA model with essentially the same cuts.[15] As shown in Figure 2.30, the reach increases significantly for a high luminosity run (here taken as 30 fb^{-1}).

2.5.2 Generic exotic signatures and the CDF II upgrade

The search for new phenomena looks for any deviation from Standard Model expectations. However, guided by theory, historical precedent (e.g. high p_T leptons), and sometimes serendipity (e.g. the CDF $ee\gamma\gamma\not\!\!E_T$ candidate event), certain generic signatures emerge: missing transverse momentum($\not\!\!E_T$), high-p_T leptons (e,μ), multi-leptons, high-p_T jets, displaced vertices, high-p_T photons, hadronic τ-decays, and highly-ionizing particles. The CDF upgrade has been designed to detect these objects with precision and efficiency.

Certain aspects of the Run IIb upgrade are needed

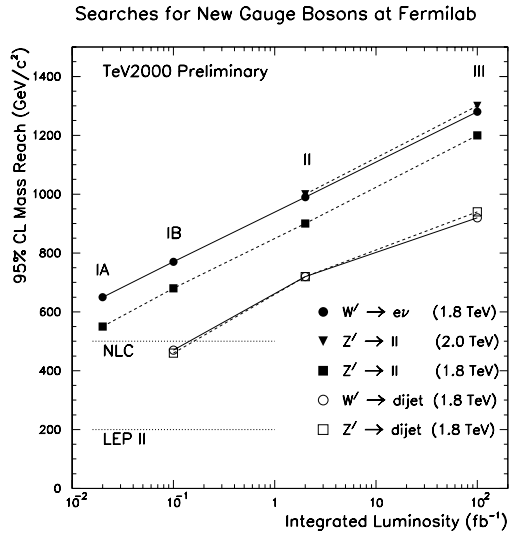

Figure 2.29: The expected mass reach, defined as the 95% C.L. lower limit on the mass vs. integrated luminosity at the Tevatron for searches for new gauge bosons. The potential to discover increasingly heavy objects grows only logarithmicly with luminosity.

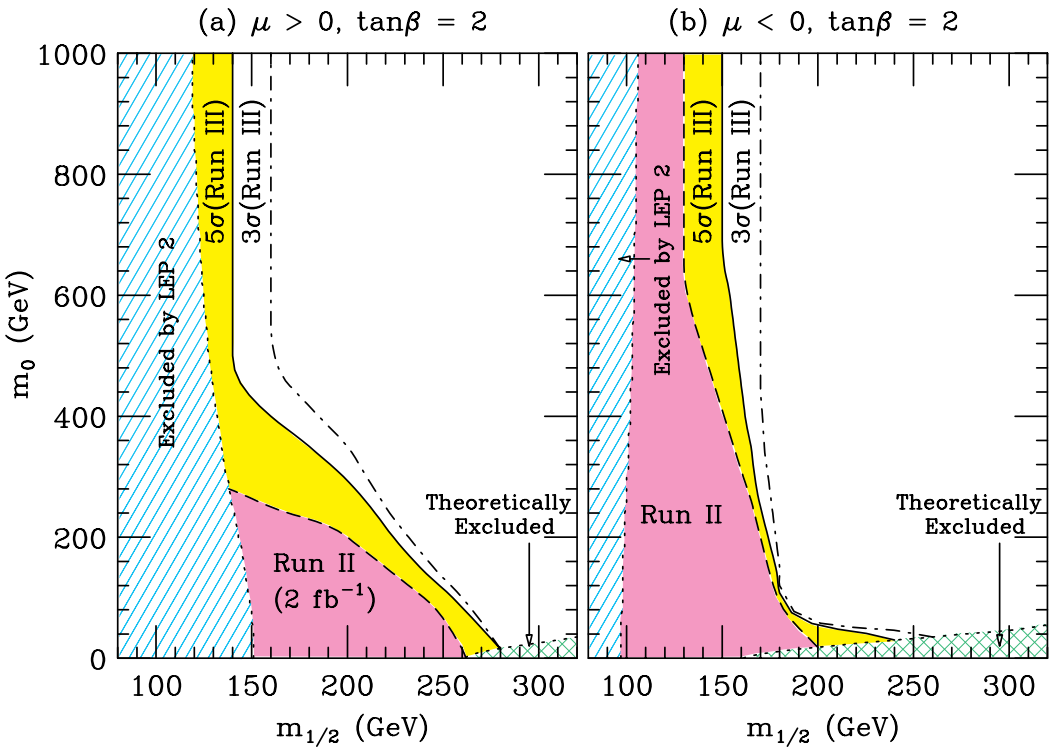

Figure 2.30: The contours of 99% C.L. observation at Run II and 5σ discovery as well as 3σ observation at Run III (30 fb^{-1}) for $p\bar{p} \to$ SUSY particles $\to 3\ell + X$ with soft lepton cuts in the $(m_{1/2}, m_0)$ plane, for $\tan\beta = 2$, (a) $\mu > 0$ and (b) $\mu < 0$. (from reference [15])

Table 2.13: SM backgrounds (fb) for low-p_T trileptons as defined in reference [15] ("soft B" cuts). (adapted from [15])

BG	σ fb
$\ell'\nu'\ell\bar{\ell}$	0.45 ± 0.003
$\ell\nu\ell\bar{\ell}$	0.20 ± 0.004
$\ell\nu\tau\bar{\tau}$	0.36 ± 0.008
$\tau\nu\ell\bar{\ell}$	0.13 ± 0.008
$\ell\ell\tau\bar{\tau}$	0.06 ± 0.001
$t\bar{t}$	0.06 ± 0.004
total	1.26
99% C.L.(2 fb^{-1})	2.5
3σ(2 fb^{-1})	2.38
3σ(15 fb^{-1})	0.87

to maintain CDF's excellent performance in the high luminosity environment. Precision tracking is clearly critical, not only for lepton detection and photon discrimination, but for identification of primary and secondary vertices. Thus the silicon detector, which will discriminate between multiple primary vertices along the interaction region, and detect secondary vertices with high efficiency and precision, is essential for the exotics program. In addition, the 'projective' modification of the inner layers of the COT will allow for continued high-efficiency tracking in the central rapidity ($|\eta| < 2$) region. Of critical importance is the ability to trigger on muons. This capability depends on scintillator timing in addition to stub finding in the muon drift chambers. In the intermediate rapidity range, this timing is provided by the CSX scintillators. These counters will need to be replaced for the high-luminosity run.

Several of the proposed upgrades will significantly enhance the performance of the detector for Run IIb in ways highly relevant to exotic searches. The addition of stereo information to the Level 1 trigger will have a major impact on signatures with multiple, low-*pt* leptons or displaced vertices. The additional Z information should significantly reduce fake rates. In addition, because Level 1 tracks are available for the Level 2 decision, this upgrade will allow for enhanced Level 2 track-based triggers, for example one based on a multi-track mass. This is illustrated in Figure 2.31 for the dimuon J/ψ trigger. In this case the additional stereo information allows the application of a mass cut which dramatically reduces the trigger rate. Stereo tracking at the trigger level will also impact the Level 1 track trigger (Track Trigger module) which is primarily aimed at selecting hadronic decays of B hadrons. Currently this module looks for pairs of tracks. We are proposing an upgrade to the Track Trigger module that will additionally trigger on three tracks. This upgrade is primarily designed to maintain the capability for triggering on displaced vertices in a high luminosity environment.

The proposal to add timing information to the readout of the central and plug Electromagnetic calorimeters will significantly enhance our capability to do physics with photons. This timing information will already be available for the hadron calorimeters in Run IIa (central hadronic timing was available in Run I); it is critical in removing noise hits as well as identifying cosmic rays. However, the hadron timing is obviously ill-suited for the timing of electromagnetic particles. In current searches for extremely rare events, cosmic ray backgrounds remain a problem. Additionally, the timing will ensure that all photons are from the primary interaction. This will be essential at high luminosity with multiple interactions (mean ~ 5) per crossing. This situation is illustrated by the $ee\gamma\gamma\not\!\!E_T$ candidate event, where the hadron calorimetry timing was available for one electron and one photon in the event (see Figure 2.32). [20] In this case, both electron and photon are both consistent with the (unoptimized) 4 ns resolution. The cosmic rays background, uniform in time, is also shown. However, no timing information is available for the plug electron candidate or the second photon. The instrumentation of the electromagnetic calorimetry with timing both for central and plug calorimeters will allow timing for all electromagnetic clusters. Additionally, a 1 ns resolution is achievable with calibration. This capability would allow for searches of long-lived particles predicted in some models of gauge-mediated supersymmetry decaying to photons.

2.5.3 Illustrative signatures in specific models

Beginning with the Tev-2000 Workshop in 1996 [21] and continuing through the more recent Physics at Run II set of workshops sponsored by Fermilab[14], a great deal of effort has gone into studying the physics potential of a high-luminosity Tevatron run. For example, the Physics at Run II workshop identified 25 distinct channels with significant discovery potential

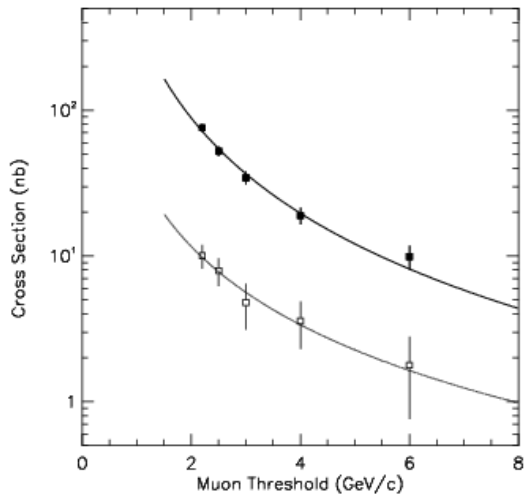

Figure 2.31: Dimuon trigger cross section vs. muon trigger p_T threshold in Run I. Solid points are for tightly matched, opposite-charge pairs. The open squares are the rates with a mass cut as would be available from the proposed Level 1 track upgrade. The fits are to a power-law form.

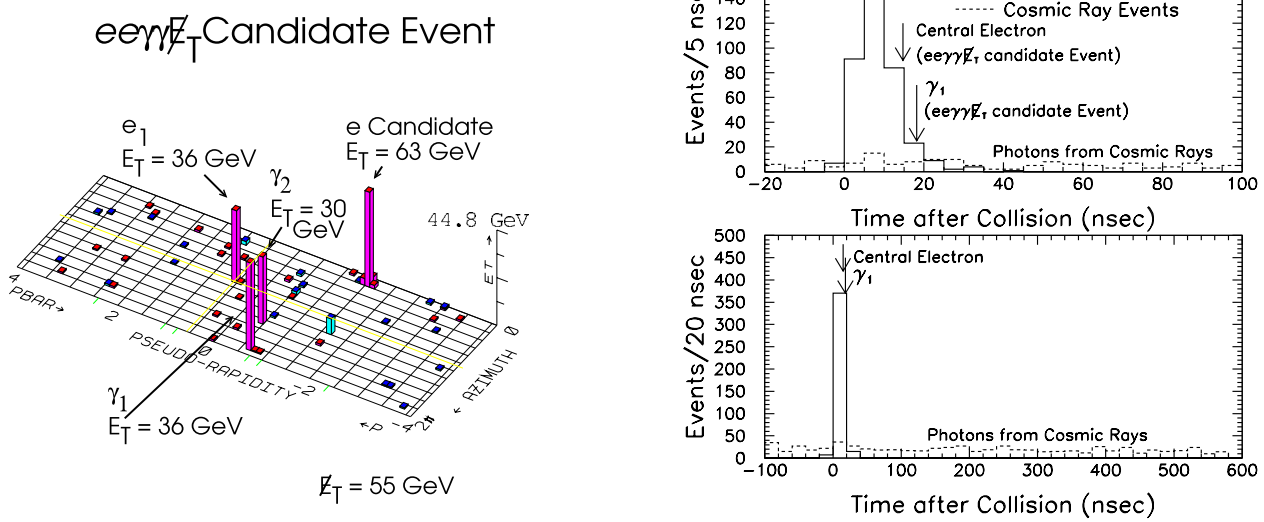

Figure 2.32: Left: The CDF event with 1 central electron, 2 central photons, a plug electron candidate, and $\not\!\!E_T$. Only the central electron and one of the photons (γ_1) has hadronic timing information. Right: The timing for the central electron and photon from the $ee\gamma\gamma\not\!\!E_T$ candidate event are consistent with having originated at the primary interaction. Shown for comparison are the timing of electrons from Z decays and the flat background from photons from cosmic rays.

for supersymmetry in Run II. We make no attempt to summerize this very large body of work here. Rather, our purpose in this section is to give a few examples in a number of important exotics channels of the discovery potential of the CDF upgraded detector with a large luminosity exposure. These examples illustrate the large potential for discovery, particularly in supersymmetric models, of physics beyond the Standard Model.

2.5.3.1 Signatures with missing transverse momentum

Missing transverse momentum ($\not\!\!E_T$), is the classic signal for R-parity conserving supersymmetry. It is important not only as a trigger and a generic signature, but as an essential component in a large number of signatures. The CDF Run I search for squarks and gluinos in the missing energy plus multijet channel excludes at 95% C.L. gluino masses below 300 GeV for $m_{\tilde{q}} \approx m_{\tilde{g}}$, and below 195 GeV independent of the squark mass. The exclusion contour at 95% C.L. in the $m_{\tilde{q}}$-$m_{\tilde{g}}$ mass plane is shown in Figure 2.33. This recent result, using a 'blind' search technique, is a significant improvement over previous searches and is starting to probe the interesting mass region for constrained supersymmetric models. In Run II we expect substantial improvement in our $\not\!\!E_T$ resolution as a result of the plug calorimeter upgrade. The addition of timing information to the electromagnetic calorimetry will also have a significant impact on analyses with $\not\!\!E_T$ as they remove an insidious type of cosmic ray backgrounds which could otherwise not be reduced.

A study of the five SUGRA points discussed above was done by the SUGRA working group for the jets plus $\not\!\!E_T$ channel.[15] The analysis assumed a detector resolution comparable to that expected for CDF II. The range of $\tilde{q}/\tilde{g}$ masses in these models are in the range $\sim (350-450)$ GeV for cases 2,3,4, with heavier masses for cases 1 and 5. With a hard cut of $\not\!\!E_T > 75$ GeV and the removal of events with $\not\!\!E_T$ correlated with jets, the background is dominated by Standard Model processes with neutrinos– top, and W/Z plus jets. The total background cross section is about 300 fb, giving signal cross sections for discovery (5σ) of 61 fb at 2 fb^{-1}, and 22 fb at 15 fb^{-1}. The signal cross sections are listed in Table 2.14. Here it can be seen that a high luminosity run is needed to be sensitive for squark and gluino masses in the range of 350-400 GeV.

Table 2.14: SUSY signal (fb) for $\not\!\!E_T$ jets events for the Tevatron for the 5 SUGRA cases (from reference [15]).

case	σ fb
(1)	5.7 ± 0.1
(2)	16.6 ± 0.2
(3)	61.9 ± 0.9
(4)	18.5 ± 0.6
(5)	1.3 ± 0.2

2.5.3.2 Signatures with high-p_T leptons

High p_T leptons are the classic signature for extra gauge bosons that are predicted in grand unified theories with gauge groups larger than SU(5). CDF has placed 95% C.L. limits of $M_{Z'} > 690$ GeV and $M_{W'} > 755$ GeV for standard model couplings. Such searches are also sensitive to quark-lepton compositeness in models where quarks and leptons share constituents. For example, the compositeness scale limit set by CDF from the dielectrons is $\Lambda^{\pm}_{LL} > 2.5(3.7)$ TeV.[17] These limits will continue to improve (albeit logarithmically) with increasing luminosity (Figure 2.34).

The possibility of detecting extra dimensions in Drell-Yan production at the Tevatron has been suggested by Hewett.[22, 23] Such extra dimensions may be detectable at the Tevatron in theories where gravity becomes strong near the weak scale. The interaction of massive gravitons with quarks and leptons gives rise to an enhancement in the cross section at high pair-mass and a forward-backward charge asymmetry. Figure 2.34 (left) shows the invariant mass distribution for dielectron pairs from CDF in Run I.[18] The agreement with the Standard Model expectation is excellent, and in particular there is no excess of events at high mass. Hewett has calculated that a 0.1 fb^{-1} data set consistent with the Standard Model constrains the effective Plank (string) scale to be greater than 990 (930) GeV depending on the sign ($\mp$) of the graviton amplitude. Shown in Figure 2.34 (right) is the projected limit as a function of luminosity.

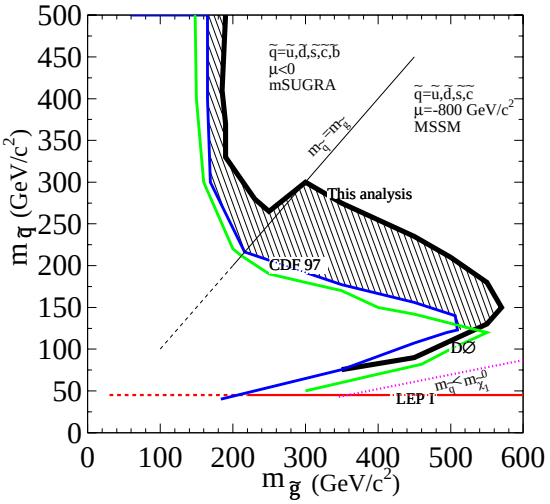

Figure 2.33: Exclusion contour at 95% C.L. in the $m_{\tilde{q}}$-$m_{\tilde{g}}$ mass plane based on based on 84 pb^{-1}of Run I data for the mSUGRA model with $\tan\beta = 3$. (From reference [16]).

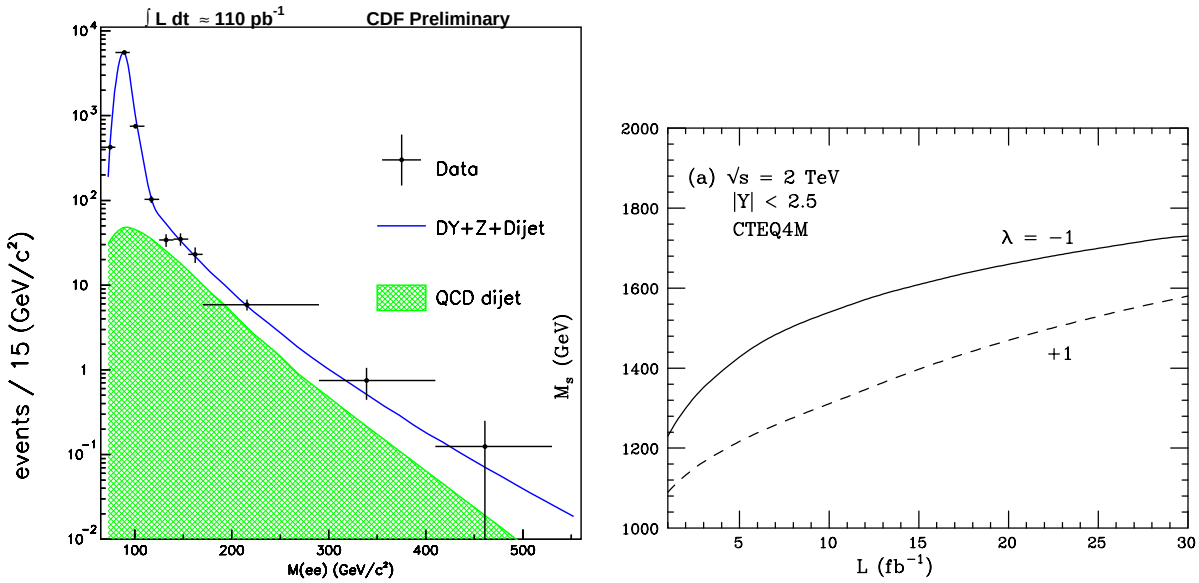

Figure 2.34: Left: The dielectron invariant mass distributions compared to background predictions from the 0.1 fb^{-1}Run I. The agreement with the standard model everywhere is excellent. Right: 95 % C.L. limit on the string scale as a function of integrated luminosity using the forward-backward asymmetry of high-mass lepton pairs. The parameter λ is the relative sign between the graviton and Standard Model amplitudes.[23]

2.5.3.3 Multi-lepton signatures

As has already been mentioned, tri-leptons are a good signature for chargino-neutralino production. Multi-lepton signatures are also predicted in models with R-parity violation and in models of gauge-mediated supersymmetry (GMSB) . For example, multileptons are predicted in a model of GMSB with nearly degenerate sleptons that share the role of next-lightest particle (NLSP).[22] In theories with GMSB, the LSP is an essentially massless, spin-1/2 Goldstino ($\tilde{G}$), the particle resulting from the spontaneous breaking of supersymmetry. The decay rate of any superpartner $\tilde{X} \to X\tilde{G}$ is proportional to m_X^5/F^2, where $\sqrt{F}$ is the symmetry breaking scale.[24] Depending on the scale $\sqrt{F}$, the NLSP may be long-lived. The Run II Workshop considered many scenarios for NLSP, including the degenerate slepton NLSP case.[25] In this case, three-body decays of $\tilde{e}_R$ and $\tilde{\mu}_R$ to $\ell\tau\tilde{\tau}_1$ are forbidden. For low $\sqrt{F}$ decays of the sleptons to $\ell\tilde{G}$ are prompt giving a signature of multi-leptons and $\not\!\!E_T$. Based on the Run I trilepton search, the number of background events was estimated to be 0.5 per fb^{-1}.[26] (The $\not\!\!E_T$ cut was increased to 25 GeV for this study.) The resulting limit is shown in Figure 2.35.

2.5.3.4 Signatures with high-p_T jets

Many extensions of the Standard Model predict exotic particles with decays to quarks and gluons which would appear as bumps or enhancements in the dijet mass spectrum. For example, the existence of a larger chiral color group, $SU(3)_L \times SU(3)_R$, would lead to massive color-octet axial vector gluons (axigluons) which would be produced and decay strongly giving a very large cross section times branching ratio to dijets.[27, 28] Technicolor models predict relatively light technihadrons, which might include color-octet technirhos that decay to dijets or color-singlet technirhos with signatures of W or Z plus dijets. [30] Models of gauged flavor symmetries have additional gauge (flavoron) bosons giving rise to an enhancement at high-mass in the dijet cross section.[10] If quarks are composite particles, then excited states of composite quarks are expected and couple to qg. New gauge bosons, W' and Z', in addition to coupling to leptons, would produce dijet mass bumps. Superstring-inspired E_6 grand unified models predict the existence of many new particles [31] including a color-triplet scalar diquark $D(D^c)$ with charge $\pm 1/3$ which couples to $\bar{u}\bar{d}(ud)$.

The dijet mass spectrum is described within errors by next-to-leading order QCD using CTEQ4HJ parton distributions.[32] In Run I we have searched for resonances and set limits on the production of high-mass resonances.[33] The data (see Figure 2.36, left) is well described by a fit to a smooth curve and resonances are excluded. The predictions for Run II are shown on the right of Figure 2.36.

Particularly important for exotics searches are b-flavor jets and therefore secondary vertex tagging. For example, in technicolor models the technipion couplings are expected to be proportional to mass.[30] Topcolor models predict a Z' and topgluons which preferentially decay to $b\bar{b}$.[34, 35] In models of supersymmetry, the stop ($\tilde{t}$) could be significantly lighter than the squarks.[36] xIn gauge-mediated supersymmetry with a higgsino-like neutralino NLSP, the neutralino will have a large branching ratio to the Higgs.[37] In Run I we searched for resonances in secondary vertex tagged dijets (see Figure 2.36) and set limits on Z'_{TopC} and topgluons. We have also searched for a fourth generation $b' \to bZ$, and a technirho decaying to $Wb\bar{b}$, and a techniomega decaying to $\gamma b\bar{b}$.[38, 39, 40] We have done a study for Run II of the higgsino-like NLSP model with the signature of $b\bar{b}\not\!\!E_T$.[25] In Figure 2.37 we have calculated the cross-section times branching ratio limit for 2, 10, and 30 fb^{-1}. It is seen that at least 10 fb^{-1}is needed to have any sensitivity in this channel.

2.5.3.5 Signatures with high-p_T photons

From Run I data we have published a detailed search for anomalous events with two isolated, central, high-p_T photons.[41, 42] The diphoton mass distribution is shown in Figure 2.38 The results are consistent with standard model expectations, with the possible exception of one event (the $ee\gamma\gamma\not\!\!E_T$ event). The $\not\!\!E_T$ distribution was used to set a limit in the light gravitino SUSY scenario. We have also looked for narrow diphoton resonances as might be the signature for a scalar-goldstino, new extra dimensions, new contact interaction, or 'bosophilic' Higgs.[43]

We have studied the prospects for Run II discovery of a bino-like neutralino in gauge-mediated supersymmetry. In this scenario, the NLSP decays to a photon plus the Goldstino. Depending on the supersymmetry breaking scale $\sqrt{F}$, this decay may or may not be prompt. In the case of prompt decays,

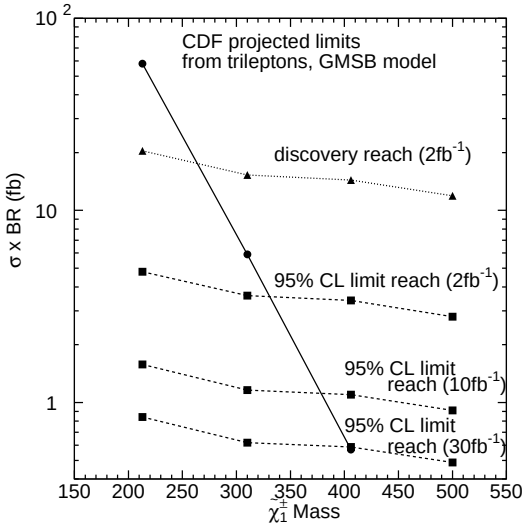

Figure 2.35: The projected Run II CDF limit on cross section times branching ratio in the degenerate slepton NLSP model. The solid line is the theoretical prediction.

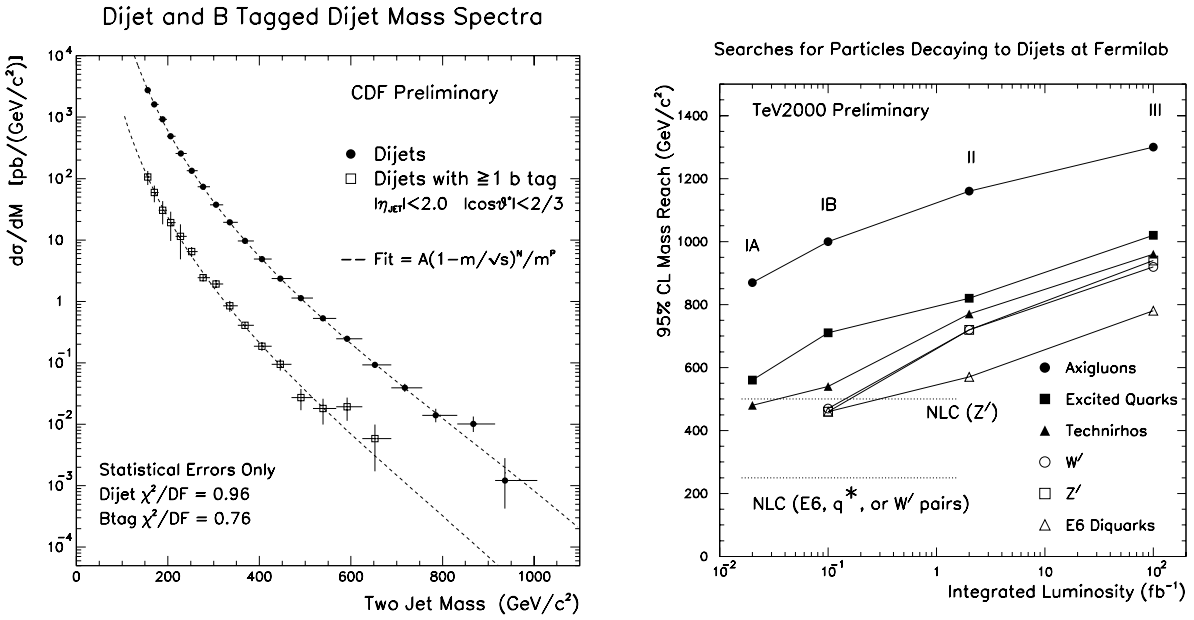

Figure 2.36: Left: The invariant mass distribution of dijets, and the invariant mass distribution with one at least one secondary vertex tag (b tag). Right: The 95% C.L. lower limit on the mass of new particles decaying to dijets versus integrated luminosity.

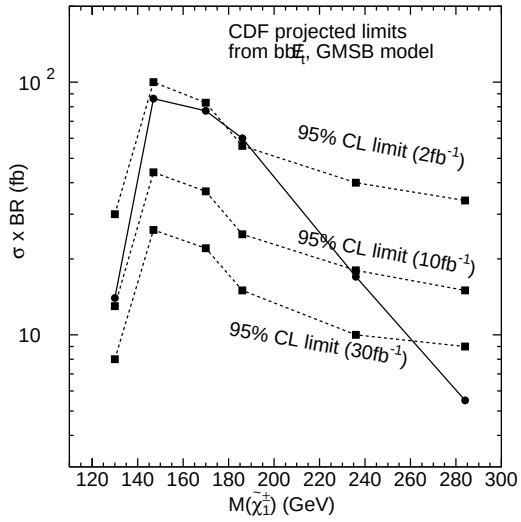

Figure 2.37: Projected Run II limits on the total SUSY cross section times branching ratio in the $b\bar{b}X\not\!\!E_T$ channel along the higgsino-like neutralino as a function of chargino mass. The solid line is the theoretical expectation.

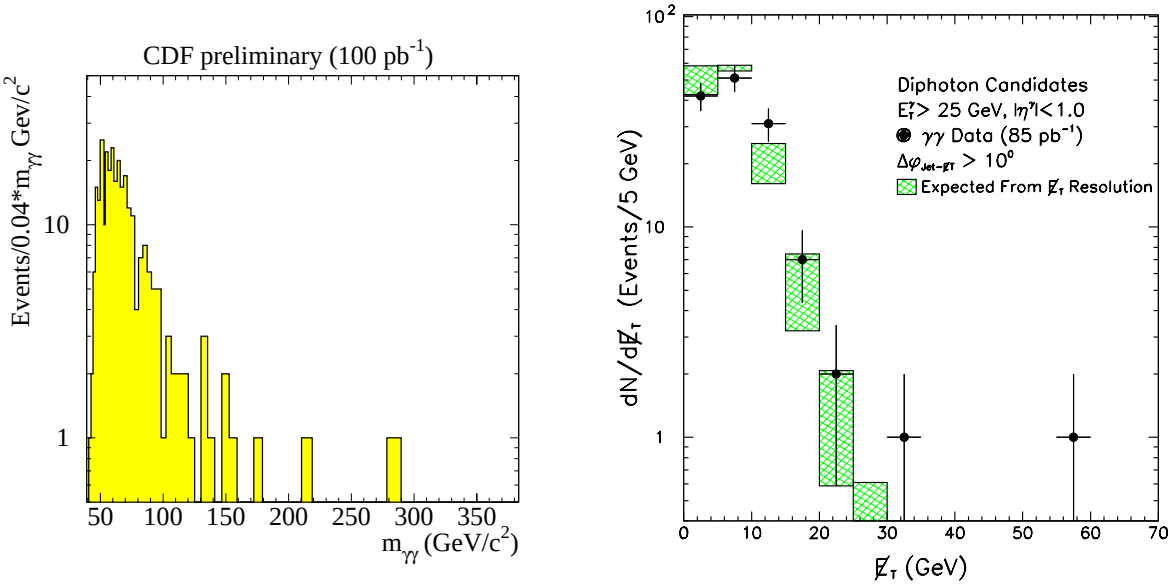

Figure 2.38: Left: The diphoton mass distribution from 100 pb^{-1} Run I data. Right: The $\not\!\!E_T$ spectrum for events with two central photons compared to the expected distribution from $\not\!\!E_T$ resolution.

we can project our sensitivity based on the Run I search. As a result of the plug calorimeter upgrade and tracking upgrades we expect a significantly enhanced acceptance to $|\eta| < 2$. This improves our efficiency by 60%. The primary background is from QCD and is estimated to be ~ 0.5 fb, based on the Run I data corrected for the increased center-of-mass energy. The projected limits as a function of neutralino mass are shown in Figure 2.39, for 2, 10 and 30 fb^{-1}. A significant increase in sensitivity is gained at the higher luminosities. In addition, the electromagnetic calorimeter timing upgrade will give a handle which can indicate that the photon is indeed from the collision; a significant improvement for searches with final state photons which suffer from cosmic ray backgrounds.

In the case of a long-lived, bino-like neutralino it is possible that a non-prompt photon would be produced. In this case, the only handle we have for this signature is the proposed electromagnetic calorimeter timing. With an expected resolution of about 1 nsec, Figure 2.39 shows the range of neutralino and Gravitino masses that would give rise to a detectable delayed signal.

2.5.3.6 Detecting hadronic τ decays

We have demonstrated that it is possible to detect hadronic decays of the τ, having measured the cross section times branching rato for $W \to \tau\nu$. [44] This technique which identifies narrow, hadronic jets is shown in Figure 2.40 from a search for third generation leptoquarks.[45] The charged particle multiplicity distribution shows that the characteristic one-plus-three prong signature is very clean. This technique can significantly increase the sensitivity to Run II exotic signatures. This is especially true in the case of supersymmetry. In SUGRA models with large $\tan\beta$, decays to taus are favored.[46] In gauge-mediated models, the stau can be the NLSP.

For example, a model studied in the SUGRA working group was a large $\tan\beta$ scenario where $\tilde{\chi}_1^{\pm}\tilde{\chi}_2^0 \to \tau\tau\tau + X$. Figure 2.41 shows the improvement in sensitivity gained by including hadronic tau decays in addition to leptonic decays in a trilepton signature. A 3σ exclusion is possible for luminosity greater than 10 fb^{-1}. [47]

2.5.4 Detecting long-lived, massive particles

Massive stable particles are possible features of several theories for physics beyond the standard model including supersymmetry, mirror fermions, technicolor, and compositeness. We have searched in the 88/89 data for heavy stable charged particles [48, 49] based upon their expected high transverse momenta, relatively low velocities (via time-of-flight), and muon-like penetration of matter. We obtained upper limits on the cross-section for the production of heavy stable particles as a function of their mass. This can be translated into a mass limit from the cross-section for any particular theory and varies from about 140 GeV for color triplets to 255 GeV for color decuplets as shown in Figure 2.42b. This analysis is currently being extended using Run I data. Rather than using time-of-flight, the analysis takes advantage of the large ionization depositions, dE/dx, expected for massive particles, with measurements in both the SVX and in the outer tracker (CTC for Run I). For example, see Figure 2.42 (left). Using half of the Run Ib data, we have obtained a preliminary limit of 190 GeV/c^2 for color triplets. The extrapolations to Run II are shown in Figure 2.42b.

In gauge-mediated supersymmetry with a stau NLSP, the stau might be quasi-stable. In such a scenario it would appear as a muon trigger with large ionization and low velocity. The sensitivity to this model in Run II is shown in Figure 2.43.[25]. The figure shows that significant sensitivity is gained by using time-of-flight. The reach, while marginal with 2 fb^{-1} becomes substantial with more than 10 fb^{-1}.

An interesting possibility for supersymmetry is that the $\tilde{\chi}_1^{\pm}$ is long-lived. [50] This happens in models where the $\tilde{\chi}_1^{\pm}$ is nearly degenerate with the LSP $\tilde{\chi}^0$, a scenario which arises naturally in anomaly-mediated models.[50, 51] In the paper by Feng *et al.*, the possibility of detecting the $\tilde{\chi}_1^{\pm}$ as a massive, stable charged particle was explored. They considered both a heavy-ionizing track trigger and an isolated stiff-track trigger. The cross section for this signal as a function of chargino mass is shown in Figure 2.44. The expected background from Run I as a function of particle mass is shown in Figure 2.45. Above 125 GeV we expect very little background. We should be able to discover $\tilde{\chi}_1^{\pm}$ with masses above 250 GeV with 15 fb^{-1}.

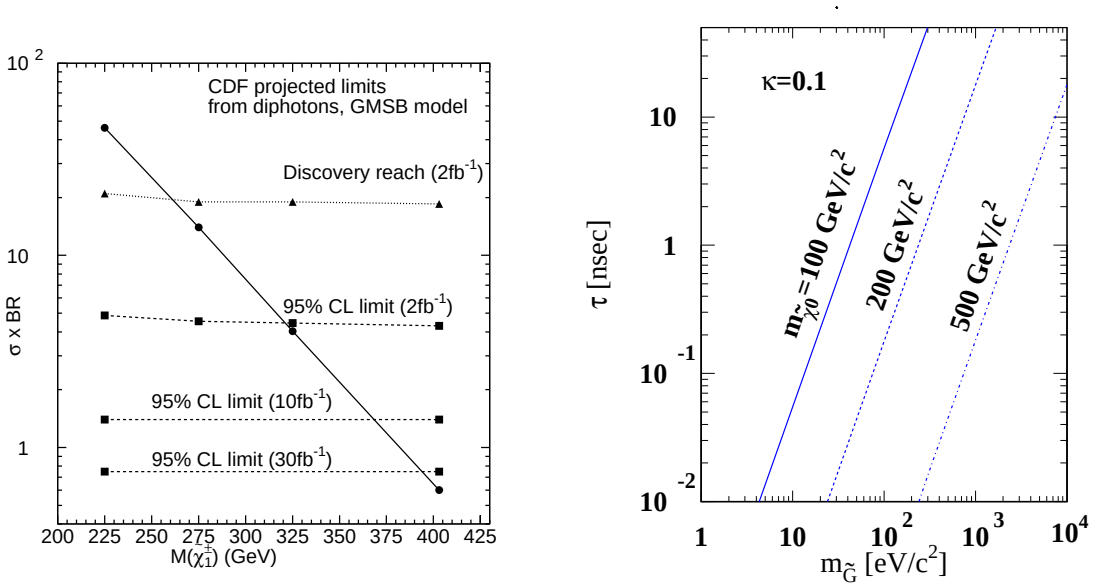

Figure 2.39: Left: Projected limits on the SUSY cross section for the bino-like neutralino NLSP in the $\gamma\gamma\not{E}_T$ channel. Right: Lifetime of the NLSP for various masses as a function of the Gravitino mass. κ is a parameter measuring the photino content of the neutralino.

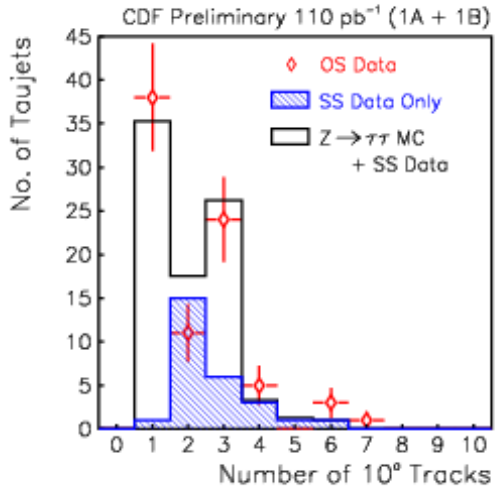

Figure 2.40: Charged particle multiplicity distribution in hadronic jets for opposite-sign Run I data compared to $Z \to \tau^+\tau^-$ Monte Carlo plus fakes estimated from same-sign data (from ref [45]).

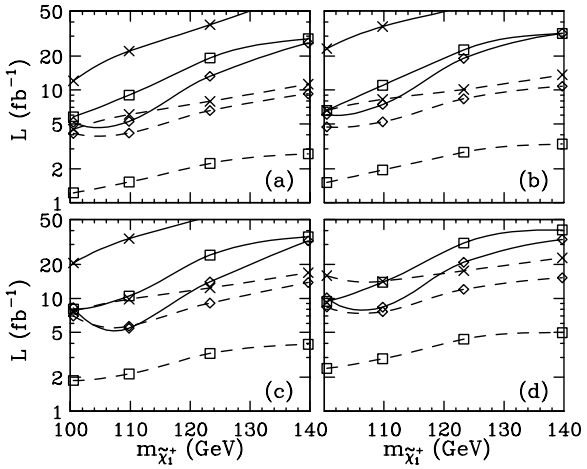

Figure 2.41: The total integrated luminosity L needed for a 3σ exclusion (solid lines) or observation of 5 signal events (dashed lines), as a function of the chargino mass $m_{\tilde{\chi}_1^+}$ from reference [47]. The plots correspond to variations of the $\not\!\!E_T$ cut and a jet veto (JV) as: (a) $\not\!\!E_T > 20$ GeV; (b) $\not\!\!E_T > 25$ GeV; (c) $\not\!\!E_T > 20$ GeV and JV ; and (d) $\not\!\!E_T > 25$ GeV and JV. The plotting symbols correspond to the following channels: trileptons ($\times$), dileptons plus a tau jet ($\Box$) and like-sign dileptons plus a tau jet ($\Diamond$).

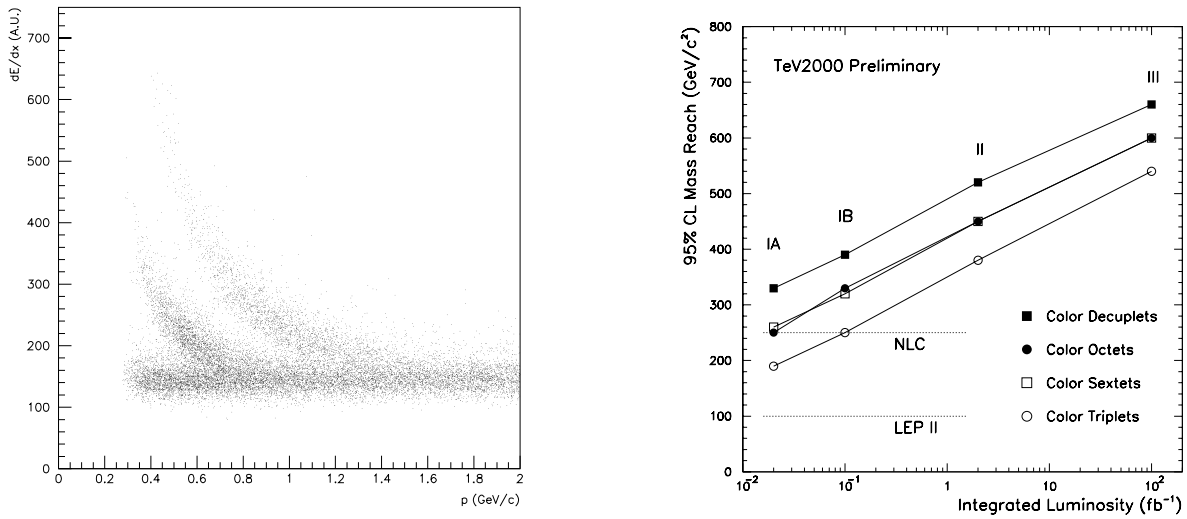

Figure 2.42: (a) A scatter plot of the dE/dx vs momentum is shown for the Run Ib silicon detector after a cut has been applied on the dE/dx from the main tracking chamber. Known particles (kaons and protons) can be clearly distinguished for $p/m < 1.2$ ($\beta < 0.6$). New massive particles would look similar but at higher momentum. (b) The expected mass reach is plotted vs. integrated luminosity at the Tevatron. The maximum mass reach of other accelerators is shown for comparison.

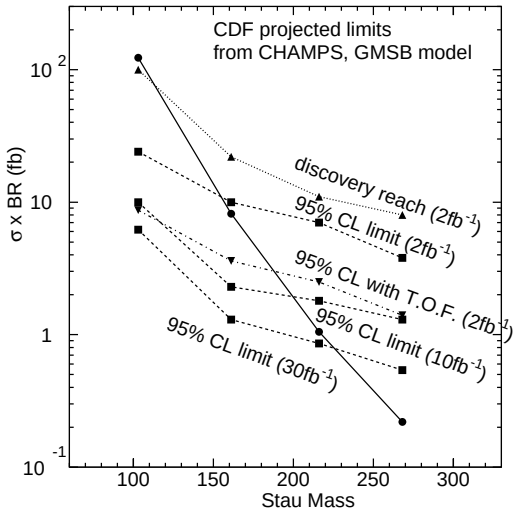

Figure 2.43: The projected limits on the cross-section times branching ratio for a long-lived stau in a NLSP stau model. Projections are shown based on dE/dx in the COT and silicon, and with an additional time-of-flight measurement assuming 100 ps timing resolution.

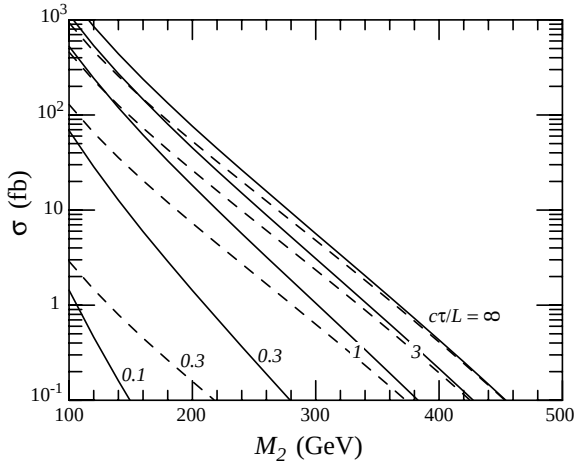

Figure 2.44: Cross section for $\tilde{\chi}\tilde{\chi}$ production (solid) with a at least one $\tilde{\chi}_1^{\pm}$ traveling a radial distance L with $|\eta| < 1.2$. The dependence on the decay length $c\tau$ is shown. Dashed contours further require the long-lived $\tilde{\chi}_1^{\pm}$ to have $\beta\gamma < 0.85$. (from reference [50])

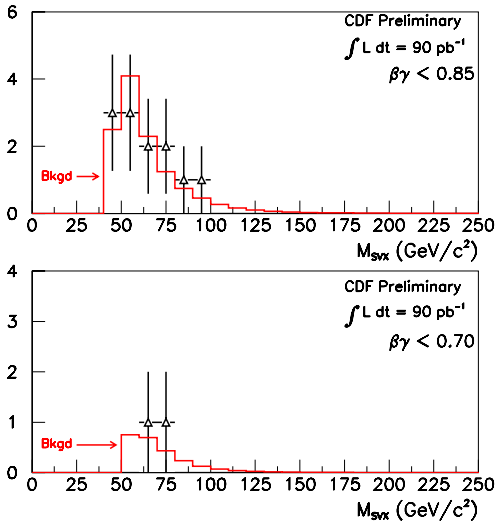

Figure 2.45: The mass distribution in 0.9 fb^{-1} Run I muon trigger data compared to the expected background. The top plot has $\beta\gamma < 0.85$; the bottom plot has $\beta\gamma < 0.70$.

2.5.5 Summary

CDF has produced most of the strongest limits to date in direct searches for physics beyond the Standard Model. This experience allows us to make realistic predictions of the physics potential of a high-luminosity run. The proposed upgrades are critical for maintaining our current tracking and muon detection capabilities in a high luminosity environment. In addition, we have proposed enhancements to the lepton triggers and to electromagnetic calorimeter timing that will significantly extend our sensitivity in many important exotics channels.

Based on detailed studies in a broad range of theoretical models, there is a large potential for discovery in Run IIb. This is particularly true in the area of theories with supersymmetry. Barring these discoveries, we will be able to place many strong constraints on theories that predict new physics beyond the Standard Model.

Bibliography

[1] M. Chanowitz, hep-ph/0104024.

[2] G. Altarelli, F. Caravaglios, G. F. Giudice, P. Gambino and G. Ridolfi, JHEP **0106**, 018 (2001) [hep-ph/0106029].

[3] G.W. Anderson and D.J. Castaño, hep-ph/9509212, Phys. Rev. **D53**, 2403 (1996).

[4] S. Dimopoulos, M. Dine, S. Raby, and S. Thomas, hep-ph/9601367, Phys. Rev. Lett. **76**, 3494 (1996); S. Dimopoulos, S. Thomas, J.D. Wells, hep-ph/9604452 and preprint SLAC-PUB-7148 (1996).

[5] S. Ambrosanio, G. Kane, G. Kribs, S. Martin, and S. Mrenna, hep-ph/9602239, Phys. Rev. Lett. **76**, 3498 (1996).

[6] S. Ambrosanio, G. Kane, G. Kribs, S. Martin, and S. Mrenna, hep-ph/9605398 (1996).

[7] K.S. Babu, C. Kolda, and F. Wilczek, hep-ph/9605408 (1996).

[8] J.L. Lopez and D.V. Nanopoulos, hep-ph/9607220 and preprint CTP-TAMU-23/96 (1996).

[9] K. Lane, and E. Eichten, BUHEP-95-11, Mar 1995; hep-ph/9503433; Phys. Lett. **B352**, 382, (1995).

[10] G. Burdman, R. S. Chivukula and N. Evans, Phys. Rev. D **62** (2000) 075007 [hep-ph/0005098].

[11] N. Arkani-Hamed, S. Dimopoulos and G. Dvali, Phys. Lett. B **429**, 263 (1998).

[12] I. Antoniadis *et al.*, Phys. Lett. B **436**, 257 (1998).

[13] N. Arkani-Hamed, S. Dimopoulos and G. Dvali, Phys. Rev. D **59**, 086004 (1999).

[14] See http://fnth37.fnal.gov/run2.html for a list of these workshops.

[15] " Report of SUGRA Working Group for Run II of the Tevatron", V. Barger, *et al.*, hep-ph/0003154.

[16] "Search for Gluinos and Scalar Quarks using the Missing Energy plus Multijets Signature", T. Affolder *et al.*, The CDF Collaboration, FERMILAB-Pub-01/084-E, hep-ex/0106001. Submitted to Phys. Rev. Lett. May 31 2001.

[17] F. Abe *et al.*, (The CDF Collaboration), Phys. Rev. Lett. **79**, 2198 (1997).

[18] F. Abe *et al.*, (The CDF Collaboration), Phys. Rev. Lett. **79**, 2191 (1997)

[19] P. Nath and R. Arnowitt, Mod. Phys. Lett. **A2**, 331 (1987); R. Barbieri, F. Caravaglios, M. Frigeni and M. Mangano, Nucl. Phys. **B367**, 28 (1991); H. Baer and X. Tata, Phys. Rev. **D47**, 2739 (1993); J.L. Lopez, D.V. Nanopoulos, X. Wang and A. Zichichi, Phys. Rev. **D48**, 2062 (1993); H. Baer, C. Kao, and X. Tata, Phys. Rev. **D48**, 5175 (1993).

[20] F. Abe *et al.*,(The CDF Collaboration), Phys. Rev. Lett. **81**, 1791 (1998); F. Abe *et al.*,(The CDF Collaboration), Phys. Rev. D **59**, 092002 (1999).

[21] The TeV-2000 Group Report, Fermilab-PUB-96/082.

[22] "Proceedings of the Tevatron Run II SUSY/Higgs Workshop" Editor: J. F. Gunion; BTMSSM Convenors: M. Chertok, H. Dreiner, G. Landsberg, J. F. Gunion, J.D. Wells, hep-ph/0006162.

[23] J. L. Hewett, Phys. Rev. Lett. **82**, 4765 (1999) [hep-ph/9811356].

[24] P. Fayet, Phys. Lett. B **70**, 46 (1977); P. Fayet, Phys. Lett. B **84**, 416 (1979); P. Fayet, Phys. Lett. B **84**, 421 (1979)

[25] "Low-Scale and Gauge-Mediated Supersymmetry Breaking at the Fermilab Tevatron Run II", R. Culbertson, *et al.*, hep-ph/0008070.

[26] F. Abe *et al.*, (The CDF Collaboration), Phys. Rev. Lett. **80**, 5275 (1998).

[27] P. Frampton and S. Glashow, Phys. Lett. **B190**, 157 (1987).

[28] C. Albajar *et al.* (UA1 Collaboration), Phys. Lett. **B209**, 127 (1988).

[29] E. Eichten and K. Lane, Phys. Lett. **B327**, 129 (1994).

[30] E. Eichten, K. D. Lane and J. Womersley, Phys. Lett. B **405**, 305 (1997) [hep-ph/9704455].

[31] J. Hewett and T. Rizzo, Phys. Rep. **C183**, 193 (1989).

[32] F. Abe *et al.*, (CDF Collaboration), Phys. Rev. D **61**, 091101 (2000).

[33] F. Abe *et al.*, (CDF Collaboration), Phys. Rev. Lett. **74**, 3538 (1995).

[34] C. T. Hill, Phys. Lett. B **266**, 419 (1991).

[35] C. T. Hill, hep-ph/9702320.

[36] H. Baer, M. Drees, R. Godbole, J. F. Gunion and X. Tata, Phys. Rev. D **44**, 725 (1991).

[37] S. Dimopoulos, M. Dine, S. Raby, S. Thomas and J. D. Wells, Nucl. Phys. Proc. Suppl. **52A**, 38 (1997) [hep-ph/9607450].

[38] F. Abe *et al.*,(The CDF Collaboration),Phys. Rev. Lett. 84 835-840 (2000).

[39] F. Abe *et al.*,(The CDF Collaboration), Phys. Rev. Lett. 84, 1110-1115 (2000).

[40] F. Abe *et al.*,(The CDF Collaboration), Phys. Rev. Lett. 83, 3124 (1999).

[41] F. Abe *et al.* (CDF Collaboration), Phys. Rev. Lett. **81**, 1791 (1998) [hep-ex/9801019].

[42] F. Abe *et al.* (CDF Collaboration), Phys. Rev. D **59**, 092002 (1999) [hep-ex/9806034].

[43] T. Affolder *et al.* (CDF Collaboration), hep-ex/0105066.

[44] F. Abe *et al.* (CDF Collaboration), Phys. Rev. Lett. **68**, 3398 (1992).

[45] F. Abe *et al.*, (The CDF Collaboration), Phys. Rev. Lett. **78**, 2906 (1997).

[46] H. Baer, C. Chen, M. Drees, F. Paige and X. Tata, Phys. Rev. Lett. **79**, 986 (1997) [hep-ph/9704457].

[47] J. D. Lykken and K. T. Matchev, Phys. Rev. D **61** (2000) 015001 [hep-ph/9903238].

[48] F. Abe *et al.* (CDF Collaboration), Phys. Rev. Lett. **63**, 1447 (1989).

[49] F. Abe *et al.* (CDF Collaboration), Phys. Rev. **D46**, 1889 (1992).

[50] J. L. Feng, T. Moroi, L. J. Randall, M. Strassler and S. Su, Phys. Rev. Lett. **83**, 1731 (1999) [hep-ph/9904250].

[51] J. L. Feng and T. Moroi, Phys. Rev. D **61**, 095004 (2000) [hep-ph/9907319].

2.6 QCD

2.6.1 Introduction

Quantum Chromodynamics, QCD, the theory of the strong interaction, is the least precisely known component of the Standard Model. In Run IIb, the QCD sector will be tested with increased precision using the production and fragmentation of jets, and the production of W/Z bosons, Drell-Yan lepton pairs, and single and double photons [1, 2]. The data samples possible with an integrated luminosity of 15 fb^{-1}, an increased center of mass energy, and an improved rapidity coverage, coupled with the increasingly sophisticated theoretical techniques developed within perturbative QCD, will allow for stringent tests of the Standard Model down to distance scales of the order of 0.1 millifermis or less.

One of the goals for Run II will be to obtain a level of precision for QCD measurements similar to those obtained at LEP. Until the turn-on of the LHC the Tevatron will remain the "high Q^2 frontier" and it's quite plausible that any new physics beyond the Standard Model may manifest itself as deviations from the predictions of QCD. The data taken will serve to determine the fundamental input ingredients of the theory, including the strong coupling constant α_s and parton distribution functions (PDFs). Next-to-leading order (NLO) QCD predictions for the inclusive jet and dijet cross sections have been available for almost a decade [3, 4, 5]. More recently, the 3 jet cross section has also been calculated to NLO [6] and the techniques to extend this to other 3-body observables such as W/Z + 2 jet are available. The inclusive W and Z cross sections are available at NNLO and an extensive 5-year program to calculate the inclusive jet cross section to that order should be complete by the start of Run IIb [7]. At NNLO, the theoretical uncertainties due to still higher orders will be greatly reduced as shown in Figure 2.46.

In the same timescale (or less), PDFs will be widely available at NNLO, leading to a precision for QCD predictions never before achieved. In addition to extending calculations to higher order, a number of other theoretical tools have been developed and are, or will be, available for Run IIb. Among the most promising of the methods is resummation. For processes involving two disparate scales, e.g. the transverse momentum (Q_T) and mass of gauge bosons (W,Z, Higgs), or processes involving large parton x values, e.g. the high E_T jet cross section, double logarithmic contributions to the cross section arise due to the imbalance of the phase space available for the radiation of real and of virtual gluons. These contributions due to the effects of soft gluon radiation need to be resummed and can lead to important changes in the QCD observables. There have been many recent calculations involving resummation relevant to collider observables [1, 2] and more progress is expected in the next few years.

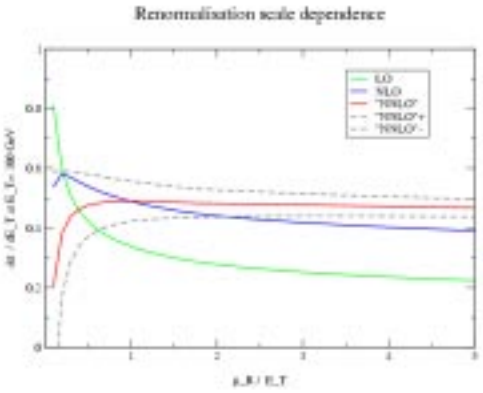

Figure 2.46: The jet cross section at an E_T value of 100 GeV/c plotted as a function of the relative renormalization scale μ/E_T. For renormalization scales within a factor of 2 of the jet energy, the renormalization scale uncertainty of the cross section prediction is reduced from 20% at leading order to 9% at NLO to a few percent at NNLO. The 3 NNLO curves correspond to 3 assumptions regarding the currently uncalculated terms for the NNLO inclusive jet cross section.

QCD-based Monte Carlo programs such as Herwig [8], Pythia [9] and Isajet [10] are used extensively in essentially all high energy physics experiments [11]. The gluon radiation from the parton showering and the resultant hadronization incorporated into the programs allows for detailed comparisons to experimental data. But, the basis for all of the above programs are $2 \rightarrow 2$ matrix elements. Parton showering provides only an approximation for more complex signatures involving multiple jets, photons, W/Zs and heavy quarks in the final state. There has been progress in incorporating exact matrix elements into the QCD Monte Carlos [12, 13] and recently a universal interface has been developed between matrix element and Monte Carlo programs that allows for the advantages of the use of the exact matrix element and the additional gluon radiation and hadronization from the parton shower [14]. The current implementation of all QCD Monte Carlo pro-

grams is at leading order, but progress has been made at extending the weighting to NLO [15], and such implementations should be available by the start of Run IIb.

2.6.2 Inclusive Jets

The inclusive jet cross section has been measured in CDF over the E_T range from 15 GeV/c to 450 GeV/c, spanning 9 orders of magnitude [16, 17]. (See, for example, Figure 2.47.) Good agreement is observed with NLO QCD [3, 5] predictions using conventional PDFs except at the highest values of transverse energy, starting at 200 GeV/c, where an apparent excess is observed. As the high Q^2 region is one where new physics may cause a deviation from NLO QCD predictions, any excess is of great interest. Similar deviations have been observed in other CDF jet cross section measurements such as the dijet mass [18], differential dijet [19] and ΣE_T [20] analyses. A detailed examination of the angular distribution for dijet production indicates that it is consistent with QCD-type production mechanisms [21].

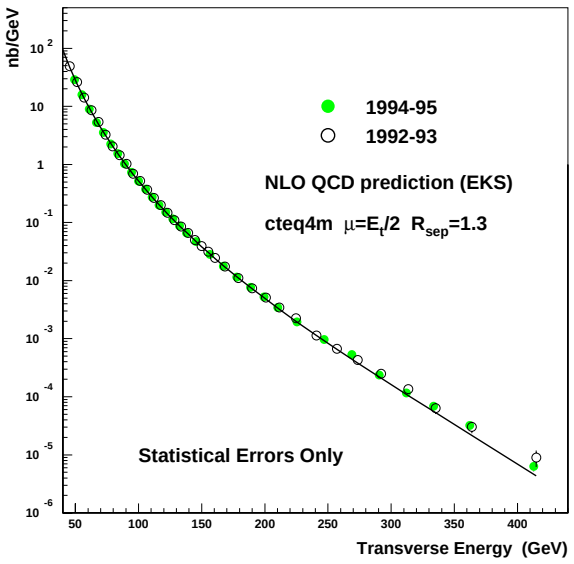

Figure 2.47: The inclusive jet cross section measurements for Run Ia and Ib.

One possible explanation for the excess of high E_T jets is that the gluon distribution at high x is larger (by a factor of 2) than conventional PDF fits have indicated. A CTEQ analysis [22, 23] has shown that such a change in the gluon distribution is possible given the constraints from the data sets included in the global PDF fits. The resulting PDF (CTEQ 4HJ and then later CTEQ 5HJ [24]) provide the best agreement not only with the CDF jet cross sections but also with D0 as well [25]. The improved agreement provided by CTEQ5HJ for the CDF Run IB inclusive jet data can be observed in Figure 2.48.

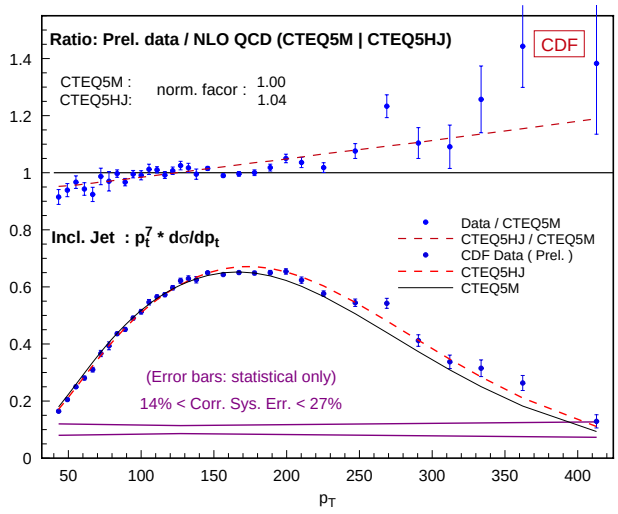

Figure 2.48: The CDF jet cross section measured in Run Ib compared to NLO predictions using the CTEQ5M and CTEQ5HJ pdf's.

A data sample of 15 fb^{-1} will enable the jet cross section to be probed for higher E_T (and x) values than were possible in Run I. In Run IIa, the jet cross section can be measured up to E_T values of approximately 550 GeV/c, extended to approximately 600 GeV/c in Run IIb. The yield of jet events in the central rapidity region in Run II can be seen in Figure 2.49 using NLO QCD predictions [26] with the CTEQ5M and CTEQ5HJ PDFs, along with a parameterization of the physics cross section observed in Run IB. In addition to the increased statistics of Run II, the increase in the center-of-mass energy from 1.8 to 1.96 TeV has a dramatic effect on the jet cross section at high E_T.

The goal of the Run II calorimeter upgrade was to provide calorimetry as precise in the forward region as in the central one. Unlike Run I, the inclusive jet cross section will be measured out to rapidity values of 3 in Run II. The number of events expected in the rapidity intervals 0.7-1.4, 1.4-2.1 and 2.1-3.0 can be seen in Figure 2.50, using predictions with both the CTEQ5M and CTEQ5HJ pdf's.

In Run I, there were approximately 20 events with an E_T value above 400 GeV/c. In Run II, the increase in energy and integrated luminosity will result in a sample of such events about 500 times as large. With this high statistics data sample, it will be possible to

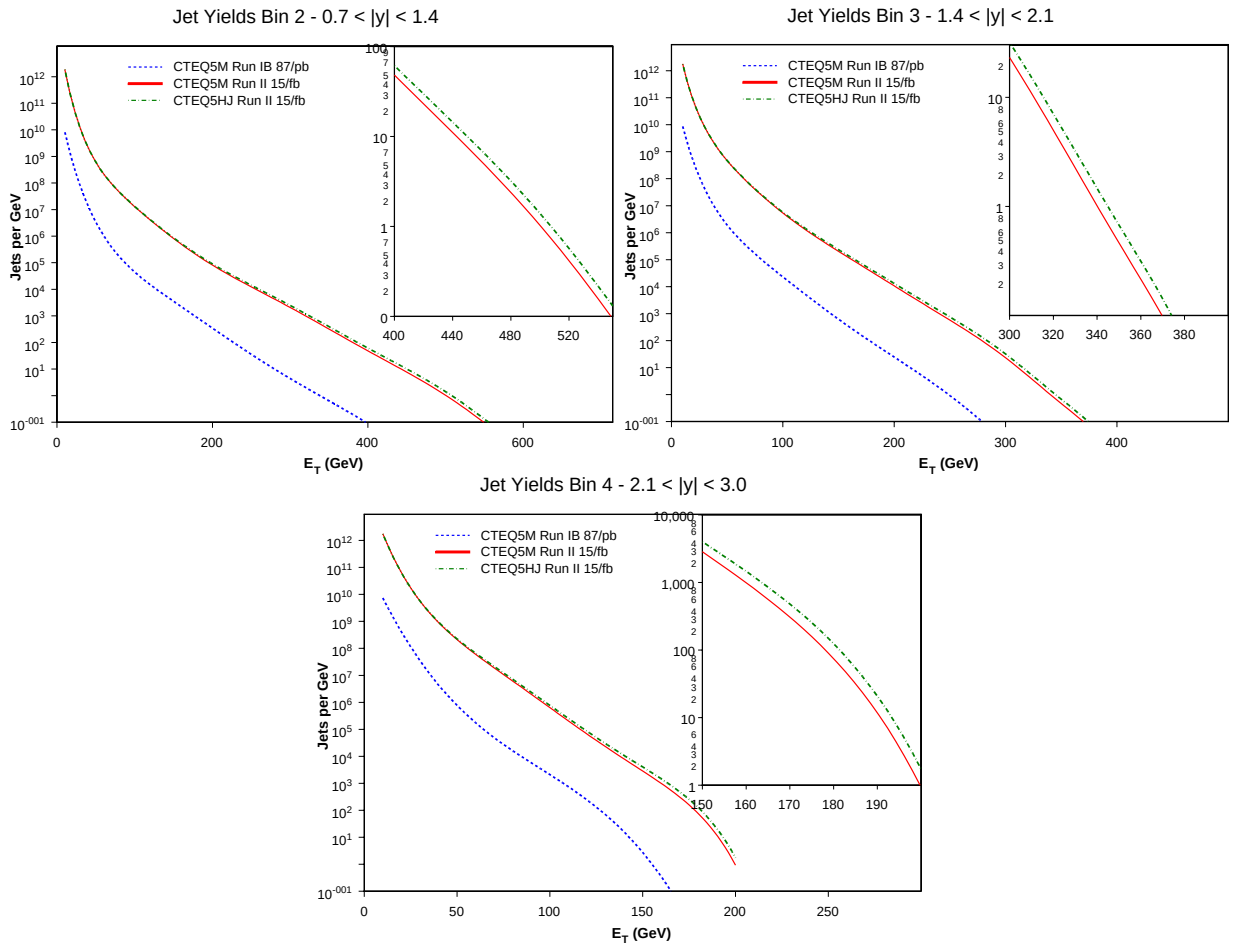

Figure 2.50: Predictions for Run Ib and Run II for the inclusive jet yield in the forward rapidity regions using the EKS NLO program and the CTEQ5M and CTEQ5HJ pdf's.

study the detailed properties of the events in order to probe more precisely the production mechanisms. Any additional $s-channel$ contributions, as for example from compositeness, to the dijet cross section will tend to flatten the angular distributions. Predictions for the dijet mass distribution are shown in Figure 2.51 for the central rapidity region and in Figure 2.52 for the full rapidity region [26]. A measurement of the dijet angular distribution should be possible out to dijet masses of the order of 1000 GeV/c^2.

In addition, one can examine the pattern of soft gluon emission in the jet events. These hadronic attenna patterns provide a tool to diagnose different patterns of color flow in high E_T events. They reflect the underlying short-distance physics and are sensitive to color coherence and interference between initial and final-state partons. These patterns may be used to distinguish between conventional QCD and new physics production mechanisms such as a possible Z-prime or compositeness [27]. In addition, it may be possible to determine if there is an enhanced gq scattering component of the high E_T jet cross section (expected with a CTEQ5HJ-like gluon distribution) compared to the dominant $q\overline{q}$ production mechanism.

As discussed in the introduction, threshold logarithms ($(ln(1-x))$, where x is the parton momentum fraction), become important when the final state object is forced to carry a large fraction ($x \rightarrow 1$) of the available center of mass energy. In this case, the radiative tail of real gluon emission is strongly suppressed. Resummation of the soft gluon radiation for this circumstance typically results in an enhancement of the cross section in the relevant kinematic region. The resummation of the threshold logs for the inclusive jet cross section at the Tevatron has been performed and found to result in only a moderate increase in the cross section in the kinematic region measured in Run I [28]. Nonetheless, it will still be important to fully consider such effects for the high E_T and x values accessible in Run IIb.

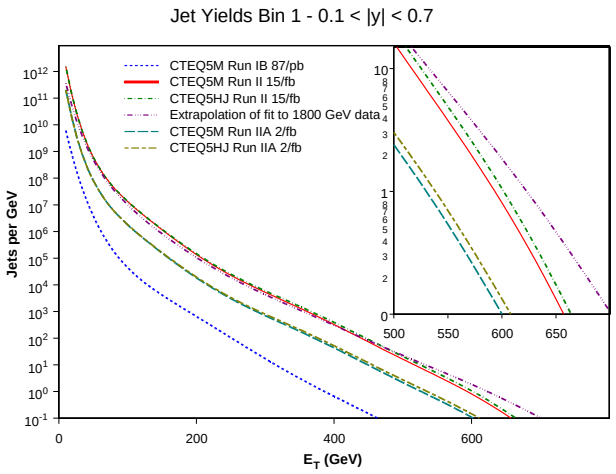

Figure 2.49: The inclusive jet cross section (number of events) in the central rapidity region for CDF. Predictions for Run Ib, Run IIa and Run IIb use the EKS [3] NLO program and the CTEQ5M and CTEQ5HJ pdf's, as well as an extrapolation of the physics curve measured in CDF in Run Ib.

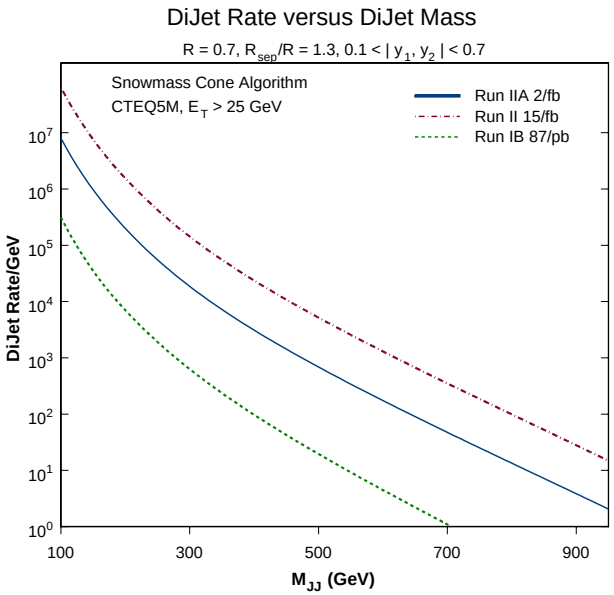

Figure 2.51: Predictions for the dijet mass distribution in the central rapidity region using the EKS NLO jet program and CTEQ5M parton distributions.

2.6.3 α_s and PDFs

An important goal of QCD analyses in CDF is the extraction of α_s and/or parton distributions from all processes for which there are both reliable data samples and reliable predictions. Examples include the inclusive jet, dijet mass, differential dijet, inclusive photon, photon + jet and W/Z/DY cross sections. The CDF inclusive jet cross section and inclusive W/Z cross sections, along with the W asymmetry have been utilized in global PDF fits. The jet cross section, in particular, has provided in the past critical constraints on the gluon distribution in the x range from .05-.20.

The inclusive jet cross section from Run IB has been used by CDF to extract a measurement of the strong coupling constant α_s [29]. A value of α_s of $0.118 \pm 0.0001(stat) \pm 0.01(exp.syst.)$ (obtained by fitting the jet cross section over the E_T range from 40 to 250 GeV/c), consistent with the world average, is obtained. More importantly, as shown in Figure 2.53, the running of α_s is measured over an extremely wide Q^2 range. The slowing of the running of α_s is a manifestation of the jet excess when using conventional PDFs.

In Run IIb, a measurement of the running coupling constant will be possible from a Q^2 of $(10\text{GeV})^2$ to over $(600\text{GeV})^2$. Deviations in the SM running of α_s may be due to loop contributions of new particles.

2.6.4 Exploring High x

The high x region can be probed more directly by measuring the differential dijet cross section, as a function of the E_T and η of the two leading jets. Assuming a $2 \rightarrow 2$ hard scattering, the event kinematic variables (x, Q^2) are related to the jet's transverse energy, E_T, and pseudorapidity, η, by

$$x_{12} = \Sigma_i \frac{E_{Ti}}{\sqrt{s}} e^{\pm \eta_i}; \qquad Q^2 = 2E_T^2 \cosh^2 \eta^* (1 - \tanh \eta^*) \tag{2.2}$$

where the sum is over all the jets in the event. The parton momentum fractions are represented by x_1 and x_2, and for a two body process the four momentum transfer in the interaction is given by Q^2. We define x_1 to be the maximum of the two momentum fractions in the event and x_2 as the minimum.

The differential dijet cross section was measured in CDF in Run Ib, requiring one jet (the trigger jet) to be in the central region ($0.1 < |\eta| < 0.7$) and the other jet to be in one of four rapidity regions. The measured cross sections and kinematic coverages can be seen in Figure 2.54.An excess similar to that observed for the inclusive jet cross section in the central region was observed.

The higher energy and larger statistics in Run IIb will enable this measurement to be extended to larger values of x and Q^2. The better calorimetry in the forward region will allow cross section measurements

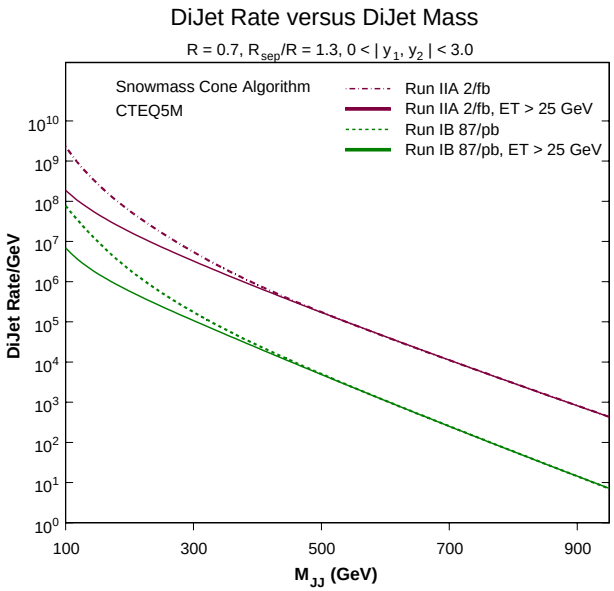

Figure 2.52: Predictions for the dijet mass distribution in the full rapidity region using the EKS NLO jet program and CTEQ5M parton distributions.

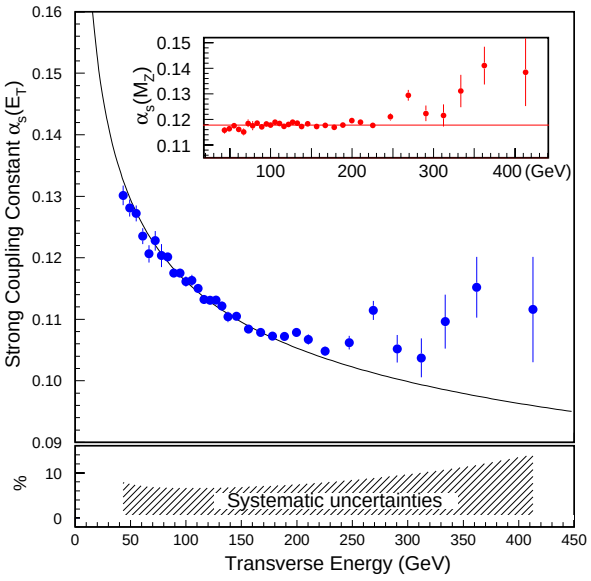

Figure 2.53: The strong coupling constant as a function of E_T measured using the CDF inclusive jet cross section in Run Ib.

where both jets are non-central.

2.6.5 W and Z production

2.6.5.1 Inclusive cross sections

The inclusive W and Z theoretical cross sections are currently known to NNLO. In addition, the cross sections are sensitive to quark distributions in an x range already very well determined by high statistics deep-inelastic scattering (DIS) and Drell-Yan (DY) experiments. Experimentally, the measurement of the W and Z cross sections have relatively low systematic errors. Approximately, 12 million $W \rightarrow e\nu$ and 1.5 million $Z \rightarrow e^+e^-$ events are expected with $15fb^{-1}$. Given the above factors, the W and Z cross sections will be extremely useful for determining the luminosity of the Tevatron, especially given the current uncertainty in measuring the total inelastic cross section. It is interesting to note that the majority of the differences in the CDF and D0 Run Ib cross sections are due to different assumptions as to the size of the total inelastic cross section. If the CDF and D0 jet cross sections, for example, are normalized to their respective W and Z cross sections, then the normalization difference essentially disappears.

2.6.5.2 W/Z p_T distributions

Double logarithmic contributions due to soft gluons arise in all of the kinematic configurations where radiation of real and virtual gluons are highly unbalanced [30]. This occurs for the the case of hard scattering production near threshold, as for example was discussed for jet production at high E_T, and for the transverse momentum distributions of vector bosons at low transverse momenta.

The W and Z p_T distributions have been extensively studied in CDF in Run IB. The distributions are well-described by resummation calculations over the entire range of measurement, as shown in Figure 2.55 for the case of Z production. In Run IIb, the W and Z p_T distributions can be extended out to 350-400 GeV/c [31]. In addition, the increased statistics and coverage will allow the measurements to be extended to new kinematic regions.

The factorization of the hadron-hadron cross sections into a hard part and into PDFs (for example, in the Drell-Yan process) can be proven if the initial-state partons probed in the hard collision have x_1 and x_2 sufficiently close to 1. This factorization picture does not necessarily apply at small x, when the probed partons lose the dominant fraction of their energy in the process of the evolution. Ultimately, at very small x the DGLAP logs become negligible in comparison to the BFKL logs. Semi-inclusive DIS

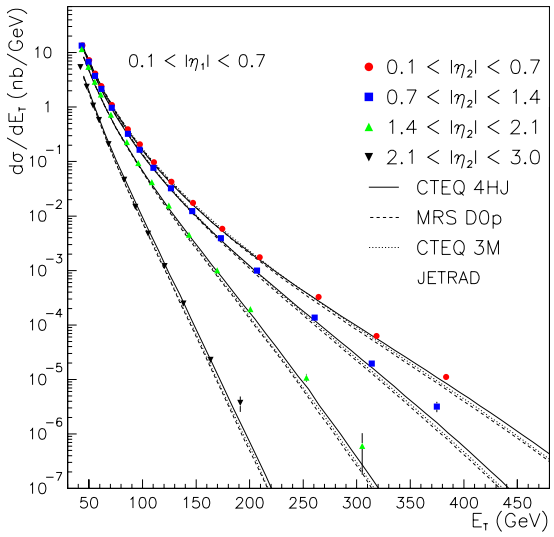

Figure 2.54: The differential dijet cross section for CDF from Run Ib.

(SI-DIS) data from HERA [32] (transverse energy flow, charged particle multiplicity) shows a consistent increase in the average q_T, when the x value is below 0.005-0.01. In the framework of the generalized factorization formalism (CSS) [33], the HERA SI-DIS data is described consistently only if one assumes the rapid growth of the non-perturbative Sudakov factor (i.e., the rapid growth of intrinsic k_T) [31]. Hence the SI-DIS HERA data may be revealing the universal transition from the DGLAP dynamics to the BFKL dynamics at x values of less than approximately 0.005-0.01, i.e., at much higher x values than is commonly assumed. This then questions the accuracy of the predictions of the conventional factorization picture for the p_T distributions at the LHC and VLHC.

At the Tevatron, a similar effect may show up in the dependence of the shape of the p_T distributions of the W and Z boson production on the rapidity of the vector boson. In order to observe this effect, it is necessary to measure distributions in the forward rapidity region. At HERA, the broadening of the q_T distributions is visible at x=0.002, which approximately coincides with the minimal x that can be achieved with Z boson production in Run IIb.In any case, it will be interesting, from the point of view of predictions for the LHC, to test the resummation formalism in this kinematic region.

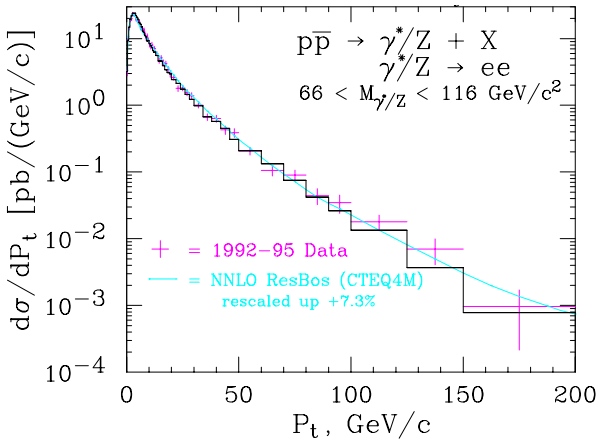

Figure 2.55: The Z p_T distribution measured by CDF in Run Ib. The data is compared to predictions from the resummation program ResBos [34] (curve) and Pythia 6.1 (histogram).

2.6.5.3 W/Z + jets

In Run I, the distributions for W/Z + n jets have been measured out to an n value of 4 (with an E_T cut on the jets of 15 GeV/c).The cross section for $W(\rightarrow e\nu)+ \geq njets$ from Run I is shown in Figure 2.56.

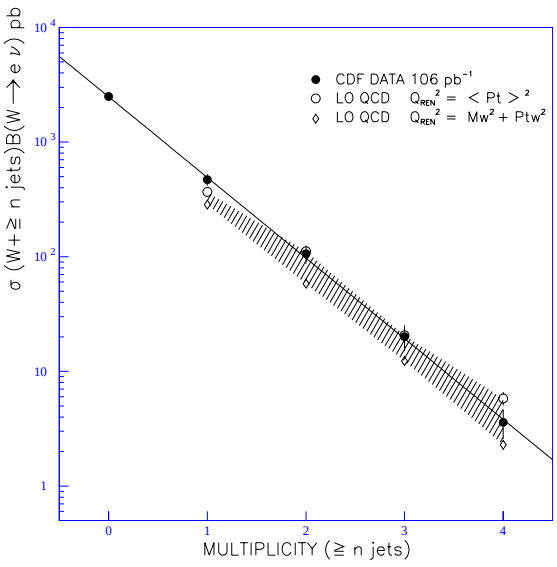

Figure 2.56: The cross section for $W(\rightarrow e\nu)+ \geq njets$ for CDF from Run I.

In RunIIb, the cross section will be measured for W/Z with up to 8 jets. Such measurements are interesting not only in their own right, but also as a check on the backgrounds for new physics involving W/Z (or leptons plus missing transverse energy) production with a large number of jets. Current calcula-

tions can cover this region, but only at leading order. Thus, it is important to have experimental measurements against which to normalize the theoretical predictions. Of particular interest are final states consisting of W/Z plus a heavy quark pair (+jets). The foremost example is $Wb\overline{b}$, the primary background for a low mass Higgs search at the Tevatron. With 15 fb^{-1}, CDF will have a sample of approximately 7500 $W(\rightarrow e\nu) + b\overline{b}$ events, 2100 of them with 1 or more additional jets (all jets required to have $|\eta| < 2.5$ and $E_T > 20$ GeV/c), 500 of them with 2 or additional jets and 90 of them with 3 or more additional jets [35]. (No efficiency or tagging corrections have been applied and the calculation is at leading order.)

2.6.6 Single and Double Photon Production

Single and double photon production at high transverse momenta have long been viewed as ideal processes for testing the formalism of perturbative QCD, as both the experimental and theoretical systematic errors have traditionally been lower than for jet production in the same kinematic range. NLO calculations are available for both processes [36, 37, 38] and NNLO calculations should be available by the start of Run IIb. [39]. The inclusive photon cross section is approximately a factor of 3000 lower than the cross section for inclusive jet production at high E_T. Given the factor of 1500 increase in statistics in Run IIb (compared to Run I), the reach for photons in Run II will be slightly less than achieved for the inclusive jet cross section in Run I, as shown in Figure 2.57 [40]. At low to moderate values of E_T, the gluon-quark (Compton) scattering subprocess dominates the isolated photon cross section while quark-antiquark scattering is the dominant subprocess at high E_T. There are backgrounds to photon production from the decay of π^os (resulting from jet fragmentation). These backgrounds are greatly suppressed by isolation cuts applied to the data, but even without explicit isolation cuts the background becomes less important as the transverse momentum of the photon is increased. The same isolation cuts also suppress Bremsstrahlung mechanisms for producing photons (the photon brems off of a quark line), which otherwise would tend to dominate the production at low E_T. Above an E_T value of 100 GeV/c, the signal fraction for the photon candidate sample approaches 100%. The current level of agreement of the CDF direct photon data with NLO QCD theory is shown in Figure 2.58. The data lies above the theory at low E_T and below the theory at higher E_T. The deviation at low E_T is believed to be due to the effects of soft gluon emission (k_T [41]), while the cause for any deviation at higher values of E_T is currently unknown. It will be extremely interesting both to understand the lower E_T region better and to probe the higher E_T region in Run II.

In addition there will be measurements with tagged final states. Run I measurements of photon plus muon events allowed for measurements of the bottom and charm content of the photon events using the relative p_T of charged tracks around the muon [42]. This sample will benefit both from the added luminosity and also from the improved detection of displaced vertices allowing for heavy flavor tagging in both the inclusive photon and muon plus photon samples.

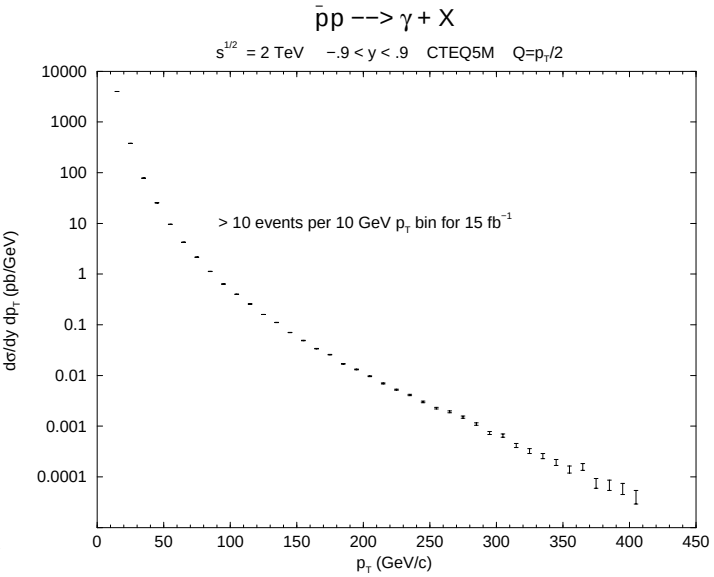

Figure 2.57: The expected reach in E_T for inclusive photon production in Run II using a NLO QCD prediction and CTEQ5M pdf's.

Diphoton production is a small cross section and will benefit greatly from the increased statistics of Run IIb. The diphoton cross section from Run Ib is plotted in Figure 2.59, as a function of the diphoton mass [43]. The backgrounds from jet fragmentation have been subtracted. The measurement is statistics-limited but good agreement is observed with the NLO QCD prediction [37]. The reach in diphoton mass in Run IIb can be observed in Figure 2.60 [44].

The dominant production mechanism for low diphoton mass is gg scattering while $q\bar{q}$ scattering dominates for higher diphoton mass values. (As for

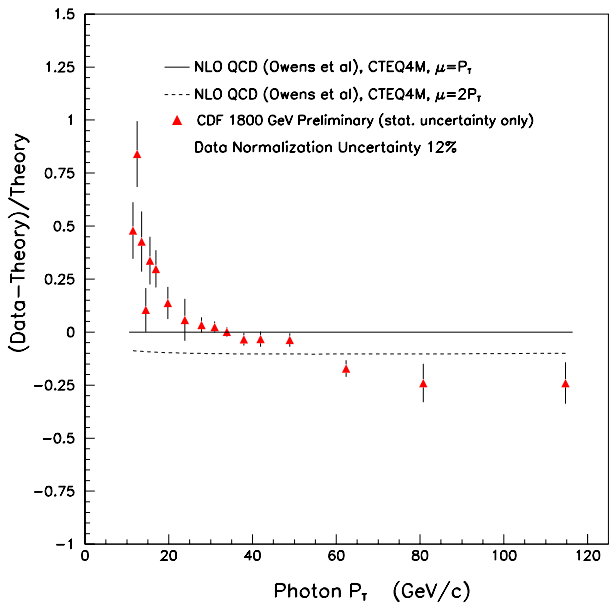

Figure 2.58: Comparison of the CDF photon cross section in Run Ib to NLO theoretical predictions [36].

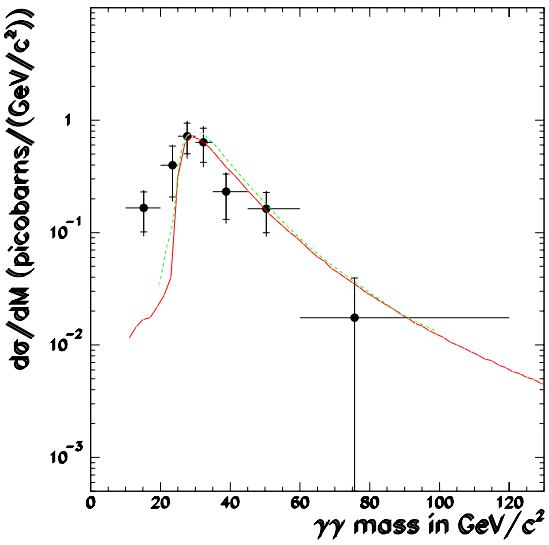

Figure 2.59: The diphoton cross section measured by CDF in Run Ib compared to NLO theoretical predictions [37].

the case of single photon production, the imposition of an isolation cut reduces the contribution from Bremsstrahlung subprocesses, which otherwise would dominate the cross section for low diphoton masses).

The understanding of the production mechanisms and yields for single and double photon production (and of the production and yield for the π^o backgrounds) is of importance for Higgs searches in the $\gamma\gamma$ decay mode at the LHC. In addition, Higgs production, both at the Tevatron and at the LHC, can be affected by soft gluon emission from initial state partons, and separation of signal and background can benefit from a reliable resummation formalism. Low mass diphoton production at the Tevatron offers an opportunity for the predictions of this formalism to be studied for gg initial states [45]. By measuring diphoton production at forward rapidities as well, the gg resummation formalism can be studied in a kinematic regime similar to that relevant for light Higgs production at the LHC.

The rapidity distribution for diphoton production (2 entries for each pair) for Run IIb is shown in Figure 2.61 [46]. A sizeable cross section is present in the forward rapidity region.

Anomalous high mass diphoton production can also serve as a signature for new physics, such as the presence of large extra dimensions [47]. Thus, an understanding of the QCD production mechanisms is crucial.

2.6.7 Diffractive Physics

Diffractive processes in high energy hadron hadron collisions are still not well understood, although great progress has been made by CDF and DØ in recent years. QCD is the fundamental theory of strong interactions but is only directly applicable to hard (large Q^2) processes for which the coupling α_S is small enough that the perturbative series converges rapidly. In every collision involving hadrons this condition is violated (after a hard scatter, hadronization takes place on all scales down to the pion mass). The process of confinement is sometimes considered to be *the* main issue in QCD. In the transition from partons to color singlet hadrons, sometimes color singlet clusters of hadrons are formed, well separated in rapidity from other color singlet clusters. These events have rapidity gaps, where there are no hadrons over a large (typically > 3 units) region of rapidity y. The largest gaps, 15 units at the Tevatron, are in elastic scattering $p\bar{p} \rightarrow p\bar{p}$. It is to be hoped that one day we will be able to predict elastic scattering on the basis of QCD. Today it is partially described by Regge theory. Regge theory is based on some sound principles such as analyticity, crossing symmetry and unitarity but it is not a complete theory. Perhaps one will be able to derive Regge Theory (or a similar theory) from QCD. Then it will be important to have as complete data as possible on diffractive

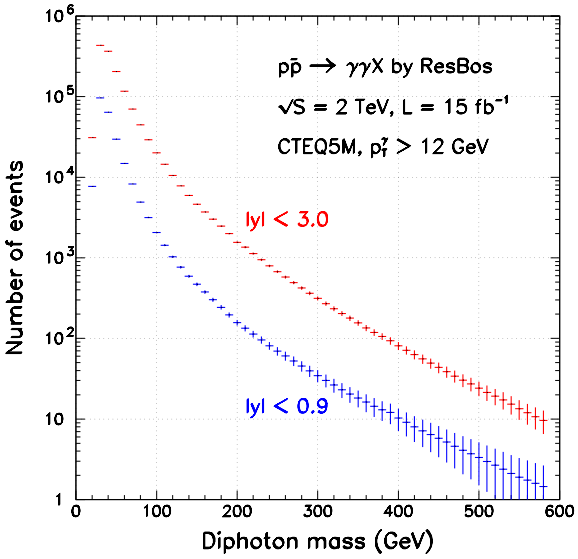

Figure 2.60: Predictions for the number of diphoton events expected in Run IIb with 15 fb^{-1}, for two different rapidity cuts on the photons, using the ResBos program.

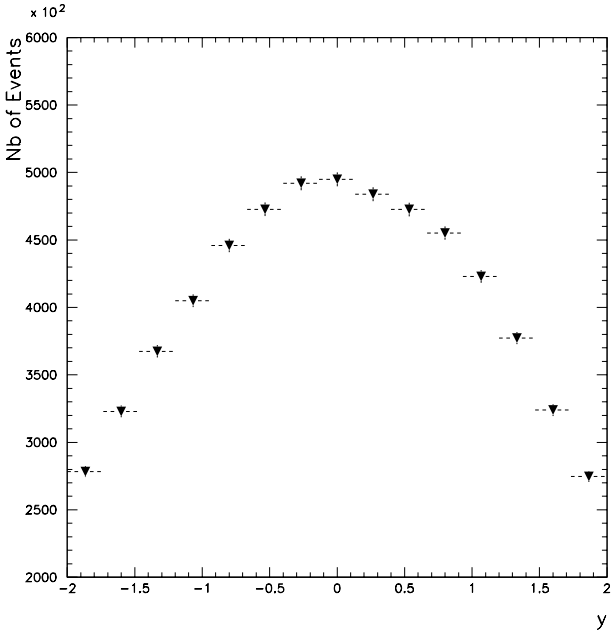

Figure 2.61: Predictions for the diphoton rapidity distribution (the rapidity of each photon is plotted separately) expected in Run IIb, calculated using the DIPHOX [38] program.

processes including elastic scattering. Up to now this has only been measured at the Tevatron out to $t = -0.6$ GeV^2, but at lower energies (ISR and S$p\bar{p}$S) there is structure at larger $|t|$ ($\frac{d\sigma}{dt}$ becomes flat). In Regge theory the 4-momentum transfered between the p and $\bar{p}$ when they scatter elastically at these high energies is almost entirely carried by a *pomeron* at low $|t|$ (and by a photon for *very* low $|t|$ which is Coulomb scattering) with a possible transition to *odderon* exchange at large $|t|$. The pomeron carries positive C-parity and the odderon negative C-parity, and it would change sign between $p\bar{p}$ and pp scattering. To first order it is believed that the "soft" (low Q^2) pomeron is 2-gluon exchange (together with multiple exchanges) and the odderon is 3-gluon exchange (two gluons cannot have C = -1). Progress in understanding diffractive (large rapidity gap) processes has come mostly from studying hard (high Q^2) interactions that have gaps and/or a leading (Feynman $x_F > 0.9$) (anti-)proton. In CDF from Run 1 we have measured diffractive production of high-E_T jet pairs, J/ψ, b-jets, and W-bosons. We have also measured double diffractive (double pomeron exchange) production of di-jets. Because these processes have different dependencies on quarks and gluons in the initial state, it has been possible to test the notion that diffraction can be viewed as the emission of a pomeron, considered like a virtual spacelike hadron with a universal structure function, and its subsequent interaction with the other beam particle. From this notion is derived the term *factorization* which if true means that one can factorize the process into the emission, propagation and interaction of pomerons. Using such a picture we have derived a "gluonic fraction" of pomerons in hard processes (Q^2 typically 2000 GeV^2) to be 0.54 ± 0.15. Importantly we have also found that factorization in hard interactions is badly violated. This conclusion comes both from comparing our diffractive cross sections with those measured in ep collisions at HERA, and from comparing our single diffractive dijet cross section with our double pomeron dijet cross section. One of the basic quantities in QCD is the structure function of the proton $F(x, Q^2)$. By comparing our diffractive data with non-diffractive data we have been able to derive, and have published, *diffractive structure functions* which can be compared with such *dsf* measured in ep collisions at HERA. We find non-universality.

A new paradigm for hard diffraction is needed. A new description should presumably also take into account another phenomenon we discovered at the Tevatron, that of large rapidity gaps between balancing high E_T jets (hard double diffractive dissociation DDD). The exchanged 4-momentum-squared across the gap is in this case of order 2000 GeV^2

where the concept of a pomeron is probably meaningless. Perhaps a better description is that a hard parton-parton scatter occurs in the normal way by gluon exchange (on a very short time scale) and on a much longer time scale another gluon (or gluons) is exchanged to cancel the color. A similar description may be adequate also for hard single diffraction (and double diffraction). The rapidity gaps would be produced by one hard and one or more soft partons but on very different time scales, so at no *one time* is there a *pomeron*. There is not yet a good universal description of these processes, and it is clear that this is a data-driven field. A lot more data on all processes (higher statistics over a larger range of kinematic variables) is needed.

In Run 1B we made diffractive studies[50] without observing the scattered p or $\bar{p}$ using large rapidity gaps to tag diffraction. We studied diffractive production of di-jets, W, b-jets, and J/ψ. We also studied rapidity gap between pairs of balancing high E_T jets, and soft double diffractive dissociation.

In Run 1C (the last 3 months of Run 1) we added three Roman pots 55 m downstream of CDF with scintillating fiber trackers to measure high x_F (low $\xi = 1 - x_F$) antiprotons. More detailed studies of single diffraction were possible and we observed double pomeron production of di-jets (central di-jets with a low ξ antiproton and a rapidity gap on the proton side). This sample of 130 events corresponds to a cross section of ≈ 44 nb, thus could have been obtained in about 5 minutes of *live time* at L = 10^{31} cm^{-2} s^{-1} given a selective trigger.

In Run 2A we have re-installed[51] the Roman pot spectrometer on the antiproton side with the same detectors but new electronics. We have installed a new set of *rapidity gap counters* along both beam pipes, called Beam Shower Counters (BSC). These will be used in some Level 1 triggers to select diffractive (and double pomeron) candidate events that occurred by themselves (no pile-up). We are installing in the October 2001 shut down a pair of MiniPlug calorimeters covering the regions $3.5 < \eta < 5.5$ ($0.5^\circ < \theta < 3.0^\circ$) on the East and West sides. These will be used both for very forward jets (for the *Jet-Gap-Jet* studies) and as rapidity gap detectors (where the edge can be varied off-line over the η coverage). The forward detectors will be read out for all CDF events, and we will be able to study hard diffractive processes (di-jet, W, Z, high p_T b-jets, etc) with several hundred times the statistics of Run 1C. For the double pomeron di-jet production, which is a subject of great interest, the gain is more like a factor 10^4 if we have an effective trigger. This means that we should be able to measure jet pairs with $E_T(jet) > 50$ GeV rather than the 7-10 GeV of the Run 1C data. We will also be able to tag the jets using the SVX tracker and measure double pomeron production of $b\bar{b}$ di-jets. It has been proposed[52] that di-jets produced in double pomeron exchange are essentially pure gluon jets, with a small admixture of $b\bar{b}$ di-jets, the light quarks being suppressed by the $J_z = 0$ selection rule. In this case we can produce samples of tens of thousands of $> 99\%$ pure gluon jets (to be compared to a present world sample, from $Z \to b\bar{b}g$ at LEP, of < 450 pure g-jets).

We will also in Run 2A study soft double pomeron exchange processes, including exclusive processes where the p and $\bar{p}$ go undetected down the beam pipes and a few central hadrons are produced ($\pi^+\pi^-, K^+K^-, \phi\phi, J/\psi\pi^+\pi^-, \Lambda\bar{\Lambda}, \Omega\bar{\Omega}, \chi_c^\circ, \chi_b^\circ$, etc). These processes probe QCD at very low Q^2, providing information on glueball and hybrid spectroscopy, and on the spin of the pomeron (through the Λ and Ω polarizations).

For Run IIb we want to continue single diffractive studies especially of the W and Z, and to be able to do these studies in the presence of multiple interactions. This can be done with high precision timing on the forward $p/\bar{p}$, matching the forward particle to the W/Z decay products using the central Time of Flight counters. However we envisage that the main thrust of our diffractive studies in Run IIb will be on double pomeron exchange, or events with both p and $\bar{p}$ having $\xi < 0.1$ and well measured, with a central massive system, especially di-jets and $b/\bar{b}$ di-jets, high p_T leptons and photons. This is the subject of a separate proposal, to be submitted[1] to the April 2002 PAC, following the Letter of Intent[53]. The proposal is to replace the existing Roman pots on the $\bar{p}$ side with new pots with silicon microstrips replacing the scintillating fiber hodoscopes and quartz Cerenkov counters (for timing) replacing the scintillator trigger counters. It is also proposed to move some Tevatron magnets to make warm space on the p side and install identical detectors there, to study the reaction $p\bar{p} \to pX\bar{p}$. Measuring both the p and $\bar{p}$ with high precision, M_X is known to about 250 MeV. The system X is measured in CDF. It is especially interesting to plot M_X when X is a $b\bar{b}$ dijet, a $\tau^+\tau^-$

[1] Subject to approval by CDF.

pair, or a $WW^{(*)}$ candidate, as it has been proposed that the Higgs boson might be observable in such interactions. If it *is* seen, its mass is measured very well ($<\approx$ 100 MeV). High-$|t|$ elastic scattering, which has not yet been measured at the Tevatron, will be measured in parallel (indeed it is used to calibrate the spectrometers). There is still disagreement among theorists on the observability of the Higgs boson with this method at the Tevatron. Nevertheless the field of high mass double pomeron exchange is unexplored territory and there have been many suggestions that it might give surprises. Timing resolution $\approx$ 50 ps in the Roman pots will minimize problems associated with pile-up at high luminosity. More details will be presented in the VFTD Proposal at the April 2002 PAC.

Bibliography

[1] See, for example, the website for the Les Houches Workshops on Physics at TeV Colliders, http://wwwlapp.in2p3.fr/conferences/LesHouches/Houches2001/ ; the proceedings for the QCD/SM section of the 1999 workshop can be found at hep-ph/0005114.

[2] See, for example, the website for the website for the Run 2 Workshop on QCD and Weak Boson Physics, http://www-theory.fnal.gov/people/ellis/QCDWB/QCDWB.html , and references therein.

[3] S. Ellis, Z. Kunszt and D. Soper,(EKS), Phys. Rev. Lett. **64** 2121 (1990).

[4] F. Aversa, M. Greco, P. Chiappetta, J.P. Guillet, Z. Phys. **C46**, 253 (1990).

[5] W.T. Giele, E.W.N. Glover and D.A. Kosower,(JETRAD), Phys. Rev. Lett., **73**, 2019 (1994).

[6] W.B. Kilgore and W.T. Giele, hep-ph/0009193.

[7] E.W.N. Glover, hep-ph/0106069.

[8] G. Corcella *et al*, JHEP **0101**, 010 (2001) [hep-ph/0011363].

[9] T. Sjostrand *et al*,Comput. Phys. Commmun. **135**, 238 (2001) [hep-ph/0010017].

[10] H. Baer *et al*, hep-ph/0001086.

[11] See, for example, the talks at the Workshop on Monte Carlo Generator Physics for Run II at the Tevatron, http://fnth31.fnal.gov/people/giele/runiimc/ .

[12] G. Corcella and M.H. Seymour, Nucl. Phys. **B565**,227(2000) [hep-ph/9908388].

[13] G. Miu and T. Sjostrand, Phys. Lett. **B449**, 313(1999) [hep-ph/9812455].

[14] E. Boos *et al*, hep-ph/0109068.

[15] See, for example, Y. Chen, J.C. Collins, N. Tkachuk, JHEP **0106**, 015 (2001) [hep-ph/0105291].

[16] CDF Collaboration, F. Abe *et al.*, Phys. Rev. Lett. **77**, 438 (1996).

[17] CDF Collaboration, T. Affolder *et al*, Phys. Rev. **D64**, 032001 (2001)[hep-ph/0102074].

[18] CDF Collaboration. T. Affolder *et al.*, Phys. Rev. D **61**, 091101 (2000).

[19] CDF Collaboration, F. Abe *et al.*, Phys. Rev. Lett. **64**, 157 (1990).

[20] CDF Collaboration, F. Abe *et al.*, Phys. Rev. Lett. **80**, 3461 (1998).

[21] CDF Collaboration, F. Abe *et al*, Phys. Lett. **B384**, 401 (1996).

[22] CTEQ Collaboration, J. Huston *et al.*, Phys. Rev. Lett. **77**, 44 (1996).

[23] H.L. Lai *et al.*, Phys. Rev. D **55**, 1280 (1997).

[24] H.L. Lai *et al*, Eur. Phys. J. **C12**, 375 (2000) [hep-ph/9903282].

[25] D0 Collaboration, Phys. Rev. Lett. **86**, 1707 (2001), [hep-ex/0011036].

[26] We would like to thank Steve Ellis for generating these figures.

[27] J. Ellis, V. Khoze, W.J. Stirling, Z. Phys. **C75**, 287 (1997) [hep-ph/9608486].

[28] N. Kidonakis, J.F. Owens, Phys. Rev.**D63**, 054019 (2001),[hep-ph/0007268].

[29] T. Affolder, C. Mesropian *et al*, submitted to Phys. Rev. Lett., [hep-ex/0108034].

[30] See, for example, the discussion by S. Catani in Reference 1.

[31] P. Nadolsky, private communication.

[32] H1 Collaboration,Phys. Lett. **B356**, 118 (1985); H1 Collaboration, Eur. Phys. J**C12**, 595 (2000); ZEUS Collaboration, Z.Phys. C**70**, 1 (1996).

[33] J.C.Collins, D.E.Soper, G. Sterman, Nucl. Phys. **B250**, 199 (1985).

[34] C. Balazs, C.P. Yuan, Phys. Rev. D**56**, 5558 (1997); C. Balazs, C.P. Yuan, Phys. Rev. D**59**, 114007 (1999).

[35] M.L. Mangano, M. Moretti, R. Pittau, [hep-ph/0108069].

[36] P. Aurenche, R. Baier, M. Fontannaz, Phys. Rev. **D42**, 1440 (1990); H. Baer, J. Ohnemus, J.F. Owens, Phys. Rev. **D42**, 61 (1990).

[37] P. Aurenche, A. Douri, R. Baier, M. Fontannaz, D.Schiff, Z. Phys. **C29**, 459 (1985); B. Bailey, J. Owens, J. Ohnemus,, Phys. Rev. D **46**, 2018 (1992).

[38] T. Binoth, J.P. Guillet, E. Pilon, M. Werlen,(DIPHOX) Eur. Phys. J. **C16**, 311 (2000), [hep-ph/9911340]; T. Binoth, J.P. Guillet, E. Pilon, M. Werlen, Phys.Rev. **D63**, 114016 (2001), [hep-ph/0012191].

[39] L. Dixon, private communication.

[40] We would like to thank J. Owens for generating this plot.

[41] L. Apanasevich *et al.*,Phys. Rev. **D59**, 074007 (1999),[hep-ph/9808467].

[42] K. Kurino, S. Kuhlmann, CDF/ANAL/CDF/CDFR/5462.

[43] Takeshi Takano, University of Tsukuba Doctoral Thesis (Sept. 1997).

[44] We would like to thank C. Balazs for the generation of this figure.

[45] C. Balazs, J. Huston, I. Puljak, Phys. Rev. **D63**, 014021 (2001), [hep-ph/0002032].

[46] We would like to thank J.P. Guillet for the generation of this figure.

[47] D. Gerdes, S. Murgia, CDF/ANAL/EXOTIC/CDFR/5694.

[48] DØ Collaboration, T. Asakawa *et al.*, Proceedings of Hadron Collider Phys. Workshop XIII Jan. 14-20, 1999, Bombay, India.

[49] A.D. Martin, *et al.*, Eur. Phys. J. **C4**, 463 (1998).

[50] The Hard Diffraction Group of CDF : Proposal for Hard Diffraction Studies in CDF, CDF-**2940**, (Feb 1995)

[51] Proposal for Hard Diffraction and Very Forward Physics with CDF in Run II, CDF-**4591**, (Aug 1997); Addendum CDF/DOC/CDF/CDFR/4833 (Nov 1998).

[52] V.A.Khoze, A.D.Martin and M.G.Ryskin, [hep-ph/0011393].

[53] A Search for the Higgs Boson using Very Forward Tracking

Detectors with CDF. LOI 920 (March 2001). CDF/PHYS/EXOTIC/CDFR/5585

2.7 *B* Physics in Run IIb

2.7.1 Introduction

The study of particles containing the bottom quark has provided valuable insights into the weak interactions and QCD: *e.g.* the long lifetime of b hadrons, the large mixing observed in the B^0–$\bar{B}^0$ system, the discovery of heavy quark symmetries and the utility of heavy quark effective theories, and the observation of "penguin" decays. This is not surprising given that the bottom quark is heavy and that its preferred charged current coupling to the top quark occurs only in virtual higher–order processes. The b hadrons provide a valuable laboratory in which to extract fundamental parameters of the Standard Model, test its consistency, and search for rare processes which are sensitive to physics beyond the Standard Model.

Measurements with b hadrons can in principle be used to extract information on 5 of the 9 elements of the CKM matrix that relates the weak–interaction and mass eigenstates of quarks. The CKM matrix can be written as:

$$V = \begin{pmatrix} V_{ud} & V_{us} & V_{ub} \\ V_{cd} & V_{cs} & V_{cb} \\ V_{td} & V_{ts} & V_{tb} \end{pmatrix} \tag{2.3}$$

or in the Wolfenstein [1] parameterization:

$$\simeq \begin{pmatrix} 1-\lambda^2/2 & \lambda & A\lambda^3(\rho - i\eta) \\ -\lambda & 1-\lambda^2/2 & A\lambda^2 \\ A\lambda^3(1-\rho-i\eta) & -A\lambda^2 & 1 \end{pmatrix} \tag{2.4}$$

given here to $O(\lambda^4)$, where $\lambda = \sin(\theta_{\rm Cabibbo})$ and the other three parameters A, ρ, and η encode the remaining two weak mixing angles and the irreducible complex phase that introduces *CP* violation.

Unitarity of the CKM matrix requires the relationship

$$V_{tb}^* V_{td} + V_{cb}^* V_{cd} + V_{ub}^* V_{ud} = 0, \tag{2.5}$$

which can be displayed as a triangle in the complex plane, as shown in Figure 2.62. The base of this triangle has been rescaled by $A\lambda^3$ to be of unit length. Also shown are the angles α, β, and γ which lead to *CP* violating effects that can, in principle, be measured with b hadrons.

The b physics goals for CDF II include:

- Observation of *CP* violation in $B^0 \to J/\psi K_S^0$ and a measurement of $\sin(2\beta)$ to ± 0.02.

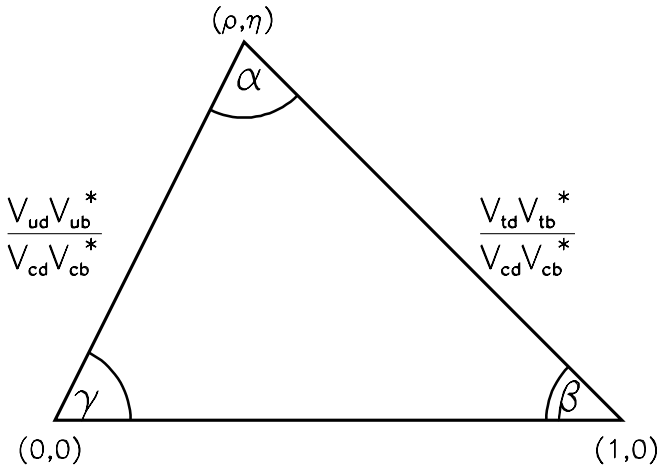

Figure 2.62: The unitarity triangle indicating the relationship between the CKM elements.

- Measurement of the *CP* asymmetries in $B_s^0 \to J/\psi\phi, J/\psi\eta^{(\prime)}$.
- Observation of *CP* violation in $B^0 \to \pi^+\pi^-$ and $B_s^0 \to K^+K^-$ and a measurement of γ to $\pm 3^\circ$.
- Observation of B_s^0 mixing and measurement of Δm_s and $\Delta\Gamma_s/\Gamma_s$.
- Observation of exclusive decays of the B_c^+ meson, allowing precise determination of its mass and lifetime.

The copious production of b hadrons of several species at the Tevatron offers the opportunity for measurements that will allow us to fully check the consistency of the CKM picture. To take advantage of the broad spectrum and high production rate of b hadrons at the Tevatron, the challenges of triggering and event reconstruction in high energy $p\bar{p}$ collisions must be successfully met.

2.7.2 The Run I CDF *b* program

CDF has demonstrated the ability to mount a b physics program exploiting the unique aspects of hadron production. More than fifty papers have been published (or are submitted and under review) in PRL and PRD by CDF on the subject. Many of the CDF results are highly competitive with measurements from LEP or CLEO and some of them are the best measurements from a single experiment. These measurements include:

- Individual b hadron masses ($B^+, B^0, B_s^0, \Lambda_b$) [2, 3]
- Individual b hadron lifetimes ($B^+, B^0, B_s^0, \Lambda_b$) [4, 5, 6]
- The *CP* violation parameter $\sin 2\beta$ [7]
- Polarization in $B^0 \to J/\psi K^{*0}$ and $B_s^0 \to J/\psi\phi$ [8]
- Observation of the B_c^+ meson [10]
- B^0 mixing and limits on B_s^0 mixing [11, 12]
- Searches for rare decays ($B^0, B_s^0 \to \mu^+\mu^-$; $B^\pm \to \mu\mu K^\pm$; $B^0 \to \mu\mu K^{*0}$; $B^0, B_s^0 \to \mu e$) [13]

CDF has also carried out several studies of B and quarkonium production and of $b\bar{b}$ production correlations [14, 15]. The QCD aspects of these results have generated much interest. In addition, they provide the understanding of B production necessary for studies of B decay.

The analyses carried out by CDF have shown that the mass resolution obtained with the CTC coupled with the vertex resolution obtained with the SVX allows us to (a) isolate fully–reconstructed B decays and (b) measure the lifetime of the decaying mesons.

One of the most interesting measurements by CDF in Run II was the first significant measurement of the *CP*-violation parameter $\sin 2\beta$ using a sample of approximately 400 $B_d^0 \to J/\psi K_s$ decays from 110 pb^{-1} of data. Using several flavor tagging methods, it was determined that $\sin 2\beta = 0.79^{+0.41}_{-0.44}$. This measurement also demonstrates CDF's ability to tag the flavor of B mesons at production, which is crucial to many of the measurements we expect to do in Run II.

2.7.3 CDF strategy for *b* physics in Run II

Recently, Babar and Belle presented measurements of $\sin 2\beta = 0.59 \pm 0.14(stat) \pm 0.05(syst)$ [16] and $0.99 \pm 0.14(stat) \pm 0.06(syst)$ [17], respectively, showing that *CP* is definitely violated in decays of B mesons, beginning a new era. The next step is acquire sufficient statistics to make precision measurements that fully constrain the unitarity triangle and the CKM matrix. Then, by making further measurements, it will be possible to explore whether the Standard Model can fully explain *CP* violation in the B sector or whether there are indications of new sources of *CP* violation.

CDF's Run II B Physics program enhances and complements those of the B factories. The e^+e^- experiments have the advantages of already collecting a significant amount of data and of having cleaner event topologies, allowing observation of more modes and higher tagging rates. The advantages of doing B physics at the Tevatron include the higher B production rates and the production of B_s^0 mesons and B baryons. Although the B factories have been running for a couple of years, if CDF acquires the expected 2 fb^{-1} of data in the next two years, it will have a measurement of $\sin 2\beta$ that is at least as good as those of the B factories. CDF's extensive experience doing B physics in Run I indicates its ability to isolate clean signals and do precision measurements. In addition, there are important measurements, such as determining Δm_s from B_s^0 mixing and searching for *CP* violation in $B_s^0 \to J/\psi\phi$, that cannot be done at the B factories, but which CDF is well suited to do.

In Run II, CDF will take advantage of the broad spectrum of b hadrons produced at the Tevatron to make measurements with B_s^0 mesons, B_c^+ mesons and b baryons as well as with B^0 and B^+ mesons. Key elements of CDF that made the Run I high–p_T physics program (for example, top and W) so successful include excellent tracking resolution, lepton identification (including dE/dx), secondary–vertex reconstruction, and a flexible and powerful trigger and data acquisition system. These same elements are also the foundation upon which a successful b physics program was built.

The strategy for CDF II is to build on our experience in Run I, to optimize the quality of information in the central region while expanding coverage, and to exploit many additional b hadron decay channels. The tracking upgrades (SVXII/ISL/COT) are expected to improve the present mass resolution while the 3D silicon tracker (SVXII) is expected to improve the vertex finding ability. The lepton and tracking coverage will be increased (SVXII, ISL and CMX/IMU). The dE/dx information from the COT will be employed for particle identification. For Run II, CDF has installed a time-of-flight (TOF) system in the space at the outer diameter of the tracking volume (COT) to provide for $K/\pi/p$ separation at low to moderate transverse momenta. From these improvements, we also expect to increase our tagging efficiencies and dilutions to $\epsilon D^2 = 9.1\%$ for B^0 mesons and to 11.3% for B_s^0 mesons.

In addition, the high–rate capability of the up-

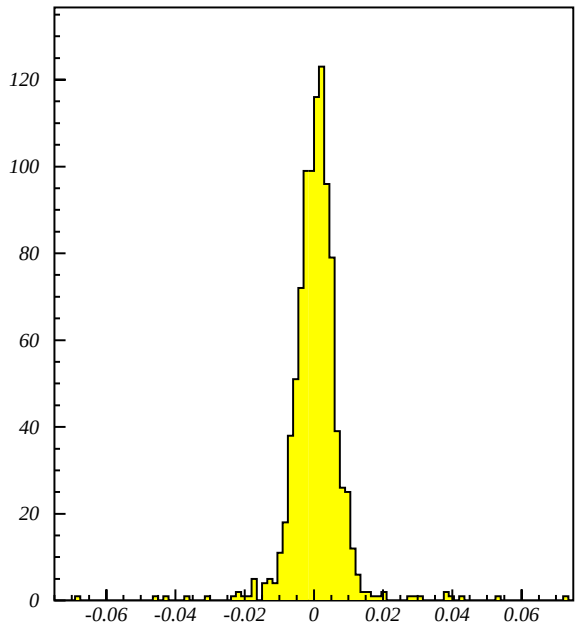

Figure 2.63: Track impact parameter distribution as determined online by the SVT during the Fall, 2000, commissioning run. The 45 μm resolution is consistent with expectations.

graded trigger/data acquisition system will enable us to handle the high luminosity of the Main Injector era while lowering thresholds and acquiring events in many more channels. Of particular importance will be the ability to form triggers based on track information alone at Level 1 (XFT) and detect the presence of tracks with displaced vertices at Level 2 (SVT). Figure 2.63 shows the impact parameter resolution obtained online with the SVT during the commissioning run in the Fall of 2000. The excellent resolution will give CDF a powerful tool for triggering on tracks that did not originate at the primary vertex, particularly the decays products of B hadrons.

Thus, the CDF II detector will provide for a competitive b physics program that has unique features and addresses a wide variety of topics of fundamental importance.

2.7.4 Plans for Run IIb

Since data is just beginning to be accumulated for Run II, the current performance of the detector cannot be fully assessed, although early evaluation of the detector performance looks very promising. However, the CDF collaboration is confident from its extensive experience doing B physics in Run I that we can accurately extrapolate to Run IIb.

It is assumed that the detector performance anticipated for Run IIa will be maintained in Run IIb. This includes the excellent momentum resolution of the COT, the electron identification capabilities of the calorimeters, and muon identification.

Of particular importance for doing B physics is the excellence secondary vertex resolution of the SVX II detector with Layer 00, expected to be less than 20 microns. It is assumed that the replacement silicon vertex detector for Run IIb will have comparable resolution and coverage as the one for Run IIa.

Since most of the measurements planned for Run IIb are not expected to be systematically limited, previous studies done for Run IIa apply or can be straight-forwardly extrapolated from the 2 fb^{-1} of Run IIa to the 15 fb^{-1} of Run IIb. This assumes that the increased instantaneously luminosity of Run IIb can be handled without needing to prescale the relevant triggers. The most important triggers for the physics discussed below are the J/ψ, inclusive lepton, two displaced track, and dimuon plus displaced track triggers. The current bandwidth needed for the J/ψ and dimuon plus displaced track triggers are a sufficiently small fraction of the total available that it is anticipated with improvement in DAQ system that these triggers will not be a limiting factor in Run IIb. The inclusive lepton trigger will be bandwidth limited, but for B physics can be augmented with a displaced track requirement, which will reduce the rate without significant loss of signal.

On the other hand, the two displaced track trigger is more problematic, since it is currently the largest single component of the available trigger bandwidth, particularly at Level 1. For Run II, CDF has investigated three displaced track trigger strategies for different Tevatron conditions (A, B, and C in table 2.15). For Run IIb, the third scenario will work, but would result in a 50% loss of signal compared to the scenario A to be used in Run IIa. To avoid this loss, the ability to select on invariant mass in the Level 1 trigger is desired. This will allow the displaced track trigger to remain efficient at an acceptable rate for two–body B hadron decays.

Several B physics measurements of importance in Run IIb are described below. The topics included here were selected because (1) the physics is inter-

	Scenario A	Scenario B	Scenario C
Luminosity (10^{32}cm^{-1}s^{-1})	< 1	1 - 2	1 - 2
Beam crossing interval (ns)	396	132	396
$p_T^{(1)}$, $p_T^{(2)}$ (GeV/c)	> 2	> 2.25	> 2.5
$p_T^{(1)} + p_T^{(2)}$ (GeV/c)	> 5.5	> 6	> 6.5
$\Delta\phi$	$< 135°$	$< 135°$	$< 135°$
Cross section (μb)	252 ± 18	152 ± 14	163 ± 16

Table 2.15: Level-1 XFT trigger cuts and cross sections for the three Tevatron operating scenarios considered.

esting, (2) the measurement is competitive or better than the corresponding measurement expected from other experiments, (3) the measurement represents a unique measurement at the Tevatron, and/or (4) the measurement illustrates requirements on the detector performance. This list of physics measurements is not exhaustive but is illustrative of the exciting B physics that will be possible in Run IIb.

2.7.5 *CP* Violation in the *B* system

The most important goal of the CDF II B physics program is to study *CP* violation in the B system. This will continue into Run IIb with an emphasis on greater precision and expansion into lower rate, but interesting, modes.

The decay $B_s^0 \to J/\psi K_s$ is the golden mode, which all experiments, including CDF, will use to make precision measurements of $\sin 2\beta$. The decays $B_s^0 \to J/\psi\phi$ and $J/\psi\eta^{(\prime)}$ are interesting because the *CP* asymmetries in the Standard Model are expected to be very small, making them very sensitive to new *CP* violating physics. Once $\sin 2\beta$ and Δm_s (see below) are precisely measured, the unitarity triangle will be fully constrained. It then becomes important to measure other properties to see if they are consistent. The other angles of the unitarity triangle are notoriously difficult to measure precisely, but CDF may have a unique opportunity to measure the angle γ very well using the decays $B^0 \to \pi\pi, K\pi$ and $B_s^0 \to KK, K\pi$. Various $B \to DK$ decays are also sensitive to γ but are statistically limited due to small branching ratios, making them ideal to pursue in Run IIb. Finally, CDF will be able to search for direct *CP* violations in various decay modes (the B physics equivalent to ϵ'/ϵ in the K system), such as $\Lambda_b \to pK, p\pi$.

2.7.5.1 *CP* Asymmetry in $B^0 \to J/\psi K_S$

For measuring *CP* violation in the B system, the decay mode most frequently discussed in the literature [18] is $B^0 \to J/\psi K_S$. *CP* violation manifests itself as an asymmetry in the partial decay rates of B^0 and $\bar{B^0}$ to the same final state, $J/\psi K_S$ (a *CP* eigenstate). This results in an asymmetry:

$$A_{CP} = (N - \bar{N})/(N + \bar{N}) \tag{2.6}$$

in the number of decays from B^0 (N) and $\bar{B^0}$ ($\bar{N}$) mesons. The asymmetry in the partial decay rates is directly related to the angle β of the CKM unitary triangle:

$$\Gamma(B^0, \bar{B^0} \to J/\psi K_S) \propto e^{-\Gamma t}[1 \pm \sin(2\beta)\sin(\Delta m t)] \tag{2.7}$$

where Δm is the mass difference between the heavy and light B meson states and t is the proper decay time. The observed asymmetry A_{CP}^{obs} will be smaller than A_{CP} by a factor known as the "dilution" D; $A_{CP}^{obs} = DA_{CP}$. The dilution receives contributions from the proper time resolution, from the method used to tag the flavor of the B meson at the time of production, and from backgrounds.

From the full data sample accumulated in Run I (110 pb^{-1}), CDF used 400 $B_d \to J/\psi K_s$ decays to measure $\sin 2\beta = 0.79^{+0.41}_{-0.44}$. We obtained this sample with a dimuon trigger that required both muons to have transverse momentum (p_T) greater than 2.0 GeV/c. For this analysis, we did not require that the events be in the SVX fiducial region, although we used SVX information if available.

For Run IIa, due to (1) the increased cross section at $\sqrt{s} = 2$ TeV, (2) increased coverage of SVX II, (3) increased muon coverage, (4) improved tagging using the TOF system, (5) lowering the P_T threshold for the dimuon trigger, (6) addition of a $J/\psi \to e^+e^-$

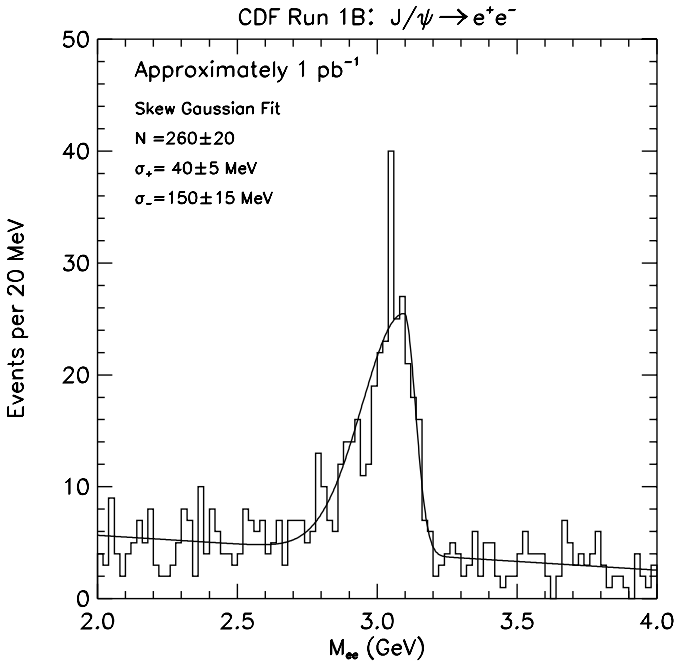

Figure 2.64: $J/\psi \rightarrow e^+e^-$ signal from a test trigger during Run I.

trigger (see figure 2.64), and (7) the increased integrated luminosity from 110 pb^{-1} for Run I to 2 fb^{-1} for Run IIa, we conservatively expect a 50-fold increase in the yield, giving 20,000 $B_d \rightarrow J/\psi K_s$ events from the dimuon channel and 8,000 from the dielectron channel. The systematic uncertainty on $\sin 2\beta$ is dominated by the uncertainty on the dilution. Since the dilution is also determined from the data, its uncertainty also scales with the statistics. Using only the dimuon events, we conservatively expect to measure $\sin 2\beta$ with an uncertainty of 0.05 in Run IIa.

Since we do not see a limiting systematic uncertainty in Run IIb or a problem with triggering, the uncertainty on $\sin 2\beta$ will also scale with the integrated luminosity, giving an uncertainty of 0.02 for the 15 fb^{-1} of Run IIb. A measurement of this precision will be very competitive with those from Babar and Belle at that time and will tightly constrain the unitarity triangle and CKM matrix.

2.7.5.2 *CP* Asymmetry in $B_s^0 \rightarrow J/\psi\,\phi$

While the *CP* asymmetry in $B^0 \rightarrow J/\psi K_S$ measures the weak phase of the CKM matrix element V_{td} in the standard convention, the *CP* asymmetry in $B_s^0 \rightarrow J/\psi\,\phi$ measures the weak phase of the CKM matrix element V_{ts}. The latter asymmetry is expected to be very small in the Standard Model, but in the context of testing the Standard Model has the same fundamental importance as measuring the more familiar *CP* asymmetries. This measurement is most accessible, if not unique, to experiments at a hadron collider.

Our Run I B_s^0 mass analysis indicates that our yield of reconstructed $B_s^0 \rightarrow J/\psi\,\phi$ events is 40% that of $B^0 \rightarrow J/\psi K_S$ (see Figure 2.65). Since the improvements for $B^0 \rightarrow J/\psi K_S$ ($\approx 20,000$ dimuon events) apply equally to $B_s^0 \rightarrow J/\psi\,\phi$, we can expect ≈ 8000 events for this decay mode in Run IIa.

The flavor tagging techniques for the B_s^0 are the same as those for the B^0, with one exception: The fragmentation track correlated with the B_s^0 meson is a kaon instead of a pion. A PYTHIA study indicates that the Time–of–Flight system, by identifying kaons, will allow us to increase the efficiency of the same-side kaon algorithm from 1.0% to 4.2% [19]. Thus, we assume a total flavor tagging efficiency (ϵD^2) for B_s^0 mesons of 11.3%

The magnitude of a *CP* asymmetry in $B_s^0 \rightarrow J/\psi\,\phi$ decays will be modulated by the frequency of B_s^0 oscillations. Thus, for a meaningful limit, we must be able to resolve B_s^0 oscillations. If we neglect ($c\tau$) resolution effects and scale from the $B^0 \rightarrow J/\psi K_s$ mode, we can expect a precision on the asymmetry of ± 0.07 from a time dependent measurement in Run IIa. However, resolution effects smear the oscillations and produce an additional dilution factor of

$$D_{res} = e^{\left(\frac{-x_s^2\sigma_\tau^2}{2\tau^2}\right)}, \qquad (2.8)$$

where $x_s = \Delta m_s/\Gamma_s$, σ_τ is the resolution on the proper decay time, and τ is the average B_s^0 lifetime. With the addition of Layer 00, we expect that the proper lifetime resolution for the SVX II will be $\sigma_\tau/\tau \approx 0.03$ [20]. For $x_s = 25$, this dilution degrades the resolution on the asymmetry by a factor of 1.3.

There is an additional complication in this mode if the $J/\psi\,\phi$ final state is not a *CP* eigenstate. If this mode were a *CP* eigenstate, then the full resolution on the *CP* asymmetry would apply. If the mode is a mixture of *CP* states, then an angular fit including the *CP* violation is needed. Studies indicate that if this mode is an equal mixture of *CP*-even and *CP*-odd states, then the resolution on the *CP* asymmetry as determined from the angular fit is degraded by a factor of roughly 2. In Run I, CDF measured the *CP* even fraction to be 0.77 ± 0.19 [8].

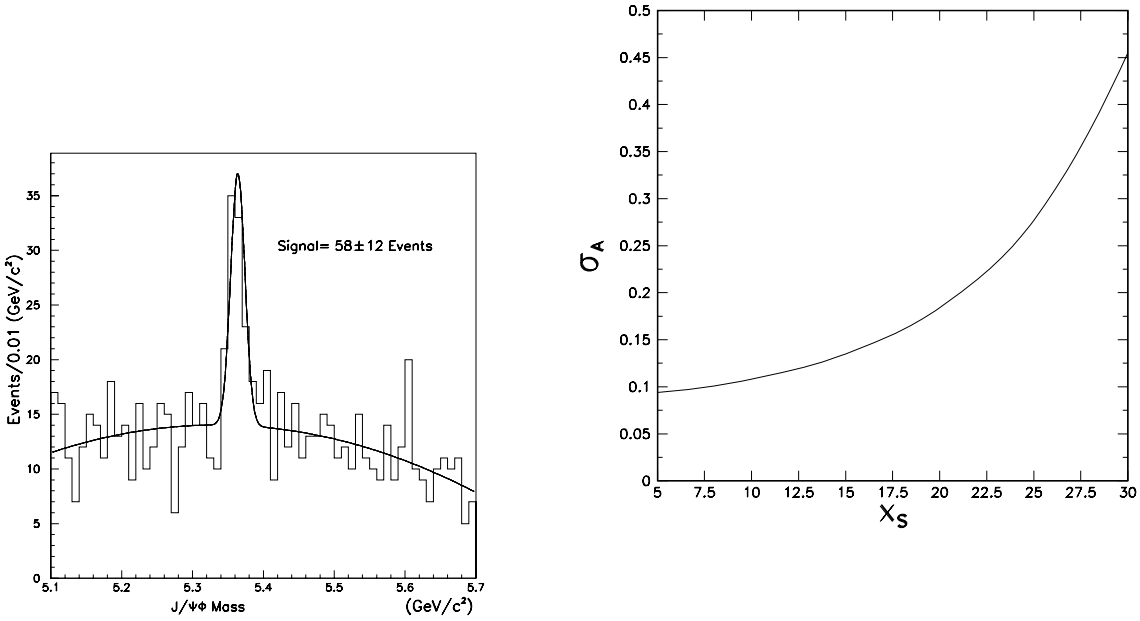

Figure 2.65: Left: The reconstructed mass distribution for $B_s^0 \to J/\psi\,\phi$ decays. SVX track information has been required for the muons from the J/ψ. Right: The uncertainty on the *CP* asymmetry for $B_s^0 \to J/\psi\,\phi$ as a function of the B_s^0 mixing parameter x_s.

With 15 fb^{-1} of data in Run 2b, $x_s = 25$, and vertex resolution comparable to Run IIa, we expect to measure the *CP* asymmetry in $B_s^0 \to J/\psi\,\phi$ with a resolution between 0.03 and 0.06, depending on the *CP* content of the final state. This is close to the Standard Model expectation of roughly 0.02, making us quite sensitive to new *CP*-violating physics in this mode.

2.7.5.3 *CP* Asymmetry in $B_s^0 \to J/\psi\eta^{(\prime)}$

Measuring the *CP* asymmetry in $B_s^0 \to J/\psi\eta^{(\prime)}$ decays is very similar to measuring it in $B_s^0 \to J/\psi\,\phi$, with two notable exceptions. First, the $J/\psi\eta$ and $J/\psi\eta'$ final states are *CP* eigenstates, so no angular fit is required and hence there is no degradation.

Second, the presence of photons in the final state (we detect the $\eta^{(\prime)}$ via its $\gamma\gamma$ decay mode) make these modes much more difficult for CDF. The CDF calorimeter was not designed to detect and measure low energy photon with very good energy resolution. However, CDF is capable of detecting these signals. Figure 2.66 shows the invariant mass of diphotons selected from our inclusive electron trigger data, which represent a data sample enhanced in $b\overline{b}$ events. Photon candidates were required to be in separate calorimeter towers, have $E_T^\gamma > 1$ GeV/c^2, and satisfy requirements on E_{had}/E_{EM}, isolation, and pulse in the strip chambers. Clear π^0 and η signals can be seen.

The resolution on the reconstructed B_s^0 mass can be improved by constraining the photons to the η or η' mass. Monte Carlo studies show that the B_s^0 mass resolution will be better than 40 MeV/c^2, which is more than a factor of two worse than our mass resolution in all charged track decays but still should be more than sufficient to observe this mode.

Scaling from the expected number of $B^+ \to J/\psi K^+$ events, the ratio of B^0 to B_s^0 production, and the expected relative branching ratios, we expect 8000 $B_s^0 \to J/\psi\eta$ events in Run IIb[9]. Studies of J/ψ events in Run I indicate that with a 40 MeV/c^2 mass resolution, the background to signal ratio should be no more than 2. Using $x_s = 25$ and a proper time resolution of $\sigma_\tau/\tau = 0.03$, we expect to measure the *CP* asymmetry in this mode with a resolution of 0.11.

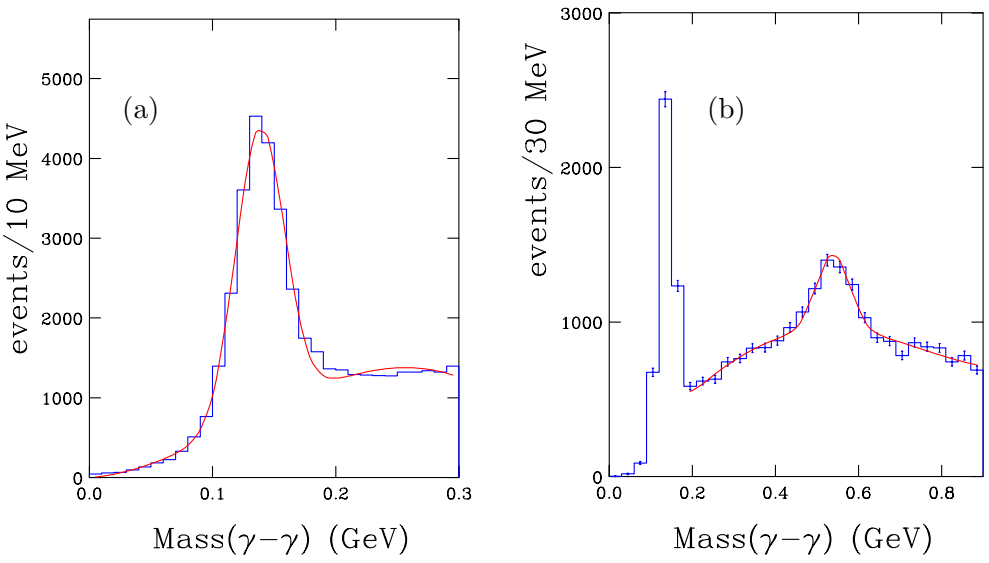

Figure 2.66: Invariant diphoton mass distribution showing (a) $\pi^0 \to \gamma\gamma$ and (b) $\eta \to \gamma\gamma$ signals in CDF Run I data.

2.7.5.4 *CP* Asymmetry in $B^0 \to \pi^+\pi^-$ and $B_s^0 \to K^+K^-$

The *CP* asymmetry in the decay $B^0 \to \pi^+\pi^-$ is often touted as a way to measure $\sin 2\alpha$. In the absence of penguin diagrams, this is certainly true. However, penguin diagrams are expected to make a significant contribution to this decay mode, greatly complicating the extraction of CKM information from the observed *CP* asymmetry.

Many studies have been done of how to obtain precision CKM information from the *CP* asymmetry, including measurement of the decay mode $B^0 \to \pi^0\pi^0$ and detailed analysis of the Dalitz plot in the similar $B^0 \to \rho\pi$ mode. These methods are complicated and difficult for any experiment and are not feasible for CDF due to the necessity of accurately and efficiency detecting π^0's.

We have investigated a very promising method suggested by Fleischer [21] that measures the CKM angle γ by relating the *CP* violation observables in the decays $B^0 \to \pi^+\pi^-$ and $B_s^0 \to K^+K^-$. The necessity of the B_s^0 mode makes this strategy unique and well suited to the Tevatron.

The decays $B^0 \to \pi^+\pi^-$ and $B_s^0 \to K^+K^-$ are related to each other by interchanging all down and strange quarks, that is, through the so-called "U-spin" subgroup of the SU(3) flavor symmetry of strong interactions. For the decay $B^0 \to \pi^+\pi^-$, the tree diagram is expected to be dominant with the penguin diagram being subdominant (but significant). For the decay $B_s^0 \to K^+K^-$, the opposite is expected, that is, the penguin diagram is expected to dominate. The strategy in reference [21] uses the U-spin symmetry to relate the ratio of hadronic matrix elements for penguins and trees, and thus uses $B_s^0 \to K^+K^-$ to correct for the penguin pollution in $B^0 \to \pi^+\pi^-$.

This strategy does not rely on "plausible" dynamical or model-dependent assumptions, nor on final-state interaction effects, as do many other methods of extracting γ. The theoretical accuracy is only limited by U-spin-breaking effects. We have evaluated the likely size of these effects and find them to be small compared to the expected experimental error on γ in Run II.

The key to measuring the *CP* asymmetries in $B^0 \to \pi^+\pi^-$ and $B_s^0 \to K^+K^-$ is to trigger on these decays in hadronic collisions. We will do this with the two displaced tracks trigger, which is a significant fraction of the Level 1 bandwidth in Run IIa. To maintain the viability of this trigger in Run IIb, we will add the ability to obtain three dimensional tracking information and make an invariant mass selection in Level 1.

Observation of these modes is further complicated by similar branching ratios for the modes $B^0, B_s^0 \to K\pi$ and the lack of good particle identification in CDF. The CLEO, Babar, and Belle experiments have

measured $Br(B^0 \to K^+\pi^-) = (17.3 \pm 1.5) \times 10^{-6}$ and $Br(B^0 \to \pi^+\pi^-) = (4.4 \pm 0.9) \times 10^{-6}$ (these are weighted averages of the results in [22]). The corresponding B_s^0 decays have not been observed, but we can make an educated guess based on SU(3) symmetry, giving

$$\begin{aligned} Br(B_s^0 \to K^+K^-) &= (F_K/F_\pi)^2 \times Br(B^0 \to K^+\pi^-) \\ Br(B_s^0 \to \pi^+K^-) &= (F_K/F_\pi)^2 \times Br(B^0 \to \pi^+\pi^-), \end{aligned}$$

where $(F_K/F_\pi)^2 = 1.3$ accounts for SU(3) breaking. Taking into account the production ratio of $f_s/f_d \sim 0.4$, we expect the following relative yields:

$$(B^0 \to K\pi) : (B^0 \to \pi\pi) : (B_s^0 \to KK) : (B_s^0 \to \pi K) \sim 4 : 1 : 2 : 0.5.$$

Based on the measured branching ratios, our observed Run I B cross sections, and Monte Carlo studies, we expect 20,000 $B^0 \to K^\pm\pi^\mp$; 5,000 $B^0 \to \pi^+\pi^-$; 10,000 $B_s^0 \to K^+K^-$; and 2,500 $B_s^0 \to K^\mp\pi^\pm$ events in Run IIa, with an expected increase of a factor of 7.5 in Run IIb. Special runs in Run I were used to estimate the signal to background to be roughly 0.4, although we expect the 3-dimensional vertexing capability in Run II to improve this. Figure 2.67 shows the expected invariant mass peak for the number of signal events above with 56,250 background events. The signals overlap, but detailed studies have shown it is possible to extract the *CP* asymmetries by exploiting the excellent mass resolution of CDF, dE/dx information from the COT, and the greatly different oscillation frequencies of the B^0 and B_s^0 mesons.

Detailed studies of the expected error on the *CP* asymmetries show that γ can be measured to $\sim \pm 10^\circ$ with a four-fold ambiguity in Run IIa, assuming that $\sin 2\beta$ is precisely known from $B^0 \to J/\psi K_s$. By allowing 20% SU(3) symmetry breaking, we estimate the theoretical uncertainty to be $\sim \pm 3^\circ$. With the increased luminosity of Run 2b, the statistical uncertainty should be $\sim \pm 3^\circ$, making this a very promising method for measurement of γ.

2.7.5.5 Measuring γ With $B_s^0 \to D_s^\mp K^\pm$ Decays

CP violation occurs in $B_s^0 \to D_s K$ decays via interference between direct decays $B_s^0 \to D_s^\mp K^\pm$ and cases where the B_s^0 first mixes to a $\overline{B}_s^0$ with the subsequent decay $\overline{B}_s^0 \to D_s^\mp K^\pm$. Since B_s^0 mixing is expected to have very small *CP* violating phase, the relative phase of these decays is $e^{i\gamma}$, and penguin contributions are expected to be small, these decays potentially give a theoretically clean measurement of γ. Since the final states are not *CP* eigenstates, there is a strong phase δ which cannot be reliably calculated with present theoretical techniques.

The time dependent decay rate for these four processes are

$$\begin{aligned} \Gamma(B_s^0 \to D_s^- K^+) = \frac{|A|^2 e^{-\Gamma_s t}}{2}\{&(1+|\lambda|^2)\cosh(\Delta\Gamma_s t/2) \\ &+(1-|\lambda|^2)\cos(\Delta m_s t) \\ &-2|\lambda|\cos(\delta+\gamma)\sinh(\Delta\Gamma_s t/2) \\ &-2|\lambda|\sin(\delta+\gamma)\sin(\Delta m_s t)\} \end{aligned}$$

$$\begin{aligned} \Gamma(B_s^0 \to D_s^+ K^-) = \frac{|A|^2 e^{-\Gamma_s t}}{2}\{&(1+|\lambda|^2)\cosh(\Delta\Gamma_s t/2) \\ &-(1-|\lambda|^2)\cos(\Delta m_s t) \\ &-2|\lambda|\cos(\delta-\gamma)\sinh(\Delta\Gamma_s t/2) \\ &+2|\lambda|\sin(\delta-\gamma)\sin(\Delta m_s t)\} \end{aligned}$$

$$\begin{aligned} \Gamma(\overline{B}_s^0 \to D_s^- K^+) = \frac{|A|^2 e^{-\Gamma_s t}}{2}\{&(1+|\lambda|^2)\cosh(\Delta\Gamma_s t/2) \\ &-(1-|\lambda|^2)\cos(\Delta m_s t) \\ &-2|\lambda|\cos(\delta+\gamma)\sinh(\Delta\Gamma_s t/2) \\ &+2|\lambda|\sin(\delta+\gamma)\sin(\Delta m_s t)\} \end{aligned}$$

$$\begin{aligned} \Gamma(\overline{B}_s^0 \to D_s^- K^+) = \frac{|A|^2 e^{-\Gamma_s t}}{2}\{&(1+|\lambda|^2)\cosh(\Delta\Gamma_s t/2) \\ &+(1-|\lambda|^2)\cos(\Delta m_s t) \\ &-2|\lambda|\cos(\delta-\gamma)\sinh(\Delta\Gamma_s t/2) \end{aligned}$$

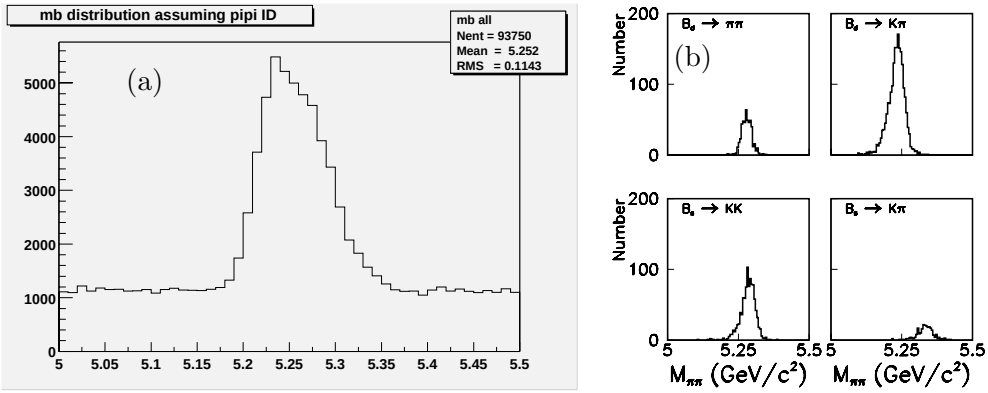

Figure 2.67: Two-track invariant mass assuming pion hypothesis for $B \to \pi\pi, K\pi, KK$, and πK states (a) added together and (b) shown separately.

$$-2|\lambda| \sin(\delta - \gamma) \sin(\Delta m_s t)\}$$

where $|A|$ is the magnitude of the $B_s^0 \to D_s^- K^+$ amplitude and $|\lambda|$ is the magnitude of the ratio of this amplitude to the one for $B_s^0 \to D_s^+ K^-$.

By fitting the time dependent decay rates for these four modes, the parameters $|A|$, $|\lambda|$, and $\delta \pm \gamma$ can be extracted. Since the rates depend on $\sin(\delta \pm \gamma)$ and $\cos(\delta \pm \gamma)$, there is a two fold ambiguity, namely, (δ, γ) and $(\delta + \pi, \gamma + \pi)$ are equivalent solutions. If $\Delta\Gamma_s/\Gamma_s$ is sufficiently small that the sinh terms cannot be resolved, then there an 8-fold ambiguity in the solutions.

The branching ratios for the decays $B_s^0 \to D_s^- K^+$ and $B_s^0 \to D_s^+ K^-$ are expected to be comparable, namely, 2.4×10^{-4} and 1.4×10^{-4}, respectively. In Run IIa, these events would satisfy the displaced track trigger. Monte Carlo studies indicate that CDF expects to reconstruct about 850 $B_s \to D_s^- K^+$ events in the Run IIa data. Studies of Run I data indicate that the signal to background ratio should be between 0.5 and 2, not including improvements that may be made with dE/dx information and 3-dimensional vertexing. With these conditions, we expect to measure $\sin(\delta \pm \gamma)$ to around 0.4 to 0.7 in Run IIa.

In Run IIb, if we can maintain the trigger rates, we would expect a factor of three improvement, which begins to place significant limits on γ, assuming that the sinh term is measurable or that δ is reliably determined theoretically (otherwise, the multiple ambiguities still allow most values of γ). However, as discussed above, the rate for the displaced track trigger is problematical in Run IIb, and since these are multibody decays, they would not pass a two-body invariant mass cut in Level 1. Another option is trigger scenario C described above, which can operate at the high instantaneous luminosities of Run IIb, but which has half the yield for signal events.

2.7.5.6 Measuring γ With $B^- \to D^0 K^-$ Decays

In a similar manner, the angle γ can be determined from the decays $B^- \to D^0 K^-$ and $B^- \to \overline{D}^0 K^-$ where the D^0 and $\overline{D}^0$ decay to both $K^\pm \pi^\mp$. Note that these modes are self-tagging and no time dependent measurement is necessary. However, the significant difference in the branching ratios limit CP violating effects to $\mathcal{O}(10\%)$.

Table 2.16 shows the branching ratios for the relevant modes. The decay $B^- \to K^- \overline{D}^0$ is particularly problematic due to the small expected branching ratio. All these decays have significant physics and combinatoric backgrounds that must be reduced to acceptable to make this method feasible. Studies show that physics backgrounds from similar modes and particle misassignments can be reduced to about the same level as the signals by using invariant mass selections and dE/dx information. These modes also have the problem that they are multi-body and hence are problematic for the displaced track trigger in Run IIb.

If the combinatoric backgrounds can be controlled and the decay $B^- \to \overline{D}^0 K^-$ measured to about 20%, then γ could be determined to about 15°.

$\mathrm{BR}(B^+ \to K^+\overline{D}^0) = 2.6 \pm 0.08 \times 10^{-4}$	CLEO
$\mathrm{BR}(B^+ \to K^+ D^0) \approx 2 \times 10^{-6}$	Estim. [23]
$\mathrm{BR}(\overline{D}^0 \to K^-\pi^+) = 1.3 \pm 0.3 \times 10^{-4}$	CLEO
$\mathrm{BR}(\overline{D}^0 \to K^+\pi^-) = 3.8 \pm 0.1 \times 10^{-2}$	PDG

Table 2.16: Estimated branching ratios of decays involved in the analysis of $B^- \to D^0 K^- \to [K\pi]K^-$ at CDF.

2.7.5.7 Direct *CP* Violation in $\Lambda_b \to pK, p\pi$

It should also be possible to observe direct *CP* violation in B decays, the analog in the B system to measuring ϵ'/ϵ in the neutral kaon system. It is most straight-forward to do this in decays where the decay products tag the flavor of the original B hadron (called self-tagging modes). Any B^+ or Λ_b mode has this feature, as do some B^0 and B_s^0 modes.

As an example, we discuss the decays $\Lambda_b \to p\pi^-$ and $\Lambda_b \to pK^-$. The asymmetry in this case is defined to be

$$A = \frac{\Lambda_b - \overline{\Lambda}_b}{\Lambda_b + \overline{\Lambda}_b}, \tag{2.9}$$

where Λ_b and $\overline{\Lambda}_b$ refer to the number of each type observed. In the Standard Model, the asymmetry for $\Lambda_b \to pK$ is expected to be about 10%, whereas the asymmetry for $\Lambda_b \to p\pi$ is predicted to be in the 20% to 30% range.

The branching ratios for these modes are not known, but are estimated to be similar to $B^0 \to \pi\pi$. Since these Λ_b decay modes will satisfy the two displaced track trigger (assuming the mass windows are chosen appropriately), the number of expected events in each mode can be scaled from the number of expected $B^0 \to \pi\pi$ and the relative production rates, giving 10,000 events in 15 fb^{-1}. An advantage to this measurement is that tagging is not necessary, thus all the events are fully available for the asymmetry measurement. The background for these modes should be no worse than for $B^0 \to \pi\pi$, and use of TOF and dE/dx may substantially reduce them. We assume a signal to background of 1 to 2.

There is also a possibility of accepting a combination that interchanges the p and the K or π, which is essentially a mistag. Using the TOF system, this can be reduced to about 10% at a 20% loss of signal.

The formula for the uncertainty on the asymmetry in the presence of background and mistagging for small asymmetries is

$$\sigma_A = \frac{1}{D}\sqrt{\frac{S+B}{S^2}}, \tag{2.10}$$

where A is the asymmetry, S is the number of signal events, B is the number of background events, $D = 1 - 2f$ is the dilution factor due to mistags, and f is the mistag rate. Thus, we expect an error on the asymmetry of about 2%, significantly smaller than the Standard Model predicted asymmetries. Note there will also be a systematic error due to the mistagging, but we should be able to keep this at the level of 1% or smaller.

2.7.6 Mixing and Lifetime Differences

One of the primary goals of CDF in Run IIa is to observe B_s^0 mixing. The ratio of oscillation frequency Δm_s to the oscillation frequency Δm_d determines the ratio $|V_{td}/V_{ts}|$ up to theoretical uncertainties on the order of 5-10%.

With the addition of Layer 00 for excellent vertex resolution and the displaced track trigger to give a large sample of exclusive decays (such as $B_s^0 \to D_s\pi$), CDF expects to have a reach in Δm_s which is far beyond the Standard Model expectation. Furthermore, once a statistically significant signal is observed in B_s^0 oscillations, the value of Δm_s has a very small statistical uncertainty. Thus, we expect that B_s^0 mixing will be observed in Run IIa, and its usefulness for determining $|V_{td}/V_{ts}|$ and constraining the unitarity triangle will be limited by theoretical uncertainties.

CDF will continue to pursue measurements of B^0 and B_s^0 mixing in Run IIb since precise knowledge of Δm_d and Δm_s is necessary for extraction of other physics signals, such as, time dependent *CP* asymmetries in B^0 and B_s^0 decays. However, we do not expect further improvements in these measurements to directly impact our understanding of CKM physics.

2.7.6.1 $\Delta\Gamma_s/\Gamma_s$

The calculation of Δm_s depends upon the evaluation of the real part of the mass matrix element. The imaginary part of the same matrix describes the decay widths of the two mass eigenstates B_s^H and B_s^L. Within the Standard Model it is possible to calculate the ratio $\Delta\Gamma_s/\Delta m_s$ [24]:

$$\Delta\Gamma_s/\Delta m_s = -\frac{3}{2}\pi\frac{m_b^2}{m_t^2}\frac{\eta_{QCD}^{\Delta\Gamma_s}}{\eta_{QCD}^{\Delta m_s}} \tag{2.11}$$

where the ratio of the QCD correction factors (η) in the numerator and denominator is expected to be of order unity [25]. This ratio does not depend on CKM parameters. Thus, a measurement of $\Delta\Gamma_s$ determines Δm_s up to QCD uncertainties. Moreover, the larger Δm_s becomes the larger $\Delta\Gamma_s$ is. Thus, as it becomes more difficult to measure Δm_s, $\Delta\Gamma_s$ becomes more accessible. Using the above expression, Browder *et al.* [25] show that if $x_s = 15$, a 7% difference in lifetime is expected.[2] They estimate that the uncertainties in calculating $\Delta\Gamma_s/\Delta m_s$ contribute an uncertainty of $\sim 30\%$ on $|V_{td}/V_{ts}|^2$ (that is, a 15% uncertainty on $|V_{td}/V_{ts}|$). This contribution to the theoretical uncertainty should be added in quadrature to the 10% uncertainty discussed in the previous section, for a total uncertainty of $\approx 20\%$.

We do not expect $\Delta\Gamma_s/\Gamma_s$ to be measured sufficiently well in Run IIa that its usefulness is dominated by theoretical uncertainties. Thus, we will continue to pursue this measurement with the higher statistics available from Run IIb.

Several techniques can be used to determine $\Delta\Gamma_s$ [26]. First, the proper time distribution of a flavor-specific B_s^0 mode (*e.g.* $B_s^0 \to D_s\ell\nu$ or $B_s^0 \to D_s^-\pi^+$) can be fit to the sum of two exponentials, although for the small lifetime differences expected, this method is not efficient and not competitive with the ones below. Second, the average lifetime of such a flavor specific mode can be compared to the lifetime of a mode that is dominated by a single *CP* state (such as $B_s^0 \to D_s\overline{D}_s$) [27]. Finally, a decay such as $B_s^0 \to J/\psi\,\phi$ can be decomposed into its two *CP* components (via a transversity analysis [28]) and fit for a separate lifetime for each component. It is noted that CDF has measured the helicity structure of the decays $B \to J/\psi K^*$ and $B_s^0 \to J/\psi\phi$ using Run Ia data [8]. The results obtained for the parity-even fractions are $0.87^{+0.12}_{-0.09}$ for $B \to J/\psi K^*$ and 0.77 ± 0.19 for $B_s \to J/\psi\,\phi$.

The statistical uncertainty on the B_s^0 lifetime from semileptonic B decays in Run II will be below 1%. The Run II expectation is for $\approx 60,000$ $B_s^0 \to J/\psi\,\phi$ events in 15 fb^{-1}. The $B_s^0 \to J/\psi\phi$ helicity structure should then be known to about 1% [3]. Using the current CDF number for the $B_s^0 \to J/\psi\,\phi$ helicity structure, with 15 fb^{-1}, $\Delta\Gamma_s/\Gamma_s$ could be determined to 0.01. Including current theoretical uncertainties of 20%, this determination of $\Delta\Gamma_s$ would either measure $|V_{td}/V_{ts}|$ or set an *upper* bound on $x_s = \Delta m_s/\Gamma_s \leq 15$. Thus, using the direct x_s measurement and $\Delta\Gamma_s/\Gamma_s$, CDF II should be able to measure $|V_{td}/V_{ts}|$ over the full range permitted by the Standard Model in Run II.

It is important to note that the discussion of B_s^0 mixing (and *CP* violation) has been in the context of the three generation Standard Model. New physics associated with large mass scales can also reveal itself through a study of the mass and width differences for the neutral B mesons [29].

2.7.6.2 $\Delta\Gamma_d/\Gamma_d$

The lifetime difference for the B^0 eigenstates is expected to be very small in the Standard Model, around 0.3%. This is smaller than probably can be measured, even in Run IIb. However, the lifetime difference is sensitive to new physics and may be as large as a few per cent in some extensions to the Standard Model, which should be measurable.

The lifetime difference $\Delta\Gamma_d/\Gamma_d$ can be measured by comparing the lifetime measured in a high statistics *CP* eigenstate mode, such as $B^0 \to J/\psi K_s^0$, to the lifetime measured in a flavor specific mode, such as semileptonic decays or $B^0 \to J/\psi K^{*0}$,$K^{*0} \to K^+\pi^-$. Note that flavor tagging is not needed here and the full statistics of the samples are available.

For the $\sim$150,000 $B^0 \to J/\psi K_s$ decays expected in Run IIb, the statistical error on the lifetime is $\sim 0.3\%$, comparable to the lifetime difference in the Standard Model. At this level, effects of backgrounds and other systematic effects are probably important, but significant deviations from the Standard Model prediction should be observable.

2.7.7 B_c^+ Decays

In Run I, CDF discovered the B_c^+ meson via its semileptonic decay $B_c^+ \to J/\psi\ell\nu X$ [10]. In Run II, we expect to observe this meson in several exclusive decay modes, making precise determination of its mass and lifetime possible.

One of the cleanest exclusive modes is $B_c^+ \to J/\psi\pi^+$. We estimate the number of expected events

[2] This large $\Delta\Gamma_s$ is possible because there are common decay modes with large branching fractions available to the B_s^0 and $\overline{B}_s^0$ (*e.g.* $D_s^{(*)+}D_s^{(*)-}$).

[3] The systematic uncertainties in the polarization measurements are dominated by the estimate of the size and helicity of the background under the B mass peak. These systematic uncertainties should scale with the square root of the number of events in the sample.

by scaling from the observed number of $B_c^+ \to J/\psi\ell\nu X$ events and theoretical predictions of the relative branching ratios [30], which range from 0.06 to 0.32. This gives us an expectation of 9 events in Run I on an observed background of roughly 6 events.

Extrapolating to Run IIb, including the detector and trigger improvements for Run II, we expect to observe about 3000 $B_c^+ \to J/\psi\pi^+$ events. These events plus those from other exclusive decays will allow us to make very precise measurements of the B_c^+ mass and lifetime.

We also note that the decay $B_c^+ \to J/\psi\pi^+$ which may exhibit a *direct CP* violating effect at the few percent level [31]. The mode is self–tagging and no time dependence is required. Any non–vanishing effect would immediately exclude the superweak model of *CP* violation. In Run IIb, for 3000 events, we expect about a 2% error on the asymmetry.

The relatively short lifetime observed for the B_c^+ (albeit with large errors) indicates the it decays primarily by decay of the charm quark, that is, via the decay $B_c^+ \to B_s^0\pi^+$. Based on the approximately 150,000 fully reconstructed B_s^0 decays we expect in Run IIb, we should observe a few hundred $B_c^+ \to B_s^0\pi^+$ decays.

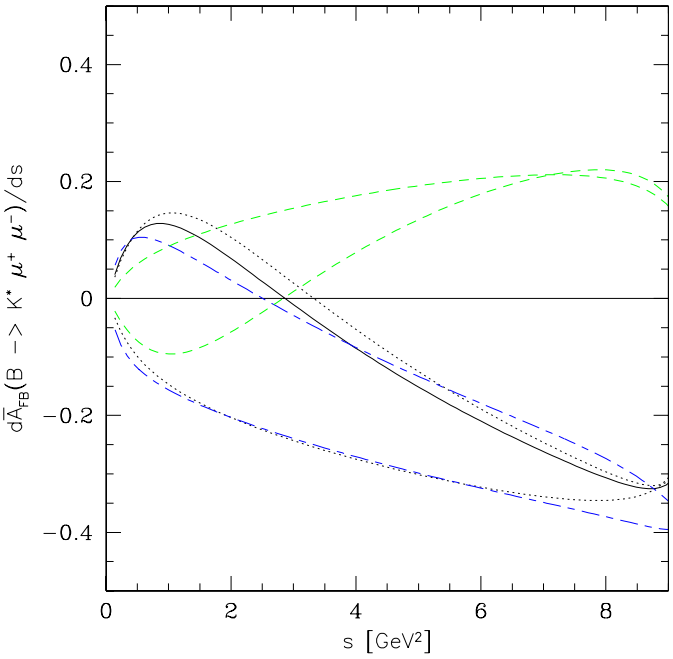

Figure 2.68: The forward-backward asymmetry in $B^0 \to K^{*0}\mu\mu$ decay as a function of $s = M^2_{\mu\mu}$ predicted by the Standard Model (solid line), the SUGRA (dotted), and MIA-SUSY (long-short dashed line) [32].

2.7.8 Rare B decays

Rare B decays provide a stringent test of the Standard Model for possible new physics effects, such as an anomalous magnetic moment of the W or the presence of a charged Higgs. Experimentally, rare decays such as $B^0 \to K^{*0}\mu\mu$, $B^0 \to \mu\mu$, and $B_s^0 \to \mu\mu$ are accessible via the dimuon trigger.

The straight dimuon trigger for muons outside the narrow J/ψ mass window will become problematical for the high luminosities of Run IIb. In Run IIa, we have implemented a dimuon trigger that requires an additional displaced track. It is expected that this trigger will be sufficient to search for rare B decays with dimuons in Run IIb.

2.7.8.1 $B^0 \to K^{*0}\mu\mu$

The decay $B^0 \to K^{*0}\mu\mu$ is expected in the Standard Model to have a branching ratio of approximately 1.5×10^{-6}. For this branching ratio, we expect to observe 36±7 events in Run IIa and 270±50 events in Run IIb with the dimuon plus displaced track trigger.

The forward-backward asymmetry A_{FB} of the muons relative to the B direction in the dimuon frame is expected to be extremely sensitive to new physics. In the Standard Model, A_{FB} is expected to cross zero as a function of the dimuon mass $M_{\mu\mu}$ at a value around 2 GeV/c^2. New physics can change, or even eliminate, where this zero crossing occurs. Figure 2.68 shows the expected forward-backward asymmetry as a function of $M_{\mu\mu}$ for the Standard Model and several possible extensions to the standard model.

Figure 2.69 shows the expected A_{FB} distribution with 50 and 400 $B^0 \to K^{*0}\mu\mu$ events after all trigger and offline requirements. The solid line in the figure corresponds to the Monte Carlo generated distribution. It is clear that the statistics in Run IIa will be marginal for extracting information on A_{FB}. The situation is still challenging in Run IIb but hopeful. We are exploring methods to best extract the zero crossing point of A_{FB}, including in the presence of backgrounds.

The statistics of Run IIb are definitely needed for this measurement. The events come from the dimuon plus displaced track trigger, which should not need to be prescaled in Run IIb.

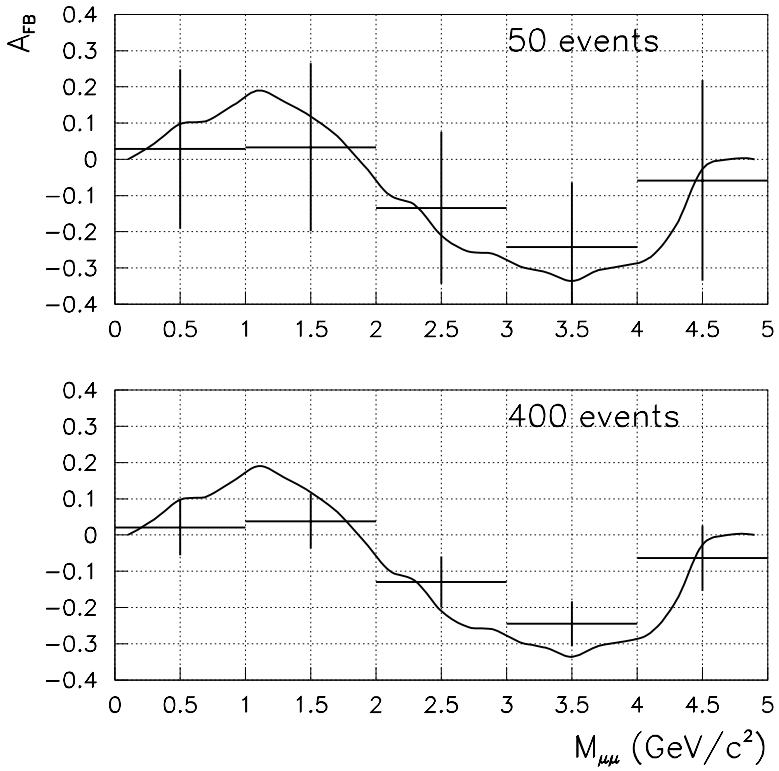

Figure 2.69: A_{FB} with 50 and 400 events of the $B^0 \to K^*\mu\mu$ signal and $S/B = 1$.

2.7.8.2 $B \to \mu\mu$

The dimuon plus displaced track trigger is also useful to search for the two-body decays $B^0, B_s^0 \to \mu\mu$, predicted to have branching ratios of 1.5×10^{-9} and 3.5×10^{-8}, respectively. Since these branching ratios are at the limits of CDF's reach, even in Run IIb, we quote "single-event sensitivities", that is, the branching ratio for which we would expect one observed event in 15 fb^{-1}.

CDF searched for these decays in Run I [13] with single-event sensitivities of

$$S(B^0 \to \mu\mu) = (2.0 \pm 0.5) \times 10^{-7} \quad (2.12)$$
$$S(B_s^0 \to \mu\mu) = (6.0 \pm 1.6) \times 10^{-7}. \quad (2.13)$$

The Run IIb expectations extrapolated from these, including the difference in trigger, muon coverage, and cross section, are

$$S(B^0 \to \mu\mu) = 2.1 \times 10^{-9} \frac{15\text{fb}^{-1}}{\int \mathcal{L}(\text{fb}^{-1})} \quad (2.14)$$
$$S(B_s^0 \to \mu\mu) = 3.5 \times 10^{-8} \frac{15\text{fb}^{-1}}{\int \mathcal{L}(\text{fb}^{-1})}. \quad (2.15)$$

Thus, for the expected Standard Model branching fractions, we would expect to not see $B^0 \to \mu\mu$ and to see a few $B_s^0 \to \mu\mu$ events.

Note that it is possible for new physics (such as a charged Higgs) to substantially increase these branching fractions, to which we would be sensitive. Also note, that we have not yet done an extensive study of the backgrounds expected at these levels, which, of course, is crucial for understanding whether we could actually see a signal above the background.

2.7.9 Radiative B Decays

In the absence of long distance effects, radiative B decays provide an alternative approach for measuring $|V_{td}/V_{ts}|$. Radiative decays are also interesting because they proceed solely through penguin diagrams. It is likely that the B factory experiments will measure B^- and B^0 radiative decays better than is possible at CDF. Still, CDF will measure radiative decays, including B_s^0 and Λ_b radiative decays, which are not accessible to the B factories.

CDF will use two methods to search for radiative penguin decays. The first identifies photons as clusters in the Central EM calorimeter. For Run II, a trigger requiring a 5 GeV EM cluster (the pho-

ton) and two tracks above 1.5 GeV/c is being implemented. From this trigger, we expect to observe $\sim$ 2700 $B^0 \to K^*\gamma$ events in 2 fb^{-1} for a branching ratio of 4.5×10^{-5}. The mass resolution of the reconstructed B is dominated by the resolution on the photon energy and is $\sim$ 140 MeV. We have studied our ability to reject combinatorial background using Run I photon data and have studied with Monte Carlo the discrimination against $B \to K^*\pi^0$ and $\rho\pi^0$ and higher multiplicity penguin decays [34]. These backgrounds are manageable. However, the offline cuts to remove background are expected to reduce the signal by about a factor of 2. The mass resolution is not adequate to separate $\gamma\rho$ from γK^* on an event-by-event basis; however, a statistical separation is possible. In addition, the COT dE/dx system should provide 1σ K-π separation in the momentum range of interest.

The second method looks for photon conversions where the electron or positron satisfies the 4 GeV electron with displaced track trigger. The probability for a photon to convert in the material around the beam pipe in Run I was $\sim$ 5%, which is expected to increase to $\sim$ 10% in Run II due to additional material in SVX II. The main advantage of the conversion method is that the B mass is calculated solely from charged tracks, giving a resolution comparable to B signals observed in Run I, that is, 20 to 30 MeV/c^2. The backgrounds are also less for the conversion sample. The improved resolution gives cleaner signals and allows separation of $B^0 \to \rho\gamma$, $B^0 \to K^*\gamma$, and $B_s^0 \to K^*\gamma$ signals. These advantages will probably make the conversion method the optimal one for Run II.

The numbers of radiative penguin decays expected in the conversion sample in Run 2 are

$$
\begin{aligned}
N(B^0 \to K^*\gamma) &= 170 \times \frac{\int \mathcal{L}(\mathrm{fb}^{-1})}{2\mathrm{fb}^{-1}} \times \frac{Br(B_d \to K^*\gamma)}{4.5 \times 10^{-5}} \\
N(B_s^0 \to \phi\gamma) &= 63 \times \frac{\int \mathcal{L}(\mathrm{fb}^{-1})}{2\mathrm{fb}^{-1}} \times \frac{Br(B_d \to K^*\gamma)}{4.5 \times 10^{-5}} \\
N(B_s^0 \to K^*\gamma) &= 2.2 \times \frac{\int \mathcal{L}(\mathrm{fb}^{-1})}{2\mathrm{fb}^{-1}} \times \frac{Br(B_d \to K^*\gamma)}{4.5 \times 10^{-5}} \\
N(\Lambda_b \to \Lambda\gamma) &= 5 \times \frac{\int \mathcal{L}(\mathrm{fb}^{-1})}{2\mathrm{fb}^{-1}} \times \frac{Br(B_d \to K^*\gamma)}{4.5 \times 10^{-5}}.
\end{aligned}
$$

Thus, the 15 fb^{-1} of Run IIb will be needed to observe the $B_s^0 \to K^*\gamma$ and $\Lambda_b \to \Lambda\gamma$ modes.

2.7.10 Semileptonic Decays

In Run II, CDF will observe large numbers of semileptonic decays of all species of B hadrons. Here, we concentrate on $\Lambda_b \to \Lambda_c\ell\nu$ decays, which are not produced in e^+e^- B factories, as being illustrative. Semileptonic decays of B hadrons are acquired via the inclusive electron and muon triggers. For B physics, the rates for these triggers can be kept under control by also requiring a displaced track.

Measuring the differential decay rate $(1/\Gamma)\, d\Gamma/dQ^2$, where Q^2 is the momentum transfer, is a stringent test of Heavy Quark Effective Theory (HQET). These tests require large data samples and so are ideally suited to Run II. In the Run I Λ_b lifetime analysis, 197$\pm$25 $\Lambda_b \to \Lambda_c\ell\nu$, $\Lambda_c \to pK\pi$ events were partially reconstructed [6]. Extrapolating to Run IIb, including the improvements in the detector and trigger, gives an expected yield of 150,000 events in 15 fb^{-1}.

Tests of HQET in Λ_b semileptonic decays could be compromised by contamination from decays of the Λ_b to higher order charmed baryons. Monte Carlo studies show that rejection of events with extra tracks having a small impact parameter with respect to the Λ_b vertex controls these backgrounds at acceptable levels.

2.7.11 $\psi(2S)$ Polarization

In Run I, CDF measured the direct production of both J/ψ and $\psi(2S)$ mesons, giving cross-sections approximately 50 times greater than those predicted by QCD using the color-singlet model. This anomalous production can be explained in nonrelativistic QCD by the inclusion of color-octet $c\bar{c}$ states in the hadronization process. A consequence of this production mechanism is that the transverse polarization of the J/ψ and $\psi(2S)$ mesons approaches 100% for transverse momenta $p_T \gg m_c$, where m_c is the charm quark mass. Measurements in Run I by CDF of the J/ψ and $\psi(2S)$ polarizations [35] did not support the color octet models, but statistics were limited at large transverse momenta, where the theory is most reliable.

In Run IIa, the uncertainties on the polarization of J/ψ's will be $\pm$0.2 at a transverse momentum of 30 GeV/c, providing a stringent test of the color octet models. However, direct J/ψ's have the problem that some of them come from decays of prompt $\psi(2S)$'s and χ states, adding some uncertainty to the inter-

pretation of the measurement. Direct $\psi(2S)$'s do not have this problem, but to measure their polarization out to comparable transverse momenta will require the statistics of Run IIb.

2.7.12 Concluding remarks

From the previous discussion it should be clear that in Run IIb CDF plans to fully exploit the copious production of all species of b hadrons at the Tevatron. We believe we will have a complete and competitive program, with unique strengths, for example, in rare decays and B_s^0 physics.

With the experience gained so far in the analyses of Run I data and the planned capabilities of the CDF II detector, we are able to confidently project our expectations for Run IIa and Run IIb which include:

- Observation of *CP* violation in $B^0 \to J/\psi K_S^0$ and measurement of $\sin(2\beta)$ to better than ± 0.02.
- Measurement of the *CP* asymmetries in $B_s^0 \to J/\psi\,\phi, J/\psi\eta^{(\prime)}$, which measure the phase of V_{ts} in the Standard Model and are sensitive to new *CP* violating physics.
- Observation of *CP* violation in $B^0 \to \pi^+\pi^-$, $B_s^0 \to K^+K^-$ and measurement of the unitarity triangle angle γ to better than $\pm 3^\circ$.
- Observation of B_s^0 mixing and precise determination of Δm_s.
- Measurement of $\Delta\Gamma_s/\Gamma_s$ to 0.01.
- Observation of exclusive decay modes of the B_c^+ meson, allowing precise determinations of its mass and lifetime.
- Observation of radiative penguin decays.
- Observation of the rare decays $B^0 \to \mu\mu K^{*0}$ and $B^\pm \to \mu\mu K^\pm$.

With these and other measurements that we will pursue with b hadrons in Run IIa and Run IIb, we expect to greatly improve the understanding of weak-interaction quark mixing and *CP* violation in the Standard Model and be very sensitive to new physics in these areas.

Bibliography

[1] L. Wolfenstein, Phys. Rev. Lett. **51**, 1945 (1984).

[2] "Measurement of the Mass of the B_s^0 Meson." F. Abe *et al.*, Phys. Rev. **D53** 3496 (1996); "Observation of the Decay $B_s^0 \to J/\psi\,\phi$ in $p\overline{p}$ Collisions at $\sqrt{s} = 1.8$ TeV." F. Abe *et al.*, Phys. Rev. Lett. **71** 1685 (1993).

[3] "Observation of $\Lambda_b \to J/\psi\Lambda^0$ at the Fermilab Proton–Antiproton Collider." F. Abe *et al.*, Phys. Rev. **D55** 1142 (1997).

[4] "Measurement of the Average Lifetime of B Hadrons Produced in $p\overline{p}$ Collisions at $\sqrt{s} = 1.8$ TeV." F. Abe *et al.*, Phys. Rev. Lett. **71** 3421 (1993); "Measurement of the B^+ and B^0 Meson Lifetimes." F. Abe *et al.*, Phys. Rev. Lett. **72** 3456 (1994); "Measurement of the B^- and $\overline{B}^0$ Meson Lifetimes Using Semileptonic Decays." F. Abe *et al.*, Phys. Rev. Lett. **76** 4462 (1996); "Measurement of B Hadron Lifetimes Using J/ψ Final States at Cdf." F. Abe *et al.*, Phys. Rev. **D57** 5382 (1998); "Measurement of the B^- and $\overline{B}^0$ Meson Lifetimes Using Semileptonic Decays." F. Abe *et al.*, Phys. Rev. **D58** 092002 (1998).

[5] "Measurement of the B_s^0 Meson Lifetime." F. Abe *et al.*, Phys. Rev. Lett. **74** 4988 (1995); "Measurement of the Lifetime of the B_s^0 Meson Using the Exclusive Decay Mode $B_s^0 \to J/\psi\,\phi$." F. Abe *et al.*, Phys. Rev. Lett. **77** 1945 (1996); "Measurement of the B_s^0 Meson Lifetime Using Semileptonic Decays." F. Abe *et al.*, Phys. Rev. **D59** 032004 (1999).

[6] "Measurement of Λ_b^0 Lifetime Using $\Lambda_b^0 \to \Lambda_c^+\ell^-\bar{\nu}_\ell$." F. Abe *et al.*, Phys. Rev. Lett. **77** 1439 (1996).

[7] "Measurement of the *CP*-violation Parameter $\sin 2\beta$ in $B^0/\overline{B}^0 \to J/\psi K_s^0$ Decays." F. Abe *et al.*, Phys. Rev. Lett. **81** 5513 (1998); "A Measurement of $\sin 2\beta$ from $B \to J/\psi K_s^0$ with the CDF Detector." T. Affolder *et al.*, Phys. Rev. **D61** 072005 (2000).

[8] "Measurement of the Polarization in the Decays $B_d^0 \to J/\psi K^{*0}(892)$ and $B_s^0 \to J/\psi\phi$." F. Abe *et al.*, Phys. Rev. Lett. **75** 3068 (1995); "Measurement of the Polarization in the Decays $B_d^0 \to J/\psi K^{*0}(892)$ and $B_s^0 \to J/\psi\phi$." T. Affolder *et al.*, Phys. Rev. Lett. **85** 4668 (2000).

[9] *CP* Violation chapter of the Proceedings of the Fermilab Workshop on B Physics at the Tevatron: Run II and Beyond (known at the Yellow Book), to be published.

[10] "Observation of the B_c Meson in $p\overline{p}$ Collisions at $\sqrt{s} = 1.8$ TeV." F. Abe *et al.*, Phys. Rev. Lett. **81** 2432 (1998); "Observation of the B_c Meson in $p\overline{p}$ Collisions at $\sqrt{s} = 1.8$ TeV." F. Abe *et al.*, Phys. Rev. **D58** 112004 (1998); "Measurement of the Branching Fraction for $B^+ \to J/\psi\pi^+$ and Search for $B_c^+ \to J/\psi\pi^+$." F. Abe *et al.*, Phys. Rev. Lett. **77** 5176 (1996).

[11] "Measurement of $B^0\overline{B}^0$ Flavor Oscillation Frequency and Study of Same Side Flavor Tagging of B Mesons in $p\overline{p}$ Collisions." F. Abe *et al.*, Phys. Rev. **D59** 032001 (1999); "Measurement of the $B^0\overline{B}^0$ Oscillation Frequency Using Dimuon Data." F. Abe *et al.*, Phys. Rev. **D60** 051101 (1999); "Measurement of $B^0\overline{B}^0$ Flavor Oscillations Using Jet Charge and Lepton Flavor Taggin in $p\overline{p}$ Collisions at $\sqrt{s} = 1.8$ TeV." F. Abe *et al.*, Phys. Rev. **D60** 072003 (1999); "Measurement of the $B^0\overline{B}^0$ Oscillation Frequency Using $\ell^- D^{*+}$ Pairs and Lepton Flavor Tags." T. Affolder *et al.*, Phys. Rev. **D60** 112004 (1999).

[12] "Search for B_s^0 Oscillations Using the Semileptonic Decay $B_s^0 \to \phi\ell X\nu$." F. Abe *et al.*, Phys. Rev. Lett. **82** 3576 (1999).

[13] "Search for Flavor Changing Neutral Current in B Meson Decays in $p\overline{p}$ Collisions at $\sqrt{s} = 1.8$

TeV." F. Abe *et al.*, Phys. Rev. Lett. **76** 4675 (1996); "Search for the Decays $B^0 \to \mu^+\mu^-$ and $B_s^0 \to \mu^+\mu^-$ in $p\overline{p}$ Collisions at $\sqrt{s} = 1.8$ TeV." F. Abe *et al.*, Phys. Rev. **D57** R3811 (1998); "Search the Decays $B_s^0, B_d^0 \to e^{+-}\mu^{-+}$ and Pati-Salam Leptoquarks." F. Abe *et al.*, Phys. Rev. Lett. **81** 5742 (1998); "Search for Flavor-Changing Neutral Current Decays $B^+ \to \mu^+\mu^- K^+$ and $B^0 \to \mu^+\mu^- K^{*0}$." T. Affolder *et al.*, Phys. Rev. Lett. **83** 3378 (1999);

[14] "A Measurement of the B Meson and b Quark Cross Sections at $\sqrt{s}$ =1.8 TeV Using the Exclusive Decay $B^\pm \to J/\psi K^\pm$." F. Abe *et al.*, Phys. Rev. Lett. **68** 3403 (1992); "Measurement of the Bottom Quark Production Cross Section Using Semileptonic Decay Electrons in $p\overline{p}$ Collisions at $\sqrt{s} = 1.8$ TeV". F. Abe *et al.*, Phys. Rev. Lett. **71** 500 (1993); "Measurement of Bottom Quark Production in 1.8-TeV $p\overline{p}$ Collisions Using Semileptonic Decay Muons." F. Abe *et al.*, Phys. Rev. Lett. **71** 2396 (1993); "Measurement of the B Meson and b Quark Cross Sections at $\sqrt{s}$ =1.8-TeV using the Exclusive Decay $B_d^0 \to J/\psi K^{*0}(892)$." F. Abe *et al.*, Phys. Rev. **D50** 4252 (1994). "Measurement of the B Meson Differential Cross Section, $\frac{d\sigma}{dP_t}$, in $p\overline{p}$ Collisions at $\sqrt{s} = 1.8$ TeV." F. Abe *et al.*, Phys. Rev. Lett. **75** 1451 (1995); "Measurement of $b\overline{b}$ Rapidity Correlations in $p\overline{p}$ Collisions at $\sqrt{s} = 1.8$ TeV." F. Abe *et al.*, Phys. Rev. **D61** 032001 (2000).

[15] "Measurement of Correlated $\mu - \bar{b}$ Jet Cross Sections in $p\overline{p}$ Collisions at $\sqrt{s}$ =1.8 TeV." F. Abe *et al.*, Phys. Rev. **D53** 1051 (1996). "Measurements of $b\bar{b}$ Production Correlations, $B\bar{B}$ Mixing and a Limit on ϵ_B." F. Abe *et al.*, Phys. Rev. **D55** 2546 (1997).

[16] "Observation of *CP* Violation in the B^0 Meson System." BABAR collaboration, SLAC-PUB-8904, hep-ex/0107013, and submitted to Phys. Rev. Lett., July, 2001.

[17] "Observation of Large *CP* Violation in the Neutral B Meson System." Belle collaboration, Phys. Rev. Lett. **87** 091802 (2001).

[18] H. Quinn, B^0–$\bar{B}^0$ *Mixing and CP Violation in B Decay*, in Review of Particle Properties, Phys. Rev. **D50**, 1632 (1994) and references therein.

[19] "Proposal for Enhancement of the CDF II Detector: An Inner Silicon Layer and a Time of Flight Detector,", CDF II Collaboration, Fermilab-Proposal-909, October 1998; "Update to Proposal P-909: Physics Performance of the CDF II Detector with an Inner Silicon Layer and a Time of Flight Detector," Cdf II Collaboration, January 1999.

[20] The CDF Collaboration, *SVXII Simulation Study and Upgrade Proposal*, CDF Note 1922, (see in particular Table 13).

[21] R. Fleischer, Phys. Lett.**B459**.306 (1999).

[22] D. Cronin-Hennessy, *et al.* (CLEO), Phys. Rev. Lett **85**, 515 (2000); K. Abe, *et al.* (Belle), Phys. Rev. Lett **87**, 101801 (2001); B. Aubert, *et al.* (Babar), Phys. Rev. Lett **87**, 151802 (2001)

[23] D. Atwood, I. Dunietz, and A. Soni, Phys. Rev. Lett. **78**, 3257 (1997).

[24] J. Hagelin, Nucl. Phys. **B193**, 123 (1981); M.B. Voloshin *et. al* Sov. J. Nucl. Phys. **46**, 112 (1987).

[25] T.E. Browder and S. Pakvasa, UH 511-814-95. See also the recent discussion by M. Beneke, G. Buchalla and I. Dunietz, SLAC-PUB-7165, HEP-PH/9605259.

[26] I. Dunietz, Phys. Rev. **D51**, 2471 (1995).

[27] I. Bigi *et al.*, in "B Physics", 2nd edition, S. Stone editor.

[28] A.S. Dighe, I. Dunietz, H.J. Lipkin and J.L. Rosner, Phys. Lett. **B369**, 144 (1996).

[29] See Y. Grossman, WIS-96/13/Mar-PH, HEP-PH/9603244; M. Gronau and D. London, Technion-PH-96-37, HEP-PH/9608430, and Y. Nir, WIS-96/31/Jul-PH, HEP-PH/9607415 for recent discussions.

[30] C. H. Chang and Y. Q. Chen, Phys. Rev. **D49**, 3399 (1994); S. S. Gershstein *et al.*, "Physics of B_c Mesons", Phys. Usp. **38**,1 (1995); S. S. Gershstein *el al.*, "Theoretical Status of

the B_c Meson", hep-ph/9803433, 24 March 1998; Rk K. Ellis, V. V. Kiselev, and A. K. Likhoded, "Theoretical Status of B_c Decays and Lifetimes", Yellow Book contribution (B Physics at the Tevatron: Run-2 and Beyond), December 1999; J. D. Bjorken, "Estimate of Decay Branching Ratios for Hadrons Containing Charm and Bottom Quarks", unpublished report (1986), http://www-theory.fnal.gov/people/ellis/Bphysics/bjorken.PDF).

[31] I. Dunietz, Phys. Lett. **B316**, 561 (1993).

[32] A. Ali, *et al.*, Phys. Rev. **D61**, 074024 (2000).

[33] A. Ali, V.M. Braun and H. Simma, Z. Phys. **C63**, 437 (1994); J.M. Soares, Phys. Rev. **D49**, 283 (1994); S. Narison, Phys. Lett. **B327** 354 (1994).

[34] F. DeJongh and M. Shapiro, *A Proposal for Observing Radiative B Decays at CDF*, CDF Note 2570; K. Kordas *et al.*, *The CDF Penguin Trigger*, CDF Note 3771.

[35] "Measurement of J/ψ and $\psi(2S)$ Polarizations in $p\overline{p}$ Collisions at $\sqrt{s} = 1.8$ TeV." T. Affolder *et al.*, Phys. Rev. Lett. **85** 2886 (2000).

[36] E. Braaten, B. Kniehl, and J. Lee, hep-ph/9911436.

Chapter 3

Run IIb Silicon Vertex Detector (SVX IIb)

3.1 Introduction

During the Spring and Summer of 2000 the CDF Run IIb silicon Working Group studied the lifetimes of all components of the CDF Run IIa silicon detectors in order to establish integrated luminosity levels that can be attained with reasonable detector performance [1]. The Working Group concluded that it was not possible to guarantee that these limits, shown in Table 3.1, can be exceeded. As a result, a substantial portion of the Run IIa detector can not be guaranteed to survive Run IIb (15 fb^{-1}) and would thus limit our ability to capitalize on the exciting physics opportunities at Fermilab before the start of LHC. In particular, there is a significant likelihood that L00, the innermost 3 layers of SVXII, and all SVXII port-cards will need to be replaced. It was also clear that the schedule for such a replacement would be driven in large part by the schedule for a new radiation tolerant SVX chip (called SVX4). A small group of engineers from LBL, Padova and Fermilab was formed and made great progress on the SVX4 chip design in the past 2 years. The first full chips are expected to be in hand during the spring of 2002. The goal for the Run IIb installation is a six month long shutdown in the first half of 2005. In order minimize the shutdown period, a complete replacement for SVXII and L00 is necessary. As discussed in the working group report, any alternative, such as a partial replacement, would require a much more extensive shutdown.

The CDF Run IIb silicon detector is designed to be a radiation tolerant replacement for the SVXII and L00 detectors that is optimized for Higgs and new particle searches while also being affordable, robust, and simple to construct and operate. To minimize development time, the design makes use of existing

Layer	Safe Lifetime (fb^{-1})	Cause of Death
L00	7.4	V_{dep}
L0	4.3 (5.6)	S/N (V_{dep})
L1	8.5 (10.9)	S/N (V_{dep})
L2	10.7	V_{dep}
L3	23 (30)	S/N (V_{dep})
L4	14	V_{dep}
L6	> 40	n/a
L7	> 40	n/a
L8	> 40	n/a
Port-cards:		
SVX-II	5.7	DOIM
ISL & L00	14.6	DOIM

Table 3.1: Safe lifetimes for each layer of SVX-II as defined in the text. In the "Cause of Death" column S/N stands for signal to noise and V_{dep} for depletion voltage.

and tested technologies to the largest extent possible. The design presented in this Chapter represents our baseline design. Some changes may be required as we learn more about the operation of the RunIIa detector. For example, between the last Technical review of the Run IIb silicon project the following changes have been made:

- The 90 deg. stereo sensors have been replaced with axial and small-angle stereo sensors.
- Layer 1 is constructed of outer layer staves significantly reducing both the cost and complexity of the project.
- Layer 1 will have axial sensors on both sides of the stave for redundant measurements in this critical region.

In addition, we are currently studying two options for the sensors on Layer 5. Under consideration are axial layers on both sides or axial on one side and an additional small-angle stereo layer on the other side. For the purposes of this document we assume that layer 5 has axial sensors on both sides, however, further study is needed to determine if double axial or small-angle information is more advantageous for Run IIb pattern recognition. The current status of those studies is presented in the next Chapter. This decision has no impact on the cost or schedule of the project. The axial and small-angle sensors are the same price. The stave construction fixtures and procedures are independent of the sensor type. A decision is only needed by the time of the order of the production sensors (currently estimated as Sept. or Oct. 2002).

3.1.1 Conceptual Design

Having established that the present SVXII and L00 will not withstand the amount of radiation that will be accumulated during Run IIb, the design of the replacement detector must address three important issues:

1. It must withstand the radiation corresponding to an integrated luminosity in excess of 15 fb^{-1} during a period of 3 years.
2. It has to be ready for installation by Jan. 2005.
3. It has to retain or improve the performance of the present device.

Parts	SVXII + L00	Run IIb
sensors	7	3
hybrids	12	2
ladders/staves	7	2

Table 3.2: Different types of parts for the SVXII, L00 and Run IIb silicon detectors.

All three of these items are addressed by the use of single sided silicon sensors. The needs of the LHC detectors at CERN have motivated a great deal of effort on the development and understanding of radiation hard silicon sensors. Studies found that single sided sensors could be designed to withstand high bias voltages and that as long as the sensors were adequately cooled, good performance could be achieved throughout the LHC, or Run IIb, operation [4]. We intend to use this type of single sided sensor for the Run IIb detector, and will actively cool the sensors to sub-zero temperatures. Similar sensors (and cooling) are already in use in L00 of the Run IIa detector. Single sided sensor technology also has the advantage of avoiding the difficulties in manufacturing and procurement of double sided sensors that were incurred during the Run IIa detector construction.

To address item 2, we have drastically reduced the number of different types of key components such as hybrids and staves (ladders in the Run IIa language). Table 3.2 summarizes the number of types of parts for the SVXII + L00 and Run IIb silicon detectors. The outer 4 layers of the Run IIb detector utilize only two types of sensor (axial and small-angle), a single type of hybrid, and account for $\simeq 94\%$ of all detector parts. In Run IIa the total number of parts was split into 6 roughly equal sets each with its own features and difficulties.

Item 2 is also addressed by keeping the existing Run IIa infrastructure for use in Run IIb. For example, the cooling and the readout are designed to fit within the Run IIa systems. We note here a few of the differences and similarities in the Run IIa and Run IIb designs. The details are presented in later sections.

The immediate implication of using single sided silicon and direct silicon cooling is an increased amount of material inside the tracking volume. Consequently, effort has been directed towards minimizing all inactive components. With respect to the SVXII (Run IIa) design, the improvements in mass are:

- Portcards and portcard cooling have been eliminated (this by itself accounts for more than 3% X_0) from the tracking volume.
- Hybrids will use a more recent materials technology enabling smaller area and less metal coverage (by a factor of two in both cases). This same technology was used for the Run IIa L00 hybrids.
- Material and measurements are more uniformly spread over a larger volume (i.e. larger radii).
- The use of intermediate strips throughout the detector provides good resolution without the price of increased readout electronics.

The result is that despite doubling the silicon contribution (by using single-sided instead of double-sided sensors) and adding cooling to the sensors, the Run IIb design is less massive than SVXII.

The mechanical design of the Run IIb detector has been optimized for ease of construction and is quite different from the Run IIa design in that only one type of stave is used on the outer 4 layers. Figure 3.1 shows an end view of the Run IIb detector. To maintain the axial tracking capabilities of the Run IIa detector, staves will have axial silicon sensors mounted on one side of a carbon fiber rohacell structure and axial or small-angle stereo sensors mounted on the other side. The use of one structural design for the outer 180 staves will significantly reduce the production time. A wedge-based geometry has the clear disadvantage of requiring different parts (detectors, hybrids, assembly and bonding fixtures etc.) for each layer. This made the construction more complex, expensive and less flexible. Details of the mechanical design can be found in sections 3.2- 3.4.

A smaller and simplified version of the Run IIa portcard (the MiniPortCard or MPC) will be used at the end of each stave on layers 1-5. To address some of the reliability issues which have become evident with the Run IIa detector, the optical components have been removed and most of the active components of the Run IIa portcard have been moved to the more accessible junction card. This reduces the mass and cooling needed and should significantly improve the robustness of the system. Our desire to use commercially available parts combined with the higher radiation environment of the Run IIb detector has independently ruled out the use of optical transmitters for the data. Copper transmission lines will be used in place of the fiber optics. Cooper lines were tested extensively in the laser test stands used during Run IIa ladder production. More details on the MPC and rest of the DAQ system are provided in section 3.5.

3.1.2 Schedule

Preparation of a detailed schedule is underway and will be presented in a separate document. However, with a planned installation date of Jan. 2005, the rough features of the schedule are clear. Based on Run IIa experience, roughly 6 months of preparation (alignment, testing, final assembly etc.) will be needed between installation of the last stave in a barrel, and having a detector ready to install at CDF. This implies that the last stave must be completed by middle of 2004. We anticipate approximately 10 months for outer layer stave production, allowing some time for ramp up. This implies that production components for the outer layers must be in hand by the middle of 2003. This is achievable if the production chips, hybrids and sensors can be ordered in the fall of 2002. It is clear from these constraints that the schedule for R&D and prototyping is very limited compared to previous projects. We have thus, at every step of the design, tried to simplify and minimize the technically challenging tasks, without compromising the performance of the detector.

Prototyping activities were initiated in 2001 (where possible) and the project is in good shape for having key components for prototype stave construction to start by the middle of 2002. The first full chips will be in hand and available for installation on hybrids and the hybrid prototyping schedule meshes well with this schedule. By July 2002, prototypes of both hybrids and chips should allow testing and evaluation to begin. Another critical component is procurement of the silicon sensors. A small prototype order of the outer layer designs has been placed so that sensors will also be available for evaluation with the chip and hybrid. Other long lead time items are the beampipe, bulkheads, L0 signal cables followed by DAQ components and power supplies.

One schedule concern is the time required to swap out the old detector and install and commission the new one. A six month shutdown period leaves essentially no contingency for installation and includes little or no time for connecting and commissioning.

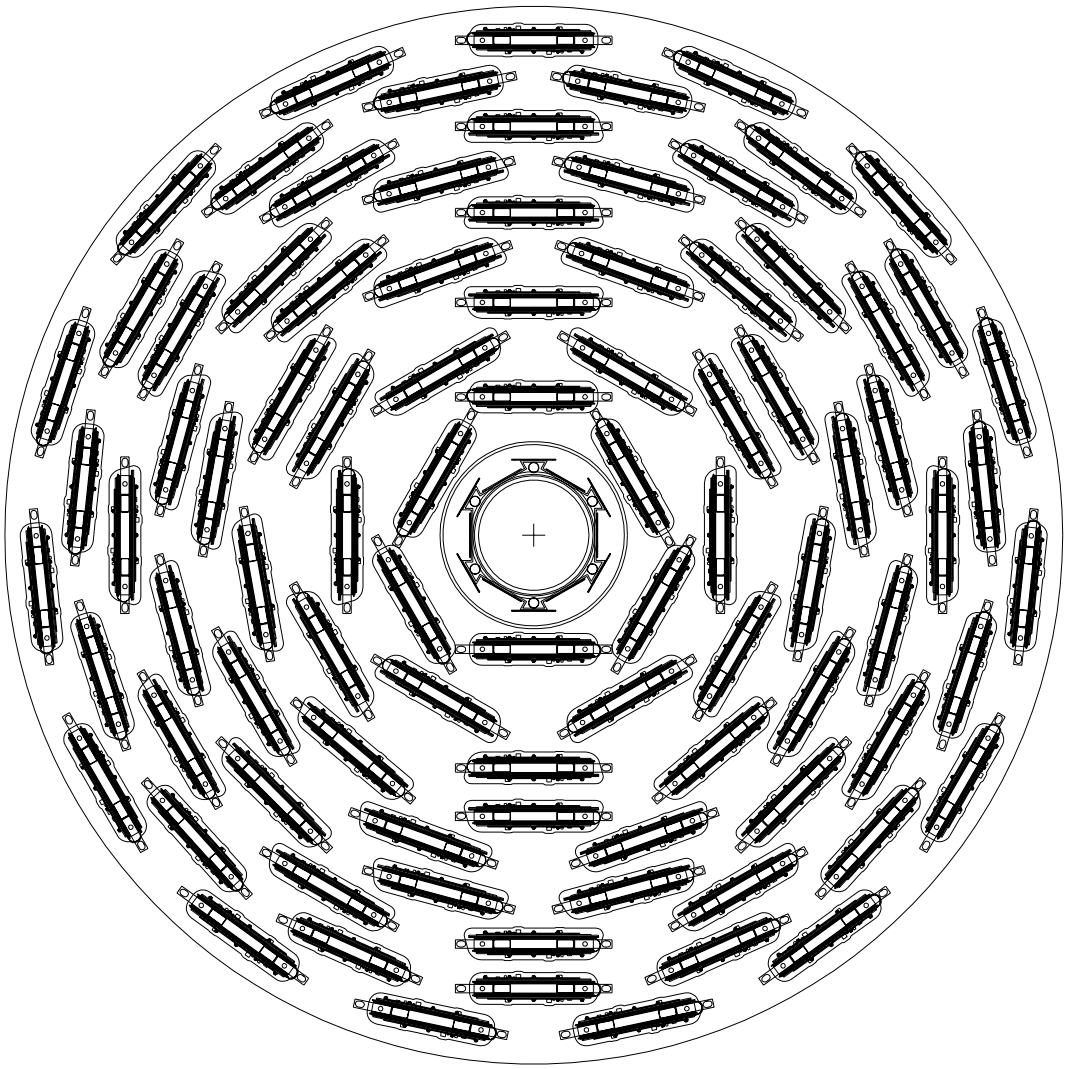

Figure 3.1: SVXIIb layout. Note that one stave design is used for the outer five layers and the innermost layer is very similar to the Run IIa L00 design.

With the experience of Run IIa to guide us, we are developing a plan to minimize as much as possible the turn-around time for the Run IIa to Run IIb transition.

The design presented in the following sections is the result of many studies, iterations and optimizations with input from mechanical and electrical engineers and physicists. We have based many of the design decisions on the experience of the previous silicon projects (SVX, SVX', SVXIIa, L00 and ISL). The structure of the document is as follows: section 3.2 describes the overall mechanical layout, the stave and barrel design, and alignment. Section 3.3 discusses the cooling system. The sensors and the fine pitch cables for the inner layer are described in section 3.4; section 3.5 covers the data acquisition system including the hybrids, the mother cables, the mini-portcards, external cables, junction cards, FIBS and power supplies. The details of the SVX4 chip are presented in 3.6. Section 3.7 compares the material in the Run IIb design with the Run IIa detector and section 3.8 describes the descoping plan. Section 3.9 concludes with a summary of the mechanical and electrical design. The subsequent chapter is devoted to a description of the simulation efforts, analysis of Run IIa data and the expected performance of the completed Run IIb silicon detector.

3.2 Mechanical Layout

3.2.1 Overview

The Run IIb detector is designed to maintain and enhance where possible the capabilities of the Run IIa detector, while allowing for quick construction and assembly as well as flexibility in terms of descoping. The new detector has 6 layers with two barrels in z, each 66 cm long. As in the Run IIa SVX detector, the staves within a layer are arranged in a castellated pattern as shown in Figure 3.1. However, to minimize the construction time, the Run IIb design has abandoned the 12-identical wedge structure of the Run IIa detector. The Run IIa portcards (and associated cables and cooling) have been removed from the tracking volume, to minimize mass and to allow the active layers to be more evenly distributed in radius. The key feature of the Run IIb design is that the outer 4 layers use identical structural elements, called staves, to support the silicon sensors. Figure 3.2 shows an isometric view of a stave. Each stave has built-in copper-kapton bus cables and cooling tubes which are sandwiched between 6 axial sensors on one side, and 6 axial or stereo sensors on the other side. Four-chip hybrids are used to read out two sensors each and are glued on the silicon (as in Run IIa). Layers 2-4 will have axial on one side and small-angle (1.2°) stereo sensors on the other side. The axial (stereo) sensors are 40.5 (43.1) mm wide and 96.4 mm in length. Layers 1 and 5 will have axial on both sides. The modularity of the outer 5 layers in ϕ, starting from the outer layer (layer 5) is 30, 24, 18, 12 and 6. The total number of staves in the outer layers is 180. Of these, 72 are double axial and 108 are axial plus 1.2° stereo. The radial locations of the Run IIb silicon layers are given in Table 3.3. The locations of the layers in the Run IIa detector are also listed.

The innermost layer (called Layer 0) is very similar to the Run IIa Layer 00 design [8]. It is a 12-fold symmetric axial layer and uses fine pitch cables between the sensors and the hybrids. The hybrids are located outside the tracking volume. One difference is that the Run IIb L0 has only one sensor and hybrid type. These are similar to the L00 2-chip modules (L00 had both one-chip and two-chip sensors and hybrids). The L0 sensors are identical to the 2-chip L00 sensors used in Run IIa; they are 14.85 mm in width and 78.5 mm in length. Two sensors are ganged together and readout by one hybrid. The length of L0 is 12 sensors plus gaps between modules for a total coverage of approximately 96 cm.

Layer 1 must provide redundancy for the axial tracking of Layer 0, but the circumferential space is very limited. We have found that the most robust layout for Layer 1 is an outer layer stave with axial sensors on both sides. The angular coverage of Layer 1 is only 85%, but the gaps are covered by the inner staves of Layer 2 as shown in Figure 3.1.

In summary, to speed construction of the Run IIb detector, we have minimized the number of different structures to be built. There are only two types of hybrid and only three types of single-sided sensors (two on the outer layers and one for Layer 0). Table 3.4 compares SVX IIb design parameters with those of the current SVX IIa design. Simulation studies of the Run IIb layout are discussed later and are compared to the Run IIa configuration. Note that the innermost layer has moved out for Run IIb. This allows for a much simpler construction procedure for this layer without degrading the impact parameter resolution. Also, the outermost layer has moved out roughly 5

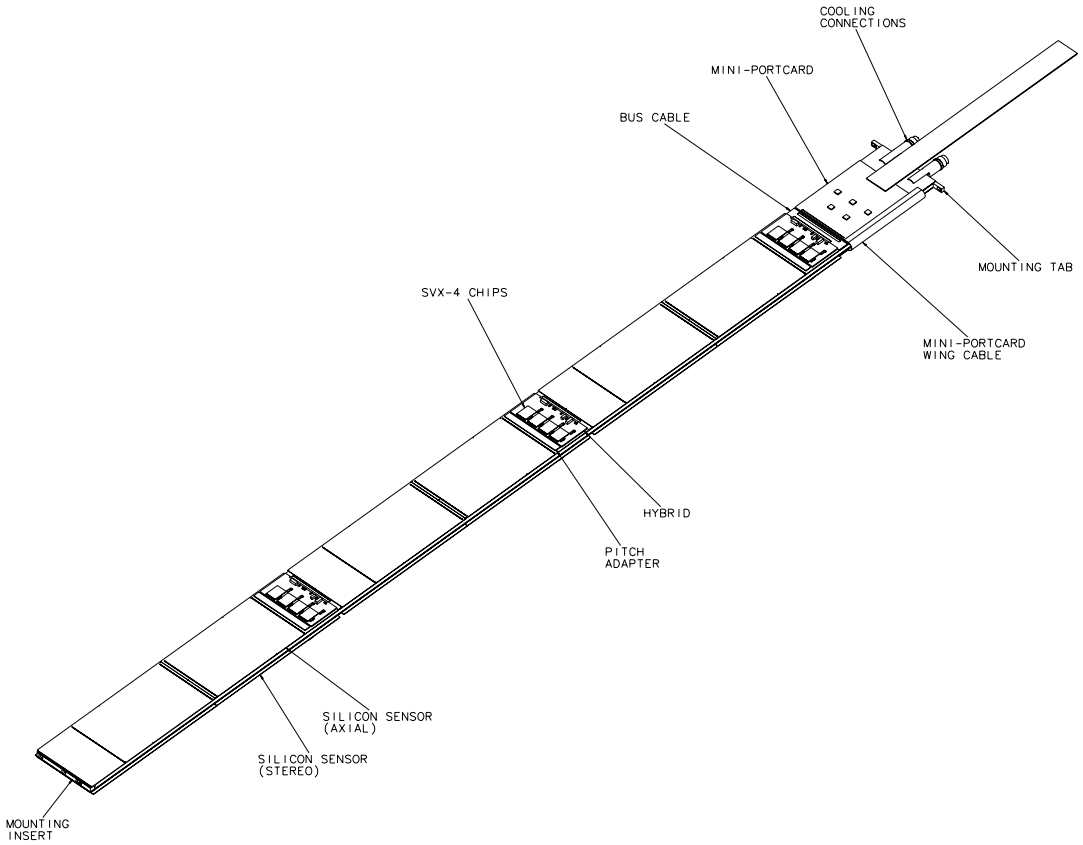

Figure 3.2: Run IIb stave design.

cm as a result of the elimination of portcards and the associated cables and cooling. An important feature of the Run IIb design is that the outer staves are essentially interchangeable. If further study shows that, for example, the outer layers should be rearranged, this will have no impact on the fixturing and prototyping for stave construction. This flexible design also allows a nonintrusive descoping plan which will be discussed in section 3.8.

3.2.2 Stave (ladder) Design

The detector is made up of three types of assemblies. The type used in the largest quantity is shown in Figures 3.2, 3.3 and 3.4 and is utilized in layers 1 through 5. The upper face of the stave is made up of three readout modules. Each module is made up of two axial sensors wirebonded together and a readout hybrid that is glued onto the silicon surface at one end of one sensor. The axial (small-angle) sensors are 96.393 mm long and 40.55 mm (43.10 mm) wide. The hybrid is fabricated on beryllia ceramic using thick-film circuitry (see Section 3.5). Its surface includes areas for four SVX4 chips, a wire bond field for bonding to a pitch adapter and a wire bond field used to connect the hybrid to the bus cable that passes underneath the silicon sensors. The hybrid is wirebonded down to this bus through a small gap between adjacent sets of sensor modules. A pitch adapter is glued to the silicon, next to the hybrid, and facilitates wirebonding between the SVX4 chip pads on the hybrid and the sensor pads. The bottom face of the stave is similar to the top, except that it is comprised of either axial (layers 1 and 5) or 1.2° stereo (layers 2-4) sensor modules. The hybrids used will be exactly the same on the axial and stereo sides and different pitch adapters will be used to match each sensor pad frame to the chips pads on the hybrids. Identical bus cable pass underneath the sensor modules on each side of the stave. These cables are connected at the end of the stave at the Mini-Port Card (MPC). The MPC processes the readout and regenerates the signals for transmission to the external DAQ system. It is mounted on the axial side of the stave past the end of the sensor modules. A small copper kapton "wing" cable is used to connect the bus cable on the stereo side of the stave to the MPC on the axial side of the stave.

The core of the stave itself is fabricated of carbon fiber composite skins on a foam core with a built-in cooling tube. The cooling tube is formed from 0.1mm walled polyetheretherketone (PEEK) plastic, which was selected for its ability to withstand radiation environments. It runs in a U-shaped path along the stave, having both its inlet and outlet beyond the active region of the detector. It provides cooling for the ϕ- and z-side sensor modules and the MPC.

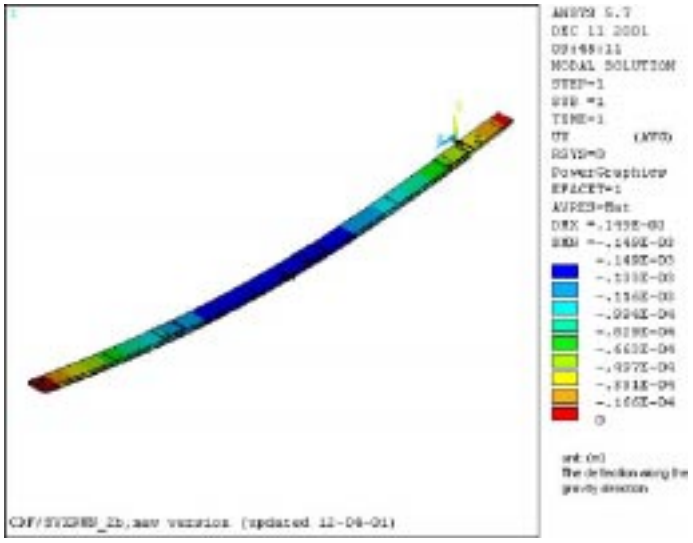

Figure 3.5: Finite element analysis of stave structure under gravity.

Stave position within the detector is registered in two locations. At the inner end of the barrel, pins extend out from the bulkhead to engage precision holes located in an Aluminum stave core insert. At the outboard end of the barrel, pins integrated into the bulkhead engage slots built into the stave core. The slots allow adjustment of the stave position within the barrel.

The emphasis on a low mass construction results in a significant sag over the length of a stave. With the staves only supported at z=0 and ±66 cm, the sag in the middle is expected to be ≈150μm. This is within the 160μm specification (see section 3.2.9). Prototype staves will be used to verify these results. Figure 3.5 shows the results of the finite element analysis of the stave structure.

The L0 configuration is very similar to the L00 detector used in Run IIa. It will be 12 fold symmetric and use sensors that are 2 chips wide (L00 alternated 1 chip and 2 chip wide sensors). A carbon fiber support structure with integrated cooling tubes will be mounted on the inner bore of each barrel and will be used to support the silicon. Six modules of two sensors each will be mounted at each ϕ location. In

Description	IIb Axial R (cm)	IIb Stereo R (cm)	Run IIa label	R(cm) IIa
Layer 0 inner	2.10		L00a	1.3
Layer 0 outer	2.50		L00b	1.85
Layer 1 inner	3.50	4.00 (0°)	L0a	2.54 (90°)
Layer 1 outer	4.35	4.80 (0°)	L0b	2.99 (90°)
Layer 2 inner	5.95	6.40 (1.2°)	L1a	4.12 (90°)
Layer 2 outer	7.475	7.925 (1.2°)	L1b	4.57 (90°)
Layer 3 inner	9.525	9.075 (1.2°)	L2a	6.52 (1.2°)
Layer 3 outer	10.90	10.45 (1.2°)	L2b	7.02 (1.2°)
Layer 4 inner	12.375	11.925 (1.2°)	L3a	8.22 (90°)
Layer 4 outer	13.750	13.30 (1.2°)	L3b	8.72 (90°)
Layer 5 inner	14.750	15.20 (0°)	L4a	10.09 (1.2°)
Layer 5 outer	16.150	16.60 (0°)	L4b	10.64 (1.2°)
Bulkhead outer radius	17.5			12.75
Screen, portcards, cables				12.75-16.5
Spacetube inner radius	17.5			16.5
Spacetube outer radius	18.5			17.5
ISL inner radius	19.5			19.5

Table 3.3: Comparison of radial locations of the axial and stereo silicon layers L00, SVXII and Run IIb. Note that in SVXII double-sided sensors were used and thus the axial and stereo radii are the same.

Detector Parameter	SVXIIb	SVX II
Readout coordinates	r-ϕ and r-z	r-ϕ and r-z
Number of barrels	2	3
Number of staves(ladders) per layer/barrel	12;6;12;18;24;30	12
Active Stave length	59.3 cm	29.0 cm
Sensor length	9.6 cm	7.2 cm
Combined barrel length	118.7 cm	87.0 cm
Layer geometry	staggered radii	staggered radii
Radius innermost layer	2.1 cm	2.44 cm
Radius outermost layer	16.6 cm	10.6 cm
r-ϕ readout pitch	50;75;75;75;75;75 μm	60;62;60;60;65 μm
r-z readout pitch	80;80;80	141;125.5;60;141;65 μm
Length of readout channel (r-ϕ)	19.4 cm	14.5 cm
r-ϕ readout chips per stave(ladder)	2*3;24;12;12;12;24	4;6;10;12;14
r-z readout chips per stave (ladder)	12;12;12	4;6;10;8;14
r-ϕ readout channels	405,504	211,968
r-z readout channels	165,888	193,536
Total number of channels	571,392	405,504
Total number of readout chips	4464	3168
Total number of detectors	2304	720
Total number of staves (ladders)	180 (+ inner layer)	180

Table 3.4: Comparison of the Run IIb silicon and the 5-layer SVX IIa. Note that the Run IIb design includes the beampipe layer (L00 in Run IIa) while the SVXII chip and channel counts do not; the number of sensors is more than twice the Run IIa count due to the use of single-sided sensors and the addition of the beampipe layer into the total. The pitch listed for the sensors is the readout pitch. All the Run IIb sensors will make use of alternate strip readout, thus, the actual sensor pitch is half that listed in the table. In Run IIa alternate strip readout was not used for the SVXII sensors.

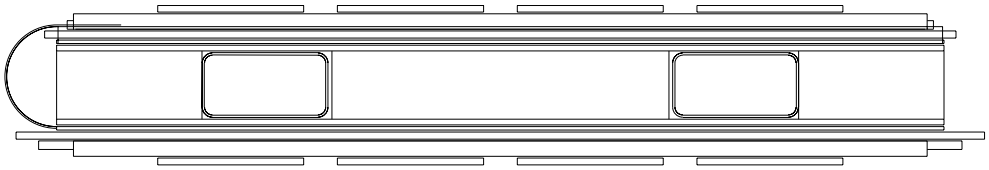

Figure 3.3: Full end view of an outer layer stave.

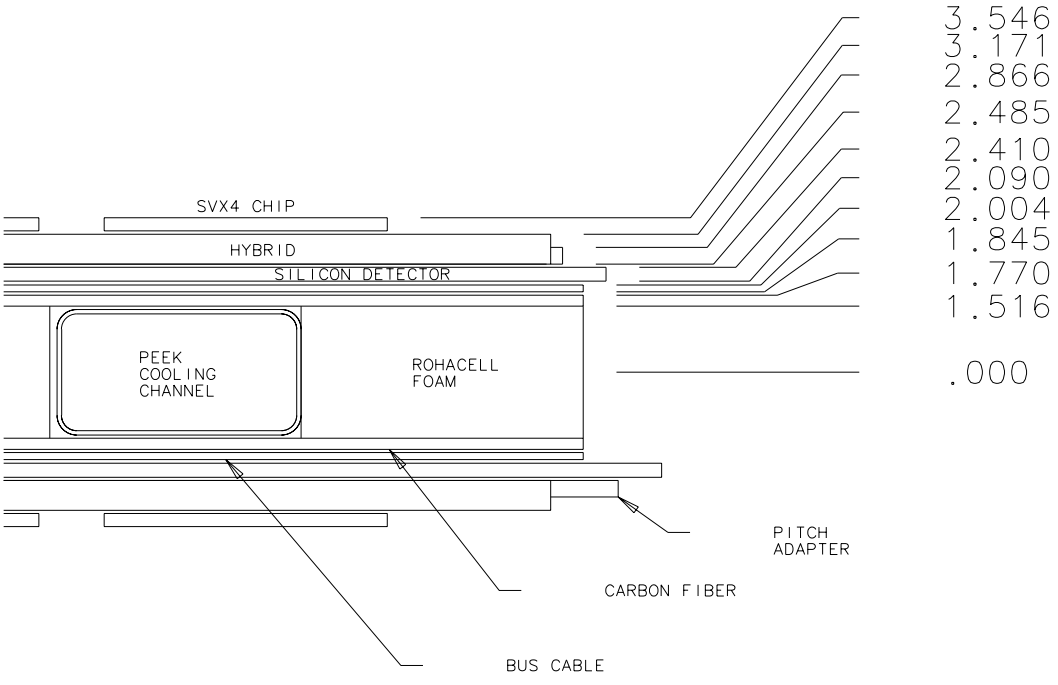

Figure 3.4: Closeup of end of a stave with dimensions (mm) of the lamination layers.

a module, the two sensors will be glued and bonded together and connected to a L00 type hybrid with a long fine pitch cable. The hybrids will be at $|z| >$ 66 cm, outside of the tracking volume. To minimize material and to fit within the allowed space, the L0 hybrids will incorporate the signal regeneration function of the MPC and a separate MPC will not be required. A consequence is that each module of L0 will form one readout chain, while on Layers 1-5 all six modules on a stave are ganged together to form one readout chain. The radial location of L0 is larger than the Run IIa L00 for several reasons. First, we wished to only use one sensor and hybrid type, namely the two-chip variety and 12 two-chip sensors simply don't fit at the L00 radius. Second, the support structure of L00 was split such that the top and bottom halves were constructed separately and then mounted on the pipe. This split structure presented difficulties with the alignment. With the present design, the L0 structure is a cylinder which fits over the large flanges at the ends of the beampipe. The new design eliminates several of the challenging aspects of the L00 design.

3.2.3 Beampipe

The design of the beampipe is very similar to the original Run IIa design. The pipe is 12 feet in length, with a 20 mil wall and provides the 1" clear aperture required by the accelerator. It is constructed out of three (or five) beryllium pipe sections. In contrast to the previous pipes, we are considering a technology, where the pipe sections are drilled rather than rolled and then brazed. The drilled pipe has the advantages that it does not have a braze joint along the full length of the pipe and it also has a more circular cross section than the rolled pipe. Information on cost and schedule for delivery for each technology are being collected at this time.

3.2.4 Bulkheads

The outer barrel staves span between precision bulkheads. The bulkheads will be constructed by gluing mounting features to a flat disk. The $z = 0$ bulkheads will have holes for installation arms and small precision pins that mate with the precision holes that are built into the end of each stave. The large z bulkheads will have holes that exceed the outer dimensions of the stave by $\geq$ 1mm such that the staves can be installed through them. Figure 3.6 shows a barrel with both bulkheads and some staves. These bulkheads and the mounting fixtures establish the precision of the barrel assembly and, therefore, must be positioned to very close tolerances. We are investigating carbon fiber and beryllium for the bulkhead material. Both have a long radiation length and high stiffness. Beryllium is much more expensive and requires a very long lead-time for machining, but may be necessary to meet the required precision.

During stave installation into the barrels, the z=0 and the outer bulkhead will be precisely aligned to each other. An inner screen will span the length of the barrel and will be glued to the inner surface of each bulkhead to maintain the bulkhead to bulkhead alignment. This structure will be supported in a rotating fixture similar to that used for construction of SVX, SVX', and SVXII. The staves will be installed through the outer bulkhead and then pinned to the z=0 bulkhead and the outer bulkhead. After stave installation is complete a cylindrical carbon fiber screen will be installed over the bulkheads and glued to them. This screen will hold the relative alignment of the bulkheads when they are removed from the rotation fixturing and will provide protection for the staves. After both barrels are complete they will be installed in a reinforced carbon fiber cylinder which spans the length to the support points on the ISL.

Figure 3.7 shows a side view of one half of the Run IIb silicon tracker, including ISL, the beampipe and the extension cylinders.

3.2.5 Spacetube

The weight of the SVX IIb detector is supported at the ends of the ISL detector using the existing kinematic mounts. The distance between these mounts is 1.95 m. A split cylindrical tube, called the spacetube, similar to that used in Run IIa will be used to span the gap between the mount points on ISL. The cylinder is split horizontally lengthwise such that the barrels can be installed from above. Figure 3.8 shows two barrels in the bottom half of the spacetube. The lower half of the cylinder will have reinforcing structures (rings and/or disks) at $z = 0$ and the $\pm$1m locations to prevent deformations of the cylinder under load. The reinforcing rings at the ends of the cylinder will also function as the structure for the beampipe supports. This open geometry leaves the detector ends accessible from above for beampipe and Layer 0 installation and for cable and plumbing dressing. Once the barrels, inner detector, and beampipe are

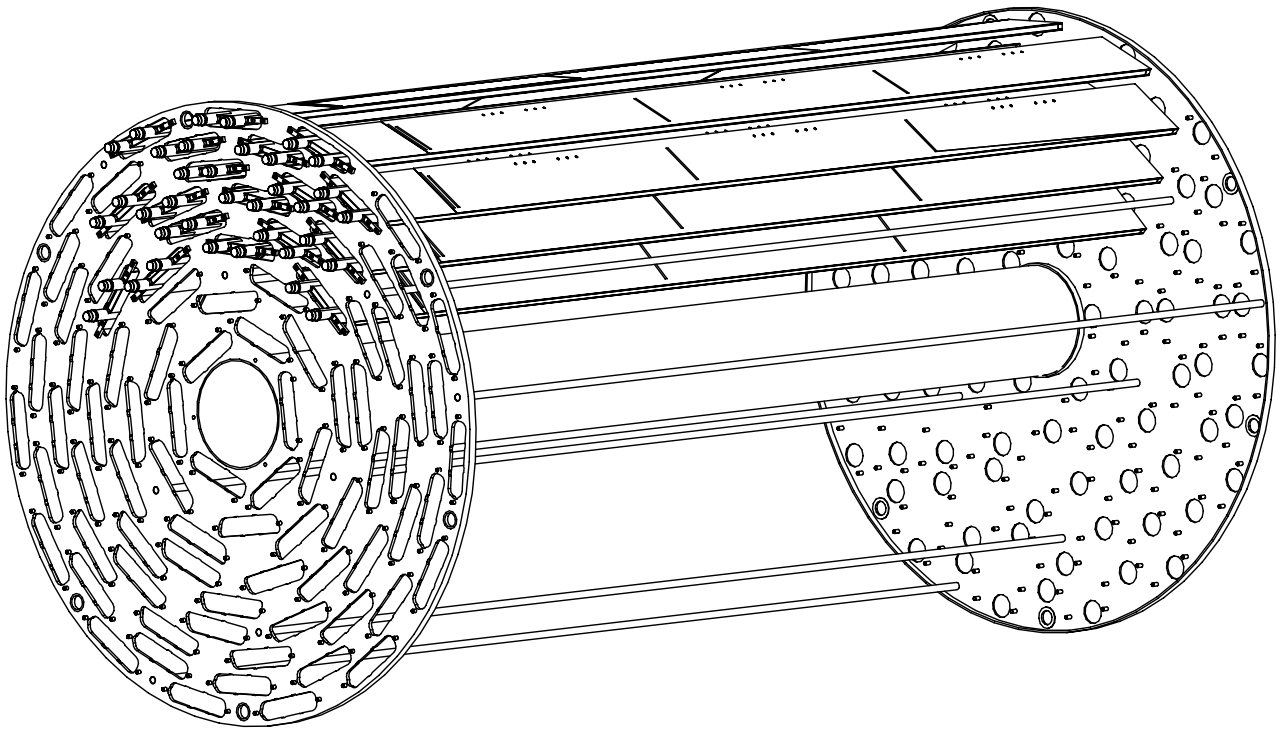

Figure 3.6: Isometric view of a barrel. Both bulkheads are visible along with a few staves. The inner bulkhead ($z \approx=0$) is on the right and the outer bulkhead is on the left. Also shown are rods connecting the bulkheads. These could be used to provide extra constraints on the bulkhead to bulkhead alignment.

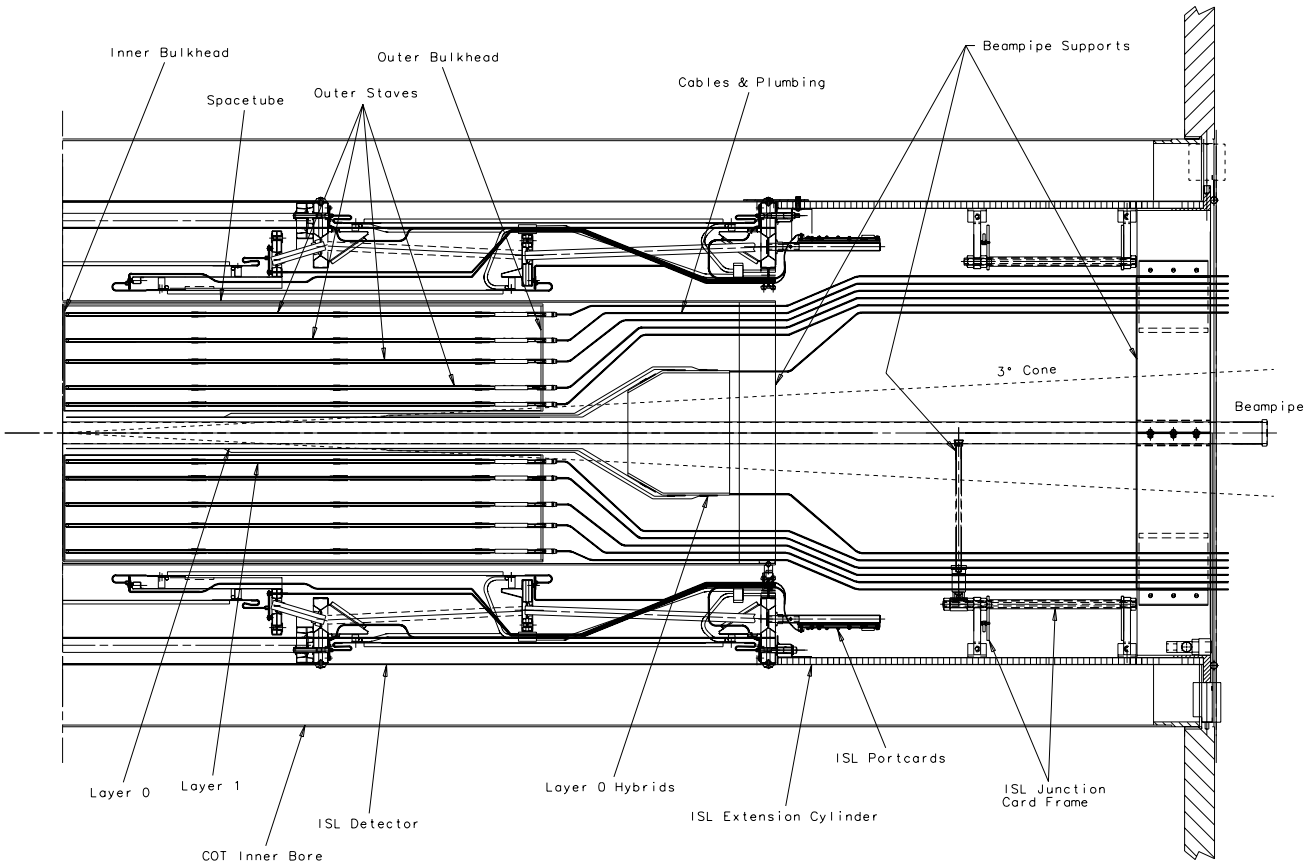

Figure 3.7: Side view of one half of the 3m long Run IIb detector. The outer bulkheads are at $|z| \approx 66$cm. The Run IIb spacetube spans the gap between the ISL mount points ($\approx \pm$ 1m). The beampipe and beampipe supports are shown along with the junction card ring and the ISL extension cylinders.

completely installed and aligned, the top and bottom halves of the cylinder will be glued together to provide maximum stiffness and support.

The alignment of the SVX IIb silicon with respect to the beam axis is critical for the operation of Silicon Vertex Trigger (SVT). Studies for Run IIa indicated that the axis of the barrels must be aligned to within a angle of 100 μrad relative to the beam axis, corresponding to a placement of about $\pm$130 μm from end-to-end along the length of the barrels. The rigid spacetube structure will maintain the precise barrel alignment after the assembly is removed from the measurement platform and inserted into ISL.

3.2.6 Barrel Assembly and Installation

Barrel assembly will occur on a precision coordinate measuring machine. Survey balls on the outer barrel bulkheads will allow the position of the internal barrel axis to be measured without direct reference to the silicon strips. Similar fiducials on the spacetube will characterize the detector's position. The kinematic mount positions on ISL are well known from measurements during SVXII/ISL construction. The new mounts on the Run IIb space tube will be positioned such that the Run IIb detector will be aligned to ISL.

After the spacetube is closed and the alignment has been reconfirmed, the assembly will be mounted on an installation fixture. The installation fixture will support SVXIIb while the ISL, mounted on a track, slides over it. SVXIIb will then be lowered onto the ISL kinematic mount points and removed from the fixture supports. ISL junction card support ring and supports for cables and cooling tubes are then arranged such that the ISL extension cylinders can slide over them. Beampipe supports are then installed. These over-constrain the pipe, and limit the amplitude of oscillations at the middle of the pipe. This installation process was used for the assembly of the Run IIa detector.

Once the installation of SVXIIb into ISL is finished, the entire 3m long assembly is transfered to the transportation cage and carried to the CDF assembly hall. Installation into the COT proceeds directly from this fixture and will follow the same procedures which were developed for installation and removal of the Run IIa detector.

3.2.7 Alignment with the Beam Axis

After the installation into the COT is complete, the position of the Run IIb silicon detector will be adjusted by moving the combined SVX/ISL assembly. The initial position of the detectors will be determined and adjusted by referencing the beampipe position (centered with respect to the silicon) to the end flanges of the COT. Survey points on the ISL and SVXIIb can also be tied to the reference system of the CDF detector. This alignment should place the detector within 1-2mm of the correct position. The detector position with respect to the beam is precisely determined using data from the $p\bar{p}$ collisions. If need be, the detector position can be readjusted by moving either the entire tracking system (COT + ISL/SVXIIb) and thus preserving their relative alignments, or by adjusting only the position of the silicon systems. Experience with Run IIa will determine if it is possible that steering of the Tevatron beams can provide this final alignment instead of moving the detectors. In either case, as in Run IIa, beam steering will be used to maintain the position and alignment of the beams between and during stores so that adjustments in the detector position should be needed only rarely.

3.2.8 Secondary Vertex Trigger (SVT)

The impact of the present detector design on the SVT trigger has been considered. The non-wedge-based geometry presents some challenges which are not present in the Run IIa SVX detector. However, similar issues were addressed in the implementation of L00 in the SVT trigger in Run IIa. The Run IIb design is compatible with the Run IIa trigger system provided a few adjustments are made to the present SVT hardware. A minimum set of modifications have been identified which would allow the use of the L2 SVT trigger with the Run IIb detector in a fully satisfactory manner.

The number of readout chains in the Run IIb detector is compatible with the SVT system and studies have found that the expected readout times are within the window allowed for the trigger at 132 ns operation. The main issue remaining is the 12-fold ϕ segmentation of the present trigger scheme. The immediate consequence of having abandoned a wedge symmetric design is the potentially unacceptable degradation of the track fitter performance since layer radii are not always constant within a ϕ seg-

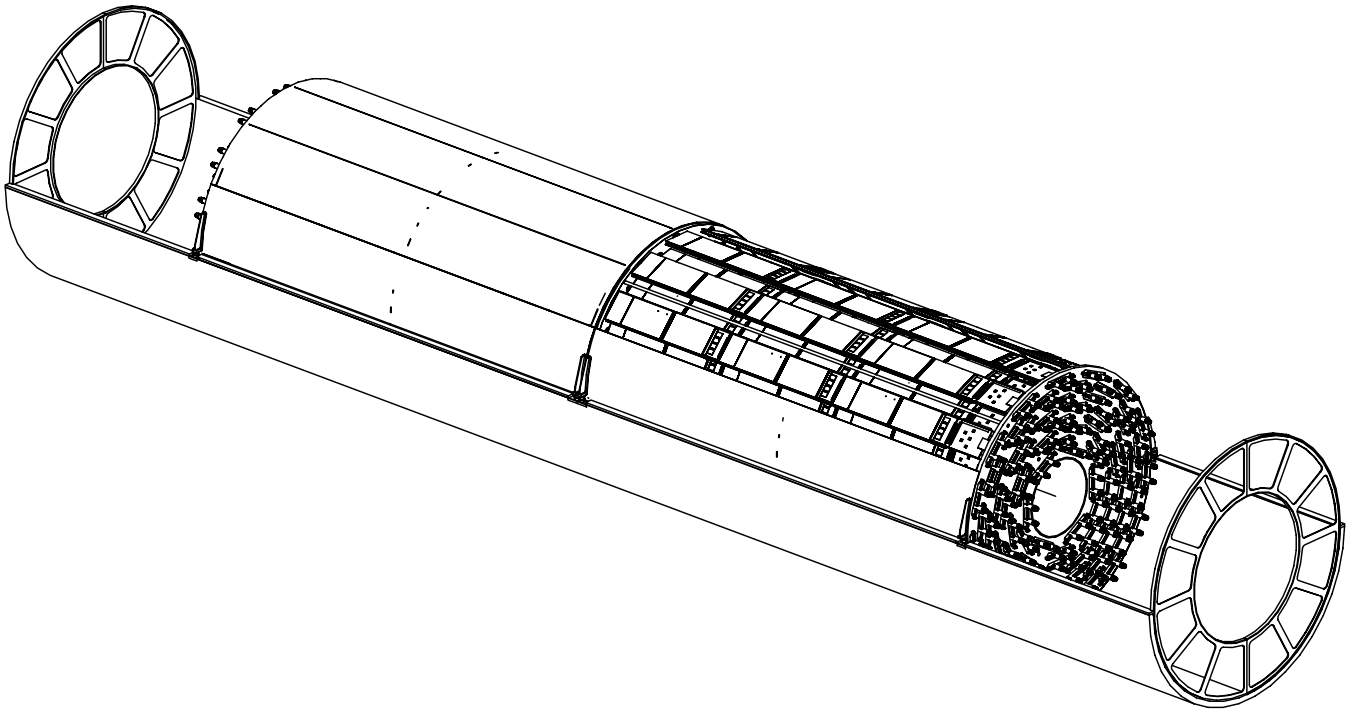

Figure 3.8: Two barrels are shown in the bottom half of the spacetube. The outer bulkheads are at $|z| \approx 66$cm. Reinforcing wheels are show at the end of the space tube. These minimize deflections of the tube and provide strain relief for cables and cooling.

ment. This degradation of performance with the present track fitter is being assessed and will determine whether a redesign of this board is needed. The cost of a redesign is included in the baseline cost estimate.

The minimal change required to the SVT is that 12 more merger boards, identical to those presently in use, need to be added to the system. These are needed for the hits from staves which span ϕ boundaries to be distributed to two different ϕ sections further upstream. This will allow the trigger decision to proceed without the additional cost of more external connections. The current SVT crates can accommodate the additional boards.

3.2.9 Alignment

The alignment requirements for SVXII were driven by the needs of the SVT trigger and these are assumed to be the same as for Run IIa. Specifically the requirements for the barrels in the space tube are:

1. slope within ± 100 μrad of nominal,
2. transverse position within ± 250 μm, and
3. longitudinal position within ± 1 mm.
4. The deflections under full load must be stable and repeatable to ± 10 μm before, during, and after installation into the ISL.
5. The thermal stability must be better than $\pm 10\mu$m over a 25^oC range.
6. The torsional deflection due to variations in the strain from the cable, cooling pipe and other asymmetric loads should be less than 10 μm at the mounting points of the detector.

These alignment tolerances are quite tight and are being reevaluated in light of the Run IIa data analysis. It is possible that they could be relaxed and thus could significantly reduce the time spent on stave construction, alignment and measurement in the barrels. A preliminary evaluation of the new specifications is given below.

To understand the assembly alignment requirements, we first note the difference between the construction position tolerance, which may be difficult to achieve, and knowledge of the position of a misaligned component, which may be easier to measure. The only significant restriction on the construction tolerance is given by the silicon–based impact parameter trigger (SVT). Since the track fits are done with constants which can be adjusted for each trajectory, all misalignments, once measured, can be corrected except for one case. This case arises because the trigger has only transverse information and thus knows a hit z position only within a silicon readout unit. Therefore, within a readout unit, the strip position uncertainty as a function of z must be limited.

To provide an approximate limit on the allowed misalignments we make the following assumptions: 15μm resolution on outer layers, 9μm resolution on the inner two layers, and 1.8% momentum resolution from the external track. Fitting these parameters and allowing for the fact that the impact parameter resolution from the trigger will include a beamspot of at least 23μm, we find that the high-momentum track resolution itself may grow as much as 100% of its nominal 9μm before the total impact parameter resolution is degraded by 5%. The actual performance of the trigger will not see this full effect since the misalignment resolution will be further masked by multiple scattering.

Next we distribute the allowed misalignments, in the form of additional hit resolution, to the layers in a pattern that tends to preserve the impact parameter resolution. We allow an additional 9μm resolution to be added to the inner layers and a 13μm resolution to be added to the outer layers.

Finally, we use an RMS analysis to interpret the allowed increases in resolution as tolerances on placement of the devices. For motions in the phi measurement direction, there is no limit since these misalignments can be removed in the SVT software. For rotations about the radial axis, we find a limits of $\pm 150\mu$rad for layer 0 and $\pm 180\mu$rad for the other layers. This applies to each readout unit (order 18cm) individually, relative to the beamline, and with no relation to the other readout units. For radial placement limits, we consider a model where silicon placement, sag, other bows, and silicon warpage all contribute to the position of the readout unit, and the radial positions are roughly equally distributed between a maximum deviation $\pm D$ from the average radius. We find the following limits on D for layers 0 to 6: 66, 67, 54, 85, 122, 160, 200μm.

This style of analysis does not address questions such as pattern recognition or χ^2 degradation, or tails of the distributions, which may not follow RMS rules

due to, for example, correlated misalignments.

In the consideration of alignment for offline reconstruction there are no assembly tolerances, only guidelines for the measurement of component positions. This approach is possible since in the offline environment any known misalignment can be corrected once we have full knowledge of the track position. A second point is that, historically, the mechanical assembly measurements of detectors have disagreed with the tracking alignment in some respect, and when they do, the track-based measurements are given the final word. A third observation is that with enough time and sufficient effort of collecting and analyzing special data sets, the silicon detector alignment can be completely aligned using tracks. We conclude that, with respect to offline, the construction alignment measurements are a matter of degree of confidence, insurance, or convenience rather than tolerances.

A feature of the Run IIb design is that the staves will be supported off the end of the silicon wafers. It should thus be possible to view the entire sensor area of the staves when they are installed in the barrels and to measure their horizontal positions to better that 10 μm in the barrel reference frame (for Run IIa only the middle 15cm of a 30 cm stave was visible). Another feature of the IIb design is that some of the layers are upside down compared to the other layers (the axial layer is on the inside rather than the outside). It will thus be possible to directly measure the Hall effect drift by taking a small amount of data with and without the magnetic field. In Run IIa this is possible only in the ISL.

In Run IIa the axial and stereo views are on the same sensor and thus very precise relative alignment was possible. In Run IIb the two views on a stave are separated by the about 5mm. Although it is not critical to position the axial and stereo sensors extremely precisely to each other, measurement of their relative positions at the level of 15μm should be possible and would be a significant time savings in commissioning.

3.2.10 Position Monitoring

A Rasnik (or similar) system for monitoring the overall position of the barrels can prove useful in detecting the large unexplained shifts observed in most detectors. Position monitors will be located on the barrels and plug directly into the existing Run IIa system.

3.3 Cooling and Gas systems

The silicon should be maintained below the temperatures listed in Table 3.5 for nominal operating conditions. In Layer 0 we expect roughly a 10 deg. difference between the coolant temperature and the temperature of the sensors and thus we anticipate the coolant temp for Run IIb will be need to -15 deg. C to achieve the goals in the table. Thermal runaway was a serious issue for the thermal design of the SVXII detector [3] where center silicon sensors in a barrel were not well-coupled thermally to the cooled bulkheads. Available heat transfer paths ran through either wirebonds, foam, or Nitrogen gas. Internal heat generated due to leakage current caused by radiation damage is therefore hard to remove and it leads to higher silicon temperatures. Since the amount of leakage current increases significantly as the temperature increases, a positive feedback system exists, potentially leading to a catastrophic thermal runaway condition if cooling is insufficient.

For the SVX IIb detector, the design integrated luminosity of 15 fb^{-1} is much higher than for SVXII, so the leakage current will be much higher. Having silicon sensors that are only loosely coupled thermally to the cooling system is simply not a design option. Each stave must therefore be equipped with its own cooling channels to couple the sensors to the coolant more directly. In this way, the issue of thermal runaway has been effectively eliminated. The nominal heat load anticipated within the detector is shown in Table 3.6. These numbers assume 400 mW per SVX4 chip, 0.27 W per sensor for internal heat generation after 30 fb^{-1} integrated luminosity (40μA/cm^2, 15^{o}C operating temp, 250 V depletion), 0.5 Watts for each transceiver (5) on the mini-PCs, and convection with a 0^{o}C environment when the fluid temperature is -15^{o}C. Note that the SVX4 chip is expected to use less power than the 420 mW SVX3D chip since the operating voltage is 2.5V instead of 5V.

The existing SVXII cooling system will be used for cooling the Run IIb detector. The Run IIa system is designed to operate at -10°C with 30% ethylene glycol by weight in water, which has a freezing point of -14°C. However, in order to achieve the specified silicon operating temperatures for layer 0 in Run IIb, the system will have to operate at a colder temperature, nominally -15°C. Therefore, the ethylene glycol percentage will be increased to 43% by weight, yielding a freezing point of about -25°C. This would allow op-

Layer	Temp. (deg. C)
0	-5
1	-5
2	+10
3	+10
4	+15
5	+15
6	+15

Table 3.5: SVX IIb temperature specifications

	Heat Load per Stave (W)
SVX4 chips (24)	9.6
Convection	4.2
MiniPC	2.5
Leakage (6 cm)	1.6
Total per stave (W)	18.3
Total Layers 2-5 (W)	3240
Run IIa SVX Detector Total(W)	2800

Table 3.6: SVX IIb Detector Heat Load

eration of the cooling system down to approximately -20°C.

As in SVXII, the cooling system is designed to operate below atmospheric pressure in the detector region. Therefore, if a leak in the system were to occur, the coolant, being under a partial vacuum, will not leak into the detector environment. The gas system for the detector will provide a continuous gas flow of nitrogen at $\approx$ 200 scfh to the detector volume. This dry gas supply keeps the silicon volume slightly over atmosphereic pressure and prevents condensation. To prevent the gas from adding heat to the system, it will be cooled near its injection region by means of a compact fluid-to-gas heat exchanger integrated into one of the plumbing return lines. This will cool the gas to nearly the coolant temperature. The gas system will be monitored to prevent impurities from entering the system.

3.3.1 Stave Cooling

A total of five inlet/outlet plumbing access slots per end of the CDF detector are currently in use for SVXII+L00 and will be available for SVX IIb. One slot will be devoted to cooling L0 and L1. The remaining 4 slots will be manifolded to provide cooling to the staves in layers 2-5. The end of the cooling channels in a stave will have aluminum fittings glued to the carbon fiber structure. Flexible tubing, similar to that used in Run IIa, will be attached to the aluminum fittings. These tubes will either attach to another stave (connecting them in series) or to a manifold. The cooling for Layer 0 sensors is embedded in the carbon fiber support structure as in the Run IIa L00. Cooling will also be provided to the hybrid support structure located off the ends of the L0 sensors.

A finite element thermal model has been developed to investigate the temperature trends in the silicon for the stave type used in layers 1 through 5. Temperatures in layer 0 silicon have not yet been studied in detail. Figure 3.9 shows the results of the modeling where a coolant temp of -15°C is assumed. The maximum temperature in the sensor occurs underneath the readout hybrid, as the SVX4 chips are the primary heat source in this region. Heat generated in the chips is spread through the beryllia hybrid substrate, which has a very high thermal conductivity. It is conducted through the adhesive to the silicon, where it is spread further, and then conducts down through the bus cable and adhesive layers to the composite skin on the stave core structure, which is constructed from high-conductivity carbon fiber. The heat is then picked up by the cooling channels running axially through the stave core. Silicon sensors without hybrids mounted on top of them have very small heat loads and are therefore maintained close to the coolant temperature. The warmest location is on the hybrid at the outer end of the stave. The heat from the other hybrids can dissipate in two directions along the stave while the heat from end hybrid is trapped on one side by the presence (and heat) of the mini portcard. The warmest portion of the stave is 0°C with a coolant temperature of -15°. In terms of radiation damage, the important number is the average temperature over a strip. The models indicate that the axial modules have average temperatures of -10°. The shortest small-angle strips directly under the hybrid end up with an average temperature of -4°C. These are well below the specifications in Table 3.5 because the operating temperature of the chiller is driven by the needs of the innermost layer.

The grouping of the staves into cooling circuits is driven by pressure drop restrictions for each cooling supply slot. To minimize the tubing at the end of the staves, one would like to connect together the maximum number of staves into one cooling circuit.

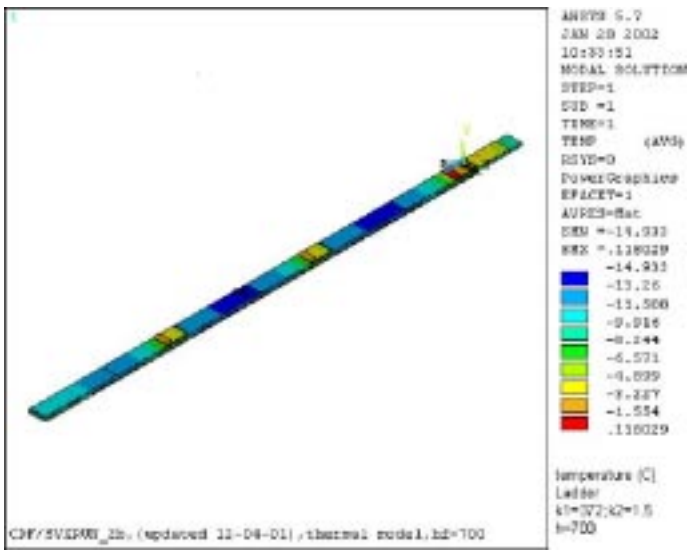

Figure 3.9: Results of finite element analysis of stave temperatures.

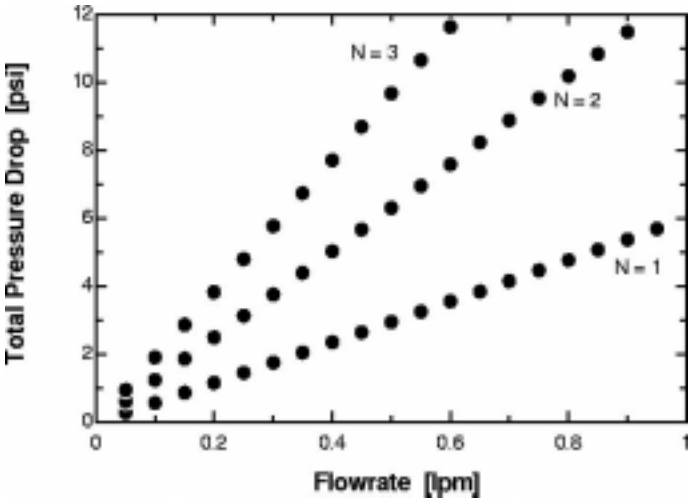

Figure 3.10: Predicted pressure drop versus flow rate for 1, 2 and 3 staves ganged in series.

However, to keep the system at subatmospheric pressures inside the detector volume, the allowed pressure drop within the detector cooling circuits in 4.5 psi. Figure 3.10 shows pressure drop versus flow rate for the configurations with 1, 2 or 3 staves connected in series. Lower flow rates result in larger difference between the inlet and outlet temperatures of the coolant. Figure 3.11 shows the pressure drop for the cases with 1, 2, and 3 staves connected in one circuit. With 3 staves connected in series, and a flow rate of 0.24 lpm, we are within the allowed total pressure drop, and the change in the coolant temperature in the 3-stave circuit is 4.3°C, or 1.4°C/stave.

As indicated above, the Run IIb design is much less sensitive than the Run IIa device to problems associated with thermal runaway resulting from radiation damage in the sensors. The effect of integrated luminosity was investigated by looking at the predicted silicon temperature in layer 2 at the beginning of the run and after 30 fb^{-1}. Only a very small difference (< 1 deg.) in the predicted temperatures was found, demonstrating that internal heat generation resulting from leakage current is not a thermal runaway concern with the Run IIb design.

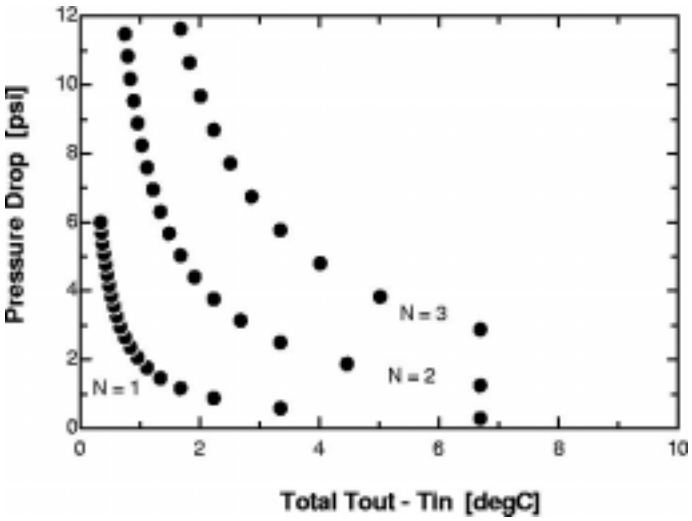

Figure 3.11: Pressure drop versus inlet-outlet temperature difference.

3.4 Sensors and fine-pitch cables

3.4.1 Radiation damage

Silicon detectors are damaged by radiation primarily through displacement of silicon or impurities from

their lattice sites (bulk damage). The other form of damage, often referred to as surface damage, is the main mechanism responsible for IC performance degradation but it has little impact on silicon detectors since their active region is mostly in the bulk away from the passivating silicon dioxide layer. As a first approximation this mechanism can be neglected since the sensors we are proposing for the Run IIb silicon detector are single-sided p^+/n. As a result of bulk damage, silicon detectors are subjected to two main mechanisms:

- increase in leakage current and thus in the overall noise
- substrate type inversion (i.e. from n-type to p-type) which affects the depletion voltage.

3.4.1.1 Run IIa Radiation Measurements

The radiation field inside the tracking volume is measured using thermal luminescent dosimeters (TLDs) placed at 145 separate locations. During the first 9 months of Run IIa the TLDs were harvested twice. The first period from February to May was dominated by beam studies and proton losses. The second period from May to October and was dominated by proton-antiproton collisions. Table 3.7 summarizes the two exposures. Figure 3.12 shows the pattern of ionizing radiation based on measurements at two radial distances from the CDF axis as a function of the position along the axis. Protons enter from the left. In this figure, we've separated the contributions from collisions (top) and losses (bottom) using the prescription:

$$D_1 = C_1 * d_{lum}(\frac{Rad}{pb^{-1}}) + L_1 * d_{loss}(\frac{Rad}{counts}) \quad (3.1)$$

$$D_2 = C_2 * d_{lum}(\frac{Rad}{pb^{-1}}) + L_2 * d_{loss}(\frac{Rad}{counts}) \quad (3.2)$$

where D_i are the measured doses on the TLDs, C_i are the collisions (luminosity in pb^{-1}) and L_i are the losses (counts) measured in the Feb-May (i=1) and the May-Oct (i=2) periods. These two equations are solved for d_{lum} and d_{loss} and the results are plotted in Figure 3.12.

3.4.1.2 Leakage Current

The leakage current is extremely sensitive to temperature, doubling every $\simeq 7^o$C. It is the junction reverse

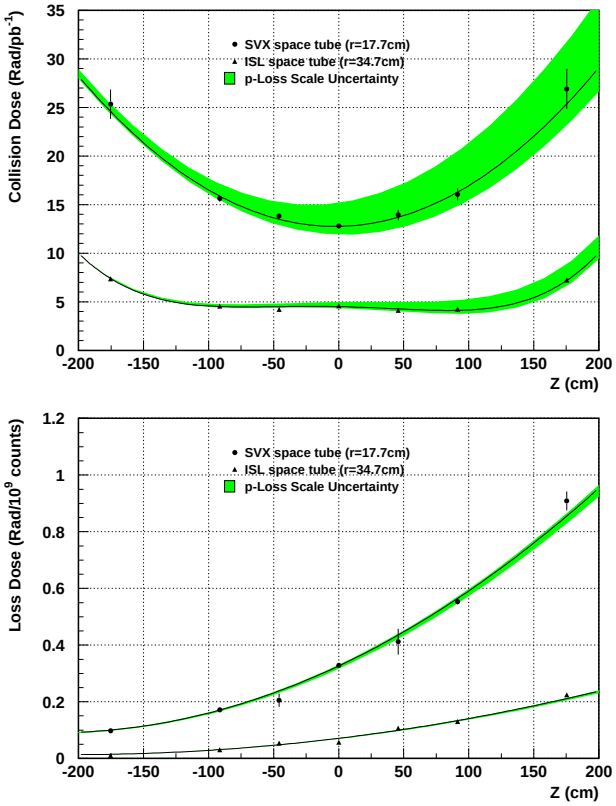

Figure 3.12: Radiation measurements and fits to Run IIa data. Ionizing radiation dose from collisions (top) and proton losses (bottom) observed by TLDs placed in the tracking volume. The data in the plots were derived from two exposures in 2001.

Period 2001	Feb-May	May-Oct.
Proton Beam (10^{19})	0.070	1.56
Pbar Beam (10^{19})	0.0082	0.137
Proton Losses (10^9)	15.3	40.9
Pbar Losses (10^9)	2.0	10.2
Del. Luminosity(pb^{-1})	0.058	10.7

Table 3.7: TLD exposure statistics

saturation current and is proportional to the silicon volume considered. The generation/recombination model predicts the following dependence of the leakage current on temperature:

$$\frac{I_{leak}(T_1)}{I_{leak}(T_2)} = \frac{T_1^2}{T_2^2} \cdot e^{[\frac{-E_g}{2k}(\frac{T_1-T_2}{T_1 T_2})]}; \qquad (3.3)$$

where T is the temperature in Kelvin, $E_g = 1.12\ eV$ is the silicon energy gap and k is the Boltzmann constant. An intense research effort over the past few years (motivated by the LHC experiments) found that the increase of leakage current with radiation is linear and is independent of the particular substrate or detector fabrication process. It is thus possible to assign a global constant to the leakage current increase with radiation:

$$I_{leak} = \alpha \cdot Volume \cdot \phi\ ; \qquad (3.4)$$

where α is the leakage current damage constant at 20^oC, Volume is the silicon volume considered and ϕ is the radiation damage fluence in 1 MeV equivalent neutron$\cdot cm^{-2}$. Detectors subjected to radiation damage exhibit an increase of leakage current which decays with time after irradiation (annealing effect) with a temperature dependent time constant. Consequently the leakage current damage constant will depend on the time and temperature history of the detector. For detectors used in a collider, the damage rate is always rather low compared to the annealing time constant and we can assume that complete annealing occurs during their operation. In this case we can use an α constant of 3.2 $10^{-17}\ A/cm$. Since our silicon detectors are AC coupled there is no direct path for the leakage into the readout chip preamplifier inputs but rather its effect is seen as a noise increase. The increase in noise is independent of the intrinsic readout chip noise and needs to be added to the latter in quadrature. Since the functioning of the SVX4 chip is based on the double correlated sample and hold concept, the noise associated with the leakage current can be shown to be:

$$ENC_{I_{leak}} = \frac{1}{\sqrt{q}} \cdot \sqrt{I_{leak} \cdot \frac{x - F(x)}{F(x)^2}} \qquad (3.5)$$

$$x = \frac{T_{int}}{\tau} \qquad (3.6)$$

$$F(x) = (1 - e^{-x}) \qquad (3.7)$$

where q is the electron charge, T_{int} is the integration time and τ is the preamplifier rise time.

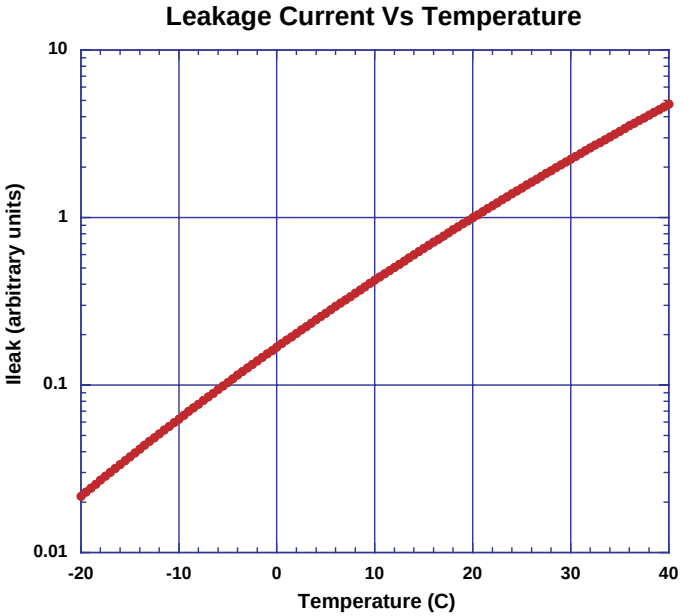

Figure 3.13: Relative variation of leakage current with temperature.

Figure 3.14 shows the component of the noise from leakage current as a function of the leakage current itself assuming $T_{int} = 113ns$ and $\tau = 45ns$. There are two handles to limit the leakage current: one is the temperature and the second is the silicon strip volume itself. In practice, though, the strip volume is defined by other considerations (resolution, occupancy, ease of fabrication etc.) and temperature remains the only control. Figure 3.13 shows the relative variation of leakage current with temperature with the arbitrary reference choice of 20^oC as the unit value. For example, lowering the temperature from 20^oC to -5^oC makes the leakage current go down by an order of magnitude. The silicon operational temperature is then set by the amount of increased noise that can be tolerated at any given radius for any type of detector (i.e. a given baseline noise and a given strip volume).

3.4.1.3 Depletion voltage

While the increase of leakage current with radiation damage is a very well understood (at least macroscopically) effect, much less so is the depletion voltage variation. This is mainly due to the fact that the donor removal rate and acceptor introduction rate (responsible for the variation of the effective dopant concentration N_{eff} and hence for the deple-

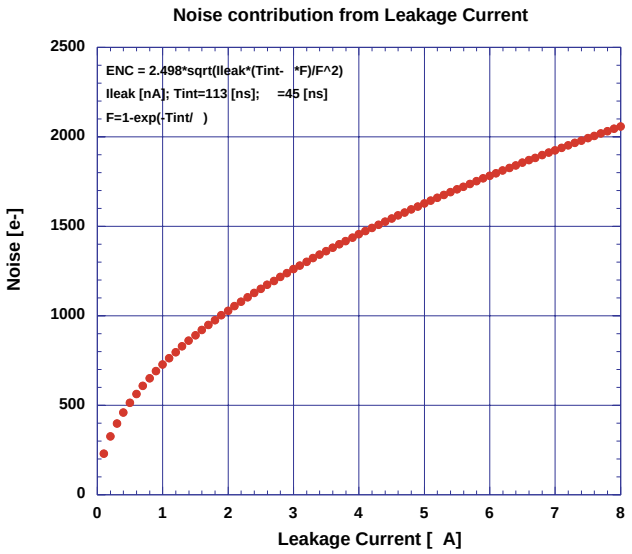

Figure 3.14: Noise (in electrons) vs Leakage current.

Parameter	Value	Unit
K_S	7.6610^{-8}	$V \cdot cm$
N_{C0}	2.510^{12}	cm^{-3}
c	2.010^{-13}	cm^2
g_C	1.7710^{-2}	cm^{-1}
d	3.010^{-2}	cm
Φ	2.210^{13}	$1\ MeV\ eq.\ n \cdot cm^{-2}$ per fb^{-1} *at* $1\ cm$

Table 3.8: Values of the parameters to determine the depletion voltage.

tion voltage) are complex mechanisms, the magnitude of which depends upon many parameters such as temperature, initial resistivity, initial concentration of various impurities, type of radiation, and even detector production processes. A further complication is that damaged bulk is subject to two types of annealing, first a beneficial annealing and then a reverse-annealing which, if not controlled, will increase the initial damage by about a factor of 2. Fortunately the reverse annealing plays a role only after considerable damage has been done (in practice only after type inversion) and can be minimized by keeping the silicon at a temperature below 5^oC. Neglecting the reverse annealing effect, we can model the variation in depletion voltage using the simplified formula:

$$\Delta N_{eff}(\Phi) = N_{C0}\, e^{-c\Phi} + g_C \cdot \Phi\ ; \quad (3.8)$$

$$V_{depletion} = \frac{q}{2K_S\epsilon_0} \cdot d^2\ |N_{eff}|\ ; \quad (3.9)$$

where N_{eff} is the effective dopant concentration, Φ is the radiation fluence, N_{C0} in the initial effective doping concentration, c is the donor removal rate, g_C is the acceptor introduction rate, d is the silicon thickness, q is the electron charge, K_S is the silicon dielectric constant and ϵ_0 is the vacuum permittivity. Table 3.8 shows the values used for our calculations and Figure 3.15 shows the predicted depletion voltages for the three innermost layers as function of luminosity. In this Figure we applied a safety factor of 1.5 to the predicted dose.

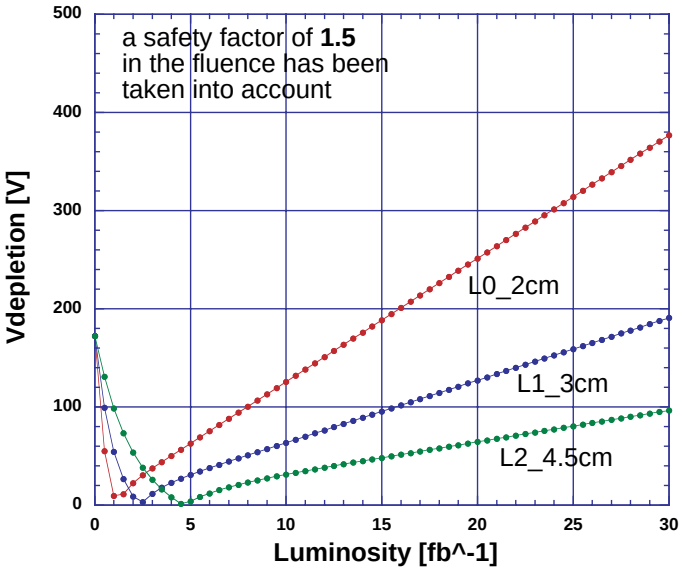

Figure 3.15: Predicted depletion voltages as a function of delivered luminosity. A safety factor of 1.5 in the expected dose has been taken into account.

3.4.2 Sensor Specifications

In this section we give a brief technical description of the sensors that will be used for Run IIb. We intend to make use of R&D performed for the LHC[4] experiments and to take advantage of the recent experience with the construction of the Run IIa silicon detectors[5, 6]. To minimize the cost, all sensors will be fabricated on 6" wafers[7] with at least two sensors per wafer. The specifications for the substrates are listed in Table 3.9. The choices of the substrate characteristics are driven by mechanical constraints as well as by radiation hardness. The specified wafer orientation has been proven to withstand fluences up to $4X10^{14}$ p/cm^2 without any change on the total capacitance of the strips [4]. The high resistivity substrate will prolong the lifetime of the sensors by delaying high voltage operation.

Parameter	Specification
Thickness	320 μm $\pm$ 15 μm
Wafer diameter	6 *inch*
Wafer type	n-type
Wafer orientation	$< 100 >$
Wafer resistivity	1.3 to 3.3 $k\Omega$-cm
Warp	$< 100\mu m$
Polish	Mirror finish on Junction side
	Ohmic side optional

Table 3.9: Properties of the wafers

Many characteristics are common to all detectors regardless of layer or stereo angle. All sensors are n-type, single-sided, AC coupled, poly biased silicon microstrip detectors with intermediate strips. As already described, the sensors have to withstand high radiation fluences. Consequently it must be possible to operate the sensors at voltages exceeding 500 V. Such results have already been achieved for Layer 00 in Run IIa. Figure 3.16 shows the breakdown voltage for all the Layer 00 sensors produced by *Hamamatsu*. The cut at 500 V still allows for a very high yield. Similar results have been achieved with other vendors like *ST Catania*[5] and *Micron Semiconductor L.t.d.*

3.4.2.1 Axial and 1.2° stereo sensors

For the innermost layer the sensors will be identical to the Layer 00 sensors[5]. The outer layer sensors are described here. Given the sensor thickness, the

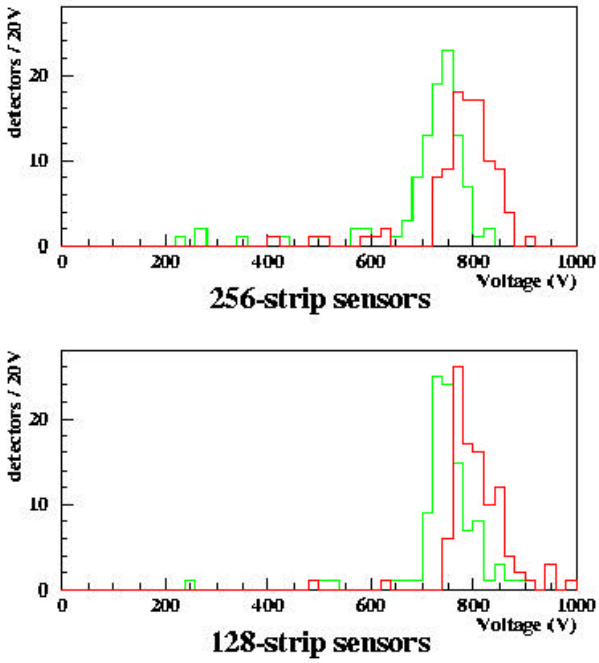

Figure 3.16: Breakdown and operational voltages of Layer 00 Hamamatsu sensor.

amount of signal collected is fixed, but the noise is strongly dependent on the sensor design. The feature sizes define the magnitude of the total capacitance of each strip which is linearly correlated with the noise performance. The total capacitance of microstrip detectors is well parameterized by formula 3.10 [4].

$$C_{tot} = (0.83 + 1.67\frac{w}{p})pF/cm \qquad (3.10)$$

A w/p (width/pitch) of 0.2 results in a capacitance per unit length of 1.16 pF/cm. Strips as long as 34 cm can then be read out by a single electronic channel without compromising the initial signal over noise. The limit on signal to noise is discussed in Section 3.6, and corresponds to 40 pF. The set of specifications for the outer axial sensors is reported in Table 3.10.

3.4.3 Inner Layer Lightweight Cables

To minimize the scattering material in the first measurement layer, the L0 construction will follow the design of the Run IIa L00 detector. The analog signals from the L0 silicon detectors are read out through lightweight cables to hybrids located outside the tracking region ($|z|$ >50cm). The material of the hybrids, chips and associated cooling are thus outside the tracking volume. A concern with these

Parameter	Specification
Active area dimensions	38.48 x 94.262 mm^2
Overall dimensions	40.55 x 96.392 mm^2
Strip pitch	$37.5\mu m$
Readout pitch	$75\mu m$
Number of strips	1024
Number of readout strips	512
Depletion Voltage	120 to 250 V
Biasing scheme	Poly resistor on one side
Poly resistor values	1.5 $\pm$ 0.5 MΩ ($<$ 10% variation within a sensor)
passivation	SiO_2 0.5-1 μm thick
Implant strip width	$9\mu m$
Implant depth	$> 1.2\mu m$
Doping of implant	$> 1x10^{18} ions/cm^3$
Width of Aluminum strip	$15\mu m$
Thickness of Aluminum strip	$> 1\mu m$
Resistivity of Aluminum strip	$< 30\Omega cm$
Coupling capacitor value	$> 12pF/cm$
Coupling capacitor breakdown voltage	$> 100V$
Total sensor current at $T = 20^\circ$ C and 500 V	$< 50nA/cm^2$
Interstrip resistance	$> 1\ G\Omega$
Total interstrip capacitance	$< 1.2pF/cm$
Bad channels	$< 1\%$ (No more than 5 per sensor)

Table 3.10: Sensors specifications for the outer axial layers

long cables is noise pickup and increase in the readout capacitance could potentially degrade the system performance. Studies with the L00 detector are in progress and the noise issues look tractable.

The cable design is essentially the same as that of L00. The pitch of the trace lines is 50 μm to match the readout pitch of the sensors. In order to reduce the inter-trace capacitance, the width of the cables expands by a factor of two for most of its length. Two overlapping cables are used for each sensor pair and they pass over the top of the silicon sensors.

The lightweight cables for Run IIa L00 were fabricated at CERN. The same CAD layout file has been transferred to a private company, KEYCOM Co.[9], to evaluate the production feasibility. KEYCOM has experience making similar lightweight cables for the Belle SVD. The cable base is 30 μm thick kapton where copper is evaporated and then plated to a thickness of 5 μm. Although we found some technical problems in the first products, the trace widths are not well controlled resulting in some breaks and bridges, optimization of the pattern and use of glass masks should solve these problems. Further R&D studies are underway, and experience with the current L00 cables will be taken into account as much as possible. In particular, the issue of noise pickup will be addressed.

Once quality cable production is established, visual inspection should be sufficient for quality assurance. The company will perform visual inspection on every cable. Small bridges could be repaired using a laser: passivation with enamel is foreseen to protect against discharges initiated from such irregular surfaces and to maintain quality for a longer term. The surfaces of the bonding pads are gold plated with nickel plating underneath. The thicknesses will be optimized through wirebonding tests. The electrical performance, such as inter-trace capacitance and trace resistivity will be tested on a sampling basis.

3.5 Data Acquisition

3.5.1 Introduction

The Run IIb silicon data acquisition will re-use most of the Run IIa system.

The complete DAQ system was designed for Run IIa
and is described in the Run IIa TDR [3].
Here we only describe new components needed for Run IIb.
The changes
from the Run IIa system are driven by changes in the
chip and the high radiation environment of Run IIb.
The SVX4 chip, as discussed in section 3.6,
with the new 0.25μm technology
will operate with 2.5V rather than
the 5V of the SVX3 chip.
This fact, combined with the new detector geometry,
requires the development of new hybrids (see
section 3.5.3).
In addition, studies by the
Run IIb working group [1] found
that the Digital to Optical
Interface Modules (DOIMS) on the SVXIIa portcards [10]
were not sufficiently radiation hard to survive the Run IIb luminosities.
These two items and their associated ramifications call for a new Port Card.
It is very difficult to obtain rad hard replacements for the DOIMs without
substantial effort and the associated schedule delay and cost. As a result,
we have chosen to use copper cables to carry the data from the portcards to
Fiber Transition Modules (FTMs). The associated modifications to the
FTMs are discussed
in section 3.5.7.
A block diagram of the new sections of the Run IIb DAQ system is shown
in Figure 3.17.
For Run IIb new portcards and junction cards are being designed.
Most components of the Run IIa portcard will be transferred
to a new junction card leaving only transceivers behind on the new mini-portcard (MPC). As shown in Figure 3.2, an MPC will be at the end of each stave and will be of minimal mass. The junction card, now called the junction portcard (JPC), will be moved outside the bore of the COT, to the face of the central calorimeter, where the COT repeater cards are mounted. The radiation dose in that region is small enough that off-the-shelf components can be used.

The active components on the new JPC's will require cooling. Sufficient cooling is available at their proposed location. The cooling required by the MPC is significantly reduced compared to the Run IIa portcards. It will be supplied by the lines which also cool the hybrids and the silicon sensors. The ISL portcards and junction cards will not be changed for Run IIb since ISL will still have SVX3 chips and they are located in a lower radiation environment than the SVXIIa portcards.

More information on the new MPC can be found in section 3.5.4. Section 3.5.5 describes the new JPC and section 3.5.6 discusses the cables which connect the MPC to the JPC and the JPC to the FTMs.

3.5.2 Readout times

The time available to read out the axial sensors is limited by the bandwidth of the trigger. The silicon vertex trigger (SVT) must produce a decision in less than 20 μsec on average for deadtimeless operation at a Level 1 accept rate of 50 kHz. The processing time of the trigger is about 10 μsec, leaving $\sim$10 μsec for readout and digitization of the $r-\phi$ data. The stereo data is read out after the $r-\phi$ producing an additional constraint on the total readout time for both. However, if many L1 triggers are rejected after 20 μsec, this will free up the L1 buffers making this constraint less important. Studies with Run IIa data have been used to estimate the allowed readout time for the Run IIb detector layout. The readout times for Run IIa ladders are added together such that they correspond sections that are roughly the same size as the proposed Run IIb staves. The studies are described in detail in reference [12]. They found that the coarser granularity of Run IIb design at low radius (particularly Layer 1) will not introduce significant deadtime in SVT.

3.5.3 Hybrids and Staves

This section describes the design of the SVXIIb readout hybrids and the stave electrical design. The design presented below assumes that each stave will contain one readout chain. Studies, with Run IIa data, of actual readout times and the execution time

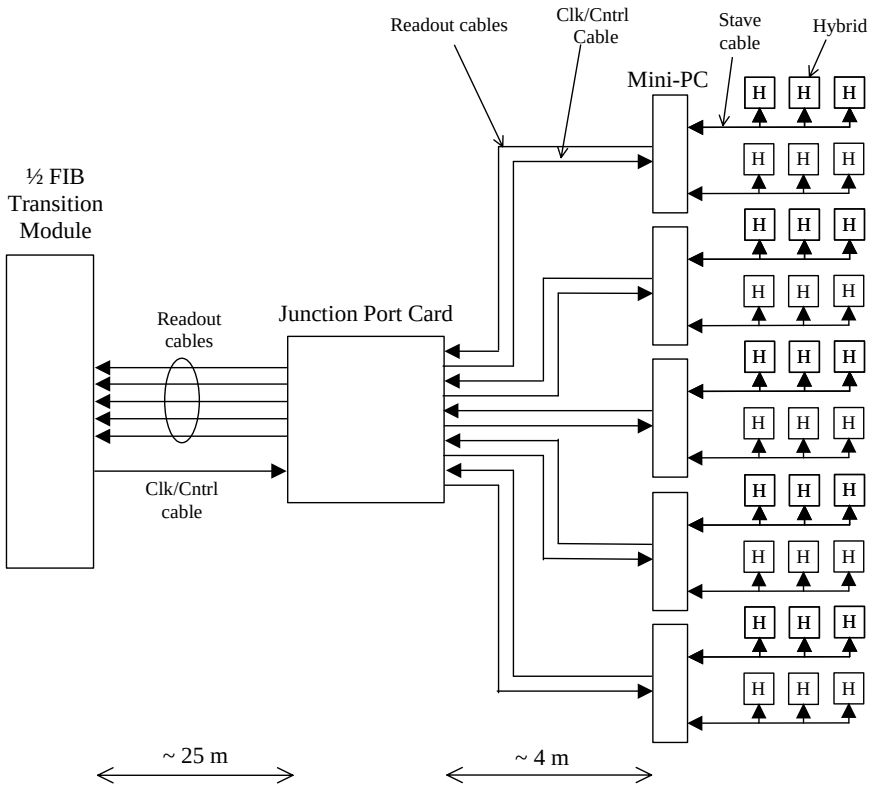

Figure 3.17: block Diagram of the new components of the Run IIb DAQ (from Hybrids to Copper FTM's)

of the SVT trigger indicate that one readout chain per stave is sufficient.

The hybrids are circuit boards which service the SVX4 front end chips. They provide an interconnect to cables from the MPC and hold additional passive components which are required for the proper operation of the SVX4 chips. Key issues connected to the hybrids are material, reliability, and fabrication. If the hybrids are in the tracking volume, as they are in SVXIIa, they add to the passive scattering and conversion burden. As interconnects to the DAQ they must be reliable. Typically, a fabrication constrained to provide reliable, fully tested and characterized hybrid assemblies has been a major portion of the labor during the construction phase of past silicon trackers.

The hybrid requirements and philosophy for SVXIIb are discussed in the Run IIb Working Group report [1]. A guiding principle was to utilize as much of the Run IIa experience with L00, SVXIIa and ISL as possible. For example, for the Run IIb hybrids we will exploit the new fine pitch thick film etched technologies which worked very successfully on L00. We will also minimize the number of distinct hybrid designs in order to simplify and expedite the construction phase. In order to limit rework, a premium is placed on reducing the number of chips on a hybrid while maintaining an efficient readout configuration. The hybrid concept and design for Run IIb have been strongly influenced by the factors discussed in the working group report report. In addition it has taken into account later experience with the installation and commissioning of the Run IIa system and constraints imposed by a practical detector layout which meets the tracking performance goals for Run IIb.

Layer 0, the beam pipe layer, is similar to the Run IIa L00 design. The hybrids will be placed outside the tracking volume and connect to single sided axial sensors via fine pitch cables. In the new design all the Layer 0 detectors and hybrids will be identical. The detectors will be 256 strips wide and the hybrid will contain two SVX4 chips. As in L00, the hybrid substrate material will be Alumina since it is placed outside the tracking volume and cooling is not a critical constraint. The performance and yield of the L00 doublet hybrid were excellent thus we expect a similar result for the new project. The new L0 hybrid will require a transceiver chip on each hybrid since insufficient space will exist for nearby mini Port Cards. Considerable experience exists with operation of the transceiver chip on the hybrid from the ISL project. The total number of hybrids required for the beam pipe layer is 72.

Layers 1-5 are double sided stave structures in which the hybrids are glued to the silicon, as described in section 3.2.2. Built into a stave is an electrical bus structure to provide signals and current to the SVX4 chips. The hybrids will be considerably smaller than previous SVXIIa and ISL designs due to the use of the fine pitch hybrid technology developed for L00. The hybrid substrate material will be BeO. There will be 6 hybrids per stave, 3 on each side. Layers 1-5 all use 4 chip hybrids on both the ϕ and the stereo sides. A total of 1080 4-chip hybrids will be needed. Unlike SVXIIa, the hybrids will not contain "finger" structures between the chips to provide local AC bypass and biasing resistors. This simplification is due again to the use of fine pitch technology. The basic design of a 4-chip hybrid is shown in Figure 3.18.

A material estimate for the stave design is discussed in Section 3.7.

As indicated above, the hybrids will be serviced by an electrical bus structure running below the detectors. The electrical bus is a copper-kapton flex cable which is laminated to the carbon fiber surfaces of the stave. The single sided silicon sensors are glued on top of the cable.

Small gaps, $\approx$3 mm wide, between detectors allow wire bonds to be placed between the bus and the hybrids. This wire bonded interconnect eliminates the need for a separate cable or connector field on each hybrid and further reduces the hybrid area. The bus uses a differential transmission line structure and is shown in Figure 3.19. The traces are arranged in an edge coupled differential configuration. Lines are 75 microns wide with a 100 micron space. Each pair is separated by a 150 micron gap. The singled ended lines which provide slow control to the SVX4 chips use the same structure but are not paired. Power and ground are provided on wide traces to avoid excessive voltage drops and go individually to each hybrid. The impedance of the bus is determined by the trace geometry and kapton thickness between the bus and the carbon fiber below and the Aluminum shield above. Calculations have placed this at 85 ohms.

Tests are in progress with SVX3D chips to study shielding and power distribution in order to avoid electrical pickup from the bus structure. A thin (12 micron) layer of Aluminum for the electrical shield

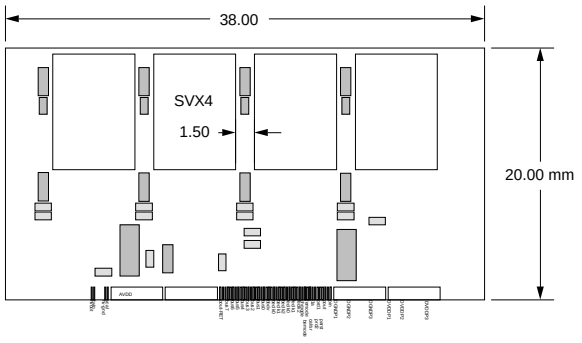

Figure 3.18: SVXIIb 4 chip hybrid used on Layers 1-5.

and a layer of Kapton to stand off the voltage on the back of the sensor has been shown to shield activity on the power and differential data lines. Some pickup can be seen due to activity on the slow control lines which are pulsed between operating modes of the SVX3 chip from 0 to 5V (CMOS) and this is still under study. The possibility also exists to run these lines differentially and install transceivers on the all the new hybrids. The situation can improve with additional shielding and with the lower voltage swings (0 to 2.5 V) in the SVX4 chip. A full understanding of these issues awaits the first full stave prototype with the new SVX4 chip.

The configuration and technology choices described above for hybrid and stave design and configuration are justified by the following considerations.

1. Material and temperature are most critical on the innermost layer. For this reason we chose to maintain the basic L00 design on the beam pipe layer with hybrids, and their heat load, outside the tracking volume.

2. Experience with the fine flex cables used on L00 for Run IIa was mixed. There are serious concerns about availability and cost for these parts in large quantities. In L00 these structures were found to be vulnerable to noise pickup although techniques for controlling this problem are largely known. Assembly of a complex structure using fine cables is awkward. For these reasons, a design which minimizes the use of fine line cables and applies them only where most appropriate was favored.

3. By placing hybrids on the silicon we can minimize dead space but this degrades the resolution in the covered regions. There is considerable power dissipation on the hybrids and this increases the cooling requirement on the silicon. For these reasons we restricted on-detector hybrids to the non-beam pipe layers.

4. The hybrids built for SVXIIa and ISL used a technology with a minimum 100 micron line and space width and 400 micron via pitch. For Run2a L00 we obtained a new technology which can accommodate 50 micron lines and spaces and 100 micron via pitch. With smaller vias and pitch we can reduce the area of the hybrid. In addition, the specific stave geometry allows us to combine trace and power/ground layers on the SVXIIb hybrids for Layers 1-5. This reduces the number of conductor layers from six to four. These space and material improvements mitigated concerns about mounting hybrids on the silicon for the non-beam pipe layers.

5. The manufacture and assembly/testing of the hybrids is a major construction burden. The SVXIIa, L00, and ISL had 13 distinct hybrid designs. For SVXIIb this has been reduced to 2 designs. We actually imposed a limit on the number of different hybrid designs on the layout configuration for the detector. This, in part, drove us to the particular stave based design adopted. With a reduced number of hybrid designs manufacturing is more efficient. Costs are reduced, particularly for the Layer 1-5 design.

For the hybrid and stave design to be viable the assembly and test process must be consistent with the schedule for Run IIb. We have considered this process and believe it can be organized to meet the required schedule. Below we elaborate on this plan.

1. The Layer 0 hybrid count is similar to L00 from Run IIa. This is a known process and went rapidly without any particular difficulty. The entire project is <100 hybrids including spares and yield. Transceiver yield on hybrids for Run IIa ISL was nearly 100%.

2. The stave layers consist of a single four chip design. All the hybrids can be produced in one or two lots from the thick film vendor. Typical manufacturing time is 8-12 weeks.

3. Figure 3.20 indicates the steps involved in assembling and testing the stave layer hybrids. All operations except the stave lamination and final stave assembly are duplications of the Run IIa assembly process. While some new mechanical fixturing will be required, all the electrical test and burn-in hardware and software from Run IIa can be re-used.

4. The stave layer hybrids are attached to the stave bus by wire bonds. In the past, the flex cable or connector attachment process was time consuming

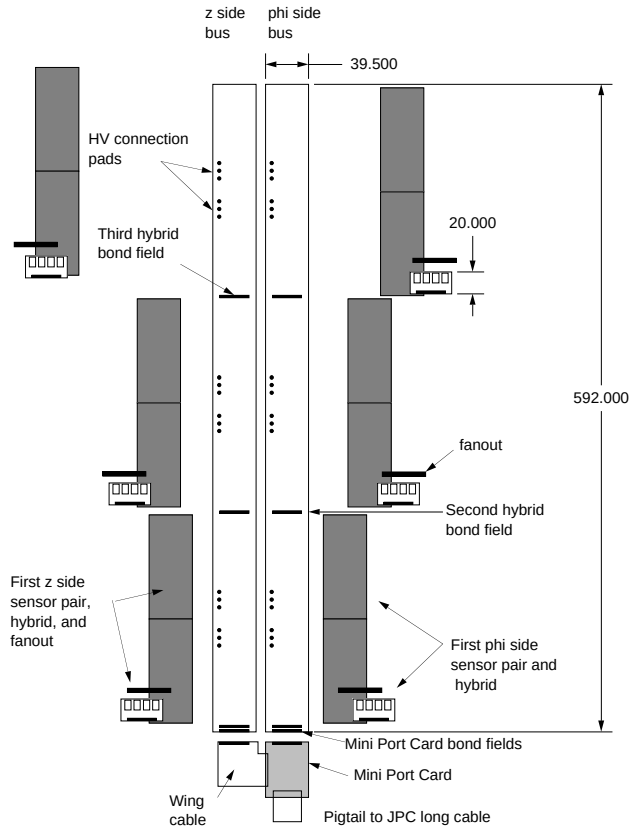

Figure 3.19: Stave bus stripline structure near the bonding region to a hybrid. Traces narrow for reasons of mechanical limitations and then widen between hybrids to maintain minimum voltage drop. HV lines are at extreme left.

and expensive. Elimination of this step represents a significant simplification.

5. Figure 3.20 indicates the rates needed from the component lines to produce one working stave per day during the construction cycle. Based upon Run IIa, this is reasonable and actually represents a lower production rate than that achieved in Run IIa.

3.5.4 Mini Port-card

The MPC will be mounted at the end of the stave and electrically connected to the end of the phi and z side stave buses with wire bonds. The MPC, as the hybrids, will be a fine pitch thick film circuit on a BeO substrate. All active circuitry will be on one side of the MPC. Each MPC will contain five transceiver chips, and by-passing and termination components. A pair of short external flex cables (pigtails) will connect the MPC to a longer cable set from the Junction Port Card. A wire bond pad field will enable connection to the phi side stave bus. An additional flex cable (the "wing") will be soldered to the MPC and will bend around to the back side of the stave. It will be glued to the Carbon Fiber core and will be bonded to the z side stave bus. Fabrication and assembly/test issues are similar to that of the hybrids. Approximately 200 MPC will be required to readout the Run IIb detector. Below we discuss the electrical design and expected performance of the MPC.

Figure 3.21 shows a block diagram of the MPC and its interconnection with the stave readout circuitry. Figure 3.22 shows the actual layout of the MPC components and bond/solder pads. The MPC main functions are to buffer the signals between the hybrids and the JPC and to connect common signals and power supplies to the ϕ and z side of the stave cable.

All communication between the MPC and the JPC use LVDS since the JPC's will be relatively far ($\approx$4 m) from the staves. The clock lines (front-end and back-end) are regenerated on the Mini-PC and sent to each hybrid using dedicated drivers and dedicated differential lines. The clock termination is mounted directly on the hybrids. The SVX4 single ended control signals (CHMODE, L1A, etc.) are transformed from differential to single ended on the MPC. Most are bussed to all hybrids in parallel but those with critical timing (L1A and PRD2) are driven individually to the phi and z sides of the stave. The data lines are shared between the two stave cables and terminated on the last hybrid of each stave bus. Bus 0:3 lines are bi-directional and the differential drivers regenerate the data in both directions, from the JPC to the hybrids and vice-versa.

An important aspect of the interconnection of the MPC with the stave flex cables is the proper termination of the differential signals to avoid reflection on the lines. We have performed simulations to understand the termination schemes. A particularly critical signal is the differential Odd Byte Data Valid (OBDV). If a glitch occurs here, the DAQ system may store incorrect information. Figure 3.23 shows the result of such simulation with OBDV terminated as shown in the block diagram. The plot shows the two differential signals (OBDV and OBDV*) arriving to the OBDV differential input gate. The hybrid

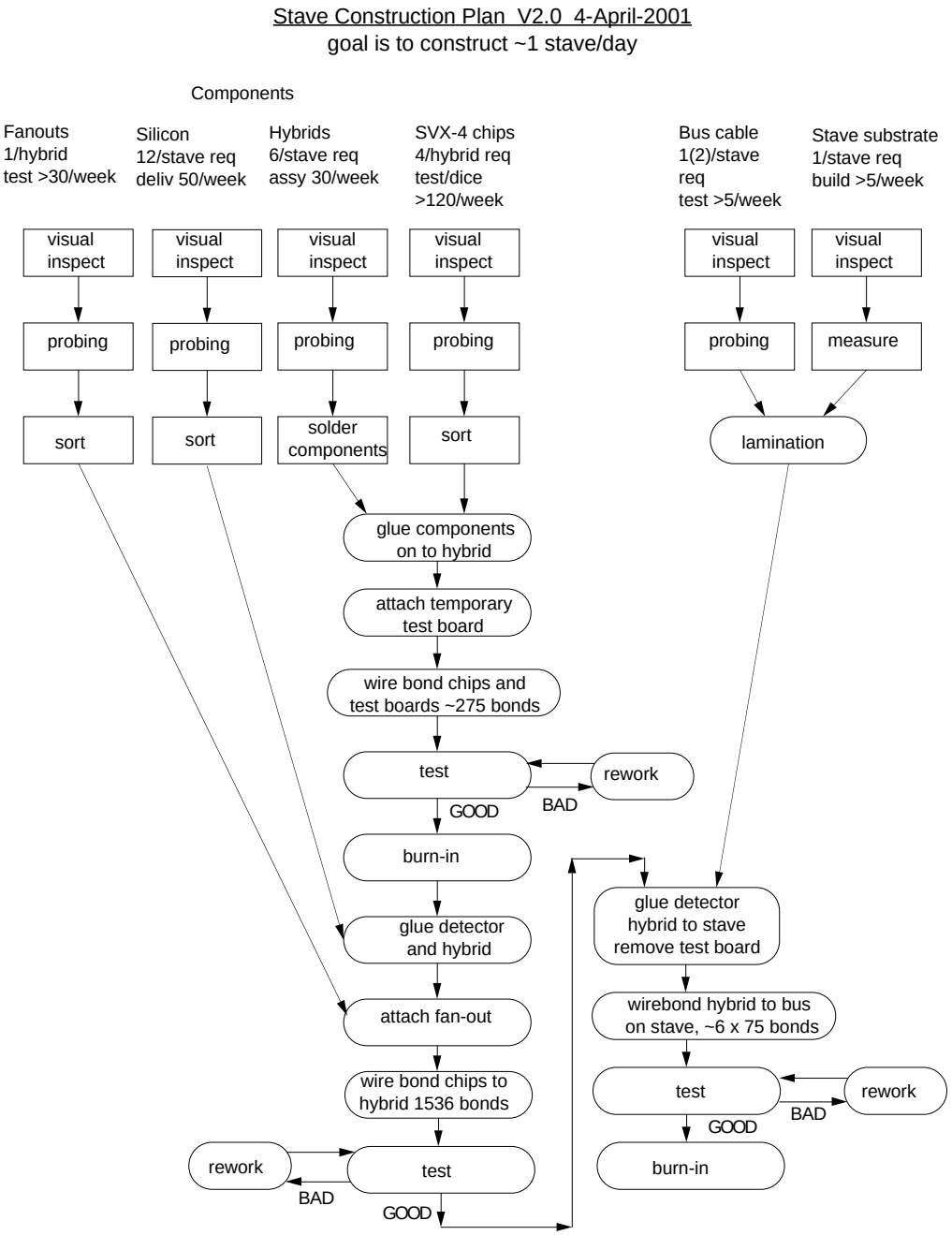

Figure 3.20: Construction and testing steps for stave hybrids

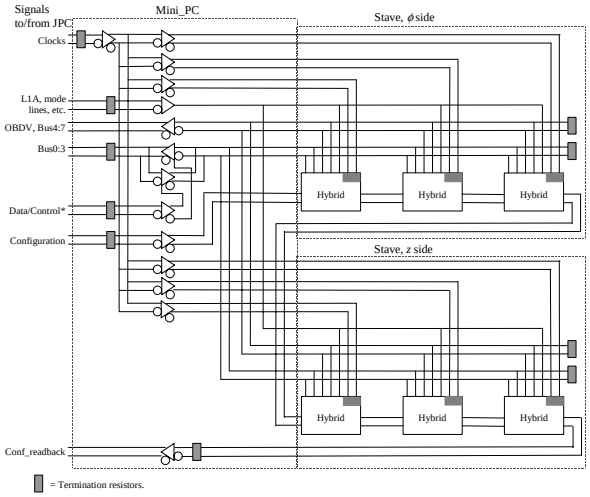

Figure 3.21: Block diagram of mini portcard and connections to hybrids on a stave

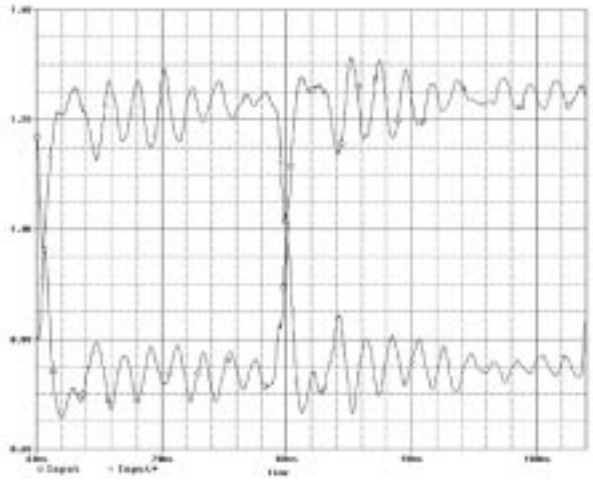

Figure 3.23: Differential Signals OBDV and OBDV*

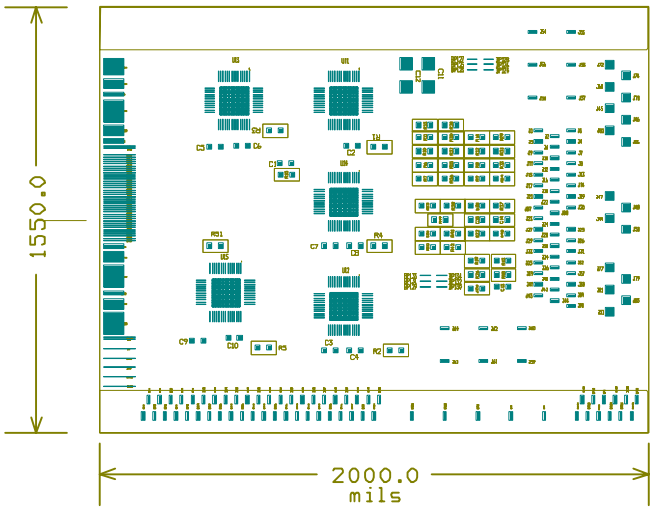

Figure 3.22: Layout of the MPC. Bond pads for the top stave bus cable are on the right. Solder pads for the wing cable are along the bottom. The solder pads on the left are for the external pigtail cables.

closer to the MPC is driving the OBDV. These simulations where done using Spice. The driver used was the Spice description model of the transceiver differential driver; the MPC, stave cables (top and bottom) and wing where simulated with a Spice lump transmission line; the wire bonds by 2 nH inductors and the chip inputs by 2 pF capacitors. Table 3.11 shows the characteristics of each transmission line of this chain. In the simulation, the stave busses on both the ϕ and z sides are 35 cm long. One can observe that, after the signals switch, there is voltage ringing but it is small enough to display a minimum differential voltage between OBDV and OBDV* of $\approx$350 mV, which insures that no glitch will happen. The ringing is produced by discontinuities on the transmission line caused by hybrids, wire bonds, capacitive load of the chips and impedance discontinuities from one type of transmission line to another (e.g., from stave cable to wing, etc.).

The MPC could use the Run IIa transceiver chips to generate the single ended 2.5V CMOS signals needed to control the SVX4 chips. Sufficient transceiver chips remain from the Run IIa project and are available to use in Run IIb. The transceiver chip was designed to operate with a 5.0V power supply. To use Run IIa chips, the non-inverting half of each differential output is converted by supplying 2.5V power to a dedicated driver current pin, and appropriately connecting ground or power to special pins that control the behavior of the differential out-

	Hybrid	Wing	Bus	MPC
Differential Z(Ω)	68	83	85	70
Substrate ε	7	3.9	3.9	7
Ground Plane				
Top (μm)	-	-	75	-
Bottom (μm)	80	100	75	120
Traces				
Length (cm)	2.5	5	35.5	5
Width (μm)	50	75	75	75
Separation (μm)	50	100	100	75
Thickness (μm)	10	18	18	10

Table 3.11: Elements and configuration of the data chain simulation.

Capacitive Load	Rise Time	Fall Time
82pF	15.5ns	16.2ns
220pF	36.2ns	42.5ns

Table 3.12: Timing of Single Ended Transceiver Output with Capacitive Load

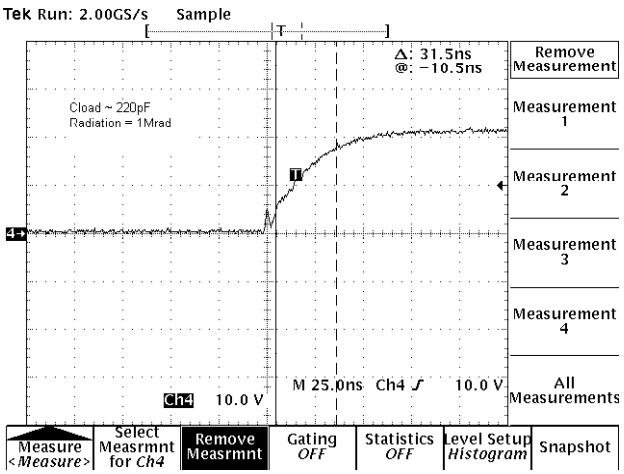

Figure 3.24: Risetime for 220pf load

puts.

Table 3.12 shows how the rise and fall times (10-90%) of the single ended transceiver output varies with different CL when configured to convert a 5.0V input to a 2.5V output. This timing was measured using a transceiver irradiated with 18 Mrad (Co60 source). The capacitive load of all six hybrids, top and bottom stave cable, MPC and wing cable is estimated in 200 pF. The achieved speed for 220 pF is fast enough for most SVX4 single ended inputs but those, as pointed before, with critical timing (L1A and PRD2) are driven individually to the ϕ and z sides of the stave to reduce the capacitance to one half (≈100 pF).

The radiation tolerance of the transceiver chips was studied by irradiating them upto a dose of 18 Mrad (Co60 source). Little degradation was seen in the signal quality for chips operated with 2.5 V output level, set to be compatible with the SVX4 chip. A second and more favorable possibility for the MPC is to use a new transceiver chip which can be designed on the same 0.25um technology of the SVX4 chip. The major advantages will be lower power dissipation and mostly the fact that a special 5V line for the transceiver chips would not be necessary. The latter results in a major savings in terms of power supplies channels and cables. At the time of writing a new transceiver chip has already been designed and submitted to MOSIS for verification with the plan of inserting it in the second svx4 chip submission. The transceiver chip occupies so little real estate in the silicon wafer that can be accomodated in the empty space left over by the svx4 chip reticule. Figures 3.24 and 3.25 show the results for 1 and 18 Mrad with 220 pF capacitive load. These studies are detailed in reference [11].

3.5.5 Junction Port Cards (JPC)

The JPC will encompass the remaining functions of the Run IIa PC and Junction Card. On the JPC the read out data will be resynchronized to reduce the skew between different data lines and increase the data reliability. Voltage regulators will be needed for each readout chain and will produce some heat load. Each JPC will have 2 voltage regulators serving each MPC since voltages on both analog and digital power supplies will need control. Each JPC will connect to 5 MPC's, since there is one readout chain per MPC. As described in the introduction, the JPC will be located outside the tracking area, on the face of the central calorimeter. This is a low radiation area, with ample cooling and space available. As a result, the JPCs can use standard printed circuit board technology and off-the-shelf components in standard packages.

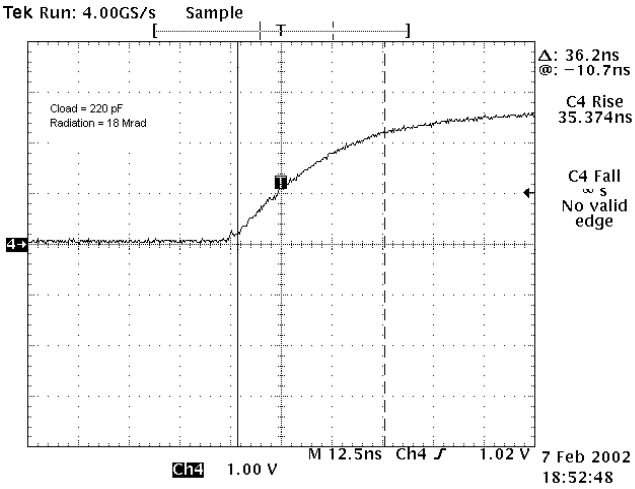

Figure 3.25: Risetime for 220 pF load and 18 Mrad dose.

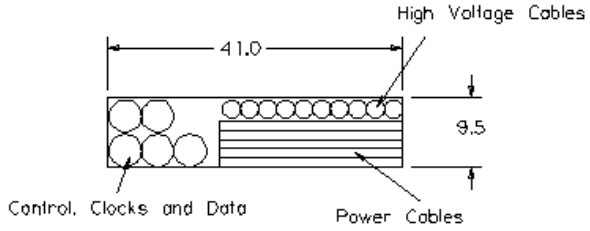

Figure 3.26: Cables from 5 staves fit easily into one of the COT slots.

3.5.6 Cables

The MPC will be have two small low mass flex pigtails ≈12 cm long soldered to it. The pigtails will connect to low mass standard cables which traverse ≈ 70 cm the end of the ISL extension cylinder (the current location of the RunIIa junction cards). At this location, connections will be made to the ≈ 4m long cables which carry the data and control signals through the cable slots to the new JPCs on the COT repeater card ring. These cables will be a custom designed copper shielded cable with ≈24 pairs of 34 AWG wires and total diameter of ≈4.5 mm. Power and high voltage will use cables similar to the cables already employed in SVXIIa. In the Run IIa each port card corresponds to five readout chains, and the cables from each portcard occupy one slot. For Run IIb, each stave is a readout chain. Figure 3.26 shows the cables from 5 staves fit easily into one slot and thus the Run IIb detector will occupy the same number of slots as in Run IIa.

¿From the JPCs the cables go to the DAQ racks and power supplies which are mounted on the walls of the collision hall. These cables are similar to the cables used in SVXIIa and are commercially available.

3.5.7 FTM's and associated modules

The use of copper data cables instead of fibers from the MPC on out, necessitates a redesign of the Fiber Transition Module (FTM). We have performed several bit error rate tests with the appropriate LVDS drivers and receivers over 30 m of copper cables to test the reliability of such transmission. For example, LVDS drivers transmitting data at 53 MWords/sec over 30 m of copper ribbon cable have shown an acceptable bit error rate of better than $4.3\text{x}10^{-16}$. This translates to one error every 3.8 hours if all SVXIIa ladders were transmitting data 100% of the time.

3.5.8 Power Supplies

The Run IIb power supply system will use the present infrastructure as much as possible to minimize costs and installation and testing time. In particular we will use the same scheme for interfacing the new power supplies with the CDF High Voltage control system (via the CAENET to VME interface board V288) allowing for the overall software infrastructure to remain the same (except for the low level specific CAEN instructions). Power supply modules will necessarily be different from the Run IIa supplies for several reasons:

1. the SVX4 chips works with 2.5 V (not 5V);
2. all special voltages related to the optical transmission lines have been dropped;
3. the organization of the power distribution is based on *staves* and not on *wedges*;
4. it is desirable to use commercially available products rather than custom made ones.

Low voltage power should be provided separately to the analog section of the chip (AVDD), the digital section of the chip (DVDD), the MPC (transceiver chips), and the JPC. High Voltage will have a single

Run2b	Volt	I_{max}(A)	SVXIIa	Volt	I_{max}(A)
DVDD	2.5	0.15/chip	DVDD	5.0	0.15/chip
AVDD	2.5	0.25/chip	AVDD	5.0	0.15/chip
TRX	5	1.0/MPC	+5VDOIM	5.0	2.8/PC
JPC	5	4.0/JPC	+2VDOIM	2.5	-1.7/PC
			DTERM	3.5	±0.15/PC
Vbias	600	0.01/half stave	Vbias	±250	0.005/Layer

Table 3.13: Power need for the present silicon system as compared to the SVXII. Currents are estimated using the minimal approach from Table 3.14.

polarity (positive) since we only have single sided detectors. Table 3.13 shows the different low and high voltage channels needed for the Run IIb silicon detector as compared to SVXIIa.

Power channels are grouped into power super-channels in order to provide power to a detector subsystem (for the SVXIIa super-channel would correspond to a ladder). A further combination of channels and super-channels capable of providing power to the part of the detector controlled by a single JPC (such a grouping for SVXIIa controls a wedge) is quite cumbersome to implement for this design (one JPC services 5 readout chains and we have 1 readout chain/stave). We are instead considering a scheme where JPCs are treated as separate channels and the natural grouping is implemented in software rather then in a physical module. Using this scheme we can count the number of channels and super-channels needed to power the system. Table 3.14 shows the counting in the model that a super-channel provides power to a single stave and consists of a single AVDD, DVDD, MPC and two Vbias (one for the axial and one for the stereo silicon detectors). As mentioned earlier in the section regarding the MPC, with the use of a new transceiver we can avoid providing the extra 5V line necessary to power the old transceivers in the MPC. The new transceiver will instead be powered by the DVDD line of the stave.

Table 3.15 compares the Run IIb approach of Table 3.14 with the present SVXIIa+ L00.

3.5.9 Failure Mode Analysis

The stave unit is highly integrated. This results in a significant reduction in mass, size, and readout and assembly complexity. The cost is increased vulnerability to single point failures. On each side of the stave there are three hybrids. All six share the output bus. In principle a failure on one can bring the entire stave down. This possibility is made significantly remote by various design and assembly features.

We currently are planning to use a special chip on each hybrid called the Priority Bypass Chip (PBC). This chip, when activated, causes the Priority and Initialization bits to bypass the hybrid. The chip is wired to both AV and DV. If DV is removed the chip is activated. Power is supplied individually to each hybrid on a stave. Thus we can activate this chip on a single hybrid if needed. The PBC would be used in a case where Priority became stuck in that particular hybrid. It would also be used in a case where a hybrid or chip took control of the data bus but would release it if DV was removed.

Failure modes effecting the consumption of analog current are potentially serious since AV cannot be turned off with DV on, and if both are off the PBC won't work. In this case we lose that hybrid and all after it on the stave. Failure modes effecting the consumption of digital current should be isolated to one hybrid if the PBC is used to bypass it. Failures of a single wirebond on a data or control line can result in either a loss of data from a single chip or the entire hybrid. In some cases the chip or hybrid could be left stuck in a state which compromises the function of the bus. In this case the PBC could be used to recover the rest of the stave. If we needed to bypass priority and the PBC failed then we could lose the stave after the offending position. If the PBC failed in such a way that it shunted Priority against our desire, then we would lose the hybrid.

On power and ground pads from the stave bus to the hybrid, multiple wire bonds will be used to reduce the danger of bond failure. On the data and control lines, the bond pads are narrow and multiple bonds may not be possible. This will however be explored with the stave prototyping program. Whenever pos-

Layer	R/O Chains	JPC	LV	HV
5	60	12	192	120
4	48	10	154	96
3	36	8	116	72
2	24	6	78	48
1	12	4	48	24
0	72	16	232	72
TOTAL (both sides)	252	56	820	432

Table 3.14: Number of R/O chains, JPCs and separate Low and High voltage channels needed. Note that the R/O chains are split evenly between the East and West sides of the detector and there are at most 5 R/O chains per JPC on each side. L0 has one R/O chain/module. For layers 1-5 the number of LV channels assumes 3/stave(AVDD, DVDD and MPC) + 1/JPC. Two HV channels per stave are assumed. For Layer 0 for LV we assume 3/module (AVDD, DVDD and one for the transceiver) + 1/JPC, and for HV we assume 1/module.

Layer	R/O Chains run2b	R/O Chains svx2+l00	LV run2b	HV run2b	LV svx2+l00	HV svx2+l00
5	60	72	192	120	144	72
4	48	72	154	96	144	72
3	36	72	116	72	144	72
2	24	72	78	48	144	72
1	12	72	48	24	144	72
0	72	48	232	72	96	60
Port Card					216	
TOTAL	252	408	820	432	1032	420

Table 3.15: Number of separate Low and High voltage channels for Run IIb as compared to SVXIIa + L00

sible, chip to hybrid bonds will be doubled up as well. Bonds from the mini-PC to the bus are critical since a loss there could compromise the entire stave.

Problems with the PBC or excessive AV current could be mitigated if the the PBC was served by a dedicated power line common to all hybrids. This will be explored in the prototyping program. Bonds to the stave and from chip to hybrid will be encapsulated with room temperature cure Sylgard 186. This material has been used extensively in the Layer00 project with excellent results. All component connections on the hybrid will use solder rather than conducting epoxy to avoid the possibility of cracks in the bond.

3.5.10 Summary

A design for the readout of the Run IIb detector has been presented. The various components have been detailed and are fairly straight forward. This system moves material further out of the tracking volume and makes maximal use of SVXIIa components and experience. The DAQ will be the same from the FTM's on up the readout chain. Although Run IIb has more channels, abandoning the wedge design has allowed us to optimize the readout chain distribution and thus the total number of DAQ chains will be smaller than in Run IIa.

3.6 SVX4 Chip

The silicon signals will be integrated, digitized, and read-out locally by a custom integrated circuit (chip) designated SVX4. The SVX4 chip is a functional replacement of the SVX3 chip used in the Run IIa silicon detectors with some important differences.

1. A lower noise and faster rise-time amplifier, which allows for larger detector capacitances.

2. Lower operating voltage (2.5V instead of 5V).

3. Enhanced radiation tolerance.

The SVX4 development work began in 2000 after it was realized that the SVX3 chip had several limitations that made it a poor candidate for instrumenting a Run IIb upgrade, and that such an upgrade would only be possible if a viable readout chip was available. The main disadvantages of the SVX3 readout chip are as follows:

1. Radiation tolerance is not adequate for Run IIb inner layers, and noise increases significantly with radiation for outer layers.

2. Amplifier noise and rise-time are unfavorable for large detector capacitance values.

3. Manufacturer (Honeywell) increased production costs to a prohibitive level.

4. Severe yield problems were encountered during Run IIa construction that were not well understood and could not be prevented for a future run.

The SVX4 chip design is complete and an engineering run submission is in progress. Full prototypes will be available in summer 2002. The design is the work of a collaboration of engineers from LBNL, Fermilab, and the University of Padova. The design targeted the 0.25μm feature size bulk CMOS process of the Taiwan Semiconductor Manufacturing Company (TSMC). This is a commercial process that is not advertised as radiation hard, but the thin gate oxide used in deep sub-micron processes is inherently "immune" to radiation damage, and by using special layout techniques developed by the RD-49 collaboration for LHC experiments, can yield devices with very high radiation tolerance. However, while the SVX4 chip is functionally a replacement for SVX3, many sub-circuits required significant redesign to adapt to the new technology. The amount of design work that has been done runs the full spectrum from the ADC, where the schematics are identical in SVX3 and SVX4, to the data memory ("FIFO"), where a completely new circuit with a radically different architecture has been implemented for SVX4. In the latter case the deep sub-micron technology is so much faster than the technology used for SVX3 that the FIFO could be built out of standard circuit elements (available as a library developed by RD-49) and a layout automatically generated using commercial software. This is in contrast to SVX3 where the FIFO was fully custom made and used innovative circuit ideas and dynamic logic to be able to perform at the required speed. Because the SVX4 chip required significant redesign, a list of specifications was produced early on to provide a frame for the engineers to work in. This list was generated jointly by CDF and D0, as D0 intends to also use the SVX4 chip in their Run IIb upgrade. The SVX4 design specifications are reproduced in Tables 3.16, 3.17, 3.18, and 3.19.

A.	General:	
1.	Input bonding pad pitch:	48μm
2.	Overall Width:	6.250mm active area. Dicing streets as close as allowed by design rules.
3.	Overall length:	$<$ 11.925mm
4.	Supply voltages:	2.25-2.75V analog, 2.25-2.75V digital.
5.	Versions:	A version is the basic "conservative" version. B version adds on-chip bypassing and front to back combined power routing.
6.	Bond pad layout:	Both version have same bond pad layout with some pads used only by CDF and others used only by D0.
7.	Bond pads:	Except Front End inputs, no wirebond pad is to be smaller than 150 $\times$ 150μm (cover layer opening). Probe pads not meant for wirebonding are exempt.
8.	Maximum Supply Voltage:	3.5V
B.	Preamp:	
1.	Input pulse polarity:	Positive.
2.	Gain (feedback capacitor):	3mV/fC.
3.	Gain uniformity (ch-to-ch):	5% or better.
4.	External load capacitance:	10pF to 50pF.
5.	Risetime 0-90%:	adjustable in a range that includes 60-100ns for any allowed load.
6.	Risetime adjustment:	4 bits minimum.
7.	Noise (ENC):	2000e^- or less for a 40pF load using double correlated sampling with 100ns integration.
8.	DC open loop gain:	$>$2500 ($>$95% charge collection from 40pF).
9.	Linearity:	Linear response for pulses up to 20fC, non-linearity $<$0.25mV at output.
10.	Dynamic range:	$>$200fC.
11.	Reset + settling time:	$<$ 1μs for any initial condition.
12.	Reset offset voltage:	Internally set to a value TBD by designers, with external override capability.
13.	Input protection diodes:	2μA DC capability to either rail. Current must not go to substrate.
14.	Calibration injection:	40fF internal cap switched to input.
15.	Calibration charge control:	1 external analog reference voltage (other voltage is AVDD, not ground).
16.	Input disable switch:	2 Config. Register bits. N.1 disables control of reset switch for channel with calibration mask bit set. N.2 determines whether reset switch is always closed or always open for disabled channels.
17.	Input Device Current:	Adjustable with configuration bits as in SVX3 but with wider range (factor of 2).
18.	Bypass capacitors:	Performance in SVX-II mode to be maintained with no external bypass capacitors closer than 10mm.

Table 3.16: SVX4 Chip specifications part 1 of 4.

C.	Pipeline:	
1.	Input Pulse polarity:	Negative.
2.	Voltage gain:	3 to 5 (in that range, fixed).
3.	Gain uniformity:	5% channel to channel.
4.	Risetime, 0-90%:	10ns to 40ns (in that range, fixed).
5.	Noise (ENC at preamp input)	$< 500e^-$.
6.	Linearity:	linear response up to 20fC at preamp input.
7.	Dynamic Range:	To Be Confirmed: >40fC at preamp input.
8.	Reset Time:	<20ns for any allowed initial condition.
9.	Pedestal uniformity:	$< 500e^-$ at preamp input channel to channel, $< 1000e^-$ at preamp input cell to cell.
10.	Bias:	Internally set with override bonding pad.
D.	ADC:	
1.	Type:	Wilkinson with real time pedestal subtraction.
2.	Voltage Ramp:	Rate adjustable with external resistor.
3.	Ramp rate "trim" bits:	3 Bits, adding binary weighted capacitors to op-amp feedback. Largest capacitor is 4x the fixed feedback capacitor. These capacitors provide a range adjustment- no fine adjustment.
4.	Ramp Linearity:	0.25% for rates between 0.1 and 1 V/μs.
5.	Ramp dynamic range:	1V.
6.	Ramp pedestal:	Same as in SVX3.
7.	Counter:	8-bit Gray code, 106MHz rate.
8.	Differential nonlinearity:	<0.5 LSB.
9.	Bias:	Internally set with override bonding pad.
E.	Data output drivers:	
1.	Type:	Complementary with "resistor current sources".
2.	Current source range:	2.5mA to 17.5mA in 2.5mA steps (3 bit adjust).
3.	Rise and fall times:	>2ns and <4ns with nominal load.
4.	Common mode:	VDD/2 nominal with T termination.
5:	Load capability:	70Ω and 20pF.
7.	Tri-state:	Outputs tristated in initialize (except if SR copy pad is bonded- see H7) and digitize modes.
8.	Single ended use:	No additional requirements.
9.	Bidirectional:	All Bus pads will be bidirectional. Only some will be used of input as well as output by CDF, but all of them will be I/O for D0.
10.	Output data skew:	>3ns between OBDV and any bus line and between any two bus lines.

Table 3.17: SVX4 Chip specifications part 2 of 4.

F.	TN-BN Pins:	
1.	Functions	The multiplexed functions of the SVX3 TN/BN pads will be separated in SVX4 to TN/BN Priority in/out dedicated sets of pads.
2.	Type, BN/TN:	"Open collector" I/O with internal pull-up.
3.	Type, Priority in:	Differential receiver (2 bond pads) same as clock receivers, with added hig Z common mode reference voltage (center tap of large R between VDD ar
4.	Type, Priority out:	Differential driver (2 bond pads) same as data bus outputs.
5.	BN/TN Internal pull-up:	$> 500\Omega$.
6.	BN/TN Pull-down current:	>10mA.
7.	BN/TN Modes:	only active in digitize mode.
8.	Priority in/out Modes:	Configuration register input/output during initialize mode. Priority passing during readout mode. Priority out high during digitize mode.
9.	Bonding pads:	This increases the number of bonding pads per chip by 4 (2 next to TN and 2 next to BN).
G.	Configuration Register:	
1.	Type:	Bit serial shift register.
2.	Cell type:	SEU tolerant shadow register.
3.	Shadow register:	Keep as in SVX3 for SEU tolerance.
4.	Clock:	Register advanced with FE clock in initialize mode.
5.	Length:	As needed.
6.	Preset:	no preset.
7.	layout rule:	Do not place configuration register cells within 75μm of a wirebond pad (they can be destroyed by missed wirebonds).
8.	Bit order:	LSB loads first on all fields.
9.	Bit Assignment:	Numbers are for illustration. Designers may add bias adjust or other system bits as needed:
	0-127:	Calibration Mask
	28:	Cal-inject signal polarity
	29:	Input disable
	30:	Disable mode (reset always on or off)
	140-144:	Bandwidth bits (left room for 5)
	145-147:	Input transistor current
	148-153:	Pipeline depth
	154:	Pipeline readout order
	155-161:	Chip ID
	162:	Real time pedestal subtraction Enable
	163:	Last channel latch
	164:	Channel 63 latch
	165:	Read all
	166:	Read Neighbors
	167-170:	Ramp pedestal
	171:	Ramp direction
	172:	Comparator polarity
	173-175:	Ramp range selection
	176-183:	Sparsification threshold
	184-191:	Counter Modulo
	192:	First chip flag (see H.9)
	193:	Last chip flag (see H.9)
	192-194:	Output driver resistor select

Table 3.18: SVX4 Chip specifications part 3 of 4.

H.	Control Functions:	(*) Denotes desirable features but not strictly required.
1.	Signal Functions:	All control signals same function as SVX3 except as noted here.
2.	Ramp and Counter Reset:	Remove Counter Reset as an independent signal. In normal mode Counter Reset is to be tied to Ramp Reset. In Dynamic Pedestal Subtraction mode Counter Reset is internally generated as in SVX3.
3.	Preamp Reset & Fe Clock:	Preamp Reset should always function independently of FE Clock state. (In SVX3 Preamp Reset can only go high while FE Clock is high).
4.	Last channel SR bit:	on=always latch chan. 127 (same "last chip flag" in SVX3).
5.	Chan. 63 latch SR bit:(*)	on=always latch chan. 63 (doubles read out speed).
6.	extra L1A:	Additional L1A pulses (beyond 4) should be ignored by the pipeline logic.
7.	OBDV (data valid) control (*):	OBDV must be driven by 1 chip per daisy chain at all times to prevent data transmission errors. This can be accomplished in SVX4 with 2 configuration register bits: First Chip (FC) and Last Chip (Different from item 5). OBDV control is given by this logic table

Pri. In	Pri. Out	FC	LC	OBDV
H	H	L	L	disabled
H	L	L	L	disabled
L	H	L	L	ENABLED
L	L	L	L	disabled*
X	H	H	L	ENABLED
X	L	H	L	disabled*
H	X	L	H	disabled
L	X	L	H	ENABLED

		* OBDV is to be disabled one BE CLOCK cycle after Pri. Out is lowered (same as in SVX3). [In the present CDF silicon system it was necessary to add logic to the port cards to implement this function, because the SVX3 does not have the FC and LC bits.]
8.	D0 Mode pad:	A special bond pad, if bonded will set the chip in D0 mode. This will multiplex I/O signals onto all Buslines and gate off the Pipeline Clock during digitize and readout operations.
9.	Test outputs:	Buffered preamp and pipeline outputs for one channel, Comparator output for 1 channel, Ramp probe point, RTPS comparator buffered input and output- all as in SVX3. Additional probe points as needed to fully test performance.

Table 3.19: SVX4 Chip specifications part 4 of 4.

¿From an operational standpoint the most significant impact of the move to deep sub-micron technology is the lower operating voltage, 2.5V instead of 5V. In order to use the SVX4 chip in a system that was designed for 5V electronics it will be necessary to shift logic levels of many signals. Fortunately the radiation tolerant "Transceiver Chip" that was developed for the present detector can be used as a level shifter although it was not designed as such. A less obvious consequence of the lower voltage is that the tolerance for voltage drops in power supply lines is greatly reduced, which has implications for power distribution and voltage regulation. Finally, the maximum achievable dynamic range of the front end amplifier is necessarily lower than in a 5V process, but this is not an issue because there is significant headroom in this parameter. As previously mentioned, significant design work was involved in generating the SVX4 chip even though it is roughly a functional replacement for SVX3. This is because the deep sub-micron process is sufficiently different from the process used for SVX3 that simply copying over the SVX3 schematics does not work in general (although it does work very well for some circuit elements). In particular, the lower voltage has implications for many circuits, but also the special design rules needed for radiation tolerance have an appreciable impact. A significant amount of simulation and design verification was performed by the engineering team. No features were left out of the engineering submission, in hope that it may work as final prototype. The schedule does however allow for one additional iteration of the design. Confidence in the viability of the first engineering submission is supported by by two main factors. Nevertheless, (1) The basic architecture of the SVX4 chip is copied from SVX3 and the desired relation between inputs and outputs is exactly known. (2) Because a standard commercial process is being used, the accuracy of simulation tools is vastly superior to what was available during SVX3 development. Even for detailed characteristics of analog circuits, measurements and simulation are seen to agree at the 5% level. This has been verified with a brief test chip program. Two sub-circuit test chips have been fabricated as part of the SVX4 development. A preamp only chip was received from the MOSIS prototyping service in February 2001, and a preamp plus pipeline and logic controller chip was received in July 2001. The former was submitted at a very early stage of the design work, and was used throughout the design process to verify simulation results and later on to check the radiation tolerance of the process. This chip was irradiated in a Co^{60} source up to a total does of 40 MRad. No measurable difference was seen in the performance (noise, risetime, etc.). Transistor thresholds did shift measurably in good agreement with prior data from the RD-49 collaboration (even though they are from a different deep sub-micron manufacturer). The second test chip has also been irradiated up to 16 MRad and no performance degradation was seen at the 5% level. Bench measurements of this chip demonstrate that all front end circuits are fully functional and meet design requirements. The noise at the pipeline output using double correlated sampling is 30% less than for SVX3D, which meets the design specification. Beyond that, this second test chip was very useful in understanding some process parameters. Through this chip it was discovered that the foundry would default to a high resistivity substrate due to certain design elements in the SVX4 chip unless specifically instructed not to (the intent for SVX4 is to use a low resistivity substrate with an epitaxial layer just as was done for SVX3). A deficiency in the design rule verification that relates to the yield of precision capacitors offered in this technology was uncovered and corrected.

Presently submission of the chip is expected March 25th and wafers should be in hand for testing by late May. Figure 3.27 shows the footprint of the SVX4 chip (internal bonding pads are not shown). The engineering run will contain two versions of the SVX4 chip: SVX4A and SVX4B. The main difference between them will be the power distribution. In SVX4B new concepts will be tested using on chip capacitance to combine power supplies, thereby reducing the number of external connections and components required. Details of power distribution mainly affect performance in dead-timeless operation, which is a system issue difficult to understand with simulations. The features explored with SVX4B go beyond simply building an SVX3 replacement and were originally introduced to address requirements of the D0 collaboration, which will not operate the chip in dead-timeless mode but may have tighter constraints that CDF on available space for components and external connections. Which chip version is more suitable for CDF (A or B) will be determined from bench tests of the engineering prototypes. If it turns out that both CDF and D0 can use the same chip ver-

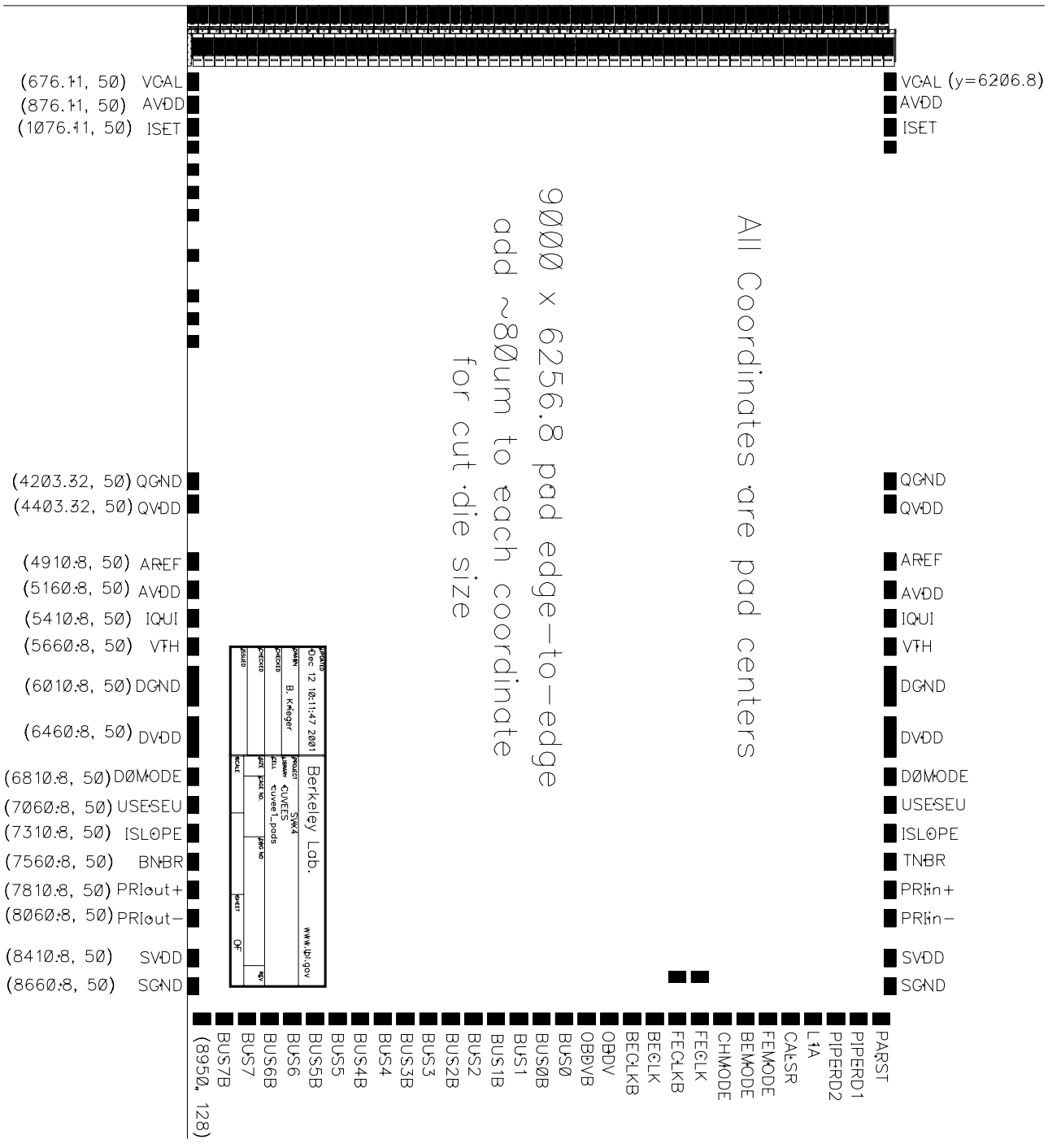

Figure 3.27: SVX4 chip pad frame specifications.

sion, a joint production run of SVX4 would be possible. This would save some fabrication costs, but more importantly would reduce the total production testing effort.

3.7 Material

An important design goal of the Run IIb detectors was minimization of material in the tracking volume. This is particularly important in the innermost layers where multiple scattering degrades impact parameter resolution. Material at larger radii can also degrade pattern recognition performance, generate secondaries, and reduce electron identification efficiency.

The material for the Run IIb detector is estimated based on the layout presented in section 3.2. Figure 3.28 shows a schematic model of the materials in a stave. The dimensions are not to scale. The total material in a stave, averaged over the stave area, is $\sim 1.8\%X_0$.

In Run IIa, the SVXII readout hybrids are mounted in the active volume to minimize acceptance loss due to gaps, and the portcards are mounted in the tracking volume to minimize the distance between the readout hybrids and portcards. The data from the SVX3D chips are converted to optical signals on the portcard. While the fibers carrying those signals out of the detector volume are low mass as expected, their power consumption is substantial so that their cooling and power cables introduce substantial mass.

For the innermost layer, minimizing material was critical, so kapton signal cables are used to locate the readout hybrids out of the tracking region. This was also required by space constraints in Run IIa. Furthermore, L00 used long kapton bus cables to carry the data from the readout hybrids to portcards which were placed at large radius and large $|z|$, outside the tracking region.

The use of single-sided silicon sensors in Run IIb doubles the contribution of silicon to the material budget since a separate sensor is used for the axial and stereo measurements. But, as can be seen in Figure 3.29, silicon accounts for only a small fraction of the material budget in the Run IIa design. There are several ways in which the Run IIb design attempts to minimize material. The innermost layer uses kapton signal cables, like Layer-00, to keep the readout electronics out of the tracking volume. This keeps the material low for the critical inner layer. The use of a universal stave for the outer layers introduces new material from the carbon fiber support structure, the direct silicon cooling which is needed for radiation hardness, and the bus cable. But, the bus cable allows the removal of the portcard and power cable material since the mini-portcard will now be mounted at the end of the staves. The use of an LVDS copper data bus instead of optical readout does not increase the material budget because the lower power and cooling requirements more than compensate for the thin copper traces in the data bus. Finally, the new readout hybrids are smaller and lower mass than in Run IIa because of the compactness of the stave design and use of new printing technologies.

The material seen by a track is dependent on z (e.g., when a track goes through a hybrid region it sees more mass than when it misses the hybrids.) Figure 3.29 shows a comparison of the Run IIa and Run IIb design for 90^o tracks as a function of z. One can see that the material budget in the Run IIa design is large. The dominant material effects arise from readout hybrids, portcards, and power cables. In Figure 3.29 for z< 1cm the Run IIa material is only silicon. From 1-3cm it is Si and portcard cables. From 3-10cm RunIIa has silicon, portcard cables and portcards; from 10-20cm it is silicon, hybrids, portcards, and portcard cables. At larger z the pattern of silicon, hybrids and portcards repeats and the portcard cables pile up. The contribution in the Run IIa design from power cables is $\sim 4\%X_0$ from $3 < |z| < 28$ cm. It rises to $\sim 8\%X_0$ beyond that. The contributions from the readout hybrids ($\sim$ 13%) can be seen for $10 < |z| < 20$ cm and $40 < |z| < 45$ cm.

The expected material contributions in the Run IIb design shown in Figure 3.29 are: $\sim 6\%X_0$ for $|z| <$ 16 cm from silicon, carbon fiber support structure, and cooling; $\sim 18\%X_0$ due to the addition of readout hybrids in the regions at 16, 34, and 54 cm; and $\sim 7\%X_0$ for the remaining regions due to the bus cable beginning at the location of the first hybrid.

3.8 Descoping

The Lab has asked us to present descoping options as part of the technical design of the Run IIb silicon detectors. There are a number of choices that should be made during the project once it is clear how the schedules are proceeding. A dramatic candidate for descoping the project is to drop the outer layer. This would reduce the number of staves by 33%, but would result in a weaker detector. Studies using the Run2a

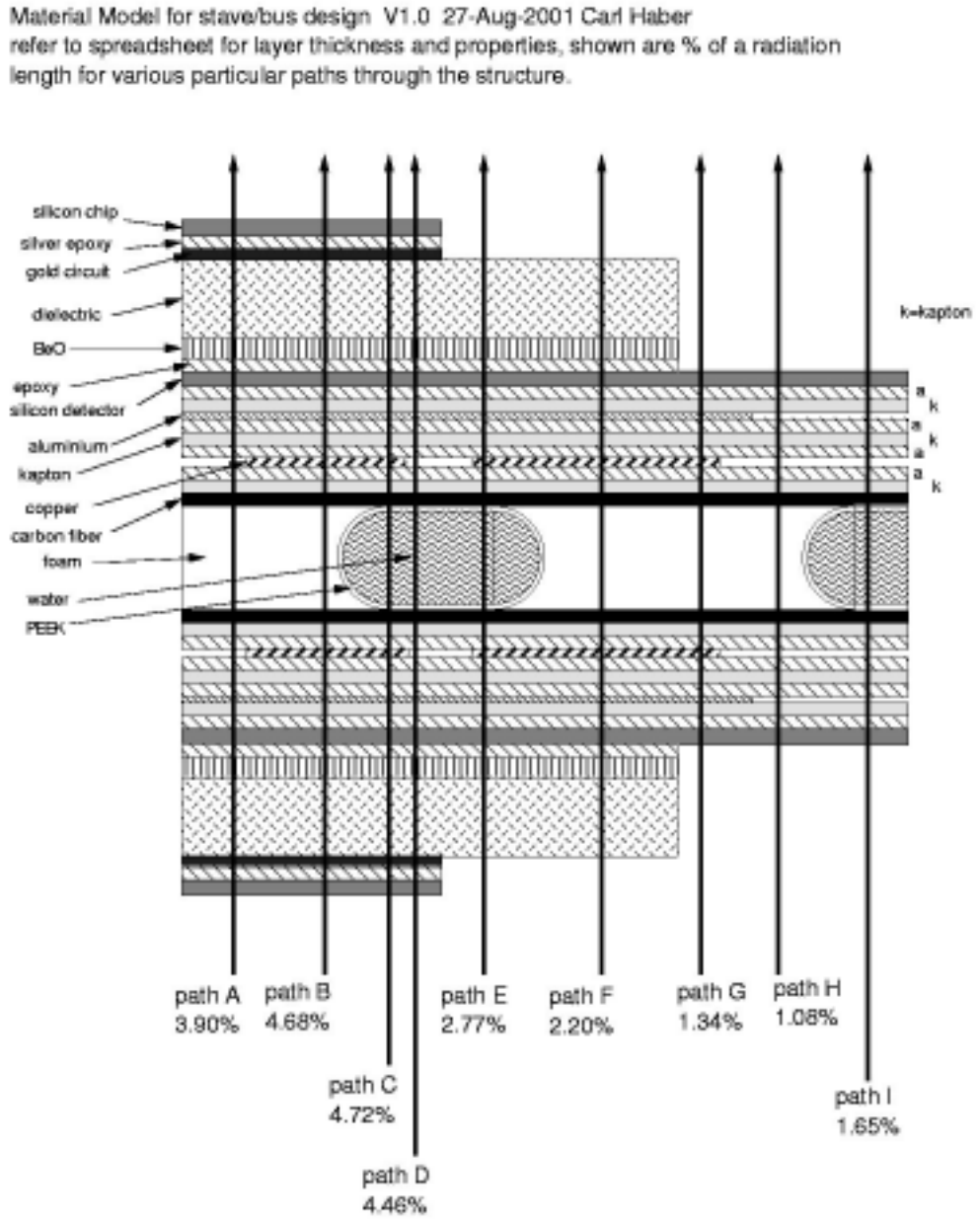

Figure 3.28: Material model for Run IIb stave design.

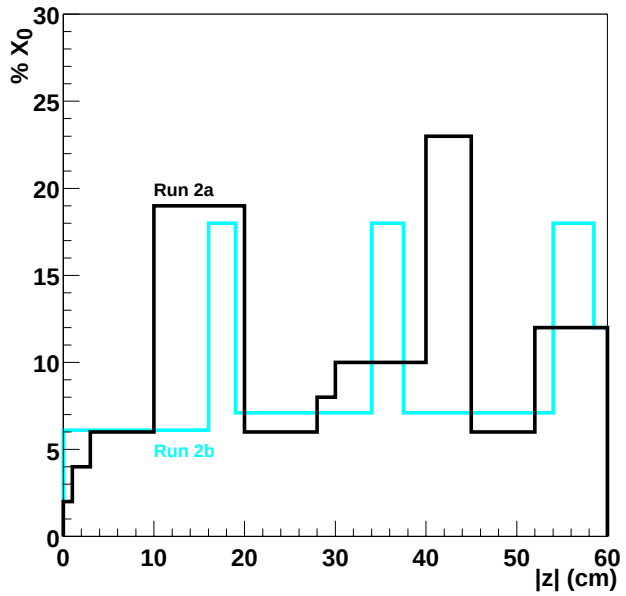

Figure 3.29: The average material of the Run IIa and Run IIb silicon detector designs is compared for normal incidence trajectories as a function of position along the beam line ($|z|$). The black curve is Run IIa. The light curve is Run IIb.

simulation package have shown that this would have a negative impact on the b-tagging efficiency and thus would reduce the Higgs search capabilities of the detector. We prefer to consider a staged approach to descoping. The design of the outer layers is such that the staves are interchangible from layer to layer. If it becomes clear late in the project that the installation schedule will not be met, it is possible to simply rearrange and/or omit staves. This could result in incomplete layers, but would be have a smaller negative impact than dropping the entire outer layer.

3.9 Summary

We have presented a design which is based in great measure on the experiences with the previous CDF silicon detectors and on the R&D in progress for the LHC detectors. We have simplified the mechanical design and minimized the expected construction time by utilizing one stave design for the majority of the layers. The $r-\phi$ tracking capabilities should match or exceed that of the Run IIa detector and the the design should be able to easily withstand the expected radiation dose from Run IIb. We feel that this Run IIb detector can be built in the alloted time and will be sufficiently powerful to fully exploit the physics opportunities presented in Run IIb.

Bibliography

[1] T. Affolder et al, Run IIB Silicon Working Group Report, CDFNOTE:5425. Submitted to PAC in Oct. 2000.

[2] Charge from PAC.

[3] The CDF Collaboration, Run IIA Technical Design Report, Preprint FERMILAB-Pub-96/390-E

[4] N. Demaria et al, NEW RESULTS ON SILICON MICROSTRIP DETECTORS OF CMS TRACKER, Nucl.Instrum.Meth.A447:142-150,2000

[5] P. Azzi at al, Results on the SGS-Thompson Low Resistivity Silicon Detectors for L00, CDF/DOC/CDF/PUBLIC/5301.

[6] G. Bolla et al, THE CDF SVX II UPGRADE SILICON DETECTOR: SILICON SENSORS PERFORMANCES, Nucl.Instrum.Meth.A409:112-116,1998

[7] G. Bolla et al, SILICON MICROSTRIP DETECTORS ON 6-INCH TECHNOLOGY, Nucl.Instrum.Meth.A435:51-57,1999

[8] CDF Collaboration, Physics Performance of the CDFII Detector with an inner silicon layer and a Time of Flight (update of Fermilab proposal P-909), CDFNOTE 5264; March 2000.

[9] KEYCOM Co., 3-40-2 Minami-Otsuka, Toshima-ku TOKYO, Japan 170-0005.

[10] Andresen, J., et.al., "The Port Card for the Silicon Vertex Detector upgrade of the Collider Detector at Fermilab," IEEE Trans. Nuclear Science, Vol. 48, pp. 504-508, June 2001

[11] Turqueti, M., Weber, M., Zimmermann, S. "C0-60 Irradiation Tests Performed for the Ten Bits Differential Transceiver (Version B)," CD/ESE/Fermilab internal Document, Feb. 2002.

[12] D. Stuart "Silicon Readout Time and Event Size with Projections for Run IIb" CDFNOTE 5887, March 2002.

Chapter 4

Silicon Detector Design

4.1 Detector Layout

For Run IIb CDF plans to replace the SVXII and L00 detectors while retaining the ISL detector. The details of the mechanical design are presented in the previous chapter. As part of an integrated tracking system, the SVXIIb detector must provide robust tracking in the high luminosity environment of Run IIb. The similarities and differences with the Run IIa design are presented below.

- Similarities
  - A low mass, high precision, beam pipe layer with axial strips only.
  - Longitudinal segmentation of 6 readout modules.
  - Operation with the displaced vertex trigger.
- Differences
  - More uniform radial distribution of layers and no electronics or cooling between the outer layer of SVX and ISL
  - Use of single-sided sensors everywhere. Double-sided layers are made up of two layers of silicon with a few millimeters of radial separation.
  - A single structure is used for the outer 5 layers and the number of staves/layer increases with radius, rather than a wedge design where the size of the sensors in a wedge grows with radius.
  - Use of an intermediate strip everywhere to improve hit resolution while also keeping the channel count as low as possible.
  - Three or four small-angle stereo (SAS) layers to improve the association with axial tracks and the overall robustness of the system at high luminosity.
  - A larger radius for the beam pipe layer.
  - A double-axial layer just outside the beampipe layer.
  - The outermost layer has the option of being a double axial layer, as described in Chapter 3, or made of axial and small-angle stereo sensors as Layers 2-4. The small-angle stereo option would be chosen if the ISL is not fully repaired or if further studies of the performance at high luminosities indicate the additional stereo measurement is more desirable. Retaining this option with Layer 5 has little impact on the cost and schedule of the project and allows us to react to the outcome of the ISL repairs.

The use of intermediate strips in the designs of all sensors is made possible by the fact that we anticipate the SVX4 readout chip will have lower noise than the SVX3D chip used in Run IIa. For moderate to high signal-to-noise ratios and readout pitches less than ~ 200 μm, intermediate strips provide better resolution with relatively little loss of two-track separation relative to sensors with the same readout pitch and no intermediate strips.

A full hit-level simulation from the Run IIb tracking system was not available to guide the design of the detector we propose to build for Run IIb. The data from Run IIa is just becoming available and the tracking (particularly in the stereo view) is in an early stage of development. Consequently, we embarked on a program of evaluating our design with a number of targeted studies along with, when available, information from the data.

The remaining portions of this chapter describe studies of the impact parameter resolution (4.2), the utility of the double axial layers (4.3), the performance of the small-angle stereo (4.4), the placement of the inner layer (4.5), pattern recognition efficiencies (4.6), and descoping options (4.7).

4.2 Impact Parameter Resolutions

We calculated impact parameter and pointing resolutions for the proposed tracker design with a simple analytic program. The program takes into account the different hit resolutions and material (radiation lengths) of each layer of silicon. The program was checked against Run Ib data where it predicted an $r-\phi$ impact parameter resolution versus p_T given by

$$\sigma_d(calculated) \;=\; \sqrt{13^2 \;+\; (34/p_T\;)^2}$$

The impact parameter resolution as a function of p_T as measured in Run Ib is shown in Figure 4.1. The fit to the data yields the parameterization:

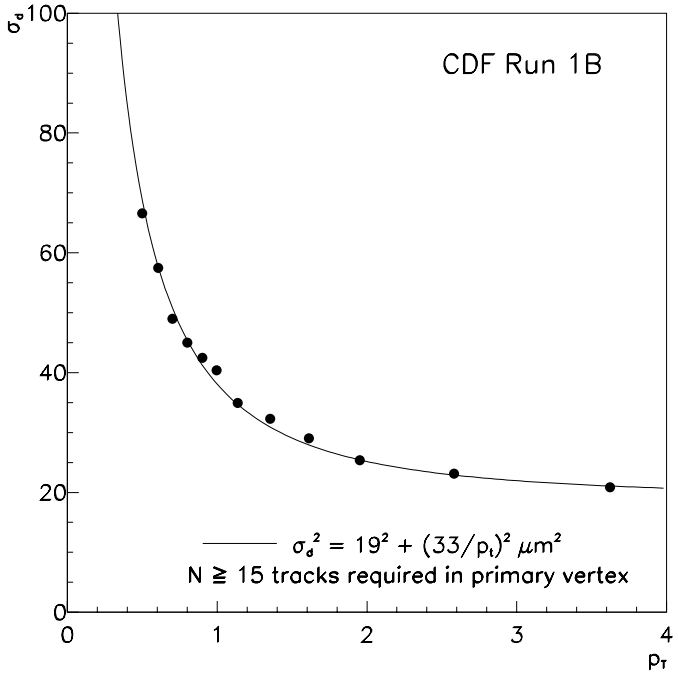

Figure 4.1: Run Ib impact parameter resolution measurement and fit to a simple parameterization.

$$\sigma_d(Run\ Ib) \;=\; \sqrt{19^2 \;+\; (33/p_T\;)^2}$$

The multiple scattering term is essentially equivalent to the calculated value. The constant terms are different because the data includes the uncertainty in the primary vertex (10 μm), as well as contributions from wedge to wedge misalignments (10μm). Adding these uncertainties in quadrature with the calculated resolution results in a constant term of ± 19 μm.

Having successfully modeled the Run Ib data, we turn to the Run IIb detector. Table 4.1 shows the radii and hit resolutions used in our calculations. Note that for axial we simply used $p/\sqrt{12}$ to determine the hit resolutions, where p is the strip pitch. For the small angle stereo (SAS) layers the hit resolution along the beam (z) direction is determined by combining information with the nearby axial layer. We thus calculated

$$\sigma_z \;=\; \sigma_\perp \times \sqrt{2}/\tan(\alpha)$$

where α is the angle between the axial and stereo strips and $\sigma_\perp$ is the hit resolution along an axis perpendicular to the strips in either the axial or small angle sensors. For the ISL (layers 6 and 7 in Table 4.1) we get a hit resolution in z of roughly 2.2 mm.

Table 4.2 shows the radii and material of the scattering planes included in our calculations. For simplicity we lump passive and active material at the average radii of the measurement layers.

Layer	Strip Angle	Radius [mm]	hit resolution [μm]
0	0^o	23.0	7.2
1	0^o	37.75	10.8
1	0^o	45.75	10.8
2	0^o	67.1	10.8
2	1.2^o	71.6	780
3	1.2^o	97.6	780
3	0^o	102.1	10.8
4	1.2^o	126.1	780
4	0^o	130.6	10.8
5	$0^o(1.2^o)$	154.5	10.8(780)
5	0^o	159.0	10.8
6	0^o	210	32.3
6	1.2^o	210	2200
7	0^o	290	32.3
7	1.2^o	290	2200

Table 4.1: Radii and hit resolutions (in $r-\phi$ and z) used to calculate impact parameter and pointing resolutions. The radii are the average of radius for the inner and outer castellations on each layer. The layer 5 sensor at 154.4mm has the option of axial or small-angle stereo sensors.

Layer	Radius [mm]	Material [% X_o]
BP	12.0	0.1
0	21.0	1.4
SC	32.0	0.5
1	42.0	2.0
2	69.0	2.0
3	100.0	2.0
4	129.0	2.0
5	157.0	2.0
6	210 (ISL)	1.4
7	290 (ISL)	1.4

Table 4.2: Radii and material of the scattering layers. BP is the material in the beampipe and SC is the material in the inner screen of the outer barrel

Following the model used in the Run Ib data, we calculate the impact parameter resolutions presented in Table 4.3. As discussed earlier in the text, the asymptotic terms do not include effects such as the uncertainty in the primary vertex ($\approx$10 μm) or misalignments ($\approx$10 μm)) and therefore are better than what we expect to measure. In fact, these effects dominate the resolution of high p_T tracks except for the case in which both hits on layer 1 and the hit on Layer 0 are missed. We find that the Run IIb design has good impact parameter resolution in $r-\phi$ and that the design is fairly robust. The resolution is not too seriously degraded if the hits are missed on Layer 1, if the correct hit on Layer 0 is still attached. This will happen $\approx$ 15% of the time due to the gaps in Layer 1. If there are hits in Layer 1 and we exclude the hit on the innermost layer while retaining its material, the multiple scattering contribution to the impact parameter resolution grows, but the resolution is still very good for high p_T tracks. It is difficult to improve the multiple scattering effects significantly since they depend mainly on the amount of material in the innermost layer which is already minimal. Reducing the material in each layer other than the innermost by a factor of 2 yields only about a 10% reduction in the multiple scattering terms shown in the table. Reducing the material would of course have other benefits such as a reduction in the rate of secondary particle production. Less material also reduces the amount of scattering at larger radii which can force tracking algorithms to use larger road sizes.

Configuration	$\sigma_d[\mu$m] Asymptotic	$\sigma_d[\mu$m] Pt = 2 GeV
All Layers	6	25
No Layer 1	7.5	27
No Layer 0	9	51
No Layer 0 or 1	15	79

Table 4.3: Impact parameter resolutions in $r-\phi$ for all axial layers (ISL + SVXIIb) and for the cases in which the tracks miss layer 1 and/or layer 0.

4.3 Double axial tracking layers

The design of the tracking system must be robust in the high luminosity environment of Run IIb. This high luminosity represents not only a challenge for the new silicon system but for the full integrated tracking system of CDF. At a luminosity of $5 \times 10^{32}\ cm^{-1}s^{-1}$ with 132ns (396 ns) bunch crossings, we expect approximately 4 (15) interactions per crossing. This will cause high occupancy in the inner layers of the COT. Pattern recognition algorithms may not be able to rely on these inner layers.

- We need to design the SVX IIb detector to be robust against the degradation of the COT. We want design the silicon to strengthen the pattern recognition in the environment of 5-10 multiple interactions.

Bottom quarks from Higgs, top quark decay or other sources are identified by a secondary vertex displaced from the primary interaction point. These b-quark jets are central and high E_t ($\beta\gamma \sim 10$), which leads to secondary vertex displacements of a few millimeters. The cores of these jets represent a challenging environment for pattern recognition algorithms. In Run I, the displacement was measured in the $r-\phi$ plane. In Run II this will again be the primary view to measure the displacement since this is the strength of the detector. When attempting to tag the secondary vertices we want the tracking algorithms to be efficient, have good impact parameter resolution, and have a minimal percentage of pattern recognition mistakes, which lead directly to false tags.

The standard CDF tracking algorithm begins with a track found in the COT and projects the track from the COT into the silicon system attaching hits first in the outer layers and working in toward the inner most silicon layers, refitting the track as silicon hits are added. This pattern recognition is performed first

in the $r-\phi$ view, making the first connection of the COT tracking into the silicon a critical step. When multiple silicon hits are present in a window around the projected track location, each hit represents the beginning of a possible reconstruction path into the inner layers. Each false path represents the possibility of a pattern recognition failure.

- Minimizing the number silicon hits on the outer layer that are considered by the tracking algorithm will reduce the potential for tracking mistakes.

In addition, studies have shown that impact parameter resolution and tracking mistakes are dominated by the pattern recognition in the inner few layers of the silicon. If hits on these inner layers are correctly assigned to the track, then good impact parameter resolution is achieved. However, if the wrong hits are assigned, then tracking mistakes occur and produce non-Gaussian tails in the resolution function. The tracks with artificially large impact parameter then can lead to false b-quark tags. Monte Carlo studies indicate that picking the wrong hit on Layer 1 nearly always leads to the incorrect hit assigned on Layer 0.

- The SVX design should have robust $r-\phi$ pattern recognition in these inner layers of silicon.

To address these bullet points above, the design includes two layers with axial sensors on both sides of the stave. We refer to these as *double-axial* layers. Layer 1 is the first double axial layer and it strengthens the pattern recognition near the beam pipe. The second double-axial layer is Layer 5 and it strengthens the connection between the COT track and the silicon system. The double axial layers assist the pattern recognition in two basic ways

- Simple redundancy of the axial layers. This ensures that a good axial hit should be present in this layer of the SVX. (Can be used as a veto if no hit is observed in either layer.)

- Providing additional information for the tracking algorithms. The two hits on the axial sensors of a double-axial layer represents a small track stub or line segment. The angular resolution of the line segment is ~ 3 mrad, comparable to the resolution in a superlayer of the COT. When a track is projected into a double-axial layer, the tracking algorithm can demand that the slope of the track stub be consistent with the slope of the projected track. This provides additional information and rejection beyond the simple hit location requirement.

To understand the impact of double axial layers we examined generator level monte carlo in $t\bar{t}$ events. For these studies, double axial staves were assumed at radii of 3.0 cm (Layer 1) and 15 cm (Layer 5). The separation between the two axial layers in a stave was 4mm. COT tracks were extrapolated to Layer 5 and Layer 1. At each layer a search for other hits within a 5σ road was performed. The slopes of all combinations of hits in the two axial sensors is computed. The difference between the slope of the COT track and all the track stubs within in the road is plotted in Figure 4.2. At Layer 5, 72% of the track stubs can be eliminated with a 3σ cut on the slope. This eliminates three-quarters of the pattern searches into the inner layers and reduces the opportunities for pattern recognition failures. Similarly 40% could be eliminated at Layer 1.

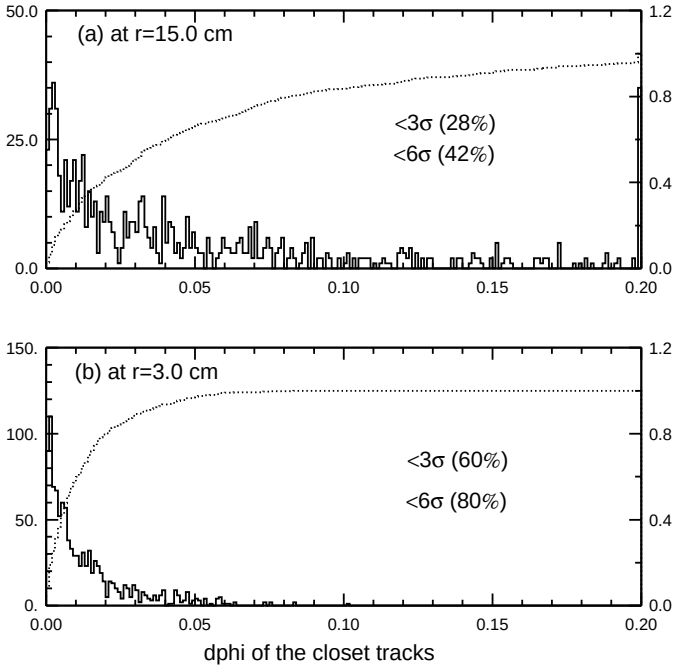

Figure 4.2: The comparison of slopes of track stubs in Layer 5 and Layer 1.

We are continuing our studies of the double-axial layers in the design. These studies uses $t\bar{t}$ events, which contain dense high-energy jets, however, we want to understand how the performance changes with multiple interactions and more detailed detector simulation. In high-luminosity the fraction of hit

combinations that we can reject may go down, however, the very case in which we want additional rejection in order to recover some of the degradation in the performance of the inner layers of the COT.

4.4 Tracking in the stereo view

The design of the stereo tracking capabilities for the Run IIb detector has undergone a number of iterations. Finally, due to concerns about the ability of the inner layers of the outer tracking chamber (COT) to survive in the Run IIb environment we have decided to concentrate on robustness in the $r-\phi$ view and simplification in the stereo view. We have eliminated the 90 degree stereo layers from the design. However, the number of small-angle stereo layers in the SVX has been increased to 3 or 4 layers (optional layer 5). The ISL provides an additional 1(2) small-angle measurements for tracks with $|\eta| < 1$ ($|\eta| > 1$). The resolution in z is worse than in Run IIa due to the elimination of the 90 deg. stereo layers, but the association of the hits to tracks will be easier. In addition, the z resolution should be sufficient to resolve multiple interactions.

We have performed a number of studies to estimate the z_o resolution and the impact from additional layers of small-angle stereo. The first study is based on an analytical calculation of the resolution. Next we use the Run IIa simulation of $t\bar{t}$ events. Finally, we examine a Run IIa data sample of J/ψ events.

Configuration	σ_z[mm] Asymptotic	σ_z[mm] $P_t = 2$ GeV
SVX L2-L5 + 1 ISL	1.4	1.4
SVX L2-L4 + 1 ISL	1.8	1.8
SVX L2-L5 Only	1.4	1.4
SVX L2-L4 Only	2.0	2.0

Table 4.4: Impact parameter resolutions in r-z view for all stereo layers and the cases in which ISL and/or layer 5 are missing. There is no significant difference for high momentum tracks and P_t=2.0 GeV/c

We begin with an analysis which follows the same structure as the presented for the r-ϕ view. The impact parameter resolution in z is calculated using the same model as Section 4.2 but using the radii and resolutions for the stereo layers listed in Table 4.1 and Table 4.2 The results are shown in Table 4.4. The configurations shown include 3 and 4 small-angle stereo layers in the SVX and the effect of having or missing a stereo hit in the ISL. The most important conclusion is that for all the configurations listed, the resolution is $\approx 1-2$ millimeters and so should be sufficient to resolve multiple interactions. Studies are underway to establish if 3 or 4 small-angle layers are needed to provide robust Run IIb operation.

The previous study relied on a parametric study of the SVX Run IIb detector. We also can use the full simulation from the Run IIa detector. While the advantage is that the Run IIa simulation models the availible data, the disadvantage is that it is using the Run IIa geometry (e.g. radii of SAS layers). Nonetheless, we can use it to study general trends related to small-angle stereo tracking. The study simulated $t\bar{t}$ events and used the current stand-alone tracking in the silicon systems to investigate:

- The z_o resolution of tracks and the effect of additional SAS layers.
- The efficiency for finding tracks (stand-alone) when different numbers of SAS layers are used.

The tracks considered were contained in the fiducial volume of the silicon system and produced at least 4 hits in axial layers and at least 2 hits in the small-angle stereo layers. In addition, at least 1 SAS hit was required in the ISL. The efficiency for finding these tracks was 65±3%, 89±1%, and 88±2% when 2, 3, and 4 small-angle layers were *available*, not necessarily used, in the SVX and ISL (see Table 4.5). Using these same tracks, the z_o resolution was determined as a function of the number small-angle stereo layers *used* in the stand-alone track fit (see Table 4.5). In both the case of efficiency and the resolution, the presence of a fourth small-angle stereo layer did not significantly increase the performance.

Available SAS Layers	Efficiency	Used SAS Layers	σ_z (mm)
2	65±3%	2	2.5
3	89±1%	3	1.3
4	88±2%	4	1.1

Table 4.5: Simulation of the track finding efficiency and z resolution when 2, 3, or 4 SAS layers are either available to or used by the stand-alone tracking algorithm.

Finally, we have also looked at the Run IIa data using the standard Outside-In (OI) tracking algorithm.

This algorithm begins with tracks from the COT, extrapolates them in to each successive layer of the silicon and associates hits in that layer to the track. A plot of the J/ψ mass from a portion of the Run IIa data is shown in Figure 4.3. In this plot, tracks are required to have at least 3 r-ϕ hits per track, and no stereo information is used. This sample of J/ψ's represents a cleaner environment than the $t\bar{t}$ Monte Carlo.

Since the ISL is currently not working in the central region (the region where the COT and OI tracking can cover), the small-angle silicon hits come only from the SVX. The data were separated into samples in which there is only one SAS layer on each track and a sample in which there are two SAS hits on each track. The difference in z for the two J/ψ tracks is shown in Figure 4.4 for both cases. We see that there is improvement when two instead of one SAS hit is associated with each track. When no SAS hits are attached, the stereo information is extrapolated from the COT and the distribution has a width of 8mm.

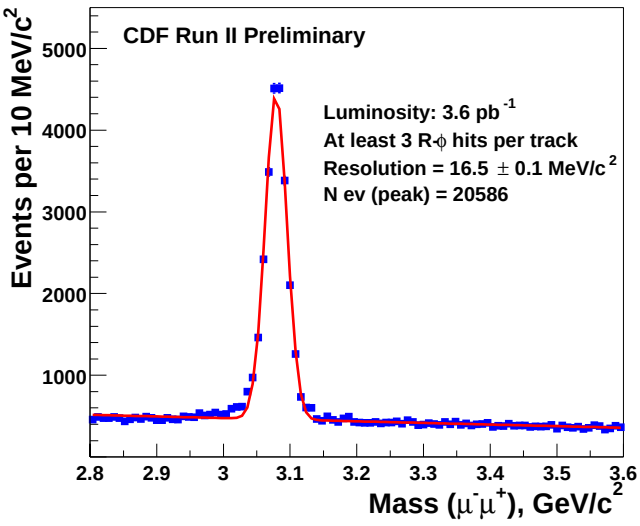

Figure 4.3: J/ψ mass from Run IIa data.

From the parametric studies, Run IIa Monte Carlo, and Run IIa data indicated that with small-angle stereo sensors we should be able to achieve a z_o resolution of ≈ 1 mm. This should be sufficient to distinguish tracks from multiple interactions. The resolution is not strongly dependent on the number of small-angle stereo layers once one gets beyond 3+1 (SVX+ISL). We are continuing our study of $r-z$ tracking as improved simulation tools and additional

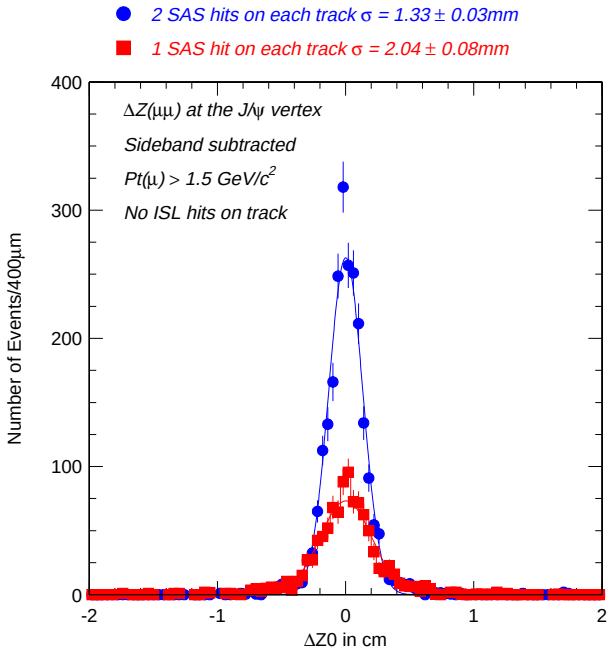

Figure 4.4: Delta z between two tracks in Run IIa J/ψ data when one or two SAS hits are attached to each track. When no SAS hits are attached the distribution has a width of 8mm from the stereo of the COT

Run IIa data become available.

4.5 Innermost Layer Placement

The radial placement of the L00 detector in the CDF Run 2a detector was determined by the spatial constraints imposed by the SVXII bulkhead and the minimum allowed radius of the beam pipe. Freed from these constraints, the question naturally arises as to what might be the optimal radial placement of the innermost silicon layer for our physics objectives in Run IIb. On the one hand, for unshared hits[1] impact parameter resolution improves as the measurement is made closer to the beamline. On the other hand, at smaller radii the frequency of shared hits increases. These hits have worse position resolution and the impact parameter measurements for tracks associated with these hits are correspondingly degraded.

To quantify the magnitude of these competing effects on the physics performance of the Run IIb detector, we have performed the following simula-

[1] Unshared hits are defined as a contiguous cluster of strips with charge over threshold produced by one and only one particle.

tion. Top events are generated with PYTHIA 6.129. These events are fed to a parameterized charge deposition model (tuned on SVX′ data and modified for general use) to simulate hits on a silicon layer of some specified geometry. The details of the geometries we considered are provided in Table 4.6. Other inputs to the Monte Carlo are listed in Table 4.7. From the charge deposited by the model, clusters are formed and classified as shared or unshared as defined above. Clusters are further classified as either splittable or unsplittable depending on whether or not an identifiable dip in the cluster charge distribution can be observed. If such a dip is observed, the cluster is split into two clusters, allowing some of the lost hit resolution to be recovered. Thus, four categories of hit resolution are obtained: unshared/unsplittable, unshared/splittable[2], shared/splittable and shared/unsplittable. For each category, mean residuals are computed statistically. Since track impact parameter resolution will depend on whether or not clusters are shared at both layer 0 and layer 1, the above procedure is employed first for the layer 1 geometry, from which shared/unshared and splittable/unsplittable fractions are obtained. The process is then repeated with the layer 0 geometry. When the hit is unshared in layer 0 it is assumed to also be unshared in layer 1. If, however, the hit is shared at layer 0, random numbers are thrown to decide if the hit is shared/unshared and splittable/unsplittable in layer 1. A parameterized impact parameter resolution is calculated for each of the 8 categories of shared/splittable clusters in layer 0 and layer 1. For each track with $|\eta| < 1$ in the simulation[3], an impact parameter error is assigned based on its L0/L1 shared/splittable classification utilizing the impact parameter resolution parameterizations calculated previously. Tracks are smeared and passed to a stand-alone version of the Run Ib secondary vertex finding algorithm, SECVTX, using cuts similar to the standard Run I cuts (the SECVTX algorithm has two passes: the first requires at least 3 displaced tracks with p_T >0.5 GeV and σ_d >2.5, the second pass requires at least two displaced tracks with $p_T > 1.0$ GeV/c and $\sigma_d > 3$). A jet with an identified and positively displaced secondary vertex, ($L_{xy}/\sigma > 3$) is considered to be tagged. For taggable b-jets, (*i.e.* jets which contain at least one track from a b-decay within the acceptance of the COT in this study), single and double tag efficiencies are computed. The entire process is repeated for each of 4 radial configurations. The relative average efficiencies for tagging one or both b jets as a function of the radius of the innermost layer are plotted in Figure 4.5. The single b tag efficiencies for the four radii as a function of the E_T of the b jet are shown in Figure 4.6.

With regard to low E_T physics one would have an *a priori* expectation that performance would be more sensitive to the radius of the innermost layer. We generated generic $b\bar{b}$ samples and again studied the performance of our b tag algorithm. The single and double b tag efficiencies for generic $b\bar{b}$ events are shown in Figure 4.7. As expected, the effect of increasing the radius of the innermost layer is more pronounced. As for $t\bar{t}$, the change in performance at a radius of 2 cm is still relatively small and the degradation is more rapid for radii above 2 cm. For completeness we show the single b tag efficiencies for the four radii as a function of the E_T of the b jet in Figure 4.8.

Based on these results, we conclude that the optimal radial placement of the innermost layer would be that of the current L00 detector at 1.5 cm. However, we also note that our estimate of physics performance is not significantly degraded in either our $t\bar{t}$ or $b\bar{b}$ generated samples if the innermost layer is placed at a radius of 2.0 cm. Moreover, placement of the innermost layer at 2.0 cm presents fewer mechanical difficulties and would reduce the radiation dose rate of this layer and increase its lifetime by a multiplicative factor of $(1.5/2.0)^{-1.7} \sim 1.63$. We thus conclude that the marginal increase in tagging efficiency gained by returning to a radius of 1.5 cm is more than offset by these other important factors.

4.6 Pattern Recognition Efficiency

This section investigates the correlations between layers and the effects of pointing resolutions in the detector design as a whole. There are two sources of hit confusion which lead to pattern recognition errors: cluster merging and lack of pointing resolution necessary to discriminate among nearby hits. Hit confusion and resulting pattern recognition errors can give prompt tracks an incorrect impact parameter.

[2]This category arises when an incident particle causes a δ-ray to propagate in the silicon and deposit charge over more strips than usual for an isolated track.

[3]For this study the impact parameter resolution was calculated with the assumption that the curvature of the track is known (e.g. is given by the COT).

L0 average radius	L0 #strips	L1 average radius	L1 #strips
1.5 cm	128/256	3.5 cm	512
2.0 cm	256	4.0 cm	512
2.5 cm	384	4.5 cm	512
3.0 cm	384	4.5 cm	512

Table 4.6: Geometries considered in the Monte Carlo Simulation.

Signal to Noise = 15:1
Intermediate strip readout
Readout strip pitch = 50 μm
Sensor thickness = 300 μm
12-fold symmetry in ϕ
0.5 cm gap at $z = 0$

Table 4.7: Inputs to the Monte Carlo Simulation.

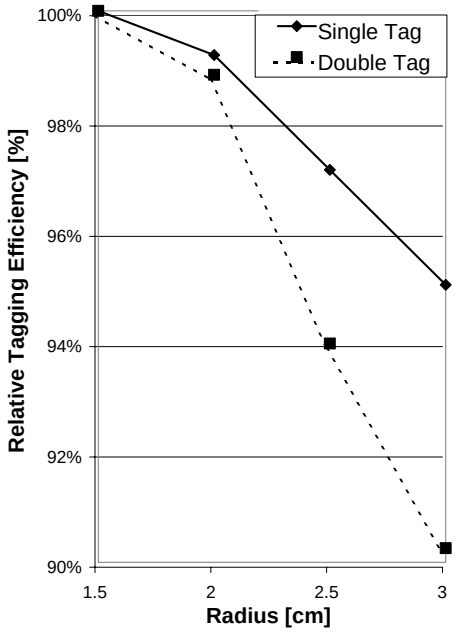

Figure 4.5: SECVTX single and double tag efficiencies in MC $t\bar{t}$ events as a function of the radius of the innermost silicon layer normalized to unity at a radius of 15 cm.

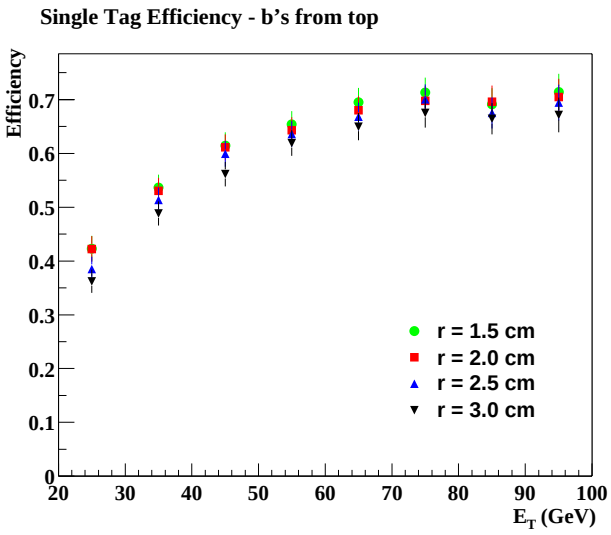

Figure 4.6: SECVTX single tag efficiencies in MC $t\bar{t}$ events as a function of the E_T of the b jet for the four radial configurations considered.

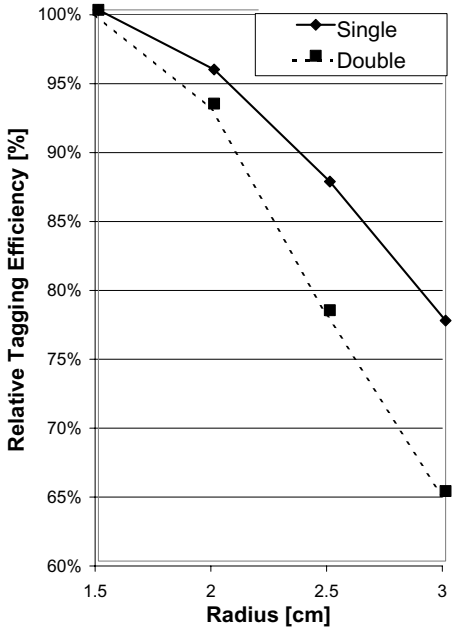

Figure 4.7: SECVTX single and double tag efficiencies in MC $b\bar{b}$ events as a function of radius of the innermost silicon layer normalized to unity at a radius of 15 cm.

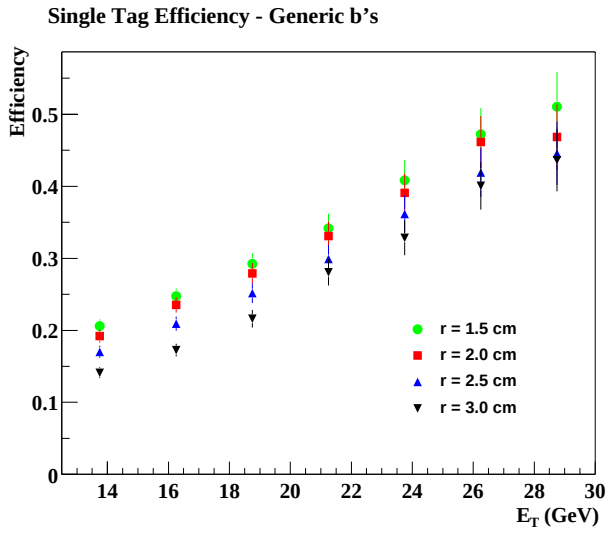

Figure 4.8: SECVTX single tag efficiencies in MC $b\bar{b}$ events as a function of the E_T of the b jet for the four radial configurations considered.

To study these effects, a simple simulation of the Run IIb detector was employed, and the same sample of $t\bar{t}$ events was used as in the previous section. The individual single-sided measurement layers are modeled as cylinders of appropriate length split in ϕ and z into individual readout units. Each layer measures a coordinate corresponding to the strip angle, including such effects as ganging. Calculation of hit separation is purely geometric. The effects of cluster lengthening due to incidence angle in both ϕ and η are also taken into account. For simplicity, particle trajectories are not perturbed by material interactions and the single-hit efficiency is assumed to be 100%. An outside-in algorithm is used to project good COT tracks through one layer of the ISL into the Run IIb detector. In each layer, the distance in the measurement coordinates to the nearest other hit is computed. If that distance is larger than both the inherent two hit resolution of the layer (2× readout pitch) or a tightly defined tracking road (3× pointing resolution into the layer), the track is considered to be successfully resolved in that layer.

As a track is successfully linked to each layer, the pointing resolution into the next layer is improved. This "tracking path" proceeds through successively more powerful layers. When the correct hit is not distinguishable, the pointing resolution to the next layer down is re-computed and an attempt is made to find the hit in that layer. In the case where the correct hit is once again distinguishable, it is assumed that the full pointing resolution to the successive layers is recovered.

When the track arrives at the innermost layer in a confused state, the layer where the unrecoverable confusion first occurred is recorded along with the reason for the failure: cluster merging or lack of pointing resolution. While many of these cases may be distinguishable with real track fitting, this allows identification of potential weaknesses and meaningful comparisons between competing designs. Figure 4.9 shows the results for b-daughter tracks in $t\bar{t}$ events that pass through all layers of each detector.

An important difference between the Run IIa and Run IIb detectors is the radius of the outermost layer. In the Run IIb design, this significantly reduces the rate of wrong hit association at the entry point. Once a correct hit at Layer 5 is associated to the COT/ISL track, the pointing into the remaining layers is improved and this increased efficiency carries through to the inner layers. As a track proceeds to lower ra-

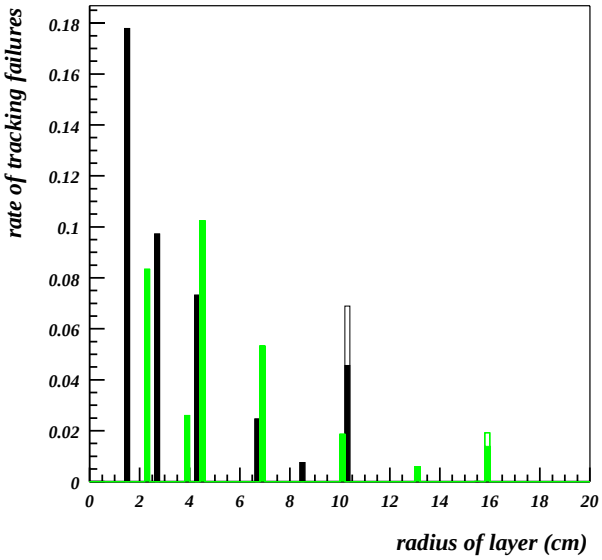

Figure 4.9: The point of origin for tracking failures in the r-ϕ view. Effects of both merging (solid) and pointing inadequacy (open) for Run IIa (black) and Run IIb (light) designs are shown.

dius, the occupancy increases and the losses due to merged hits increases. In the Run IIb design, Layer 1 shows a larger fraction of lost tracks due to merged hits than the Run IIa design, although they are at similar radius. This is in part due to the larger pitch of the Run IIb sensors and due to the large incident angle of the 6-fold Layer 1 Run IIb design. Failure in inner axial sensors of Layer 1 are ∼2%, while the failures in the inner axial sensor of Layer 5 are negligible. This shows that the occupancy and the resulting confusion at the radius of Layer 1 is such that a track can have a good hit on the outer Layer 1 and still, 2% of the time, it will point to merged or confused hit on the inner Layer 1. Layer 0 has much smaller pitch and incident angles than Layer 1 and thus the number of failures due to merged hits is reduced rather than increased for this step to lower radius. At the very small radius of the Run IIa L00 there is significant loss due to merged hits, although the pitch and incident angles are very similar to the Run IIb L0.

The overall performance is obtained by summing the number of tracking failures at each layer. The Run IIb design has a rate of potential tracking failures of 31%, compared to 45% in the Run IIa design. These studies indicate that the Run IIb detector will be a stronger and more robust tracking device than the Run IIa detector and thus should be able to better resolve the complicated tracking situations which will be present in the Run IIb luminosity environment.

4.7 Descoping

As mentioned earlier, the Lab has asked that we investigate descoping options as part of the technical design. In particular, dropping layer 5 would reduce the number of staves by 60 (30%). Alternatively, dropping Layer 4 would reduce the number of staves by 48 or 27%. Either of these could potentially reduce the time to complete the project, 3-4 months assuming a rate of production of 1 stave per day.

The discovery of the Higgs is the focus of Run IIb and the tagging of b-jets is critical to that effort. The Higgs Working Group found a direct relationship between the significance of a potential Higgs discovery (σ), the integrated luminosity required (L) and the efficiency for b-tagging (ϵ):

$$\sigma \propto L * \epsilon^2. \tag{4.1}$$

Figure 4.10 shows a plot of the Higgs mass reach for a 5σ discovery for 30 fb^{-1} (15 fb^{-1} each for CDF and D0) as a function of the b-tagging efficiency. On the plot 1.0 corresponds to a tagging efficiency of 65%. A 4% reduction in the tagging efficiency corresponds to 3 GeV less mass reach or alternatively, an increase of 8% in the amount of luminosity required.

Unfortunately the full Run IIb simulation was not well enough understood for these studies so we use the well tested Run IIa detector simulation. The ISAJET Monte Carlo was used to generate a sample of $t\bar{t}$ events which were then fed through the Run IIa simulation package. The effect of dropping a layer was studied by deleting layers in the detector configuration in the simulation. The standard Run IIA Outside-In (OI) tracking algorithm in the $r-\phi$ view was run on the simulated events. The efficiency for tagging b jets was measured along with the percentage of fake tracks. A jet is considered tagged as a b-jet if the L_{xy} for the jet is more than 3σ from the primary vertex. A track is defined as fake if the impact parameter (d0) is more than 3σ from the true d0.

Four configurations were considered and the results are shown in Table 4.8. Configuration A is the full

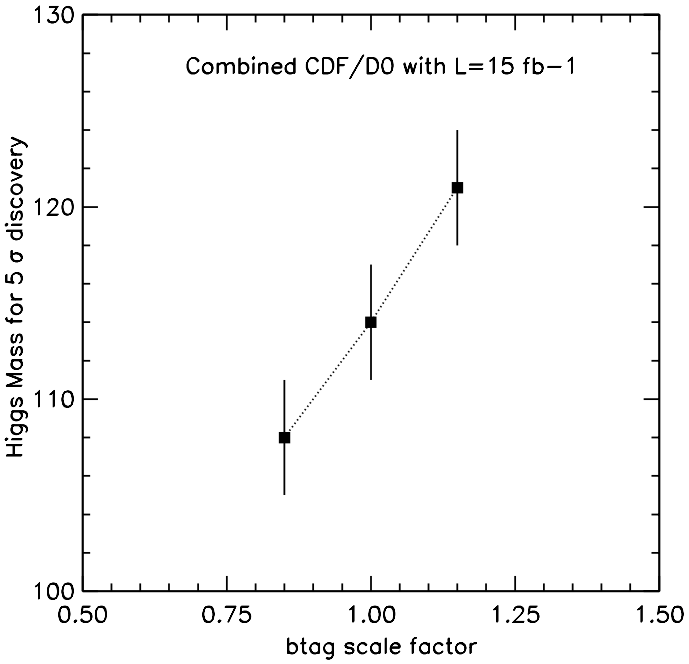

Figure 4.10: Higgs mass reach for a 5σ discovery as a function of the relative b-tagging efficiency for an integrated luminosity of 30 fb^{-1} (15 each for CDF and D0). The b-tagging efficiency is relative to 65%.

	B-tag eff. (%)	% Diff.	Fakes(%)	% Diff.
A	58.8	-	7.7	-
B	56.3	-4	8.9	+16
C	51.3	-12.6	9.5	+23
D	51.0	13.3	8.7	+13

Table 4.8: Percentage B-tagging efficiency and fake tracks for different configurations of the Run IIa detector. Note that the tagging algorithm is still under development and thus the absolute numbers are expected to improve. A is the full Run IIa detector, B is without Layer 5 of SVXII. Configurations C and D assume the inner layers of the COT are dead; C has dropped layer 5 of SVXII, D has dropped layer 4 of SVXII. The statistical uncertainty on the tagging efficiency is 1.3% and it is 0.5% on the percentage of fake tracks.

Run II system: there are hits in L00, 5 layers of SVXII, hits in ISL and a good track from the COT. This is compared (configuration B) to the case in which Layer 5 of SVXII is dropped. In configuration C and D the inner layers of the COT are considered dead (which could potentially happen due to high occupancy and/or aging) and either Layer 4 (D) or 5 (C) are dropped. In addition we found that the the loss of the inner two layers of COT, without dropping a layer of SVXII was roughly equivalent to configuration B (dropping Layer 5, but not the COT layers). Note that the tagging algorithm is still in the early stages of development. The absolute numbers presented in the table do not represent the expected ultimate performance, but rather provide a basis for comparison of different configurations.

The numbers shown in the table represent a minimum reduction. The reduction in tagging efficiency from dropping an outer layer could be compounded by degraded performance in the COT due to aging and/or high occupancies. For example, additional fakes would force tighter cuts and thus an additional reduction in efficiency. The effects of multiple interactions at high luminosity have also not been included. This study concentrated on the central region where outside-in tracking could be used, however, the effect of dropping an outer layer on the forward region, where stand-alone tracking must be used, will be greater.

In summary, we have investigated the effects of dropping a layer using the Run IIa simulation. We found that the loss of a layer would adversely affect our ability to tag b-jets which is critical for the discovery of the Higgs in Run IIb.

4.8 Conclusions

The silicon detector we propose for Run IIb is a conservative design. Indications from the Run IIa data are that the occupancies and the associated difficulties in a higher luminosity environment must not be ignored. As a result we have added more axial layers at small radius and large radius. In addition, the 90 deg. stereo layers have been exchanged for small angle stereo layers. This degrades the resolution in the stereo view to of order 1mm (still sufficient for identification of primary vertices), and significantly improves the association of the correct hits to tracks. We feel the Run IIb detector will be able to operate well in the Run IIb environment and has the capabilities needed for the search for the Higgs.

Bibliography

[1] L3 note 1666, 1995, "Helicoidal tracks", J. Alcaraz.

[2] CDF/DOC/SEC_VTX/PUBLIC/1790, 1998, "Tracking in the SVX", H.Wenzel.

[3] CDF/DOC/TOP/PUBLIC/2946, 1995, "The SVX′ MC Simulation" H.Y.Chao et al.

Chapter 5

Calorimetry

5.1 Introduction

Most of the proposed upgrades to the CDF calorimetry are related to the Central Electromagnetic Calorimeter (CEM), one of the few remaining pieces of the original CDF detector. The CDF Central Calorimeter was baselined in 1981, before Run -2, and was designed for instantaneous luminosities of 10^{30} and integrated luminosities of 1 pb^{-1}. The demands placed on this detector by the physics analyses continually increase. The proposed upgrades are in two parts: 1) replace the slow gas detectors on the front face of the calorimeter with faster scintillator versions that have better segmentation, and 2) add timing information to both the Central and Endplug Electromagnetic calorimeters to filter out cosmic ray backgrounds.

5.2 Central Preshower Detector

5.2.1 Motivation

The CDF Central Preshower (CPR) and Central Crack (CCR) detectors will be replaced with an integrated scintillator detector. This would happen at the time the silicon detector is replaced for Run IIb. There are many reasons for this replacement: 1) The CPR is a slow wire chamber that integrates over several crossings and has relatively poor segmentation. This combination will lead to very high occupancies in Run IIb, crippling electron and photon identification. 2) Even with the modest occupancies in Run IIa, the current CPR segmentation makes it difficult to use in more sophisticated analyses such as improving jet resolutions. 3) With 10 fb^{-1} the CPR is expected to have collected 0.1 C/cm, where wire aging has typically caused significant degradation in performance, sometimes beginning with much smaller doses. 4) The thin gas layers of the CPR and CCR have much worse pulse height resolution than a scintillator detector. This is important for both electron identification and improving resolutions with a dead material correction. 5) We have an opportunity to build a much better detector for a relatively small cost. This is possible because we intend to reuse the Run IIa electronics and make use of the CDF experience in building similar detectors for the Run IIa upgrade.

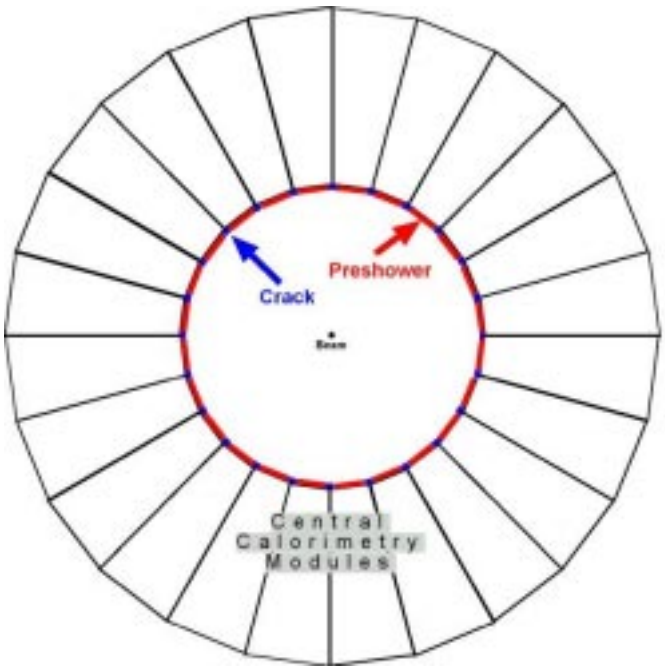

Figure 5.1: Diagram of central calorimetry wedges and the location of the preshower and crack detectors.

5.2.2 Run I Physics Using the CPR and CCR

The most important uses for preshower detectors such as the CPR are: 1) improving electron identification, 2) separating single photons from meson back-

grounds, 3) improving jet resolutions for new physics searches such as the search for the Higgs. The CPR has been used extensively in electron identification in CDF. It provides about a factor of two to three more rejection of charged pions that pass all other cuts using tracking, calorimetry, and shower maximum information. This extra rejection has been crucial in soft electron ID for b jet tagging, as was shown in the first top evidence paper and displayed in Figure 5.3.

Secondly, the CPR has been used in numerous publications involving photon identification. The shower maximum detectors cannot resolve single photons from meson decays above 35 GeV since the angular separation between the two photons is too small. The CPR uses photon conversion rates which are energy independent. It was used initially to extend the QCD measurement of direct photons by more than 100 GeV in photon p_T, as shown in Figure 5.4. More recently the CPR has been used to estimate backgrounds to signals of exotic physics that include photons. New physics is expected to come at higher p_T, in a region where the shower maximum detector has no discriminatory power. It is crucial to maintain this photon identification capability for possible new signals in Run II. As the next section will show, with the luminosities possible in Run IIb, the occupancy of the current detector will be too large for photon identification.

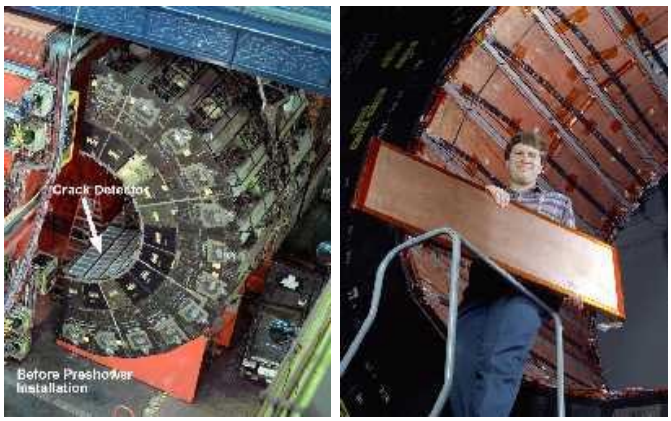

Figure 5.2: Photographs of one arch of twelve calorimetry wedges, pulled away from the beamline. The Run I preshower and crack detectors are seen lining the inner surface of the arch in the right photograph.

The use of the preshower detector to improve the energy resolution of a jet is a relatively new idea for Run II. It is well known that improving dijet mass resolution will be important in finding various new physics signals such as the Higgs, as shown in Figure 5.5. An improvement of 30% in the mass resolution (from 15% to 10%) means a factor of two less luminosity is needed to discover the Higgs. The preshower detector may help improve jet resolutions in several ways, these studies are now underway. The first way the preshower detector helps jet resolutions has already been used in Run I, in the electron b-tag in top quark events mentioned above. Due to the presence of the neutrino in these jets, CDF corrects the energy of these jets differently than those with no electron. This improves the overall energy resolution of the b jet, but no one has studied in detail precisely how much. The second way the preshower detector can help jet resolutions is by correcting for energy loss in the dead material in front of it, which the ZEUS experiment has successfully done with their scintillator-based preshower detector. We have simulated 2 GeV photons in the proposed preshower detector and found a 20% improvement in the energy resolution. Since photons provide 30% of the total jet energy, this is a 6% improvement in a jet resolution, an important contribution. A third way the preshower can help is by tagging low momentum tracks that shower in the dead material and do not escape, leaving zero energy in the calorimeter. Finally, a preshower detector can be used in other ways to improve jet resolutions in algorithms incorporating charged tracking. Since the tracking resolution is so much better than the calorimeter, the main challenge is to estimate the remaining electromagnetic (and neutral hadron) component of the jet. Charged tracks complicate this since they shower in the EM calorimeter, whereas preshower detectors can be used to estimate this contribution to the EM energy. The current CPR detector makes this difficult since a single cell spans five calorimeter towers, possibly collecting showers from other particles in the jet. A preshower detector where each cell is confined to a single calorimeter tower, such as the one in this proposal, is desirable for this purpose.

The current CDF central crack chambers (CCR) have not been directly involved in a CDF publication, but they have been checked for large pulse heights in all of the rare events CDF has observed. Their usefulness in other ways has been recently illustrated by a search for a Z peak in dielectron events, where one electron passed into a crack. Figure 5.6 shows a comparison of the Z peak measured when using the electron + track 4-vector and when one uses the electron + crack energy 4-vector. This indicates the

capability of tagging high energy photons in the crack region in events which may contain new physics. The crack covers about 8% of the central detector, and in events with multiple EM objects such as the famous $ee\gamma\gamma Met$ event the possibility of one object hitting the crack is quite high. If we are lucky enough to get a sample of such events then doing measurements of this physics will require crack tagging of photons. Irrespective of the source of this single event, if SUSY is producing signals with photons as some suggest, there will be a large variety of new physics with photons and missing E_T and other objects. Crack tagging of high-energy photons will become even more important. The current crack chamber is a very thin gas layer that would be much improved with a scintillator replacement, integrated with the new preshower detector.

The CDF preshower and crack detectors are expected to play important roles in Run II physics such as soft electron tagging of b jets, photon identification in SUSY events or other new physics, and improving jet resolutions for mass bump searches such as the Higgs. The next section will explain why the CPR in particular will be severely degraded or completely useless in the high-luminosity Run IIb era.

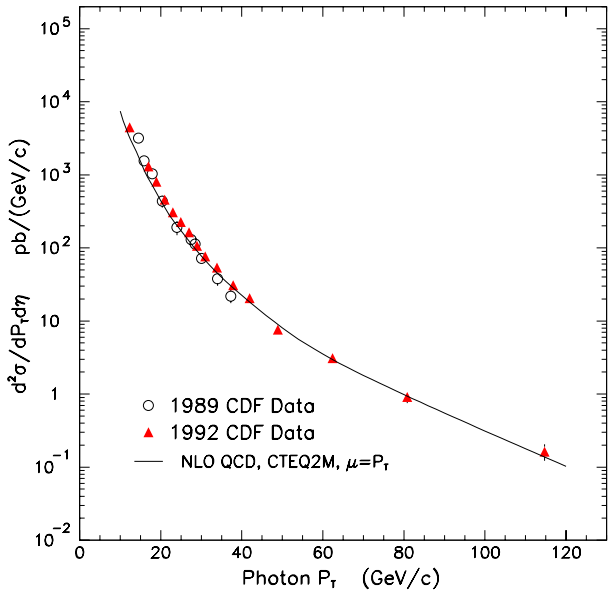

Figure 5.4: Direct photon cross section from 1989 (before CPR installation) and from 1992 using the CPR. The cross section was extended by almost 100 GeV in photon Pt.

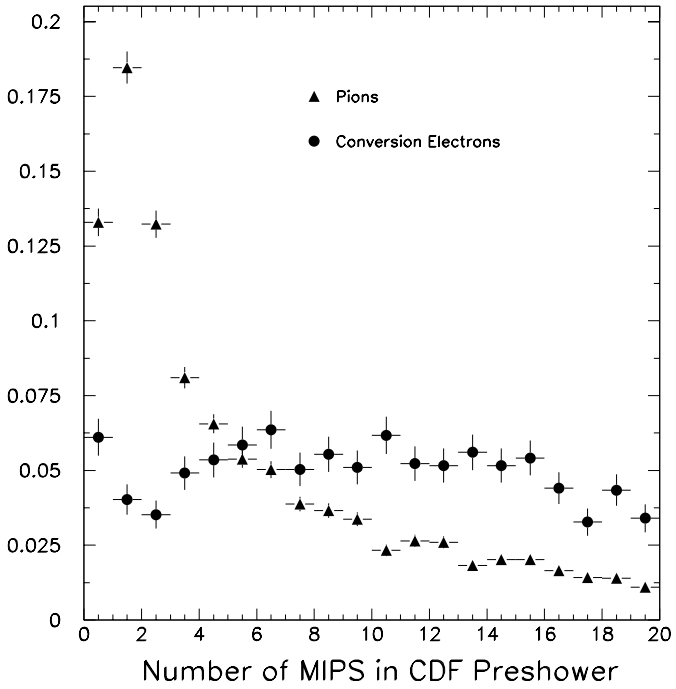

Figure 5.3: CPR response to electrons and charged pions as shown in the top "evidence" PRD.

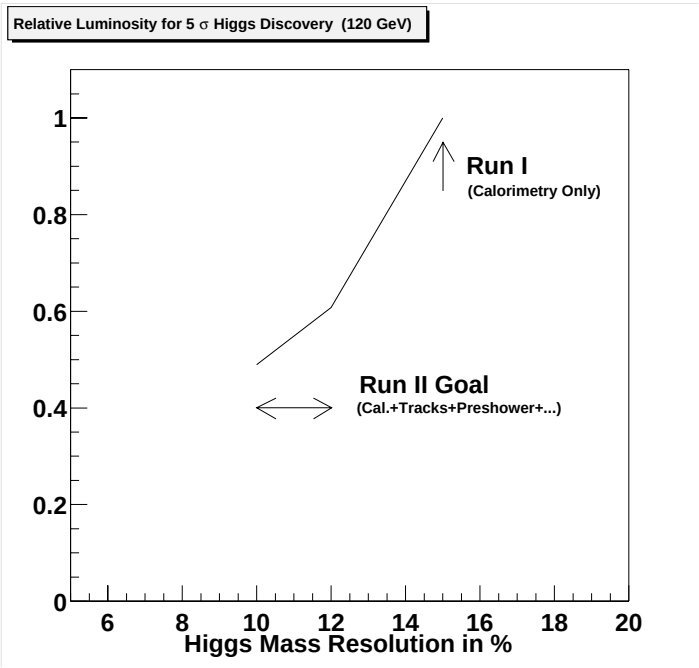

Figure 5.5: Relative improvement in luminosity needed for a Higgs Boson discovery, as a function of mass resolution.

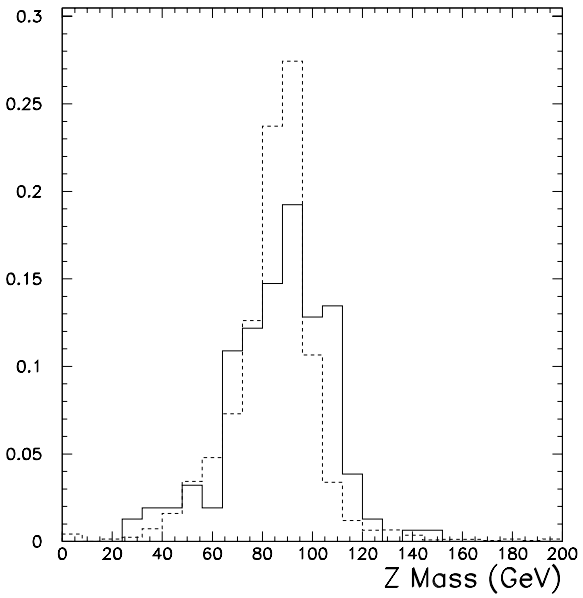

Figure 5.6: Dashed line is Z peak using electron + track, the solid line is electron plus Crack Chamber pulse height for electrons that went into the ϕ crack.

5.2.3 Occupancy Issues

The occupancy and segmentation issues discussed in this section are only relevant for the preshower detector. The current crack chambers are not sensitive to MIPS or soft photons like the CPR and the proposed crack chambers have the same segmentation as the previous ones. The CPR is a slow wire chamber and, based on early results from Run II, it appears that integrating over four crossings will be necessary to collect a significant fraction of the charge. One concrete example of a problematic scenario is if the peak Run IIb luminosities reach 6x10^{32}, with 108 bunches and 132 ns spacing. This will give rise to 5 minimum bias events per crossing. With the CPR integrating over 4 crossings, the detector will have to deal with over 20 minimum bias events! A second concrete example is the TDR situation of luminosities reaching 2x10^{32}, but with 36 bunches and 396 ns spacing. This results in 6 minimum bias events per crossing. With the CPR integrating over only two crossings in this case, a total of 12 minimum bias events are present in the CPR. With these two examples it is possible to extrapolate to any other possibility. We present Figure 5.7 as evidence of the serious difficulties the CPR could have in Run IIb. The figure shows the Run II CPR pulse height distribution in the case of overlapping 20 minimum bias events, it has an occupancy of 64%. The technique to identify photons at high p_T is to count the fraction of events in the zero bin, since single photons convert less often than multiple photons. The conversion frequency for a single photon is between 60% and 65%, so close to the background occupancy from minimum bias events that discrimination will not be possible. Similar difficulties arise for electron identification. Obviously there is a continuous degradation of performance with increasing luminosities; here we have only mapped out one possibility. But this discussion indicates that the occupancy problems in Run IIb are real. The proposed detector design will reduce the occupancy from overlapping minimum bias events by more than x10. This is accomplished by improving the detector speed with a scintillator replacement, as well as improving the detector segmentation.

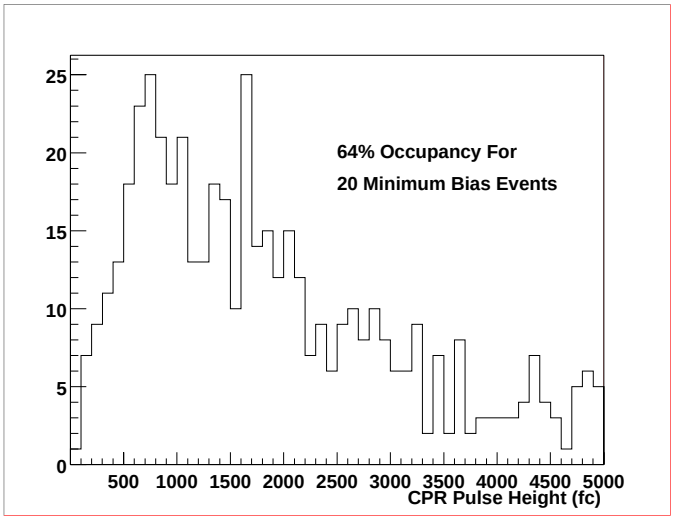

Figure 5.7: CPR run IIa pulse height for 20 overlapping minimum bias events. This background occupancy is 64%, for comparison the conversion frequency for a single photon is between 60% and 65%. The photon cross section is derived from counting the fraction in the zero bin. The occupancy of the estimated underlying event will make this very difficult.

5.2.4 Overview of Detector Design for Run IIb

The relatively limited budget available for the Run IIb upgrades necessitates a limited budget for the CPR upgrade. In this spirit, we plan to re-use the existing electronics channels currently employed in the readout of the existing CPR and CCR detectors, thus removing one of the largest components

of the cost for any new detector system. At the time that the present CPR was constructed, the technology did not exist for the convenient design of a scintillator-based device to fulfill the same purpose. In the intervening years, advances in the production of wavelength-shifting (WLS) and clear plastic optical fibers have allowed for the design of scintillator detectors with WLS fiber readout with almost arbitrary segmentation and essentially complete hermeticity. Such a design has already been implemented in CDF in the plug electromagnetic and hadronic calorimeters and in the plug preshower detectors, as well as in many other experiments such as CMS and MINOS.

The new CPR will be placed in the space currently occupied by the old CPR and CCR. Figures 5.1 and 5.2 show the location of the Run I detectors in both diagrams and pictures. They cover the front face of the forty-eight central calorimetry wedges. These wedges are arranged into four "arches" of twelve wedges, which can independently be moved away from the beamline for access to the inner surface.

The new CPR should be sensitive to minimum ionizing particles (MIPS). A yield of 5 photoelectrons per MIP is sufficient for this purpose. The CCR scintillator is forced to be thinner, on the order of 6 mm, than that used for the CPR. This will result in less light but the yield should still be sufficient for the CCR functionality since it is measuring showers, not MIPs. Due to its location in the central rapidity region and at a relatively large radius, there should be little impact from radiation damage on the performance of the CPR2, even at the highest foreseen luminosities.

A radial space of 2.8 cm is available for the CPR detector and a space of 7 mm is available for the CCR. The basic design of the new CPR involves 2 cm thick scintillator tiles, segmented in η and in ϕ, as shown in Figure 5.8 along with the mechanical shell design (discussed more in the next section). The amount of scintillator needed for the new CPR is relatively modest, of the order of 50 m^2. The 2 cm scintillator has been produced by the Dubna group in CDF and is available in the quantities needed for the new CPR. The scintillator sheets will be cut into tiles and will have grooves for the WLS fibers machined in them using the facilities that are present in Lab 8 at Fermilab. Prototype tiles have been created from the Dubna scintillator using the Lab 8 tooling. The scintillator was found to be particularly easy to machine and there should be no problem with producing the required number of tiles in the timescale available.

These tiles will be read out by 1.0 mm diameter WLS fibers embedded in a roughly circular ("sigma-shaped") groove (see Figure 5.9) machined in one surface of the tile to a depth of 4 mm (and with a width of 1.5 mm). Such a groove shape maximizes the light yield and uniformity while keeping the fiber bending to a minimum. The depth of the groove allows for 3 turns of fiber to be used in order to increase the percentage of the scintillator light absorbed by the fibers; the width of the groove optimizes the combination of ease of fiber insertion and the minimization of machining of the tile. A number of commercial vendors are capable of producing quality fibers, both WLS and clear, to the specifications needed for this project. Tests are being conducted on fibers from Kuraray, Bicron and Polihitech to determine the best combination of quality and price. The fibers will be held in the groove with the use of a specially extruded polyurethane O-ring that will be placed in the groove. The O-ring will also extend 2 mm above the surface of the tile to serve as a mechanical protection for both the surface of the tile and the clear fibers.

Also, to improve the light yield, the end of the WLS fiber remaining in the tile groove will be diamond-polished and will have a thin aluminum coating sputtered onto it. The process of depositing an aluminized mirror on a polished fiber end (and then applying a protective coating) was developed for CDF and has become routine in the facility located in the Fermilab village. The tiles for each wedge will be assembled into a "tray" formed by a 2.5 mm aluminum shell. The edges of the tiles will be painted white using a titanium dioxide paint in order to optically isolate the tiles. Thin polyethylene spacers will be used to mechanically separate the tiles and to protect the paint from abrasion.

After exiting the tiles, the WLS fibers will be spliced to 1.0 mm diameter clear fibers (fibers in which no WLS dopants have been added to the polystyrene) using fiber splicing technology originally developed for the CDF plug calorimeter upgrade. Splicing to clear fibers prevents the extra light loss from the transit from the tile to the edge of the detector through WLS fibers. The splicing machines and the expertise to use them remain at Fermilab. The clear fibers will then be routed on top of the scintillator tiles to the high eta edge of each wedge, as shown in Figure 5.10, where they will be glued into a number of plastic shell optical connectors. The

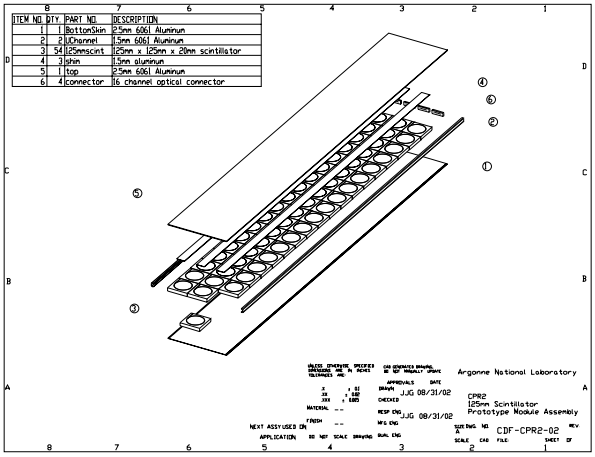

Figure 5.8: Exploded view of the current preshower upgrade design.

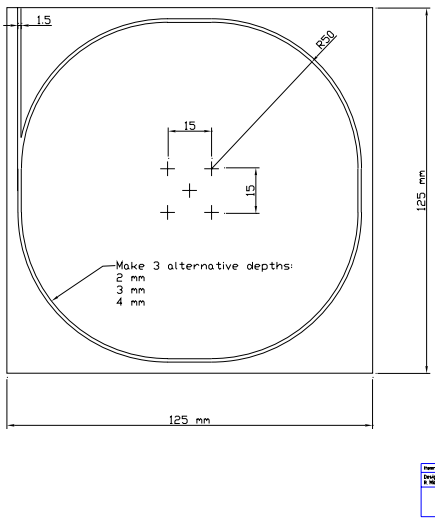

Figure 5.9: Groove cut into the scintillator tiles.

polyethylene spacers mentioned previously will extend approximately 1 mm above the surface of the tile and will have grooves that will organize the routing of the clear fibers. As mentioned previously, the splicing and mirroring will take place at Fermilab using Fermilab personnel. The spliced fibers will be assembled into pigtails at Michigan State University by glueing the fibers into plastic connectors and then machining the connector surface using a diamond polisher present at MSU. The plastic connectors will be precision machined in the MSU machine shop. The quality of the pigtails will be tested using an ultraviolet light scanner originally developed for pigtail production for the endplug project.

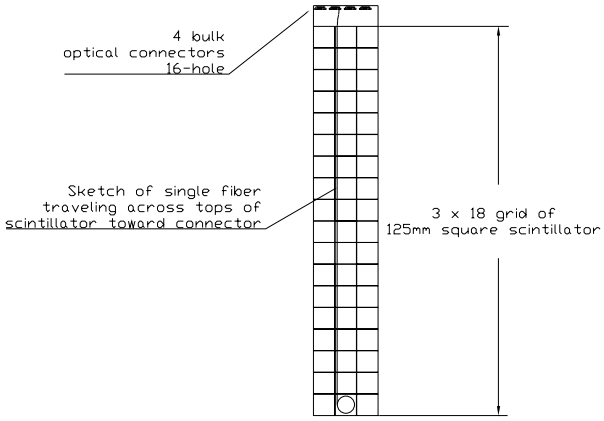

Figure 5.10: Sketch of the scintillator tile layout and fiber rout of a single fiber in the preshower detector.

Each CPR module will be enclosed in an aluminum shell that will provide both mechanical integrity and optical isolation for the detector. The current design for the shell is shown in Figure 5.12, and is relatively simple. It consists of three tiles across, 2.5 mm aluminum covers, and 1.5 mm aluminum U-channels on the end to provide support. An FEA analysis of this configuration has been performed at ANL, and a sag of 0.5 mm is expected with only a single support in the middle of the counter. We plan to support the counters in at least four locations, as the current CPR chambers are supported. In addition, a full-scale mechanical prototype has been built using fake tiles made of PVC, and deflections consistent with the FEA analysis have been measured.

An optical cable consisting of roughly 5 m of clear polystyrene fibers (1.1 mm diameter) covered by a light-tight sheath will route the light signals from the edge of the CPR through the crack to the back of

each wedge of the central calorimeter. There, each optical cable will terminate in a "cookie" which will be coupled to the front surface of a MAPMT. There is a "step-up" in fiber diameter in order to reduce any effects from any possible misalignment between the pigtails and the optical cables. As for the pigtails, the connectors and cookies will be precision-machined in the MSU machine shop.

Reusing the electronics for the CPR/CCR implies two SMD cards per wedge or 64 channels. Note that modification of central SMQIE/SQUID electronics is not required. The design plan is to retain ten CCR channels and allocate the remaining 54 channels to the CPR. With this segmentation, tower-based information could be used in the optimized jet resolution algorithm.

The CCR scintillator tiles will have linear grooves machined down the center to a depth of 2 mm. As in the CPR, the WLS fibers will be spliced to clear fibers of the same diameter after leaving the tiles and the clear fibers will terminate in plastic connectors at the edge of the CCR detector. There an optical cable will transmit the light to a MAPMT at the back of the wedge. The CCR will be contained in a separate mechanical/optical structure formed from 1/32 inch aluminum.

Each MAPMT will have 16 pixels and thus will have 16 optical channels mapped to it. There will be a total of five optical cables per wedge. Three of the optical cables will have 16 CPR channels, one will have 6 CPR channels and one will have 10 CCR channels. The latter two cables will terminate in cookies that will fit together in a "jigsaw" fashion on one MAPMT.

The four 16 channel PMTs required for each wedge will be mounted in a light tight PMT box. The design of the box is shown in Fig. 5.11. The optical cable terminates in a cookie that is mounted with screws into a plate at the bottom of the box. A mu metal shield surrounds each cookie and PMT. A polarized ring aligns the PMT to the cookie and also maintains an air gap of .010 inch between the fiber ends and the face of the PMT. The PMT is held by a spring clip that is inserted into the open end of the mu metal shield. Short cables are used to collect the signals onto a 34 pin connector that will mate with 16 coaxial cable pairs. The cover, the mu metal shield, and the mating ring comprise a light baffle to make the box light tight.

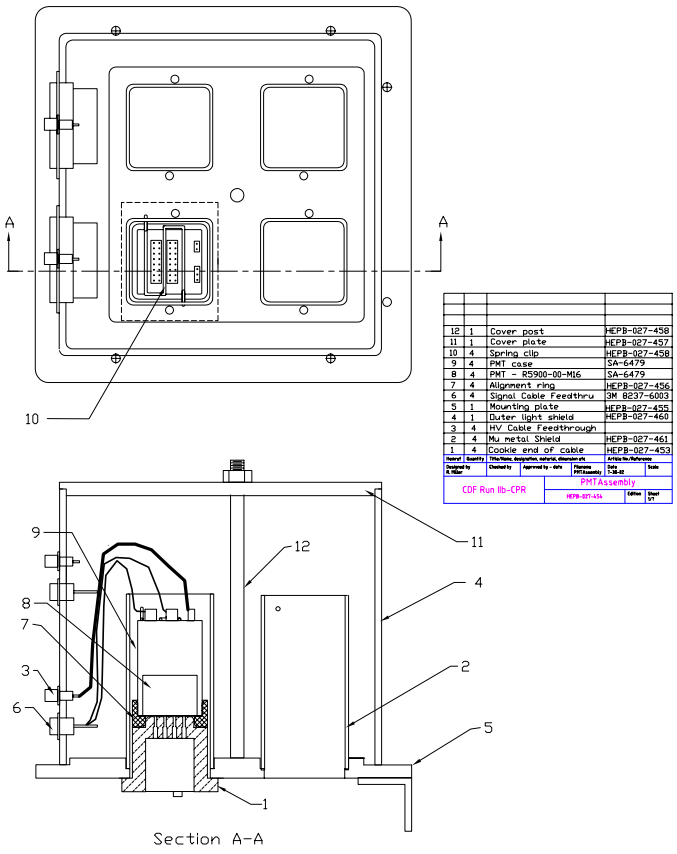

Figure 5.11: Sketch of the phototube box design.

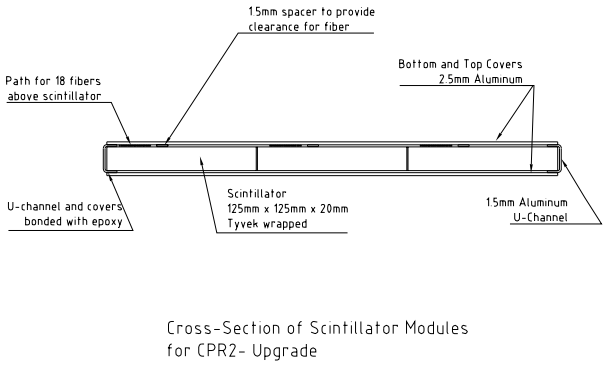

Figure 5.12: Cross section of the preshower design, showing 3 tiles across inside an aluminum shell.

5.2.5 Phototube Test Results

The readout of the detector is by the use of R5900 multi-anode PMT's (MAMPT's) manufactured by Hamamatsu. This is the same tube used for the endplug shower maximum detector. This is a 16 channel device with pixel size of 4.5X4.5 mm^2. With one detector channel per pixel, each wedge of the CPR will require 4 MAPMT's, for a total of 192 plus 10% spares for a total order of 220 MAPMT's.

We present results from a preliminary test performed at the Rockefeller University on ten Hamamatsu R-5900 MAPMT's purchased by the University of Tsukuba as part of the ongoing CPR2 R&D program. Specifications by the manufacturer are shown in Table 5.1. Individual tubes may deviate substantially from the values given by the manufacturer. It is important to measure these characteristics and verify that each tube conforms to the appropriate and acceptable ranges.

In the production run of phototubes, the University of Tsukuba will perform the task of testing the phototubes. Their teststand, utilizing two lasers, one fast and one slow, is just now being commissioned. For this reason these phototubes were tested at Rockefeller with a teststand that was used for production testing of the CDF Endplug Shower Maximum detector phototubes, as well as the CDF Miniplug phototubes.

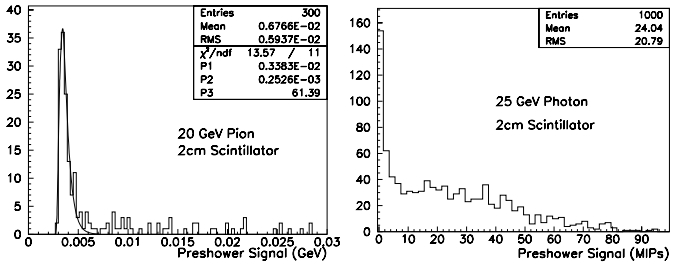

Figure 5.13: Left: the MIP signal is determined by non-interacting 20 GeV pions in the Preshower detector. Right: the Preshower response to a 25 GeV photon expressed in MIP equivalent.

In the test stand at the Rockefeller HEP Lab, we are studying the channel response uniformity, the single photoelectron response, the cross talk and the linearity, in order to optimize the voltage divider design for the CPR2 requirements. As a result of our GEANT simulation, it would be desirable to read out signals from the Preshower in the range 1-100 MIP's. Fig. 5.13 shows the MonteCarlo result for a 25 GeV photon. In the current front-end electronics, the SMQIE chip has a 13 bit dynamic range, measuring charge up to 100 pC with a resolution of 12.5 fC.

For the test we use a light sealed 'test box' which contains a light emitting diode (LED) embedded into a rectangular prism of lucite. The purpose of the lucite is to act as a 'light mixer' distributing the LED light uniformly among a set of clear fibers mounted in holes drilled in a delrin 'cookie' in a pattern matching that of the MAPMT photocathode pixels. This unit tests a single MAPMT unit at a time. The LED has been pulsed with a signal from a pulse generator at 1KHz and 50 ns wide. A couple of attenuators before reaching the LED have been used for a fine adjustment of the LED light intensity, and a light filter in front of the MAPMT has been used for the single photoelectron measurement. The testing is carried out on ten MAPMTs manufactured by Hamamatsu Corporation, divided in two groups: five (serial numbers KA2399, KA2409, KA2437, KA2440, KA2443) are a tube assembly of type H6568-MOD with an extra 17th channel, sum of the 16 channels, from the last dynode; while the remaining five (KA2402, KA2419, KA2467, KA2571, KA2633) are H6568 without dynode signal. All of them have a normal bleeder cicuit (equally divided circuit).

The uniformity of the LED light across the 4×4 cookie channels has been measured with three MAPMTs, and the measurement has been repeated after rotating each tube by 90°, 180° and 270°. Variations shown by these measurements are within ± 3 %.

The readout system employed for this test was a CAMAC based LeCroy 2249W 11-bit 12-channel charge integrating ADC, with a sensitivity of 0.25 pC/count, controlled by a National Instrument 'Labview' data acquisition software.

To check the reproducibility of the measurement using this setup, the output of one MAPMT was also measured repeatedly after (i) turning off/on the pulse generator which fires the LED, (ii) turning off/on the high voltage supply which powers the MAPMT, and (iii) re-mounting the MAPMT before each measurement. The variation in ADC counts is less than 1 % in cases (i) and (ii), and about $1 \sim 2$ % in case (iii).

For each MAPMT, our tests consist of a measurement of the ADC counts as a function of the variation of the input voltage, and a channel–to–channel uniformity response between the sixteen anode outputs. The MAPMT under study has a base resistor divider of $\sim 4M\Omega$. The base circuit, shown in Fig. 5.15,

draws approximately 0.2 mA at 800 Volts. The maximum allowed voltage for these PMTs is 1000 Volts.

Figure 5.14: Left: The Hamamatsu R-5900 MAPMT has a 1 squared inch cross-section; Right: The test stand at the Rockefeller Lab.

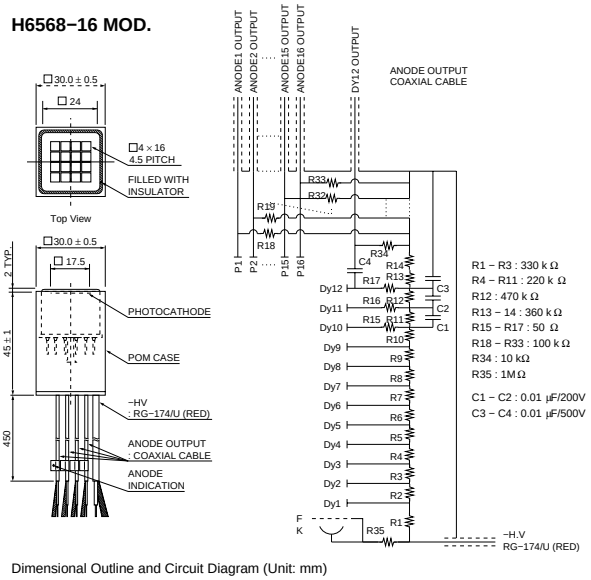

Dimensional Outline and Circuit Diagram (Unit: mm)

Figure 5.15: Schematic drawing of the Hamamatsu H6568-16 MOD (R5900-16) MAPMT base under study for the CPR2 detector.

A crucial issue is the uniformity of inter–pixel response. We measured the channel to channel uniformity of the ten MAPMTs under test. The channel with the highest output counts is assigned to the 100% value, and all other channels are normalized to that channel. Figure 5.16 shows the measurement for five of the ten MAPMTs tested. The dashed lines in the plot correspond to a relative variation in response between channels of a ratio 2:1. The reproducibility of our measurements is within about 5% to 10%, in the range from 600 V up to 850 V applied to the MAPMT. Figure 5.17 compares our MAPMT calibration results to the Hamamatsu specifications. For all of the ten tested MAPMT's, the two calibrations agree within ±15%.

The MAPMT's under test have a high gain, which ranges from $2 \cdot 10^5$ to $3 \cdot 10^7$ for voltages from 600V to 1000V. They have normal bleeder cicuits (equally divided circuits). We want to study the linearity of the response, as Hamamatsu also produces a "tapered bleeder" version of the base, which allows for a better pulse linearity. Use of these bleeder circuits improves pulse linearity 5 to 10 times than that obtained with normal bleeder circuits, but with a gain about ten times smaller at the same voltage.

We varied the voltage between 640V and 820V in 20 V increments, and measured the charge of the output signals. Fig. 5.18 shows a good linearity in the range 660V-760V, where most likely the detector will be operated, but deviations from linearity already start at 800V.

We also studied the single photoelectron response, by means of a combination of two attenuators before the LED and a light filter between the LED and the MAPMT.

The single-electron response can be measaured with light pulses so attenuated that the probability of each pulse giving rise to only one photoelectron is much greater than the probabilty of its giving rise to more than one.

If fluctuations in the number of photons per light pulse follows a Poisson distribution, so will the number $n_{k,i}$ of photoelectrons emitted in response to them:

$$P(n_{k,i}) = \frac{(\bar{n_{k,i}})^{n_{k,i}}}{n_{k,i}} \cdot e^{-\bar{n_{k,i}}}$$

Thus the probability of no photoelectron being emitted is $P(0) = e^{-\bar{n_{k,i}}}$; the probability of only one being emitted is $P(1) = -\bar{n_{n,k}} \cdot e^{-\bar{n_{n,k}}}$; and the probability of more than one being emitted is $P(n_{k,i} > 1) = 1 - P(0) - P(1)$. Since the ratio $P(n_{k,i} > 1)/P(1)$ tends toward $\bar{n_{k,i}}/2$ as $\bar{n_{k,i}}$ tends toward zero, it is evident that it is possible to so attenuate the light pulses that the probability of more than one photelectron being emitted per pulse is negligible compared with that of only one being emitted. In practice single-electron operation is obtained by so attenuating the

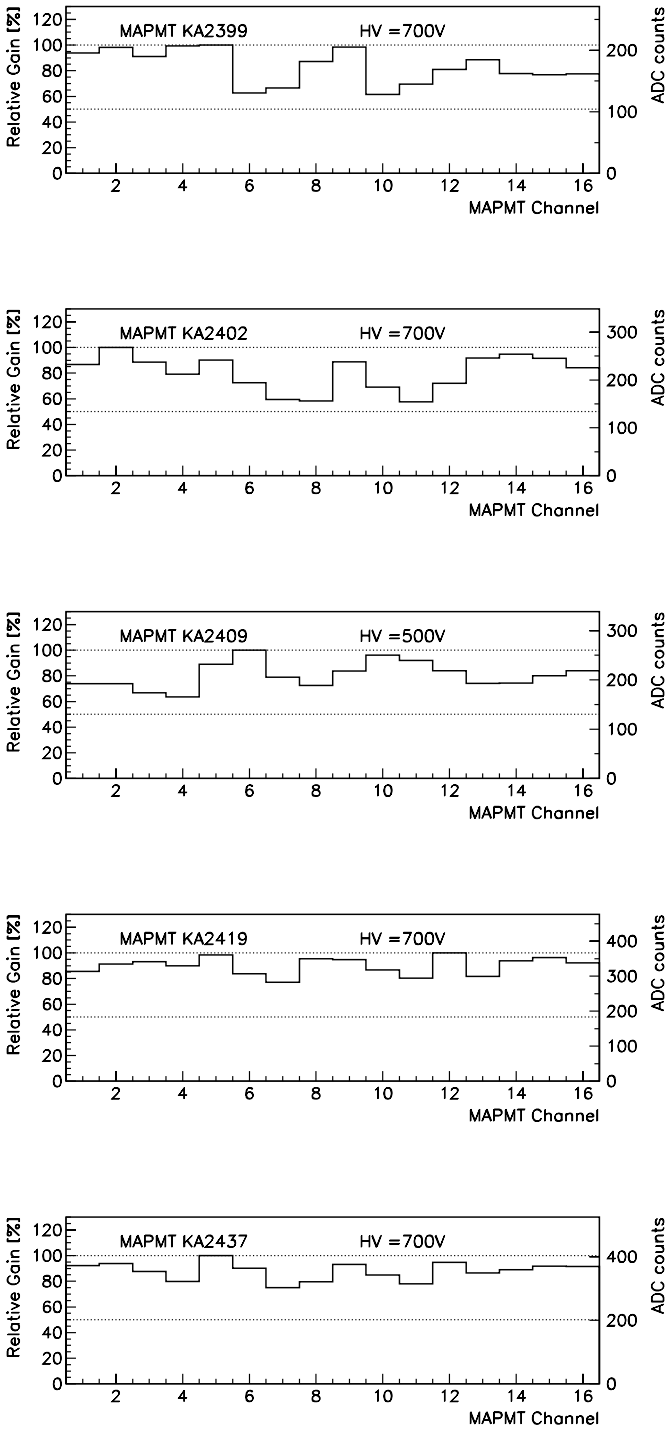

Figure 5.16: Channel–to–channel relative gain for the sixteen output signals of five of the ten MAPMTs under study. The dashed lines represent a variation in response of a ratio of 2:1.

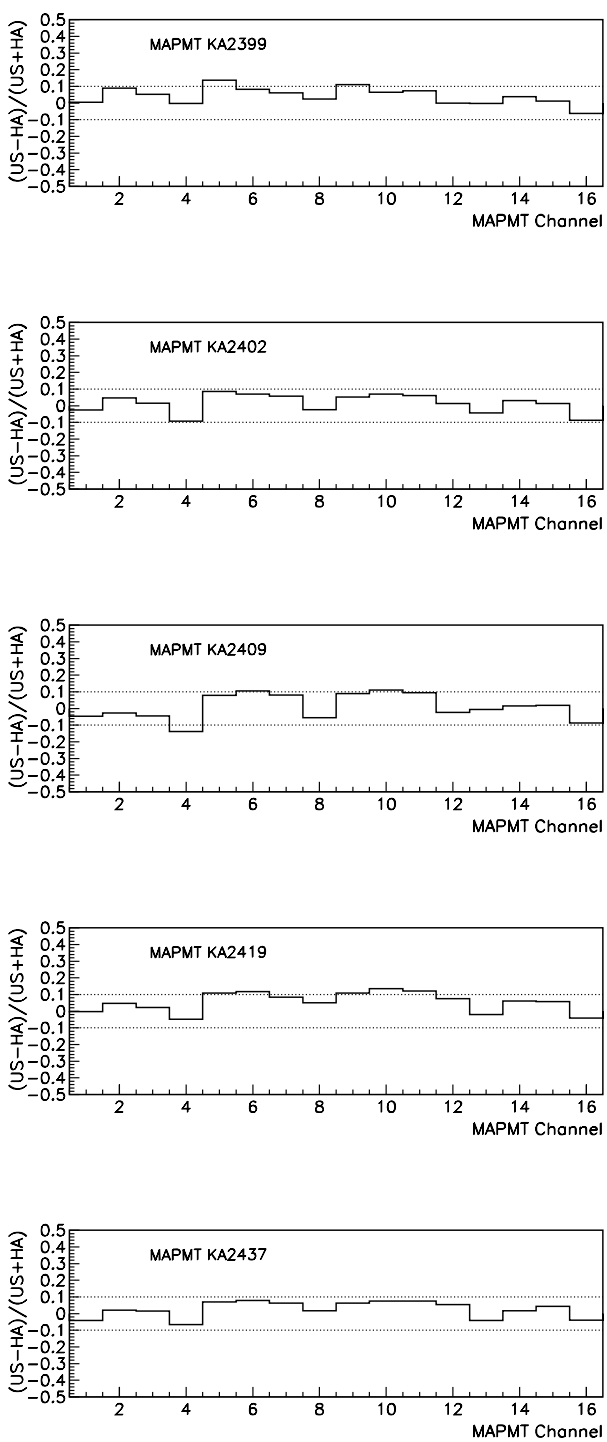

Figure 5.17: Our bench measurements (US) are compared to the Hamamatsu specifications (HA). The dashed lines in the plot correspond to a relative variation of ±10%.

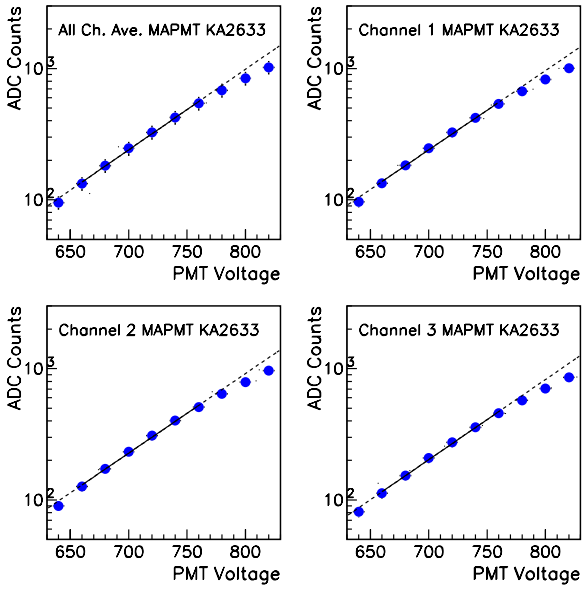

Figure 5.18: The average ADC counts are plotted as a function of the MAPMT voltage for all the channels and individually for the first three channels of the MAPMT. An exponential fit has been performed on six data points between 660V and 760V.

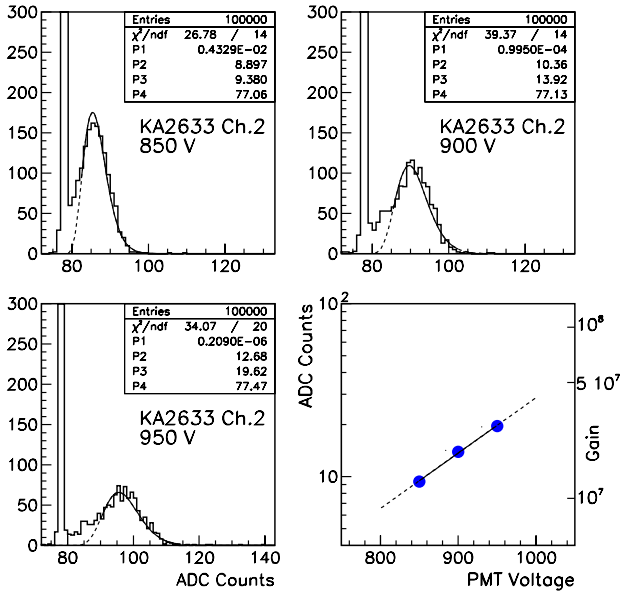

Figure 5.19: Single photoelectron response of one channel (ch. 2) of MAPMT n.KA2633 at three different voltages. The data are fitted with a *Polya distribution*, $P(m) = [m(mG/G_0)^{m-1} \cdot e^{-mG/G_0}]/\Gamma(m)$. The parameter $p3 = G_0$ corresponds to the pulse height for single photoelectrons.

light that less than one anode pulse occurs per hundred light pulses. The ratio $P(n_{k,i} > 1)/P(1)$ is then less than $5 \cdot 10^{-3}$.

Therefore the LED light in our test stand has been attenuated at the level of having less than 1,500 anode pulses out of 100,000 light pulses. In order to separate the single photoelectron peak from the pedestal, the MAPMT has been operated at high voltage/gain. Three measurements at 850V, 900V and 950V respectively, showed a linear shift of the single-photolectron peak.

The distributions in fig. 5.19 are fitted with a *Polya distribution*, i.e.

$$P(m) = \frac{m(mG/G_0)^{m-1}}{\Gamma(m)} \cdot e^{-mG/G_0}$$

which is appropriate for describing single photoelectron pulse height distributions. In the fits in fig. 5.19, $p1$ is the normalization constant, $p2$ the parameter m, $p3$ the parameter G_0, and $p4$ the pedestal mean value.

At 950V the MAPMT became somewhat noisy and the single photoelectron peak much broader.

As a cross-check of what mentioned above, fig. 5.20 shows the response of the same channel of the MAPMT n.KA2633, but now with more light resulting in a smaller (pedestal signal)/(anode signal) ratio. The contribution from two or more photoelectrons is visible in the tail of the distribution, especially at higher voltage. However, the position of the single photoelectron peak did not move much.

Cross talk studies were also performed. The cross talk deserves careful treatment as it may affect both the pattern recognition and the energy reconstruction. Analysis of this effect will provide an important gauge for MAPMT testing and calibration.

This is a two-fold effect and includes the effect of light leaking from the fibers into the neighboring channels. In addition, there is another source of cross talk from the electrons traveling down the dynodes and spuriously hitting the neighboring channels: we will call this "electronic" cross talk.

We pulse individual fibers by masking all other fibers with black tape and determine the signal leakage to the neighboring pixel in one of the MAPMT. We then rotate the MAPMT by 180 degrees relative to the light source to determine the source of the cross talk. The signal leakage is about 1.5–2.0% to each of the four neighboring pixels. This includes the

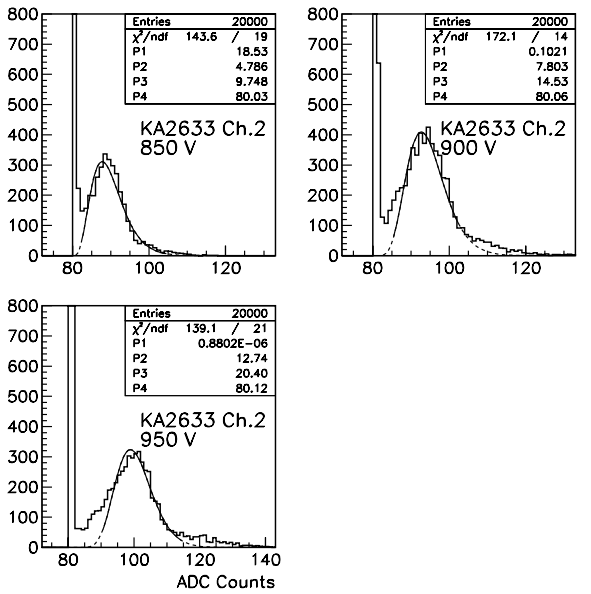

Figure 5.20: Single photoelectron response of one channel (ch. 2) of MAPMT n.KA2633 at three different voltages. With more light it is now possible to see the contribution from more than one photoelectron in the distribution tail.

Parameter	description/value
Window material	borosilicate
Quantum Efficiency	13%
Anode dark current	1 nA
Linearity	0.5 mA
Cross–talk	1%
Anode Uniformity	1:3
Photocatode material	bialkali
Spectral Response	300 to 650 nm
Number of stages	12
Anode	array of 4×4
Pixel Size	4 mm × 4 mm
Maximum High Voltage	1000 Volts
Rise time	$\leq$ 1 nsec

Table 5.1: Specifications of the R-5900 16–channel MAPMT produced by Hamamatsu.

"pedestal value" of a few counts. After we subtract the pedestals as derived from the "far–away" channels, we measure a signal leakage of about 6% into the four neighboring channels. The result does not change when we rotate the MAPMT by 180 degrees. The result is consistent with the "electronic" cross talk of $\sim$ 4% indicated in the specifications from Hamamatsu. In Table 5.1 the cross talk is $\sim$ 1% per channel.

5.2.6 Detector Prototype Test Results

Prototype modules have been constructed at both Argonne and Pisa using the 2 cm thick scintillator produced by Dubna. Grooves have been cut in eight tiles of this scintillator by Fermilab Lab 8, and a six-tile 1-tower module has been constructed and tested at ANL. The tiles were wrapped in Tyvek. In Pisa, nine tiles of a second sheet of this scintillator have been cut and grooved and tests are beginning on these as well. In neither case have the ends of the fibers been mirrored, nor have the WLS fibers been spliced to clear fibers upon exiting the tile. Therefore the current preliminary results on light yield should be considered a lower limit.

The ANL tests have used the same Cesium source mapper used for those Minos production modules built at ANL. The six tiles had 4 different configurations of groove depth and numbers of loops of fibers within the groove. All six tiles worked well in the scan, but two of the tiles were not able to be completely covered by the range of the source mapper in it's current configuration. Therefore in Figure 5.21 we present the results for the four tiles that were completely scanned. The x-axis is the source position in arbitrary units, the y-axis is a number proportional to the phototube current, corrected for relative phototube gains. The top figure shows the two tiles that had 4 mm grooves and three loops of fibers, while the bottom figure shows the two tiles that had 2 mm grooves and only one loop of fiber. The three loop tiles had a response a factor of 1.5 larger than the one loop tiles, therefore the baseline design for the preshower detector is to use three loops. Within an individual tile, a bow shape is normally seen in the response due to increased response around the fiber itself. This is very consistent with what is seen in the CDF EndPlug calorimeter. Tile 1 was a special corner tile, and the left side of its response was reduced by extra material in the corner of the module absorbing photons before detection, thereby not giving the expected bow-shaped response. Overall uniformity is quite good between tiles 3 and 4 (better than 5%), and also between tiles 1 and 2 although tile 2 has an average response 10% lower than tile 1. The cause of this is under investigation. But since tiles are easily calibrated in-situ with both cosmics and MIPs,

and will be completely mapped before installation, a 10% variation among tiles is easily corrected for if it remains in the production modules.

The absolute light output from MIPs cannot be directly measured from this photon source, but an important relative determination can be made. The production Minos modules are known to produce 12 photoelectrons/MIP at the detector location where the attentuation length effects of the fibers are minimal. Immediately following the CPR tests a Minos module was mapped, and the response of this Minos module using the same teststand and phototube was 1/2 of the CPR. Since the scintillator for the CPR is twice as thick as Minos, we expect twice the current in the CPR if the response/MIP is the same between CPR and Minos. Therefore our best estimate of photoelectrons/MIP from the ANL tests is 12. Cosmic ray tests at ANL are being setup.

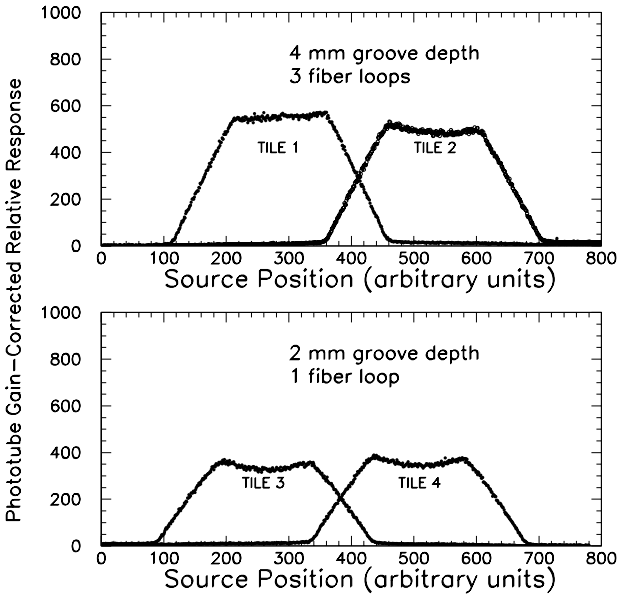

Figure 5.21: Source scan of four tiles of the 6-tile preshower prototype assembled at ANL.

The Pisa setup is a cosmic ray teststand, and the first MIP peak from a CPR prototype is shown in Figure 5.22. This was taken with a WLS fiber from PoliHiTech that was 50 cm long, and with only one loop in the tile. Optical grease was used to improve the contact between scintillator and fiber. The peak response indicates 11 photoelectrons/MIP, consistent with the ANL result but achieved in a different way. Given these results, and the fact that other known improvements to light output have not yet been implemented at either ANL or Pisa such as mirrored fibers, it seems clear that the specification of 6 photoelectrons/MIP will be easily achieved.

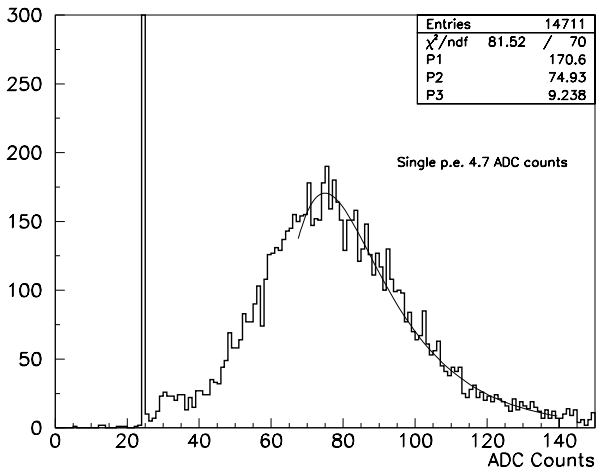

Figure 5.22: Cosmic ray MIP peak from the Pisa prototype.

5.2.7 Summary

The CDF Central Preshower and Crack detectors are playing an important role in RunII physics, and will be upgraded with a scintillator replacement to maintain and enhance its capabilities. The research and development program is well underway at four institutions in the U.S. (FNAL,ANL,MSU,Rockefeller), two institutions in Italy (Pisa and Rome), and at the University of Tsukuba in Japan. The design choices have been made to minimize cost and technical risk.

5.3 Electromagnetic Calorimeter Timing

5.3.1 Introduction

The CDF Collaboration plans to add timing information into the readout of the central and plug electromagnetic calorimeters (CEM and PEM) for Run IIb using a technique similar to the hadron TDC (HADTDC) system[1] [1, 2]. This upgrade, known as the EMTiming project, would significantly improve the potential of the CDF detector to do high-P_T searches for new physics in data samples with photons in the final state in two crucial ways:

1. It would reduce the backgrounds due to cosmic ray and beam halo sources and improve our sensitivity for important and difficult searches such as Supersymmetry (SUSY), Large Extra Dimensions (LED), anomalous couplings in $W\gamma/Z\gamma$ events etc.;

2. It would provide a vitally important handle that could confirm or deny that all the photons in unusual events, such as the $ee\gamma\gamma\not\!\!E_T$ candidate event [3] (see Figure 5.23) or in the CDF excess of $\ell\gamma\not\!\!E_T$ events [4], are from the primary interaction.

Additionally, with enough calibration data, the timing information would give us the possibility of searching for very long-lived particles which decay (1-10 nsec) into photons (for more detail see [1] and references therein).

5.3.1.1 Overview

Timing information from the calorimeter readout has been a part of the CDF detector since it was first commissioned in 1985. The HADTDC system in particular has been a powerful tool to help reject coarse backgrounds from cosmic rays and other non-primary interactions such as beam-gas or main ring splash. Adding timing information to the readout of the CEM and PEM has been suggested periodically over the years as well, but was not seen as necessary for the primary physics goals of the collaboration.

However, since the observation of the $ee\gamma\gamma\not\!\!E_T$ candidate event and the end of Run I, there are many

[1]For more information on this project please visit http://hepr8.physics.tamu.edu/hep/emtiming/

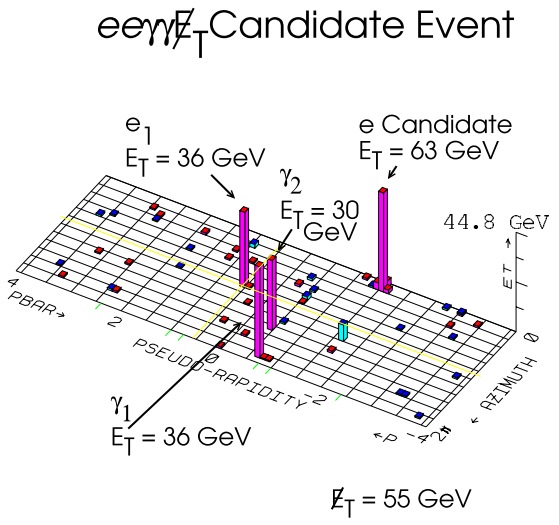

Figure 5.23: A LEGO display of the Run I CDF $ee\gamma\gamma\not\!\!E_T$ candidate event.

new and important search channels which were not envisioned when the detector was originally built. For example, there is now an enormous amount of interest in new models of SUSY, LED, Higgs decays, and other theories which encourage searches for anomalous events with photons, and in many cases photons and $\not\!\!E_T$. From the earliest days of the models, and in many cases as part of their creation, CDF has played a central role. Despite the fact that the detector was not optimized for these searches, there are a number of analyses which either have been published in PRL/PRD, or will be submitted in the near future [3, 4, 5, 6, 7].

From an experimental stand point, it is now clear that timing information for each photon could play a major role in any discovery. The primary reason for this is that in each search cosmic rays or beam related backgrounds can interact with the detector and produce an additional photon and associated $\not\!\!E_T$ which is unrelated to the event. Timing information would go a long way to reduce these insidious backgrounds and give us a vital handle that each photon in the event is from the primary interaction. For example, in the Run I search for SUSY and LED in the $\gamma + \not\!\!E_T$ channel, cosmic ray backgrounds dominate all other SM backgrounds by a factor of 2 [5]. Figure 5.24 shows the E_T^γ distribution of the data and the background predictions from cosmic rays. Unfortunately, it is very difficult to reduce these backgrounds as there are striking similarity between the distribution of the identification variables for photons from real events

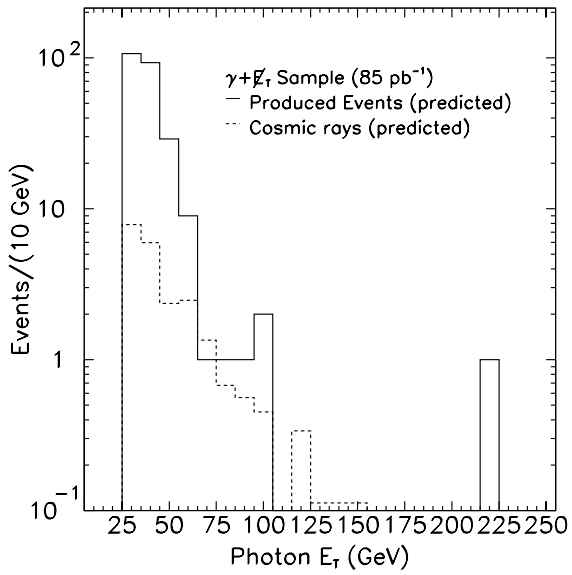

Figure 5.24: A prediction of the produced number of events in the data in 85 pb^{-1} in the $\gamma + \not\!\!E_T$ channel. Here we have folded out the HADTDC efficiency for all E_T^γ. The dashed line shows the contributions from cosmic rays.

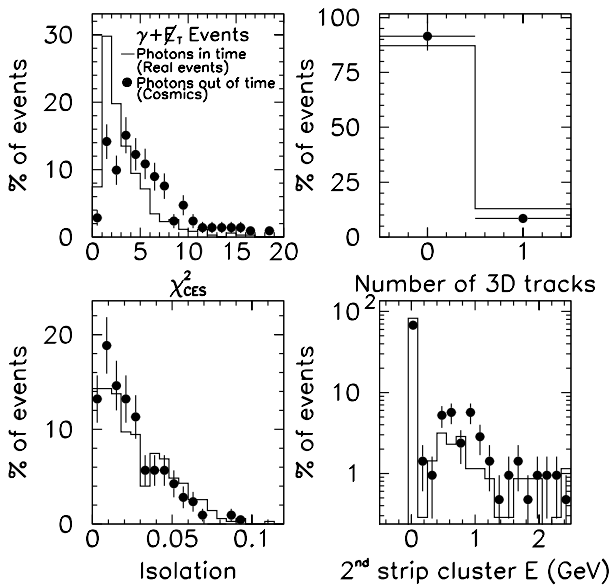

Figure 5.25: A comparison of the identification variable used to identify photons in the data from cosmic rays and from photons from the primary collision. The two distributions are largely indistinguishable.

and those from cosmic rays. See Figure 5.25. For these reasons it is clear that powerful and efficient tools are required to reject this background.

One such tool is the time of arrival of the photon relative to the collision time. In Run I, we were able to use the small amount of leakage energy into the hadronic calorimeter to fire the HADTDC system. While this method is powerful, as detailed below, it is very inefficient for low E_T photons (with a strong E_T bias) and has a bias towards more impure samples (fake photons from jets have a larger probability of depositing more energy in the HAD than prompt photons, and thus have a larger probability of firing the HADTDC system). The EMTiming project would be fully efficient for both the central and plug Run IIb and have no such biases.

A second important point is that timing information would also provide a vitally important handle that confirms that all the photons in unusual events are from a real collision. While, the CDF $ee\gamma\gamma\not\!\!E_T$ candidate event [3] and the events in the CDF $\ell\gamma\not\!\!E_T$ excess [4] are perhaps tantalizing hints of new physics; currently the detector cannot tell us if all the photons in these events are even from the primary interaction. The EMTiming project would help answer this question and would thus go a long way to improve the robustness of any potential discovery.

We begin with the physics motivation for new particle searches and the theories which predict photons in the final state. We continue with a description of why adding the EMTiming project would make a major contribution and then briefly describe the hardware, cost, schedule and manpower requirements.

5.3.2 Searching for New Physics with Photons

The primary motivation for searching in photon final states is that the photon is likely to be a good probe of new interactions, particularly SUSY. More generally, its applicability is potentially far greater as it is the only one of the three $SU(2) \times U(1)$ gauge bosons that couples to both chiralities (L and R sectors *i.e.*, V vs. V–A or V+A) and is therefore more likely to couple to any new gauge sector. While the heavy vector bosons are also likely to couple, the photon has detection advantages over both W's and Z's as the final state particle. Photons have a better kinematic resolution and they do not suffer a sensitivity loss from branching ratios and momentum sharing between the decay products.

While final state photon searches have advantages, looking at events with photons and $\not\!\!E_T$ can have provide even greater sensitivity. There are very few stan-

dard model backgrounds which produce photons and $\not\!\!E_T$, allowing a fairly clean sample with the exception of one insidious background: cosmic rays. The bottom line is that there are a number of important and different types of searches for new physics that can be done with photons in the final state. The experimental hints from Run I, coupled with the large number of well-motivated theoretical models makes the photon final state a compelling place to look.

5.3.2.1 Theoretical Models

A large number of new physics models make a strong case that the prospects for discovery at the Fermilab Tevatron are excellent. The most well studied model is SUSY.

The two main SUSY breaking models which have recently come into favor, now predict photons in the final state. Super-gravity models [8] could produce events which decay down to neutralinos, N_2, such that the decay $N_2 \rightarrow \gamma N_1$ dominates, or $N_1 \rightarrow \gamma\tilde{G}$ [9]. In some gauge-mediated SUSY breaking models (GMSB) [8, 10, 11] all SUSY cascade decays can end in $N_1 \rightarrow \gamma\tilde{G}$, and all events have 2 photons and (some) $\not\!\!E_T$. The SUSY signals are of particular interest, as they provide a natural explanation for the $ee\gamma\gamma\not\!\!E_T$ candidate event.

Other important possibilities include:

- R-parity violating SUSY models with light gravitinos as the LSP [12];
- Grand unified theories which, for example [13], can produce heavy neutrinos which decay via $\nu_E \rightarrow \gamma n_E$;
- Composite models of quarks and leptons which, for example [14], produce excited leptons which can decay via $e^* \rightarrow e\gamma$;
- Models with new dynamics which, for example [15, 16], produce anomalous production of $W\gamma$ and $Z\gamma$ events;
- Models with LED [17] (or SUSY [18]) can predict the emission of electromagnetic radiation in Graviton or Gravitino production, respectively, producing events with the $\gamma\not\!\!E_T$ final state signature;
- Models of fermiophobic Higgs bosons [19] which can decay via $H \rightarrow \gamma\gamma$, often produced with heavy vector bosons.

5.3.2.2 Quasi-Model-Independent Searches

While there are a large number of theories that predict new particles which decay to photons, with or without $\not\!\!E_T$, a potentially far more powerful motivation is based on the idea that we have not yet correctly formulated the mechanism of electroweak symmetry breaking. This suggests that there is a good chance that the data will point the way first and perhaps the observations already noted are the first hints. There are now strong new techniques, the "cousins" methods, signature based searches and Sleuth [3, 6, 20], for making these types of exploratory searches both quantitative and systematic and we intend to use them.

5.3.2.3 Future Possibilities: Long-Lived Particles which Decay to Photons

It is possible that with enough time and calibration data ($W \rightarrow e\nu$) the system would allow for a new class of searches for long-lived particles which decay to photons. In a GMSB scenario where $\tilde{G}$ and N_1 are the LSP and NLSP, the $\tilde{G}$ mass is expected to be in the range between 1 eV/c^2 and 10^4 eV/c^2 [11]. This can lead to an N_1 which can decay via $N_1 \rightarrow \gamma\tilde{G}$ with lifetimes of order (1-10 nsec). If we can calibrate the timing to be $\approx$1 nsec, the system should be powerful enough to study this class of models. The current HADTDC system has approximately 4 nsec of timing resolution [21]. The resolution possibilities are still under study [22]. The issues of how efficiently the photon identification will do with photons which originate from a displaced vertex will also have to be studied.

5.3.2.4 Physics Summary

To summarize, there is a compelling case to do physics with photons in the final state, and the EMTiming project would play a central role in reducing cosmic ray background and enhancing the robustness of any potential signal. Any set of Tevatron searches (SUSY, Higgs, LED etc.), must contain the $\gamma\not\!\!E_T + X$, $\ell\gamma\not\!\!E_T + X$, $\gamma b\not\!\!E_T + X$, and $\gamma\gamma\not\!\!E_T + X$ channels where the photons are promptly produced and vulnerable to experimental problems. In addition we expect that the robustness of the charged lepton channels of measurements of SM $W\gamma/Z\gamma$ will be enhanced by the EMTiming system. New channels such as $Z\gamma$ in the $\nu\nu\gamma$ channel may potentially open. Perhaps

with enough calibration data we can even search for long-lived particles that decay to photons.

5.3.3 The EMTiming Project

The EMTiming upgrade is similar to the HADTDC system in that both use the same hardware designs to record the time of arrival of any energy deposited in the EM and HAD calorimeters respectively. In Run I, the HADTDC system was used to find the 'timing' of those few photon candidates which have energy "leakage" out of the CEM and into the CHA [23]. This method is very powerful in separating backgrounds. Figure 5.26 shows a comparison of the timing in the HADTDC's for promptly produced particles and for cosmic rays. As shown in the figure, prompt particles have a distribution which is centered at the time of flight from the collision point to the calorimeter with a resolution of a few nsec. Cosmic rays are spread evenly as a function of time. Rejection of cosmic ray backgrounds using timing in the calorimeter clearly has excellent rejection power, and allows for a straight forward method of background estimation.

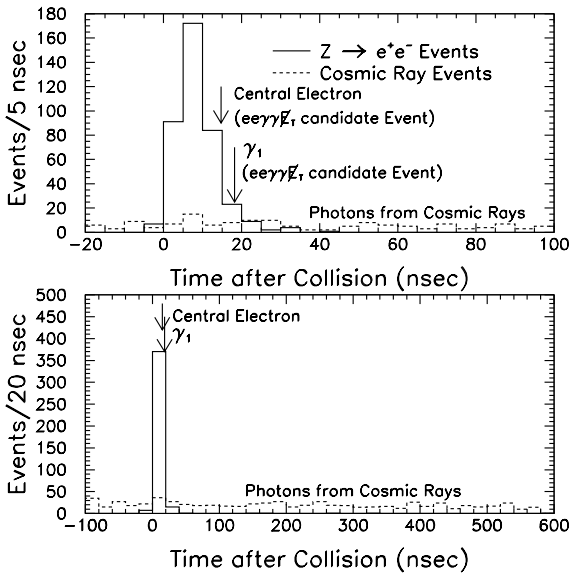

Figure 5.26: A comparison of the timing information for electrons from $Z \rightarrow ee$ and cosmic rays events using the central hadron calorimeter in Run I. Note that for true electrons the distribution is centered at the time of flight from the collision point to the calorimeter and that the unoptimized resolution is a few nsec. Cosmic rays are spread evenly as a function of time as expected. The arrows indicate the timing of two of the four EM clusters in the CDF $ee\gamma\gamma\not\!\!E_T$ candidate event. Only three of the four were in the central part of the calorimeter, and only two deposited enough energy to fire the HADTDC's with the photon just barely above threshold.

Unfortunately, even though many photons deposit some energy in the HAD, the efficiency of getting timing information is often not high. Figure 5.27 shows that the inefficiency in Run I is a strong function of the E_T of the photon; it has an efficiency of roughly 20% for $E_T^\gamma = 20$ GeV and a plateau around 100% above about 80 GeV, and was only instrumented for the central calorimeter. In Run II the PHA calorimeter is also instrumented and preliminary results for Run II are shown in Figure 5.28. Both CHA and PHA show an improvement over Run I as the central TDC energy threshold is lower, and the plug is now instrumented. However, the noise/activity in the plug requires a higher leakage energy threshold and has a larger inefficiency than the central for small E_T. In contrast, we expect that the EMTiming system would be fully efficient for all useful photon energies for both small and large η.

While the timing from the HADTDC system is clearly beneficial, the inefficiency is deadly in many standard analyses. To illustrate this, Figure 5.29 shows the kinematics from an ensemble of two photon events from Gauge Mediated SUSY model. The two curves in Figure 5.29 compare the expected number of timed events using the EMTiming and HADTDC timing (using Run I numbers) systems. From the figure, it is clear that it would not be a robust search technique to require all photon candidates in every $\gamma\gamma\not\!\!E_T$ event be timed using the HADTDC system. However, to make a numeric comparison, we note that the event yield would be doubled by the EMTiming system.

Another useful way to benchmark the additional sensitivity of the EMTiming system is to compare the event yield of standard model production of $Z(\rightarrow \nu\nu)\gamma \rightarrow \gamma + \not\!\!E_T$ events with and without the system. Results from SUSY and LED, modulo production cross sections and differences in mass scales, are comparable. Figure 5.30 compares the expected yield of timed events from the EM and HAD calorimeters for the central detector only (where the HADTDC system is most efficient). The mean photon energy lies in the region of low HADTDC efficiency and is falling exponentially. In the Run I $\gamma + \not\!\!E_T$ analysis [5], in order to make a robust search the E_T^γ thresholds were raised to 55 GeV where the HADTDC system is almost fully efficient. With the

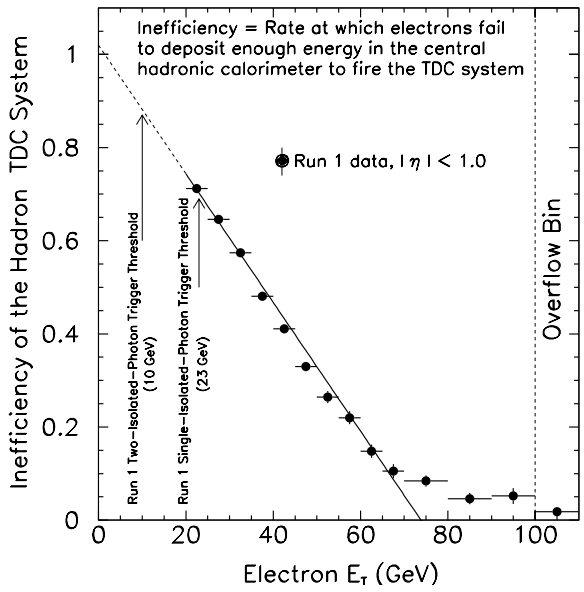

Figure 5.27: Inefficiency for electrons to have enough energy deposited in the hadronic calorimeter to fire the TDC's and be within the timing window for Run I. We assume that the efficiency for electrons and photons are equal since their shower characteristics are similar for the amount of energy deposition in the HAD. Note that the region to the right of the vertical dashed line is all events above 100 GeV.

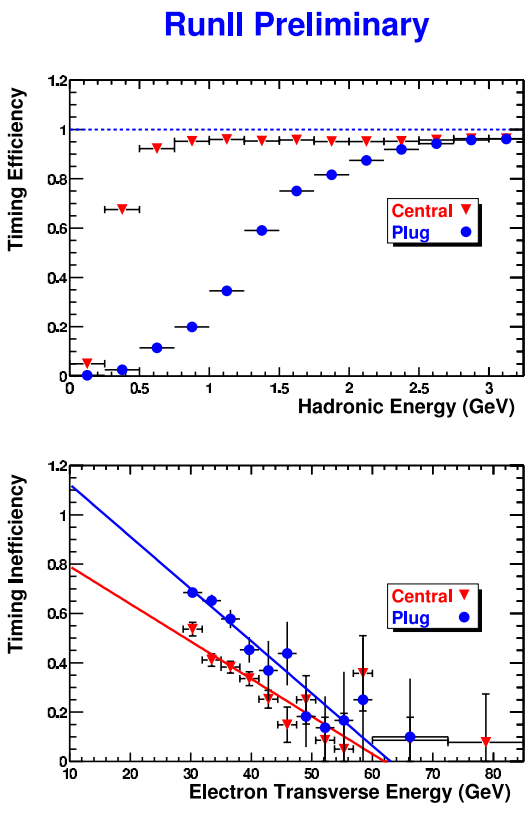

Figure 5.28: The Run II HADTDC timing efficiency. The top plot shows the efficiency to fire as a function of deposited energy in the CHA and PHA respectively. The bottom plot shows the inefficiency for electrons to have enough energy deposited in the hadronic calorimeter to fire the TDC's.

EMTiming system, we would be fully efficient for all events which pass the $\gamma + \not\!\!E_T$ trigger thresholds of 25 GeV each. Comparing the predictions above 55 GeV and above 25 GeV, we expect a factor of 30 improvement in event yield. Perhaps with enough data, we could do a measurement of $\bar{p}p \rightarrow Z(\rightarrow \nu\bar{\nu}) + \gamma + X$ in Run IIb. This process has the advantage over the $\ell^+\ell^-\gamma$ channel by a factor of 3 in the branching ratio, and almost a factor of 2 in the acceptance. We note that D$\emptyset$, which has a pointing calorimeter and has no such problems with cosmic ray backgrounds, has produced the dominant $Z\gamma$ measurement to date from the Tevatron by using the $\gamma\not\!\!E_T$ channel [24].

Using a SUSY scenario of $\tilde{G}\tilde{G}\gamma$ production, we estimate that the EMTiming system, and just lowering the threholds to 50 GeV, would improve the cross section limits in the $\gamma + \not\!\!E_T$ analysis by a factor of two over the HADTDC system alone. This improvement should improve the limits on $\sqrt{F}$ by 20 GeV. See Figure 5.31. Further improvements are possible, but will require a new analysis to reduce the next-most dominant backgrounds which were not previously considered.

5.3.3.1 Tell-tale Handles in Important Events

The efficiency loss in using the HADTDC's to do *a priori* photon physics searches is disappointing. However, *a posteriori* this inefficiency could undermine a potential discovery or cause an embarrassing mirage. The pressing nature of having a high efficiency timing measurement is illustrated in Figure 5.26 which also contains the timing for the two electron and two photon candidates in the $ee\gamma\gamma\not\!\!E_T$ candidate event. Three of the four objects were in the central calorimeter and the other in the plug. *A priori*, from the kinematics of the two photon and electron candidates, we expected 1.4 of them to fire the HADTDC system (there was no timing in the plug so there was no possibility for the PEM cluster). The data fluctuated in our favor and two of the four deposited enough energy in the HAD to fire the

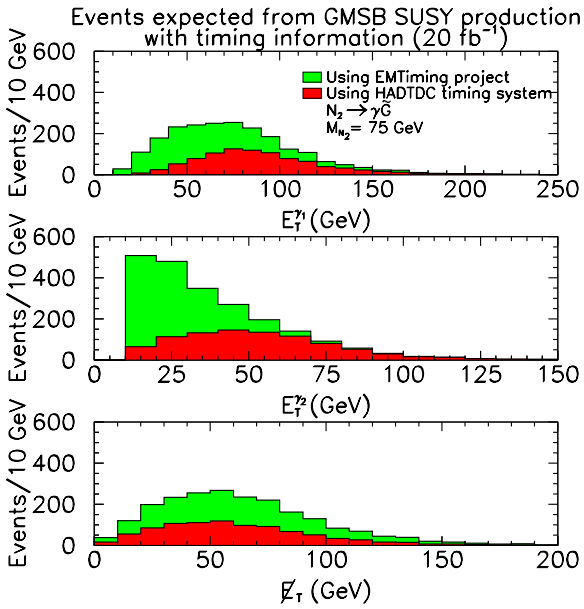

Figure 5.29: Histograms of the distributions of photon E_T and $\not\!\!E_T$ in a gauge-mediated model of SUSY [3]. The light shaded histogram shows the predicted signal with timing information available in electromagnetic calorimeters. The dark shaded histogram shows the predicted signal with no timing available from EM calorimeters.

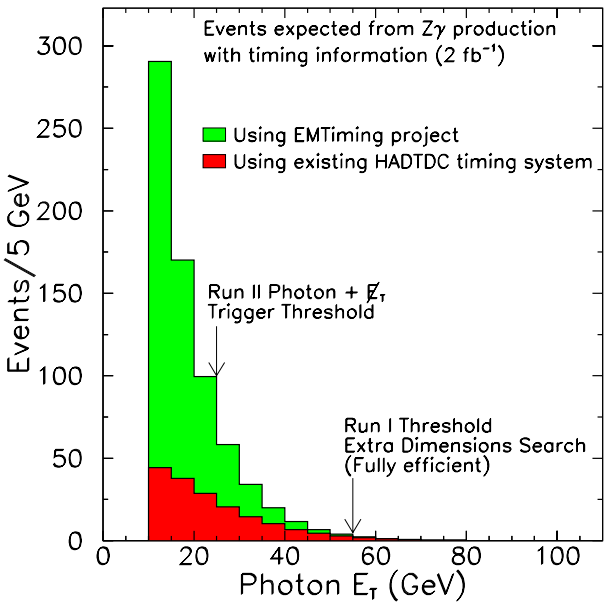

Figure 5.30: The prediction for the photon E_T spectrum from $Z\gamma$ events. The light and dark shaded curves shows the expected yield of timed events from the EMTiming and HADTDC systems in Run II. Note that the Run I $\gamma + \not\!\!E_T$ analysis required a photon E_T of 55 GeV. The $\gamma + \not\!\!E_T$ trigger threshold is at 22 GeV and reducing the kinematic requirement would increase the event yield by a factor of 30. One can also see that number of photons which would be timed from $Z\gamma \to \ell\ell\gamma$ which come in on the leptonic triggers would be even larger.

TDC's. We note that the photon was barely above threshold. The fact that both the electron and one photon are in time is actually quite an interesting result as it helps confirm that at least part of the event is from the primary collision. For Run II, even with the PHA timing, the efficiency of the plug is low (again see Figure 5.28) and the probability of tagging all four clusters is of the order of 5% as compared to the ≈100% for EMTiming.

The cosmic ray contamination to diboson events ($W\gamma/Z\gamma$) in the charged lepton decay modes is expected to be small, but can cause large disruptions. For many years, electroweak measurements of anomalous couplings in diboson production have been seen as fairly robust since the charged lepton has a strong handle from the tracking chamber. However, the recent CDF excess in the $\ell\gamma\not\!\!E_T$ channel has called this into question [4]. There is a serious worry that since the photon and any $\not\!\!E_T$ have no timing handle that the events are vulnerable to errors which affect both the counting experiments and the kinematic distributions. For example, a $W \to e\nu$ event with a cosmic ray would look like a $W\gamma$ event with anomalous $\not\!\!E_T$, and while the background estimates indicate that the contribution from cosmics is small, only about half of the photon events in the $\ell\gamma\not\!\!E_T$ sample had timing information in them. Similar problems could occur in $Z \to ee$ events. An overlapping cosmic ray would give an $ee\gamma\not\!\!E_T$ signature, which has no significant direct SM backgrounds. Similarly, and perhaps more interestingly, with the large number of $W\gamma$ and $Z\gamma$ events expected in Run II, the possibility of observing a fake $e\gamma\gamma\not\!\!E_T$ event becomes daunting.

Using the HADTDC readout to infer that a photon is part of the primary collision also has systematic problems. For example, since the timing is based on the hadronic energy deposited, there is a bias toward photons which have more hadronic energy associated with it i.e., more likely to be a fake from a jet. A second more difficult problem, is that since it only takes a small amount of energy in the HAD to fire the TDC system (approx 50% efficient at 0.5 GeV), hadrons from the underlying event can cause the system to fire even if the primary photon does not. Thus, even in the $ee\gamma\gamma\not\!\!E_T$ candidate event the photon for which there is HADTDC timing information (γ_1 in

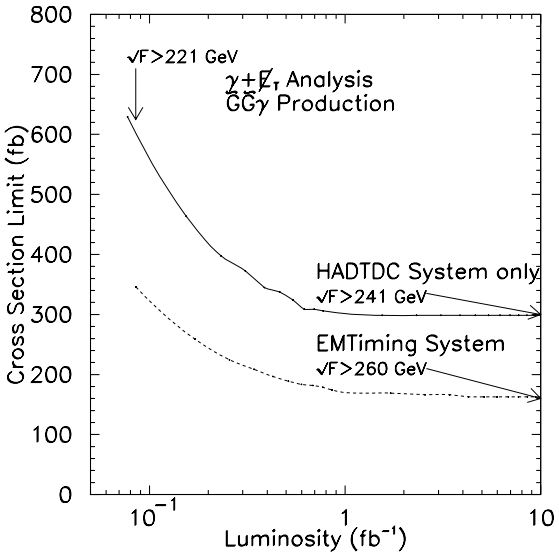

Figure 5.31: A comparison of the expected 95% C.L. limit on $\tilde{G}\tilde{G}\gamma$ production in the $\gamma + \not\!\!E_T$ channel using the HADTDC and EMTiming systems.

Figure 5.26), there is a finite probability that the photon is in fact out of time, but appears in time because energy from the underlying event fired the TDC. Preliminary studies suggest that about 5% of the time a cosmic ray which is out of time with the collision will have underlying event which will deposit enough energy in the HAD to fire the TDC system. The EMTiming system would be far less sensitive to such problems since we are firing directly on the large amount of energy deposited, and we can tune the threshold to be in the few GeV range.

While there are estimates as to the rate at which cosmics can contribute photons to an already existing event (and such estimates appear to be negligible [3]), it is clear that statistics are a worry in a sample of a few events, and an even greater worry in a sample of one event. Direct timing for both the CEM and PEM are, and would have been, of great benefit in these two important instances. We will never know if these events are due to an overlap. It is certainly possible that this type of problem could occur in the future and the EMTiming system would allow for all photon candidates (in both central and plug, for large and small E_T) to have the necessary timing information to negate this effect

5.3.4 Hardware, Cost, Schedule and Manpower

The hardware for this system is designed to mimic that of the hadron calorimeter TDC system as much as possible. However, we have made a small number of changes in an effort to minimize both the cost and the risk by making the entire system connectorized. This would allow us to recreate the the existing system and put it back exactly as it is today with minimal effort. Since there is no new technology in this design, we have not supplied a great deal of technical detail in this summary. More details can be found in Refs. [1, 2]. The path, which is illustrated in Figure 5.32, is:

$$\text{PMT/Base} \overset{\text{Cable}}{\longrightarrow} \text{Transition Board} \overset{\text{VME Backplane}}{\longrightarrow} \text{ASD} \overset{\text{Cable}}{\longrightarrow} \text{TDC} \overset{\text{VME}}{\longrightarrow} \text{Readout}$$

In this system the signal comes out from the phototube and collected with the tubes from the rest of the wedge on a transition board which is on the backside of a calorimeter readout VME crate. All the lines are passed through the VME backplane into an Amplifier Shaper Discriminator (ASD) which effectively turns the signal into an LVDS digital pulse suitable for use by a TDC. The signal is sent out of the front panel of the ASD, and upstairs to a TDC which is then readout into the event. Figures 5.33 and 5.34 show the individual components used in the CEM and PEM respectively.

Currently there are 960 CEM phototubes, none of which have a base that is compatible with readout for timing. To remedy this we are using a custom splitter to the CEM output [25] using low-cost, off-the-shelf components. The splitter itself is a fully passive element designed to be completely connectorized so that it may easily installed (or de-installed if necessary) in the system. Currently the CEM phototubes are readout using custom bases which have the anode connected to a 25' RG174 cable via a LEMO connector. The other end of this cable is soldered directly onto a transition board which is attached to the ADMEM system which integrates the charge to give a full energy measurement. The splitter is designed to be inserted directly into the PMT base, have the original LEMO/PMT end of the ADMEM line go to the primary output of the splitter (using a female LEMO connector on the splitter), and have the secondary (split) line go to an ASD transition

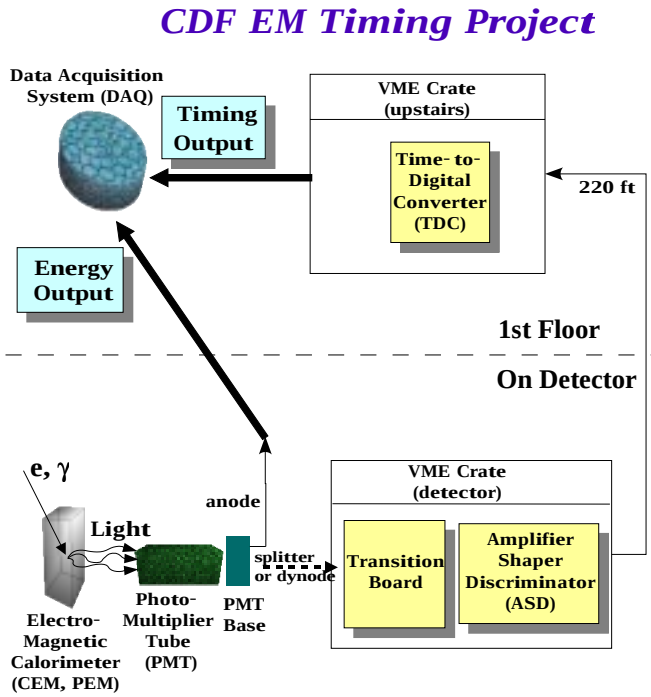

Figure 5.32: Layout of the EMTiming project.

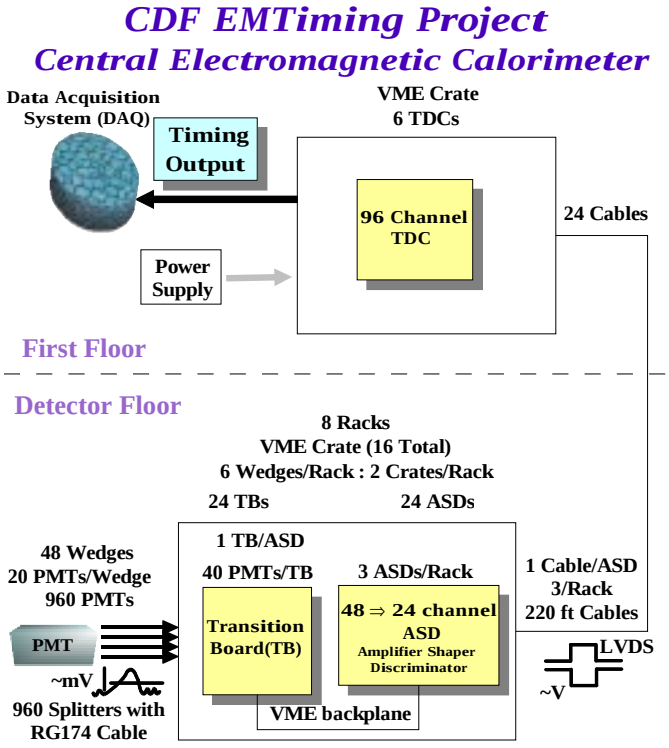

Figure 5.33: Layout of the central electromagnetic calorimeter components for the EMTiming project.

board for use in the TDC system. Figure 5.35 shows a circuit digram of the splitter and Figure 5.36 shows a photograph of a working prototype. The splitter works by inductively coupling the primary line (to the CEM ADMEM's) to the secondary output, and the grounds are not connected. The primary output loses a negligible amount of the charge which is used for the energy measurement and the secondary line only takes ≈15% of the output voltage for use to fire the ASD/TDC system.

There have been many tests of the splitter both on the test bench and on the detector itself. Figure 5.37 shows an oscilloscope picture of signals from a test bench and using a signal generator. From the figure, there is no discernable difference between the input shape and height before and after inserting a splitter into the system. Testing the splitter with an ADMEM shows that the amount of charge collected is the same for all tested energies. Figure 5.38 shows an example of the ADC counts with and without a splitter with a pulse height corresponding to of approximately 40 GeV. Figures 5.39 and 5.40 show similar results with and without a splitter for pedestal and readout values using the LED calibration system in-situ on the detector. The splitter shows no effect on the readout other than to shift the signal arrival time at the ADMEM by ≈1 nsec.

As a test of the efficiency and noise on the split signal, we find that for energies high relative to the ASD threshold that the splitter fires the ASD/TDC system with 100% efficiency at just above 1 nsec resolution, see Figure 5.41, with resolution dominated by the 1 nsec TDC resolution. There is no evidence of mis-firing[2] of the TDC or extra energy deposited into the ADMEMs from the splitter. This is shown in Figure 5.42 which shows the number of times the TDC fires around the LED firing. The full chain from CEM PMT all the way to the readout of the TDC has been established on the detector in-situ, proving that the system works as expected.

The PEM also has 960 phototubes, however those bases already have a dynode output designed into the base, so no modification is required. This system will look virtually identical to the HADTDC system except instead of having the cables soldered to the ASD transition board, we will use LEMO connectors to make cable installation easier and decoupled from

[2]We note that preliminary studies have no mis-firings in any of our LED tests. This means that at 95% C.L. there is less than a 0.1% chance in 132 nsec that the TDC will mis-fire due to spurious noise picked up by the splitter.

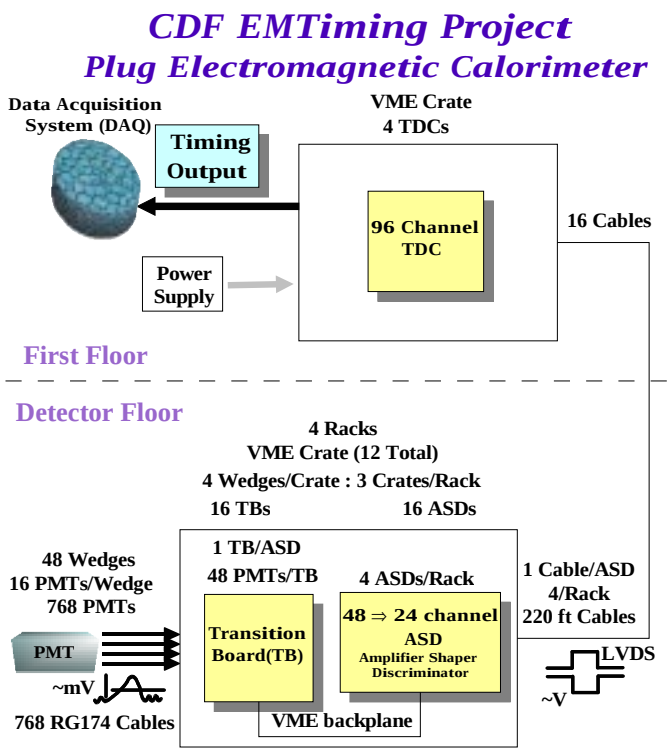

Figure 5.34: Layout of the plug electromagnetic calorimeter components for the EMTiming project.

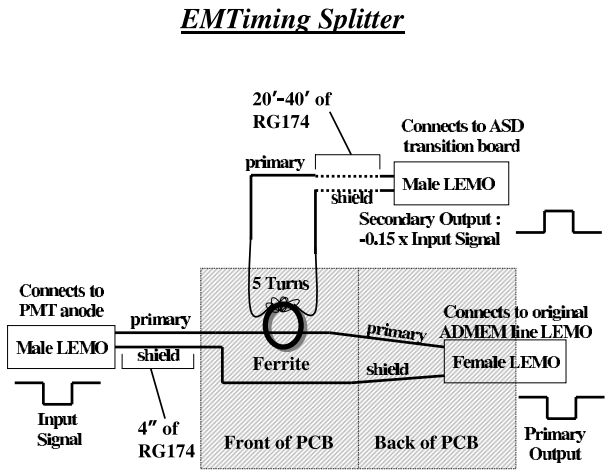

Figure 5.35: A circuit diagram of the EMTiming splitter for the central calorimeter.

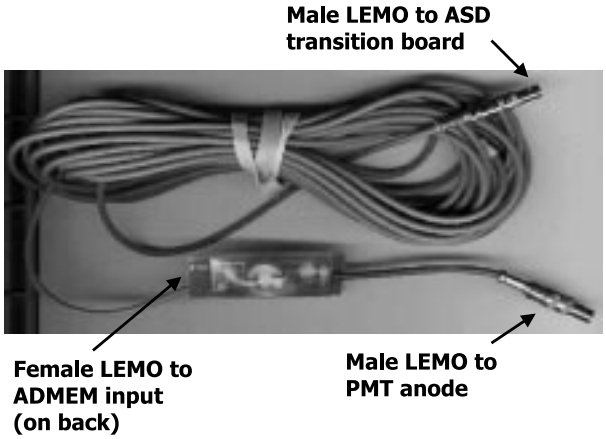

Figure 5.36: Photograph of a working prototype EMTiming splitter for the central calorimeter.

the ASD/TB installation. This will also make testing and debugging easier. We are only instrumenting the 768 towers with the smallest η as this significantly reduces the number of cables and boards in the system.

The electronics requirements are similar to those for the HADTDC system. The equipment needed includes 40 Transition boards, 40 ASD boards, 10 TDC boards, a TDC crate, and around 2000 cables. The parts are detailed in Table 5.2. No new technology needs to be researched or developed. Everything re-uses equipment or designs. Working prototypes of the splitter harness exist and in tests have functioned as expected. Prototypes of the PEM cable harness, which is simply RG174 with LEMO and AMP connectors are in progress and are following the existing designs which are currently being used in the PHATDC system. New boards with the same ASD design are being produced. New transition boards are being built with virtually identical layout to those used in the WHA except instead of 36 channels they take in 48 channels. The long cables from the ASDs on the detector floor to the TDC on the first floor are identical to those used in HADTDC system for the short stretch from the TDC patch panel to the TDC, except that they are 220 feet in length. We have chosen these cables since we do not have the same cable to cable slewing requirements in the trigger, nor the muon system routing requirements, and this allows us to use these cheaper, lighter, more flexible cables which also contain three times as many lines per cable. Prototypes of these cables have been bench-tested using the same LVDS driver/receiver chip sets on the ASD/TDC boards and the same output signals from the ASD's. Overnight tests have been shown to have 100% efficiency, adequate sample and hold times, and only add ≈25 psec of jitter to the timing resolution which is comparable to the system in use. The TDC's which are currently in the existing system are being replaced, and we are recycling 10 from the currently existing pool. The TDC

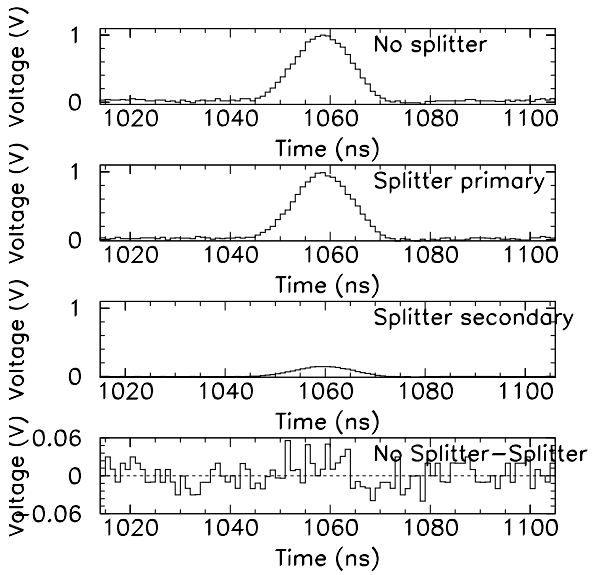

Figure 5.37: Scope results for the EMTiming splitter for a 1 volt input pulse from a signal generator. The top plot shows the generator directly into the scope. In the next plot a splitter is used and the distribution is taken from the primary output, with the secondary output shown in the following plot. The splitter and no-splitter outputs are virtually identical as shown in the difference plot which is on the bottom.

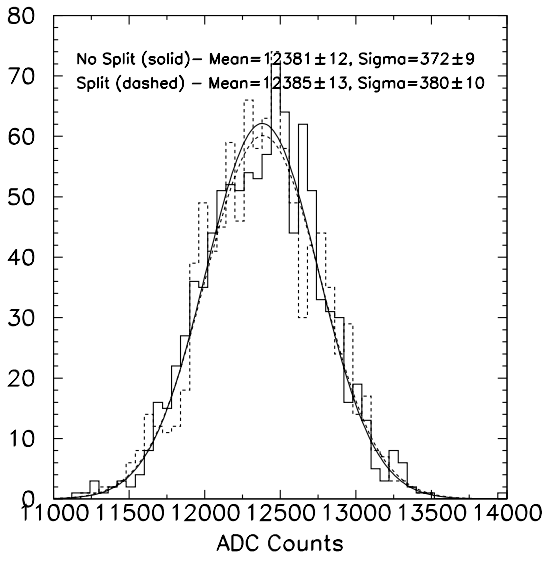

Figure 5.38: The charge deposition in the ADMEM, measured in ADC counts, with and without the EMTiming splitter for a PMT pulse corresponding to about 40 GeV on a test bench. Both the means and widths are identical within statistical errors. Similar results for other energies can be found in Ref. [2].

crate and Tracer will be taken from spares with the power supply and crate processor purchased off the shelf.

5.3.4.1 Work Required Prior to Start of Run IIb

There are several tasks that need to be completed before the beginning of the Run IIb shutdown. The parts for the splitters and PEM cables must be procured, and harnesses for both assembled. The transition boards and ASD's will need to be built. The ASD→TDC cables will need to be purchased. We will re-use the existing TDC boards, and the TDC crate parts will be recycled or purchased off the shelf. All the work above, including the upstairs TDC crate, can be done ahead of the Run IIb shutdown so that the only installation work that needs to be done during the shutdown is inserting the ASD/TB into the existing crates and running the cables. This will allow adequate time for testing. We note that we have many of the parts already in hand, most having been recycled, and many of the rest of the small parts are off-the-shelf items which are either in stock or have short lead times.

5.3.5 Summary and Conclusions

To summarize, the EMTiming project will augment the readout of the central and plug electromagnetic calorimeters for Run IIb to include timing information by adding hardware similar to that in the existing HADTDC system. This upgrade would significantly improve the potential of the CDF detector to do physics in samples with photons in the final state in two main ways: 1) It would reduce the cosmic ray backgrounds for important and difficult searches and measurements in a way which allows for significantly lower E_T^γ thresholds, larger η acceptance and with a flat efficiency as a function of E_T; 2) It would provide a vitally important handle to help confirm that all the photons in unusual events, such as the $ee\gamma\gamma\not\!\!E_T$ candidate event, are from the primary interaction. With sufficient calibration data, there is even the possibility of searching for very long-lived particles which decay into photons.

In Run II, even with twenty times the data, in the case that we do see a statistically significant excess of such events, it is still likely to be at relatively low statistics and we will need all the background rejection we can get. Furthermore, as in the case for the

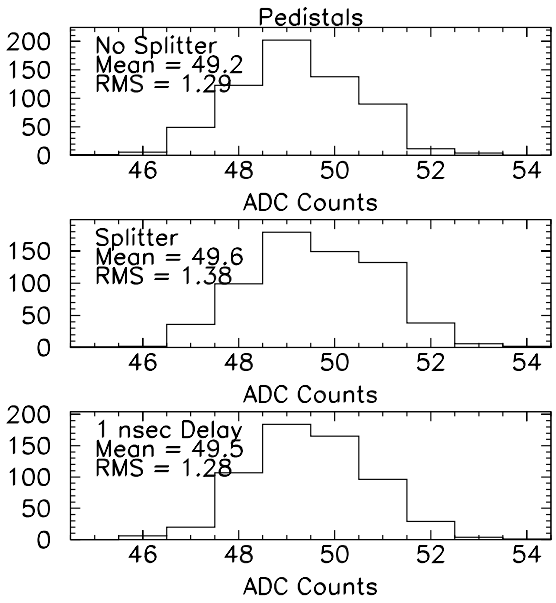

Figure 5.39: The number of ADC counts as measured by a CEM PMT/ADMEM combination on the detector using LED pedestal runs. The top plot shows the results for no splitter, the middle plot for the splitter and the bottom plot for a 1 nsec delay to take into account systems present timing window settings. As expected there are negligible differences between them.

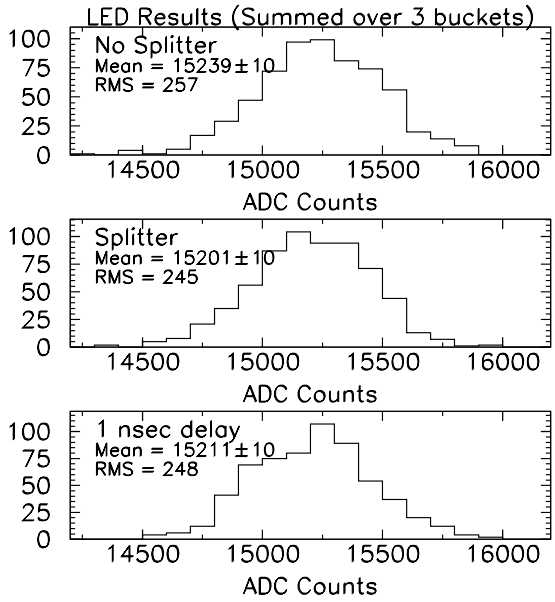

Figure 5.40: The number of ADC counts as measured by a CEM PMT/ADMEM combination on the detector using LED data runs. The top plot shows the results for no splitter, the middle plot for the splitter and the bottom plot for a 1 nsec delay to take into account systems present timing window settings. As expected there is negligible differences between them.

$ee\gamma\gamma\not{E}_T$ candidate event, even the most lenient critics will want to see that on a case-by-case basis any unusual events containing photons (and especially those with $\not{E}_T$) are not due to cosmic ray sources. In these cases, with no model to guide the experimenter on ways to verify an explanation, timing information is crucial.

We believe that the significant physics prospects provide adequate justification for this project. There is no new technology which needs to be developed so there are virtually no technical risks. Ultimately, the bottom line is that for a modest cost we can significantly extend the discovery potential for certain types of new physics.

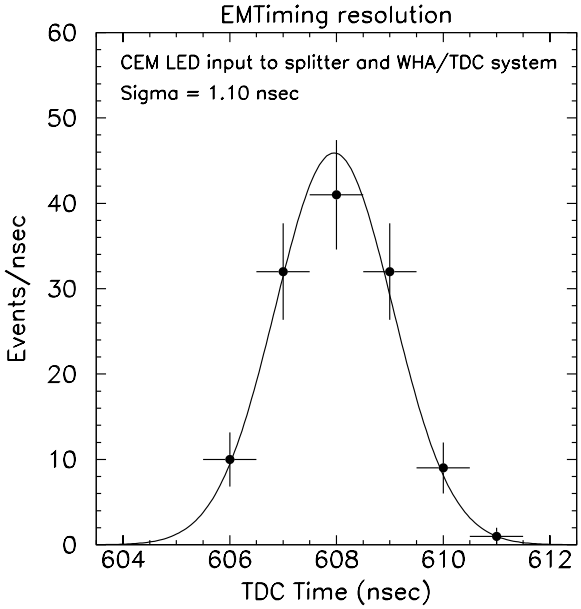

Figure 5.41: Measurement of the intrinsic timing resolution of the EMTiming System using the CEM LED's and a splitter hooked up into a WHA HAD TDC channel.

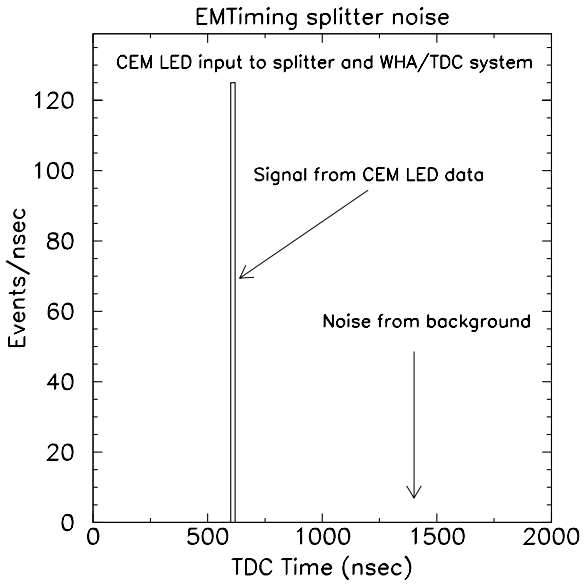

Figure 5.42: This plot shows the time of arrival distribution of the light deposited by the LED in the PMT of the CEM. We note that all the events are within about a nsec of each other, and that the TDC never fires otherwise. This shows that no noise is picked up by the splitter which might make the TDC fire.

CEM	main units	spares	Comments
Splitter Harness			
LEMO Cannon	960	96	EPL.00.250 NTN
RG174 cable	23,040ft	2,304ft	RG174→TB, ≈30 ft/cable
Male LEMOs	960	96	FFS.00.250.NTCE31
Lemo-ettes	960	96	FFS.00.250.NTCE31
Ferrite Torroid	1,200	120	Phillips TX/13/7.1/4.8-3E27
Wire, ties & shrink wrap	1	0	
Circuit boards	30	0	UC dwg A-2508, 40 splitter/board
Transition Board (TB)	24	3	
24 Channel ASD Board	24	3	
ASD→TDC cable	24	8	3M 3756/68,3M 10168-8100-EE
96 Channel TDC Board	6	1	
Crate	1		
Crate Power Supply	1		
Tracer	1		
Crate Processor	1		
PEM	main units	spares	Comments
PEM Harness			
M Lemo connectors	768	77	FFS.00.250.NTCE31
RG174 cable	17,664ft	1,766ft	RG174→TB, 23 ft/cable
Ferrule	1,000	0	AMP 1-332056-0
Socket	1,000	100	AMP 51565-1
20 pin Connector	96	10	AMP 201356-1
Housing	100	6	AMP 204087-1
Female Jackscrew Kit	100	6	AMP 200867-1
Male Jackscrew Kit	100	6	AMP 200868-1
Transition Board (TB)	16	2	
24 Channel ASD Board	16	2	
ASD→TDC cable	16	4	3M 3756/68, 3M 10168-8100-EE
96 Channel TDC Board	4	1	

Table 5.2: Parts list for the EMTiming project.

Bibliography

[1] D. Toback *et al.*, "Proposal to Add Timing Information Into the Readout of the Central and Plug Electromagnetic Calorimeters," CDF Note 5518.

[2] For more information on this project please visit http://hepr8.physics.tamu.edu/hep/emtiming/

[3] CDF Collaboration, F. Abe *et al.*, Phys. Rev. Lett. **81**, 1791 (1998) and Phys. Rev. D. **59**, 092002 (1999); D. Toback, Ph.D. dissertation, Univ. of Chicago (1997).

[4] CDF Collaboration, D. Acosta *et al.*, Phys. Rev. Lett. **89**, 041802 (2002) and Phys. Rev. D 66, 012004 (2002). J. Berryhill, Ph.D. dissertation, Univ. of Chicago (2000).

[5] CDF Collaboration, D. Acosta *et al.*, hep-ex/0205057, submitted to Phys. Rev. Lett.

[6] CDF Collaboration, T. Affolder *et al.*, Phys. Rev. D **65**, 052006 (2002).

[7] CDF Collaboration, T. Affolder *et al.*, Phys. Rev. D. **64**, 092002 (2001).

[8] S. Ambrosanio *et al.*, Phys. Rev. Lett. **76**, 3498 (1996).

[9] S. Dimopoulos, M. Dine, S. Raby, and S. Thomas, Phys. Rev. Lett. **76**, 3494 (1996).

[10] J. L. Lopez and D. V. Nanopoulos, Mod. Phys. Lett. A **10**, 2473 (1996).

[11] For example, see S. Ambrosanio, G.L. Kane, G.D. Kribs, S. Martin, and S. Mrenna, Phys. Rev. **D** 54, 5395 (1996).

[12] B. C. Allenach, S. Lola, and K. Sridhar, Phys. Rev. Lett **89**, 011801 (2002).

[13] J. L. Rosner, Phys. Rev. D. **55**, 3143 (1997).

[14] U. Baur, M. Spira, and P. M. Zerwas, Phys. Rev. D. **42** 815 (1990); E. Boos, A. Vologdin, D. Toback and J. Gaspard, Phys. Rev. **D** 66, 013011 (2002).

[15] A. D. De Rujula, M. B. Gavela, P. Hernandez, and E. Masso, Nucl. Phys. B **384**, 3 (1992).

[16] M. Baillargeon *et al.*, hep-ph/9603220 (1996).

[17] N. Arkani-Hamed, S. Dimopoulos, and G. Dvali, Phys. Lett. **B429**, 263 (1998).

[18] A. Brignole, F. Feruglio, M. L. Mangano, and F. Zwirner, Nucl. Phys. B **526**, 136 (1998); Erratum-ibid. B **582**, 759 (2000).

[19] H. Haber, G. Kane, and T. Sterling, Nucl. Phys. B **161**, 493 (1979); A. Stange, W. Marciano, and S. Willenbrock, Phys. Rev. D. **49**, 1354 (1994); M.G. Diaz and T. Weiler, hep-ph/9401259 (1994); A.G. Akeroyd, Phys. Lett. B **68**, 89 (1996).

[20] DØ Collaboration, B. Abbott *et al.*, Phys. Rev. D. **62**, 092004 (2000); DØ Collaboration, B. Abbott *et al.*, Phys. Rev. D **64**, 012004 (2001); DØ Collaboration, B. Abbott *et al.*, Phys. Rev. Lett. **86**, 3712 (2001).

[21] P. Onyisi, "Efficiency of central and wall hadron timing information for cosmic ray discrimination for Run 1," CDF Note 5460; M. Cordelli *et al.*, "Timing calibration of CDF hadron calorimeters", CDF Note 5856.

[22] D. Toback and P. Wagner, "Simulation of the Calorimeter Timing System," CDF Note 5866.

[23] S. Kuhlmann, "Timing Information For Central Photons and the ee$\gamma\gamma$MET Event," CDF Note 4256.

[24] DØ Collaboration, S. Abachi *et al.*, Phys. Rev. Lett. **78**, 3640 (1997). DØ Collaboration, S. Abachi *et al.*, Phys. Rev. D. **57**, 3817 (1998).

[25] H. Frisch, M. Goncharov, H. Sanders and D. Toback, "The CEM Timing Splitter", CDF Note in progress. For the latest version see Ref. [2].

Chapter 6

Run IIb Trigger & Data Acquisition Upgrades

6.1 Introduction

To cope with the higher luminosity of Run IIb, the CDF detector needs to upgrade several components of its front-end electronics, trigger and data acquisition system. The fundamental structure of the trigger and readout systems are unchanged from the existing Run IIa detector. The upgrades outlined here are required to handle the higher density environment, higher data rates, and larger data volumes provided by the Tevatron in Run IIb.

In this chapter, we outline five distinct projects designed to insure that the entire CDF detector will be fully efficient throughout Run IIb. These upgrades are discussed in the sections listed below:

- A time-to-digital converter (TDC) replacement for the Central Outer Tracker (COT) [Section 6.3].
- An upgraded fast track processor (XFT) [Section 6.4].
- An upgraded silicon vertex tracker (SVT) [Section 6.5].
- An upgrade of the Level 2 decision crate (L2) [Section 6.6].
- An upgrade to the event builder switch and Level 3 processor farm [Section 6.7].

Before specifying the details of these projects, we will outline the trigger and data acquisition needs of the detector in Run IIb.

6.2 System Requirements

In this section, we briefly outline the constraints imposed upon the CDF Run IIb front-end, trigger and data acquisition systems. Further details on the performance of the detector and the requirements on the trigger and DAQ system can be found in Ref. [1].

6.2.1 Luminosity Design Guidelines

As stated in Chapter 1, the baseline Run IIb accelerator configuration is 396ns bunch spacing, with the potential to move to 132ns operation. The design specification followed here is a maximum instantaneous luminosity of 4×10^{32} cm^{-2}s^{-1} with 396ns bunch spacing, corresponding to an average of 10 $p\overline{p}$ interactions per bunch crossing. In most cases, 132ns operation is implicitly allowed in our system. In the case of the XFT IIb system, specific provisions are made for 132ns bunch spacing that will be discussed in Section 6.4.

6.2.2 CDF Triggers for Run IIb

Trigger cross section estimates are important for establishing the operating requirements for the Run IIb system. The experiment will be devoted to high-p_T searches, including the Higgs boson and Supersymmetry. The trigger budget is estimated by extrapolating the relevant Run IIa trigger cross sections. This extrapolation is done over an order of magnitude in instantaneous luminosity, so some care is required in interpreting the results [2].

The trigger strategy will include high-p_T electrons and muons; missing energy triggers; multi-lepton triggers; and b-jet triggers. Although the benchmark for the Run IIb upgrades is the Higgs boson

search, discovery is by no means assured. It is imperative that CDF carry out a broad program of high-p_T physics, including detailed study of the properties of the top quark and searches for other possible new phenomena such as supersymmetry, technicolor, large extra dimensions, high mass gauge bosons, compositeness, and additional fermion generations. Here we summarize the Higgs triggers, followed by the triggers aimed at the rest of the high-p_T program.

In the following sections, we outline our baseline trigger strategy for Run IIb. The trigger cross section estimates are based upon a linear extrapolation from existing Run IIa data.

6.2.2.1 Higgs Searches

The search for a low mass Higgs Boson ($M_H < 135\,\mathrm{GeV}/c^2$) focuses on associated production of the Higgs with a W or Z. The dominant decay mode of the Higgs in this mass region is expected to be $b\bar{b}$, with $\tau\tau$ possible at large $tan\beta$. The trigger requirements depend on how the W or Z decays. If it decays into an electron or muon, we capture it with inclusive high-p_T lepton triggers. For Z decay into $\nu\bar{\nu}$, we trigger on $\not\!\!E_T$+ jets or on b-jets. In addition, there are a number of calibration triggers for measuring detection efficiencies, background rates, and energy scales and resolutions. Table 6.1 summarizes the rates for these triggers.

Trigger	Rates at 4×10^{32} cm^{-2}s^{-1}		
	L1	L2	L3
e/μ	2,327 Hz	250 Hz	22 Hz
ν	4,401 Hz	130 Hz	9 Hz
calibration	2,940 Hz	117 Hz	16 Hz
Total	9,668 Hz	497 Hz	47 Hz

Table 6.1: Summary of trigger rates for Higgs search triggers at $\mathcal{L} = 4 \times 10^{32}$ cm^{-2}s^{-1}. These triggers are important for many other high-p_T physics analyses.

6.2.2.2 Other High-p_T Searches

The triggers listed in Table 6.2 are needed to carry out a broad high-p_T physics program at the energy frontier. These are complementary to the triggers listed in Table 6.1.

Trigger	σ_{L1}(nb)	σ_{L2}(nb)	σ_{L3}(nb)
High-p_T jets	19,000	60	17
$t\bar{t}$ (all hadronic)	(overlap)	50	5
$\tau\bar{\tau}$	5,000	50	4
$\not\!\!E_T + \tau$	(overlap)	50	4
High-E_T photons	13,500	110	21
di,tri-leptons	1,000	190	45
Total	38,500	660	96
Total rate	15,400 Hz	264 Hz	38 Hz

Table 6.2: Summary of triggers necessary for the CDF Run IIb high-p_T physics program. The estimated rates shown are for an instantaneous luminosity of $\mathcal{L} = 4 \times 10^{32}$ cm^{-2}s^{-1}.

6.2.3 Summary of Trigger/Bandwidth Requirements

Based upon the trigger cross sections for the relevant high-p_T triggers in Run IIa, we project the Run IIb system to require: 25kHz of Level 1 accept rate, 750Hz of Level 2 accept rate and 85Hz of Level 3 accept rate at $\mathcal{L} = 4 \times 10^{32}$cm^{-2}s^{-1} with 396ns bunch spacing. Burst rates will be somewhat larger. As mentioned above, due to the limited luminosity in Run IIa to date, these estimates arise from linear extrapolations over a very large range.

The trigger rates, bandwidth and data volume requirements for the Run IIb CDF detector are the primary motivation for the upgrades discussed in the following sections. In each section, we describe the limitations of the existing system and our plan for alleviating these limitations through targeted improvements to specific pieces of the CDF trigger and data acquisition system.

6.3 TDC Upgrade

The Run IIa time-based systems (COT, muons and hadron timing) utilize custom TDCs constructed by the University of Michigan specifically for the CDF experiment. They are performing well in the Run IIa system, and are meeting their technical specifications in terms of performance. The Run IIa TDCs will continue to be adequate for the Run IIb muon and hadron timing systems, as well as the new electromagnetic calorimeter timing system.

In the case of the COT, the data volume will continue to grow as the luminosity increases. At Run IIb

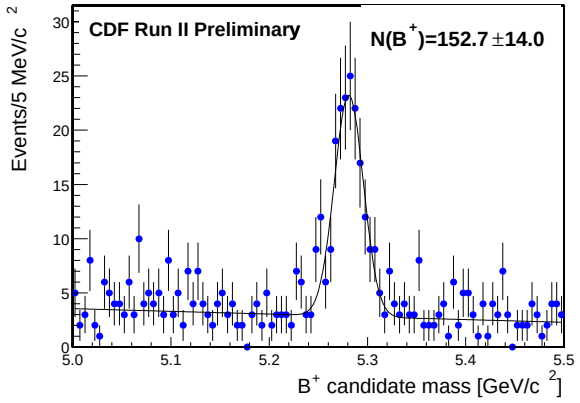

Figure 6.1: Fully reconstructed $B^{\pm} \rightarrow J/\psi K^{\pm}$ events. The 15.3 MeV/c^2 width is consistent with expectations for a well-aligned system with ∼1ns timing resolution.

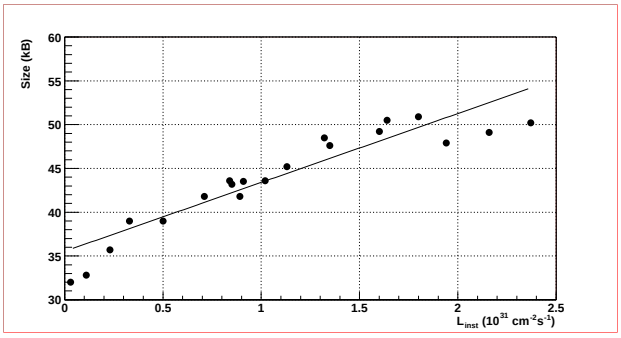

Figure 6.2: Average data volume produced by the COT as a function of luminosity as seen in Run IIa data. This plot is for a mix of random triggers. This data plus Monte Carlo have been used to extrapolate to Run IIb conditions.

luminosities, the current system will not be able to handle the data volume and data rate provided by the COT. In this section, we describe a replacement for the Run IIa time-to-digital converters (TDCs).

6.3.1 CDF Central Outer Tracker

For the Run IIa detector, a new open-celled drift chamber, the Central Outer Tracker (COT) was constructed. The COT has a superlayer structure, with 12 wire layers per superlayer. The 8 total superlayers consist of 4 axial and 4 stereo layers. The axial layers are utilized in the Run IIa Level 1 track trigger (XFT). The COT has a total of 30,240 sense wires. The cell geometry was constructed so that the maximum drift time is less than the beam crossing interval, so that pile-up is not a problem. In 396ns operation, an argon–ethane (50/50) mixture is used that provides a maximum drift time of ∼240ns. In the case that the Tevatron changes over to 132ns operation, the gas mixture will be changed to Ar:Et:CF_4 and the maximum drift time will be ∼110ns.

The chamber signals are processed by custom ASICs mounted directly on the chamber face. This ASIC, known as the ASDQ chip, performs pulse amplification, shaping and discrimination. The ASDQ additionally provides a width-encoded charge measurement that is used for particle identification by specific ionization (dE/dx). The discriminated signals are driven off the chamber face as differential LVDS signals to a series of repeater boards mounted on the detector endwall. The repeater boards drive the signals to the TDC boards which reside in VME crates mounted on the detector endwalls.

Each TDC board handles 96 wires, resulting in 315 TDCs in the COT system. These TDC boards are distributed over 20 VME crates. The Run IIa TDCs have 1ns time binning, multi-hit functionality and additionally provide signals for the Level 1 tracking trigger (XFT).

6.3.2 Performance of the Run IIa System

The Run IIa COT system is performing well. Tracks are reconstructed with very high efficiency and excellent momentum resolution. Figure 6.1 shows a reconstructed $B^{\pm} \rightarrow J/\psi K^{\pm}$ signal from Run IIa data. The measured mass depends upon properly calibrated detector material and magnetic field value, while the measured width depends upon chamber alignment and timing resolution. The width of the signal shown here is $15.3 \pm 1.7\,\mathrm{MeV}/c$, which is consistent with expectations based upon a well-aligned COT with ∼1ns timing resolution. Although we have not yet explicitly unfolded the alignment and timing contributions, this clearly indicates that the system is working well and very good timing resolution has been achieved.

6.3.3 Extrapolation to Run IIb

Even with current luminosities seen in Run IIa, a clear growth trend can be seen in the COT data volume. This can be seen in Figure 6.2 which shows the COT occupancy as a function of instantaneous luminosity. The architecture of the current system gives a rise in both data processing time and readout time as the occupancy grows. Readout rates at or beyond

300Hz can not be maintained at higher luminosities with the existing system due to [3, 4]:

- **TDC on-board data processing.** In the current system, processing is performed upon Level 2 accept. As the data volume grows, so does the processing time. Any significant processing time that occurs after the Level 2 accept results in system deadtime.

  In the case of the COT readout, the growth in data volume with luminosity translates directly into longer on-board processing time. Even below Run IIb luminosities, this on-board processing will affect system deadtime.

- **VME Readout.** Each TDC in the crate is read-out serially by VME block transfer. The readout time grows with data volume.

  The fundamental limitation to VME backplane transfer is less than 14MB/s. This bandwidth limitation is exceeded in Run IIb.

- **Data transfer.** The existing CDF readout structure brings the data through the TRACER via VME transfer and then to a TAXI link to the VRB. The TRACER→TAXI→VRB link will be unable to handle the data volume provided by the TDCs.

  The fundamental limitation to the TAXI link is 12MB/s. This bandwidth limitation is exeeded in Run IIb.

To summarize, the TDCs for the COT need to be replaced due to both deadtime and data transfer considerations. Even if the existing TDCs were deadtimeless, the existing readout architecture would not satisfy the Run IIb performance needs. The new TDC will address all of these issues.

6.3.4 Run IIb TDC Specifications

Based upon our understanding of the Run IIa COT and TDC systems, as well as the trigger and data acquisition requirements outlined earlier in this section, we have developed a detailed set of technical specifications for the Run IIb COT TDC system [5].

We outline a few of the primary specifications:

- The TDC boards must be fully compatible with the existing CDF data acquisition architecture
- The system must be able to handle burst rates of 50kHz Level 1 accept rate and 1.1kHz Level 2 accept rate, with deadtimeless Level 1 operation and less than 2% deadtime Level 2 operation.
- The readout time must remain below 500μsec for the anticipated Run IIb COT data volume,
- The TDC architecture must allow for significant on-board data compression.
- The TDC must deliver timing information to the Level 1 track trigger processor (XFT).

The muon, and calorimeter timing systems will continue to utilize the Run IIa TDCs throughout Run IIb. As stated above, the Run IIa TDCs are working well and will continue to do so in those systems.

6.3.5 TDC Technical Design

The new design satisfies or exceeds all of these specifications and will be built to be fully backward compatible with the Run IIa TDCs. This will facilitate testing and commissioning of the new system, and allow a staged approach to implementing all of the features of the new TDC.

6.3.5.1 Overview

The design of the new TDC is shown in Figure 6.3 and is primarily based upon the commercially available Altera Stratix FPGA. Some of the details of the technical design are provided in the following sections, here are the important points:

- The new TDC will be plug-compatible with the existing TDC. No changes to the COT input or XFT outputs will be needed. The existing CDF clock, TRACER and custom CDF signals will be retained.
- The actual time-to-digital functionality is performed with a commercial FPGA.
- The new TDC will be utilized in the COT system only.
- The hit-data is processed upon a Level 1 accept. This renders the deadtime of the TDC system insensitive to data volume, as the data processing is performed in parallel with the Level 2 trigger.

- Although the new TDC will support the existing CDF readout structure, it will additionally allow for a high speed readout path that will bypass the Tracer→TAXI link. The data will still be shipped to a VRB. This will be a changeover from non-SVX to SVX-style readout, although the readout will begin upon Level 2 accept.

6.3.5.2 Design

The Stratix FPGA family includes a number of features which make it well-matched to this application:

- high bandwidth (840 MHz) differential inputs (equivalent to 1.2ns binning.)
- ∼two megabits of configurable memory
- high speed logic performance
- moderate price

The Run IIa TDC is a 9U VME board that handles 96 channels per board. To maintain compatibility in cabling, signal inputs and front-end calibration needs, we will utilize 48 LVDS inputs per Stratix chip, with two Stratix chips per TDC board. The input signals from the COT are differential, constant-current LVDS pairs. In addition to the LVDS input to the chip, in internal multiplexer will select a choice between the COT signals and calibration signals from the TRACER. The Altera chip has internal termination resistors that will replicate the input termination used in the existing system. This minimizes connections required at the input pin area.

The input to the Stratix has a high speed deserializer which perfectly matches the application needed here. The deserialize factor is 10, meaning that the serial stream will be broken into to a stream of 10 bit parallel words. Since this deserialization is the actual analog-to-digital conversion on input to the Altera, the remainder of the system, including the routing of the FPGA is digital.

The clocking for the LVDS inputs will be driven with a global clock which will come from a master phase-locked loop (PLL) on the chip. A phase-locked loop synchronized to the CDF clock will multiply the frequency by 11. The 83.33MHz signal will drive the clocks of the LVDS inputs and the entire logic tree. The master PLL will have a frequency of 83.33MHz. Our requirement is to generate a clock at 10 times the 83.33 MHz signal to give a synchronous sampling period of exactly 1.2ns. Studies using Run IIa data of COT tracking indicate that 1.2ns time binning yields a negligible contribution to resolution.

Two 10 bit shift registers are placed immediately after the words are first formed to source the signals to a majority logic block which generates trigger data for the XFT, discussed in the following section. The data then enters a holding buffer which is a two port memory with 512 locations. The chip global address for this function is a simple counter. The read port is generated as an programmable offset from the write address. This serves as a delay to wait for the time of the Level 1 accept.

Upon Level 1 accept, the data is written into one of four selected Level 2 buffers, each having a range of 384ns. The address generators for these memories are also chip global. There are two sets of Level 2 buffers, one to handle the data as it is copied from the input buffer, and a second one that holds the data after edge-detection has been performed. There are four copies of the two types of Level 2 buffers to conform to the CDF DAQ architecture. Buffer management is controlled by the Trigger Supervisor.

There will be two edge-detection processors per chip, each serving 24 channels. A programmable channel-enable bit will allow the operator to disable hot channels. The hit-encoding logic will detect edges to level changes that exist for a minimum of five time intervals of 1.2 ns. This logic will be executed with look-up tables internal to the FPGA. This will allow flexibility by downloading the contents of this table to select minimum pulse width. This circuit has been simulated and can operate in under 10ns period. This stage edge-detection stage operates synchronously.

The output of the edge-detection processor will determine the word count and the bit position of the transitions. The word count is 12ns per interval and the position is 1.2ns per bit. A simple addition will determine the full time position relative to the start of the event. A time-subtraction subtraction can give the time span from the previous transition. Since all processes are pipelined, these additional tasks will merely add latency and not effect the rate. There will one such processor per twenty four channels. In this stage, the hit data will be compressed using a Huffman compression algorithm.

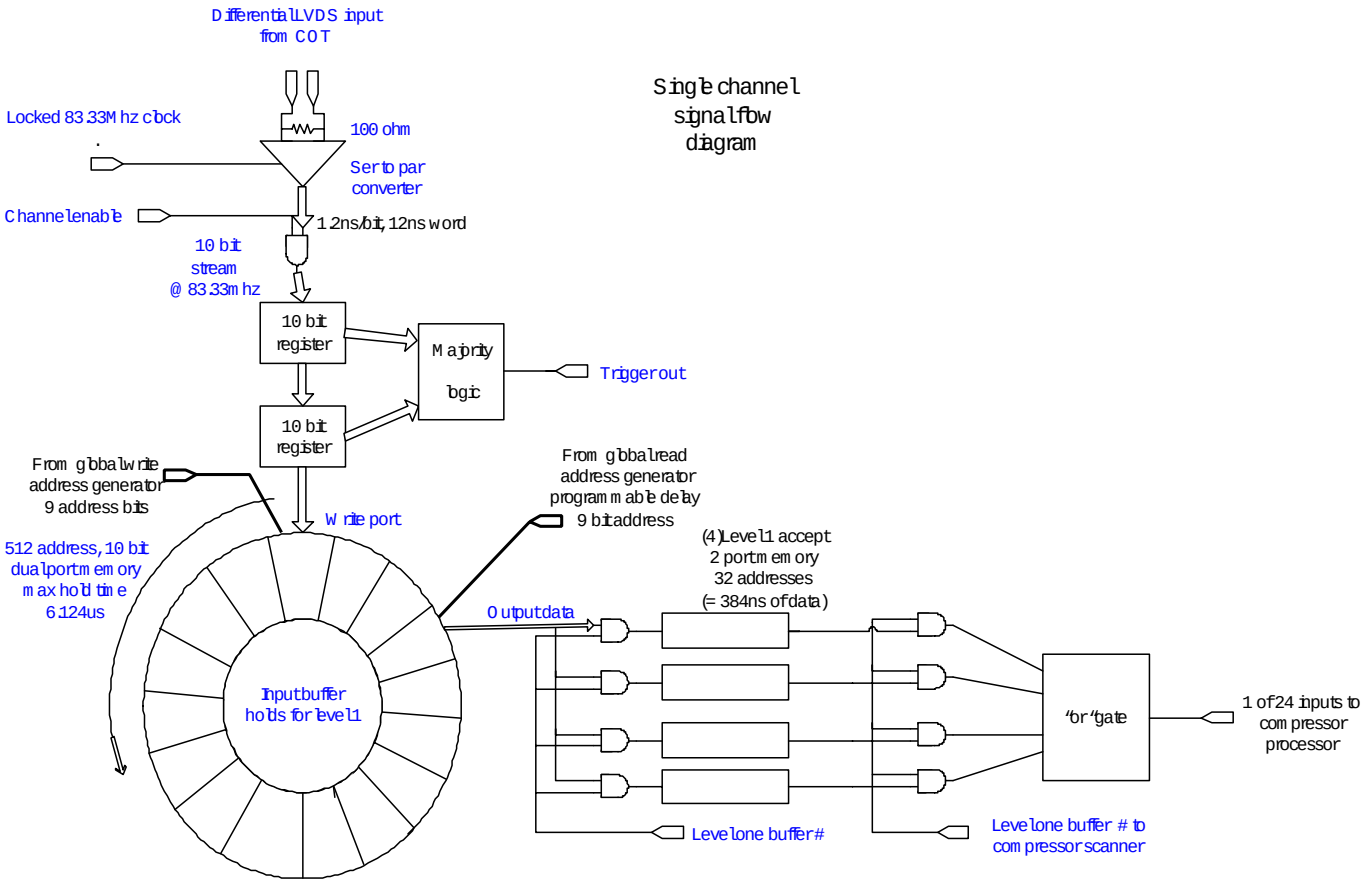

Figure 6.3: New TDC block diagram. All of the functionality shown here is carried out within the primary FPGA.

6.3.5.3 VME Readout

The design of the TDC will allow for two possible readout paths, one that is identical to the present system, a second that bypasses the TRACER→TAXI link.

In the existing readout path, the hit-data is loaded into a single FIFO for each 96-channel board. The FIFOs for the boards (typically 15 TDCs per VME crate) are read serially over VME by block transfer to the crate CPU. In "spy" mode, the TRACER actually grabs the data as it is being read by VME and loads the data into an on-board FIFO. The data is then sent by TAXI link to the VRB. Retaining the functionality of the existing readout system will aid and simplify commissioning of the TDC system.

At Run IIb luminosities, however, the existing readout mechanism is not sufficient. Each TDC will be equipped with a front panel fiber optic G-link output. An additional data-concatenation board will reside in each crate. The board will accept input from the local TDCs by G-link, concatenated the data and then send it by G-link to the VRB. Since the VRB already handles G-link format, the changes to the existing system are minimal. A concatenation board will reside in each TDC crate and have full access to CDF-specific signals for timing and buffer identification.

6.3.5.4 XFT Interface

In the existing system, input signals are split off and sent to both the TDC ASIC and the mezzanine board. The TDC mezzanine board, known as the XTC board, performs its own coarse time-to-digital conversion. The XTC is effectively a two-bit TDC. Data from the XTC is sent out synchronously to a transition module that drives the signals to the XFT finder boards in the first floor counting room over Ansley cables.

The remainder of the XFT system will be discussed in the following section. Here we describe the XTC

functionality that will reside on the new TDC. The flexibility of the Altera FPGA allows us to move the XTC functionality into the TDC board itself. Upon data capture in the deserializer section, we will split the digital signals off into a secondary path for trigger processing. The 10-bit grouping utilized in the TDC will be retained for trigger processing.

The approximate time binning will be three times finer than in the Run IIa system. This will give approximately 40ns time bins. The trigger signals will be driven directly from the Stratix chips using the provided LVDS outputs which reside on the chip. To maintain compatibility with the existing TDC transition module, the signals will be converted to TTL and driven to the transition module through the J3 connector. The transition modules and cables are retained from the Run IIa system and will drive hit data for the trigger at 45.5MHz up to the XFT finders residing in the first floor counting room.

6.4 XFT Upgrade

6.4.1 Introduction

The trigger for Run II incorporates charged track information in the Level 1 trigger decision. The tracks are found by the eXtremely Fast Tracker (XFT) and the resulting track list is sent to the eXTRaPolation system (XTRP) for distribution and matching with other Level 1 primitives such as electromagnetic clusters (for electron identification) and muon stubs (for muon identification). The XFT track list is also sent from the XTRP to the SVT for identification of displaced tracks at Level 2. The XFT identifies tracks in r-ϕ only, using the four axial layers of the COT. This device is presently in operation in Run IIa and is operating well, as summarized below. The device was designed with the following luminosity scenario:

- $\mathcal{L} = 1 \times 10^{32}\mathrm{cm}^{-2}\mathrm{s}^{-1}$, 396ns bunch spacing, <int/crossing> ~ 3
- $\mathcal{L} = 2 \times 10^{32}\mathrm{cm}^{-2}\mathrm{s}^{-1}$, 132ns bunch spacing, <int/crossing> ~ 2

Given that the XFT was designed for a brand new drift chamber, the COT, we had no data to estimate the occupancy. The occupancy estimates came from Run I extrapolations.

Two things have changed. One is that the baseline for Run IIb assumes a bunch spacing of 396nsec, and an initial store luminosity of $\mathcal{L} = 4 \times 10^{32} cm^{-2} s^{-1}$. The mean number of interactions in this environment is ~ 12, a factor of ~ 4 above our design goal. In addition, the occupancy in the COT is about a factor of two above our initial extrapolations from Run I. As a result, the performance of the XFT is compromised in this busy environment. To address these problems, and to recover our present good performance of the XFT in Run IIb, we propose the following upgrade:

- A replacement of the core pattern recognition chips of the XFT segment Finder and segment Linker [6]. The CDF collaboration has proposed an upgrade of the TDC, which will provide an opportunity to send more precise (by a factor of 3) timing information to the XFT. The upgrade of the pattern recognition chips of the XFT will allow us to utilize this additional information, and recover our momentum and ϕ_0 resolution, and reduce our fake tracks. Most of the present XFT system would be reused in this upgrade. The layout of the upgraded Finder and Linker board would be almost identical to the present designs: the major change would be in the replacement of the core chips, and the firmware implemented on these chips.

- An addition of a single stereo measurement [7] to the existing XFT tracks. The XFT identifies tracks in r-ϕ only, using the four axial layers of the COT. Since both the electron and muon subsystems are segmented in z, the ability to extrapolate and match XFT tracks in the z view could prove extremely useful in reducing fake lepton triggers. Also, supplemental tracking trigger information will be crucial in controlling fake rates which will feed directly into displaced vertex trigger. The stereo measurement would be made in the outermost stereo layer (SL7) of the Central Outer Tracker (COT). The stereo segment Finding would be done in exactly the same manner as the axial segment finding is presently done. The primary change would be in how the stereo segments are output to the next stage in the trigger.

Although the baseline for Run IIb assumes a bunch spacing of 396nsec, the Lab has indicated that the trigger must be able to work if the bunch spacing is reduced to 132nsec. In this scenario, transmitting more precise timing information to the XFT

cannot be done without upgrading the cabling and support infrastructure (*i.e.* transition cards). The upgraded system will then revert back to the present coarse timing information. Some degradation in performance will result, although it will not be as severe, since 132nsec running will result in fewer interactions per crossing then comparable luminosity at 396nsec running. However, the stereo segment finding still provides rejection even with coarse timing information, and serves as insurance in case the bunch spacing is reduced to 132nsec.

In the remainder of this chapter, we summarize current XFT performance, indicate how the performance will degrade with additional interactions, and describe in detail how the new system will be constructed.

6.4.2 XFT Performance: Current and Extrapolated

6.4.2.1 Momentum and ϕ Resolution

We have measured the XFT track p_T and ϕ resolution in data events containing a high p_T lepton as well as in monte carlo $t\bar{t}$ events. In the data, the XFT track is compared against tracks reconstructed with the offline tracking algorithm. In monte carlo the XFT track is compared against simulation level particles (OBSP). The resolution distributions (see Figure 6.4) are fit to the sum of two Gaussian distributions. The resolution value is taken as the limits of the 68% confidence interval centered on the mean.

To understand how the resolutions change as we increase the number of interactions, minimum bias events were added to the data and monte carlo samples. For the data, we added events collected with a minimum bias trigger. In the monte carlo, we generated samples with additional interactions according to the CDF *MBR* generator. We added a Poisson-mean of 5 and 10 additional events to the samples. For each sample, we measured the p_T and ϕ resolution and performed our fitting procedure. Figure 6.5 summarizes the evolution of the resolutions as a function of the number of additional interactions. We perform these measurements with the XFT algorithm requiring $\geq$10 hits per layer (2-Miss) and $\geq$11 hits per layer (1-Miss). We see a significant degradation of the performance of the XFT between 5-10 interaction per crossing.

We should emphasize that the current running conditions of the XFT is the $\geq$10 (2-Miss) mode. This is governed by the single hit efficiency of the COT. We are currently investigating the possibility of changing to the $\geq$11 (1-Miss) algorithm. The 1-Miss mode improves the resolution slightly and reduces the number of fake (false) XFT tracks (see Section 6.4.2.2), but at the cost of reduced tracking finding efficiency.

6.4.2.2 Track Rates

While the resolutions are one measure of the performance of the XFT, another important characterization of the performance is the rate at which tracks are found. This is quantified in the efficiency of finding true tracks and the rate at which fake tracks are reported. Because of the XFT algorithm, we don't expect a large impact on the efficiency. However, the rate of fake tracks is a concern. Reporting false tracks increases the trigger rates and consumes precious bandwidth in the trigger.

We have investigated the rate of tracks in two samples, data and monte carlo. In the data, we looked only at the rate that XFT tracks were found. We did not separate true tracks from fake tracks in events that had merged minimum bias events [1]. Figure 6.6 shows the rate (XFT tracks/Event) for several p_T thresholds and operating conditions for the XFT (1-Miss vs 2-Miss). Note: Recall that the data sample that is being used is the high p_T ($\geq$18 GeV) electron sample, so there is at least one high p_T track in each event. The important issue is the trend of the track rates versus the number of additional interactions. Although the true and fake XFT tracks are not separated in this case, it is interesting to note that the difference between the 2-Miss and the 1-Miss is almost entirely due to fake tracks found with the 2-Miss algorithm (*i.e.* loss in efficiency of the 1-miss case can only account for a $\sim$5% difference in rates).

We have repeated this process in monte carlo of minimum bias events (no hard scatter). However, in this case since we know the true tracks that have been generated, we can separate the fake XFT tracks from the true tracks. Figure 6.7 shows the rate of *fake* XFT tracks per event in minimum bias events as a function of the number of additional interactions. Note the factor 900 (200) increase in fake tracks per event in moving from 2 interactions per crossing to 10 interactions per crossing, when allowing up to 2 (1) misses per segment.

[1] Currently, it is technically difficult to do this in the merged events.

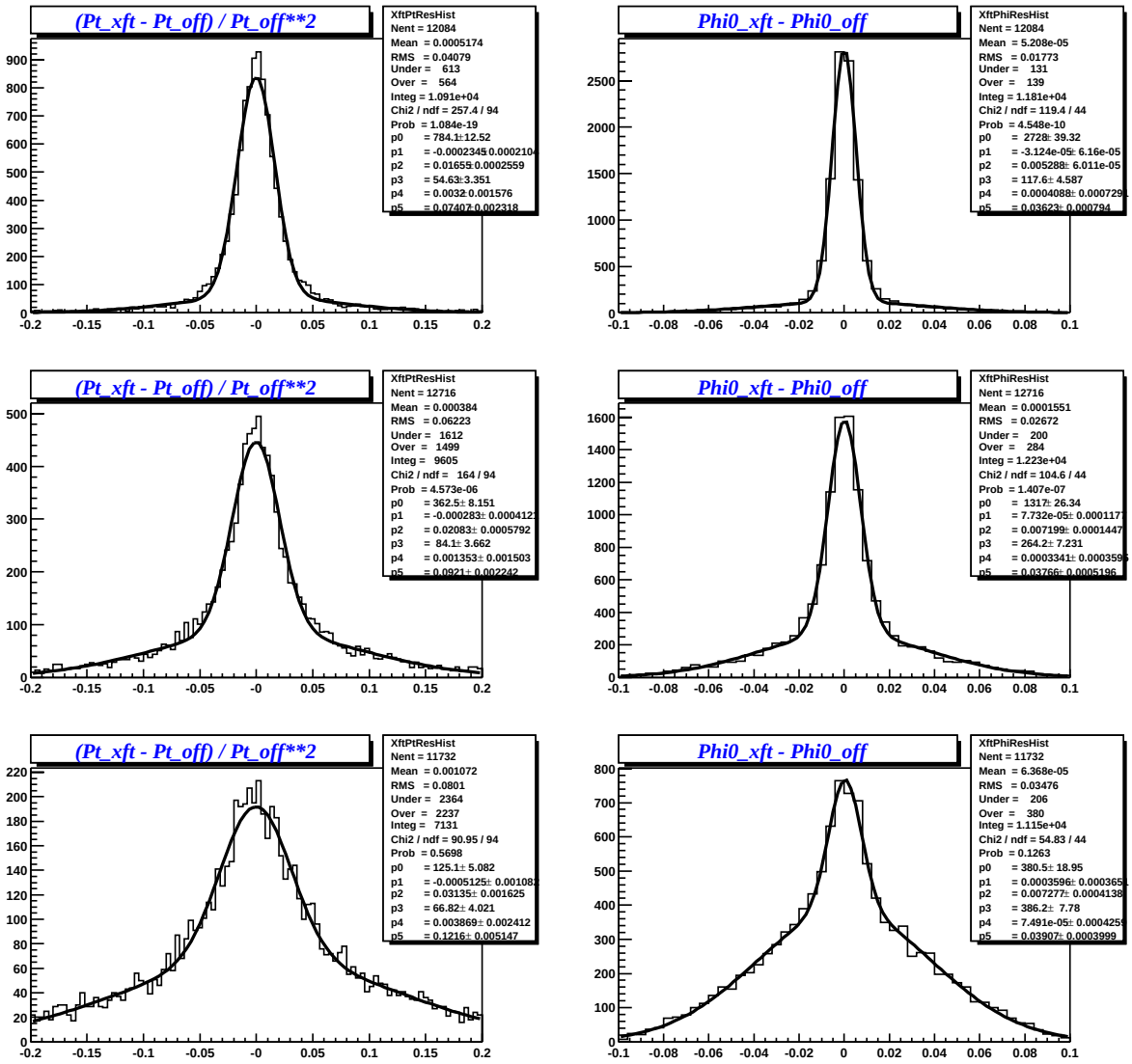

Figure 6.4: The p_T (left) and ϕ (right) resolution for XFT tracks in a data sample of high p_T inclusive electrons. The top set of plots is without any additional minimum bias events added to the data. The second set of plots is with a 5 (mean of Poisson) additional interactions added and the third set of plots is with 10 added. For these XFT tracks, 10 or more hits per superlayer are required (2-Miss).

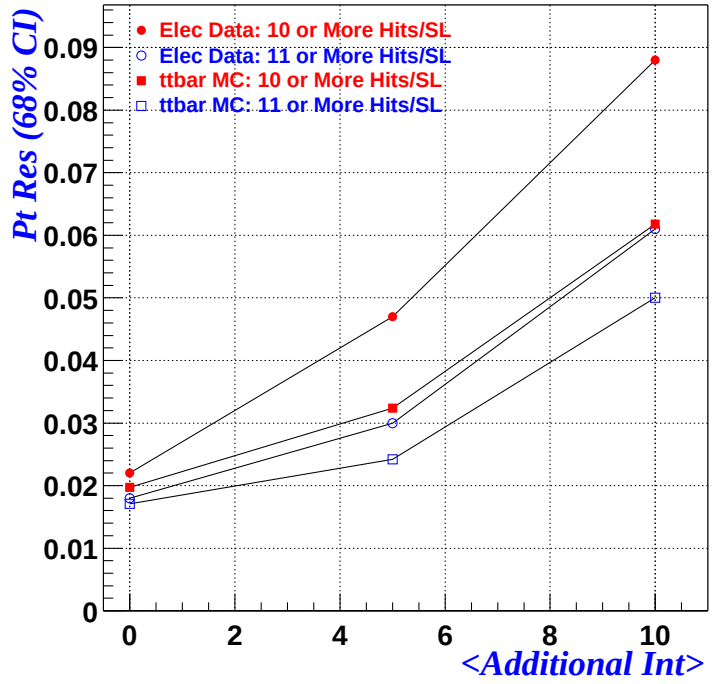

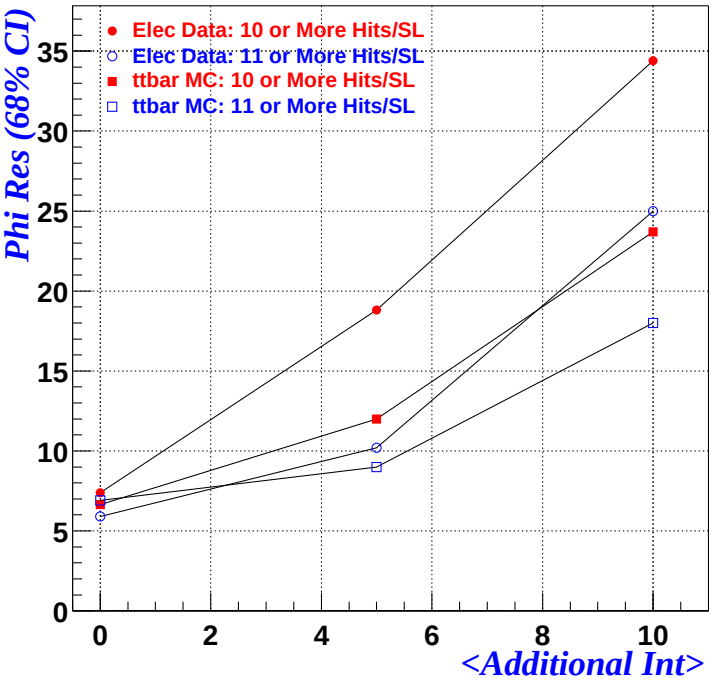

Figure 6.5: The p_T (top) and ϕ (bottom) resolution as a function of the number of additional interactions. The circles represent high p_T inclusive electron events and the squares are $t\bar{t}$ monte carlo. The filled points are requiring 10 or more wires hit in each superlayer (2-Miss) and the open points are requiring 11 or more wires hit in each superlayer (1-Miss). The ϕ resolution is given in terms of milliradians and the p_T resolution is given by $\Delta p_T/p_T^2$ in units of $(\mathrm{GeV/c})^{-1}$.

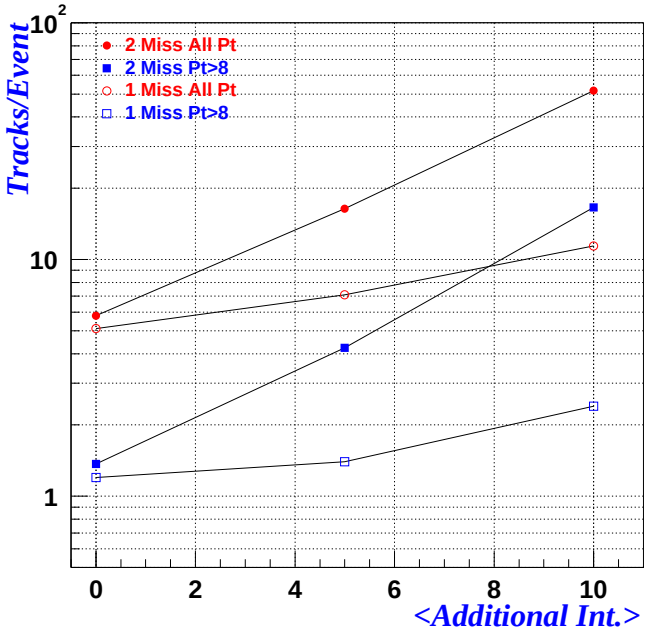

Figure 6.6: The rate of XFT tracks in high p_T inclusive electron events as a function of the number of additional interactions. The circles are for all XFT tracks with $p_T >$ 1.5 GeV/c. The squares are for tracks with $P_t > 8$ GeV/c. The closed points are allowing 2 misses (require 10 or more hits) per superlayer. The open points are allowing on 1 miss (require 11 or more hits) per superlayer.

6.4.2.3 Summary

With the current XFT hardware, the track trigger processor should work well through Run 2A and up to instantaneous luminosities of 1×10^{32} cm^{-2}-sec^{-1}, at a bunch spacing of 396nsec. This corresponds to about 3 (mean) interactions per crossing. It may be necessary to operate the XFT with the 1-Miss design for the higher luminosities of Run 2A. Ongoing studies indicate that this incurs an acceptably small loss in track finding efficiency. However, as the XFT is pushed beyond ~5 interactions per crossing (well beyond its design point) the performance is significantly degraded even with the 1-Miss design. Upgrades and improvements to the track trigger are likely necessary for operation at the 5-10 interactions per crossing of Run 2B.

6.4.3 Expected Performance of an Upgraded XFT

In this section, we outline how the axial and stereo upgrade of the XFT will address the shortcomings of

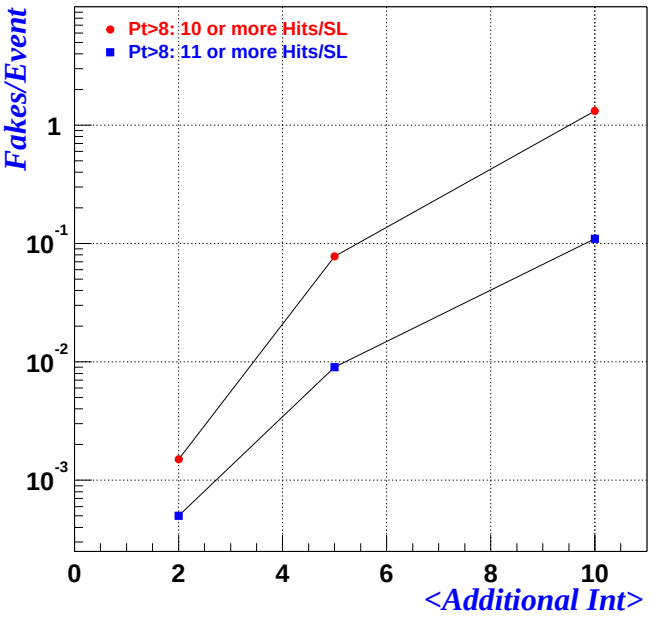

Figure 6.7: The rate of **fake** XFT tracks in minimum bias monte carlo events.

the current device in RunIIb.

6.4.3.1 Impact of a Upgraded Axial XFT

The degradation of the XFT in Run IIb will be in 3 areas: momentum resolution, ϕ_0 resolution, and fake XFT tracks. The loss of resolution is tied to occupancy in the COT much higher than designed for, due primarily to the large number of interactions per crossing. A primary cause of fakes is two unrelated tracks crossing in the outer two layers. These tracks combined with general occupancy in the inner layers lead to the XFT finding fake high momentum tracks, a problem which is greatly exacerbated by the higher luminosity running. However, the XFT performance can be recovered by:

- Better segment finding: Better segment finding will reduce the number of spurious pixels reported to the Linker. This should lead to more precisely measured momentum and ϕ position.

- Better linking of the segments: In a dense environment such as is the case at high luminosity, valid pixels from low momentum (but still interesting) segments will still make it through to the Linker. If these two segments are close in ϕ in the outer two layers, they could be mistaken as a much higher momentum track. By providing finer slope information, the Linker should be able to reject tracks which come from two valid, but unrelated tracks.

To understand how a new XFT design can reject fake tracks, we first need to establish how well the current XFT measures the p_T of a segment in the outer two layers. The resolution in p_T for segment finding is shown in Figure 6.8. This plot is made for those segments the XFT identifies as "both" signs of low p_T, or high p_T. Two choices are shown, one with a bin ~4 GeV, the other with a nominal bin of ~8 GeV. The turn-on curves are consistent with a resolution of approximately 0.20 $(\mathrm{GeV/c})^{-1}$.

Using a toy MC, and the resolution of the hit finding in the current XFT, we would calculate the p_T resolution to be 0.20 $(\mathrm{GeV/c})^{-1}$. So this is a good match with what we actually see in the data.

We use this same toy MC to estimate what our resolution would be if we improved the hit resolution of the XTC by a factor of 3. This would change the information provided to the Finder from two bins corresponding to a simple *prompt* or *delayed* hit, to 6 bins of timing information per wire. This same toy as used above indicates that our expected resolution in p_T for the outer two layers would improve to 0.06 $(\mathrm{GeV/c})^{-1}$. This factor of 3 improvement in resolution should help both in fake rejection, as well as in the final reported XFT track p_T and ϕ resolution.

To understand how much fake rejection can we expect for this sort of resolution, we first verified first that fake tracks come predominantly from multiple tracks generating segments in the outer two layers. The plot Figure 6.9 shows the slope difference between the XFT track and the nearest MC track. The top plot is for matched XFT tracks, the bottom is for fake XFT tracks. Note that it is possible that the true track is in fact nearby, but that it happens to not be the nearest. In any case, it is easy to see that fake tracks are very different from a real XFT track. Figure 6.10 shows how many tracks contribute to either fake or real tracks. If a single track is the closest at each of the 4 segments, this corresponds to 1. If four different tracks contribute, then this corresponds to 4, and so on. As expected, real XFT tracks come from real single tracks. However, fake tracks are generated by multiple tracks which happen to be mis-reconstructed by the Linker as a real track. This effect becomes more pronounced as the mean number of interactions increases.

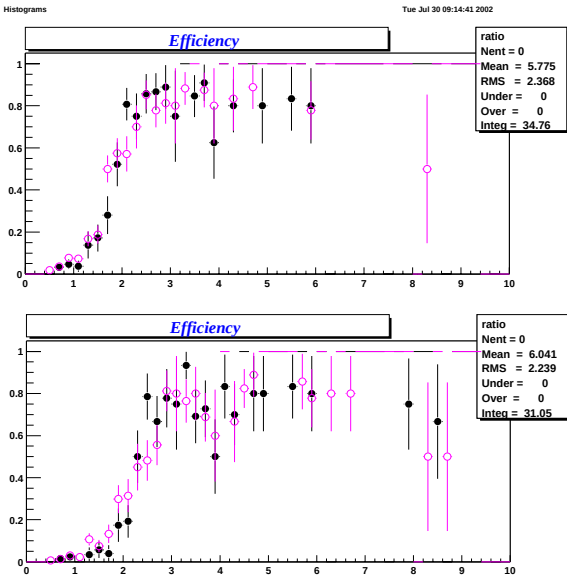

Figure 6.8: The efficiency to identify an XFT segment high momentum.

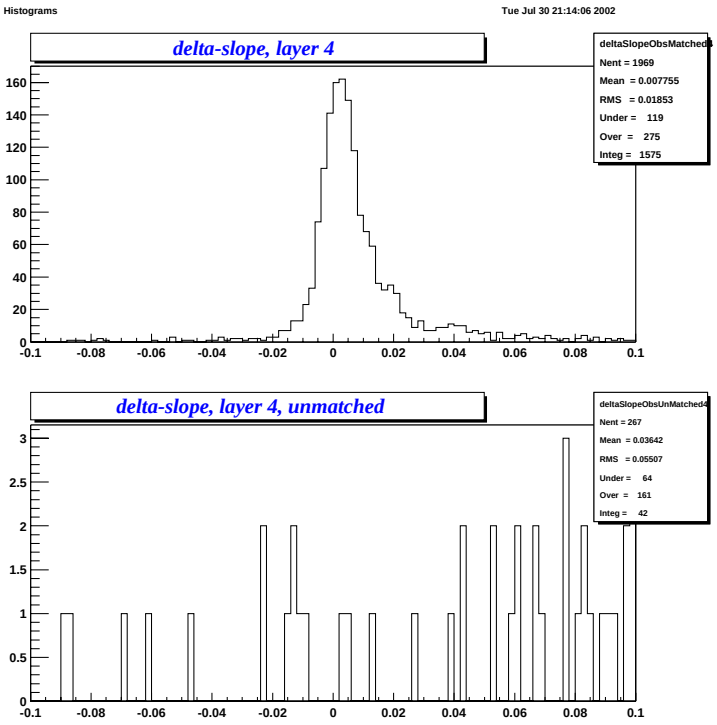

Figure 6.9: The difference in slope between a found XFT tracks and the nearest true Monte Carlo track. The top plot is for XFT tracks which have been matched to Monte carlo tracks (reals), while the bottom is for XFT tracks which were not matched to Monte Carlo tracks (fakes).

Armed with this information, we then implemented the following algorithm:

- For each XFT track (fake or real) we take the outer two segments. We find the monte carlo track which comes closest to this segment. We then smear this true p_T by the expected segment resolution of 0.06 $(\mathrm{GeV/c})^{-1}$. Based on this smearing, we decide if the "measured" p_T is above threshold for this segment. We set the threshold to be 5 GeV. If above this, then the segment is marked as "high p_T".
- In linking the two segments, we require that both segments be marked as high Pt.
- We then examine the efficiency for the sample of XFT tracks to pass this additional requirement.

Note that it is still possible to find tracks with p_T lower than 5 GeV/c. The purpose of this study is to determine how many of the "High Pt" fake tracks will fail this requirement, as well as seeing how many true high p_T tracks would pass this requirement.

The results are shown in Figure 6.11. Note that the x-axis is in p_T Bin, with bins 47-48 being the infinite momentum bins. The plateau region spans momenta from -10 GeV/c to infinite to $+10$ GeV/c.

- The average efficiency for high p_T real tracks is $\sim$95%, indicating that we retain high efficiency for the tracks we need to keep.
- The average efficiency for high p_T fake tracks is $\sim$10%, indicating that the improved resolution is extremely effective at removing fakes.

By utilizing the full 396nsec to send more precise information, we can improve the resolution of the XFT and gain an important handle on controlling fake tracks.

6.4.3.2 Results Using the Full Simulation

The above results come from a toy Monte Carlo, and so represent a crude estimate of how well improved timing resolution could lead to improved XFT performance. There does exist a full simulation of the Run IIA XFT, which has been extensively studied and verified using Run IIA data. In order to get an improved estimate of the performance of an upgraded XFT, we have modified this simulation to use the additional timing information we would expect in Run IIB (392ns mode). The additional information impacts the segment finding stage of the XFT, and we have not yet modified the segment linking stage. We

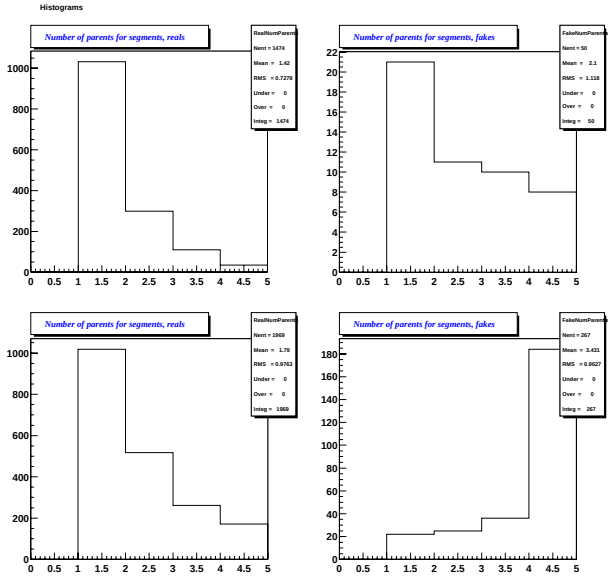

Figure 6.10: The number of Monte Carlo particles which contribute to the 4 segments of an XFT track. The distribution for XFT tracks well matched to Monte Carlo particles are shown on the left, while poor matches (fakes) are shown on the right. The top two plots are for $t\bar{t}$ events with no additional interactions overlaid, while the bottom two plots are $t\bar{t}$ events with 5 additional interactions (on average) overlaid.

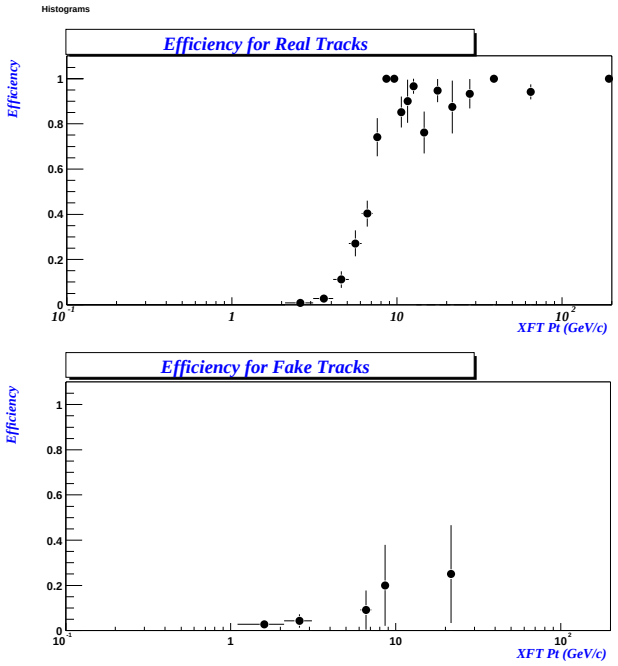

Figure 6.11: The efficiency for XFT tracks to pass the requirement that the outer two segments be high momentum, using the expected resolution of the Run IIb device.

reanalyzed the inclusive high P_T data sample using this improved segment finding. The results are shown in Figure 6.12. We see a substantial improvement in both the P_T and ϕ resolutions. It is important to note that these studies left the segment linking portion *unchanged* from Run IIA. Passing additional information, such as segment slope, from the Finder to the Linker portion of the XFT should provide further improvements on the resolution. Additional improvements may also be possible from additional optimization of the algorithms (*e.g.* ranges of the 6 time bins, etc.).

We have also estimated the impact of the improved timing and slope information on the rate of fakes. For this study we used Monte Carlo minimum bias events with multiple interactions. We measured the rate of fake tracks above 8 GeV/c. For this study we included both the additional timing information for the segment finding and additional slope information in the segment linking. We found that the additional information reduced the number of fake high tracks by about an order of magnitude. This is similar to the result based on analysis of the segment slope resolution.

6.4.3.3 Impact of Stereo Segment Finding

The current version of the XFT only uses 4 of the 8 superlayers of the COT. It does not make use of the four layers that have their sense wires tilted a few degrees with respect to the beam line. These are the so called stereo layers. As charged particles transverse the stereo layers, they will leave a track segment just like the axial COT layers only the apparent ϕ location of the track stub will be shifted with respect to the axial positions. This shift is proportional to the z position of the stub. The algorithm to find these stubs in the stereo layer is identical to the algorithms used for the axial layers, and nearly identical hardware boards could be used for this purpose[2]. Having a stereo segment available for the trigger can be used in two basic ways:

- **Provide Z-Pointing to Tracks:** Having a stereo segment can provide pointing in the z-direction. This turns the 2-D $(r-\phi)$ XFT tracks into a pseudo-3D track. The resolution in the z-direction at the outer stereo layer of the COT is about 6 cm assuming two-bin timing from the

[2]The only difference would be how wire information is distributed on the Finder board and what format the results were driven off the board.

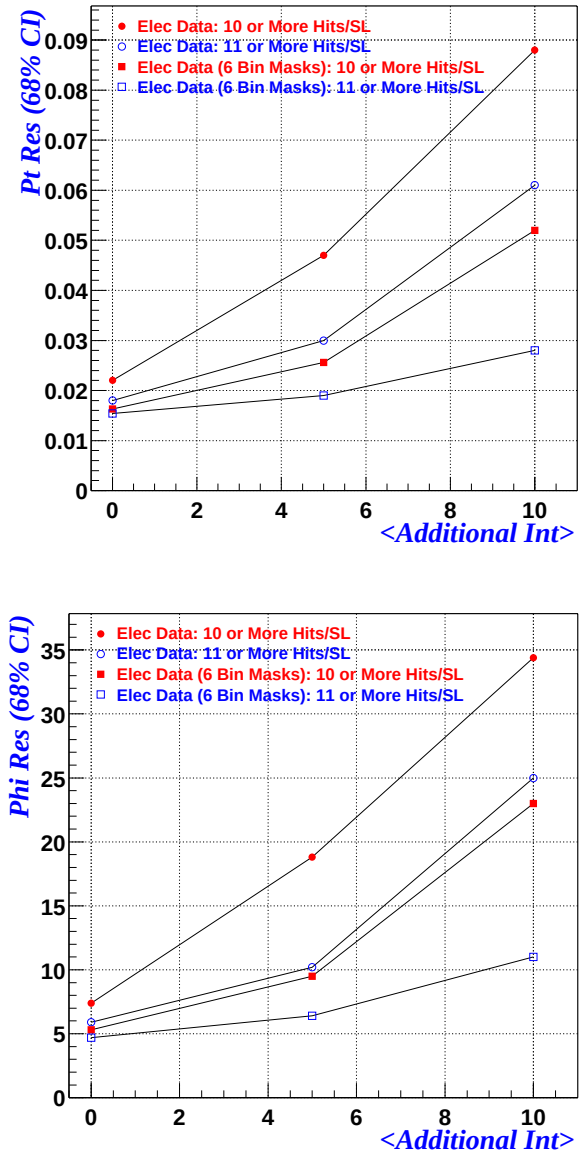

Figure 6.12: The P_T (top) and ϕ (bottom) resolution as a function of the number of additional interactions. The sample is high P_T inclusive electron events (Run IIA Data). The circles represent the performance of the XFT with 2 time bins used for segment finding (Run IIA design) and the squares represent a simulation of an XFT using 6 time bins for the segment finding (Run IIB design). The Run IIB results do not include the benefit from using additional information for the segment linking portion of track finding, which should improve these resolutions further. The filled points are requiring 10 or more wires hit in each superlayer (2-Miss) and the open points are requiring 11 or more wires hit in each superlayer (1-Miss). The ϕ resolution is given in terms of milliradians and the P_T resolution is given by $\Delta P_T/P_T^2$ in units of $(\mathrm{GeV/c})^{-1}$.

XFT front-end. This will allow a coarse pointing into the EM calorimeter and more importantly into the muon chambers. This information can be very helpful for eliminating spurious lepton triggers. For instance, hits in the muon chambers from beam halo may line up in $r-\phi$ with a real physical track. However, if we know that track is not pointed toward the muon stub in the z-direction, we can eliminate that as a trigger candidate. In addition, z information will allow us to form "invariant mass" triggers.

- **Confirmation Segment to Reduce Fakes:** A true 2-D XFT track should have a segment in the outer stereo layer. However, we have seen that fake XFT tracks are often the result of connecting lower p_T segments from *different* physical particles. Therefore, in some of the fake XFT tracks, no stereo segment will be present. We can use the stereo segment as a "confirmation" that the track is a real track. We have investigated the power of this confirmation by considering minimum bias monte carlo. In the monte carlo we required that there be a physical particle that pass through the region in the outer stereo layer for the 2-D tracks to be "confirmed". We then looked at the reduction of the fake rate after this requirement was imposed. The results are shown in Figure 6.13. We see that we can achieve about an order of magnitude reduction in the fake tracks with this confirming segment. In the figure, the fake rate is measured when we have run the 11 or more (1-Miss) version of the XFT algorithm. In fact, the order of magnitude reduction of the fakes is independent of whether we use the 1-Miss or the 2-Miss algorithms.

6.4.4 Upgrade XFT System Overview

A block diagram of the XFT System is shown in Figure 6.14. The architecture of the XFT system consists of three main subsystems along with the medium of transport of data between the three subsystems. The task of each subsystem is as follows:

- Hit Classification: This task is currently performed by the XTC module.
- Segment Finding: The Finder modules perform segment finding within the axial superlayers of the COT, reporting found segments to the Linkers.

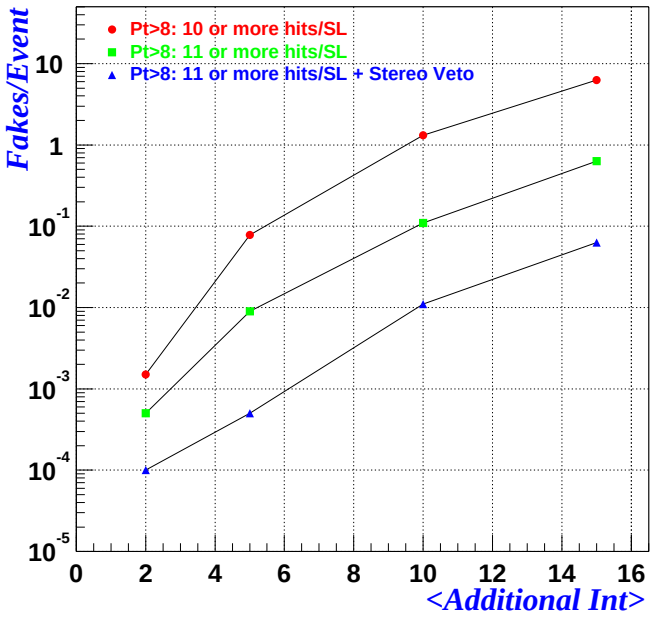

Figure 6.13: The rate of fake XFT tracks per event as measured in Minimum Bias Monte Carlo events versus the mean number of interaction per crossing. The results are shown for the 132 ns two time bin resolution of the hits on the XFT front end. The two top curves show the rate for running with a 10 or more (2-Miss) and 11 or more (1-Miss) design. These curves are identical to those shown in Figure 6.7. The bottom curve shows the rate when using the 11 or more (1-Miss) algorithm and requiring a segment in the out stereo as confirmation of the track.

- Segment Linking: The Linker modules perform segment linking of segments from the four axial superlayers in the COT.

The basic change to the axial XFT system will be in providing more finely segmented timing information to the Finder modules, which in turn will allow more detailed segment information to be sent to the Linkers. This additional information will allow us to preserve out capabilities in the more dense environment of Run IIb. Additionally, a new set of stereo Finder modules will be added, used to find segments in the outermost stereo layer (called SL7). The segments add 3D capability to the Level 1 trigger, and allow matching in z to both the electron and muon chambers.

In designing the upgrade, we will reuse as much of the present system as possible, only rebuilding those parts which cannot work within the new system.

In the upgraded device, the XTC functionality will be provided by the upgraded TDC module. The electronic and cables used to transmit the data to the Finder (the COT transition cards, the ansley cables, and the Finder Transition cards) will be reused in the new system. The Finder Modules and Linker Modules will be replaced.

The Finder modules consist of 3 basic sections:

- An input capture section, using registers and XILINX FPGAs to capture and align the data from the XTC's. This section will be duplicated in the upgraded Finder Module.

- The segment finding section, using FPGA's referred to as the Finder Chips. The present design uses Altera 10K series FPGA's. These devices will be replaced with Altera Stratix series FPGA's, which will allow us to utilize the expanded input data from the XTC's. The stereo Finders are implemented in exactly the same fashion as the axial Finders.

- The Pixel transmissions section, which transmits the Finder pixel data to the either the Linker using channel link technology (for the axial Finders) or to the Stereo Association Modules (for the stereo Finders, described later). This current section of the Finder module will be duplicated in the upgraded design of the axial Finder modules. We will use the existing cables to transmit the data from the axial Finder Modules to the Linker Modules.

The Linker modules consist of 3 basic sections:

- An input capture section, using channel link receiver. This section will be duplicated in the upgraded design.

- The segment linking section, using FPGA's referred to as the Linker Chips. The present design uses Altera 10K series FPGA's. These devices will be replaced with Altera Stratix series FPGA's, which will allow us to utilize the expanded input data from the Finders. We have some preliminary results in targeting our *current* Run IIA design for these devices, which are described in section 6.4.11.

- The track transmission section, which transmits the Linker track data to the XTRP for distribution to the rest of the trigger system. This section will be duplicated in the upgraded design.

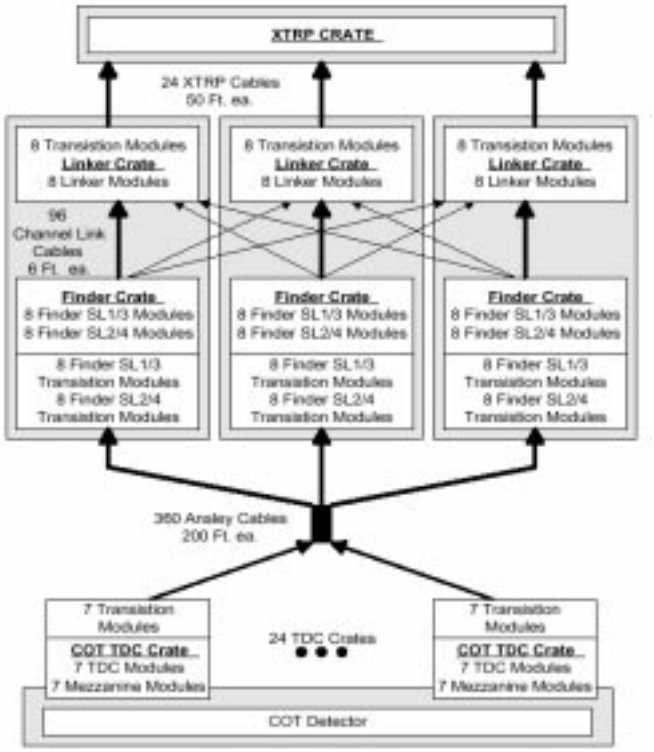

Figure 6.14: Diagram of the XFT system.

The Linker Output Modules are separate VME boards which reside in the crates with the Linker Modules. These boards drive the data on cables to the XTRP. The Linker Output Modules and the XFT–XTRP cables will be reused in the upgraded design.

The current system was designed to handle new crossings every 132 nsec. Since new data will only appear every 396 nsec, we use this additional time to send more information between subsystems. As one can see, the change in the system is limited to the FPGA's used to do the basic pattern recognition. We will not change the basic rate a data transfer from subsystem to subsystem. In the sections below, we describe in more detail each of the upgraded XFT subsystems. We will note which parts of each subsystem will be reused from the current system.

The upgraded XFT System begins with the upgraded COT TDC's in the CDF collision hall. This module will classify the hits on the COT wires as occurring in 1 or more of six time bins and send that information to the COT transition module at the back of the COT TDC crate. The transition module drives the data at 45.5 MHz, with Low Voltage Differential Signal (LVDS) technology, onto Level 1 Trigger cables that carry the COT wire data 220 ft to the Finder module crates. Finder Transition modules receive the data and send it across a customized VME backplane to the Finder modules. Finder modules find track segments and report them to Linker modules in another crate. The Finder data is transported to the Linker with the use of LVDS Channel Link technology running at 210 MHz. Linker modules accept segment data from four separate Finder modules. A Linker module uses the Finder data to link together four segments(each from a separate axial COT superlayer) to form a track. Information from a found track is sent to a Linker Transition module which drives the track information to the XTRP system via LVDS technology running at 15 MHz.

6.4.5 The XTC Module

Presently, the XTC module is a small card that plugs into a TDC module. The upgraded TDC module for Run IIb will be responsible for this functionality. The primary change in the functionality of the XTC in the upgraded system will be its capability to transmit finer time information. The maximum drift length in present running conditions is approximately 210 nsec, and this is not expected to change for Run IIb. The upgraded XTC will still transmit data to the Finder at 22nsec, but will use the full 396nsec to transmit the data. This allows for the possibility of sending up 3 times the data, or 6 bits of information per wire rather than the present 2. The Finder design outlined below will take advantage of this new time information.

Each TDC module contains 96 channels and receives discriminated COT signals from eight adjacent COT cells in a given superlayer(each cell has 12 wires). The data(hits) on the 96 wires is compared to precision reference timing signals generated from the 132ns CDF_CLK. The TDC associates the data with 1 or more of six time bins.

These bits are driven off the TDC modules through the VME J3 backplane and onto the transition board as single-ended TTL levels every 22ns, i.e. 6 times the basic 132ns clock rate. In addition control bits such as Word zero, Beam zero, and a data strobe are sent. The full 396 nsec between crossings will be necessary to send 6 bits of hit data per wire.

6.4.6 XTC To Finder Transmission

The XTC to Finder link consists of the following pieces of hardware:

- 168 COT TDC Transition modules
- 360 Ansley cables
- 60 Finder Transition Modules
- 3 Custom VME J3 backplane

All of these pieces will be reused in the upgraded system

The COT TDC transition module receives single ended TTL level prompt and delayed data from the XTC module. The transition module converts it to Low Voltage Differential Signaling (LVDS) technology and drives the data directly onto two Ansley cables. The Ansley cable is a 200 foot flat cable with 25 differential signal channels. There are three wires per channel consisting of a balanced pair of adjacent signal wires and a ground wire which provides isolation from the next channel. The cable has characteristic impedance of about 125 ohms. The rise-time is less than 7nsec (10% to 50% pulse height) and the cross-talk is less than 3%. The cable delay channel to channel varies less than +/- 1nsec. Up to eight Ansley cables will be plugged into each Finder transition module. The transition module contains receivers, which convert the LVDS signals back to single-ended TTL signals, followed by buffers which reshape the single-ended signals. The custom J3 VME backplane directs the reshaped prompt and delayed data from the Finder Transition module into the Finder Module. The backplane will act to feed through all "core" Ansley cables and also to provide for the transmission of "neighbor" data from slot to slot if needed. Neighbor data must travel at most one slot across the backplane.

6.4.7 Finder Module Design

The Finder is designed to look for valid track segments in a given COT axial superlayer. Architecturally, the Finder Modules have been broken down into two types of modules. Each type of Finder Module will span 15 degrees of the COT. The SL1/3 Finder module will contain the logic for dealing with COT Axial Superlayers 1 and 3. The SL2/4 Finder, will contain the logic for dealing with COT Axial Superlayers 2 and 4. Figure 6.15 shows a block diagram of a Finder module.

The main logic of these modules will reside in the Finder circuits. Axial superlayers 1, 2, 3 and 4 will be instrumented with 48, 72, 96 and 120 Finder circuits respectively. Each Finder circuit is implemented in an Altera FPGA device. Each Finder FPGA receives it core input from a single Ansley cable and some additional information from "neighbor" cables. The Finder FPGA outputs track segment information that is passed to Linker Modules. A valid track segment is found whenever a predefined number of wires in a given 12 wire set(mask) have hit information on them. A valid segment is identified by 12 pixels, each with 3 slopes, for Axial superlayers 1 and 2. Segments are identified by 6 pixels, each with 6 possible slopes, for Axial superlayers 3 and 4. A SL1/3 Finder Module will contain two SL1 Finder FPGAs and four SL3 FPGAs. There will be a total of 24 of these modules which will be spread out over 3 crates, with a total of 8 per crate. The custom J3 VME backplane requires that SL1/3 Finder modules be located in slots 4-11 A SL2/4 Finder Module will contain three SL2 Finder FPGAs and five SL4 FPGAs. There will be a total of 24 of these modules which will be spread out over the three Finder crates for a total of 8 per crate. The custom J3 VME backplane requires that SL2/4 Finder modules be located in slots 13-20.

The Finder module logic can be broken down into two sections: Control Logic and Data Flow. The data flow through the board starts with the Input and Alignment section followed by the Finder section and finally onto the Pixel Data Transmission section. With the implementation of reprogramable devices there exist many diagnostic methods for testing the Finder module as a single unit or within the XFT system. The board will be designed with diagnostic modes for the Alignment, Finder and Pixel sections. The diagnostic designs in general allow the reprogramable parts to be used as drivers or receivers with internal read/writeable RAM blocks that are capable of holding data to be driven or received.

6.4.7.1 Control Logic

Control Logic includes: Clock circuitry, Flash RAMs, and various FPGAs that perform the tasks of communicating with the VME system for control and error monitoring. These blocks are all implemented in Xilinx 4000E series FPGAs. They are configured with the use of a serial EPROM on when power is applied or the reset button is engaged. The Finder module also implements a JTAG interface and Boundary Scan chain to provide a method for testing for infras-

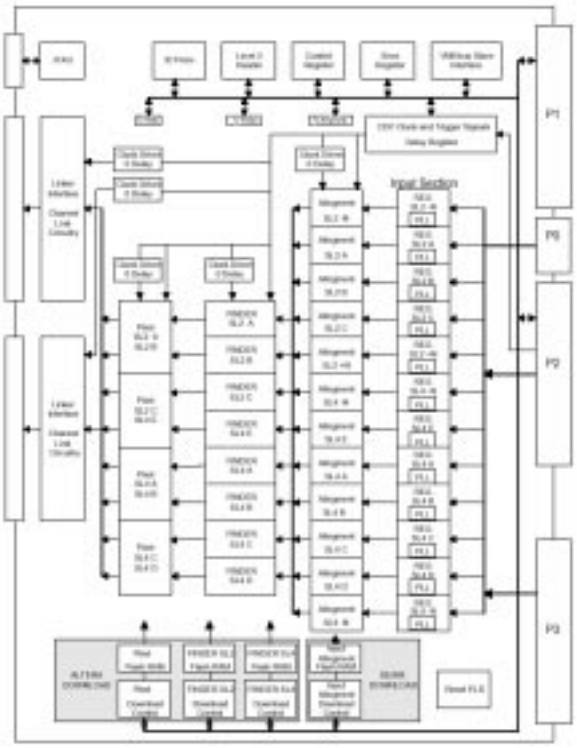

Figure 6.15: Finder SL24 Module Block Diagram.

tructure and interconnect defects.

It is possible to control the phasing of all clock and trigger signals on the Finder module. This is necessary to insure proper alignment of the raw data. The Finder board clocks are all derived from the 132ns CDF_CLK signal found on the VME backplane. The use of a programmable skew clock buffer such as the Cypress CY7B991 (Robo Clock) allows for clock multiplication to derive a 33ns and 66ns clock.

The Finder module will implement a modified version of a VMEbus slave interface. Only 32 bit aligned data transfers will be supported; these may be either single word transfers or block transfers. Only extended (32-bit) addressing modes will be supported. All modules will be assigned a unique geographical address through use of backplane pins on VME64extension backplane. Finder modules will respond to the following address modifier codes: 09, and 0B. The VME_SLAVE design is implemented in a Xilinx XC4013E-3PQ240 FPGA.

The CONTROL_REGISTER provides a 32 bit register that is used to control functions in the Alignment, Finder and Pixel chips. The main functions are reset, loop and download.

The ERROR_REGISTER is used to register and count the Word_0 and Beam_0 errors generated in the Alignment and Finder chips.

The LEVEL 2(L2) HEADER WORD block provides a means to identify the Finder board and also the time at which a level 1 accept occurred with respect to the CDF Beam Zero signal. L2 accepts a hard coded board type, serial number and geographical address to identify the board. An 8 bit R/W register identifies the Finder boards pipeline depth. When a LEVEL 2 buffer is read from the Finder board the first 32 bit word that is read comes from the L2 FPGA and is used as a 'Header' for that LEVEL 2 data.

The ALTERA Download block consists of three Xilinx FPGAs which act as controllers for three Flash RAMs. The three sets are used to configure the Altera chips. The design provides a means to control the Flash RAM that contains the download program.

The XILINX Download block consists of a Xilinx FPGA which act as controller for a Flash RAM. The data in the Flash RAM is used to configure the 12 or 14 ALIGNMENT FPGAs.

The Flash RAMs on the Finder board are used to hold the Finder, Pixel and Alignment chips designs. The Flash RAMs are AMD AM29F040B-90PC or AMD AM29F080B-90SC devices.

The ID_PROM contains the board serial number, board type and module description.

6.4.7.2 Data Flow

- Input Section - Capturing the Ansley Cable Data Since the Ansley cables are presenting data every 22ns, a conservative approach has been taken, and an "input" stage will be used to receive the output of each Ansley cable. This input stage will make use of data registers that will be capable of 100 MHz synchronous operation, and phase lock loop(PLL) devices to regenerate the 22ns clock signal. The data registers used are the Cypress CY74FCT162823T 18-bit registers and the PLL are the Cypress CY7B991-7JC or Robo Clock devices. The input data from each Ansley cable will be registered by a signal formed by taking the edge "Strobe" signal coming from the same Ansley cable, running it through an individual Robo Clock, doubling its frequency, and allowing for phase adjustment. The registered data along with the regenerated 22ns clock is forwarded to the Alignment section.

- Alignment Section - Aligning data to Finder

clock
The Alignment function is implemented in 12(Finder SL2/4 modules) or 14(Finder SL1/3 modules) Xilinx XC4005E FPGAs. These reprogramable devices implement the design shown in the block diagram of Figure 6.16. Each FPGA is responsible for aligning the data from an individual Ansley cable to the 33ns on-board clock.

The Alignment FPGA design works by allowing the various 22ns registers to be used as storage areas while the data is being transferred to another block of registers operating off the 33ns clock system. The design works since the two clocks are a fraction of the 132ns CDF_CLK system. In general three time slices of the 16-bit data arriving at the 22ns rate are registered and held for 66ns. During that 66ns those 48-bits are transferred to another 48 bit register operating off the 33ns clock. Those 48 bits are then de-multiplexed into two time slices of 24-bits of data and sent to the output registers at the 33ns rate. The 24 bits of data along with 'Beam 0', 'Word 0', 'Error' and 'Operate' are registered with the 33ns clock signal before they are sent to the output pins and onto the Finder chips. The "Operate" bit will be set and remain set once a "Beam 0" signal occurs. The "Error" bit is set if there are not 6 consecutive 22 time bins of the "Beam 0" signal "OR" if there is more than one 22ns "Word 0" signal in 18 consecutive 22ns time bins. The "Error" bit moves along to the Finder in sync with the input data. The design also forwards the individual "Beam 0 Error" and "Word 0 Error" bit to an output pin and onto the Error register of the board.

- Finder Section
  The Finder section of the XFT system performs the job of identifying track segments in a given Axial superlayer of the COT. Finder circuits flag "hits" by setting pixels which indicate the position and/or slope of an identified track segment.

  Each Finder will report 36 bits for each COT cell. The bits are arranged as a combination of pixel positions (6 or 12 total), and slope information. A "hit" is identified to have occurred whenever at least 9, 10 or 11 out of 12 wires in a mask have been hit.

  The Finder function is targeted for the Altera Stratix FPGA devices. These reprogrammable devices implement the Finder design shown in the block diagram of Figure 6.17.

  The Finder FPGA operates as follows: The four time slices of data are received every 132ns along with pertinent neighbor cell information. That data is time de-multiplexed into a 140 bit register that contains the prompt and delayed wire information. Those 140 bits are transferred to a multiplexer that selects a group of them(the group size is superlayer dependent) every 33ns to forward to a Mask set. The Mask set consists of a large number of 12 bit masks(the number of masks is superlayer dependent). Within each mask the number of misses is counted. A miss is a wire without prompt or delayed information. If the number of misses is 3 or less, a pixel that relates to a segment in that cell is turned on. There are separate MASK designs files that look for 1, 2 or 3 misses for each of the superlayers. The pixel information is registered every 33ns and transferred to the output pins.

  The Finder FPGA also contains a Level 1 pipeline and four Level 2 buffers that store prompt and delayed wire information for VME readout.

- Pixel Data Transmission

  This portion of the system is logically identical to the present system, except for the amount of slope information that will be delivered to the Linker. In the present system, Each Finder reports 12 pixels per cell to the Linker system, every 132nsec. In the upgraded system, the Finders have more information available per pix, up to 3 times or 36 bits per cell. We still transmit the information at a rate of 12 pixels per cell every 132 nsec, so the transmission circuitry on the Finder does not need to change.

  Each Finder module must present two copies of its pixel and slope information to the Linker Modules. This task is performed using a FPGA called the Pixel Chip and Channel Link drivers. The Pixel chip duplicates and forwards two Finder chips worth of information to two separate groups of three(Finder SL1/3) or four(Finder SL2/4) Channel Link drivers which in turn forward the information to different Linker modules. The Channel Link devices(National Semiconductor's

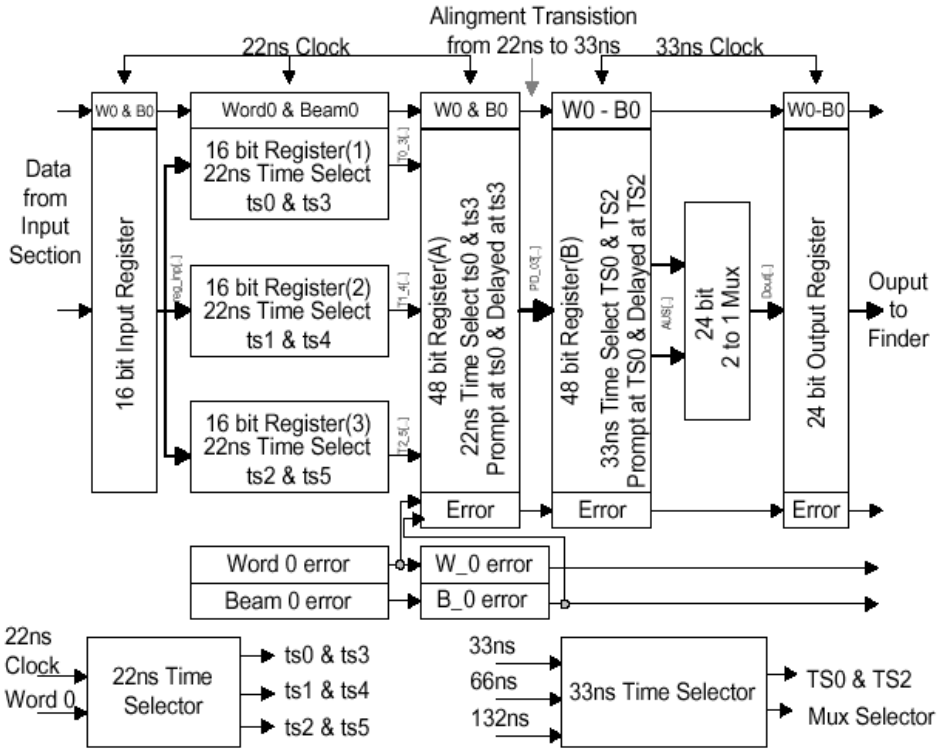

Figure 6.16: Alignment FPGA Block Diagram.

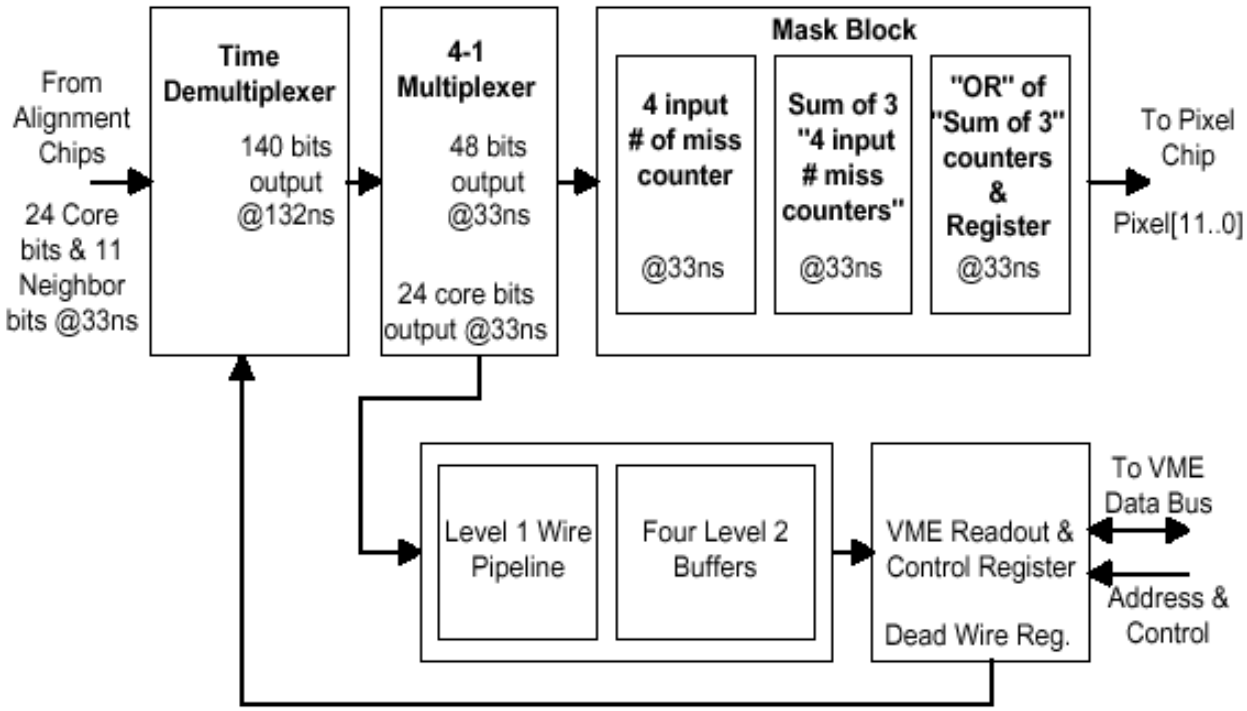

Figure 6.17: Finder FPGA Block Diagram.

DS90CR281/282 28-bit pair) consist of a driver and receiver pair. The driver is located on the Finder board and the receiver is located on the Linker board. Channel Link devices are grouped together to reduce the number of connectors and cables between the modules.

The Pixel Chip designs are implemented in the Altera Flex 10K EPF10K20RC240-3 FPGA for superlayers 2, 3 and 4 and the Altera EPF10K50RC240-3 FPGA for superlayer 1 The Pixel chip performs three functions:

- Combine the Pixel data from two Finder chips into a single 28 bit word.
- Duplicate that information and drive it through separate individual output pins to individual Channel Link drivers.
- Provide a Level 1 pipeline and four Level 2 buffers for Pixel data for VME readout.

6.4.8 Finder To Linker Transmission

The link between the 48 Finder modules and 24 Linker modules consists of 96 round cables and numerous National Semiconductor's DS90CR281/282 28-Bit Channel Link devices. Each Linker module receives pixel data from four separate Finder modules on four separate round cables. The Finder module drives pixel data to two different Linker modules on two separate round cables.

Each Finder module implements two groups of 3(SL1/3 modules) or 4(SL2/4 modules) National Semiconductor's DS90CR281 28-Bit Channel Link drivers grouped together. The DS90CR281 driver converts 28 bits of data into four LVDS data streams every clock cycle(33ns). This same clock is phase-locked and transmitted in parallel with the data streams over a fifth LVDS link. A group of eleven DS90CR282 Channel Link receivers on the Linker module convert the LVDS data streams back into TTL data in sync with eleven individual Channel Link output clock signals. The output clock signals are derived from the transmitted LVDS clock signals through a phase lock loop. The data on the LVDS pairs will be transmitted at 7 times the clock frequency. The LVDS clock signal is transmitted at the phase lock loop frequency.

The cable run from Finder Modules to Linker Modules will be short with most of the runs being six to ten feet in length. The cables are made out of 3M 3600 series cable and 3M Mini D Ribbon connectors.

A SL1/3 Finder module utilizes an 18 pair cable with 36 pin connectors and the SL2/4 Finder module utilizes a 25 pair cable with 50 pin connectors.

6.4.9 Linker Module Design

The Linker module has the responsibility of linking segments between the axial superlayers of the COT to form a track. The segments which are defined by pixels are found by the Finder modules. The Linker is separated into 288 ϕ slices of 1.25 degrees. Each slice has a dedicated chip with the task of finding tracks within the slice. The tracks found by the Linker chips are passed to the XTRP for extrapolation to other portions of the detector and used in the Level 1 trigger decision. A block diagram of the Linker module is shown in Figure 6.18. The Linker Module will be redesigned to process more detailed information from the Finder Module.

The Linker system will consist of 24 identical 9U VME modules each with 12 Linker chips. The modules reside in three Linker crates (8 cards in each crate) that are located above the Finder crates in the three XFT racks in the first floor counting room.

The Linker module as with the Finder module can be divided into two sections - Control logic and Data flow. The data flow through the Linker board starts with the receiving of pixel data by the Channel Link receivers. That received data is aligned to the board clock in the Input Formatter section which forwards the data to the Linker chips for track identification and finally onto the Output Formatter. A number of different diagnostic designs have been made for the Input Formatter, Linker and Output Formatter section. These diagnostic designs allow the reprogrammable parts to be used as drivers or receivers with internal read/writeable RAM blocks that are capable of holding data to be driven or received.

6.4.9.1 Control Logic

Control Logic includes: Clock circuitry, Flash RAMs, and a VME_SLAVE that performs the tasks of communicating with the VME system for control and error monitoring. The Linker module also uses a JTAG interface for testing and programming.

The Linker board implements a modified version of a VMEbus slave interface in a Altera Flex 10K EPF10K30RC240-3 FPGA. Only 32 bit aligned data

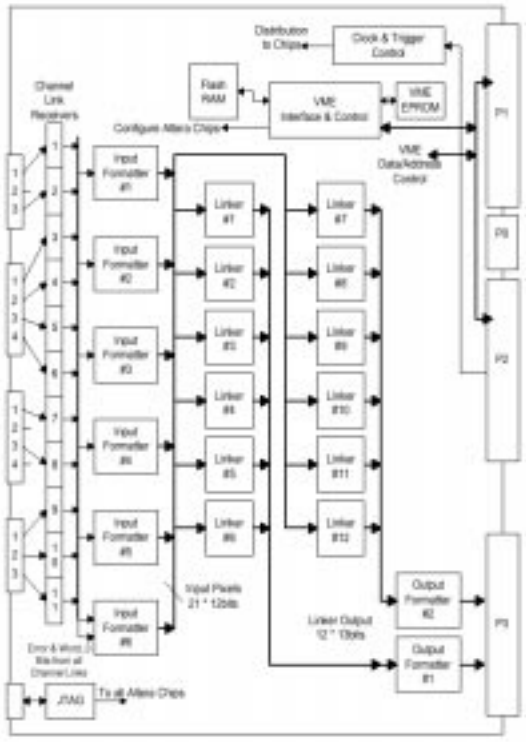

Figure 6.18: Linker Module Block Diagram.

transfers will be supported; these may either be single word transfers or block transfers. Only extended (32bit) addressing modes will be supported. The interface controls the loading of programs into the on board Flash RAM along with the download of the Flash RAM data to the Formatter and Linker FPGAs.

The onboard 33nsec, 66nsec, and 132nsec clocks are all derived from the CDF_CLK. The onboard 132nsec clock is phase shifted from the backplane CDF CLK using the DS1020 silicon delay line from Dallas Semiconductor. This chip allows delays of up to 256 nsec, in 1 nsec increments. The delayed clock is then manipulated in a scheme similar to the Finder modules using the Cypress CY7B991-7JC or Robo Clock. The resulting clock signals are redistributed throughout the module with National Semiconductor's Low skew clock buffer CGS2534V.

6.4.9.2 DataFlow

- Input Formatter

  There are 6 Input Formatter chips per board which are implemented in Altera Flex 10K EPF10K40RC240-3 FPGAs. The Input Formatters latch the data from the Channel Link receivers using the Channel Link output clocks, then synchronize the data to the on-board 33nsec clock. The output is distributed to the Linker chips. The Input chips also contain the pixel data level 1 pipeline and four level 2 buffers for VME readout. The 6th Input Formatter chip is also used for error checking: comparing word_zero, beam_zero and start bits from all Channel Link receivers.

- Linker chips

  The Linker chips are currently implemented in Altera Flex 10K EPF10K50RC240-3 FPGAs. These devices do not contain enough internal logic elements in make use of the addition information from the Finder Modules. Therefore, in the new design, the Linker Chips will use Altera's Stratix series FPGA. Each Linker chip accepts information from 6 Input Formatter chips, and searches for the best track. There are 12 Linker chips per board, each covering 1.25 degrees for a total coverage of 15 degrees per module Figure 6.19 shows a block diagram of the Linker chip.

  The Linker chip operates as follows: Each Finder sends the information from the 4 COT cells it processes to the Linker in 12 12bit words, 1 word every 33nsec. These words then have to be timedemultiplexed so the Linker can look at all cells in parallel, for all 4 superlayers. The inputs to the 12 Linker chips are slightly different, and so this routine is different for each Linker chip. There is a twofold symmetry in the Linker, which allows the number of stored roads to be cut in half. Effectively, each Linker is then arranged as two subLinkers, which we call A and B. T

  he pixels for Linker A and B are passed on to the road finding logic. There are $\sim$ 1200 4layer Roads implemented in the chip logic. Each road is stored as the "AND" of 4 pixels, one from each layer. The road finding outputs a 96 bit p_T word every 66ns. Each bit in this word corresponds to a valid track found with a given p_T bin.

  The 96 bit p_T word is presented to the "Best p_T Track" which determines what p_T to report. The BEST p_T logic is designed to report the median p_T bin of this cluster of p_T bins. In addition, the BEST p_T logic must handle the case where more

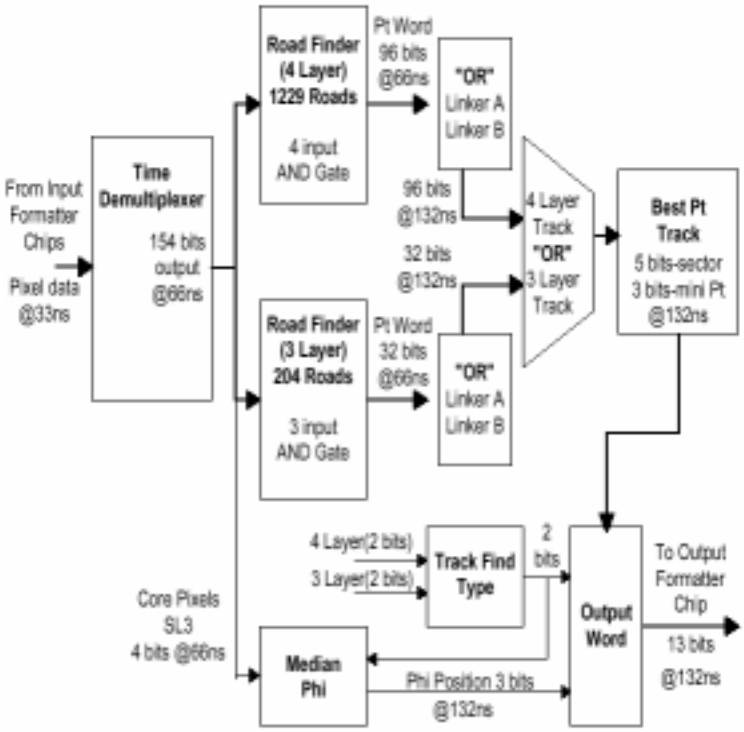

Figure 6.19: Linker FPGA Block Diagram.

than one track passes through a given Linker chip. The bias at present when this occurs is to select the cluster of p_T bins which is higher in p_T and then report the median of this cluster. The output of "Best p_T Track" is a 8 bit word with p_T and charge information: 3 bits of miniPt and 5 bits of section p_T .

The "Median ϕ" block looks at the 8 pixels reported from the Finder for superlayer 3 and determines a simple median of the pixels, outputting a 3 bit word. Remember that tracks are found in subLinkers A and B. If no track is found in a given subLinker, the pixels for superlayer 3 for that subLinker are masked off.

The Linker outputs information on the best track found every 132nsec. The output is 8 bits of p_T , 3 bits of ϕ, and 3 bits of code. The eight p_T bits are 3 bits of miniPt and 5 bits of section p_T . Only 7 bits are required to uniquely specify a p_T, but for space reasons this conversion is done in the Output Formatter chip.

- Output Formatter

  There are 2 of these chips per board implemented in Altera Flex 10K EPF10K30RC240-3 FPGAs. Each chip inputs 14 bits of data from 6 Linker chips every 132nsec. The Output Formatter forms the 7 bit p_T word using the 3 bit Mini p_T and 5 bit Section p_T from the 6 Linkers. In addition the Output Formatter implements the level 1 pipeline containing 78 bits(12 bits per Linker chip) of Linker information(p_T, ϕ, Track isolation). Duplicate tracks near the boundaries of the region covered by each Linker chip are removed and the tracking information is multiplexed into 4 data words that are sent out sequentially (every 33ns) to the XTRP system.

6.4.10 Linker TO XTRP Transmission

The found track information provided by the Linker module is transmitted one slot across the VME backplane to a Linker Output Module which converts the single ended signals to LVDS signals using National Semiconductor DS90CR31 devices. The LVDS drivers transmit the data across 50 feet of shielded twisted pair cable to a transition module in the XTRP crate. The 100 conductor twisted pair cable is produced by AMP inc. and uses the Amplimite .050 Subminiature D connectors. The transition modules use AMP 100 pin right angle Amplimite connectors.

The Linker Output Modules will be redesigned to accommodate the transmission of tracking information to a new Stereo Association Module. The current cables to the XTRP will be retained.

6.4.11 Upgraded Linker Implementation Results

As mentioned, each Run IIA Linker board contained a total of 21 Altera Flex10K-series FPGA's. In the development of the Run IIA Linker system, we used the Altera MAX+PlusII software package to simulate the timing and logic of the Altera FPGA's, and this software package was extremely reliable.

Altera has a new software package called Quartus, which is used for the programming and design of their Stratix series devices. The package can import files targeted originally for the Flex10K chips, and this has allowed us to quickly determine how much resources of a Stratix chip would be used by our Run IIA design. We have also used it to determine how fast the Stratix devices run compared to the Flex10K.

Our initial target device for the upgraded Linker chips is the Stratix EP1S25. This device has roughly 10 times the number of logic elements compared to the Flex10K50 device which is used for the RunIIA linker chips. In targeting this device, we have found:

- The standard Linker chip design uses $< 12\%$ of the logic resources of the EP1S25.
- Based on the maximum operating frequency, we expect to be able to run the devices about a factor of 3 faster than the current Run IIA devices. In implementing the Run IIA design, with no attempt at optimization of the time, we find the design run 30% faster using the Stratix devices.
- The Stratix comes equipped with a large number of LVDS I/O pins, and built in phase locked loops (PLLs) for clock multiplication and I/O SERDES transmitter/receiver circuitry. This has the potential to dramatically reduce the total chip count on the Linker (and by extension, the Finder) boards.

We expect that the upgraded linker will contain approximately 4 times the number of roads as the current Run IIA design, so fitting the upgraded design into a Stratix device should be easily possible.

6.4.12 XFT Stereo Segment Finding

Below we summarize the design and implementation of segment finding in the stereo layers of the COT. This design is very similar to the axial layer segment finding of the existing XFT system. Documentation of the XFT can be found on the web [8] and a more detailed description of stereo segment finding is in [7].

6.4.12.1 Design

In the current XFT system, the Finder searches for high-p_T track segments in each of the four axial superlayers of the Central Tracker. Each found segment is characterized by a mean ϕ position in the axial superlayer, called a pixel. Pixels are found by looking at TDC hit information in four neighboring COT cells and making a comparison to predefined sets of hit patterns, or "masks", that are consistent with good track segments. A mask will change depending on the ϕ of the track and its angle through the cell (or p_T). All possible masks for tracks with $p_T \geq 1.5$ GeV/c are part of the Finder PLD design for a given superlayer. Every 132 nsec the Finder outputs 12 bits per cell (12 pixels for the inner two axial layers, 6 pixels times 2 slopes for the outer two axial layers) to the Linker system.

The stereo segment finding works almost exactly like the segment finding for the axial layers. In defining the masks, we assume that the stereo angle is zero. The total number of masks needed to identify track segments with p_T greater than 1.5 GeV/c is 300. As with the outer 2 axial layers (SL6 and SL8), we divide each cell into 6 pixels.

The measurement of the z coordinate of a track in a stereo layer of the COT requires an identified track in the r-ϕ plane associated with a measurement of the ϕ position of the track segment in the stereo layer. This association is performed by matching a pixel in SL6 of the track to a range of pixels in SL7. The range depends on the p_T (or curvature) of the track and the stereo angle. If the track passes through the stereo layer at a z coordinate other than z=0, there will be an apparent difference in ϕ between the extrapolated position of the r-ϕ track at the stereo layer (denoted ϕ_{exp}), and the measured ϕ position of the track segment in the stereo layer(denoted ϕ_{fnd}). The z coordinate is given by the following expression:

$$z = \tan\left(\phi_{exp} - \phi_{fnd}\right) \cdot \frac{1}{S} \qquad (6.1)$$

where S is a constant dependent on the "stereo angle". For COT stereo layer 7, $S = 2.75 \times 10^{-4}$. Based on the expected resolution in ϕ_{exp} and ϕ_{fnd}, we can expect a resolution on z at SL7 of better than 6 cm.

6.4.12.2 Implementation

The stereo Finders are implemented using Altera's programmable logic devices populating 9U VME cards, just as for the axial Finders. By definition, a single Finder PLD looks for valid track segments in each of 4 neighboring COT cells. Since the total number of cells in SL7 is 432, the required number of Finder PLDs is 108. Due to the size and inflexibility of the Ansley cables, we are limited to a practical maximum of 8 Finders per board. We plan to use 6 Finders per board. This makes each board identical, and also allows room for the circuitry needed to format the data before sending it to other Level 1 or Level 2 boards (described in section below). Using 6 Finders per board, we need a total of 18 stereo Finder boards. Since each VME crate has 21 slots, of which 2 are taken up by the controller and tracer, we can fit all the stereo Finder boards into a single crate.

Many parts the existing XFT Finder system design may be used for stereo segment finding without requiring any changes. These include the TDC transition module, the Ansley cables(we have enough in hand), Finder transition module, and the Finder cPLDs. However there are some changes. A new Finder backplane will be needed as it is responsible for routing neighbor wires from slot to slot. The data input section and Finder cPLD section of the Finder board will remain the same, but the output data driving sections will need to be changed. On the axial Finder boards, National channel links are used to drive the output to the Linker boards. This should be replaced with a design to drive the data to Level 1 or Level 2 boards.

6.4.13 Stereo Segment Linking

To include stereo information in Level 1, we will replace the Linker Output Modules (LOM), which simply buffer the linker output prior to shipping to the XTRP, with a new version (LOM II) that would perform two functions:

- buffer the linker output prior to shipping to the XTRP (as is done currently)
- send a duplicate copy of the linker output to the Stereo Association Module (SAM).

The Stereo Association Modules (SAM) would reside in a nearby Stereo Matching/Track Trigger (SMTT) crate. Twelve SAM modules would reside in the SMTT crate, each module covering 30° of azimuth. Each SAM would take as input the track data from two linkers and several cables of stereo segment data from the stereo finders using channel links. There are 18 stereo finders, each one handling 20° of azimuth. Each one would have four channel-link based outputs, two copies for each 10° half of the board. Having the duplicates allows for overlaps in the regions in going from the 18 stereo finders to 12 SAMs. The SAM would perform several functions

- Associate the appropriate 36 bits of stereo data with each 2D XFT track, using look-up maps
- Pipeline and buffer the 3D tracks for readout by L2 and DAQ
- Provide tracks to the Track Trigger 3D system

The interaction between the SAMs, Track Trigger and the Level 2 trigger would be very similar to the XTRP/Track Trigger system in the current Run 2A trigger. In the existing system, the XTRP databoards pass track data to the Track Trigger on dedicated backplane lines. Additionally, the XTRP Clock/Control Board supervises the creation of a sparsified list of tracks that are transmitted to the SVT and Level 2.

In the new system, the SMTT crate would have a Clock/Control Board, 12 SAMs and the Track Trigger 3D board. The interaction between the SAMs and the Track Trigger 3D, as well as the generation of a sparsified list of 3D tracks for Level 2 would then be identical to the current implementation in the XTRP/Track Trigger system.

The stereo association performed by the SAMs would be performed synchronously and in parallel. Additionally, the SAMs would have Level 1 pipelines and Level 2 buffering so that the system can be readout in diagnostic mode. The only aspect to the SAMs which is not identical to functions currently performed in the XTRP databoards is the stereo association. The SAMs will require a three stage procedure. In the first stage, the axial track information is used to determine a set of possible stereo patterns for that track. In the second stage, the stereo patterns

are tested against the found patterns (produced by the stereo finders). The third stage would then compile the full track information (axial + stereo) and put that information into a Level 1 pipeline. Additionally, the SAMs will interact with the Track Trigger, which is discussed in the next section.

6.4.14 The Track Trigger 3D

In the first stage of the stereo association, each track will be tested against a momentum threshold. If that track is above the threshold, then that track is identified as a track that will be processed by the Track Trigger board. For each 15° wedge, up to two tracks can be sent to the Track Trigger board. This algorithm and interaction with the 12 SAMs is identical to the XTRP/Track Trigger interface in the current system.

The Track Trigger decision will be generated based upon the kinematic information from each track: transverse momentum (p_T), charge, azimuthal angle (ϕ), isolation and dip angle (θ). The system will support up to 16 different types of triggers, but is limited to quantities calculated for single tracks or pairs of tracks. Regardless of these quantities, the Track Trigger will generate an auto-accept if the charged track multiplicity is greater than six.

Functionally, the Track Trigger 3D will use lookup tables loaded into static RAM. These tables take advantage of the azimuthal symmetry of the tracking chamber and XFT. In order to perform these operations quickly, lookups for track-pairs are done in parallel. The Track Trigger looks at up to 15 possible pairs of tracks (all possible pair-combinations of up to 6 tracks) and generate up to 16 different trigger decisions [9].[3]

6.4.15 Timing

The Level 1 trigger timing constraints will be met by performing the stereo association and Track Trigger 3D algorithms in parallel with the remainder of the Level 1 trigger. In the current system, the XFT tracks are sent to the XTRP, where calorimeter and muon extrapolations are performed in addition to the Track Trigger functions. The new system only has to meet the requirement that the Track Trigger 3D decision bits arrive at preFred within the Level 1 decision time. There are no other intermediate timing milestones that are required.

For a given event, the stereo track segments are available at the same time that the axial track segments are available. Stereo association can not begin until the axial finders have completed their axial segment matching. After that, the tracks are transmitted to the SAMs and stereo matching can begin. Based upon our experience with the XFT and XTRP, we know that transmission of data and unpacking can be done in two 132ns clock cycles. The lookups and associated logic will take an additional 3-4 clock cycles, followed by 3-4 clock cycles to generate the trigger decisions. Based upon these estimates, the stereo tracking trigger path will be done before the Level 1 electron and muon triggers.

6.4.15.1 3D tracking performance

We have implemented a version of the stereo segment finding algorithm in the XFT standalone simulation. For both the axial layers and the stereo layer, the Finder is implemented using a database of masks. The association of SL7 segments to 2D XFT tracks is done by considering all segments in a valid window around the 2D XFT track. Details of this study can be found elsewhere [7], but as an example of the performance we consider the difference between the true z position and the XFT determined z position. This is shown in Figure 6.20 for a sample of simulated tracks. In this simulation, the track p_T was flat from 1.0 to 10.0 GeV/c. Tracks from an average of 2 minimum bias events were overlaid on these Monte Carlo events to simulate the effect of occupancy in the COT in Run 2. These distributions do not degrade appreciably if the average number of overlaid minimum bias events is increased to 10. The z coordinate is given by equation 1. The uncertainty on the z position is determined by how well we measure the two phi positions. In this case, the uncertainty is dominated by the extrapolation uncertainty on ϕ_{exp}, which comes from the 2D XFT track measurement errors on p_T and ϕ_{SL6}. The z position resolution is $\sim$ 6cm for the overlap of both the 2 and 10 minimum bias events.

6.5 SVT Upgrade

The SVT trigger, designed for CDF's Run IIa silicon detector, requires minor adaptation to accommodate

[3] The Track Trigger sends 16 trigger bits to preFred. We reserve 1 of those bits to signify > 6 tracks, leaving 15 independent triggers that can be generated.

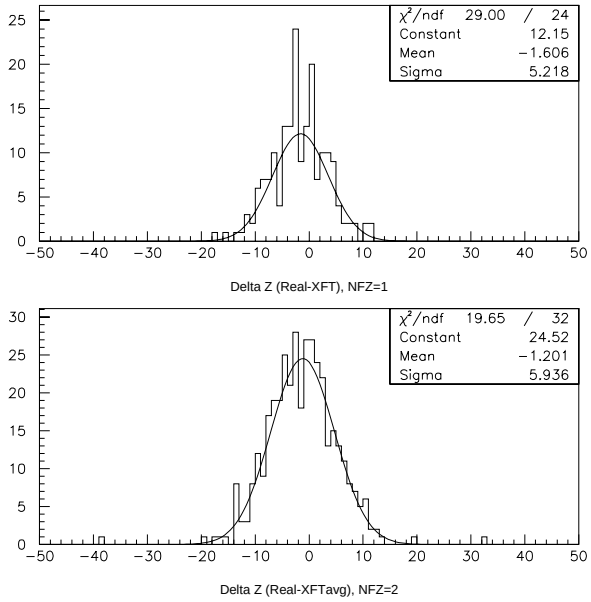

Figure 6.20: Top plot: Difference between the true z position and the XFT z position at outer stereo layer for one and only one valid stereo segment near XFT track. Bottom plot: Same when two valid stereo segments near XFT track. For both plots the average number of overlaid min-bias events is 2.

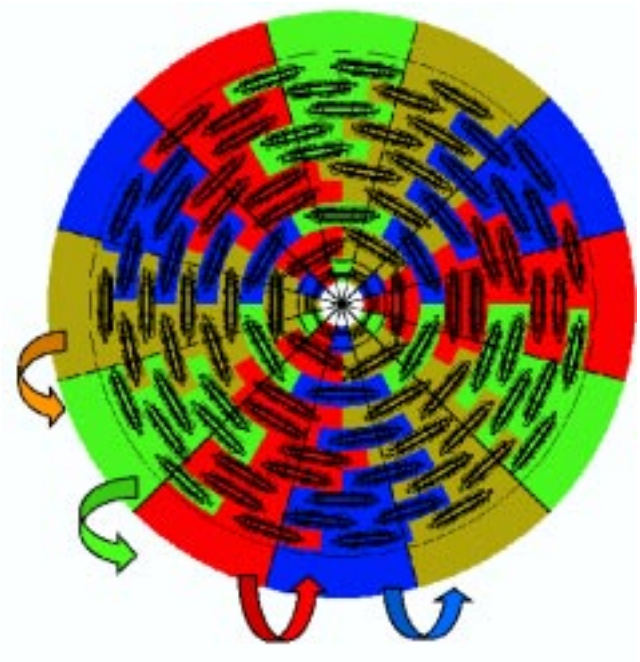

Figure 6.21: The SVX Run IIb geometry mapped onto the SVT geometry. To account for the staves that cross wedge boundaries, data is processed by hit finders in wedge N and wedge $N+1$. This function will be performed by additional Merger boards.

the geometry of the Run IIb silicon detector. Two of SVT's Run IIa design assumptions must be relaxed for Run IIb. First, the twelve-fold symmetry of SVX-II, which permits twelve identical SVT "wedges" to process data independently, will no longer exist. Second, a given set of linear track fitting coefficients can no longer span 30° in azimuth, because the radius of each silicon layer varies from stave to stave within a 30° sector. Relaxing these two assumptions requires, respectively, the construction of twelve additional Merger boards of an existing design and an extension of the Track Fitter design to allow the choice of fit coefficients to depend upon the pattern of hit coordinates within each azimuthal sector.

The existing SVT is constructed as twelve identical sets ("wedges") of VME boards. Each wedge of SVT performs strip clustering, track finding, and track fitting for 30° of the Run IIa detector in azimuth, without exchanging data with other SVT wedges. Tracks crossing wedge boundaries are not identified. The detector readout (from FIBs to VRBs, via a set of fiber-optic splitters to provide a copy of the data for SVT) is organized such that the raw data from a given 30° slice of SVX-II are sent to the clustering (Hit Finder) boards in the corresponding SVT wedge.

In Run IIb, track finding and fitting will still be performed independently for each 30° sector in azimuth, but hit data from some staves in the outer detector layers must be shared among two SVT wedges. This can be seen in Figure 6.21, which shows the implicit SVT geometry mapped onto the SVT IIb detector. The data sharing must be implemented within SVT because a given stave's raw data can only be sent to one Hit Finder board. Each Hit Finder board already has two output connectors, only one of which is currently used. The Hit Finders can be programmed to send each silicon cluster to the first output, the second output, or both, depending on the cluster's position within a stave. The detector will be cabled such that data received by SVT wedge N's Hit Finders will be needed in wedge N or $N+1$, never $N-1$.

In Run IIa, each SVT wedge contains a single Merger board (four inputs, two identical outputs), which concatenates lists of clusters from three Hit Finders and a list of drift chamber tracks from the XTFB board (XTFB feeds all twelve wedges) and sends them to an Associative Memory Sequencer board and a Hit Buffer board. In Run IIb, SVT wedge N will contain a second Merger board, which

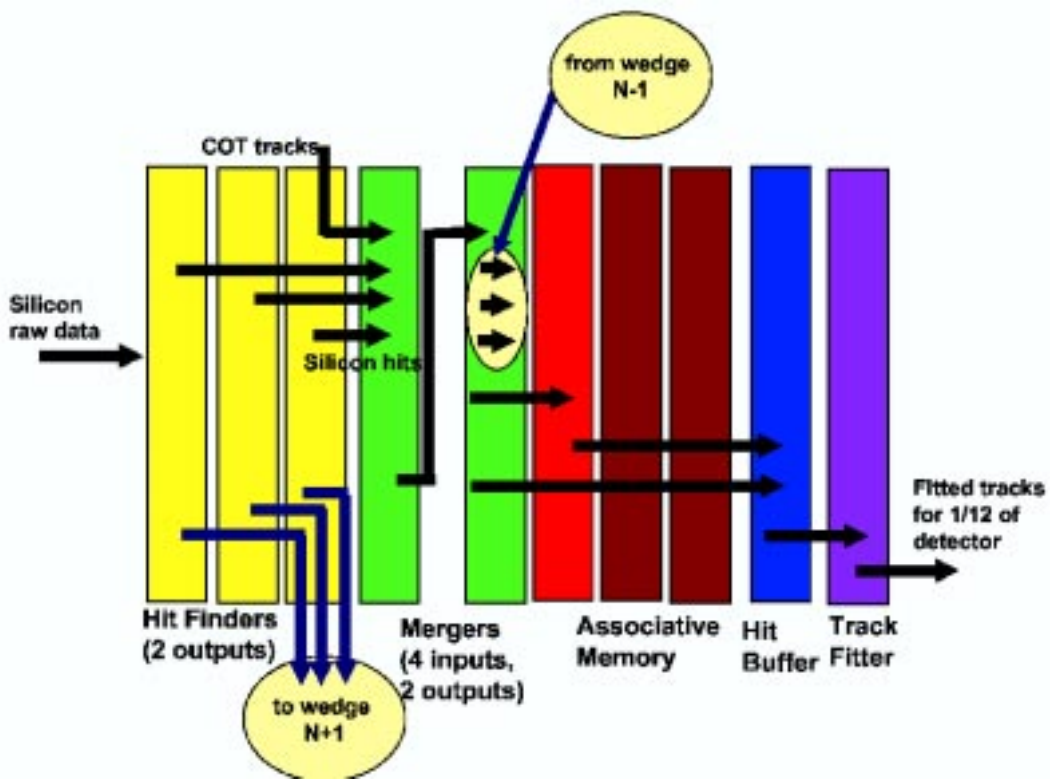

Figure 6.22: SVT data flow in Run IIb. The additional Merger boards will allow data to be passed to wedge $N+1$ from wedge N. This accounts for the Run IIb SVX geometry while retaining the Run IIa SVT framework.

concatenates the first Merger's output and the clusters forwarded by wedge $N-1$'s three Hit Finders. The second Merger's two outputs will feed the AMS and Hit Buffer; the first Merger's second output will be unused. This is shown in Figure 6.22. The current SVT crates can accommodate the additional boards. To minimize added cable bulk, the Track Fitters will move from the "wedge" crates into unused space in the "fan-in" crate, and the added Mergers will occupy the Track Fitters' current positions. (Track Fitters and Mergers have no P3 connection and can occupy any SVT crate position.)

The number of readout chains in the Run IIb detector is compatible with the SVT system and studies have found that the expected readout times are within the window allowed for the trigger at 132 or 396 ns operation.

The current SVT Track Fitters perform a fast (250 ns), linearized fit using FPGAs and lookup memories. Each fit transforms six measured coordinates (drift chamber curvature, drift chamber azimuth, and four silicon cluster positions) into three fitted parameters (curvature, azimuth, and transverse impact parameter) and three "constraint" values that can be squared and summed to form a χ^2 goodness of fit. The linear fit is essentially a matrix multiplication and vector sum,

$$(c, \phi, d, \chi_1, \chi_2, \chi_3) = \vec{p} = \vec{p}_0 + V \cdot \vec{x} \qquad (6.2)$$

whose coefficients and offset are precomputed. To reduce the number of bits needed in FPGA multiply operations, the offsets are indexed by the road number found in the SVT pattern recognition stage:

$$\vec{p} = \vec{p}_0^{\,\text{road}} + V \cdot \left(\vec{x} - \vec{x}^{\,\text{road}}\right) \qquad (6.3)$$

Each Track Fitter's coefficients can vary by bulkhead (z segment) within the detector and according to which four of the five SVX-II layers have hits available to fit, but they can not vary by road number. The uniformity of the Run IIa detector geometry allows each set of fit coefficients to span a wedge.

The Run IIb Track Fitter will closely resemble the Run IIa design, allowing a large fraction of the existing schematic diagram and firmware to be reused. The principal change is to use FPGAs and SRAMs

available today at a cost comparable to the components used on the existing Track Fitters, which allows us to increase the number of possible coefficients per wedge by a factor of eight and to make the choice of coefficients depend upon the road number. Preliminary studies indicate that replacing each current set of fit coefficients with eight sets, indexed by road number, will be adequate to represent the stave geometry of the Run IIb detector.

6.6 Level 2 Decision Crate Upgrade

6.6.1 Introduction and Motivation

In this section, we describe an upgrade for CDF's L2 decision crate for Run IIb. We start with an overview of the CDF Run II trigger, and then describe the requirements for the L2 decision crate, including the various data paths, sizes and timings. We briefly describe the Run IIa system. Next, we explain what the requirements are for the next phase of CDF (Run IIb) and how we intend to meet those requirements, incorporating lessons learned from the Run IIa project. We conclude with a brief summary.

6.6.1.1 CDF Trigger architecture in Run II

Fig. 6.23 shows part of the CDF Run II three level trigger system. Level-1 (L1) and Level-2 (L2) use custom-designed hardware to find physics objects based on subsets of the detector information, as shown in the Figure. Level-3 uses the full detector resolution to reconstruct complete events in a processor farm. The goal of each stage in the trigger is to reject a sufficient fraction of the events to allow processing at the next stage with acceptable dead time.

The L1 system is a synchronous 42 stage pipeline. When an event is accepted by the L1 trigger, all data is moved to one of four L2 buffers in the front end electronics, and trigger data is sent to the asynchronous L2 system. Here, some limited event reconstruction is performed and a final L2 decision is performed by custom processors in what is called the "Global Level 2 Trigger" in the diagram. It is this subsystem of the L2 trigger that we propose upgrading for Run IIb.

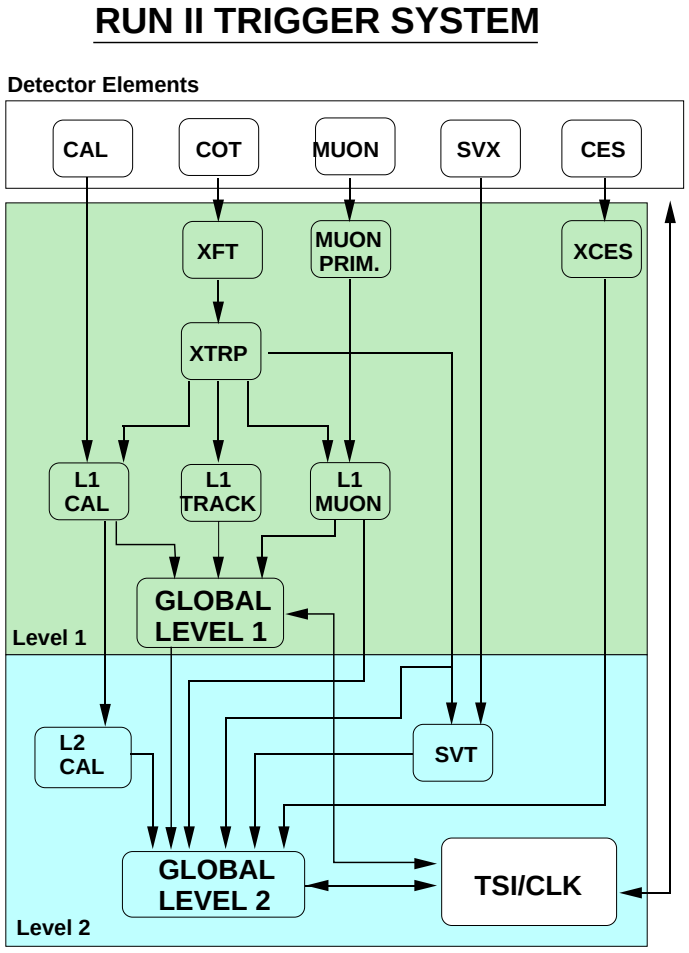

Figure 6.23: CDF Run II Trigger architecture, adapted from Reference [10]. Note that the L3 farm is not shown in the picture.

	L1	XTRP	SVT†	L2 Cal†	L2 Iso†	Shower Max†	$\mu^\dagger$	ΣE_T, $\not\!\!E_T$
Tracks	⋆	⋆	⋆					
Jets	⋆	⋆	⋆	⋆				
e's	⋆	⋆	⋆	⋆	⋆	⋆		
γ's	⋆			⋆	⋆	⋆		
μ's	⋆	⋆	⋆				⋆	
τ's	⋆	⋆			⋆			
ΣE_T	⋆							⋆
$\not\!\!E_T$	⋆							⋆

Table 6.3: Examples of the physics objects used in L2 decisions. Each row represents a physics object, and each column represents a trigger primitive. For a given row, the trigger primitives that are used to make the physics object are marked with a star (⋆). Those primitives that are first available in L2 or where new information is available in L2 are marked with a †. This is not an exhaustive list.

6.6.1.2 Level 2 Trigger Functionality and Requirements

By way of a review, we will describe the requirements of the L2 decision crate in Run II. The L2 decision crate makes the final L2 trigger decision based on primitives that have been created in the L1 trigger, and those found in two other L2 sub-systems, the Silicon Vertex Tracker (SVT) and the L2 Calorimeter (L2Cal). Additionally, the ShowerMax information is first available to the trigger in L2,[4] and an improved azimuthal (ϕ) measurement is available in the μ trigger system. L2 also has at its disposal all trigger objects used in L1, such as XFT tracks, ΣE_T and $\not\!\!E_T$ information, and the full description of the L1 decision in the form of the 64 L1 trigger bits.

These primitives must be quickly acquired and merged into physics objects in order to allow the trigger to make its decision. For instance, electrons are found by matching tracks to calorimeter clusters and the ShowerMax system. Table 6.3 shows the connection between some of the physics objects used in L2 and which trigger primitives are required to make them. After the primitives are acquired, the trigger applies basic kinematic requirements on the newly created physics objects or correlated sets of physics objects, and counts how many such objects or sets of objects exist to see if the required trigger criteria are met. Based on these requirements, the job of the L2 trigger decision system can be split into two parts: *loading* data and *processing* data. *Loading* describes how long it takes from a Level 1 accept (L1A) for the data to be available for processing such that a decision can be made. *Processing* describes how long it takes to unpack the data, form objects and make a decision based on simple kinematic cuts on objects or correlated sets of objects.

For Run IIa, the L2 trigger requirements are defined in [10, 11]. The L2 trigger is required to receive data at a L1A rate of $\sim$40 kHz, and accepts as many as $\sim$ 300 events per second, with a DAQ + trigger dead time of $\sim$ 10%. According to [11], attaining a mean loading time of 10 μs and a processing time of 10 μs plus an event-to-event exponential tail of mean 1.75 μs assures that the criteria will be met.

6.6.1.3 Overview of the Run IIa L2 Decision Crate and Data Paths

The Run IIa L2 decision crate is designed to operate as a *two stage pipeline*. The goal is to be simultaneously loading one event while processing the preceding event. During the loading stage, the dedicated L2 hardware subsystems find and send downstream calorimeter clusters (L2Cal) and tracks in the silicon detector (SVT). These data are then transferred into the memory of the L2 processor nodes via the interface boards. In the second stage, the data is unpacked and the trigger algorithms are evaluated to make the L2 decision. The final decision is then negotiated with the Trigger Supervisor (TS). Due to the nature of the pipeline implemented in the decision crate, all L2 decisions are made in L1 accept order.

[4] The ShowerMax system is labeled as XCES in Fig. 6.23. In L2, the XCES information is received by RECES cards. For the purpose of this section, the two names will be used interchangeably.

Card	MB Type	System	Quantity	Link	VME
L1Int	master	L1 trigger bits	1	LVDS†	no
XTRPList	master	XFT tracks	1	LVDS*	yes
SVTList	master	SVT tracks	1	LVDS*	yes
Clist	master	L2 clustering	1	HotLink	no
IsoList	master	L2 isolation	1	Taxi	no
μlist	master and slave	L2 μ	1	HotLink	yes
RECES	slave	ShowerMax	4	Taxi	no

Table 6.4: L2 interface cards in the Run IIa L2 decision crate. The XTRPList and SVTList boards differ only in firmware. All told, the crate will ultimately hold ten interface cards of six different types. The link column indicates what type of connection exists for the inputs to these boards. As indicated by † and $\star$, the LVDS cables in the L1 board differ from the TrackList cables. The *VME* column indicates whether a system's data is available via a VME interface. All TL2D readout occurs via processor node's VME readout.

The current L2 decision crate is based on a dual-bus architecture. The crate consists of two distinct classes of boards. The *interface cards* are the connection to the rest of the trigger system. They receive trigger primitives from other L1 and L2 trigger subsystems and pass this information to the other type of board, the *processor node*. Currently, there are six different custom interface cards. Table 6.4 shows a list of interface boards. The connection between the interface boards and the processors is via a custom 128-bit wide backplane referred to as the *Magic Bus* [12]. All trigger data flows from the interface cards to the processor nodes on the Magic Bus; while configuration and readout is via the processor node's VME interface. Interface boards can either be Magic Bus masters, Magic Bus slaves, or both. Magic Bus masters broadcast their data onto the Magic Bus, where it is received by all processor nodes simultaneously. Data from Magic Bus slaves can be retrieved by an individual processor on an as-needed basis. This means that data is both pushed into the processors (via direct memory access (DMA)) and pulled from the interface cards in this architecture (via programmed I/O (PIO)). This architecture choice (DMA or PIO) is made to minimize the Magic Bus bandwidth requirements for each interface type.

The processor nodes in Run IIa are custom computers based on 64 bit, 500 MHz DEC Alpha processors (which are obsolete) with both a VME interface and a Magic Bus interface. All processor interactions on the Alpha board occur via a Peripheral Component Interconnect (PCI) bus. VME access to the processor is available via a VME-to-PCI bridge; similarly, Magic Bus access is available via a Magic Bus to PCI interface. The baseline specification for Run IIa calls for four such nodes in the decision crate. However, currently, we have not run with more than one node.

Table 6.5 shows the event data size for various L2 trigger objects at the present luminosity, $\mathcal{L} = 1 \times 10^{31}$ cm^{-2} s^{-1}. The numbers are based upon system performance in August 2002. n is an estimate of the mean (high tail) of the Run IIa occupancy based on data. The high tail is defined as the average plus $3 \times$ RMS. Muon and RECES input data are of fixed-length. Only the Region-of-Interest (RoI) data needs to be sent to CPU memory. In the Run IIa system, the muon and RECES RoI data is pulled by the processor node while processing the event.

The current loading time is dominated by the SVT/SVX processing time. While the mean total Magic Bus transfer time is ~ 5 μs, the SVT tracks only arrive at the L2 decision crate's front panel ~ 25 μs after a L1A, significantly later than the 10 μs goal. As the processor node waits for all data to arrive before analyzing the event, the total loading time is therefore defined by the arrival of the SVT tracks.[5] As of August 2002, the processing time for a single Alpha node is ~ 25 μs on average with significant tails; however, it is believed that aggressive optimization of the code and Alpha processor firmware could reduce this processing time to ~ 15 μs. This level of performance will allow this system to satisfy the Run IIa needs.

[5] There is a simultaneous effort ongoing to speed up the SVX readout and SVT processing time.

System	Object	Object Size (bits)	mean(tail) n	Mean (Tail) Size @L2 inputs (bits)	Mean(Tail) Size into CPU mem (bits)
SVT	track	117	1.2(7)	140(819)	same
XTRP	track	21	8.4(31)	176(651)	same
L1	L1 bits	96/evt	fixed	96 (96)	same
CList	cluster	46	1.9 (7)	87(322)	same
Iso	cluster	145	1.9 (7)	275(1015)	same
μ	muon	11K/evt	fixed	11K(11K)	RoI only: $<$ 1K
RECES	shower	1.5K/evt	fixed	1.5K(1.5K)	RoI only:$\sim$ 0.1K
Average total data size				13.3K(15.4K)	$<$ 1.9K(4K)

Table 6.5: Data sizes for various L2 trigger objects at $\mathcal{L} = 1 \times 10^{31}$ cm^{-2} s^{-1}. The numbers are based on system performance as of August 2002. n is an estimate of the mean (high tail) of the Run IIa occupancy based on data. The high tail is defined as the average plus 3 $\times$ RMS. Muon and RECES input data are of fixed-length. Only the Region-of-Interest (RoI) data needs to be sent to CPU memory. In the Run IIa system, the muon and RECES RoI data is pulled by the processor node while processing the event. The RoI numbers are a rough estimate.

System	Object	Object Size (bits)	mean(tail) n	Mean (Tail) Size @L2 input(bits)	Mean (Tail) Size into CPU mem(bits)
SVT	track	117	3 (12)	351(1404)	351(1404)
XTRP	track	21	19(76)	399(1596)	399(1596)
L1	L1 bits	96/evt	fixed	96 (96)	96 (96)
CList	cluster	46	7 (28)	322(1288)	322(1288)
Iso	cluster	145	7 (28)	1015(4060)	1015(4060)
μ	muon	11K/evt	fixed	11K(11K)	RoI only: $<$ 1K
RECES	shower	1.5K/evt	fixed	1.5K(1.5K)	RoI only:$\sim$ 0.1K
Average data size				14.7K(21K)	$<$ 3K(10K)

Table 6.6: Data sizes for various L2 trigger objects at $\mathcal{L} = 4 \times 10^{32}$ cm^{-2} s^{-1}. n is an extrapolation of the mean (high tail) of the occupancy to the Run IIb luminosity at $\mathcal{L} = 4 \times 10^{32}$ cm^{-2} s^{-1} with 10 interactions per crossing. The extrapolation is done by taking the high p_T occupancy of Run IIa data and adding 10 minimal bias events. The high tail is defined as the average plus 3 $\times$ RMS of the high p_T occupancy. For this extrapolation, no attempt has been made to take into account any growth terms. Muon and RECES input data are of fixed-length. Only the RoI data needs to be sent to CPU memory. In the Run IIa system, the muon and RECES RoI data is pulled by the Alpha while processing the event.

6.6.1.4 Requirements and Motivation for a Level 2 Upgrade

It is clear that CDF needs to be ready for an unexpectedly complicated trigger environment for Run IIb. Our system must be able to handle a peak Run IIb luminosity of $\mathcal{L} = 4 \times 10^{32}$ cm^{-2} s^{-1}, where we will see an average of ten interactions per crossing. This implies that the average data size will increase substantially, and, consequently, the combinatorics will grow in processing multi-object triggers. As a consequence, CDF will need to improve both the loading stage and the processing stage of the L2 decision system.

As the occupancy in the detectors increases with luminosity, the time it takes the L2 clustering and silicon tracking subsystems to find trigger primitives increases, as does the number of primitives found. To maintain the goal of a $\sim$10 μs loading stage, the increase in latency and data size of the upstream L2 subsystems must be offset by an increase in effective bandwidth of the L2 decision crate to transfer the trigger primitives into CPU memory.[6] For instance, in the case of L2 clustering, each additional cluster adds 1 μs of latency to the arrival time of the cluster data into the L2 decision crate. According to Tables 6.5-6.6, in Run IIa, the mean arrival time is therefore 2 μs, while in Run IIb, the mean arrival time will be 7 μs.

With the increase in data size, the amount of processing increases for single-object and multi-object triggers. To maintain similar performance as the Run IIa system in the processing stage, the higher demand on the processor must be offset by increased CPU power.

Table 6.6 shows an extrapolation of trigger data size to the expected peak Run IIb luminosity $\mathcal{L} = 4 \times 10^{32}$ cm^{-2} s^{-1}. The extrapolation is done by taking the high p_T occupancy of Run IIa data and adding 10 minimum bias events. The high tail is defined as the average plus 3 $\times$ RMS of the high p_T occupancy. In this extrapolation, no attempt has been made to take into account any growth terms.

Uncertainty of the trigger requirements

As mentioned in Section 6.2.2, the process of making an estimate for the increase of the amount trigger data includes signficant uncertainty. For instance, non-physics growth terms are as yet unknown and were not included in Table 6.6. Based upon our experience with Run Ib data, which at peak luminosities had had several interactions per crossing, many trigger cross sections experienced growth terms. For example, the muon trigger rates grew quickly with luminosity due to additional accidental coinicidences between tracks and muon stubs. These non-linear growth in rates place an additional burden on the trigger system as a whole, but particularly the Level 2 trigger system. The large uncertainty in the triggering requirements make it clear that a key component of any new L2 decision crate must be the ability to adapt to changing trigger environments. For instance, out-of-order event processing could be used to mitigate the effects of long tails in processing times for particularly busy events, and data could be suppressed early in the trigger chain if it is not needed for the decision to alleviate bandwidth needs.

Long-term maintenance

The long-term maintenance of the trigger crate must be kept in mind. The easiest way of providing long-term maintenance is to minimize the number and types of objects that must be maintained. Relying on commercial or externally supported components in as many places as possible allows us to reduce the load on CDF resources for long-term maintenance. The judicious use of such components also makes for clear upgrade paths of links and processors if the conditions warrant such upgrades.

Ability to Test and Commission

As the Run IIa to Run IIb transition is expected to be short, any new system must be commissioned *before* the end of Run IIa and be able to come up with a high degree of certainty. Past experience has shown that for systems without adequate testing capabilities, the commissioning process can be long and require considerable beam time, thereby, impacting the physics running. In order to achieve the goal of a minimum length transition period, any new system should be built with self-testing capabilities.

Summary of Requirements and Motivation

In summary, the uncertainty of the Run IIb triggering environment, the increase in occupancy at high

[6] Alternatively, one could upgrade the upstream systems to decrease their latency; however, this option is significantly more expensive.

luminosity, the obsolescence of the Run IIa L2 processors, the need to provide long-term maintenance and the uncertainty of the Run IIb triggering environment drives the need for an upgrade to the L2 decision crate. A new system must be flexible enough to handle Run IIb challenges and simple enough to assure long-term maintainability.

6.6.1.5 The Pulsar Approach

We propose to meet these requirements in a design based on the Pulsar board [13]. The Pulsar board was originally designed and constructed as a general purpose L2 test stand tool, but inherent in this design is the ability for the Pulsar to be a universal interface card.. In this approach, all trigger fragments are converted and merged into a self-describing data format by a universal interface card. The common data stream is then transferred via a standard link into a commodity processor, where the decisions are made. The only custom element in this system is the universal interface board. The Pulsar is that interface board.

In the next Section, we will describe the Pulsar board-level design, the standard link used and how we combine these elements into the new system. We will show this design can not only meet the required Run IIb bandwidth, but that it is flexible enough to adapt to the evolving Run IIb trigger challenge. Finally, we will show that the system is designed in such a manner as to allow rapid prototyping, commissioning and integration, and require minimal long-term maintenance.

6.6.2 Pulsar Approach

The Pulsar project started as a way to provide some of the internal and external test functionality missing from the Run IIa L2 Decision crate. However, the Pulsar board also designed to be a universal interface card. The board has all the L2 decision crate's interfaces and can either sink or source data for each path. The general design philosophy of Pulsar is to use one type of motherboard (with a few powerful modern FPGA's and SRAM's) to interface any user data with a standard link through the use of custom mezzanine cards. This makes Pulsar a *universal interface card*. CERN S-Link [14] is chosen as the standard link for Pulsar. Using S-Link, Pulsar can communicate with commodity processors via commercially available, high bandwidth S-Link to PCI/PMC (**P**CI **M**ezzanine **C**ard) interface cards.

S-Link is a CERN specification for an easy-to-use FIFO-like data link which can be used to connect front-end to read-out at any stage in a data flow environment. It is a standard that defines interfaces of source and destination sides of a point-to-point High Energy Physics (HEP) oriented data link, and it has been used in many HEP experiments (*e.g.* NA48 and COMPASS) and will be used at future LHC experiments (ATLAS, CMS, LHCb) where high bandwidth is required.

In summary, in the Pulsar approach, we propose to use one motherboard, one custom mezzanine card for HotLink fiber data, one custom mezzanine card for Taxi fiber data, and two CERN S-Link mezzanine cards for sending and receiving S-Link.

6.6.2.1 Baseline Pulsar System Configuration

Fig. 6.24 shows the baseline configuration for the new Level 2 trigger decision crate. We use a total of eight Pulsar boards to receive event fragment trigger data from the L1 trigger, XTRP, SVT, Muon trigger, L2 Calorimeter, L2 Isolation and ShowerMax. These interface versions of the board gather data from each subsystem, package it, and send it downstream. Each Pulsar board has access to the full L1 decision information and the L1 trigger tracks. This data can be used to reduce the data volume, by keying on the L1 information to decide if the data will be needed in the L2 trigger decision, or by only sending region-of-interest data downstream based on, for example, matches between tracks and muon stubs.

It is important to note that the implementation of the L2 Pulsar scheme requires **no** modification of any of the existing elements that provide data for Level 2. This means that all of the front-end and Level 1 trigger systems that provide data for Level 2 will be unmodified in going to the Run IIb system.

Each Pulsar merges event data fragments from multiple sources into one stream. The final Pulsar, the Global Processor Controller, streams the complete data packet into a CPU where L2 decision algorithms are run. The Global Processor Controller receives the trigger decision from the CPU and negotiates the L2 decision with the Trigger Supervisor(TS). Raw input data for each Pulsar can be saved in one of four DAQ buffers, and upon L2A, all Pulsar

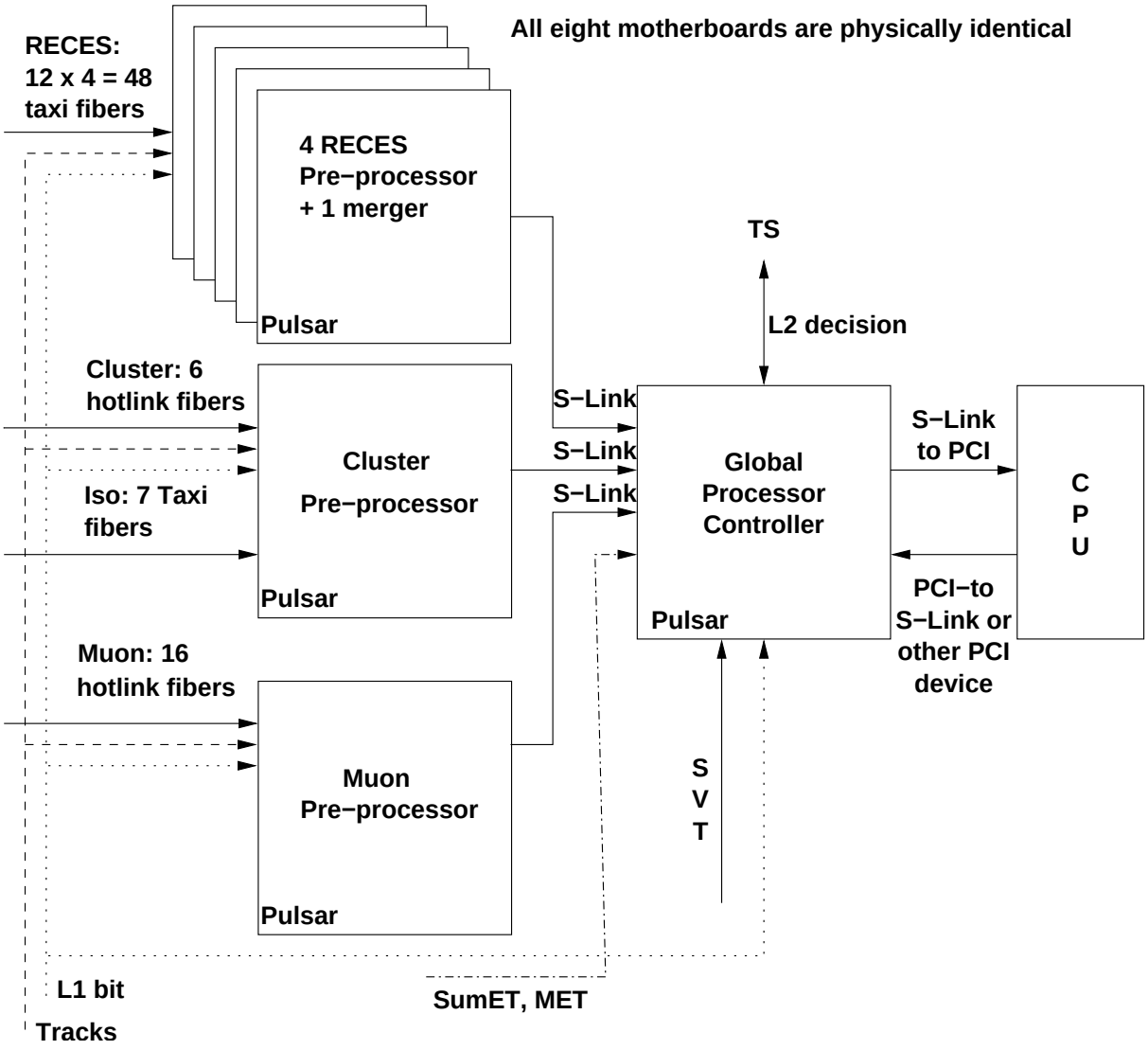

Figure 6.24: L2 Pulsar baseline configuration. The system lives in one CDF crate with a P2-style pass-through backplane in the P3 position. In total, eight physically identical Pulsar boards receive all L2 data. The final decision is made in a commodity CPU, which is connected to the crate via a S-Link to PCI card. The S-Link to PCI interface has a raw bandwidth of 260 MB/s per channel, while the S-Link bandwidth is 160 MB/s.

boards can make the data available to readout over VME.

The crate itself is a standard CDF VME crate with a pass-through backplane using P2-style (160 pin DIN) connectors in the P3 position. Since each Pulsar board is double width and takes 2 slots, eight Pulsar boards will take 16 slots in the baseline configuration.

6.6.2.2 Overview of Pulsar Board Design

Pulsar (as **Puls**er **a**nd **R**ecorder) is a 9U VME board. Fig. 6.25 shows the Pulsar block diagram. Each Pulsar has four mezzanine card slots. Data is received from these mezzanine card slots, processed and validated. Similarly, L1 and XFT or SVT track data is received via dedicated connections. Finally, data is sent downstream via one of two S-Link channels on the P3 connector to either another Pulsar board or to a commodity CPU. In addition, one connector is compatible with the TS-L2 protocol.

The Pulsar motherboard is dominated by three FPGA's: two *DataIO* FPGA's and one *Control/Merger* FPGA. Each DataIO FPGA provides the interface to two mezzanine cards. The DataIO FPGA's function is to receive data from the mezzanine cards, do any path-specific manipulation and error checking, and convert the data into S-Link format. While it is not strictly necessary, the use of a standard, self-describing data format is very useful. First of all, it makes the firmware design in both DataIO and Control FPGA very similar; secondly, the data will identify itself downstream and one can pack other information (such as buffer number, L1 trigger information and error conditions) in the header and trailer at each stage to allow robust error checking.

The Control FPGA merges data from the two DataIO FPGA's and sends the data to the P3 connector, again in S-Link format. In addition to the 9U VME board, a simple VME64x transition module is required. This card sits in the same slot as the Pulsar. It consists of two Common Mezzanine Card (CMC)[7] connectors for the two S-Link channels driven by the Control/Merger FPGA on the P3 connector. In addition, there are spare signal lines to the P3 connector from this FPGA.

[7]CMC is an IEEE draft standard for a family of mezzanine cards designed to be used interchangeably on VME, VME64, VME64x and CompactPCI cards. P1386/Draft 2.4a.

The four mezzanine card slots on the Pulsar motherboard are also CMC compatible and are designed to hold either custom mezzanine cards or S-Link mezzanine cards. There are two types of custom mezzanine cards, Hotlink and Taxi, which are used to interface with other L2 systems.[8] Each custom mezzanine card accepts four fibers, so that a total of 16 fibers can be accommodated per Pulsar board. The ability to plug in S-Link mezzanine cards allows Pulsars to be chained: any Pulsar can accept the output of up to four Pulsars using CERN's Link Source Cards (LSC's) and Link Destination Cards (LDC's).

The L1 and track data is handled somewhat differently than the fiber data. A look at Table 6.3 reminds us that all trigger objects require L1 trigger decision information (as CDF's trigger is path-driven) and many require tracks. In order to distribute the task of making objects out of trigger primitives, L1 bits and tracks are distributed to each FPGA. The L1 bits can be used to suppress data that isn't required for a trigger decision at an early stage. Track data can be used to only pass data in a region of interest downstream, thereby again reducing the data size, or, in a more ambitious approach, to create physics objects.

We choose Altera 20K400 APEX FPGA's in a 652 pin BGA package for both the DataIO and Control/Merger FPGA. This choice is largely driven by IO requirements, as this chip has roughly 500 User-IO pins. In addition to an internal 26KB memory, each DataIO FPGA also is connected to a $128K \times 36$ fast SRAM (CY7C1350).

The DataIO FPGA and Control/Merger FPGA are very similar in their functionality. Each takes two data streams and merges them into a common stream. The DataIO FPGA also must accommodate the differences between various mezzanine cards and do any necessary pre-processing; however, this functionality can be cleanly separated from the overlapping functionality. The core firmware is similar in all FPGA's on all incarnations of the Pulsar in the new system. See Sec. 6.6.2.3 for more details.

We will briefly describe how a Pulsar based system will accommodate each L2 data path. Fig. 6.24 shows their position in a baseline Pulsar based system configuration.

Pulsar as a pre-processor for the muon data path

[8]See Table 6.4 for a listing of which systems use which links.

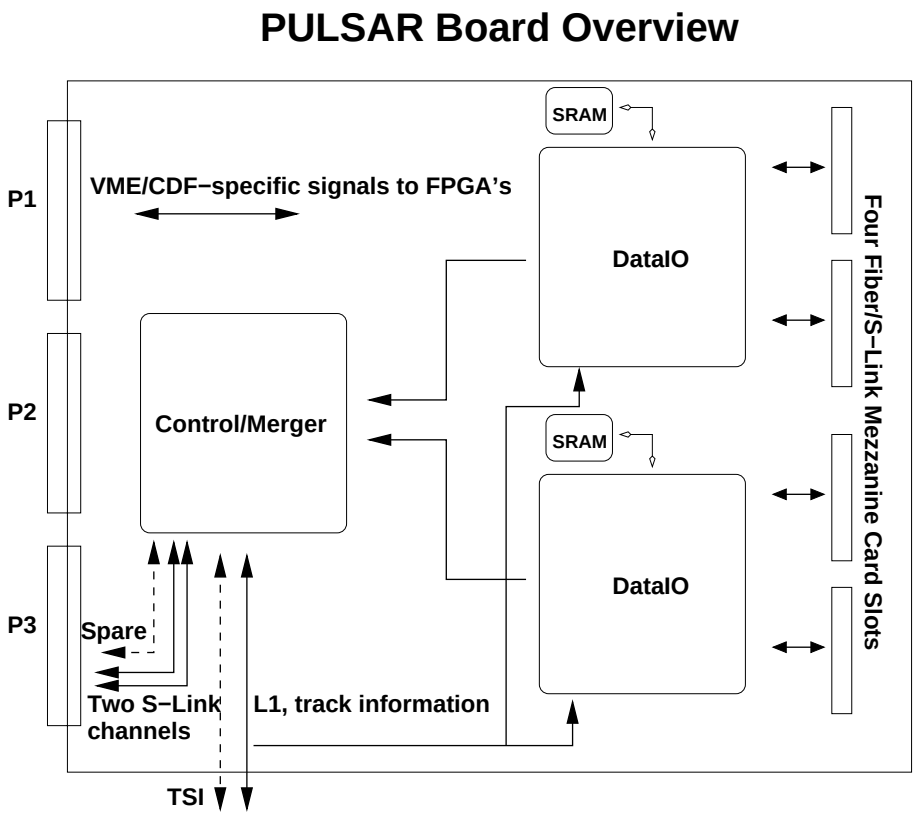

Figure 6.25: Pulsar board block diagram. The 9U double width board has four mezzanine connections that accept custom mezzanine cards for CDF-specific fiber data and CERN S-Link cards. Three FPGA's of two types receive and merge the data from the mezzanine cards. All FPGA's are visible to the VME backplane and all see the CDF-specific P2 signals. The board is compatible with a standard CDF VME crate. The board also has an interface to the CDF Trigger Supervisor (TS) and inputs for trigger track data and L1 trigger bit data.

Level 2 Muon trigger data is transferred via 16 Hotlink fibers into the Level 2 decision crate. Each muon word is packed into 4 hotlink 8-bit words, though only 24 bits are significant. The baseline implementation packs this data into 32-bit words and sends it downstream for analysis.

Because the muon data is not zero-suppressed upstream, the data volume is large- about 1.3KB per event. There are several strategies for reducing the data volume. The simplest way to suppress muon data is to check Level 1 trigger bits and see if muon data is needed for the Level 2 decision, and, if not, send an empty packet downstream. Another option is to zero-suppress the data itself. Finally, one also has the option to use the on-board SRAM as a look-up table to match tracks with muon stubs and only send those stubs that have matches.

One Pulsar board can receive all 16 fibers with four Hotlink mezzanine cards.

Pulsar as a pre-processor for the Cluster and Isolation data paths

As with the muon case, the clustering data arrives on HotLink mezzanine cards. The cluster data is of variable length; information from one cluster is spread over several fibers. The cluster trigger data is transferred to the Level 2 decision crate via 6 hotlink fibers and one LVDS cable. One cluster's worth of information is encoded into 6 hotlink words per fiber over a total of 6 fibers. The information from the LVDS cable marks the end of the event. One Pulsar board can receive the data via two mezzanine cards and all CLIST data will be visible to one DataIO FPGA. The DataIO FPGA can then generate the cluster summary information and convert the data into S-Link format.

The Isolation data path case is similar to the cluster path. Here, six Taxi fibers carry the data, and one Taxi fiber carries the control information such as end-of-event bits. One DataIO FPGA can receive the Isolation trigger via two Taxi mezzanine cards.

One Pulsar board with two Hotlink mezzanine cards and two Taxi mezzanine cards can be used to receive both Cluster and Isolation data.

Pulsar as a pre-processor for the RECES data path

The RECES data path has 48 fibers, each fiber covers one wedge (east or west side) and the data is of fixed length. We plan to use four Pulsar boards each with 4 Taxi mezzanine cards to sink the RECES data and one additional Pulsar with 4 S-Link mezzanine cards to merge all the RECES data into one data stream. If the large RECES data volume is an issue, strategies similar to those described in the muon case can be used to reduce the data volume.

Pulsar as a processor controller

The Processor Control Pulsar will act as a S-Link merger to merge all the data from S-Link LDC mezzanine cards. It will also merge the SVT data and pack data from the whole event into a single S-Link package. Once all data fragments are received from all subsystems for each event, the Processor Control Pulsar will send the data to a commodity CPU via S-Link. Using a separate PCI slot, the CPU running the Level 2 decision algorithm can return the trigger decision information back to the Pulsar board Control FPGA via either a PCI to S-Link card, or another commercial PCI card with a simple custom daughter card. The Pulsar Control FPGA will then handshake with the Trigger Supervisor to finish the L2 process.

6.6.2.3 Pulsar firmware

The firmware for the Pulsar is written in VHDL, the Very High Speed Integrated Circuit (VHSIC) Hardware Description Language. The source code is maintained in a CVS repository. The task of the firmware is to take several data streams, merge them into a single common data stream in S-Link format, and send it downstream for further processing.

All Pulsar boards share the bulk of their firmware. Fig. 6.26 shows the basic merging data flow that is common to both the DataIO and Control/Merger FPGA in all boards. Data is tagged by its L1A FIFO information, which brings with it the L1A, L1R, and buffer numbers for the event. This information is placed in the data header and sent to a merge/verify/suppress stage. Data from the input sources is sent to the same stage. This stage reformats the data as required and fills the data part of the L2 data bank. Finally, a trailer is filled with any error flags. Fig. 6.27 shows the merge/verify/suppress stage in some detail. The main features in this figure are the three boxes labeled *unifier, validator* and *object creator/ data suppressor*. The unifier merges the incoming data streams into a single output data

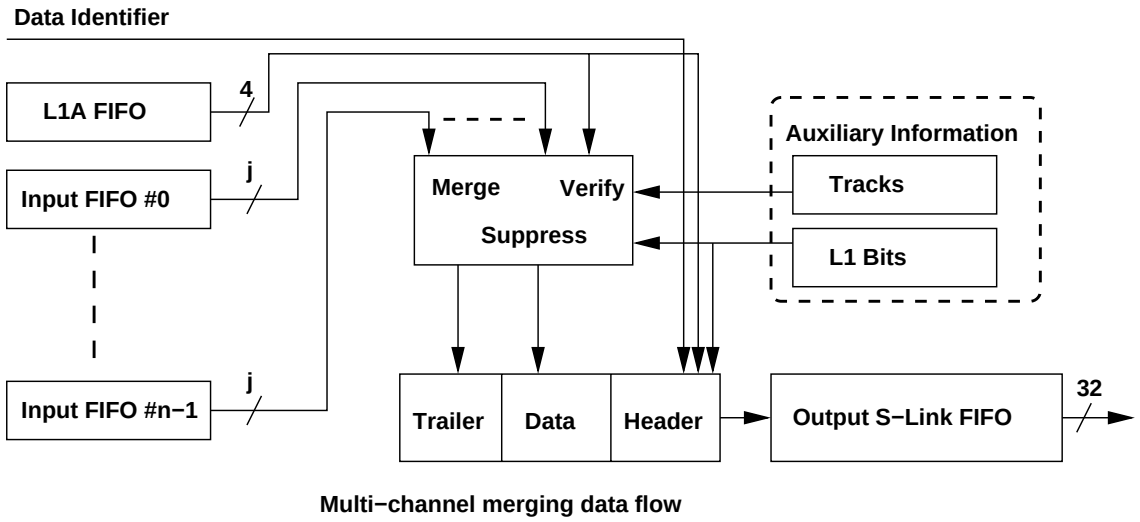

Figure 6.26: Basic merger firmware data flow. The data identifier is stamped into the header to show the data's origin. The input FIFO's can be S-Link channels, fiber data from the mezzanine cards, or the output of a previous merging stream, as long as it is in a FIFO. For DataIO merging, the input data streams are $j = 8$ bits wide. For S-Link input data streams, $j = 32$. The total number of streams n is two in the case of S-Link and the Controller/Merger FPGA and can be up to eight in the DataIO FPGA with fiber mezzanine cards.

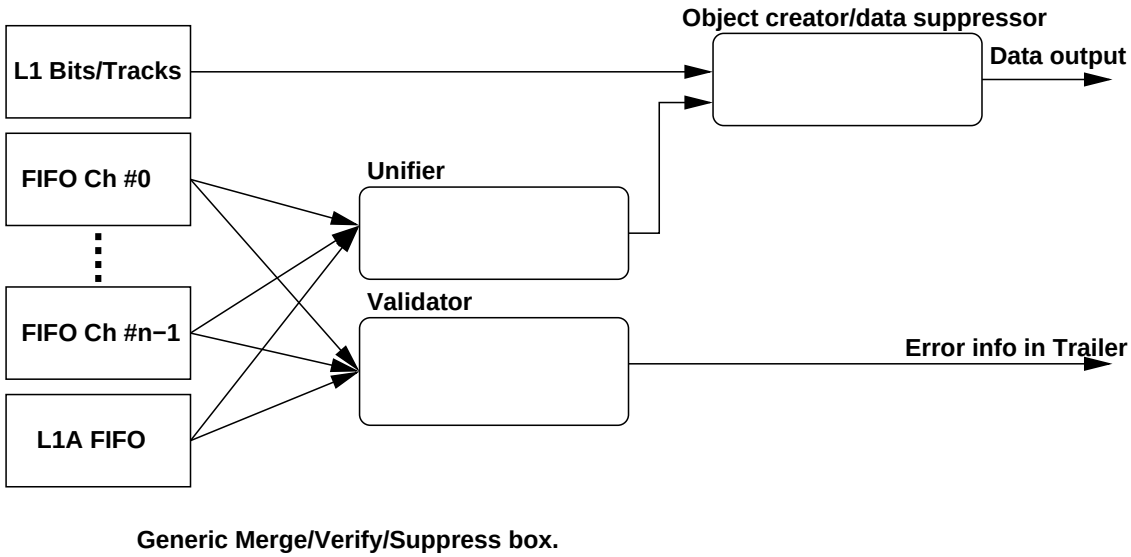

Figure 6.27: Generic view of merge/verify/suppress. Data from n FIFO channels is sent to both a unifier and a validator. The unifier does any necessary data manipulation such as final clustering, or packing into a 32-bit format. The resultant data from the unifier is sent to the object creator/data suppressor, which can be used to either generate physics objects or suppress un-needed data. In the baseline configuration, this box is a no-op and all data is passed downstream. The output of this process gets sent downstream. The FIFO data stream is also sent to a validator to check data integrity. The results of this integrity check are put in the data packet trailer. The unifier and merger are the only parts of the firmware that require customization for each subsystem. The creator/suppressor is optional and can be omitted completely.

stream, possibly manipulating the data in the process. The validator receives a copy of the incoming data stream and checks for data integrity. Any problems are tagged and put into the event trailer. The optional suppressor can be used to reduce data volume in cases where simply passing all data would challenge the bandwidth. This box will be a pass-through in most cases, as bandwidth is not expected to be an issue. As track data is available to the suppressor, matches between tracks and muon stubs, ShowerMax hits or calorimeter clusters can also be performed. In addition to the raw data, physics objects as in Table 6.3 could be created and passed downstream.

Fig. 6.28 shows an explicit example of the merge/verify/suppress box. The merger concatenates data coming from upstream sequentially, one FIFO stream at a time. This merged data stream is suppressed via a L1 bit mask. If none of the L1 bits in this event match the bit mask, we know that these data are not required for the trigger decision. An empty data packet will be sent downstream, and the data are only stored locally in one of the four DAQ buffers for the Level 2 data bank (TL2D) readout. The validator compares the buffer numbers in the incoming data stream to the event buffer number as received from the CDF backplane. Any errors are marked in the trailer.

A large amount of the firmware infrastructure is common to all Pulsar boards. This is possible as the fundamental process of moving and merging data is, in fact, identical. This makes the firmware requirements for the upgrade project manageable and maintainable.

6.6.2.4 Pulsar S-Link to PCI interface: bandwidth issues

Many S-Link cards, PCI/PMC interfaces and test tools are already commercially available, and new S-Link cards and S-Link to PCI interfaces are being developed at CERN to meet the bandwidth challenges in the LHC era. Each link itself can move data at 160 MB/s speed (40MHz clock with 32-bit data). A Simple S-Link to PCI interface card (SSPCI) has been available for many years and it has a raw bandwidth of 130 MB/s (achieved 100 MB/s on 33MHz/32-bit PCI bus). The newly available 32-bit S-Link to 64-bit PCI interface card (S32PCI64) is a high speed follow up of the SSPCI. It is designed for highly autonomous data reception and has a raw bandwidth of 260 MB/s [15].

A recent performance test in a laboratory environment indicates that one can achieve up to 150 MB/s data throughput with one S32PCI64 interface, and 300MB/s data throughput with two S32PCI64 interfaces on the fast PCI 66MHz/64-bit bus. The ultimate performance of the S32PCI64 will depend on the type of CPU architecture used. The performance tests described above were performed (at CERN) using PCs with a SuperMicro motherboard based on the ServerWorks LE chip-set. The memory of these PCs is fast enough to sustain the full speed of a 64bit / 66MHz PCI (520 MB/s) [16].

In summary, the bandwidth S-Link devices can provide is already comparable to or better than the S-Link bandwidth itself (160 MB/s). The bandwidth will continue to improve as CERN develops new S-Link to PCI interface cards . Of particular interest is the FILAR project, an S-Link to PCI interface which could handle four 160 MB/s links at once.

6.6.2.5 Final Decision-making: CPU choices

The baseline proposal for the final decision-making CPU is driven by two design requirements:

- high bandwidth into CPU memory
- low latency response time

We propose to address these issues via a server-class Intel-based CPU. We do not expect the processor to be CPU-bound, but instead will need high bandwidth, low-latency access to memory. While workstation or desktop systems may not fit these requirements, server-class systems do. In order to assure low-latency, we expect to require a real-time operating system. The freely available RTLinux, an open-source hard real-time Linux extension, is our proposed target OS [17].

6.6.2.6 Flexibility with Pulsar design

The Pulsar design is flexible in both the board configuration and in the ways in which the full system can be put together. While the baseline system is straightforward, more powerful scenarios are possible at the cost of somewhat more complex firmware programming. These improvements can be implemented as needed over time; thus the initial firmware requirements are modest.

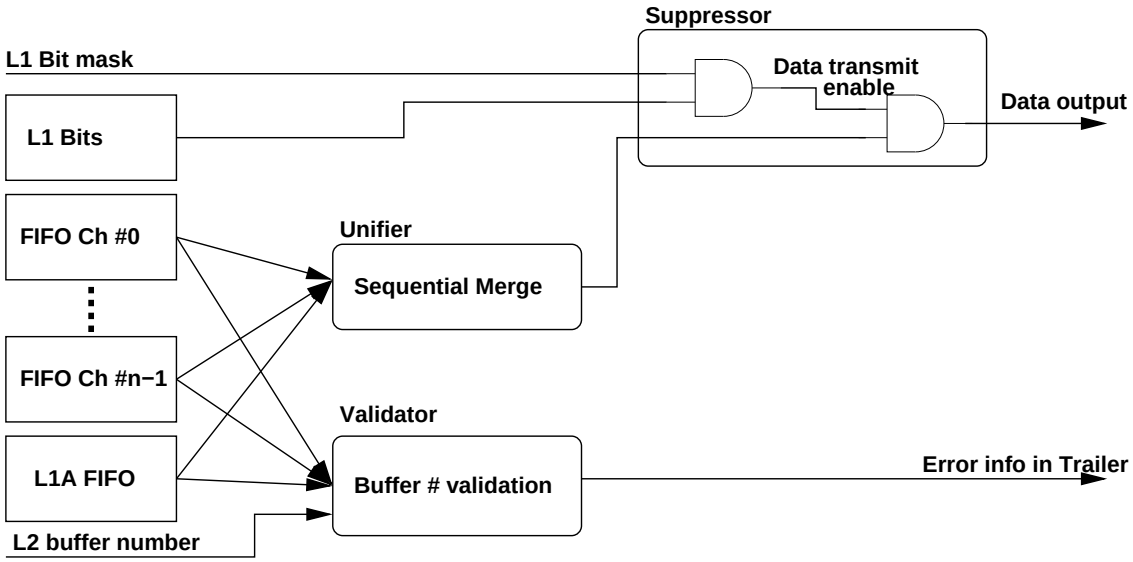

Figure 6.28: Concrete example of the merge/verify/suppress box in Fig. 6.26. In this case, data from the FIFO channels is merged sequentially. The data is suppressed from output to reduce bandwidth requirements if the L1 bits indicate that this data is not required for a decision. In addition, the buffer number from the L1A FIFO is compared to the buffer number in the data, and any mismatches are stamped into the trailer.

Board Level Flexibility

The board-level flexibility is illustrated by Pulsar's ability to manipulate the data it receives from upstream. As discussed in Sec. 6.6.1.2, the L2 trigger makes decisions based on simple trigger requirements on trigger objects it has assembled from various primitives that originating from other trigger subsystems. The creation of trigger objects very often requires combining different trigger data from different data paths; in Run IIa, this work was done in the Alpha processor. The Pulsar design provides the option to combine different data paths (and thus create trigger objects) at earlier stages, as many data paths are already visible at the pre-processor stage.

For example, it is possible to define muon objects inside the muon pre-processor DataIO FPGA's since both the muon trigger data and track trigger data are available for track and muon stub matching. The fast SRAM's attached to the two DataIO FPGA's can be used as look-up tables for this purpose. The same can be said for electrons in the RECES (merger) pre-processor. By creating physics objects at an early stage and packing them into S-Link data package, the task for the trigger algorithm code running inside a commodity CPU will be less CPU intensive, thus reducing the processing time. This may only become significant if the trigger data sizes and fakes rate increase significantly beyond present projections.

System Level flexibility

Option to use multiple PCI slots

One could use more than one PCI slot for data transfer into a CPU's memory. For example, one can send a certain data fragment, such as ones with long latency, or large data size, on a separate PCI slot. This way, the CPU doesn't have to wait for all the data fragments to arrive before processing the event. This would improve the overall performance, since not all data fragments are needed for L2 trigger decision making for every single event. For example, one limitation in the Run IIa system is the late arrival of data from the SVT, which in turn is limited by silicon readout time. The fraction of triggers requiring SVT data will be reduced in Run IIb. If silicon readout time is a limitation in Run IIb, the SVT data arrives late, it can be sent on a separate PCI slot, allowing the CPU to process the other triggers before the SVT data arrives.

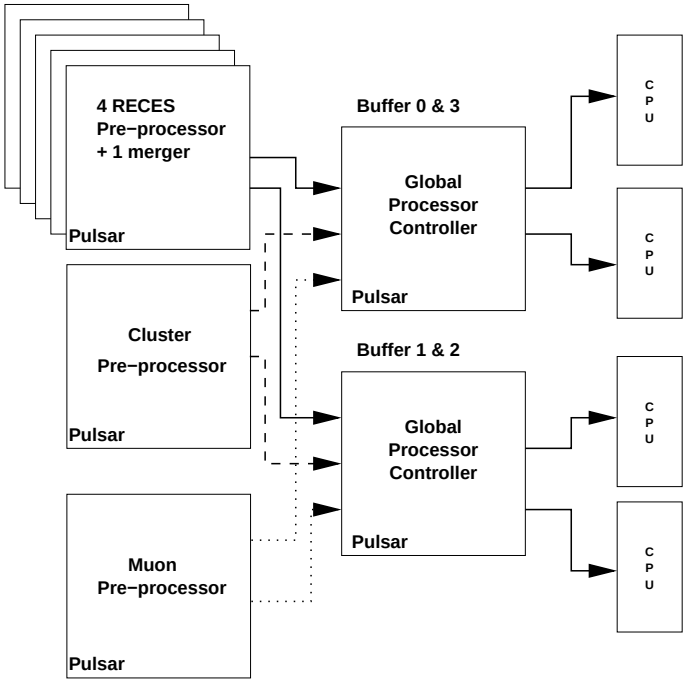

Figure 6.29: Possible Pulsar configuration with one CPU per L2 buffer.

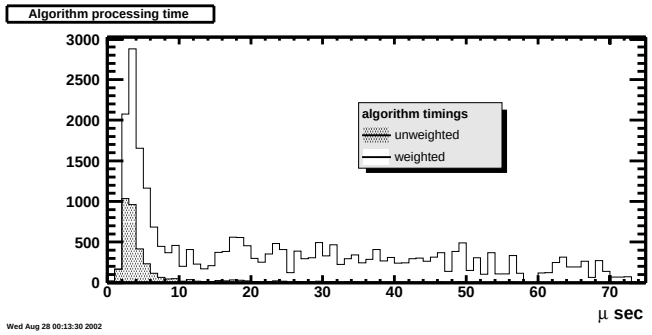

Figure 6.30: Contribution of tails to the L2 algorithm timings for the Run IIa system. The time shown is the measured algorithm processing time in μs for a beam collisions run. This time is a fraction of the total processing time in one of the two pipeline stages. The hatched time (labeled *unweighted*) shows the number of events which contribute to each time bin. A small tail is visible out to large times (~ 50 μs) and extends throughout the histogram. The unhatched histogram shows the weighted histogram, where each bin entry is weighted by the value of edge of the current bin. This weighting shows the equal-time contributions from the tails, and shows in this particular scenario, while the number of events in the tails is small, their impact is quite large.

Option to use multiple CPU's for L2 decision processing

Pulsar is designed in such a way that it allows one to use more than one CPU as Level 2 processors. This is possible because Pulsar has two S-Link ports via P3. The simplest expansion to the baseline configuration is to use 2 CPU's for L2 decision. This can be easily done by letting Pulsar send data via two S-Link output ports instead of one. One could either let the two CPU's run different algorithms on the same event, or run the same algorithm on different events. Similarly, it is possible to configure the system to use 4 CPU's.

One interesting example is to use four CPU's running the same trigger algorithm on different events. Each pre-processor can send out its data on one of its S-Link output ports depending on the buffer number of the event, as is shown in Fig. 6.29. For example, one can have buffer 0 and 3 events sent to S-Link output one, and buffer 1 and 2 events to be sent to S-Link output two. There will be two Pulsar boards acting as Processor Controllers. One receives data for events with buffer 0 or 3, and the other receives data for events with buffer 1 and 2. Each Processor Controller Pulsar then sends each buffer event on one of its S-Link output ports to a CPU. This way, one can have four CPU's running L2 algorithms with each CPU dedicated for a given buffer.[9] In fact, this is a better way to take full advantage of having a four buffer system. The advantage of running the system this way is to avoid the situation where one long tail event can prevent the other three events from being processed.

Our experience with the current system shows that this effect can be quite substantial. Fig. 6.30 shows the distribution of algorithm times as measured on an unbiased sample of L1A's in a Run IIa physics data sample. The algorithm time shown here is the time spent evaluating the trigger algorithms themselves, once data has been unpacked and ignoring all other overhead sources. The hatched histogram shows a distribution that peaks at $\sim 6\mu$s with a substantial tail (hatched histogram, labeled *unweighted* in the plot). The effect of these tails can be seen in the unhatched histogram (labeled *weighted*). Here, each entry is weighted by the time at the lower bin edge, such that equal areas in the plot represent equal time spent processing L2 algorithms. We see that the small number of events in the tail contribute as much to the total processing time as the events in the bulk

[9] Recall that CDF front-end electronics and trigger is a four buffer system at L2.

of the distribution.

As in this case, contributions due to events with long tails could be significant in the Run IIb trigger environment, and the strategy of one CPU per L2 buffer can be used to minimize this effect. [10]

6.6.2.7 Pulsar testability

As mentioned earlier, the Pulsar board was originally designed and built as a universal L2 test stand tool. As such, not only can it sink data but also it can source data for each L2 trigger data path. The source and sink Pulsars will be physically identical at hardware level, but they will have different firmware and mezzanine cards. The data source versions of Pulsar can be used to test the data sink versions of Pulsar (i.e., interface boards). In addition, a few data source Pulsars can be used to provide all the inputs from upstream subsystems and therefore to test the whole L2 decision crate in a stand-alone mode. The data source Pulsar allows the user to load a large number of events with different data size and latency. In this way it can mimic different luminosity running conditions. There is no new hardware involved, the data source and data sink Pulsars are identical at hardware level. In this sense, Pulsar is designed to have Built-In-Self-Test (BIST) capability. This modern practice for electronics with large FPGA's has proven to have positive effect on turn-on times. This test stand tool feature of Pulsar will not only speed up the commissioning of the new system, but also makes the long term maintenance much easier.

6.6.3 Comparison between Run IIa system and proposed Run IIb system

From a functional point of view, both the Run IIa system and the proposed Pulsar system for Run IIb are quite similar. Both are designed to collect different trigger primitive data from different paths and create trigger objects to make L2 trigger decisions quickly. However, the architecture and actual implementation details of the proposed Pulsar system departs in a significant way from that of the existing L2 decision crate. The Pulsar system is designed not only to take full advantage of the technology and design techniques available to us now and that will be available in the near future, but the design is also based upon lessons learned from the current system. In order to highlight the differences between the two approaches, this section compares the two systems in some detail.

6.6.3.1 Data transfer

The Run IIa system is based on a mixed data push and pull architecture.[11] This approach was necessary because some of the data paths have large data size (notably the muon system with ∼1.3 KBytes per event), and simply pushing all the data downstream requires much higher bandwidth. Instead, as shown in Table 6.5, the current system was designed to only push the smaller data packets. The processor node pulls region-of-interest data on demand from the large data size systems while processing the event. This approach eases the bandwidth requirement at the cost of complicating the event transfer and processing. This inhomogeneous environment has two effects:

1. In the case of multiple processor nodes, each processor node must individually pull the data that is not available via broadcast. If the data is only required by one node, this is irrelevant; however, if more than one node require the same non-broadcast information, it must be retrieved multiple times.

2. Pulling and pushing data ties together the two stages of the pipeline. In the pipeline mode, one event is being pushed into the processor memory while the previous event is simultaneously being processed. In a mixed push-pull architecture, the processing stage and the loading stage are vying for the same resource, the Magic Bus backplane and PCI bus.

The Pulsar system is a completely push-based system. All required data is sent to the processor. Due to the fundamentally higher bandwidth of S-Link, the need for data reduction is less severe. Any necessary reduction is done in the form of data suppression in the interface boards, as described in Section 6.6.2.1.

[10] An additional question is whether the decisions for L1 buffers have to be sent in L1 FIFO order. The design specification for the CDF DAQ was for each system to have addressable L2 buffers, so that just this type of out-of-order processing would be possible. The SVX sub-detector is unique in that it does not have addressable buffers and instead behaves more like a FIFO in readout. The possibility of out-of-order trigger decisions requires further study.

[11] In *Push* mode, the interface board is a Magic Bus master. In *Pull* mode, the board is a Magic Bus slave. See Table 6.4.

6.6.3.2 VME Readout of TL2D bank

In the Run IIa system, the TL2D bank for VME readout is formed by the processor node. The processor formats the bank on L2 accept, and the resources that are used to read out the data (PCI bus to memory) are the same as are used for the loading the next event. This contention for a limited resource, the PCI bus, effectively reduces the available bandwidth into the processor node's memory. Both the present and next event must, by design, compete for PCI bus bandwidth.

In the proposed Run IIb system, the readout is distributed across the universal interface cards. Each interface board has the CDF-standard four DAQ buffers for VME readout upon L2A. These readout buffers are filled on every event, regardless of the L2 decision. The final bank formation occurs in the VME crate controller. The processor node is not involved in the bank formation, and can solely concentrate on trigger decision processing. This approach completely decouples the readout task and L2 decision processing.

We also plan to make all raw data available to VME readout, in addition to the processed information that is sent to the processor. This will be an important debugging tool that is not uniformly present in the current system.

6.6.3.3 Implementation: Uniformity, Maintainablilty and Diagnostic Capability

In addition to the architectural differences, the system implementation is quite different in the two generations of systems. The number of custom boards and the emphasis of debugging capabilities is very different, which has wide-ranging effects.

Uniformity and Maintainability

The Run IIa design uses seven custom PCB's as interface boards,[12] a custom computer for the final decision, and a custom backplane to connect the two classes of boards. The large number of custom interface cards perform essentially identical roles. This non-uniformity was among the root causes of the long commissioning period of the Run IIa system. The primary problem encountered in the commissioning of the Run IIa system was the inability to reliably transfer data across the Magic Bus from the interface boards into the processor node. In particular, the arbitration mechanism was unreliable and suffered from low noise tolerance. During this time, lessons learned in the bus arbitration on one interface board did not automatically transfer to the next board, as each had implemented the same arbitration circuits differently. Each interface board's Magic Bus interface had to be debugged individually.

The non-uniformity also implies that a larger spares pool is required for the lifetime of this system: as each board requires two spares, a total of 14 spare L2 interface boards must be maintained.

In the proposed Run IIb system, there is *one* custom component: the Pulsar board. We take advantage of the fundamental similarity between the different data paths. As described in Sec. 6.6.2.3, each path is handled by a Pulsar board with slight variations in the firmware and two simple mezzanine cards. All the infrastructure, such as passing data downstream, is common, and therefore must only be understood once. This will allow the proposed system to be commissioned more rapidly and maintained more simply than the current system. Only one motherboard must be supported, and therefore we can maintain a smaller total pool of spares, again reducing the strain of long-term maintenance.

The interconnect among Pulsar boards is performed via externally supported S-Link hardware from CERN. The final decision is made in a commercial CPU. CPU's can be upgraded with minimal cost to take advantage of ever-increasing CPU power, and the system can take advantage of CERN's continuing research into S-Link for LHC experiments.

Diagnostic Capability

Another lesson learned from the Run IIa commissioning experience was the importance of building a system with testing in the design from the onset. The Run IIa system did not have a testing specification written into the system description, and, as a result, each interface board implemented varying degrees of testing capabilities. For instance, many interface boards do not provide VME access to their data. System testing was performed on an ad-hoc basis, and no standard set of test suites was developed. As mentioned in the introduction to Sec. 6.6.2, the Pulsar project started as an attempt to provide some of the missing test capabilities to the Run IIa project by providing a realistic, uniform data source

[12] See Table 6.4.

for all inputs to the L2 decision crate. The importance of this capability is evident by the fact that CDF chose to devote resources to a test stand so late in the process of developing the Run IIa system.

As a result, the Pulsar system was designed with diagnostic capability as a requirement. Both the Run IIa system and the Run IIb system will profit from the Pulsar in its test stand modus. With its data sourcing abilities, board- and system-level commissioning can occur away from the beam and before the nominal system replacement time. The universal interface card modus is also thoroughly testable. We provide access to the data flow at every stage as every FPGA is available via VME. The use of the S-Link data format provides a robust error checking capability. Each data fragment identifies itself downstream, and is stamped with error checking information from checks performed in the firmware. These tools allow errors to be quickly isolated to a particular part of the system, at which point the offending problem can be diagnosed. The testing strategy for the proposed Run IIb system is therefore dual: in-situ debugging and monitoring capabilities combined with an extensive ex-situ test stand in the form of physically identical Pulsar boards in their test stand configuration.

6.6.3.4 System Performance

The performance differences between the two systems are defined by three criteria:

1. Raw bandwidth
2. Overhead
3. Architectural differences

Raw bandwidth is simply the ability to get data into the processor to allow it to make a L2 decision. This encompasses both the Magic Bus or S-Link bandwidth and the bandwidth into the processor node's main memory for the appropriate system. The actual bandwidth differs from the raw bandwidth by the amount of overhead for transmitting data. Finally, architectural differences can amend these comparisons.

As described in Sec. 6.6.1.3, the current L2 system is a two-stage pipeline. This implies that two events can be in L2 at the same time. The bandwidth is to first order limited by the slower of the two stages. The baseline Run IIb system is architecturally the same. To achieve the canonical 40 KHz L1A rate, each stage needs to have an average latency of ~ 10 μs. For this type of system, the smaller the latency of the slower pipeline stage, the higher the allowed L1 bandwidth. In what follows, we will compare these two stages in both approaches from system performance point of view.

Loading Stage Latency

The latency for the loading stage is the time it takes to transfer trigger primitives into memory of L2 processor. This latency depends on factors both outside (such as SVX-SVT processing time) and within the L2 decision crate. Here we assume that the SVX-SVT processing time will be improved for Run IIb, so we focus only on the decision crate performance. In what follows, we briefly describe the latency for the existing system and then compare that latency with the proposed design. For the sake of comparison, we will assume that the data size is the same for the Run IIa and Run IIb cases.

Run IIa Loading Stage Latency

For the Run IIa system, the list of items that affects the throughput into memory and hence the latency of the first stage are the raw Magic Bus bandwidth, the bandwidth into the processor node's PCI bus memory, and the overhead associated with the transfer.[13] The Magic Bus raw bandwidth is $\sim$ 80MB/s ($128b$/200ns). The principal Magic Bus overhead is the need to distribute the bus mastership. The total per-event overhead for this is estimated to be ~ 1 μs. The Alpha has a 64 bit PCI bus running at 33MHz which leads to an theoretical PCI DMA bandwidth into memory of 260 MB/s. The effective bandwidth is only about 20-80 MB/s. The actual transfer rate is limited by memory access time and other PCI activity (such as the read-out of TL2D bank and interference between the loading and processing pipeline stages due to the mixed push-pull architecture, as outlined in Sec. 6.6.3.1). As the bandwidth of a pipeline is determined by its slowest stage, the bandwidth of the Run IIa loading stage is the effective PCI DMA bandwidth, 20-80 MB/s.

As discussed in Sec. 6.6.3.1, the fraction of events which require data to be pulled (for RECES or muon systems) also increases the latency. RECES and

[13] These numbers reflect system performance as of August 2002.

Muon data is read over Magic Bus by the processor node while processing the current event and at the same time the loading of next event over Magic Bus is on-going. This class of events contribute to the latency in a complicated way.

Proposed Run IIb Loading Stage Latency

In the new system, the latency for the first stage depends on the S-Link raw bandwidth, the time it takes to format and merge input data into S-Link format on the Pulsar boards, the bandwidth of the S-Link to PCI interface and the overhead associated with that. Since the new system has a data-push-only architecture, one cannot simply compare the raw bandwidth of S-Link with that of Magic Bus. Generally speaking, bandwidth demand will be higher in a data pushing only system. However, the Pulsar can suppress data at early stages. The S-Link raw bandwidth is 160 MB/s with 32-bit data words transferred by a 40 MHz clock. The time it takes to format and merge data into S-Link (i.e., the time it takes for data to go through each Pulsar board) can be short, as the task is done with fast modern FPGA's. This time is expected to be below 1 μs per Pulsar board based on initial VHDL simulation results. The latency for data to go through both the pre-processor Pulsar and the Processor Controller Pulsar is expected to be ~ 2 μs.

The raw bandwidth for the new S-Link to PCI interface (S32PCI64) is about 260MB/s. As mentioned in Section 6.6.2.4, recent performance tests at CERN indicate that one can achieve up to 150 MB/s data throughput with one S32PCI64 interface and 300 MB/s data throughput with two S32PCI64 interfaces. Unlike the Alpha case, memory in server-type processors is fast enough to sustain the full speed of a 66 MHz/64-bit PCI bus (520 MB/s). The test at CERN also shows that the overhead is quite small – about $1-2$ μs. Therefore, the S-Link to PCI bandwidth is well matched with the S-Link bandwidth.

With greater than a factor of two increase in effective bandwidth compared to the Run IIa system, the only subsystem data one needs to suppress is the muon data path. As shown in Table 6.5, the raw data size of the muon path is 1.3KB per event. Without suppression, this path requires 52 MB/s bandwidth on average at 40 KHz L1A rate, which does not leave a lot of headroom. In Sec. 6.6.2.2, we showed how the muon data can be suppressed inside the pre-processor Pulsar based on the L1 trigger decision information or based on the data itself. In Run IIb, roughly 10% of the L1 accepted events require muon information for the L2 decision. We expect less than 10% of the data to remain after zero suppression. All other subsystems' data sizes are much smaller (more than one order of magnitude) and can be transferred downstream without modification.

In summary, bandwidth does not seem to be an issue for the new system with this data-push-only architecture.

Latency for the Processing Stage

As described in Sec. 6.6.1.3, in the processing stage, data is unpacked from memory, physics objects are created and trigger algorithms are evaluated to make the L2 decision. Besides the dependence on event data size and complexity, the latency for this stage also depends CPU performance, memory access speed, L2 to TS handshake time, and any board configuration overhead.

Latency for the Processing stage for the Run IIa system

For comparison, we break out some of the times for the Run IIa system.[14] The algorithm processing time includes:

1. The time to unpack L1 trigger bits and scalers. With the current system this is about 2 μs.
2. Algorithm running and data unpacking, which is about 13 μs on average for the current system.
3. Error checking inside CPU, which takes about 1.1 μs.

The L2 to TS handshake time includes:

1. Starting TSI handshake which currently has 2 μs overhead (PCI writes).
2. Building the TL2D bank, which takes 1 μs for L2R and 71 μs for L2A.
3. Ending TSI handshake takes about 2 μs

The board configuration time mostly includes the Alpha DMA configuration setup time (~ 5 μs) and checking for an event in the L1 FIFO (~ 1 μs). Note that the board configuration time is not parallel with either processing time or Magic Bus transfer time.

[14] Based upon system performance as of August 2002.

Latency for the Processing stage for the proposed Run IIb system

Architecturally, the proposed Run IIb system is very similar to the Run IIa system for event processing. Therefore, the latency dependence for the second stage will be similar. There are a few differences. We use a faster, more modern CPU used instead of DEC Alphas, with faster access to memory and a larger on-chip cache for both data and instructions.[15] A high speed S-Link to PCI interface will be used instead of custom Magic Bus to PCI interface using the PCI bus in the processor node. The overhead is smaller for data transfer (including DMA setup time) since the S-Link to PCI interface (S32PCI64) is designed for highly autonomous data reception. L2 to TS handshake is expected to be around 1 μs. Unlike the Run IIa system, the decision-making processors are not involved in the formation of the TL2D bank (see Sec. 6.6.3.2).

As discussed above, with the two stage pipeline in the current system, the L2 decisions have to be made in L1A order. This means that all events are processed in the order that they are received. In Sec. 6.6.2.6, we discussed how the presence of long tails in the processing time introduces large dead time. The baseline proposal for the upgrade has similar architectural limitations, but due to the flexibility inherent in the design, the *Pulsar system can be reconfigured* to better handle this situation, as described in the above Section.

Summary Of the Performance Comparison

In summary, with the baseline design of the proposed system, the performance is expected to be much improved over the existing system. The combination of high S-Link bandwidth and data-reduction ability in the pre-processor gives the proposed system more than sufficient bandwidth to handle the increased throughput demand for Run IIb. By using faster, modern CPU's with high memory bandwidth and larger caches, we decrease the latency of the processing stage as well. As described in Section 6.6.2.6, with the extra flexibilities both at board level and at the system level, it is expected that the proposed new system can meet the trigger challenges in Run IIb with more than enough safety margin in terms of performance.

[15] In the current system, the on-chip cache is limited to the 48 KB L2 cache. The L3 cache has been disabled.

6.6.4 Summary

With 396 ns bunch spacing and ten interactions per crossing at $\mathcal{L} = 4 \times 10^{32}$ cm^{-2} s^{-1}, the Run IIb trigger environment will be very challenging. There is a large uncertainty in the extrapolation of the trigger uncertainty in the extrapolation of the trigger data size from the Run IIa environment. The current L2 decision crate was designed and built in the mid to late 1990's based on technology available at that time. The design is based on a custom bus (Magic Bus), several custom processors and many different custom interface boards. Due to the increase in occupancy and the uncertainty of conditions in Run IIb, we think it prudent to increase the bandwidth and processing power while simplifying the design and reducing the maintenance overhead.

The L2 decision crate is a critical subsystem for the entire experiment and our physics program depends crucially on its performance in Run IIb. We propose here to upgrade the L2 decision crate. The upgrade is based on a **single custom universal interface board** (Pulsar) design, plus CERN S-Link interface cards and commodity processors. The first generation of Pulsar and mezzanine boards have been designed and constructed. The new design departs from the previous implementation for the existing L2 decision crate. A standard HEP supported link is used instead of a custom backplane to transfer trigger data into CPU memory. Level 1 trigger and track trigger information are made available to all FPGA's for each Pulsar board. This design feature is driven by physics requirements, providing flexibility in performance. In addition, by choosing S-Link as the standard link, the new system can be easily upgraded to better S-Link to PCI cards and more powerful processors as they become available. This new system is designed to have sufficient safety margin and flexibility in performance to meet the Run IIb trigger challenges, to have built-in self-test capabilities to speed up the commissioning process and to ease the long term maintenance effort all the way through Run IIb.

6.7 Event-Builder and Level-3

The maximum bandwidth theoretically achievable with the existing Run IIa system is 15 channels $\times$ 16 MBytes/s = 240 MBytes/s. In practice about 60% of this limit has been achieved in benchmarking tests with simulated data sizes corresponding to

the expected detector occupancy. It is likely that the performance under test conditions can be further improved to about 80% of the theoretical limit after tuning the system. The performance when processing real data depends crucially on the load balancing among the various ATM switch inputs.

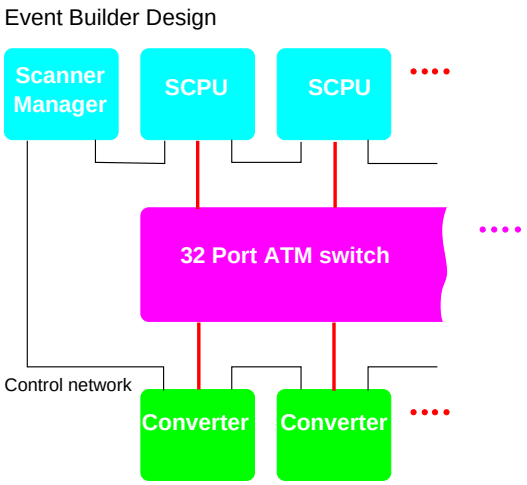

Figure 6.31: Event-Builder design for Run IIa.

To match the requirements quoted in the introduction of this chapter, a sustained rate of 750 Hz which corresponds to a data throughout of 375 MBytes/s assuming the events are 500 kBytes, the existing system needs to be upgraded. For the Event-Builder upgrade a sustained bandwidth of at least 400 MBytes/s is required to take into account load imbalancing in the ATM inputs and fluctuations in the data size.

The conceptual design of the Level-3 Trigger PC farm will not need an upgrade since it is practically extensible to any size by adding additional processor nodes. Estimating the real CPU power needs of the PC farm in Run IIb is more uncertain than estimating the bandwidth needs for the Event-Builder. Therefore only the achievable performance increase per PC is discussed. The number of PCs has to be adjusted according to the required CPU.

6.7.1 Limitations of the Existing System

The typical Event-Builder and Level-3 PC farm design schemes are shown in Figures 6.31 and 6.32. There are 15 Scanner CPUs providing input for the ATM switch and 16 Level-3 subfarms receiving the event fragments to assemble the event and process it. Per subfarm a total of 16 processor nodes are

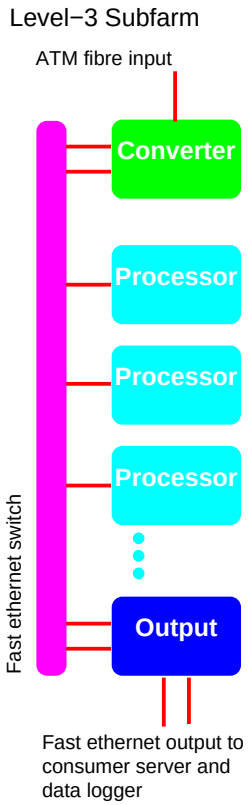

Figure 6.32: Scheme of a Level-3 PC Subfarm for Run IIa. A total of 16 subfarms are used in Run II.

available at Run IIa startup. When analyzing the data flow through the Event-Builder and Level-3 PC farm, two different types of limitations are identified: *throughput limitations* and *processing power limitations*. Processing power limitations are overcome by purchasing additional CPUs. The Level-3 trigger algorithms have to be adjusted to perform with the available CPU and still preserve the desired physics.

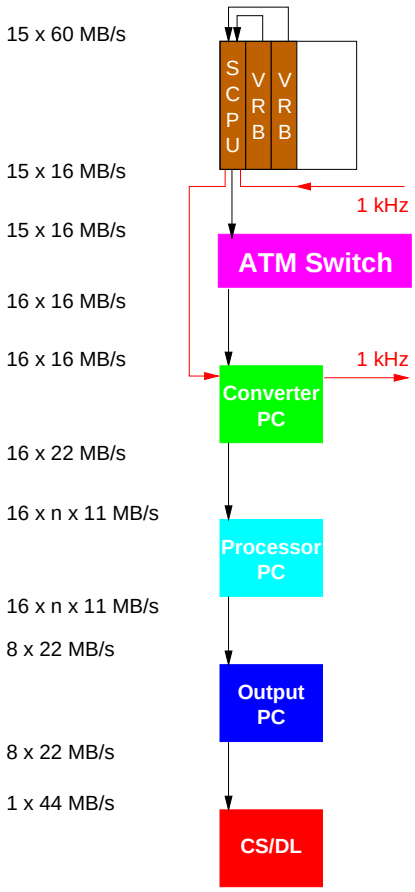

Figure 6.33: Event-Builder and Level-3 PC Farm: scheme of possible throughput limitations, where n is the number of processor nodes.

Analyzing the dataflow through the Event-Builder and Level-3 PC farm several possible throughput limitations are distinguished as illustrated in Figure 6.33:

1. control network performance of the Event-Builder (rate limit)
2. at the Event-Builder input (VRB crate)
3. at the PC farm entry which are the converter nodes
4. internally in the processing farm; fast ethernet
5. at the Level-3 output to the Consumer Server and Data Logger (CS/DL)

The Event-Builder limitations for the data throughput are about 240 MBytes/s given by the 15 ATM input connections (OC3 standard). With event sizes of 250 kBytes the control network therefore has to function properly up to 1 kHz, and this performance has been demonstrated.

Both, 240 MBytes/s data throughput and 1 kHz event rate, are upper limitations and the real performance will be less, depending on parameters such as the load balancing per ATM input, the fluctuations of the event fragment length and so on. With the present experience a sustained rate of about 600-800 Hz of 250 kBytes events is the practical limit of the system.

The input into the Level-3 PC farm on the other hand is less problematic since there is one more output OC3 connection for a total of 16. The fact that the converter node contains many PCI cards, i.e. SCRAMNet, ATM, quadruple fast ethernet, has so far not caused any problem. The two fast ethernet output connections have a sustained rate through the converter node of more than 20 MBytes/s while the OC3 input connection provides 16 MBytes/s maximum input.

For the subfarm internal network the maximum rate of 16 MBytes/s is subdivided to at least 8 PCs which is a comfortable rate for a 24 port fast ethernet switch.

The output node is connected through two fast ethernet connection each to the processor nodes and to the Consumer Server and Data Logger. Even without rejection one output node is able to handle a complete subfarm. Assuming a reasonable event rejection rate an output node could handle the input of more than 2 subfarms on its own. No limitations are expected in that layer. Extension to include more PCs is trivial since fast ethernet switches serving up to 64 ports exist on the market. Concerning the Consumer Server and Data Logger side the Level-3 PC farm, software has been designed to communicate with a farm implementation of this device. The extension is trivial and hardware is available off-the-shelf.

6.7.2 Event-Builder Maintenance and Upgrade

In this section the efforts involved in the Event-Builder upgrade are described. The present system should be able to handle a sustained data throughput of 144-200 MBytes/s and a maximum rate of 600-800 Hz. These numbers are compatible for event sizes up to 250 kBytes. The proposed upgrade scenario is based on the assumption that the CDF data acquisition has to be able to run efficiently at sustained data throughput of 400 MBytes/s and rates of 750 Hz. The event size is allowed to grow up to 500 kBytes which seems reasonable taken the latest estimates.

Upgrade scenarios replacing the ATM switch technology completely using for example Gigabit Ethernet or MyriNet have not been investigated into detail. Both technologies provide the appropriate performance on paper but more studies would be needed to seriously propose them. A serious evaluation of Gigabit ethernet and MyriNet solutions are being worked on. Replacing the existing ATM switch with its more powerful successor is considered a safer option at present, since it involves a minimal upgrade to the existing system in terms of hardware and software. The disadvantage of this solution is that it is somewhat more expensive.

6.7.3 Upgrading the ATM Network

The natural upgrade path for Run IIb is to switch from the present OC3 to OC12 ATM links and buy the new switch ASX 4000 from Marconi or an equivalent device. Switch ports based on the OC12 standard provide 4 times the bandwidth of the corresponding OC3 ports. This corresponds to a theoretical limit of close to 1000 MBytes/s, $60 - 80\%$ of which ought to be achievable in practice if there were no other bottlenecks.

The system limitations are then likely to be not the ATM switch but instead:

- VRB readout bandwidth via VME: 1000 MBytes/s spread evenly over 15 VME crates results in a 67 MBytes/s bandwidth requirement within each VME crate. This can not be achieved with present VME hardware and protocols. Benchmarks of the D64 read/write bandwidth for a MVME2600 came close to 50 MBytes/s. The useful bandwidth is probably as low as 30-40 MBytes/s resulting in 450-600 MBytes/s sustained throughput rate for the Event-Builder. This rate exceeds the maximum required performance of 400 MBytes/s and a maximum rate of 1.5 kHz as discussed above.

- The present system is limited to about 1 kHz Level-2 accept rate due to the maximum message passing rate over the SCRAMNet ring. This limitation is not due to the hardware but the software. To go beyond this the message passing protocol needs to be upgraded.

- The Converter nodes presently feed their subfarms via two fast ethernet links on a 4 port card. The output bandwidth is doubled by making use of all four ports without additional hardware. The total bandwidth through the converter nodes is then up to 48 MBytes/s which matches the performance of the ATM connection.

A sustained Event-Builder bandwidth of 450-600 MBytes/s is achievable in this scenario. Past experience has shown that in the Event-Builder the usage of the ATM switch is sufficiently different from its commercial use in the telephone industry. This implies that commercially available drivers have to be modified in a non-trivial way. This is expected to be the largest software development effort in this scenario.

6.7.4 Level-3 PC Farm Upgrade

At present it is too early to provide reliable estimates of the CPU needs for the Level-3 PC farm over the course of Run IIb. Instead it is pointed out that the performance/price ratio has roughly doubled every 1.5 years in the past. A replacement of the obsolete PCs in 2004 will therefore probably quadruple the present processing power.

6.7.5 Event Builder/Level 3 Upgrades: Conclusions

To adjust the Event-Builder and the Level-3 PC Farm to the needs of the upcoming Run IIb an extension of the data throughput to up to 400 MBytes/s and a maximum rate of 1 kHz are envisaged.

The present Event-Builder system can deal with up to 144-200 MBytes/s or 600-800 Hz which is insufficient for the Run IIb requirements. For higher per-

formances a straightforward extension of the ATM switch from OC3 to OC12 optical fibers is foreseen. The upgraded version is able to deal with rates as high as 1 kHz and data throughput of 450-600 MBytes/s.

The Level-3 requirements for Run IIb are less well defined at this stage. It seems that a replacement of the in 2004 obsolete PCs with the same number of PCs and a further extension by roughly half of that system should cover the needs of the experiment.

Bibliography

[1] P. Azzi *et al.* "Report from the Run IIb Committee." `http://www-cdf.fnal.gov/upgrades/run2b/run2b_task_force/`

[2] Y.K. Kim *et al.* "CDF Triggers for Run IIb."

[3] M. Martinez and A. Meyer, CDF Note 6065 (2002).

[4] A. Meyer *et al.* CDF Note 5824 (2002).

[5] A. Mukherjee *et al.* "Specifications for the Run IIb TDC System."

[6] R. Hughes, B. Winer CDFNote 6059(2002), "XFT Upgrade for Run2b".

[7] J. Hoftiezer *et al.* CDFNote 4300(1997), "XFT3D: A Proposal for Adding Stereo Segment Finding and 3D XFT tracking in the Trigger".

[8] http://cdfpc2.mps.ohio-state.edu/xft/xft_home.html

[9] N. Eddy, K. Pitts, M. Kasten, "Expression of Interest: CDF Track Trigger 2".

[10] R. Blair *et al* (CDF II Collaboration), *The CDF Run II Detector Technical Design Report*, 1996. FERMILAB-Pub-96/390-E.

[11] H. Kasha, M. Schmidt. "CDFII Trigger/DAQ Simulations Including the SVXII Readout," 1997. CDF/DOC/TRIGGER/CDFR/4213.

[12] C. Murphy, M. Campbell, "The Level 2 Magic Bus," 1997. See `http://umaxp1.physics.lsa.umich.edu/cdf/documents.htm\#Upgrade`.

[13] `http://hep.uchicago.edu/~thliu/projects/Pulsar/`

[14] H. C. van der Bij *et al*, "S-Link, a Data Link Interface Specification for the LHC Era," 1997. Published in the *Proceedings of the Beaune 97 Xth IEEE Real Time Conference*. See also `http://hsi.web.cern.ch/HSI/s-link/`.

[15] W. Iwanski *et al*, "Designing an S-LINK to PCI Interface using an IP core." Article presented at the 12th IEEE-NPSS Real Time Conference, June 4-8, Valencia (Spain). See also `http://hsi.web.cern.ch/HSI/s-link/devices/s32pci64/`.

[16] Markus Joos, CERN, private communication. See also `http://documents.cern.ch/archive/electronic/other/agenda/a0281/a0281s1t21/transparencies/Sw_robin.pdf`.

[17] M. Barabanov, "A Linux-based Real-Time Operating System." M.S. thesis, New Mexico Insitute of Mining and Technology, Socorro, New Mexico, 1997. See also `http://fsmlabs.com/community/`.

Chapter 7

Installation

The installation of the CDF detector for Run IIb can be scheduled with high reliability due to the experience obtained throughout the Run IIa project. Since the start of the project, the CDF detector has been rolled into the collision hall twice, once for the engineering run and then again for the Run IIa physics run. Between those two detector roll-in periods, the CDF detector was removed from the collision hall so that the prototype "barrel 4" silicon detector could be removed and the final IIa silicon detector installed. The steps for removal of the central detector are reversible. Thus we are able to use the experience and detailed schedules from the Run IIa installation to predict with a high degree of confidence the amount of time required to complete the Run IIb installation.

In Run IIa, the completed silicon detector (SVX/ISL and beam pipe) was delivered to the CDF assembly building on 16 January 2001. At the time of the delivery, the central detector had been parked in the assembly hall and fully prepared to accept this device. That preparation included removal of the end plugs, construction and alignment of the rail system used to install the detector and the installation of the silicon readout and infrastructure cables in the 30^o slots. The silicon detector arrived at the assembly building mid morning and was installed inside the COT that same workday. Once installed, the beam pipe was given a nitrogen purge, alignment surveys were completed and the silicon "inch worm" motion system was tested to make sure it was functioning properly. Once this work was complete, the process of closing up the detector in preparation for the move into the collision hall begun - scaffolding and rail insertion system was removed, the end plugs were remounted on the detector and properly cabled up, and detector services (water, gas, AC power) were disconnected. This entire process took a bit longer than one week.

Once the silicon detector was installed and the detector "buttoned-up" such that it could be moved into the collision hall - the roll-in process of the central detector from the assembly hall to the collision hall began. Using a crew of 8 men and an array of hydraulic cylinders, the central detector was pulled and pushed into position. When everything is working well, this crew is capable of moving the detector about 6 feet per hour. Hence the total journey took approximately 4 days including the final survey and final positioning. With the central detector properly positioned, the water, AC power, gas, and cryogenics had to be established. The end plugs were opened so that the beam pipe could be connected to the low beta quad magnets and final cabling of the silicon detector could begin. At the same time, muon shielding steel was installed, the North CMP muon wall was installed, the north east and north west CMX arches were put into final position and the 1200 ton shielding door was closed. These tasks along with an entire laundry list of other items were completed in 5 weeks. The CDF collision hall could be interlocked for Tevatron operation on 27 February 2001, a mere 6 weeks after the arrival of the silicon detector. At that time, the detector still required three additional weeks for completion of the silicon detector cabling and testing.

There is nothing unique about Run IIb. The operations required for its successful installation are exactly the same as the steps outlined above - steps that have been completed twice in the past three years with the same schedule. Thus the removal of the detector from the collision hall and the extraction of the existing silicon system should be accomplished in six weeks, this job is essentially a reversal of the Run IIa installation.

The disassembly of the silicon detector and the installation of the Run IIb detector into the ISL will take place at the silicon facility. The period of time

when the ISL is at the silicon facility is essentially the time period that CDF has to complete its other upgrades both in the collision hall and on the detector itself. The total amount of time available to work on these other upgrades is 14 weeks. The 14 weeks is determined by taking the sum of the 3 numbers; the 8 weeks that the ISL is resident at the silicon facility for the new SVX installation, the 3 weeks required to remove the old detector and the 3 weeks needed for the insertion of the Run IIb silicon package. In this 14-week time period, the central arches are pulled out so that the preradiator upgrade can be accomplished, old silicon cables are removed and new ones installed, EM timing modifications are performed, TDC's are replaced and a variety of small collision hall access issues are addressed. In short, this is a busy time with all sorts of activity on and around the detector. These activities do not "drive" the roll-in schedule however. Most of the tasks mentioned above require 8 or fewer weeks out of the available 14. The exception is the pre radiator installation, which will require 12 of the 14 weeks.

We have considered other installation scenarios where the central detector would remain in the collision hall. The goal of such an alternative installation approach would be to improve on the 12-14 week turn around time required for the full detector installation. If an alternative approach were found to be successful, it would either allow for additional contingency on the overall installation schedule or else shorten the "ready for collisions" date. When evaluating these new options, we considered them based on time-savings, the schedule risk including contingency for such operations, the amount of engineering and designer time required to accomplish such a plan, and the potential risk to the detectors themselves.

The CDF silicon detector is a single object - as such it is quite long. Thus in order to install this device, a substantial amount of space is required just to position the device in front of the central tracker such that it can be installed inside the central tracking volume. The only way to achieve this kind of space is to remove the end plug calorimeter from the rail system that it rests on, transfer its load to some other structure and then pull it back sufficiently far that the new silicon detector can be installed. In order to create that kind of room in our collision hall, the low beta quadrupole magnets have to be removed, the west side IMU steel motion system has to be removed, and each of the 200 ton "half moon" pieces of IMU shielding steel have to be pushed back in the collision hall as far as they can go. With the magnets removed, the IMU steel pushed back and the end plug transferred to some sort of mounting and transport system, the West end plug can be moved far enough back that the silicon detector can be installed. None of the steps described above are "show stoppers". Given enough time and sufficient engineering resources, each task can each be executed safely in our collision hall. However, these tasks are complicated and we have never done them before. It is hard to say with certainty that they, as a group, can be accomplished without incident at a sufficiently quick pace such that there is an improvement in our overall schedule.

Furthermore, leaving the detector inside the collision hall complicates other matters as well. This plan would make the preradiator and EM timing upgrades at the very least, difficult and quite possibly impossible to complete. Other cabling tasks and access tasks are made much more difficult with the detector in the collision hall.

In short, performing the Run IIb upgrade with the detector permanently resident inside the collision hall is believed to be of the same scope as a full detector roll out. Furthermore it puts into jeopardy many of the other upgrades planned for the central detector. Any schedule improvement imagined by this approach is small, and must have large contingency. We prefer to repeat the installation procedure that has been done before and summarized in table 7.1.

Activity	Duration (weeks)	Contingency
CDF "Roll out"	4	20%
SVX II/ISL extracted	3	25%
Silicon at Si. Det.	8	100%
SVX IIb/ISL installation	3	25%
CDF "Roll in"	4	20%
SVX IIb/ISL connection	12	50%
Total	34	50%

Table 7.1: Summary of CDF RunIIb installation

Chapter 8

Publications

1. "Transverse-momentum Distributions of Charged Particles Produced in $\bar{p}p$ Interactions at $\sqrt{s} = 630$ and 1800 GeV," F. Abe et al., The CDF Collaboration, Phys. Rev. Lett. 61, 1819 (1988).

2. "The CDF Detector: An Overview," F. Abe et al., The CDF Collaboration, Nucl. Instrum. Methods A271, 487 (1988).

3. "Measurement of the Inclusive Jet Cross Section in $\bar{p}p$ Collisions at $\sqrt{s} = 1.8$ TeV," F. Abe et al., The CDF Collaboration, Phys. Rev. Lett. 62, 613 (1989).

4. "Measurement of W Boson Production in 1.8 TeV $\bar{p}p$ Collisions," F. Abe et al., The CDF Collaboration, Phys. Rev. Lett. 62, 1005 (1989).

5. "Limits on the Masses of Supersymmetric Particles from 1.8 TeV $\bar{p}p$ Collisions at CDF," F. Abe et al., The CDF Collaboration, Phys. Rev. Lett. 62, 1825 (1989).

6. "Dijet Angular Distributions from $\bar{p}p$ Collisions at $\sqrt{s} = 1.8$ TeV," F. Abe et al., The CDF Collaboration, Phys. Rev. Lett. 62, 3020 (1989).

7. "Measurement of the Mass and Width of the Z° Boson at the Fermilab Tevatron," F. Abe et al., The CDF Collaboration, Phys. Rev. Lett. 63, 720 (1989).

8. "Search for Heavy Stable Particles in 1.8 TeV $\bar{p}p$ Collisions at the Fermilab Collider," F. Abe et al., The CDF Collaboration, Phys. Rev. Lett. 63, 1447 (1989).

9. "K_s^0 Production in $\bar{p}p$ Interactions at $\sqrt{s} = 630$ and 1800 GeV," F. Abe et al., The CDF Collaboration, Phys. Rev. D40, 3791 (1989).

10. "Search for the Top Quark in the Reaction $\bar{p}p \rightarrow$ Electron + Jets at $\sqrt{s} = 1.8$ TeV," F. Abe et al., The CDF Collaboration, Phys. Rev. Lett. 64, 142 (1990).

11. "Search for New Heavy Quarks in Electron-Muon Events at the Fermilab Tevatron Collider," F. Abe et al., The CDF Collaboration, Phys. Rev. Lett. 64, 147 (1990).

12. "Measurement of the Ratio $\sigma(W \rightarrow e\nu)/\sigma(Z \rightarrow ee)$ in $\bar{p}p$ Collisions at $\sqrt{s} = 1.8$ TeV," F. Abe et al., The CDF Collaboration, Phys. Rev. Lett. 64, 152 (1990).

13. "Two-Jet Differential Cross Section in $\bar{p}p$ Collisions at $\sqrt{s} = 1.8$ TeV," F. Abe et al., The CDF Collaboration, Phys. Rev. Lett. 64, 157 (1990).

14. "Measurement of $D^\star$ Production in Jets from $\bar{p}p$ Collisions at $\sqrt{s} = 1.8$ TeV," F. Abe et al., The CDF Collaboration, Phys. Rev. Lett. 64, 348 (1990).

15. "Jet-Fragmentation Properties in $\bar{p}p$ Collisions at $\sqrt{s} = 1.8$ TeV," Phys. Rev. Lett. **65**, 968 (1990).

16. "Measurement of the W-Boson Mass," F. Abe et al., The CDF Collaboration, Phys. Rev. Lett., 65, 2243 (1990).

17. "Search for a Light Higgs Boson at the Fermilab Tevatron Proton-Antiproton Collider," F. Abe et al., The CDF Collaboration, Phys. Rev. D41, 1717 (1990).

18. "Two-Jet Invariant Distribution at $\sqrt{s} = 1.8$ TeV," F. Abe et al., The CDF Collaboration, Phys. Rev. D41, 1722 (1990).

19. "Pseudorapidity Distributions of Charged Particles in $\bar{p}p$ Interactions at $\sqrt{s}$ = 630 and 1800 GeV," F. Abe et al., The CDF Collaboration, Phys. Rev. D41, 2330 (1990).

20. "Top-Quark Search in the Electron + Jets Channel in Proton-Antiproton Collisions at $\sqrt{s}$ = 1.8 TeV," F. Abe et al., The CDF Collaboration, Phys. Rev. D43, 664 (1991).

21. "Measurement of the W-Boson Mass in 1.8 TeV $\bar{p}p$ Collisions," F. Abe et al., The CDF Collaboration, Phys. Rev. D43, 2070 (1991).

22. "Measurement of the W-Boson p_T Distribution in $\bar{p}p$ Collisions at $\sqrt{s}$ = 1.8 TeV," F. Abe et al., The CDF Collaboration, Phys. Rev. Lett. 66, 2951 (1991).

23. "Measurement of $\sigma B(W \rightarrow e\nu)$ and $\sigma B(Z^0 \rightarrow e^+e^-)$ in $\bar{p}p$ Collisions at $\sqrt{s}$ = 1800 GeV," F. Abe et al., The CDF Collaboration, Phys. Rev. D44, 29 (1991).

24. "Measurement of QCD Jet Broadening in $\bar{p}p$ Collisions at $\sqrt{s}$ = 1.8 TeV," F. Abe et al., The CDF Collaboration, Phys. Rev. D44, 601 (1991).

25. "A Determination of $\sin^2\theta_W$ from the Forward-Backward Asymmetry in $\bar{p}p \rightarrow Z^0X \rightarrow e^+e^-X$ Interactions at $\sqrt{s}$ = 1.8 TeV," F. Abe et al., The CDF Collaboration, Phys. Rev. Lett. 67, 1502 (1991).

26. "Measurement of the e^+e^- Invariant-Mass Distribution in $\bar{p}p$ Collisions at $\sqrt{s}$ = 1.8 TeV," F. Abe et al., The CDF Collaboration, Phys. Rev. Lett. 67, 2418 (1991).

27. "Search for $W' \rightarrow e\nu$ and $W' \rightarrow \mu\nu$ in $\bar{p}p$ Collisions at $\sqrt{s}$ = 1.8 TeV," F. Abe et al., The CDF Collaboration, Phys. Rev. Lett. 67, 2609 (1991).

28. "Measurement of the $Z\,p_T$ Distribution in $\bar{p}p$ Collisions at $\sqrt{s}$ = 1.8 TeV," F. Abe et al., The CDF Collaboration, Phys. Rev. Lett. 67, 2937 (1991).

29. "Measurement of $B^0\bar{B}^0$ Mixing at the Fermilab Tevatron Collider," F. Abe, The CDF Collaboration, Phys. Rev. Lett. 67, 3351 (1991).

30. "A Lower Limit on the Top Quark Mass from Events with Two Leptons in $\bar{p}p$ Collisions at $\sqrt{s}$ = 1.8 TeV," F. Abe et al., The CDF Collaboration, Phys. Rev. Lett. 68, 447 (1992).

31. "Inclusive Jet Cross Section in $\bar{p}p$ Collisions at $\sqrt{s}$ = 1.8 TeV," F. Abe et al., The CDF Collaboration, Phys. Rev. Lett. 68, 1104 (1992).

32. "Lepton Asymmetry in W Decays from $\bar{p}p$ Collisions at $\sqrt{s}$ = 1.8 Tev," F. Abe et al., The CDF Collaboration, Phys. Rev. Lett. 68, 1458 (1992).

33. "A Search for New Gauge Bosons in $\bar{p}p$ Collisions at $\sqrt{s}$ = 1.8 TeV," F. Abe et al., The CDF Collaboration, Phys. Rev. Lett. 68, 1463 (1992).

34. "Topology of Three Jet Events in $\bar{p}p$ Collisions at $\sqrt{s}$ = 1.8 TeV," F. Abe et al., The CDF Collaboration, Phys. Rev. D45, 1448 (1992).

35. "Properties of Events with Large Total Transverse Energy Produced in Proton-Antiproton Collisions at $\sqrt{s}$ = 1.8 TeV," F. Abe et al., The CDF Collaboration, Phys. Rev. D45, 2249 (1992).

36. "A Limit on the Top Quark Mass from Proton-Antiproton Collisions at $\sqrt{s}$ = 1800 GeV," F. Abe et al., The CDF Collaboration, Phys. Rev. D45, 3921 (1992).

37. "Measurement of the Isolated Prompt Photon Cross Section Measurement in $p\bar{p}$ Collisions at $\sqrt{s}$ = 1.8 TeV," F. Abe et al., The CDF Collaboration, Phys. Rev. Lett. 68, 2734 (1992).

38. "Measurement of the Ratio $\sigma \cdot B(W \rightarrow \tau\nu)/\sigma \cdot B(W \rightarrow e\nu)$ in $p\bar{p}$ Collisions at $\sqrt{s}$ = 1.8 TeV," F. Abe et al., The CDF Collaboration, Phys. Rev. Lett. 68, 3398 (1992).

39. "A Measurement of the B Meson and b Quark Cross Section at $\sqrt{s}$ = 1.8 TeV Using the Exclusive Decay $B^{\pm} \rightarrow J/\psi\,K^{\pm}$," F. Abe et al., The CDF Collaboration, Phys. Rev. Lett. 68, 3403 (1992).

40. "A Measurement of the Production and Muonic Decay Rate of W and Z Bosons in $p\bar{p}$ Collisions at $\sqrt{s}$ = 1.8 TeV," F. Abe et al., The CDF Collaboration, Phys. Rev. Lett. 69, 28 (1992).

41. "Limit on the Rare Decay $W^{\pm} \rightarrow \gamma + \pi^{\pm}$ in $\bar{p}p$ Collisions at $\sqrt{s} = 1.8$ TeV," F. Abe et al., The CDF Collaboration, Phys. Rev. Lett. 69, 2160 (1992).

42. "The Dijet Angular Distribution at $\sqrt{s} = 1.8$ TeV," F. Abe et al., The CDF Collaboration, Phys. Rev. Lett. 69, 2897 (1992).

43. "Search for Squarks and Gluinos from $p\bar{p}$ Collisions at $\sqrt{s} = 1.8$ TeV," F. Abe et al., The CDF Collaboration, Phys. Rev. Lett. 69, 3439 (1992).

44. "Inclusive J/ψ, ψ' and b-Quark Production in $\bar{p}p$ Collisions at $\sqrt{s} = 1.8$ TeV," F. Abe et al., The CDF Collaboration, Phys. Rev. Lett. 69, 3704 (1992).

45. "Limits on the Production of Massive Stable Charged Particles," F. Abe et al., The CDF Collaboration, Phys. Rev. D, Rapid Communications, 46, R1889 (1992).

46. "A Measurement of Jet Shapes in $\bar{p}p$ Collisions at $\sqrt{s} = 1.8$ TeV," F. Abe et al., The CDF Collaboration, Phys. Rev. Lett. 70, 713 (1993).

47. "A Measurement of the Bottom Quark Production Cross Section using Semileptonic Decay Electrons in $\bar{p}p$ at $\sqrt{s} = 1.8$ TeV," F. Abe et al., The CDF Collaboration, Phys. Rev. Lett. 71, 500 (1993).

48. "Search for $\Lambda_b \rightarrow J/\psi\,\Lambda^0$ in $p\bar{p}$ Collisions at $\sqrt{s} = 1.8$ TeV," F. Abe et al., The CDF Collaboration, Phys. Rev. D, Rapid Communications, 47, R2639 (1993).

49. "Study of Four-jet Events and Evidence for Double Parton Interactions in $p\bar{p}$ Collisions at $\sqrt{s} = 1.8$ TeV," F. Abe et al., The CDF Collaboration, Phys. Rev. D47, 4857 (1993).

50. "Measurement of the Cross Section for Production of Two Isolated Prompt Photons in $p\bar{p}$ Collisions at $\sqrt{s} = 1.8$ TeV," F. Abe et al., The CDF Collaboration, Phys. Rev. Lett. 70, 2232 (1993).

51. "Measurement of the Dijet Mass Distribution in $p\bar{p}$ Collisions at $\sqrt{s} = 1.8$ TeV," F. Abe et al., The CDF Collaboration, Phys. Rev. D48, 998 (1993).

52. "A Prompt Photon Cross Section Measurement in $\bar{p}p$ Collisions at $\sqrt{s} = 1.8$ TeV," F. Abe et al., The CDF Collaboration, Phys. Rev. D48, 2998 (1993).

53. "Comparison of Jet Production in $\bar{p}p$ Collisions at $\sqrt{s} = 546$ and 1800 GeV," F. Abe et al., The CDF Collaboration, Phys. Rev. Lett. 70, 1376 (1993).

54. "A Measurement of Jet Multiplicity in W Events Produced in $\bar{p}p$ Collisions at $\sqrt{s} = 1.8$ Gev," F. Abe et al., The CDF Collaboration, Phys. Rev. Lett. 70, 4042 (1993).

55. "The Center-of-Mass Angular Distribution from Prompt Photons Produced in $p\bar{p}$ Collisions at $\sqrt{s} = 1.8$ TeV," F. Abe et al., The CDF Collaboration, Phys. Rev. Lett. 71, 679 (1993).

56. "A Measurement of the Bottom Quark Production Cross Section in 1.8 TeV $p\bar{p}$ Collisions Using Muons from b-Quark Decays," F. Abe et al., The CDF Collaboration, Phys. Rev. Lett. 71 2396 (1993).

57. "Inclusive χ_c and b-Quark Production in $\bar{p}p$ Collisions at $\sqrt{s} = 1.8$ TeV," F. Abe et al., The CDF Collaboration, Phys. Rev. Lett. 71, 2537 (1993).

58. "A Search for First-Generation Leptoquarks in $\bar{p}p$ Collisions at $\sqrt{s} = 1.8$ TeV at CDF," F. Abe et al., The CDF Collaboration. Phys. Rev. D, Rapid Communications, 48, R3939 (1993).

59. "Observation of the Decay $B_s^0 \rightarrow J/\psi\,\phi$ in $\bar{p}p$ Collisions at $\sqrt{s} = 1.8$ TeV," F. Abe et al., The CDF Collaboration, Phys. Rev. Lett. 71, 1685 (1993).

60. "Search for Quark Compositeness, Axigluons and Heavy Particles using the Dijet Invariant Mass Spectrum Observed in $p\bar{p}$ Collisions," F. Abe et al., The CDF Collaboration, Phys Rev. Lett. 71, 2542 (1993).

61. "Measurement of the Average Lifetime of B-Hadrons Produced in $p\bar{p}$ Collisions at $\sqrt{s} = 1.8$ TeV," F. Abe et al., Phys. Rev. Lett. 71, 3421 (1993).

62. "Measurement of Drell-Yan Electron and Muon Pair Differential Cross-Sections in $\bar{p}p$ Collisions

at $\sqrt{s} = 1.8$ TeV," F. Abe et al., The CDF Collaboration, Phys. Rev. D, Rapid Communications, 49, R1 (1994).

63. "Search for the Top Quark Decaying to a Charged Higgs in $p\bar{p}$ Collisions at $\sqrt{s} = 1.8$ TeV," F. Abe et al., The CDF Collaboration, Phys. Rev. Lett. 72, 1977 (1994).

64. "Search for Excited Quarks in $p\bar{p}$ Collisions at $\sqrt{s} = 1.8$ TeV," F. Abe et al., The CDF Collaboration, Phys. Rev. Lett. 72, 3004 (1994).

65. "Measurement of the B^+ and B^0 Meson Lifetimes," F. Abe et al., The CDF Collaboration, Phys. Rev. Lett. 72, 3456 (1994).

66. "Measurement of the Ratio $\sigma B(W \rightarrow e\nu)/\sigma B(Z \rightarrow e^+e^-)$ in $\bar{p}p$ Collisions at $\sqrt{s} = 1.8$ TeV," F. Abe et al., The CDF Collaboration, Phys. Rev. Lett. 73, 220 (1994).

67. "Evidence for Top Quark Production in $\bar{p}p$ Collisions at $\sqrt{s} = 1.8$ TeV," F. Abe et al., The CDF Collaboration, Phys. Rev. D 50, 2966 (1994).

68. "Evidence for Top Quark Production in $\bar{p}p$ Collisions at $\sqrt{s} = 1.8$ TeV," F. Abe et al., The CDF Collaboration, Phys. Rev. Lett. 73, 225 (1994).

69. "A Measurement of the B Meson and b Quark Cross Sections at $\sqrt{s} = 1.8$ TeV using the Exclusive Decay $B^0 \rightarrow J/\psi K^*(892)^0$, F. Abe et al., The CDF Collaboration, Phys. Rev. D 50, 4252 (1994).

70. "Measurement of the Small Angle Antiproton-Proton Elastic Scattering at $\sqrt{s} = 546$ and 1800 GeV," F. Abe et al., The CDF Collaboration, Phys. Rev. D 50, 5518 (1994).

71. "Measurement of the $\bar{p}p$ Single Diffraction Dissociation at $\sqrt{s} = 546$ and 1800 GeV," F. Abe et al., The CDF Collaboration, Phys. Rev. D 50, 5535 (1994).

72. "Measurement of the Antiproton-Proton Total Section at $\sqrt{s} = 546$ and 1800 GeV," F. Abe et al., The CDF Collaboration, Phys. Rev. D 50, 5550 (1994).

73. "Evidence for Color Coherence in $p\bar{p}$ Collisions at $\sqrt{s} = 1.8$ TeV," F. Abe et al., The CDF Collaboration, Phys. Rev. D. 50, 5562 (1994).

74. "W Boson + Jet Angular Distribution in $p\bar{p}$ Collisions at $\sqrt{s} = 1.8$ TeV," F. Abe et al., The CDF Collaboration, Phys. Rev. Lett. 73, 2296 (1994).

75. "A Precision Measurement of the Prompt Photon Cross Section in $p\bar{p}$ Collisions at $\sqrt{s} = 1.8$ TeV," F. Abe et al., The CDF Collaboration, Phys. Rev. Lett. 73, 2662 (1994).

76. "Search for Top Quark Decaying to a Charged Higgs Boson in $\bar{p}p$ Collisions at $\sqrt{s} = 1.8$ TeV," F. Abe et al., The CDF Collaboration, Phys. Rev. Lett. 73, 2667 (1994).

77. "Direct Measurement of the W Boson Width," F. Abe et al., The CDF Collaboration, Phys. Rev. Lett. 74, 341 (1995).

78. "The Charge Asymmetry in W-Boson Decays Produced in $p\bar{p}$ Collisions at $\sqrt{s} = 1.8$ TeV," F. Abe et al., The CDF Collaboration, Phys. Rev. Lett. 74, 850 (1995).

79. "Observation of Rapidity Gaps in $\bar{p}p$ Collisions at 1.8 TeV," F. Abe et al., The CDF Collaboration, Phys. Rev. Lett. 74, 855 (1995).

80. "Measurement of W-Photon Couplings with CDF in $p\bar{p}$ Collisions at $\sqrt{s} = 1.8$ TeV," F. Abe et al., The CDF Collaboration, Phys. Rev. Lett. 74, 1936 (1995).

81. "Limits on Z-Photon Couplings from $p\bar{p}$ Interactions at $\sqrt{s} = 1.8$ TeV," F. Abe et al., The CDF Collaboration, Phys. Rev. Lett. 74, 1941 (1995).

82. "Search for New Gauge Bosons Decaying into Dielectrons in $\bar{p}p$ Collisions at $\sqrt{s} = 1.8$ TeV," F. Abe et al., The CDF Collaboration, Phys. Rev. D, Rapid Communications, 51, 949 (1995).

83. "Observation of Top Quark Production in $\bar{p}p$ Collisions with CDF Detector at Fermilab," F. Abe et al., The CDF Collaboration, Phys. Rev. Lett. 74, 2626 (1995).

84. "Search for Charged Bosons Heavier than the W in $p\bar{p}$ Collisions at $\sqrt{s} = 1800$ GeV," F. Abe et al., The CDF Collaboration, Phys. Rev. Lett. 74, 2900 (1995).

85. "Kinematical Evidence for Top Pair Production in W + Multijet Events in $p\bar{p}$ Collisions at $\sqrt{s}$ = 1.8 TeV," F. Abe et al., The CDF Collaboration, Phys. Rev. D 51, 4623 (1995).

86. "Search for New Particles Decaying to Dijets in $p\bar{p}$ Collisions at $\sqrt{s}$ = 1.8 TeV," F. Abe et al., The CDF Collaboration, Phys. Rev. Lett. 74, 3538 (1995).

87. "Measurement of the B_s Meson Lifetime," F. Abe et al., The CDF Collaboration, Phys. Rev. Lett. 74, 4988 (1995).

88. "A Measurement of the Ratio $\sigma \cdot B(p\bar{p} \to W \to e\nu)/\sigma \cdot B(p\bar{p} \to Z^0 \to ee)$ in $p\bar{p}$ Collisions at $\sqrt{s}$ = 1800 GeV," F. Abe et al., The CDF Collaboration, Phys. Rev. D 52, 2624 (1995).

89. "Measurement of the W Boson Mass," F. Abe et al., The CDF Collaboration, Phys. Rev. Lett. 75, 11 (1995).

90. "Search for Squarks and Gluinos via Radiative Decays of Neutralinos in Proton-Antiproton Collisions at $\sqrt{s}$ = 1.8 TeV," F. Abe et al., The CDF Collaboration, Phys. Rev. Lett. 75, 613 (1995).

91. "Properties of High-Mass Multijet Events at the Fermilab Proton-Antiproton Collider," F. Abe et al., The CDF Collaboration, Phys. Rev. Lett. 75, 608 (1995).

92. "A Search for Second Generation Leptoquarks in $p\bar{p}$ Collisions at $\sqrt{s}$ = 1.8 TeV," F. Abe et al., The CDF Collaboration, Phys. Rev. Lett. 75, 1012 (1995).

93. "Limits on WWZ and WWγ Couplings from WW and WZ Production in $p\bar{p}$ Collisions at $\sqrt{s}$ = 1.8 TeV," F. Abe et al., The CDF Collaboration, Phys. Rev. Lett. 75, 1017 (1995).

94. "Measurement of the B Meson Differential Cross-Section, $d\sigma/d_{pT}$, in $p\bar{p}$ Collisions at $\sqrt{s}$ = 1.8 TeV," F. Abe et al., The CDF Collaboration, Phys. Rev. Lett. 75, 1451 (1995).

95. "Identification of Top Quarks using Kinematic Variables," F. Abe et al., The CDF Collaboration, Phys. Rev. D, Rapid Communications, 52, 2605 (1995).

96. "Measurement of the Polarization in the Decays $B_d \to J/\psi K^{\star 0}$ and $B_s \to J/\psi\phi$," F. Abe et al., The CDF Collaboration, Phys. Rev. Lett. 75, 3068 (1995).

97. "Measurement of the W Boson Mass," F. Abe et al., The CDF Collaboration, Phys. Rev. D 52, 4784 (1995).

98. "Study of $t\bar{t}$ Production in $p\bar{p}$ Collisions Using Total Transverse Energy," F. Abe et al., The CDF Collaboration, Phys. Rev. Lett. 75, 3997 (1995).

99. "Υ Production in $p\bar{p}$ Collisions at $\sqrt{s}$ = 1.8 TeV," F. Abe et al., The CDF Collaboration, Phys. Rev. Lett. 75, 4358 (1995).

100. "Measurement of Correlated μ-$\bar{b}$ Jet Cross Sections in $p\bar{p}$ Collisions at $\sqrt{s}$ = 1.8 TeV," F. Abe et al., The CDF Collaboration, Phys. Rev. D53, 1051 (1996).

101. "Reconstruction of $B^0 \to J/\psi K^0_S$ Ratios of Branching Ratios Involving $B \to J/\psi K^{(\star)}$," F. Abe et al., The CDF Collaboration, Phys. Rev. Lett. 76, 2015 (1996).

102. "Search for the Rare Decay $W^{\pm} \to \pi^{\pm} + \gamma$," F. Abe et al., The CDF Collaboration, Phys. Rev. Lett. 76, 2852 (1996).

103. "Measurement of $\sigma B(W \to e\nu)$ and $\sigma B(Z^0 \to e^+e^-)$ in $p\bar{p}$ Collisions at $\sqrt{s}$ = 1.8 TeV," F. Abe et al., The CDF Collaboration, Phys. Rev. Lett. 76, 3070 (1996).

104. "Measurement of the Mass of the B^0_s Meson," F. Abe et al., The CDF Collaboration, Phys. Rev. D53, 3496 (1996).

105. "Search for Gluino and Squark Cascade Decays at the Fermilab Tevatron Collider," F. Abe et al., The CDF Collaboration, Phys. Rev. Lett. 76, 2006 (1996).

106. "Search for Charged Higgs Decays of the Top Quark Using Hadronic Tau Decays," F. Abe et al., The CDF Collaboration, submitted to Phys. Rev. D January 5, 1996. Fermilab-PUB-96/004-E.

107. "Search for Chargino-Neutralino Production in $p\bar{p}$ Collisions at $\sqrt{s}$ = 1.8 TeV," F. Abe et al.,

The CDF Collaboration, Phys. Rev. Lett. 76, 4307 (1996)

108. "Measurement of the B^- and $\bar{B}^0$ Meson Lifetimes Using Semileptonic Decays," F. Abe et al., The CDF Collaboration, Phys. Rev. Lett. 76, 4462 (1996)

109. "Search for Flavor-Changing Neutral Current B Meson Decays in $p\bar{p}$ Collisions at $\sqrt{s} = 1.8$ TeV," F. Abe et al., The CDF Collaboration, Phys. Rev. Lett. 76, 4675 (1996)

110. "Inclusive Jet Cross Section in $\bar{p}p$ Collisions at $\sqrt{s} = 1.8$ TeV," F. Abe et al., The CDF Collaboration, Phys. Rev. Lett. 77, 438 (1996).

111. "Properties of Jets in Z Boson Events from 1.9 TeV $\bar{p}p$ Collisions," F. Abe et al., The CDF Collaboration, Phys. Rev. Lett. 77, 448 (1996)

112. "Measurement of Λ_b^0 Lifetime Using $\Lambda_b^0 \to \Lambda_c^+ \ell^- \bar{\nu}$," F. Abe et al., The CDF Collaboration, Phys. Rev. Lett. 77, 1439 (1996).

113. "Measurement of the Lifetime of the B_s^0 Meson Using the Exclusive Decay Mode $B_s^0 \to J/\psi\phi$," F Abe et al., The CDF Collaboration, Phys. Rev. Lett. 77, 1945 (1996).

114. "Forward-Backward Charge Asymmetry of Electron Pairs Above the Z^0 Pole," F. Abe et al., The CDF Collaboration, Phys. Rev. Lett. 77, 2616 (1996).

115. "Further Properties of High-Mass Multijet Events at the Fermilab Proton-Antiproton Collider," F. Abe et al., The CDF Collaboration, Phys. Rev. D54, 4221 (1996)

116. "Ratios of Bottom Meson Branching Fractions Involving J/ψ Mesons and Determination of b Quark Fragmentation Fractions," F. Abe et al., The CDF Collaboration, Phys. Rev. D54 6595 (1996). Fermilab-PUB-96/119-E.

117. "Measurement of the $\gamma + D^{*\pm}$ Cross Section in $\bar{p}p$ Collisions at $\sqrt{s} = 1.8$ TeV," F. Abe et al., The CDF Collaboration, Phys. Rev. Lett. 77, 5005 (1996). Fermilab-PUB-96/152-E.

118. "Measurement of $b\bar{b}$ Production Correlations, $B^0\bar{B}^0$ Mixing, and a Limit on ϵ_B in $p\bar{p}$ Collisions at $\sqrt{s} = 1.8$ TeV," F. Abe et al., The CDF Collaboration, Phys. Rev. D55 2546 (1997).

119. "Observation of $\Lambda_b^0 \to J/\psi\Lambda$ at the Fermilab Proton-Antiproton Collider," F. Abe et al., The CDF Collaboration, Phys. Rev. D55 1142 (1997). Fermilab-PUB-96/270-E.

120. "Measurement of the Branching Fraction $B(B_u^+ \to J/\psi\pi^+)$ and Search for $B_c^+ \to J/\psi\pi^+$," F. Abe et al., The CDF Collaboration, Phys. Rev. Lett. 77, 5176 (1996).

121. "Observation of W^+W^- Production in $\bar{p}p$ Collisions at $\sqrt{s} = 1.8$ TeV," F. Abe et al., The CDF Collaboration, Phys. Rev. Lett. 78, 4536 (1997).

122. "Further Properties of High Mass Multi - Jet Events at the Fermilab $\bar{p}p$ Collider," F. Abe et al., The CDF Collaboration, Phys.Rev. D54, 4221 (1996)

123. "Measurement of Dijet Angular Distributions at CDF," F. Abe et al., The CDF Collaboration, Phys. Rev. Lett. 77, 5336 (1996), Erratum-ibid. 78, 4307(1997)

124. "The CDF-II Detector: Technical Design Report," The CDF-II Collaboration (R. Blair et al.). Fermilab-PUB-96-390-E, Nov 1996. 234pp.

125. "Search for Third Generation Leptoquarks in $\bar{p}p$ Collisions at $\sqrt{s} = 1.8$ TeV," F. Abe et al., The CDF Collaboration, Phys.Rev.Lett. 78, 2906-2911 (1997)

126. "Observation of Diffractive W Boson Production at the Tevatron," F. Abe et al., The CDF Collaboration, Phys.Rev.Lett. 78, 2698-2703 (1997)

127. "Search for New Particles Decaying to Dijets at CDF," F. Abe et al., The CDF Collaboration, Phys.Rev. D55, 5263-5268 (1997)

128. "J/ψ and $\psi(2S)$ Production in $\bar{p}p$ Collisions at $\sqrt{s} = 1.8$ TeV," F. Abe et al., The CDF Collaboration, Phys.Rev.Lett. 79, 572-577 (1997)

129. "Search for Gluinos and Squarks at the Fermilab Tevatron Collider. F. Abe et al., The CDF Collaboration, Phys.Rev. D56, 1357-1362 (1997)

130. "Production of J/ψ Mesons from χ_c Meson Decays in $\bar{p}p$ Collisions at $\sqrt{s} = 1.8$ TeV. F. Abe et al., The CDF Collaboration, Phys.Rev.Lett. 79, 578-583 (1997)

131. "Measurement of Diffractive Dijet Production at the Tevatron. F. Abe et al., The CDF Collaboration, Phys.Rev.Lett. 79, 2636-2641 (1997)

132. "First Observation of the All Hadronic Decay of $t\bar{t}$ Pairs. F. Abe et al., The CDF Collaboration, Phys.Rev.Lett. 79, 1992-1997 (1997)

133. "Search for Charged Higgs Decays of the Top Quark using Hadronic Decays of the Tau Lepton. F. Abe et al., The CDF Collaboration, Phys.Rev.Lett. 79, 357-362 (1997)

134. "Measurement of Double Parton Scattering in $\bar{p}p$ Collisions at $\sqrt{s} = 1.8$ TeV. F. Abe et al., The CDF Collaboration, Phys.Rev.Lett. 79, 584-589 (1997)

135. "The $\mu\tau$ and $e\tau$ Decays of Top Quark Pairs Produced in $\bar{p}p$ Collisions at $\sqrt{s} = 1.8$ TeV. F. Abe et al., The CDF Collaboration, Phys.Rev.Lett. 79, 3585-3590 (1997)

136. "Double Parton Scattering in $\bar{p}p$ Collisions at $\sqrt{s} = 1.8$ TeV. F. Abe et al., The CDF Collaboration, Phys.Rev. D56, 3811-3832 (1997)

137. "Properties of Six Jet Events with Large Six Jet Mass at the Fermilab $\bar{p}p$ Collider. F. Abe et al., The CDF Collaboration, Phys.Rev. D56, 2532-2543 (1997)

138. "Properties of Photon plus Two Jet Events in $\bar{p}p$ Collisions at $\sqrt{s} = 1.8$ TeV. F. Abe et al., The CDF Collaboration, Phys.Rev. D57, 67-77 (1998)

139. "Search for New Gauge Bosons Decaying into Dileptons in $\bar{p}p$ Collisions at $\sqrt{s} = 1.8$ TeV. F. Abe et al., The CDF Collaboration, Phys.Rev.Lett. 79, 2192-2197 (1997)

140. "Limits on Quark - Lepton Compositeness Scales from Dileptons Produced in 1.8 TeV $\bar{p}p$ Collisions. F. Abe et al., The CDF Collaboration, Phys.Rev.Lett. 79, 2198-2203 (1997)

141. "Search for New Particles Decaying into $b\bar{b}$ Produced in Association with W Bosons Decaying into e Neutrino or μ Neutrino at the Tevatron. F. Abe et al., The CDF Collaboration, Phys.Rev.Lett. 79, 3819-3824 (1997)

142. "Search for Flavor Changing Neutral Current Decays of the Top Quark in $\bar{p}p$ Collisions at $\sqrt{s}$ = 1.8 TeV. F. Abe et al., The CDF Collaboration, Phys.Rev.Lett. 80, 2525-2530 (1998)

143. "Search for First Generation Leptoquark Pair Production in $\bar{p}p$ Collisions at $\sqrt{s} = 1.8$ TeV. F. Abe et al., The CDF Collaboration, Phys.Rev.Lett. 79, 4327-4332 (1997)

144. "Dijet Production by Color - Singlet Exchange at the Fermilab Tevatron. F. Abe et al., The CDF Collaboration, Phys.Rev.Lett. 80, 1156-1161 (1998)

145. "Measurement of the Differential Cross-Section for Events with Large Total Transverse Energy in $\bar{p}p$ Collisions at $\sqrt{s} = 1.8$ TeV. F. Abe et al., The CDF Collaboration, Phys.Rev.Lett. 80, 3461-3466 (1998)

146. "Properties of Jets in W Boson Events from 1.8 TeV $\bar{p}p$ Collisions. F. Abe et al., The CDF Collaboration, Phys.Rev.Lett. 79, 4760-4765 (1997)

147. "The Jet Pseudorapidity Distribution in Direct Photon Events in $\bar{p}p$ Collisions at $\sqrt{s} = 1.8$ TeV. F. Abe et al., The CDF Collaboration, Phys.Rev. D57, 1359-1365 (1998)

148. "Measurement of the $B^0 - \bar{B^0}$ Oscillation Frequency in $\bar{p}p$ Collisions using πB Meson Charge FLavor Correlations at $\sqrt{s} = 1.8$ TeV. F. Abe et al., The CDF Collaboration, Phys.Rev.Lett. 80, 2057-2062 (1998)

149. "Measurement of the Top Quark Mass and $t\bar{t}$ Production Cross-Section from Dilepton Events at the Collider Detector at Fermilab. F. Abe et al., The CDF Collaboration, Phys.Rev.Lett. 80, 2779-2784 (1998)

150. "Measurement of the $t\bar{t}$ Production Cross-Section in $\bar{p}p$ Collisions at $\sqrt{s} = 1.8$ TeV. F. Abe et al., The CDF Collaboration, Phys.Rev.Lett. 80, 2773-2778 (1998)

151. "Measurement of the Top Quark Mass. F. Abe et al., The CDF Collaboration, Phys.Rev.Lett. 80, 2767-2772 (1998)

152. "Measurement of B Hadron Lifetimes using J/ψ Final States at CDF. F. Abe et al., The CDF Collaboration, Phys.Rev. D57, 5382-5401 (1998)

153. "Observation of Hadronic W Decays in $t\bar{t}$ Events with the Collider Detector at Fermilab. F. Abe et al., The CDF Collaboration, Phys.Rev.Lett. 80, 5720-5725 (1998)

154. "Searches for New Physics in Diphoton Events in $\bar{p}p$ Collisions at $\sqrt{s}$ = 1.8 TeV. F. Abe et al., The CDF Collaboration, Phys.Rev.Lett. 81, 1791-1796 (1998)

155. "Search for Chargino - Neutralino Associated Production at the Fermilab Tevatron Collider. F. Abe et al., The CDF Collaboration, in Phys.Rev.Lett. 80, 5275-5280 (1998)

156. "Observation of $B^+ \to \psi(2S)K^+$ and $B^0 \to \psi(2S)K(892)^{*0}$ Decays and Measurements of B Meson Branching Fractions into J/$\psi and \psi(2S)$ Final States. F. Abe et al., The CDF Collaboration, Phys.Rev. D58, 072001 (1998)

157. "Search for the Rare Decay $W^\pm \to \pi^\pm + \gamma$ in $p\bar{p}$ Collisions at $\sqrt{s}$ = 1.8 TeV. F. Abe et al., The CDF Collaboration, Phys.Rev. D58, 031101 (1998)

158. "Search for the Rare Decay $W^\pm \to D^\pm(S)\gamma q$ in $p\bar{p}$ Collisions at $\sqrt{s}$ = 1.8 TeV. F. Abe et al., The CDF Collaboration, Fermilab-PUB-98-110-E, Apr 1998. 14pp.

Published in Phys.Rev. D58, 091101 (1998)

159. "Observation of B_c Mesons in $p\bar{p}$ Collisions at $\sqrt{s}$ = 1.8 TeV. F. Abe et al., The CDF Collaboration, Phys.Rev. D58, 112004 (1998)

160. "Measurement of the $\sigma(W+ >= 1Jet)/sigma(W)$ Cross-Section Ratio from $p\bar{p}$ Collisions at $\sqrt{s}$ = 1.8 TeV. By CDF Collaborations (F. Abe et al.). Phys.Rev.Lett. 81, 1367-1372 (1998)

161. "Search for Longlived Parents of Z0 Bosons in $p\bar{p}$ Collisions at $\sqrt{s}$ = 1.8 TeV. By The CDF Collaboration (F. Abe et al.). in Phys.Rev. D58, 051102 (1998)

162. "Observation of the B_c Meson in $p\bar{p}$ Collisions at $\sqrt{s}$ = 1.8 TeV. F. Abe et al., The CDF Collaboration, Phys.Rev.Lett. 81, 2432-2437 (1998)

163. "Improved Measurement of the B and $\bar{B}^0$ Meson Lifetimes Using Semileptonic Decays. F. Abe et al., The CDF Collaboration, Phys.Rev. D58, 092002 (1998)

164. "Measurement of the CP Violation Parameter $\sin(2\beta)$ in $B^0_D/\bar{B^0_D} \to$ J/ψK^0_S Decays. F. Abe et al., The CDF Collaboration, Phys.Rev.Lett. 81, 5513-5518 (1998)

165. "Measurement of the $B^0_D/\bar{B^0_D}$ Flavor Oscillation Frequency and Study of Same Side Flavor Tagging of B Mesons in $p\bar{p}$ Collisions. F. Abe et al., The CDF Collaboration, Phys.Rev. D59, 032001 (1999)

166. "Searches for New Physics in Diphoton Events in $p\bar{p}$ Collisions at $\sqrt{s}$ = 1.8 TeV. F. Abe et al., The CDF Collaboration, Fermilab-PUB-98-206-E, Jun 1998. 57pp.

Published in Phys.Rev. D59, 092002 (1999)

167. "Search for Second Generation Leptoquarks in the Dimuon plus Dijet Channel of $p\bar{p}$ Collisions at $\sqrt{s}$ = 1.8 TeV. F. Abe et al., The CDF Collaboration, Phys.Rev.Lett. 81, 4806-4811 (1998)

168. "Measurement of the B^0_s Meson Lifetime using Semileptonic Decays. F. Abe et al., The CDF Collaboration, Published in Phys.Rev. D59, 032004 (1999)

169. "Search for Higgs Bosons Produced in Association with a Vector Boson in $p\bar{p}$ Collisions at $\sqrt{s}$ = 1.8 TeV. F. Abe et al., The CDF Collaboration, Phys.Rev.Lett. 81, 5748-5753 (1998)

170. "Search for the Decays $B^0_S, B^0_D \to e^\pm\mu^\pm$ and Pati-Salam Leptoquarks. F. Abe et al., The CDF Collaboration, Phys.Rev.Lett. 81, 5742-5747 (1998)

171. "Events with a Rapidity Gap Between Jets in $p\bar{p}$ Collisions at $\sqrt{s}$ = 630-GEV. F. Abe et al., The CDF Collaboration, Phys.Rev.Lett. 81, 5278-5283 (1998)

172. "A Measurement of the Lepton Charge Asymmetry in W Boson Decays Produced in $p\bar{p}$ Collisions. F. Abe et al., The CDF Collaboration, Phys.Rev.Lett. 81, 5754-5759 (1998)

173. "Search for New Particles Decaying TO $b\bar{b}$ in $p\bar{p}$ Collisions at $\sqrt{s}$ = 1.8 TeV. F. Abe et al., The CDF Collaboration, Phys.Rev.Lett. 82, 2038-2043 (1999)

174. "Measurement of Z0 and Drell-Yan Production Cross-Section using Dimuons in $p\bar{p}$ Collisions at $\sqrt{s} = 1.8$ TeV. F. Abe et al., The CDF Collaboration, Phys.Rev. D59, 052002 (1999)

175. "Measurement of the Top Quark Mass with the Collider Detector at Fermilab. F. Abe et al., The CDF Collaboration, Phys.Rev.Lett. 82, 271-276 (1999), Erratum-ibid.82, 2808-2809 (1999)

176. "Search for a Technicolor Omega(T) Particle in Events with a Photon and a B Quark Jet at CDF. F. Abe et al., The CDF Collaboration, Phys.Rev.Lett. 83, 3124-3129 (1999)

177. "Kinematics of $t\bar{t}$ Events at CDF. F. Abe et al., The CDF Collaboration, Phys.Rev. D59, 092001 (1999)

178. "Search for the Decays $B_D^0 \to \mu^+\mu^-$ and $B_S^0 \to \mu^+\mu^-$ in $p\bar{p}$ Collisions at $\sqrt{s} = 1.8$ TeV. F. Abe et al., The CDF Collaboration, Phys.Rev. D57, 3811-3816 (1998)

179. "Search for Third Generation Leptoquarks from Technicolor Models in P ANTI-P Collisions at $\sqrt{s} = 1.8$ TeV. F. Abe et al., The CDF Collaboration, Phys.Rev.Lett. 82, 3206 (1999)

180. "Search for R-Parity Violating Supersymmetry using Like Sign Dielectrons in $p\bar{p}$ Collisions at $\sqrt{s} = 1.8$ TeV. F. Abe et al., The CDF Collaboration, Phys.Rev.Lett. 83, 2133-2138 (1999)

181. "Measurement of $b\bar{b}$ Rapidity Correlations in $p\bar{p}$ Collisions at $\sqrt{s} = 1.8$ TeV. F. Abe et al., The CDF Collaboration, Phys.Rev. D61, 032001 (2000)

182. "A Search for $B_s^0 - \bar{B_s^0}$ Oscillations Using the Semileptonic Decay $B_S^0 \to \phi$ Lepton+ X Neutrino. F. Abe et al., The CDF Collaboration, Phys.Rev.Lett. 82, 3576-3580 (1999)

183. "Measurement of B Quark Fragmentation Fractions in the Production of Strange and Light B Mesons in $p\bar{p}$ Collisions at $\sqrt{s}$=1.8 TeV. F. Abe et al., The CDF Collaboration, Phys.Rev. D60, 092005 (1999)

184. "Measurement of the Associated $\gamma + \mu^{\pm}$ Production Cross-Section in $p\bar{p}$ Collisions at $\sqrt{s} = 1.8$ TEV. F. Abe et al., The CDF Collaboration, Phys.Rev. D60, 092003 (1999)

185. "Measurement of the $B_d^0 - \bar{B_d^0}$ Oscillation Frequency using Dimuon Data in $p\bar{p}$ Collisions at $\sqrt{s} = 1.8$ TeV. F. Abe et al., The CDF Collaboration, Phys.Rev. D60, 051101 (1999)

186. "Measurement of $B^0 - \bar{B^0}$ Flavor Oscillations using Jet Charge and Lepton Flavor Tagging in $p\bar{p}$ Collisions at $\sqrt{s} = 1.8$ TeV. F. Abe et al., The CDF Collaboration, Phys.Rev. D60, 072003 (1999)

187. "Search for the Flavor Changing Neutral Current Decays $B^+ \to \mu^+\mu^-K^+$ and $B^0 \to \mu^+\mu^-K^{*0}$. By CDF Collaboration (T. Affolder et al.). Phys.Rev.Lett. 83, 3378-3383 (1999)

188. "Search for Technicolor Particles in Lepton plus Two Jets and Multijet Channels in $p\bar{p}$ Collisions at $\sqrt{s} = 1.8$ TeV. By CDF Collaboration (T. Affolder et al.). Fermilab-PUB-99-141-E, May 1999. 10pp. Submitted to Phys.Rev.Lett.

189. "Measurement of the $B^0 - \bar{B^0}$ Oscillation Frequency using $l - D^{*+}$ Pairs and Lepton Flavor Tags. By CDF Collaboration (T. Affolder et al.). Phys.Rev. D60, 112004 (1999)

190. "Observation of Diffractive Beauty Production at the Fermilab Tevatron. By CDF Collaboration (T. Affolder et al.). Phys.Rev.Lett. 84, 232-237 (2000)

191. "The Transverse Momentum and Total Cross-Section of e^+e^- Pairs in the Z-Boson Region from $p\bar{p}$ Collisions at $\sqrt{s} = 1.8$ TeV. By CDF Collaboration (T. Affolder et al.). Phys.Rev.Lett. 84, 845-850 (2000)

192. "A Measurement of $\sin(2\beta)$ from $B \to J/\psi K_S^0$ with the CDF Detector. By CDF Collaboration (T. Affolder et al.). Phys.Rev. D61, 072005 (2000)

193. "Measurement of B Quark Fragmentation Fractions in $p\bar{p}$ Collisions at $\sqrt{s} = 1.8$ TeV. By CDF Collaboration (T. Affolder et al.). Phys.Rev.Lett. 84, 1663-1668 (2000)

194. "Search for a Fourth Generation Quark More Massive than the Z0 Boson in $p\bar{p}$ Collisions at $\sqrt{s} = 1.8$ TeV. By CDF Collaboration (T. Affolder et al.). Phys.Rev.Lett. 84, 835-840 (2000)

195. "Measurement of the Helicity of W Bosons in Top Quark Decays. By CDF Collaboration (T. Affolder et al.). Phys.Rev.Lett. 84, 216-221 (2000)

196. "Search for a W' Boson via the Decay Mode $W' \to \mu\nu_\mu$ in 1.8 TeV P - ANTI-P Collisions. F. Abe et al., The CDF Collaboration, Phys.Rev.Lett. 84, 5716-5721 (2000)

197. "Production of $\Upsilon(1S)$ Mesons from χ_B Decays in $p\bar{p}$ Collisions at $\sqrt{s} = 1.8$ TeV. By CDF Collaboration (T. Affolder et al.). Phys.Rev.Lett. 84, 2094-2099 (2000)

198. "Search for Scalar Top and Scalar Bottom Quarks in $p\bar{p}$ Collisions at $\sqrt{s} = 1.8$ TeV. By CDF Collaboration (T. Affolder et al.). Phys.Rev.Lett. 84, 5704-5709 (2000)

199. "Observation of Orbitally Excited B Mesons in $p\bar{p}$ Collisions at $\sqrt{s} = 1.8$ TeV. By CDF Collaboration (T. Affolder et al.). Phys.Rev. D64, 072002 (2001)

200. "Search for Scalar Top Quark Production in $p\bar{p}$ Collisions at $\sqrt{s} = 1.8$ TeV. By CDF Collaboration (T. Affolder et al.). Phys.Rev.Lett. 84, 5273-5278 (2000)

201. "Search for the Charged Higgs Boson in the Decays of Top Quark Pairs in the $e\tau$ and $\mu\tau$ Channels at $\sqrt{s} = 1.8$ TeV. By CDF Collaboration (T. Affolder et al.). Phys.Rev. D62, 012004 (2000)

202. "A Measurement of the Differential Dijet Mass Cross-Section in $p\bar{p}$ Collisions at $\sqrt{s} = 1.8$ TeV. By CDF Collaboration (T. Affolder et al.). Phys.Rev. D61, 091101 (2000)

203. "Search for Color Singlet Technicolor Particles in $p\bar{p}$ Collisions at $\sqrt{s} = 1.8$ TeV. By CDF Collaboration (T. Affolder et al.). Phys.Rev.Lett. 84, 1110-1115 (2000)

204. "Search for New Particles Decaying to $t\bar{t}$ in $p\bar{p}$ Collisions at $\sqrt{s} = 1.8$ TeV. By CDF Collaboration (T. Affolder et al.). Phys.Rev.Lett. 85, 2062-2067 (2000)

205. "Diffractive Dijets with a Leading $\bar{p}$ in $p\bar{p}$ Collisions at $\sqrt{s} = 1800$ GeV. By CDF Collaboration (T. Affolder et al.). Phys.Rev.Lett. 84, 5043-5048 (2000)

206. "Limits on Gravitino Production and New Processes with Large Missing Transverse Energy in $p\bar{p}$ Collisions at $\sqrt{s} = 1.8$ TeV. By CDF Collaboration (T. Affolder et al.). Phys.Rev.Lett. 85, 1378-1383 (2000)

207. "Search for Second and Third Generation Leptoquarks including Production via Technicolor Interactions in $p\bar{p}$ Collisions at $\sqrt{s} = 1.8$ TEV. By CDF Collaboration (T. Affolder et al.). Phys.Rev.Lett. 85, 2056-2061 (2000)

208. "Direct Measurement of the W Boson Width in $p\bar{p}$ Collisions at $\sqrt{s} = 1.8$ TeV. By CDF Collaboration (T. Affolder et al.). Phys.Rev.Lett. 85, 3347-3352 (2000)

209. "Measurement of J/ψ and $\psi(2S)$ Polarization in $p\bar{p}$ Collisions at $\sqrt{s} = 1.8$ TeV. By CDF Collaboration (T. Affolder et al.). Phys.Rev.Lett. 85, 2886-2891 (2000)

210. "Dijet Production by Double Pomeron Exchange at the Fermilab Tevatron. By CDF Collaboration (T. Affolder et al.). Phys.Rev.Lett. 85, 4215-4220 (2000)

211. "Measurement of the Top Quark P_T Distribution. By CDF Collaboration (T. Affolder et al.). Phys.Rev.Lett. 87, 102001 (2001)

212. "Measurement of $d\sigma/dy$ for High Mass Drell-Yan e^+e^- pairs from $p\bar{p}$ Collisions at $\sqrt{s} = 1.8$ TeV. By CDF Collaboration and D0 Collaboration (T. Affolder et al.). Phys.Rev. D63, 011101 (2001)

213. "Measurement of the Top Quark Mass with the Collider Detector at Fermilab. By CDF Collaboration (T. Affolder et al.). Phys.Rev. D63, 032003 (2001)

214. "Measurement of the Decay Amplitudes of $B^0 \to J/\psi K^*$ and $B_S^0 \to J/\psi\phi$ Decays. By CDF Collaboration (T. Affolder et al.). Phys.Rev.Lett. 85, 4668-4673 (2000)

215. "Measurement of the W Boson Mass with the Collider Detector at Fermilab. By CDF Collaboration (T. Affolder et al.). Phys.Rev. D64, 052001 (2001)

216. "Test of Enhanced Leading Order QCD in W Boson plus Jets Events from 1.8 TeV $p\bar{p}$ Collisions. By CDF Collaboration (T. Affolder et al.). Phys.Rev. D63, 072003 (2001)

217. "Search for Neutral Supersymmetric Higgs Bosons in $p\bar{p}$ Collisions at $\sqrt{s}$ = 1.8 TeV. By CDF Collaboration (T. Affolder et al.). Phys.Rev.Lett. 86, 4472-4478 (2001)

218. "Search for the Supersymmetric Partner of the Top Quark in $p\bar{p}$ Collisions at $\sqrt{s}$ = 1.8 TeV. By CDF Collaboration (T. Affolder et al.). Phys.Rev. D63, 091101 (2001)

219. "Measurement of the Two Jet Differential Cross-Section in $p\bar{p}$ Collisions at $\sqrt{s}$ = 1800GeV. By CDF Collaboration (T. Affolder et al.). Phys.Rev. D64, 012001 (2001)

220. "First Measurement of the Ratio $B(T \to WB)$ / $B(T \to WQ)$ and Associated Limit on the CKM Element $|V_{TB}|$. By CDF Collaboration (T. Affolder et al.). Phys.Rev.Lett. 86, 3233-3238 (2001)

221. "Production of χ_{c1} and χ_{c2} in $p\bar{p}$ Collisions at $\sqrt{s}$ = 1.8 TeV. By CDF Collaboration (T. Affolder et al.). Published in Phys.Rev.Lett. 86, 3963-3968 (2001)

222. "Measurement of the $t\bar{t}$ Production Cross-Section in $p\bar{p}$ Collisions at $\sqrt{s}$ = 1.8 TeV. By CDF Collaboration (T. Affolder et al.). Phys.Rev. D64, 032002 (2001)

223. "Measurement of the Inclusive Jet Cross-Section in $p\bar{p}$ Collisions at $\sqrt{s}$ = 1.8 TeV. By CDF Collaboration (T. Affolder et al.). Phys.Rev. D64, 032001 (2001)

224. "Search for Narrow Diphoton Resonances and for $\gamma\gamma$+W/Z Signatures in $p\bar{p}$ Collisions at $\sqrt{s}$ = 1.8 TeV. By CDF Collaboration (T. Affolder et al.). Fermilab-PUB-01-073-E, May 2001. 30pp. Submitted to Phys.Rev.D

225. "Double Diffraction Dissociation at the Fermilab Tevatron Collider. By CDF Collaboration (T. Affolder et al.). Fermilab-PUB-01-063-E, May 2001. 20pp. Submitted to Phys.Rev.Lett.

226. "Search for Gluinos and Scalar Quarks in $p\bar{p}$ Collisions at $\sqrt{s}$ = 1.8 TeV using the Missing Energy plus Multijets Signature. By CDF Collaboration (T. Affolder et al.). EFI-01-22, Fermilab-PUB-01-084-E, Jun 2001. 7pp. Submitted to Phys.Rev.Lett.

227. "Cross-Section and Heavy Quark Composition of Photon + μ Events Produced in $p\bar{p}$ Collisions. By CDF Collaboration and D0 Collaboration (T. Affolder et al.). Fermilab-PUB-01-087-E, Jun 2001. 15pp. Submitted to Phys.Rev. D

228. "Searches for New Physics in Events with a Photon and B Quark Jet at CDF. By CDF Collaboration (T. Affolder et al.). Jun 2001. 40pp. Submitted to Phys.Rev. D

229. "Measurement of $d\sigma/dm$ Forward Backward Charge Asymmetry for High Mass Drell-Yan e^+e^- Pairs from $p\bar{p}$ Collisions at $\sqrt{s}$ = 1.8 TeV. By CDF Collaboration (T. Affolder et al.). Fermilab-PUB-01-116-E, Jun 2001. 7pp. Submitted to Phys.Rev.Lett.

230. "Searches for New Physics in Events with a Photon and B-Quark Jet at CDF. By CDF Collaboration (T. Affolder et al.). Fermilab-PUB-01-097-E, Jun 2001. 40pp. Submitted to Phys.Rev. D

231. "Search for Quark Lepton Compositeness and a Heavy W' Boson using the Electron Neutrino Channel in $p\bar{p}$ Collisions at $\sqrt{s}$ = 1.8 TeV. By CDF Collaboration (T. Affolder et al.). Jul 2001. 11pp.

232. "Charged Particle Multiplicity in Jets in $p\bar{p}$ Collisions at $\sqrt{s}$ = 1.8 TeV. By CDF Collaboration (T. Affolder et al.). Fermilab-PUB-01-106-E, Jul 2001. 6pp. Submitted to Phys.Rev.Lett.

233. "Double Diffraction Dissociation at the Fermilab Tevatron Collider. By CDF Collaboration and D0 Collaboration (T. Affolder et al.). Jul 2001. 10pp. Submitted to Phys.Rev.Lett.

234. "Observation of Diffractive J/ψ Production at the Fermilab Tevatron. By CDF Collaboration (T. Affolder et al.). Jul 2001. 9pp. Submitted to Phys.Rev.Lett.

235. "Search for New Heavy Particles in the W Z0 Final State in $p\bar{p}$ Collisions at $\sqrt{s}$ = 1.8 TeV. By CDF Collaboration (T. Affolder et al.). Fermilab-PUB-01-219-E, Aug 2001. 7pp.

236. "A Study of $B^0 \to J/\psi K^{*0}\pi^+\pi^-$ Decays with the Collider Detector at Fermilab. By CDF Col-

laboration (T. Affolder et al.). Fermilab-PUB-01-232-E, Aug 2001. 6pp.

237. "Measurement of the Strong Coupling Constant from Inclusive Jet Production at the Tevatron $p\bar{p}$ Collider. By CDF Collaboration (T. Affolder et al.). Aug 2001. 6pp.

238. "Study of the Heavy Flavor Content of Jets Produced in Association with W Bosons in $p\bar{p}$ Collisions at $\sqrt{s} = 1.8$ TeV. By CDF Collaboration (D. Acosta et al.). Fermilab-PUB-01-253-E, Sep 2001. 77pp. Submitted to PHYS REV D

239. "Diffractive Dijet Production at $\sqrt{s} = 630$ GeV and 1800 GeV at the Fermilab Tevatron. By CDF Collaboration (T. Affolder et al.). Sep 2001. 9pp. Submitted to Phys.Rev.Lett.